University of Alberta

Experimental Observations on River Ice Accumulations

by

Daniel Healy   ©

A thesis submitted to the Faculty of Graduate Studies and Research in partial fulfillment

of the requirements for the degree of Doctor of Philosophy

in

Water Resources Engineering

Department of Civil and Environmental Engineering

Edmonton, Alberta

Spring 2006

Canada

Abstract

River ice jams present a serious threat to life and property. The advancement of knowledge pertaining to river ice jams is impeded by a lack of quantitative data describing their evolution. Venturing on top of an ice jam for the purpose of collecting data is prohibitively dangerous and due to the difficulties associated with the prediction on the timing and location of their occurrence, organizing data collection efforts are not logistically practical. The safe and economic alternative is to collect data on a physical model under controlled laboratory conditions.

A hydraulic model of ice jam processes and a data collection system were designed for the purpose of obtaining continuous time-series data describing water levels, ice jam thickness, flow velocities, ice cover progression, and discharge data during the formation of a model ice jam. The results of 40 tests are presented in this thesis. Two primary testing scenarios were explored: the first series of tests investigated ice jams formed under a constant supply rate of flow (carrier discharge); the second series of tests investigated ice jams formed by destabilizing an initial ice jam by a rapid increase in discharge to form a new thicker stable ice jam.

Detailed analyses of velocity data obtained under stable ice covers for eight different Canadian rivers were conducted to establish the feasibility of using unique point velocities to describe the channel average velocity. The success in finding these unique relationships for natural irregular channels extended confidence in the use of index velocity methods during the experimental investigations.

The work presented in this thesis represents the first comprehensive set of data describing the dynamics nature of ice jam evolution under a constant carrier discharge and the dynamic response of the resulting stable ice jam accumulations to a rapid increase in carrier discharge. This work also presents the first published attempt at obtain discharge estimates under an ice jam during formation. These data contribute to an improved understanding in ice jam evolution and will facilitate validation of dynamic ice jam computational models.

Acknowledgement

The author would like to thank Dr. David Chanasyk, Dr. Robert Ettema, Dr. Selma Guigard, Dr. Mark Loewen, and Dr. Peter Steffler for committing their time and effort in reviewing this thesis.

The author would also like to thank Sheldon Lovell and especially Perry Fedun for their assistance and expertise essential for setting up the experimental apparatus and instrumentation.

Lastly, the author would like to thank Dr. Faye Hicks for her unwavering support and positive encouragement throughout the author's work. Dr. Hicks offered unconditional guidance as an experienced mentor, treated the author with great respect throughout all collaborated efforts, and extended understanding as a valued friend.

Table of Contents

List of Figures

List of Tables

List of Symbols

a acceleration

α contact angle between a liquid and a solid

b coefficient relating $V_{channel}$ to V_{Gauss}

B width of the channel or ice jam width

C_i coefficient describing cohesion in an ice jam

C_o coefficient relating to the internal strength of an ice jam

D depth of flow

ϕ coefficient of friction describing the internal strength of an ice accumulation

F Froude number

ϕ internal angle of friction analogous to the angle of repose for a cohesionless soil

F_ϕ internal strength of an ice accumulation

F_{Gs} downslope component of force due to gravity in an ice accumulation

F_{Gv} vertical component of force due to gravity in an ice accumulation

f_i friction factor associated with ice-affected portion of flow

f_i friction factor associated with ice-affected portion of flow

f_o composite friction factor for the flow under the ice cover

f_o composite friction factor for the flow under the ice cover

Fr   dimensionless ratio of inertial to gravity forces – Froude Number

F_τ internal strength of an ice accumulation

F_W downslope component of weight in an ice accumulation

g acceleration due to gravity

γ_e effective unit weight of an ice jam (used in the jam stability equation)

h depth of flow under the jam

η depth of flow non-dimensionalized by the depth to the phreatic surface

H depth from the bed to the phreatic surface

$H(f)$ transfer function describing the frequency response of an assumed system

$h_{initial}$ average depth of flow under the initial accumulation

k parameter

K_o flow parameter for a given flow rate per unit width

K_x passive pressure coefficient

L characteristic dimension of length

L_{jam} length of the ice jam

M characteristic dimension of mass

μ coefficient characterizing the internal strength of an ice accumulation

m coefficient relating $V_{channel}$ to V_{Gauss}

M measure of the uniformity of the probability and velocity distribution

μ coefficient defining the internal strength of the ice accumulation

m_b exponent associated with the roughness at bed boundary

μ_{fluid} dynamic viscosity of the fluid

m_i exponent associated with the roughness at ice boundary

n Mannings roughness coefficient

p porosity of the ice accumulation

p_o stagnation pressure

p_s static pressure

q is the discharge per unit width of channel

r density of the fluid

ρ density of water

Re   dimensionless ratio of inertial to viscous forces – Reynolds Number

ρ_{fluid} density of the fluid

ρ_i density of ice

R_i hydraulic radius of the ice-influenced portion of the flow

S stream slope

S_f friction slope

s_i specific gravity of ice

$\sigma_{surface}$ surface tension

T characteristic dimension of time

t ice jam thickness defined by the jam stability equation

t_{avg} average ice jam thickness

t_{eq} equilibrium ice jam thickness

τ_t represents the applied forces under the ice cover resulting from the flow

t_{jam} thickness of the ice jam

t_{obs} observed average thickness of the main jam body

u streamwise average velocity at distance y above the bed

U average velocity under the ice cover

u_{max} maximum velocity in a channel cross section

$u_{maxdepth}$ maximum point velocity for the panel of maximum flow depth

u_{probe} velocity immediately upstream of the tip of the Prandtl tube

u_ξ streamwise average velocity at distance ξ above the bed

V average velocity

$V_{channel}$ average channel velocity

$V_{dynamic}$ theoretical wave speed for a dynamic wave

V_{Gauss} average Gauss point velocity

V_h average velocity under the jam

$V_{initial}$ average velocity under the initial accumulation

$V_{kinematic}$ theoretical wave speed for a kinematic wave

V_{max} maximum vertically averaged panel velocity for the cross section

$V_{maxdepth}$ vertically averaged velocity for the panel of maximum flow depth

V_u average open water channel velocity approaching the ice cover

We   dimensionless ratio of inertial to surface tension forces – Weber Number

x streamwise distance from the leading edge of the model ice jam

Ω dimensionless discharge

ξ transformation of the actual distance above the bed

$X(f)$ autospectral density of $x(t)$

$x(t)$ excitation to the linear time-invariant ADV-PT system expressed as a time series

ξ_{max} constant

y vertical distance above the bed

$Y(f)$ autospectral density of $y(t)$

$y(t)$ response of the linear time-invariant ADV-PT system expressed as a time series

1.0 Introduction

The primary objectives of the work embodied by this thesis were:

- to design an experimental arrangement that would facilitate hydraulic modeling of river ice jam formation;

- to collect continuous time series data describing fundamental ice jam parameters during ice jam formation (i.e. depth, ice jam thickness, and flow rate); and

- to improve our understanding of ice jam formation processes as a result of these modeling and data collection efforts.

An experimental arrangement was successfully designed which allowed for the development of ice jams under controlled laboratory conditions. A total of 40 tests were conducted on ice jams formed under a constant flow rate and an additional 40 tests were conducted on ice jams formed by shoving due to a rapid increase in discharge – these tests are presented in Chapters 3 and 4. Chapter 2 provides the basis for the methods used in Chapters 3 and 4 to estimate discharge beneath an ice jam as it forms.

This thesis is presented in a paper format following the guidelines for thesis preparation set forth by the Faculty of Graduate Studies and Research, University of Alberta. Three core papers constitute the bulk of this thesis. Chapter 2 presents the first of these three papers and is presented as it was published in the Canadian Journal of Civil Engineering (Healy and Hicks 2004). Chapters 3 and 4 are slightly expanded versions of two papers

1

that are currently under review for publication in the American Society of Civil Engineering Journal of Cold Regions Engineering (Healy and Hicks *under review*). Where the published journal paper versions refer to this thesis for details relating to the experimental arrangement, procedures, methods, and complete experimental results, the papers presented in Chapters 2 through 4 refer to selected sections in the appendices. The last section in the appendix contains a paper presented by the author at the 16th International Symposium on Ice (Healy, Hicks, and Loewen 2002). The author chose to include this paper in this thesis since it relates directly to the papers presented in this thesis and forms the basis, in part, for some of the future research recommendations in Chapter 5.

What follows is a background of the current understanding of river ice jam theory as relevant to the work presented in this thesis. Also included in this chapter are reviews of publicly available, computational models used for simulating river ice jams, and of relevant field and experimental investigations on river ice jams. Lastly, the capability of the model arrangement used in this study to act as an analogue of real river ice processes is addressed.

1.1 Background

Previous work by the author offers a detailed review of much of the literature pertaining to river ice jam theory (Healy 1997). For the convenience of the reader, relevant portions of this work are provided herein (some of which has been adapted and expanded to provide a background review more relevant to the work presented in this thesis).

2

"An ice jam is a stationary accumulation of fragmented ice or frazil that restricts flow" (IAHR Working Group on River Ice Hydraulics 1986). Ice jams vary in size and shape in accordance to the prevailing hydraulic, geometric, and meteorological conditions during their development, and the formation processes of ice jams vary depending on these conditions. They typically form when there is a local reduction in ice transport capacity or when a flux of detached ice floes is arrested for any reason (Beltaos 1995).

Ice jams are generally classified in three ways: by the season during which the jam is formed; by the dominant formation processes; and, by conditions at the toe of the jam. A closer look at the mechanisms behind ice jam development illustrates the rationale for these classifications.

The season used to identify the "type" of jam relates to the hydraulic and meteorological conditions under which the ice jam was formed (e.g. winter versus spring, or warm weather versus cold). The most common terminology used to distinguish these "types" of jams refers to the time of formation, either freeze-up or breakup. Freeze-up jams, as the name implies, form during the freeze-up period in late fall or early winter and are typically formed from the accumulation of a combination of loose frazil ice or slush and developed frazil ice pans or floes. In sub-zero temperatures, cohesion, due to freezing between the ice floes, often adds strength to freeze-up jams. Breakup ice jams typically occur during the spring as the ice is broken up mechanically by the hydraulic and buoyant forces of rising waters (resulting from spring runoff). Temperatures are usually above freezing and cohesion effects are negligible.

3

A more physically based method of ice jam classification relates to the dominant processes during ice jam formation. In this approach, the initiation and development of an ice accumulation is considered, such as when individual frazil pans or ice floes being carried downstream with the flow are impeded by an obstruction (such as a stationary ice cover). Once they come to rest at the obstruction, subsequent ice floes will stop against the upstream edges of the arrested ice floes. The incoming ice floes experience a downward force and subsequent overturning moment due to flow separation and acceleration effects at the leading edge of the advancing accumulation. When the buoyant forces are large enough to overcome the downward forces due to the momentum and accelerating flow at the leading edge, the individual floes will remain in place, on the surface, arranging themselves edge to edge to comprise a "juxtaposed" ice cover. In this case, the leading edge of the accumulation progresses upstream at a rate which is a direct function of the supply rate of ice floes. An ice cover forms which, for all practical purposes, is of a thickness equal to the average thickness of the ice floes comprising the jam.

"Hydraulic thickening" occurs when the hydrodynamic forces on the individual ice floes at the leading edge exceed the forces due to buoyancy, causing these ice floes to submerge. Once submerged, floes may deposit under the floating ice cover somewhere just downstream of the leading edge, or they may become entrained in the flow and be swept further downstream under the ice cover. Entrained floes may be deposited under the accumulation somewhere further downstream, if lower velocities are encountered, or they may be swept downstream past the ice accumulation to reemerge downstream of the

4

obstruction.

As the head of the accumulation propagates upstream, the downslope component of ice weight within the ice jam increases. Also, the total shear load exerted by the water flow along the underside of the ice accumulation increases, since the surface area of the ice cover is increasing. These increasing forces are resisted by internal strength of the ice accumulation, which is primarily a function of its thickness. When the internal stresses can no longer support the forces due to the shear under the accumulation and the weight of the accumulation, the ice jam will collapse or "shove" in a telescoping manner until the thickness is adequate to support these applied forces.

The dominant formation processes also give rise to the classical definition of "wide" and "narrow" channel ice jams which was first proposed by Pariset et al. (1966). The narrow jam classification is based on the fact that the internal resistance of an ice jam is a function of ice thickness and does not depend on the width of the channel. In contrast, as an ice accumulation progresses upstream, the downslope component of ice weight and the shear force due to fluid drag on the underside of an ice cover increase more quickly on a wide river than on a narrow river. Thus, shoving will occur sooner in a wide channel than in a narrow channel. Because of this, ice jams thickened by shoving are often referred to as wide channel jams and ice jams thickened hydraulically are often referred to as narrow channel jams.

The toe of an ice jam is the downstream limit of the ice accumulation. However, it represents a region more than a specific point or boundary. Little is known about the

5

physical behavior of this region or its exact configuration, other than that it is different than from that of the rest of the jam (Beltaos and Wong 1986). For ice jams of the "wide" channel type, it has been observed that grounding may occur at the toe as a result of the ice accumulation coming into contact with the bed due to progressive thickening and shoving of the ice cover. Grounded ice jams are more likely to occur during breakup than at freeze-up because the individual ice floes are typically stronger, the ice accumulation tends to be thicker (because cohesion effects due to freezing are negligible), and the interstices which allow the passage of flow through a grounded accumulation are larger (Beltaos 1995).

The so-called wide channel ice jams described above are known to form the most severe types of ice jams in terms of ice thickness and resulting high water levels. These jams are governed by the applied hydraulic and gravitational forces which are offset by the internal strength of the jam. The formulations describing the strength of these types of jams are based on well known soil mechanics theories. This leads to perhaps the most fundamental assumption behind the development of ice jam mechanics theory which considers a mass of detached ice floes analogous to a cohesionless granular material. The pioneering work on ice jam mechanics by Pariset and Hausser (1966) was based on the following assumption:

"The fact that ice jams are formed by a mass of detached floes gives rise to the assumption that the mechanics of the phenomenon are independent of the rheological properties of ice." Following this basic assumption a number of very similar relationships describing the stability of a wide channel ice jam have been developed by

6

applying a force balance to an ice jam accumulation (e.g. Pariset et al. 1961 & 1966, Uzuner and Kennedy 1974 & 1976, and Beltaos 1978 & 1979). The following equation as presented by Ashton (1986) represents the typical formulation of the widely accepted jam stability relationship expressed in terms of the ice jam thickness, t, under steady state conditions.

[1-1] $\quad t\dfrac{\partial t}{\partial x} = a + bt + ct^2$

where

$$a = \dfrac{\tau_i}{2K_x\gamma_e}; \quad b = \dfrac{\rho_i gS - 2C_i/B}{2K_x\gamma_e}; \quad c = \dfrac{-C_o}{K_x B}; \quad \gamma_e = \dfrac{\rho_i g}{2}(1-p)(1-\dfrac{\rho_i}{\rho})$$

where

t is the thickness of the ice jam;

K_x is the passive pressure coefficient – usually taken as $\tan^2(45^\circ + \phi/2)$

ϕ is the internal angle of friction of the ice jam

C_i is a coefficient relating to the cohesion of the ice jam

C_o is a coefficient relating to the internal strength of the accumulation ($C_o = \tan\phi$)

B is the width of the ice jam

τ_i is shear stress exerted by the flow on the bottom of the ice jam

7

p is the ice jam porosity

S is the stream slope

ρ is the density of water

ρ_i is the density of ice

g is the acceleration due to gravity.

Term a defines the drag forces applied to the underside of the ice jam due to the flow. Term b is the down-slope component of combined weight of the ice rubble and water within the ice jam. Term c describes the forces within the ice jam resisting the applied forces in terms a and b. The term γ_e describes the effective unit weight of the ice jam. Most public domain computational ice jam profile models combine a form of equation [1-1] with a gradually varied flow relationship to compute a steady state ice jam profile defining the phreatic water surface, top of ice jam and bottom of ice jam profiles. These and more sophisticated computer models which allow for unsteady flow conditions are described in more detail below.

1.2 Available Computational Ice Jam Models

The computational ice jam models available to the public can be divided into those which are capable of handling steady state flow conditions and those which can handle unsteady flow conditions. In the first grouping there are three predominantly used steady state ice jam profile models, namely, RIVJAM, ICEJAM, and HEC-RAS.

8

The RIVJAM model (Beltaos et al. 1986; Beltaos 1988 & 1993) computes the longitudinal variation in ice thickness and water surface profile for a cohesionless, wide channel ice jam. RIVJAM also accounts for seepage through the fragmented ice cover which allows for flow through grounded accumulations of ice. The model combines the calculation of the longitudinal variation in jam thickness with the analysis of one dimensional, gradually varied flow under steady state conditions for open channels, resulting in a system of two ordinary differential equations: the first representing a relationship for jam stability; and the second representing a gradually varied flow approximation.

The ICEJAM model (Flato and Gerard 1986; Flato 1988) was developed to calculate the thickness and water surface profiles for a cohesionless, wide channel ice jam with a floating toe. For this floating toe configuration, the "seepage" through the interstitial spaces in the ice cover is neglected. The model computes the longitudinal variation in ice jam thickness together with the one dimensional, steady, gradually varied flow, resulting in a system of two ordinary differential equations.

The U.S. Army Corps of Engineers' HEC-RAS model (Daly and Vuyovich 2003) was designed to perform one-dimensional steady and unsteady flow river hydraulic calculations. It is widely used for the computation of gradually varied flow open water and ice covered profiles of known geometry. It also has the capacity to compute "wide-river" ice jam profiles under steady flow conditions. The HEC-RAS model employs essentially the same ice jam formulation as the ICEJAM model.

The jam stability equation carries a very similar formulation in all three of these models. The primary difference between the three models is in the way in which the toe conditions are approximated, the computational approach, and the user interface. Healy and Hicks (1997) provided a detailed comparison between the RIVJAM and ICEJAM models. The approach to computing a steady state ice jam profile used by HEC-RAS is very comparable to that used by the ICEJAM model. The HEC-RAS model is much more "user friendly" than both the RIVJAM and ICEJAM model and to the author's knowledge HEC-RAS is the most widely used tool for computing steady state ice jam profiles.

More advanced models attempt to model ice jam processes under dynamic conditions (unsteady flow). The two most widely known publicly available one-dimensional unsteady ice jam models are the RICEN model developed by Shen et al. (1995) and the simultaneous solution model developed by Zufelt and Ettema (1997, 2000). These models more or less follow the conventional theory of the ice jam behaving as a consolidated mass of particles is analogous to the wide channel jam relationship described in equation [1-1]. A major difference in the these two models is that the simultaneous solution model presented by Zufelt and Ettema (1997, 2000) accounts for the momentum effects of the arriving ice.

The RICEN model is an extension of the RICE model (Lal and Shen 1991) which simulated: water temperature and ice discharge distributions; evolution of frazil ice into ice pans; frazil transport and accumulation under the cover; ice jam formation and evolution; and skim ice and boarder ice formation and growth. Refinements of this

10

model were made primarily in the ice process simulation component to include: supercooling of the water; anchor ice formation; a more sophisticated method for frazil transport and accumulation; wind effects; and flow resistance due to moving ice. The model consists of two primary parts: an unsteady flow module for a channel network including ice; and a thermal and ice condition simulation module. Calculations are passed between these two modules to come to a solution in an iterative manner.

Zufelt and Ettema's simultaneous solution model (1997, 2000) simulates the dynamic failure and reformation of an ice jam. The model couples unsteady flow and ice movement by simultaneous solution of the one-dimensional unsteady equations of mass and momentum for both water and ice. The solution simultaneously solves four equations describing the depth of flow, water velocity, ice velocity, and ice thickness. Momentum forces have largely been absent from formulations describing the thickness of an ice jam, however, based on a series of experiments on ice jam shoving Zufelt (e.g. 1990, 1992, 1996) strongly suggested the importance of ice momentum in contributing to the resulting thickness of a shoved accumulation. The application of their model suggested that the equilibrium theory approach may underestimate actual water levels for a given carrier discharge.

1.3 Field Investigations

To date, only crude estimates on ice jam thickness in the field have been collected. Where thickness has been documented, it has generally been deduced from the thickness of remnant ice left on river banks (shear walls) after a jam has subsequently released and

11

passed downstream (e.g. Beltaos and Burrell 1990). In one instance, a small ice jam was documented along the Thames River, Ontario, during the winter months some time after the ice jam froze in place (Beltaos and Moody 1986). When it was deemed safe to venture out on top of the ice jam, thickness was measured by drilling holes through the frozen accumulation. The thickness data were collected for a period of up to one month after the ice jam had formed.

Spyros Beltaos from the National Water Research Institute, Burlington, Ontario, experimented with a profiling device for measuring ice jam thickness in the field (Beltaos et al. 1996). Seven ice jam events were profiled between 1990 and 1996 and results are available in a paper on hydraulic roughness or ice jams by Beltaos (2001). These attempts to collect ice jam profile data in the field represent steady state ice jam conditions after a stable accumulation has formed, and thus do not indicate to researchers how an ice jam evolves during its formation.

Martin Jasek (1997, 1999) studied dynamic processes of ice jam releases during river ice breakup. However, his research focused on ice jam surge and velocity data resulting from the release of ice – not ice jam formation. An ongoing research program led by Faye Hicks from the University of Alberta has resulted in the successful implementation of a remote water level monitoring network (consisting of 7 water level recorders) along the Athabasca River, upstream of Fort McMurray, Alberta. To date hydrographs describing ice jam release events have been successfully captured for events occurring during the breakup seasons of 2001, 2002, and 2003 (Kowalczyk and Hicks 2003, 2004). The focus, however, was on ice jam release and not ice jam formation.

12

1.4 Experimental Investigations

The advancement of knowledge in the study of ice jams has been slowed by a lack of quantitative data describing even the most fundamental ice jam characteristics (thickness and carrier discharge). The difficulty in obtaining field data is due to the unpredictable nature of ice jam formation and the inherent dangers associated with navigating on top of or near an ice jam for the purpose of collecting field data. Logistically, it is difficult to plan a field data collection program not knowing where and when an ice jam may form. A safe, economical, and practical alternative to obtaining detailed field data is to conduct investigations under controlled laboratory conditions where both qualitative (descriptive) and quantitative data can be obtained more readily.

Many of the experimental ice jam studies to date have been case specific, as opposed to generic process models. Lever and Gooch (1997) conducted tests on a 1:10 scale model ice control structure (ICS) in a refrigerated testing facility. The ICS was designed to arrest an ice run and form an ice jam to minimize ice related flooding and damage to inhabited areas downstream of the ICS. For this model, ice was allowed to form in a supply tank and within portions of the modelled reach. Ice was then released from the holding tank into the modelled reach where the ice eventually impacted on the ICS and depending on the hydraulic conditions, a jam formed upstream of the ICS. A variety of hydraulic conditions and ICS geometries were tested. The focus of the study was on the performance of the control structure and limited data on parameters describing the resulting ice jam accumulations were reported. Steady state water surface profiles and varying inflow and outflow hydrographs were measured and reported; ice jam thickness

13

profiles were not measured in this study. The control structure performed well in the model tests and the prototype was reported to have operated successfully for several years after installation.

In addition, most experimental investigations to date have been for steady state flow conditions. One of the more comprehensive experimental investigations was conducted by Saadé and Sarraf (1996) who studied ice jam profiles in a horizontal, rectangular flume under steady state conditions. The focus of the work was aimed at defining the characteristic shape of the water surface profile resulting from the development of a stable ice jam. Steady state water surface and thickness profiles were obtained for a series of 12 tests. The ice jam accumulations were formed under a constant discharge and were reported to evolve into their final stable arrangement by the processes of "erosion, shoving and telescoping". The results of the analysis found that the ice jams formed typical profiles where the upstream 90% of length of the ice jam carried a linear relationship (characterized as the gradually varying region) and the downstream 10% (rapidly varying region) of the ice jam carried a non-linear relationship. The investigators found this characterization applied to a variety of model ice geometries made of wood and polyethylene. materials which included an shape of water tests were designed so as to investigate and anaylsithe development of a water surface profile for an ice jam

The work of Zufelt (e.g. 1990, 1992, 1996) represents perhaps the most comprehensive set of published unsteady experimental ice jam studies prior to the work presented herein. A series of experiments were conducted using both real and plastic model ice to observe

14

and document the process of ice jam shoving and thickening. Two sets of tests were conducted where quantitative data were taken, while the observations for the remaining "visualization tests" were largely qualitative. The first set of experiments determined some of the properties of the model ice material based on ice jams formed under steady discharge in a horizontal bed flume. For these experiments, detailed measurements were taken on the resulting water surface, ice thickness, and velocity profiles. From these measurements, values of the composite, bed, and under ice friction factor were calculated and values on the jam stability parameter μ, associated with the plastic beads were estimated. The second series of experiments were conducted in a sloped-bed flume. For these tests measurements on ice jam thickness, extent, water velocity, water surface slope, and depth were obtained from steady state ice jam profiles. These data combined with the friction factors and jam stability coefficient determined in the first series of tests facilitated comparison of the observed ice jam profiles with those predicted by equilibrium theory.

For the visualization experiments, a series of tests using real model ice and plastic beads was carried out. For both cases, a uniform layer of ice pieces was developed under very low flow conditions. The flow rate was then increased to the initial flow level for the test and the cover was allowed to juxtapose and rearrange into a ice accumulation of roughly 1 to 2 pieces thick. Then the flow rate was increased in steps until the ice jam became unstable and shoving and thickening of the accumulation ensued. Zufelt and Ettema (1997) identified two distinct types of ice jam failure that were observed for both the real ice and plastic bead visualization experiments. These failure modes related to the initial

15

flow rate and ice jam thickness and the relative increase in flow rate (over the initial value).

The failure modes were called "progressive jam failure" and "complete jam failure". Details on these failure modes are given by Zufelt and Ettema (1997). Loosely described, the progressive failure mode the jam fails in an incremental manner from the upstream end and progresses downstream towards the toe region. For the complete failure mode, the entire jam fails and moves en masse. They defined a 50% relative increase in flow rate as the demarcation point between the two modes of failure, where progressive jam failure was observed for relative increases less than 50% and complete jam failure was observed for increases over 50%. The investigators found that multiple discharge steps were required to fail the initial accumulation and the resulting failed accumulations often thickened beyond the thickness estimated from current ice jam thickness formulations (e.g. equation 1-1). These findings suggest the importance of the contribution of ice momentum forces towards the resulting thickness profiles. A momentum parameter is absent from current ice jam stability formulations and the authors went on to develop a numerical model which included momentum effects. These modelling efforts were described briefly above.

1.5 Model Similarity Requirements

Experimental models are limited as to how well the can act as a true analogue of their prototype counterpart. By using dimensional analysis techniques, similarity criteria can be established and provide a means for assessing the experimental model's quality in this

16

regard. Similarity criteria are used to relate processes occurring at different scales, with the concept being that when the similarity criteria are satisfied, the processes modeled at different scales are the same. For a model to be considered a true analogue of the prototype, it must satisfy requirements for geometric and dynamic similarity. The primary limitation in hydraulic modeling typically lies in achieving dynamic similarity; the problem usually being that the fluid (water) used in the model is the same as for the prototype. Fortunately, certain force ratios used to define criteria for dynamic similarity tend to dominate others and if care is taken to ensure dynamic similarity for these dominant forces, then the model can be expected to be a satisfactory analogue for the dominant physical processes of interest.

"The four primary units or dimensions involved in hydraulic modeling are length, time, temperature, and either weight or mass" (Shen 1979). The characteristic dimensions that will be used to describe similarity ratios herein will be length, L, time, T, mass, M, and temperature, Θ.

For strict geometric similarity, the length ratio between model and prototype must be constant for all parts of the model and prototype. However, it is not uncommon for the vertical scale in river models to be distorted. Natural rivers generally have a wide aspect ratio where the horizontal dimension, X, is generally 2 orders of magnitude greater than the vertical scale Y. To achieve sufficient depths, model widths would be prohibitively large and vertical scale that is different than the horizontal scale is accepted.

For dynamic similarity, the forces acting throughout the entire flow field must be in a

17

similar ratio and "since the forces acting on the fluid elements will thus control the motion of these elements, it follows that dynamic similarity will yield similarity of flow patterns. Consequently, the flow patterns will be the same in the mdoel as in the prototype if geometric similarity is satisfied and if the relative forces acting on the fluid are the same in the model as in the prototype (Roberson and Crowe 1993)". This last requirement brings into focus the dimensionless numbers which describe the relative forces acting in the flow field. It is convenient to describe the relevant force ratios with respect to the inertial force, $F_{inertial}=Ma$, where M is the mass of the fluid and a is the acceleration. The primary forces of importance, along with the inertial forces, were forces due to pressure differences, gravity forces, viscous forces, and surface tension. The ratio of the inertial force to these additional forces describe the following familiar non-dimensional terms (White 1986):

[1-2]   Pressure force ratio (Euler number), $Cp = \dfrac{\text{pressure force}}{\text{inertial force}} = \dfrac{\Delta p}{1/2\rho_{fluid}V^2}$,

[1-3]   Froude number, $Fr = \dfrac{\text{inertial force}}{\text{gravity force}} = \dfrac{V}{\sqrt{gL}}$,

[1-4]   Reynolds number, $Re = \dfrac{\text{inertial force}}{\text{viscous force}} = \dfrac{\rho_{fluid}VL}{\mu_{fluid}}$,

[1-5]   Weber number, $We = \dfrac{\text{inertial force}}{\text{surface tension force}} = \dfrac{\rho_{fluid}V^2 L}{\sigma_{surface}}$,

where: p is pressure, V is velocity, L is a characteristic length scale, μ_{fluid} is dynamic

18

viscosity of the fluid, ρ_{fluid} is the density of the fluid, g is acceleration due to gravity, and $\sigma_{surface}$ is surface tension. For the model to be considered analogous to the prototype, these dimensionless parameters should be equivalent between the model and prototype.

The following attempts to describe the ability of the physical model, used in this study, to describe selected river ice processes in a manner considered analogous to similar river ice processes in full scale streams. The processes under consideration for this investigation were divided into hydrodynamic processes and ice processes. While hydraulic and ice processes work together, their separate treatment allowed for a more manageable presentation.

With respect to modeling the dominant hydraulic processes, the Weber number was not considered to be a dominant force parameter since there was only a single fluid being modeled and sufficient depths and velocities were maintained. Sun and Yang (1986) suggested that surface tension forces could be neglected for flow depths greater than about 1.5 cm and surface velocities greater than approximately 23 cm/s (the minimum velocity for gravity waves in free surface flows). In this investigation, flow depths and surface velocities of the approaching flow exceeded these values.

Given that the fluid (water) used in this investigation was the same for model and prototype, simultaneous satisfaction of Reynolds number and Froude number similarity could not be achieved. However, for sufficiently high Reynolds numbers (larger than roughly 2,000), viscous forces are small compared to inertial forces. Reynolds numbers for the studies herein ranged from 27,000 to 43,000 and were considered large enough to

19

leave the Froude number as the dominant parameter for achieving dynamic similarity. Froude numbers for the experiments ranged from roughly 0.10 to 0.15, which are plausible Froude numbers for natural streams.

Presuming that similarity of the dominant hydraulic processes was achieved, the remaining similarity requirements related to the ice processes and more specifically to the model ice material. The processes studied in this investigation did not require modeling the strength of the individual floes, and for this case, properly sized rigid model ice pieces with the appropriate buoyancy can be used (Wuebben 1995). For this study, piece size and mixture was chosen to approximate typical size distributions and floe-size-to-river-width ratios found in the field. Figure 1.1 presents photos of the surface of an ice jam generated during the model study and one observed in the field for comparison. The vertical scale ratio of the model-to-prototype ice thickness (1:100) was about an order of magnitude greater than the geometric scale relating the hydrodynamic processes (1:5 to 1:10). The average width of most of the model ice floes was 5 cm and by assuming the same range of geometric scales relating to the hydrodynamic processes (1:5 to 1:10) the model was representing prototype ice floe widths of 25 cm to 100 cm.

Since the model ice is essentially a non-wetting material, it was possible that surface tension forces would affect the behaviour of the smallest of model ice floes. There was no feasible way of identifying the magnitude of surface tension effects relating to the model ice material and efforts were made to minimize surface tension effects by keeping the model ice material wet between tests. So long as the ice floes are sufficiently thick, surface tension forces that may influence the behaviour of the model ice jam processes

20

were believed to be minimal. A more detailed treatment on model ice surface tension and the non-wetting tendency of the model ice material is provided in Appendix A.

Qualitative observations supported the assumption that the model ice floes (with the possible exception of a small portion of pieces that were roughly 2 mm thick) were not significantly influenced by surface tension effects. First, the general observed behaviour of floes being entrained by the flow at the leading edge exhibited classical underturning behaviour described in the literature (e.g. Daly and Axelson 1990; Coutermarsh and McGilvary 1993). Secondly, there were no visible impacts on the majority of the model ice pieces within the region most susceptible to surface tension effects. The presence of what will be called herein as a capillary wake (Figure 1.2) was observed approximately one channel width upstream from the leading edge of the accumulation. The presence of this wake suggested a zone of low flow and possibly a very thin recirculation zone near the surface upstream of the leading edge of the cover. When very thin pieces of material (e.g. paper or cardboard) were introduced to the surface of the flow upstream of the capillary wake, there was an abrupt reduction in velocity once they encountered and passed across the capillary wake. They would then often stop up short of, and circulate around in, the vicinity of the leading edge. However, the model ice pieces used in the investigation would pass over the capillary wake and encounter the leading edge of the accumulation with no visible reduction in velocity – the capillary wake zone appeared to have no visible impact on the behaviour of the model ice pieces. These observations increased the author's confidence in assuming that, even with the apparent presence of surface tension effects, their impact on the overall behaviour of the ice accumulation was

21

minimized by keeping the ice wet most of the time.

In addition to the usual force ratios used to establish dynamic similarity with respect to the hydraulic processes, Ashton (1986) defines the following force ratios used to establish dynamic similarity for fragmented accumulations of ice:

$$[\text{1-6}] \quad \frac{F_\phi}{F_{Gs}} = \frac{\text{internal strength of the accumulation}}{\text{downslope component of force due to gravity}},$$

$$[\text{1-7}] \quad \frac{F_{Gv}}{F_{Gs}} = \frac{\text{vertical component of force due to gravity}}{\text{downslope component of force due to gravity}},$$

$$[\text{1-8}] \quad \frac{F_W}{F_{Gs}} = \frac{\text{downslope component of the weight of the accumulation}}{\text{downslope component of force due to gravity}},$$

$$[\text{1-9}] \quad \frac{F_\tau}{F_{Gs}} = \frac{\text{shear force exerted by the flow on the bottom of the accumulation}}{\text{downslope component of force due to gravity}}.$$

And simultaneous satisfaction of these force ratios requires that:

$$[\text{1-10}] \quad \left[\tan^2\left(45^\circ + \frac{\phi}{2}\right)\right]_{\text{ratio}} \frac{Y_{\text{ratio}}}{X_{\text{ratio}}} = 1,$$

$$[\text{1-11}] \quad (1 - s_i)_{\text{ratio}}(1 - p)_{\text{ratio}} \frac{X_{\text{ratio}}}{Y_{\text{ratio}}} = 1,$$

where: Y_{ratio} denotes the vertical scale ratio, X_{ratio} denotes the horizontal scale ratio, ϕ is the internal angle of strength of an ice accumulation, s_i is the specific gravity of ice, and p is the porosity of the accumulation. White (1986) and Ashton (1986) provide a good

22

background on the dimensional analysis techniques used to develop equations [1-2] through [1-11].

The model ice material in this investigation had an internal strength value of $\phi_{dry} = 29°$ while in a dry condition and when wetted and floating in water an internal strength value of $\phi_{buoyant} = 46°$. Appendix A outlines the rationale and methodology for estimating these internal strength coefficients. For real ice jams there are, currently, no methods for making direct measurements of $\phi_{prototype}$; however, estimates of $\phi_{prototype}$ can be made based on values of the much used jam stability parameter, $\mu = (1 - p)\tan\phi_{prototype}$. The generally accepted range for the jam stability parameter, μ, is 0.8 to 1.3 and p is usually take to be 0.4 (Ashton 1986; Beltaos 1995); this would imply values of $\phi_{prototype}$ ranging from 53° to 65°. Equation [1-10] suggests that when models are distorted in the usual way such that $Y_{ratio} > X_{ratio}$ the ratio of the internal strength parameter, ϕ_{ratio}, is less than unity; given the aforementioned values for ϕ_{model} and $\phi_{prototype}$ this general trend is supported in equation [1-10]. Values for model ice jam porosities, p_{model}, were found to be greater than 0.4 suggesting that the usual distortion described by $Y_{ratio} > X_{ratio}$ in equation [1-11] was not followed; therefore for plausible ratios of p_{ratio} and ϕ_{ratio}, simultaneous satisfaction of the similarity requirements described by equations [1-10] and [1-11] was not possible. Ashton (1986) suggested that "this must be accepted as a scale effect, or it may be an argument for using model ice particles that differ in density from ice".

1.6 Estimating Discharge under an Evolving Ice Jam

Included in this thesis is the first documented attempt at estimating flow under a developing ice jam. For the experimental work described in Chapters 3 and 4 a unique approach to obtaining discharge estimates under the ice jam was devised. The basic approach was to introduce velocity probes into the flow along the channel centerline at measurement locations where continuous depth and ice thickness were observed. The velocity probes provided an estimate on the vertically averaged velocity at the channel centerline. A major part of that work was to confirm the existence of a unique relationship between the section average velocity under the ice jam and vertically averaged velocity at the channel centerline (index velocity). The section average velocity combined with the observed depth of flow and constant channel width provide estimates on discharge beneath the ice jam at the measurement locations.

Chapter 2 establishes the existence of unique relationships between average channel velocity and index velocity for natural channels and for the experimental arrangement used in this investigation. Chapter 2 provides a basis for the techniques used to estimate discharge under an evolving ice jam in Chapters 3 and 4.

24
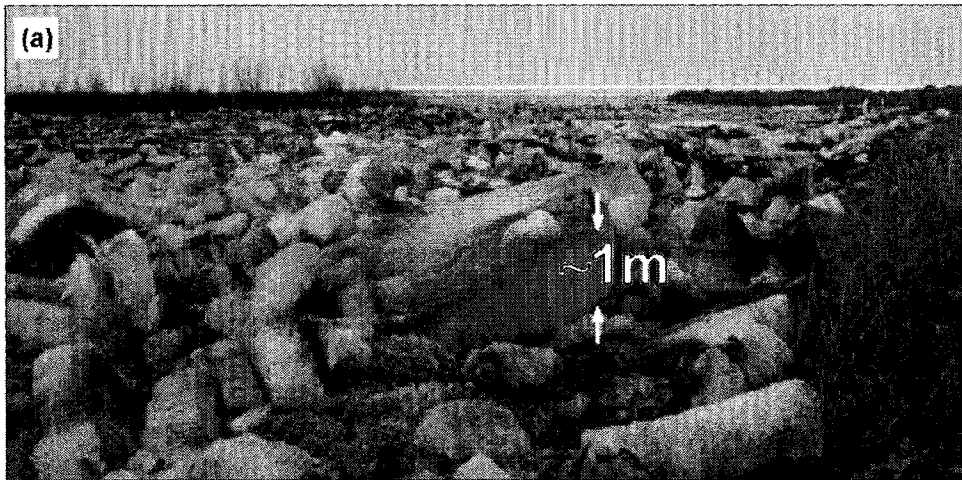
Ice Jam at Hay River, Alberta (photo by R. Gerard)
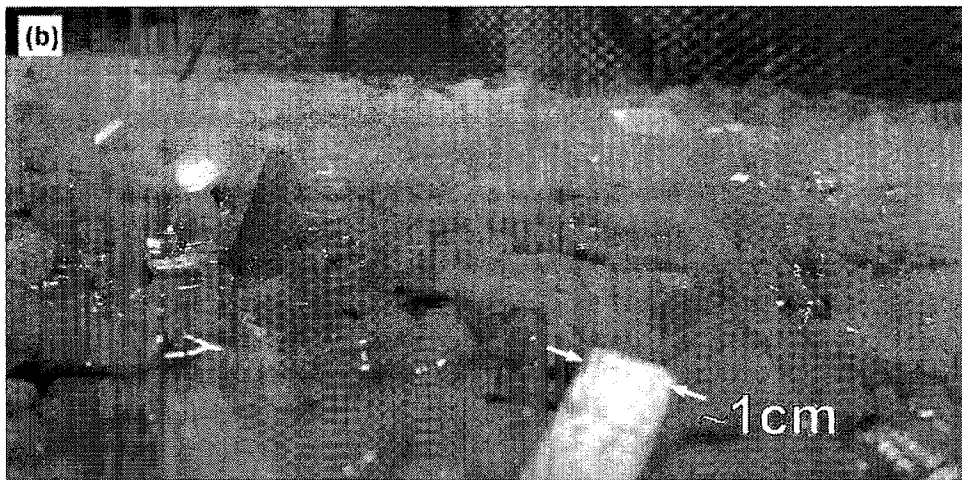
Experimental Ice Jam, University of Alberta (photo by D. Healy)

Figure 1.1. Surface views of (a) real ice jam and (b) an experimental model ice jam.

25
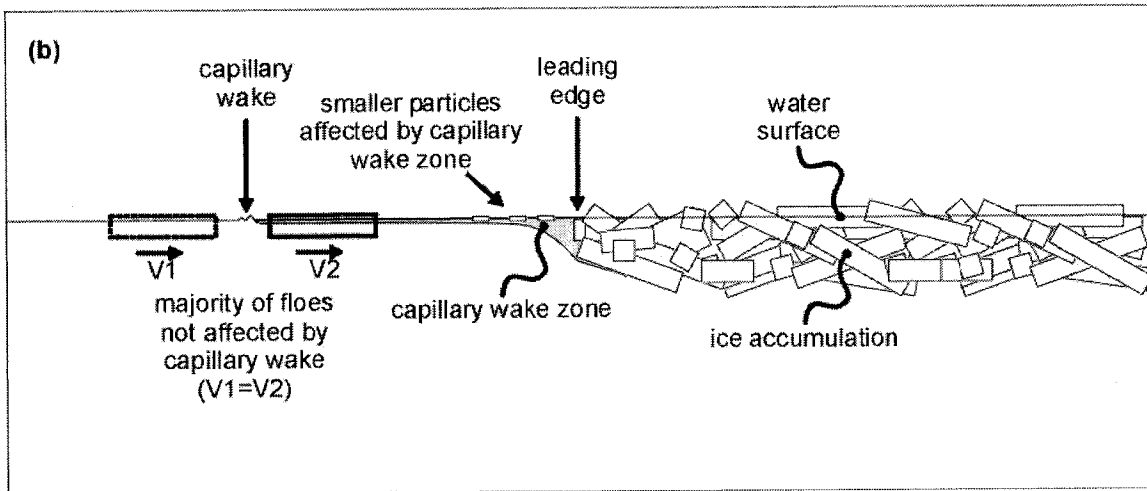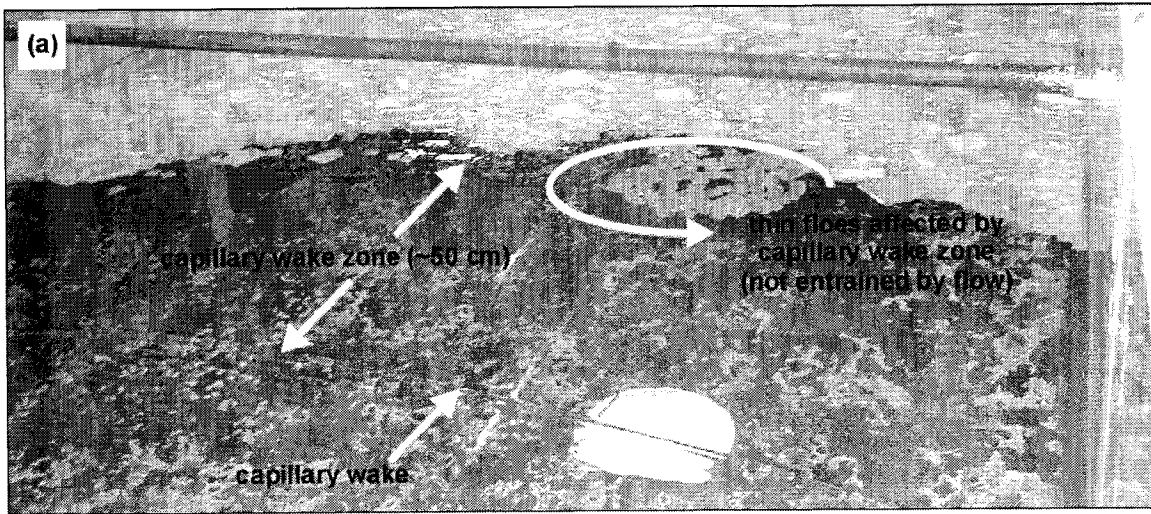
Figure 1.2. Capillary wake zone upstream of the leading edge of a model ice jam.

1.7 References

Ashton, G.D. 1986. River and lake ice engineering. Water Resources Publications, LLC, 485 p.

Beltaos, S. 1978. Field investigation of river ice jams. IAHR Symposium on Ice Problems, Lulea, Sweden, pp. 355-371.

Beltaos, S. 1979. Flow resistance of fragmented ice cover (ice jams). Canadian Hydrology Symposium, Vancouver, Canada (NRCC No. 17834), pp. 93-126.

Beltaos, S. 1988. Configuration and properties of a breakup jam. Canadian Journal of Civil Engineering, 15(4): 685-697.

Beltaos, S. 1993. Numerical computation of river ice jams. Canadian Journal of Civil Engineering, 20(1): 88-89.

Beltaos, S. 1995. River ice jams. Water Resources Publications, LLC, 372 p.

Beltaos, S. 2001. Hydraulic roughness of breakup jams. ASCE Journal of Hydraulic Engineering, Vol. 127, No. 8, pp. 650-656.

Beltaos, S., and Burrell, B.C. 1990. Ice breakup and jamming in the Restigouche River, New Brunswick: 1987-1988 observations. National Water Research Institute, NWRI Contribution 90-169, 25 p.

Beltaos, S., Ford, J.S., Burrell, B.C. 1996. Remote measurements of ice jam thickness

profiles. IAHR International Symposium on Ice, 13th, Beijing, China, Proceedings. Vol.2: Beijing, Chinese Hydraulic Engineering Society, pp. 577-584.

Beltaos, S., and Moody, W.J. 1986. Measurements on the configuration of a breakup jam. National Water Research Institute, NWRI Contribution 86-123, 37 p.

Beltaos, S., and Wong, J. 1986. Downstream transition of river ice jams. ASCE Journal of Hydraulic Engineering, 112(2): 91-110.

Countermarsh, B.A., and McGilvary, W.R. 1993. Static analysis of floating ice block stability. Journal of Hydraulic Research, Vol. 31, No.2, pp. 147-160.

Daly, S.F., and Axelson, K.D. 1990. Stability of floating and submerged ice blocks. Journal of Hydraulic Research, Vol. 28, No. 6, pp. 737-752.

Daly, S. F., and Vuyovich, C. M. 2003. Modeling river ice with HEC-RAS. Proceedings of the 12th Workshop on River Ice, Canadian Geophysical Union - Hydrology Section, Comm. on River Ice Processes and the Environment, Edmonton, Alberta, pp. 280-290.

Flato, G. 1998. Calculation of ice jam profiles. M.Sc. thesis submitted to the Department of Civil Engineering, University of Alberta, Canada, 176 p.

Flato, G. and Gerard, R. 1986 Calculation of ice jam thickness profiles. Proceedings of the Fourth Workshop on Hydraulics of River Ice, Montreal, pp. C3.1-C3.25.

Healy, D. 1997. A comparison of the ICEJAM and RIVJAM icejam process models. M.Sc. thesis submitted to the Department of Civil and Environmental Engineering,

28

University of Alberta, Canada.

Healy, D., Hicks, F. and Loewen, M. 2002. Unsteady velocity profiles under a fixed floating cover. Proc. 16th IAHR International Symposium on Ice, IAHR, Dunedin, New Zealand, Vol. 1, pp. 83-90.

Healy, D., and Hicks, F. 2004. Index velocity methods for winter discharge measurement. Canadian Journal of Civil Engineering, Vol. 31, No.3, pp. 407-419.

Healy, D., and Hicks, F. *(under review)*. Experimental study of ice jam formation dynamics. ASCE Journal of Cold Regions Engineering.

Healy, D., and Hicks, F. *(under review)*. Experimental study of ice jam thickening under dynamic flow conditions. ASCE Journal of Cold Regions Engineering.

IAHR Working Group on River Ice Hydraulics. 1986. River ice jams: a state-of-the-art report. IAHR Ice Symposium, Iowa City, pp. 561-594.

Jasek, M.J. 1997. Ice jam flood mechanisms on the Porcupine River at Old Crow Yukon Territory. Proceedings of Ninth Workshop on River Ice, Fredericton, NB, pp. 351-370.

Jasek, M.J. 1999. Analysis of ice jam surge and ice velocity data. Proceedings of Tenth Workshop on River Ice, Winnipeg, MB, pp. 174-184.

Kowalczyk, T.and Hicks, F. 2003. Observations of dynamic ice jam release on the Athabasca River at Fort McMurray, AB. Proceedings of the 12th Workshop on River Ice. 18-20 June 2003, Canadian Geophysical Union - Hydrology Section, Comm. on

River Ice Processes and the Environment, Edmonton, AB, pp. 369-392.

Kowalczyk, T. and Hicks, F. 2004. Analysis of ice jam release surges on the Athabasca River near Fort McMurray, AB. Cold Regions Engineering and Construction Conference, May, 2004, Edmonton, AB, 14 p.

Lal, A.M. and Shen, H.T. 1991. Mathematical model for river ice processes. ASCE Journal of Hydraulic Engineering, Vol. 117, No. 7, pp. 851-867.

Lever, J.H. and Gooch, G. 1999. Model and field performance of a sloped block ice control structure. Proceedings of the 14th IAHR Symposium on Ice: Ice in Surface Waters, Shed (ed.), Potsdam, N.Y., 27-31 July 1998, Vol. 2, pp. 647-657.

Pariset, E., and Hausser, R. 1961. Formation and evolution of ice covers in rivers. Transactions of the EIC, Vol. 5, No. 1, pp. 41-49.

Pariset, E., Hausser, R., and Gagnon, A. 1966. Formation of ice covers and ice jams in rivers. Journal of the Hydraulics Division, Vol. 92, No. HY6, pp. 1-24.

Roberson, J.A., and Crowe, C.T. 1993. Engineering fluid mechanics. Fifth edition. Houghton Mifflin Company. 785 p.

Saade, Raafat G. Sarraf, S. 1996. Phreatic water surface profiles along ice jams – an experimental study. Nordic Hydrology, Vol. 27, No.3, pp. 185-201.

Shen, H.W. 1979. Modeling of rivers. John Wiley and Sons, New York, New York, 900 p.

30

Shen, H.T., Wang, D.S., and Wasantha Lal, A.M. 1995. Numerical simulation of river ice processes. ASCE Journal of Cold Regions Engineering, No. 9, Vol. 3, pp. 107-118.

Sun, Z.C. and Yang, B. 1986. On the law of similarity of hydraulic model for ice floe. Proceedings of the 8th International Symposium on Ice, International Association for Hydraulic Research, Iowa City, Iowa, U.S.A., Vol. 2, pp. 49-59.

Uzuner, M.S., and Kennedy, J.F. 1974. Hydraulics and mechanics of river ice jams. IAHR Report No. 161, 158 p.

Uzuner, M.S., and Kennedy, J.F. 1976. Theoretical model of river ice jams. Journal of the Hydraulics Division, 102(HY9), pp. 1365-1383.

White, F.M. 1986. Fluid Mechanics. 2nd Edition. McGraw Hill, New York. 732 p.

Wuebben, J. 1995. Physical modeling. *in* River ice jams. S. Beltaos, ed., Water Resources Publications, LLC, 372 p.

Zufelt, J.E. 1990. Experimental observations of shoving and thickening: Comparison to equilibrium thickness theory. IAHR Proceedings of the International Symposium on Ice, 10th, Espoo, Finland, 1990, v.1: 500-510.

Zufelt, J.E. 1992. Modes of ice cover failure during shoving and thickening. IAHR Proceedings of the International Symposium on Ice, 11th, Banff, Alberata, Canada, v.3: 1507-1514.

Zufelt, J. E. 1996. Ice jam dynamics. Ph.D. thesis submitted to the Department of Civil and Environmental Engineering, University of Iowa, 203 p.

Zufelt, J.E., and Ettema, R. 1997. Unsteady ice jam processes. CRREL Report No. 97, U.S. Army Cold Regions Research and Engineering Laboratory, Hanover, N.H.

Zufelt, J.E., and Ettema, R. 2000. Fully coupled model of ice jam dynamics. ASCE Journal of Cold Regions Engineering, Vol. 14, No. 1, pp. 24-41.

2.0 Index Velocity Methods for Winter Discharge Measurement[1]

2.1 Introduction

Across Canada, water quality issues are becoming a critical concern in winter, since this is typically when the lowest flows occur, and therefore when effluent dilution capacity and oxygen replenishment are at a minimum. Increasing pressures on water quantity and quality, in response to economic development, have resulted in a need to be able to accurately quantify river discharge throughout the entire year, rather than just in the open water season. However, currently the only reliable method for determining discharge under ice affected conditions is to conduct direct measurements. This involves the use of a current meter to obtain point velocity measurements at (typically) two points in the flow depth, at more than 20 vertical panels across a channel. These point measurements are then integrated over the flow area to determine the total discharge. Pelletier (1989) provides a detailed description of typical practices for streamflow gauging under ice affected conditions in both Canada and the USA. Generally, the frequency of such "direct" measurements is limited because of cost and access.

---

[1] This chapter was published in the Canadian Journal of Civil Engineering, 2004, Vol. 31, No.3.

33

Obtaining direct measurements during the ice-affected period also presents safety concerns for operational staff. Determining when the ice cover is safe is difficult, and will become a more frequent concern if climate change results in thinner, more intermittent, ice covers. Working for extended periods of time during cold weather also makes operating equipment and recording field notes difficult.

Because of the cost and logistical difficulties associated with direct measurement, winter discharge estimates may be inferred from as few as two direct measurements over a 6 month winter period (Moore et al. 2002). For those extended periods between actual measurements, discharge estimates are usually based on conceptual and/or statistical interpretation of the measured data (Hamilton et al. 2001). Melcher and Walker (1992), who explored a variety of methods using three streams in Iowa, found that the use of interpolation between measured values resulted in errors in excess of 25% in more than 40% of cases. Hicks and Healy (2003) found that during the early breakup period, minor ice movement in the vicinity of gauging stations can lead to errors of up to 300% in the published discharge data. Hamilton et al. (2001) found that errors in daily estimates of winter discharge using conventional methodologies can exceed 500% in the most extreme cases.

It is highly desirable to be able to conduct much more frequent field visits to streamflow gauging sites than is done in operational practice at present. One way to achieve this would be to have a means of measuring ice affected discharge in a much more expedient manner. Recent research by Fulton (1999) and colleagues at the United States Geological Survey (USGS) indicates that, for the open water case, accurate discharge measurements

34

can be deduced on the basis of a single point velocity measurement. Specifically, knowledge of the magnitude and location of the maximum point velocity in a measurement section can facilitate determination of the mean velocity for the entire section. This in turn is used with a measured stage and known channel geometry (to obtain flow area) to provide the streamflow discharge. Of course, this method requires a priori knowledge of the location of the maximum velocity panel, something that Fulton (1999) has found can be identified based on surface velocities. Clearly this location must also be known a priori for the ice covered case, to apply this method. This and other practical issues for the ice application are considered in this paper.

2.2 Maximum versus Mean Velocity Relationships

The vertically averaged velocity for a section can be defined by unique point velocities (Teal and Ettema 1994), however, these point velocities do not necessarily relate directly to the mean channel velocity. Investigations by Chiu (1988, 1989) indicated that there exists a unique relationship between the maximum point velocity and mean channel velocity for the open water case. By applying probability relationships and the concept of entropy to velocity distributions a unique relationship for mean channel velocity to maximum point velocity was found (Chiu 1988, 1989). This relationship can be described as:

$$[2\text{-}1] \quad u_\xi = \frac{u_{max}}{M} \ln\left[1 + (e^M - 1)\frac{\xi}{\xi_{max}} \right],$$

where: u_ξ is the streamwise average velocity at distance ξ above the bed; ξ is a

35

transformation of the actual distance above the bed; $u_{\max}$ is the maximum velocity in a channel cross section; and M and $\xi_{\max}$ are constants. The parameter M is a "measure of the uniformity of the probability and velocity distributions" and $\xi/\xi_{\max}$ "is equivalent to the probability of velocity, randomly sampled in a channel section, being less than or equal to u_ξ" (Chiu 1988). For details on the basis of this model, the reader is referred to Chiu (1988, 1989).

Chiu et al. (1993) provided an appropriate representation of the transformed coordinate system, represented by ξ, for the special case of axis-symmetric flows (e.g. pipe flow) and Wang (1993) suggested a diatonic expression for the transformed coordinate system for asymmetric flows. However, to the author of this thesis's knowledge, a continuous expression for ξ that is applicable over the entire depth for asymmetric flows has not yet been developed.

Before pursuing the development of such a relationship, it is appropriate to verify the existence of a unique relationship for the maximum point velocity to the mean channel velocity under ice covered flows. In fact, a number of other index velocity values that were thought to be potentially useful from a practical perspective were also considered. For example, without prior knowledge of the location of the maximum point velocity in the section, it would be difficult to measure it directly in the field without reverting back to conducting detailed measurements across the entire section. In contrast, locating the maximum depth in the cross section would be a much simpler task. Therefore, the potential for obtaining useful velocity information from the panel of maximum depth was

36

also explored. In all, four possible index velocity definitions were selected for consideration in this investigation:

- the maximum point velocity for the entire cross section, u_{max};

- the maximum vertically averaged panel velocity for the cross section, V_{max};

- the maximum point velocity for the panel of maximum flow depth, $u_{maxdepth}$; and

- the vertically averaged velocity for the panel of maximum flow depth, $V_{maxdepth}$.

2.3 Available Data and Analyses

2.3.1 Experimental Data

Velocity profiles were measured in the laboratory under two different "ice" covered conditions: velocity profile measurements taken under a fixed floating cover (plastic mat) with a rough underside; and, velocity profile measurements taken under a cohesionless mass of model ice rubble, resulting in a significantly rougher "ice" boundary than was provided by the floating mat. Experiments for both cases were conducted in the 30.5 m long recirculating flume located in the T. Blench Hydraulics Lab at the University of Alberta. Figure 2.1 presents a schematic of the experimental setup used for this investigation. The rectangular flume had 0.91 m high side walls and a width of 1.22 m. The bed was sheet metal (though rusted and rough in texture) and the walls were made of Plexiglas. Mannings n for the channel, under open water flow conditions, ranged from 0.020 to 0.025.

37

For the tests described herein, discharges ranging from 35 to 65 L/s were supplied to the head tank (representing the range of discharges allowed by the experimental arrangement). The flow entering the flume was conditioned with a combination of flow straighteners in the floor of the head tank and a bank of 1.2 m long, 200 mm diameter steel pipes positioned on the floor immediately downstream of the head tank. At the downstream end of the flume, water levels were controlled with a 150 mm high broad crested weir along with a series of adjustable vertical vanes spaced across the channel. The slope of the flume was set to 0.00164. For more details describing the experimental setup and measurement methods the reader is referred to Healy and Hicks (2001) and Healy et al. (2002).

2.3.2 Field Data

As part of Water Survey Canada's (WSC) Estimation of Discharge Under Ice Project (Walker and Wang 1993), detailed velocity profile data were collected at a number of gauging sites across Canada and data collected from 26 of these sites were made available to the authors. Eight sites had adequate data for this investigation; specifically, those sites for which measurements were available on four or more different dates (each corresponding to a different streamflow) were selected for detailed investigation. Table 2.1 presents these sites, along with their typical flow ranges for the relevant winter months, as published in Environment Canada's HYDAT archive.

2.3.3 Data Analyses

Figure 2.2 illustrates some typical velocity profiles taken from the WSC field

38

observations. Most of the vertical distributions of time-averaged velocities were characterized by a two-power law shape (Figure 2.2a and c). However, in some instances the observed profiles appeared to have no coherent profile shape (Figure 2.2d), while in other instances only a few points in the observed profile strayed from an otherwise two-power law shape (Figure 2.2b). There are a number of plausible explanations for these deviations, primarily attributable to physical effects. Where point velocities are averaged over an insufficient time interval, secondary flows, large scale turbulent structures, or localized effects due to irregular geometries can be important. In fact, the WSC measurement protocols recommend average point velocities be obtained over a 45 second interval. With longer sampling intervals less "scatter" in the data would be evident and the velocity profiles would take on a smoother shape. Even in a prismatic channel under controlled laboratory conditions, the authors have observed such effects. The presence of frazil ice can also be a cause for measurements to deviate significantly from an idealized profile. Cold and miserable working conditions exacerbate the likelihood of possible measurement errors due to equipment malfunction or insufficient sampling periods. For these reasons it was hypothesized that a theoretical fit to the observed data might help to minimize the distorting effects of some of these measurement "errors", thus improving any unique relationships between velocities.

A simple, two-power law expression was preferred over the probabilistic model described previously since, without any prior knowledge as to where the maximum velocity location is, it is difficult to systematically apply the diatonic function suggested by Wang (1993). The two-power law expression chosen for this study follows that developed by

39

Tsai and Ettema (1994) and can be described as:

$$[2\text{-}2] \quad u = K_o \left(\frac{y}{D}\right)^{1/m_b} \left(1 - \frac{y}{D}\right)^{1/m_i},$$

where: u is the streamwise average velocity at distance y above the bed; K_o is a flow parameter for a given flow rate per unit width; D is the depth of flow; and m_b and m_i are exponents associated with boundary roughness at bed and ice cover, respectively.

The MATLAB© software package facilitated the application of equation [2.2] to the observed data; sample fits are illustrated in Figure 2.2. A minimum of 4 points were required by the curve fitting method and, of a total of 1006 velocity profiles analyzed for the 8 sites, 945 (94%) had four or more points. Those 61 remaining (6%), with four or fewer points, corresponded to shallow measurement panels which were generally located adjacent to the channel banks (i.e. not in the panels containing the maximum point velocities).

Providing curve fits to all the observed velocity profile data helped to facilitate the determination of the index velocities. These index velocity values obtained from curve fits agreed very well with those determined directly from the observed data (as illustrated in Figure 2.3). For the rare instances where curve fitted values differed noticeably from the observed values, the difference could largely be attributed to "erroneous" data, particularly for maximum point velocity values that strayed from an otherwise parabolic velocity distribution (Figure 2.2b). Therefore, for clarity and concise representation of the primary observations of this study, mostly curve fitted data are discussed.

2.4 Observed Relationships between Index and Mean Velocities

2.4.1 Experimental Data

For all of the experimental tests, the maximum point velocities were found to occur at the channel centerline (as was expected due to confirmed flow symmetry). Figure 2.4a and b represent the observed centerline velocity profiles with the corresponding curve fits for experimental data collected under a floating rubber mat and under a cohesionless mass of model ice, respectively. Velocity profiles were measured for both cover conditions at discharges of approximately 35, 45, 55, and 65 L/s. Figure 2.4c and d represent a comparison between the observed maximum velocities and the measured mean channel velocity for the experimental data collected under a floating rubber mat and under a cohesionless mass of model ice, respectively. For both of these cases, there appears to be a strong and unique relationship between the maximum point velocity and the mean channel velocity.

2.4.2 Field Data

The next issue to investigate was whether a unique relationship occurs for asymmetric flows in natural channels with irregular geometry. For each of the eight hydrometric stations selected for analyses (see Table 2.1), index velocities u_{max}, $u_{maxdepth}$, V_{max}, and $V_{maxdepth}$, were all compared to the mean channel velocity. Figures 2.5 through 2.20 present the results of the analyses for the entire field measurements considered in this investigation in the form of two-figure sets corresponding to each WSC hydrometric station indicated in Table 2.1.

41

Direct measurements were taken near the open water stream flow gauges indicated in Table 2.1. The stream gauging sites are usually selected so that the open water rating curve relationship is unique. The reaches where these gauges are located are generally straight uniform and there are usually no prominent channel features upstream or downstream of the gauging station that would interfere with the uniqueness of the rating curve relationship. It was expected that the direct winter discharge measurement stations were located within these reaches; however, the exact location of these measurement stations is unknown.

In each set, the first of these two figures provides a visual representation of the observed velocity data for all measurement dates in the form of isovel plots. Indicated on this first set of figures are the locations of the maximum point velocity, u_{max}, (denoted by a circle) and of the velocity profile (panel) with the maximum vertically averaged velocity, V_{max} (denoted by a heavy vertical line). The ice cover thickness is also shown (shaded), and the vertical lines within the depicted ice cover locate the panels (i.e. the locations across the section where the velocity profiles were measured). The second figure of each set summarizes the relationship between the index velocities and the mean channel velocity, for all of the measurement dates at that WSC station location.

The relative "quality" of these relationships was quantified by comparing the coefficient of determination (R^2) obtained for linear equations fit to the relationships and the resulting linear equation along with the corresponding R^2 values are included with the plots. In the discussions that follow, the relative value of the fit is described qualitatively based on the absolute R^2 value as follows: *good* denotes R^2 values greater than 0.90; *fair*

42

denotes R^2 values between 0.60 and 0.90; and *poor* denotes R^2 values less than 0.60. Since most of the sample sizes were small, the p-values associated with the cross-correlation of the variables for each site are also included on the plots as an additional measure on the "quality" of the index velocity relationships.

While the data for most of the eight hydrometric stations analyzed in this study suggested a relationship between mean channel velocity and index velocities, the relative quality of these relationships varied from site to site. Factors thought to affect the quality of the relationships that could be evaluated with the available data were: the consistency on the location of index velocities u_{max} and V_{max}; and the complexity of the channel geometry. Other factors that were thought to be of importance, yet could not be evaluated with the available data, included: the presence of frazil ice; possible backwater and drawdown effects due to local ice-affects; and complicated flow structures introduced from significant channel irregularities upstream or downstream of the measurement section.

2.4.2.1 Consistency in the location of index velocities u_{max} and V_{max}

The positions of the index velocities u_{max} (maximum point velocity in the section) and V_{max} (maximum panel velocity in the section), for the experimental tests conducted in a rectangular channel, were consistently located at the channel centerline. For the natural channels with irregular geometry, the consistency in the locations of u_{max} and V_{max} was more difficult to assess since different reference points were used for the horizontal stationing on each measurement date. Consequently, it was not possible to accurately quantify the sensitivity of index velocity to positional error. However, by inspection of

43

the cross section plots (the first figure of each paired set described above) it was possible to give a reasonable qualitative assessment on the consistency of the location of index velocities. The location of $u_{maxdepth}$ and $V_{maxdepth}$, by definition, coincided with the panel of maximum depth of flow. However, this location does not necessarily correspond to the location of maximum depth over the entire section. The horizontal location of the panel with the maximum depth of flow would vary depending on the choice of panel locations along with any thickness variations across the channel.

Based on the initial observations of this study, the horizontal position of both u_{max} and V_{max} tended to be relatively consistent for half of the hydrometric stations examined in this study, such as the Oldman River (Figure 2.5), the Red Deer River (Figure 2.7), the Little Smoky River (Figure 2.15), and the Yellowknife River (Figure 2.17). Two of the stations were considered to be consistent roughly three quarters of the time (i.e.: the North Saskatchewan River (Figure 2.9), and the Yukon River (Figure 2.19)). For the remaining two stations, located on the Pembina River (Figure 2.11) and the Halfway River (Figure 2.13), the horizontal location of u_{max} and V_{max} were considered inconsistent. For the Pembina River there was no apparent explanation as to why the horizontal locations of the index velocities were inconsistent. For the Halfway River the location of index velocities appeared to have moved from the left side of the channel during the 1990 measurement season to the right side during the 1991 measurement season. Even though the location of the index velocity moved from year to year, a good relationship between the index velocity and the average channel velocity was maintained (see Figure 2.14). It was noted by inspection of Figure 2.13 that the channel geometry itself had changed

44

between the 1990 to the 1991 winter seasons. This would suggest the importance of channel geometry on influencing the location of maximum velocities.

Given the qualitative nature of this analysis it was difficult to deduce the presence of any strong correlations between the consistent nature of the location of index velocities and the quality of their respective index velocity to mean channel velocity relationships. However, the quality of a relationship between index velocity and mean channel velocity did not appear to depend on the consistency of the horizontal location of the index velocity. For example, while the location of u_{max} for the Oldman River appeared consistent (Figure 2.5), there was no apparent relationship between index velocity and mean channel velocity ($R^2 = 0.00$). Conversely, while the location of u_{max} for the Pembina River appeared inconsistent (Figure 2.11), the relationship between index velocity u_{max} and mean channel velocity was good ($R^2 = 0.97$).

2.4.2.2 Complexity of Channel Geometry

Virtually all of the sites considered in this investigation were considered to have relatively simple geometry in the absence of an ice cover. At a first glance some of the cross sections may appear to be somewhat complicated but this is due to the exaggerated vertical scale that amplifies otherwise small irregularities. However, the presence of ice can complicate the geometry of the effective flow area. For example, on the Oldman River (Figure 2.5) the flow appears to be divided into two cells that become increasingly distinct as the ice cover thickness increases. While it was apparently not an issue for the data provided for this investigation, the presence of frazil ice would certainly have

45

potential for creating a complicated flow area.

The Oldman River (dual flow cells case) represented the most complex geometry and had index velocities relationships based on u_{max} and V_{max} giving coefficient of determinations for their linear curve fits of 0.00 and 0.01, respectively. For this case at least, the complex geometry may appear to have contributed to the existence of poor index velocity relationships. However, it is interesting to note that relationships based on index velocities corresponding to the panel of maximum depth ($u_{maxdepth}$ and $V_{maxdepth}$) were considered fair to good ($R^2 = 0.85$ and $R^2 = 0.98$, respectively).

2.5 Using Index Velocity Methods for Determining Stream Flow

To the author's knowledge, there have been no published semi-analytical models relating maximum point velocities to mean channel velocities for asymmetric (ice covered) flows in natural channels. However, the data in this study suggest such a relationship exists and developing a suitable analytical model is a worthwhile pursuit. In addition to u_{max}, other index velocities (i.e. V_{max}, $u_{maxdepth}$, and $V_{maxdepth}$) show promise as suitable indicators for deducing mean channel velocities.

Figure 2.21 provides a visual summary of all the index velocity methods examined in the study. For each measurement date the percent variation of the mean channel velocity from the line of best fit is plotted. Within each of the subfigures (Figure 2.21a through d) thick horizontal lines separate the index velocities corresponding to a particular hydrometric station and the resulting subdivisions created by these thick horizontal lines are hereafter referred to as "windows". Each window within Figure 2.21 provides a

46

visual representation of the quality of the index velocity relationships – more specifically, the variation of the data about each corresponding line of fit. The coefficient of determination (R^2) describing the quality of fit of each index velocity relationship is also included in each window. Previous investigations (Pelletier 1988, 1989) suggest the error of current winter discharge measurement methods is approximately 4 to 8%. These estimates are based on direct measurement of the velocity and depth under a competent ice cover and include uncertainties relating to: estimates on the cross sectional area; point velocity sampling time; point velocity descretization; current meter errors; and integration techniques. Inspection of Figure 2.21 suggests that the index velocity relationships, developed in this study, provide estimates on mean channel velocity within errors of approximately 5%. Presumably, errors on area estimates for these methods would be similar to current methods, consequently, discharge estimates based on index velocity methods would be expected to have errors slightly greater than 5%.

2.5.1 Practical Considerations

The practical considerations under discussion were aimed at the development of an improved streamflow measurement program using index velocity methods. The first consideration relates to the choice of measurement location. Ideally, the measurement station would be located at a section where there exists a strongly unique relationship between index velocity and mean channel velocity. Channel sections with the following characteristics were considered to be most desirable: simple planform and streamwise geometries; free of frazil ice; and minimal backwater or drawdown effects.

47

The choice of index velocity can be largely based on practical considerations as well. Overall, the location of index velocities u_{max} and V_{max} appear to be fairly consistent. However, for those occasions where their locations vary, finding u_{max} and V_{max} would require obtaining velocity data for virtually the entire cross section and the amount of labour and time to do so would exceed that required by current practices, thus defeating the intent of pursuing an index velocity approach for measuring stream flow. Alternatively, index velocities corresponding to the location of maximum depth of flow ($u_{maxdepth}$ and $V_{maxdepth}$) provide a simpler alternative and based on the observations of this study, give comparably good index velocity relationships for the mean channel velocity. Another alternative would be to choose index velocities situated at a constant location within the cross section (preferably at a deep section in the channel where higher velocities are expected). Unfortunately, the data provided for this study did not facilitate examination of this type of index velocity since panel locations were not referenced to a common horizontal datum. Therefore, for future studies it is recommended that a horizontal control be created to ensure measurements are taken at the same location each measurement date. This would also facilitate quantification of any errors associated with positional error.

Other practical considerations relating to the implementation of a modified program relate to cost, safety, and accuracy issues. The costs associated with each discharge measurement relate to the frequency of discharge measurements over the winter season and thus become of practical importance. Naturally, an appropriate economic evaluation on the potential benefits of modifying an existing program would be expected. For

48

remote sites, the economics may suggest no apparent gain by adopting a modified method for reasons relating to travel time, limited daylight hours, and so forth. Consequently, an increase in frequency in discharge measurements may not prove to be more feasible for these cases. Where access is not limited and those cases where resources weigh less on costs not associated directly with data collection like transportation for example, an increase in frequency could be anticipated. Also, where safety is of paramount importance, a reduction in time spent on the cover can reduce the cumulative risk of successive discharge measurements.

Under current measurement methods, over 40 point velocity observations are typically acquired and any errors associated with individual measurements become less significant when they are effectively averaged with all the other point observations. However, when relying on a single or relatively few point velocity observations, greater care must be taken to ensure an accurate measurement is acquired. Generally, the greatest errors in point measurements can be attributed to inadequate sampling time and the typical sample time for point velocity measurements in practice is 40 to 50 seconds (Pelletier 1988). Carter and Anderson (1963) found that the standard deviation of error ratios about a mean of zero could be reduced by roughly half when the sample interval was increased from 45 seconds to 3 minutes. Therefore, the authors recommend extending the sampling time to an appropriate interval to minimize errors associated with the sampling interval. Finally, to further assist in interpretation of the data used for streamflow estimates, detailed information on local ice and meteorological conditions should be recorded.

2.5.2 Recommendations for Additional Field Programs

While the data examined in this study strongly suggest that index velocity methods provide a promising alternative to the current practice, additional field investigations are recommended before the implementation of a full-scale streamflow measurement program. An ideal program would, through the reduction of data, improve operations with an acceptable loss of information. The aim of the additional field investigations would be to obtain a more comprehensive data set that would further verify the existence of the unique index velocity relationships found in this study and explore in greater detail potential factors affecting the quality of the resulting index velocity relationships. By ensuring horizontal control, additional index velocities could be examined, like those occurring at a constant location in the channel such as the thalweg. Any future field program would aid in the development of a streamflow measurement protocol specific to the particular site investigated and provide an outline for the development of similar protocols at other sites. The protocols may vary slightly from site to site; for example, the choice of index velocity may vary. The site-specific nature of index velocity relationships is further highlighted by Figure 2.21 where a moderate trend in the Yukon data was indicated and suggested the index velocity relationship experienced an upwards shift in the curve from year to year. While there appears to be no apparent explanation for this shift given the available data, its existence suggests that, at least given the current set of data, index velocity relationships are unique to each site and may require adjustment over time. Also, with further detailed investigations the cause of such a shift may be better understood.

50

A typical measurement protocol using $u_{maxdepth}$ and or $V_{maxdepth}$ might be as follows. First a sufficient number of detailed measurements would be required to develop a satisfactory index velocity relationship. As the measurement program progressed, additional detailed measurements would be taken to improve the index velocity relationship and track any changes that may be due varying channel conditions. A detailed measurement would follow closely to the current measurement practice which involves the use of a current meter to obtain point velocity measurements at (typically) two points in the flow depth, at more than 20 vertical panels across a channel. These point measurements are then integrated over the flow area to determine the total discharge. A detailed velocity profile would then be taken at the hole with the maximum depth of flow.

Once a suitable index velocity relationship describing the mean channel velocity had been established, subsequent measurements would be less labour intensive. First a sufficient number of holes would be drilled across the measurement section to measure the transverse variation in ice thickness (required to determine the flow area); these holes could be drilled using a small auger driven by a handheld cordless drill. Next a detailed velocity profile would be obtained at the location with the maximum flow depth – this provides index velocities $u_{maxdepth}$ and $V_{maxdepth}$. The mean channel velocity would then be deduced from either or both index velocities and subsequently multiplied by the flow area to determine the discharge. The authors foresee such a method as being less labour intensive and time consuming than the current practice and would conceivably facilitate an increased frequency of winter streamflow measurements. In addition, these methods lend themselves well to the potential for more sophisticated measurement programs that

employ some form of automated measurement method.

2.6 Conclusions

The data examined for the eight hydrometric stations studied in this investigation strongly suggest the existence of a unique relationship between index velocities and the mean channel velocity. The consistency of the locations of maximum point and panel did not appear to have any strong correlation to the quality of the index velocity relationships obtained. However, it appeared that the relative complexity of the channel geometry could have an impact on index velocity relationships, and that the presence of an ice cover can contribute to the relative complexity of the channel.

The development of an analytical model describing index velocity relationships complemented by a more rigorous field investigation is necessary to increase the level of confidence in using such methods in a full scale operation program.

Table 2.1. Winter gauging station summary data.

WSC Station ID	Station Name	Drainage Area (km^2)		Typical Discharge Values (m^3/s) Min.	Avg.	Max.
05AA023	Oldman River near Waldron's Corner	1,440	Jan	0.13	2.43	8.30
			Feb	0.76	2.34	8.00
05CE001	Red Deer River at Drumheller	24,800	Jan	1.98	11.5	23.4
			Feb	1.98	11.8	27.6
			Mar	2.80	29.4	326
05GG001	North Saskatchewan River at Prince Albert	131,000	Jan	11.2	63.7	194
			Feb	16.5	65.0	172
			Mar	14.7	70.9	329
07BC002	Pembina River at Jarvie	13,100	Dec	0.680	6.84	30.5
			Jan	0.623	4.95	16.1
			Feb	0.538	4.25	10.8
07FA006	Halfway River near Farrell Creek	9,350	Jan	7.00	12.2	21.0
			Feb	7.10	10.8	17.2
			Mar	7.20	11.6	26.7
07GH002	Little Smoky River near Guy	11,100	Dec	0.596	6.97	20.2
			Jan	1.08	5.24	14.5
			Feb	0.651	4.84	34.0
			Mar	2.05	7.45	59.0
07SB002	Yellowknife River at Outlet of Prosperous Lake	16,300	Dec	11.4	33.2	63.6
			Jan	13.0	28.7	53.8
			Feb	13.0	28.7	53.8
			Mar	12.2	23.5	39.2
			Apr	11.7	21.1	35.2
09AH001	Yukon River at Carmacks	81,800	Jan	153	310	517
			Feb	142	284	456
			Mar	136	262	435
			Apr	139	268	960

53
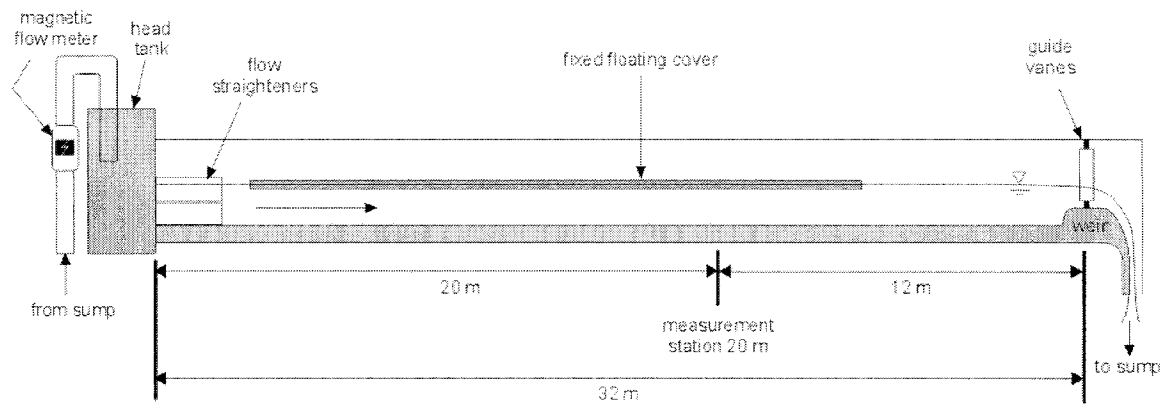
Figure 2.1. Experimental flume schematic.
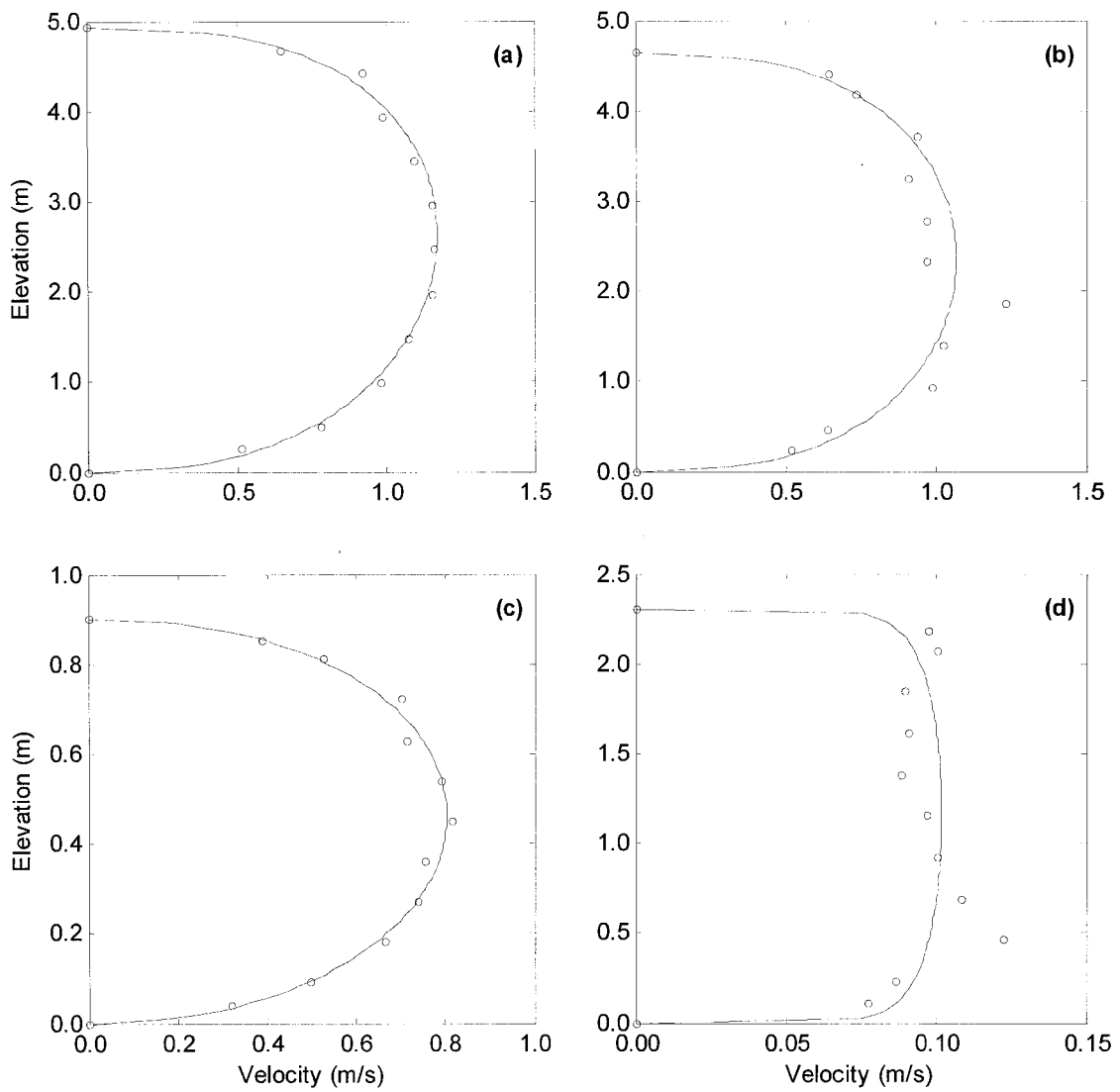
Figure 2.2. Sample velocity profile data obtained from the field.
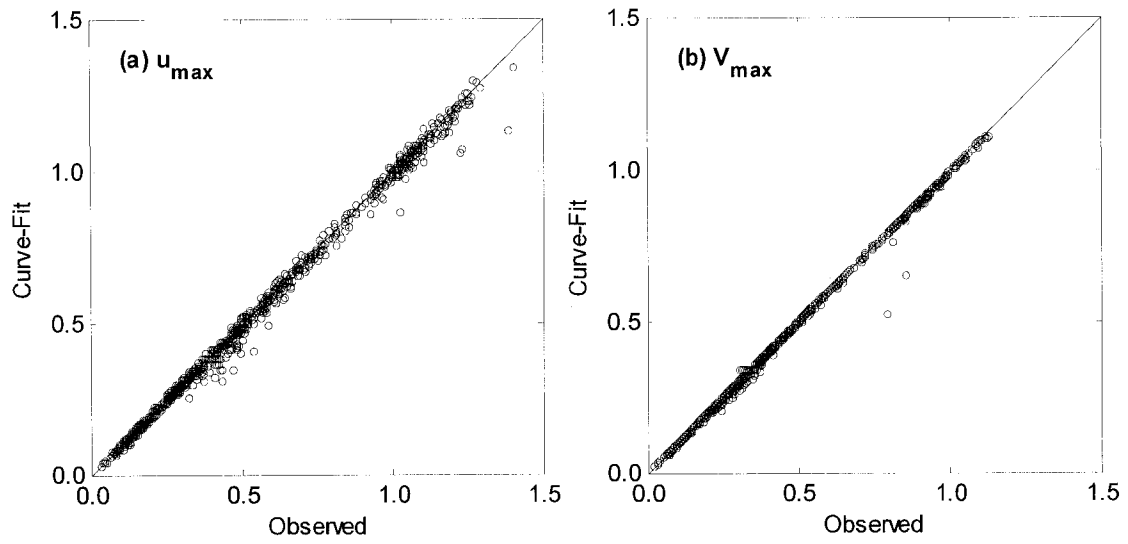
Figure 2.3. Comparison between observed and curve fitted data for (a) u_{max} and (b) V_{max} (units: m/s).

56
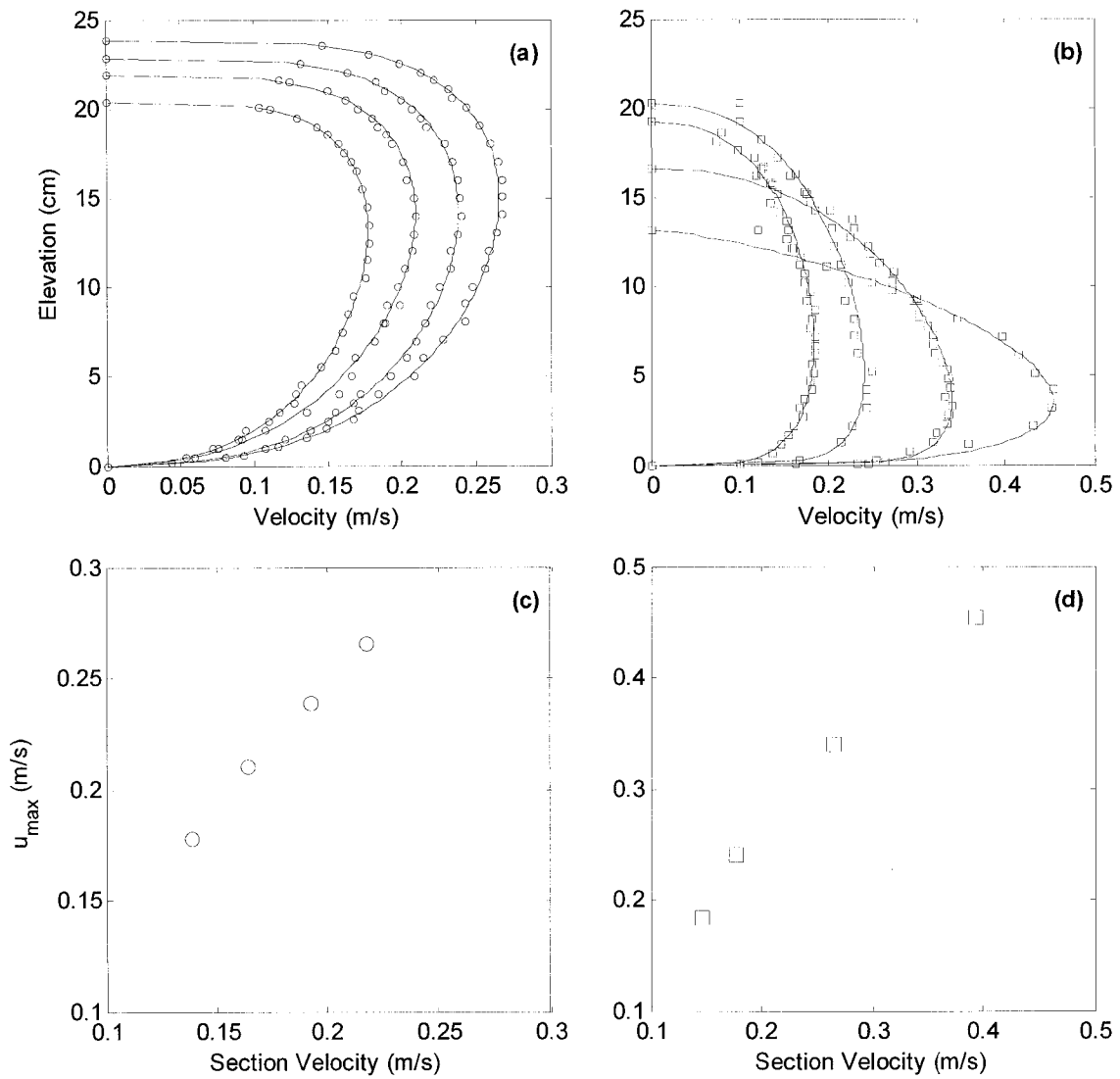
Figure 2.4. Experimental velocity profile data for: (a) velocity profiles under a floating plastic mat; (b) velocity profiles under a mass of model ice rubble; and u_{max} versus average section velocity for: (c) the floating plastic mat; and (d) the model ice rubble.

57
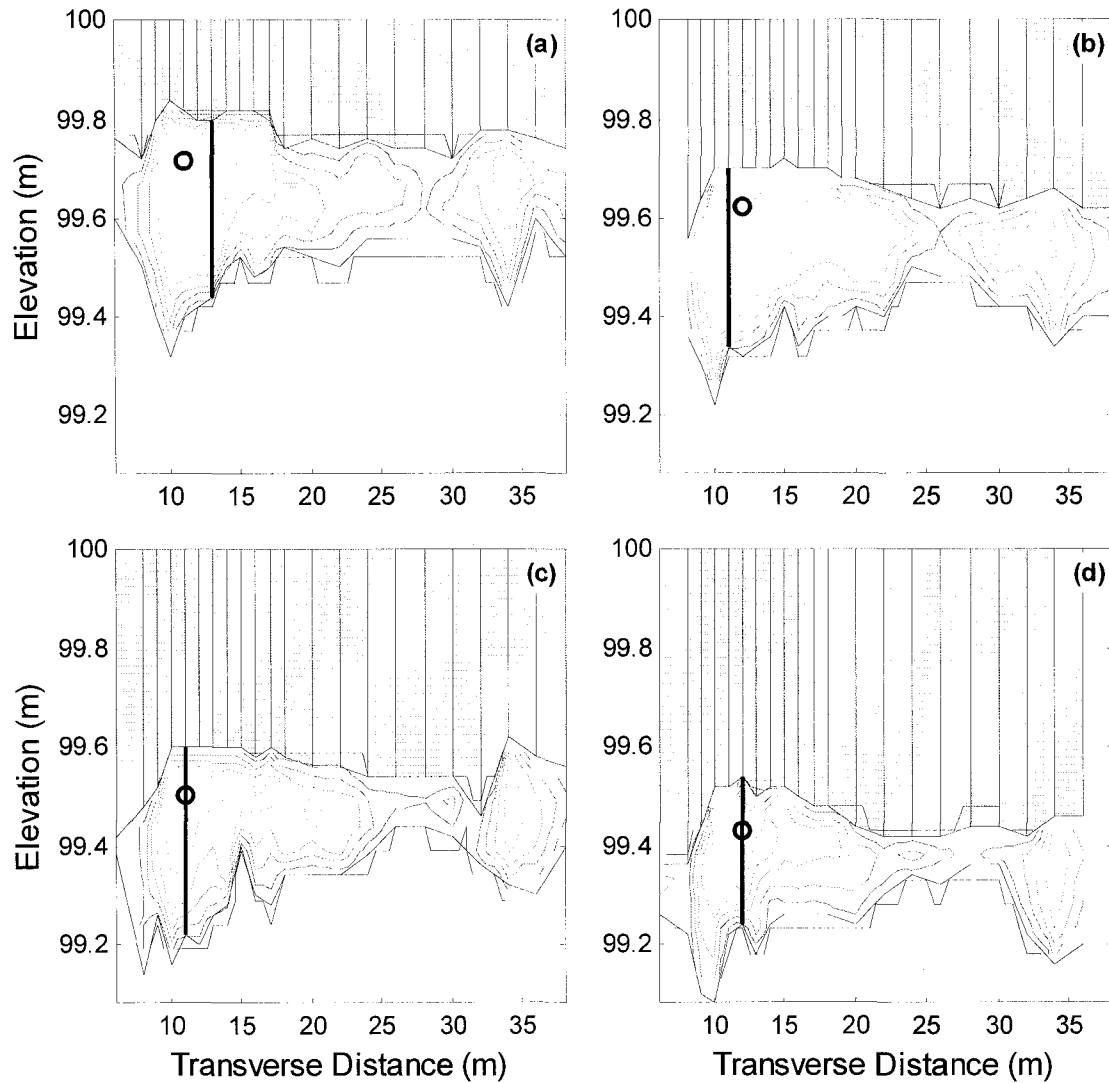
Figure 2.5. Velocity contour data for Oldman River near Waldron's Corner (05A0023): circle indicates location of u_{max} and heavy vertical line indicates location of V_{max} (contour interval = 0.1 m/s): (a) 03-Jan-90, (b) 23-Jan-90, (c) 12-Feb-90, (d) 28-Feb-90.

58
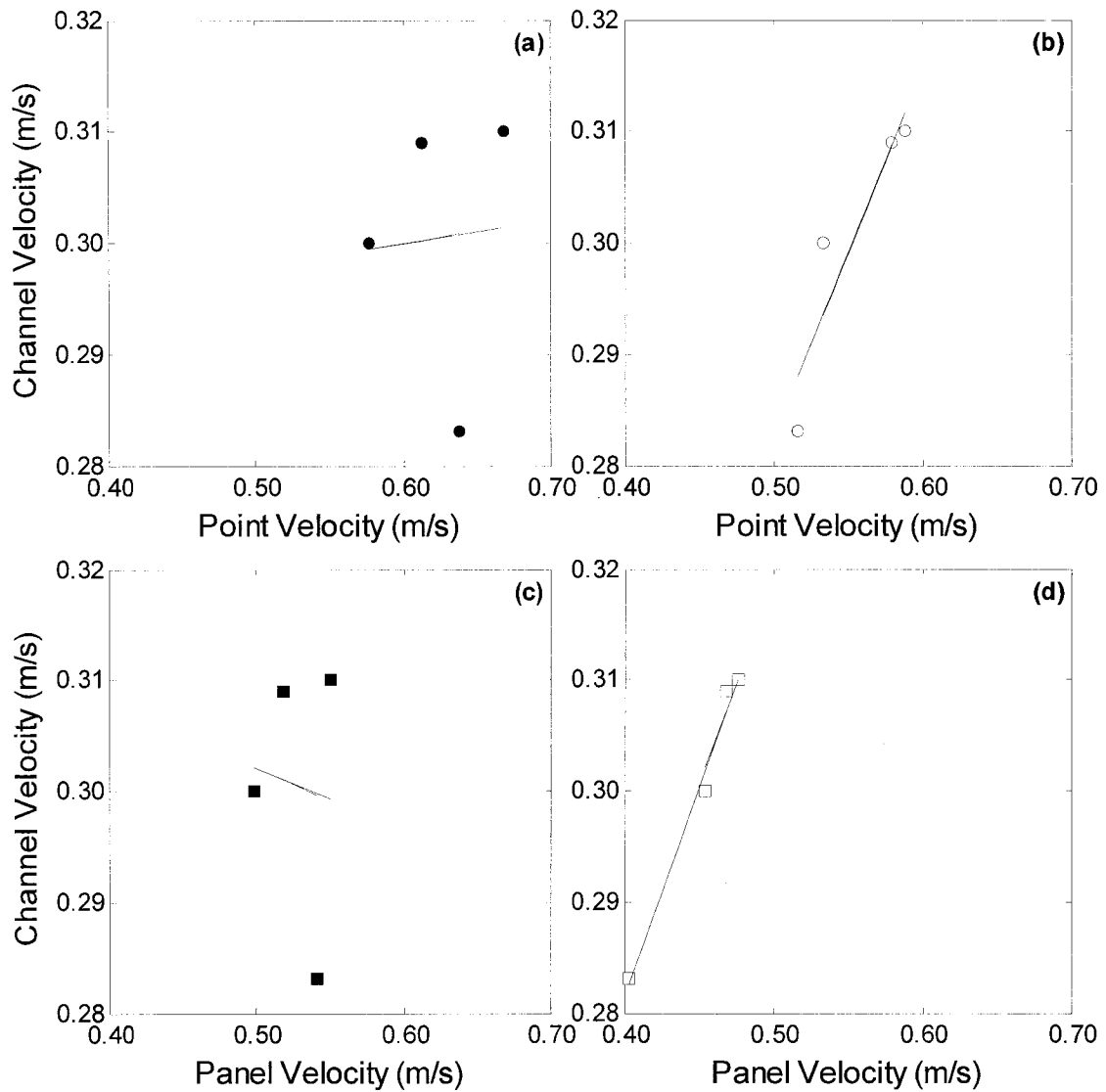
Figure 2.6. Summary data for Oldman River near Waldron's Corner (05A0023): circles denote point velocities; squares denote panel velocities; closed symbols denote maximum values over the entire cross section; open symbols denote values obtained at the panel of maximum depth: (a) u_{max} ($R^2 = 0.00$, p = 0.93), (b) $u_{maxdepth}$ ($R^2 = 0.85$, p = 0.08), (c) V_{max} ($R^2 = 0.00$, p = 0.90), (d) $V_{maxdepth}$ ($R^2 = 0.98$, p = 0.01).

59
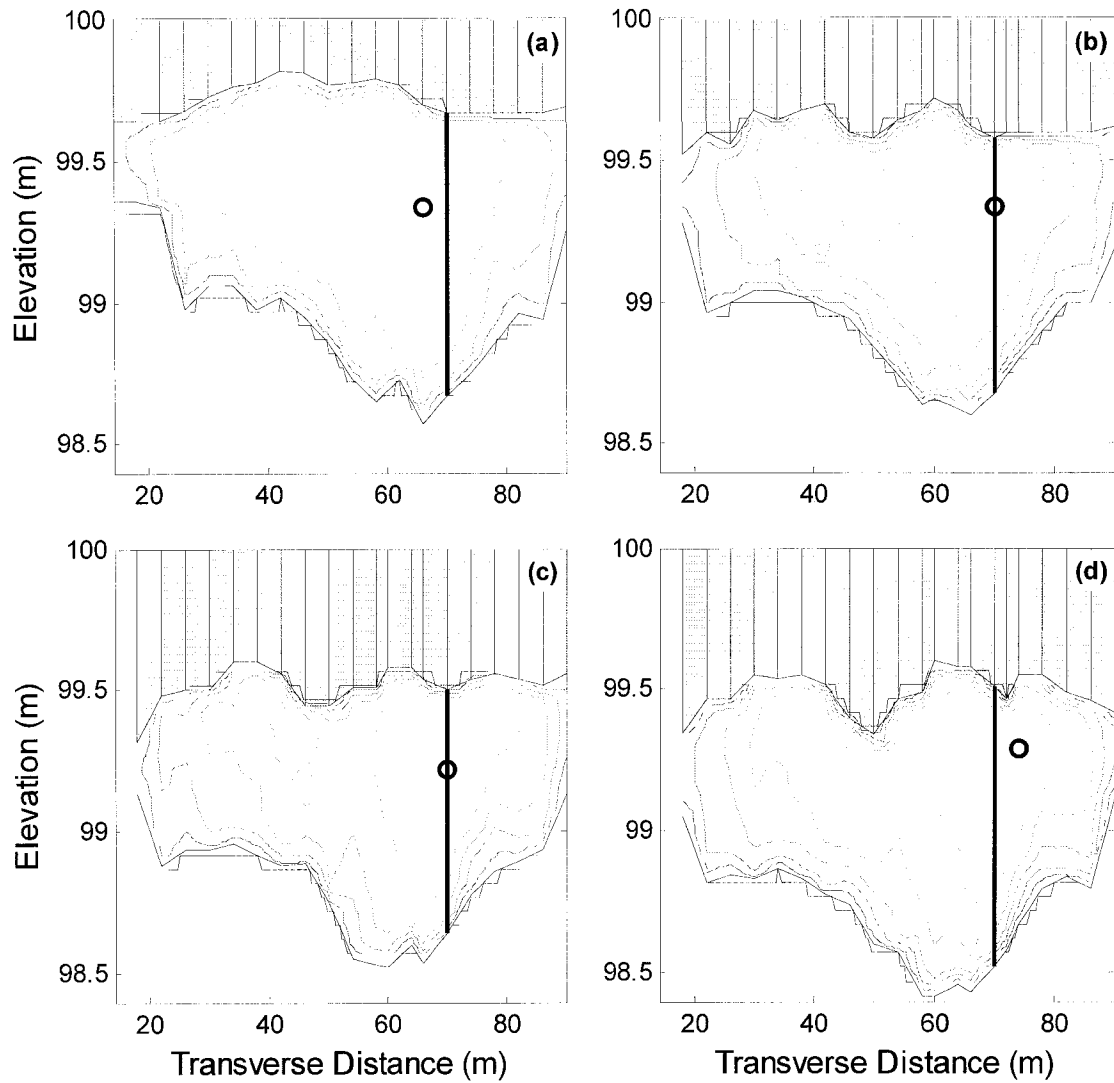
Figure 2.7. Velocity contour data for Red Deer River at Drumheller (05CE001): circle indicates location of u_{max} and heavy vertical line indicates location of V_{max} (contour interval = 0.1 m/s): (a) 03-Jan-90, (b) 23-Jan-90, (c) 13-Feb-90, (d) 07-Mar-90.

60
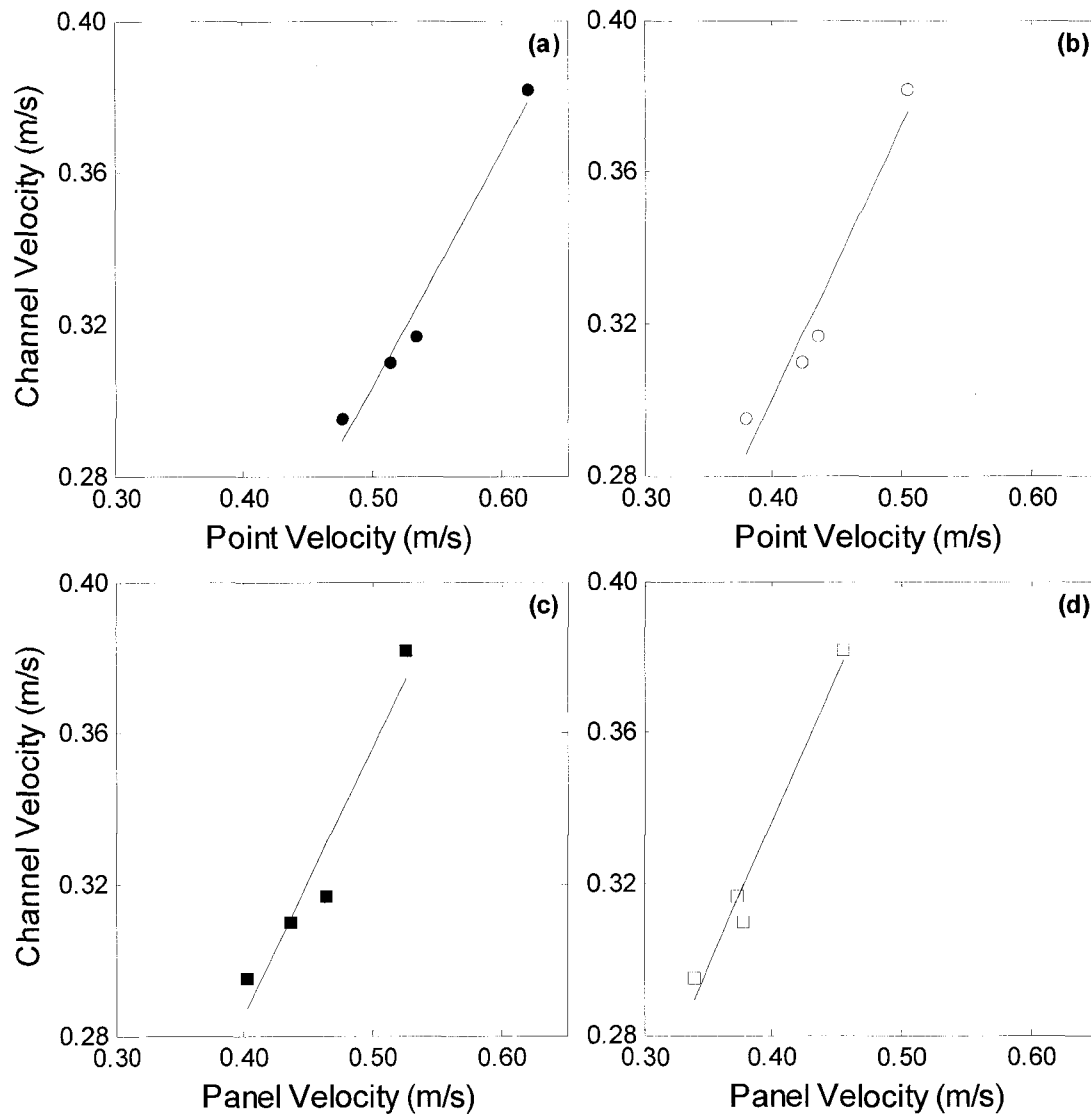
Figure 2.8. Summary data for Red Deer River at Drumheller (05CE001): circles denote point velocities; squares denote panel velocities; closed symbols denote maximum values over the entire cross section; open symbols denote values obtained at the panel of maximum depth: (a) u_{max} ($R^2 = 0.98$, p = 0.01), (b) $u_{maxdepth}$ ($R^2 = 0.94$, p = 0.03), (c) V_{max} ($R^2 = 0.93$, p = 0.04), (d) $V_{maxdepth}$ ($R^2 = 0.97$, p = 0.02).

61
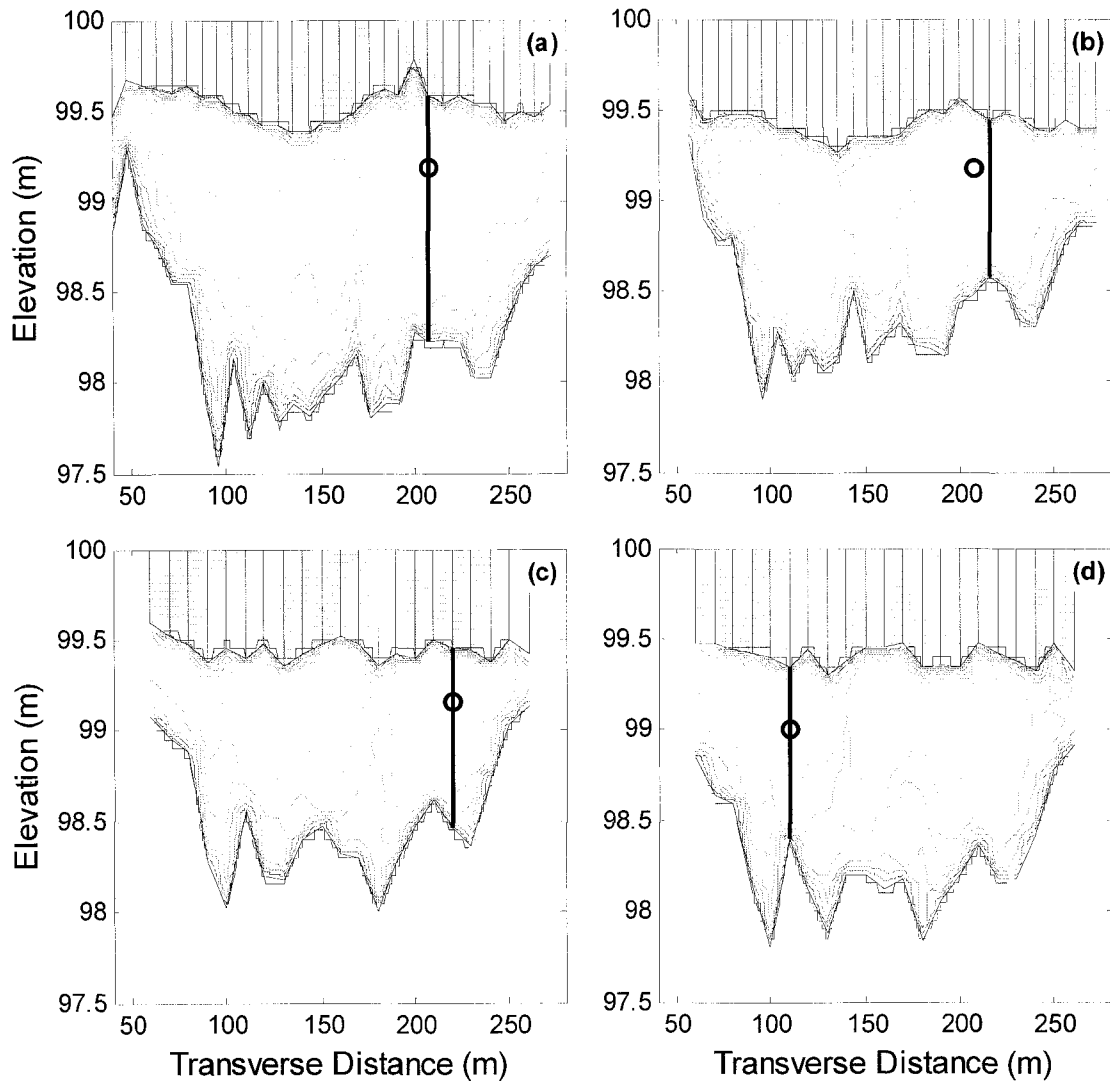
Figure 2.9. Velocity contour data for North Saskatchewan River at Prince Albert (05GG001): circle indicates location of u_{max} and heavy vertical line indicates location of V_{max} (contour interval = 0.1 m/s): (a) 11-Jan-90, (b) 01-Mar -90, (c) 15-Jan-91, (d) 06-Feb-91.

62
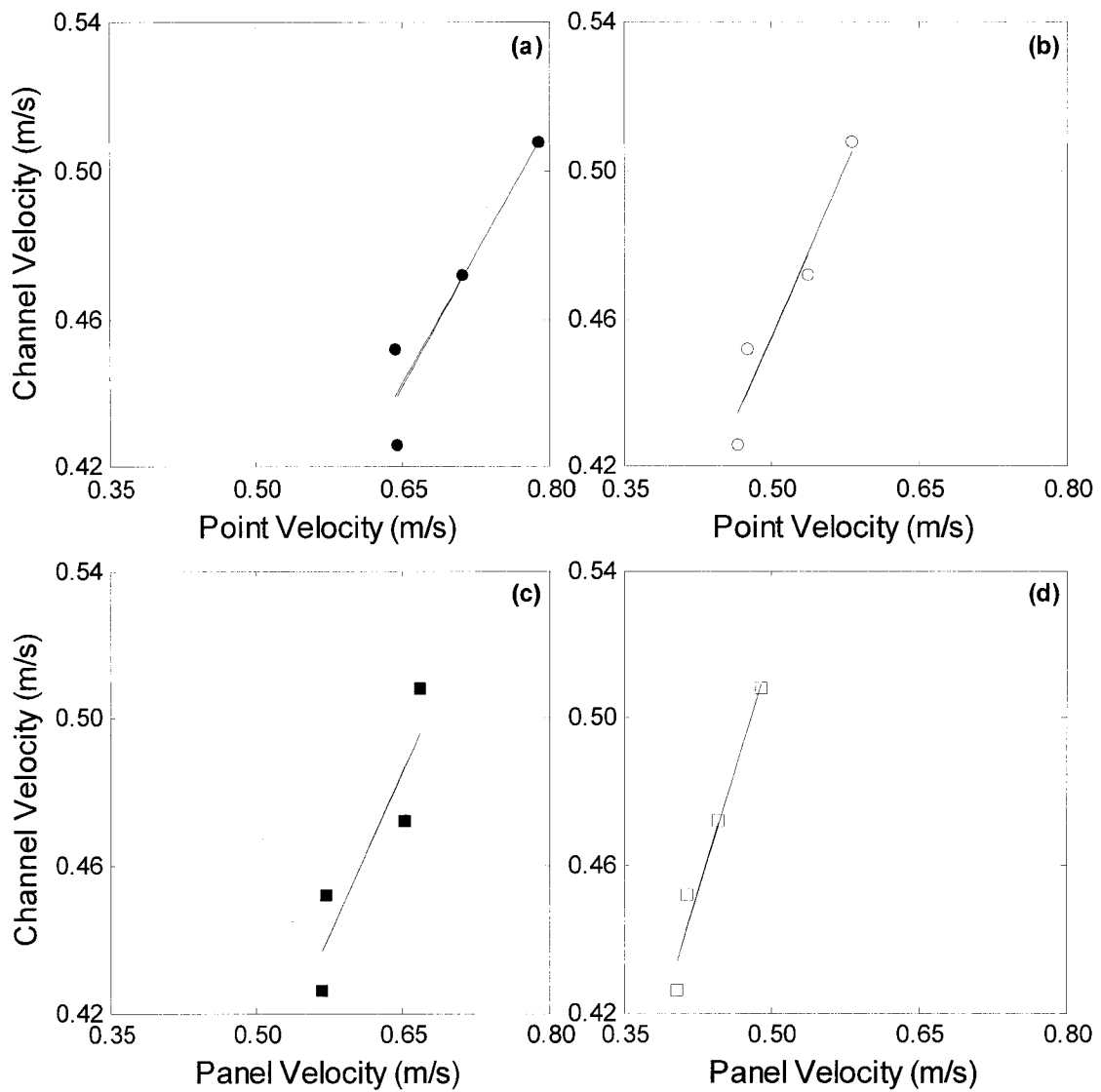
Figure 2.10. Summary data for North Saskatchewan River at Prince Albert (05GG001): circles denote point velocities; squares denote panel velocities; closed symbols denote maximum values over the entire cross section; open symbols denote values obtained at the panel of maximum depth: (a) u_{max} ($R^2 = 0.90$, p = 0.05), (b) $u_{maxdepth}$ ($R^2 = 0.93$, p = 0.03), (c) V_{max} ($R^2 = 0.82$, p = 0.10), (d) $V_{maxdepth}$ ($R^2 = 0.96$, p = 0.02).

63
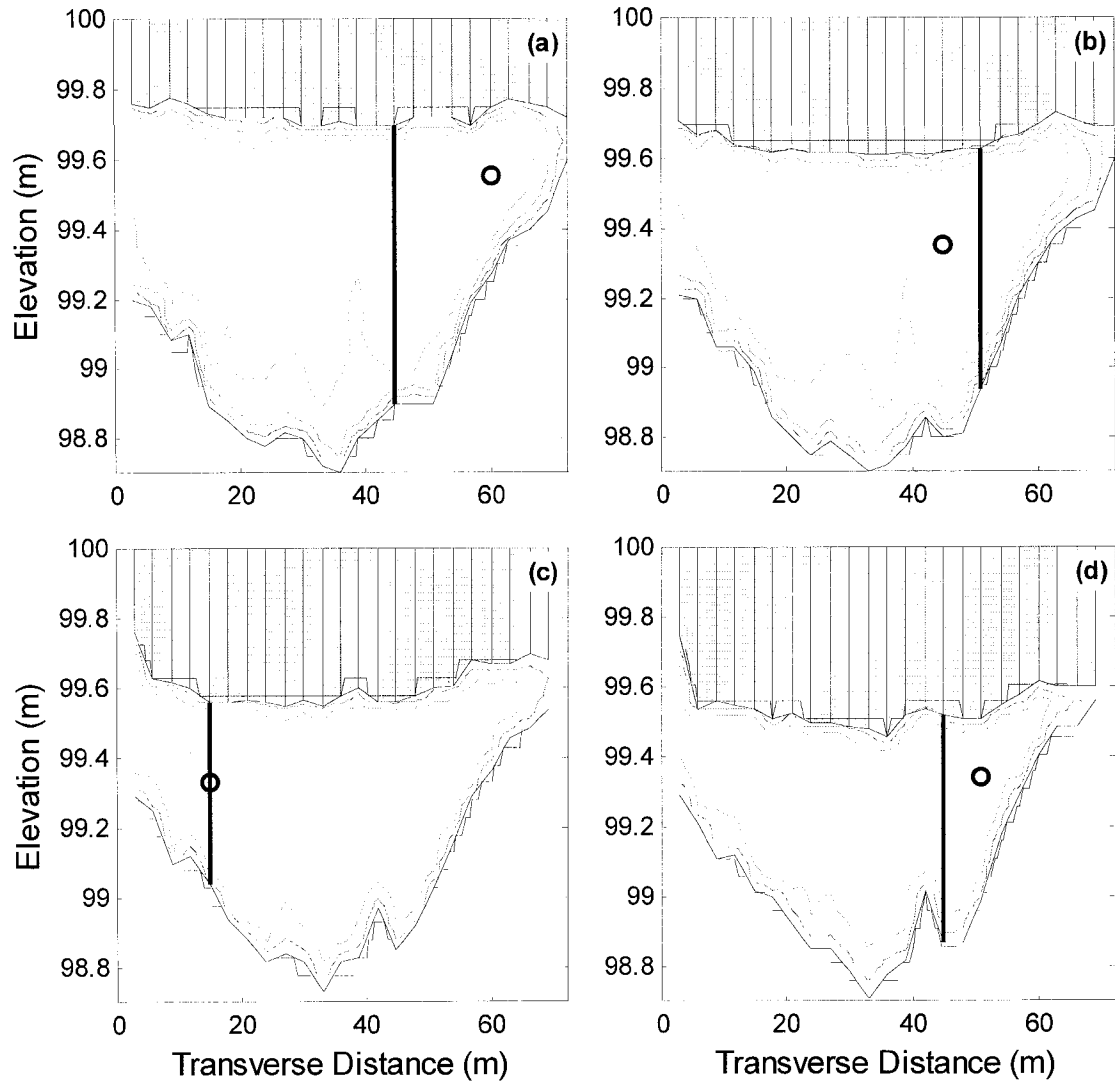
Figure 2.11. Velocity contour data for Pembina River at Jarvie (07BC002): circle indicates location of u_{max} and heavy vertical line indicates location of V_{max} (contour interval = 0.1 m/s): (a) 12-Dec-89, (b) 03-Jan-90, (c) 24-Jan-90, (d) 13-Feb-90.

64
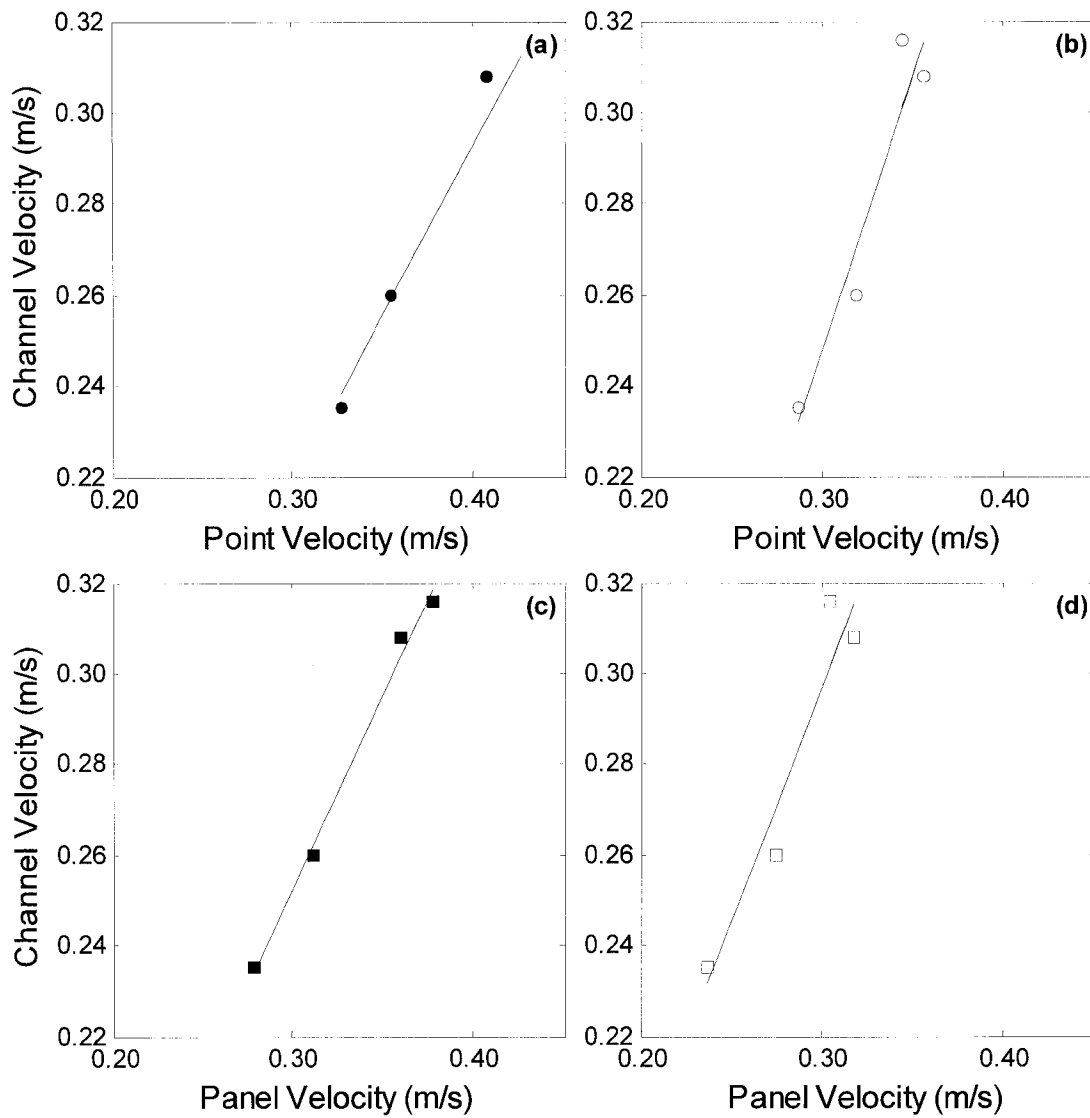
Figure 2.12. Summary data for Pembina River at Jarvie (07BC002): circles denote point velocities; squares denote panel velocities; closed symbols denote maximum values over the entire cross section; open symbols denote values obtained at the panel of maximum depth: (a) u_{max} ($R^2 = 0.97$, p = 0.02), (b) $u_{maxdepth}$ ($R^2 = 0.91$, p = 0.04), (c) V_{max} ($R^2 = 0.99$, p = 0.00), (d) $V_{maxdepth}$ ($R^2 = 0.92$, p = 0.04).

65
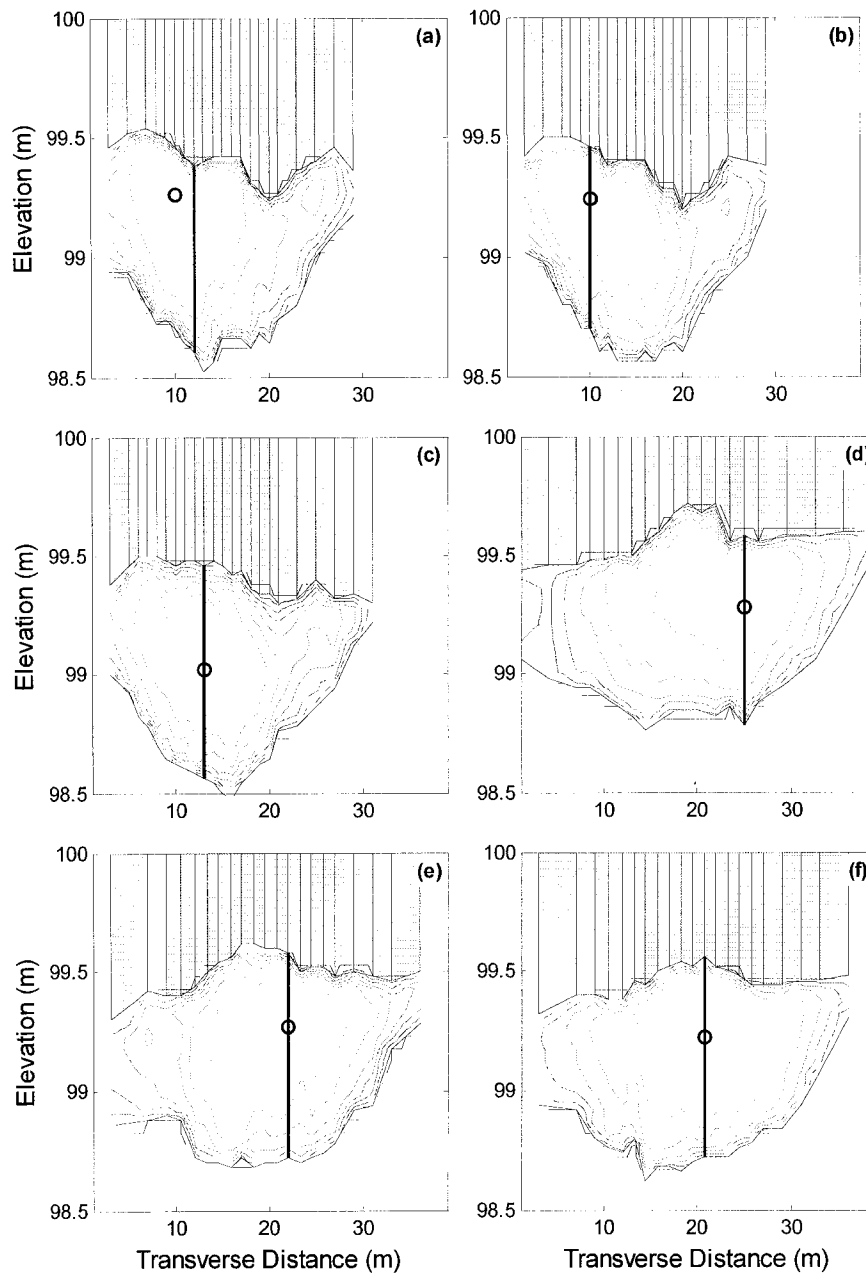
Figure 2.13. Velocity contour data for Halfway River near Farrell Creek (07FA006): circle indicates location of u_{max} and heavy vertical line indicates location of V_{max} (contour interval = 0.1 m/s): (a) 02-Feb-90, (b) 22-Feb-90, (c) 16-Mar-90, (d) 14-Jan-91, (e) 05-Feb-91, (f) 26-Feb-91.
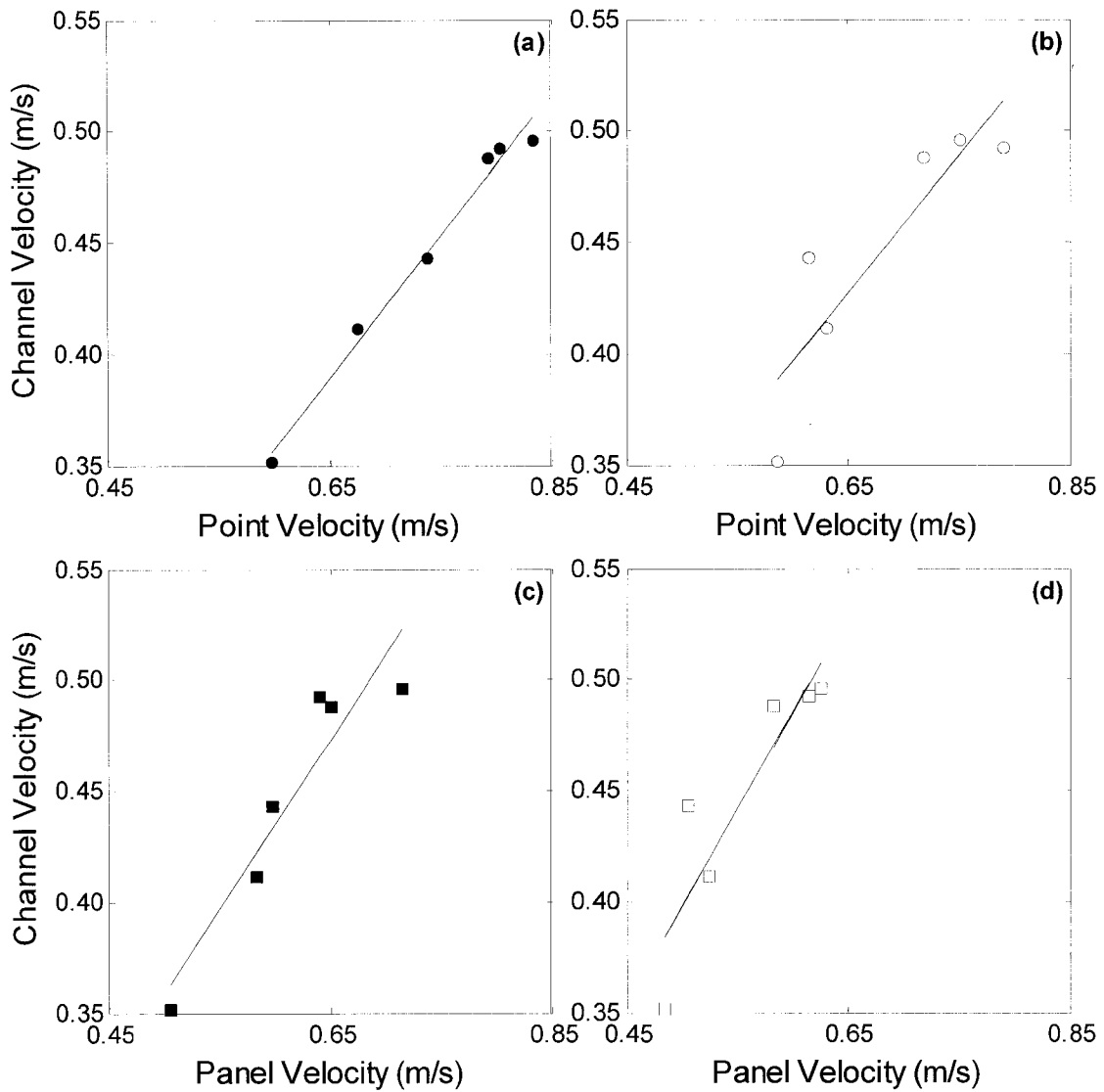
Figure 2.14. Summary data for Halfway River near Farrell Creek (07FA006): circles denote point velocities; squares denote panel velocities; closed symbols denote maximum values over the entire cross section; open symbols denote values obtained at the panel of maximum depth (note: symbols with additional outline indicate 1990 data) :

(a) u_{max} ($R^2 = 0.98$, p = 0.00), (b) $u_{maxdepth}$ ($R^2 = 0.78$, p = 0.02), (c) V_{max} ($R^2 = 0.88$, p = 0.01), (d) $V_{maxdepth}$ ($R^2 = 0.80$, p = 0.02).

67
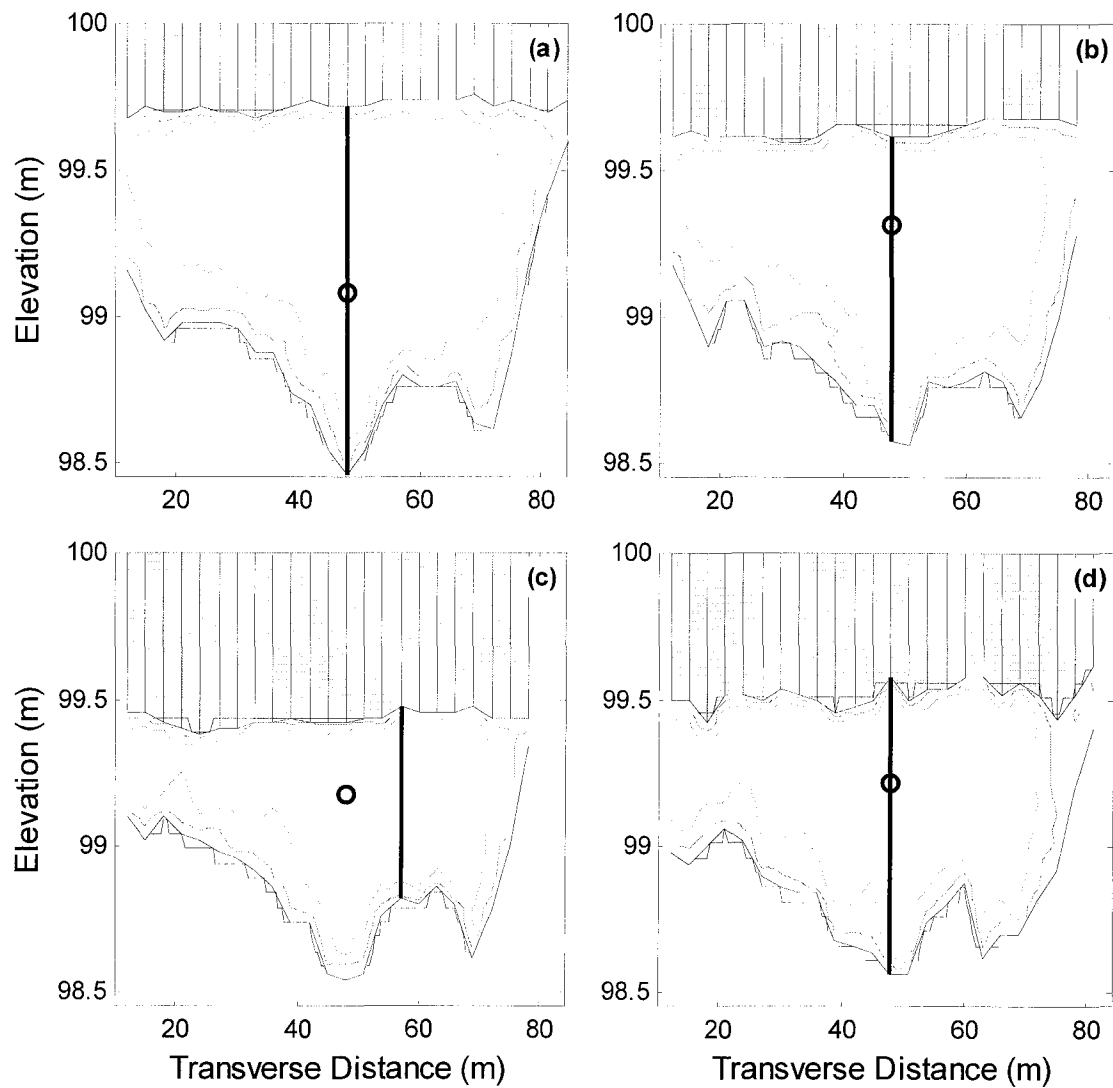
Figure 2.15. Velocity contour data for Little Smoky River near Guy (07GH002): circle indicates location of u_{max} and heavy vertical line indicates location of V_{max} (contour interval = 0.1 m/s): (a) 13-Dec-89, (b) 10-Jan-90, (c) 05-Mar-90, (d) 15-Mar-90.

68
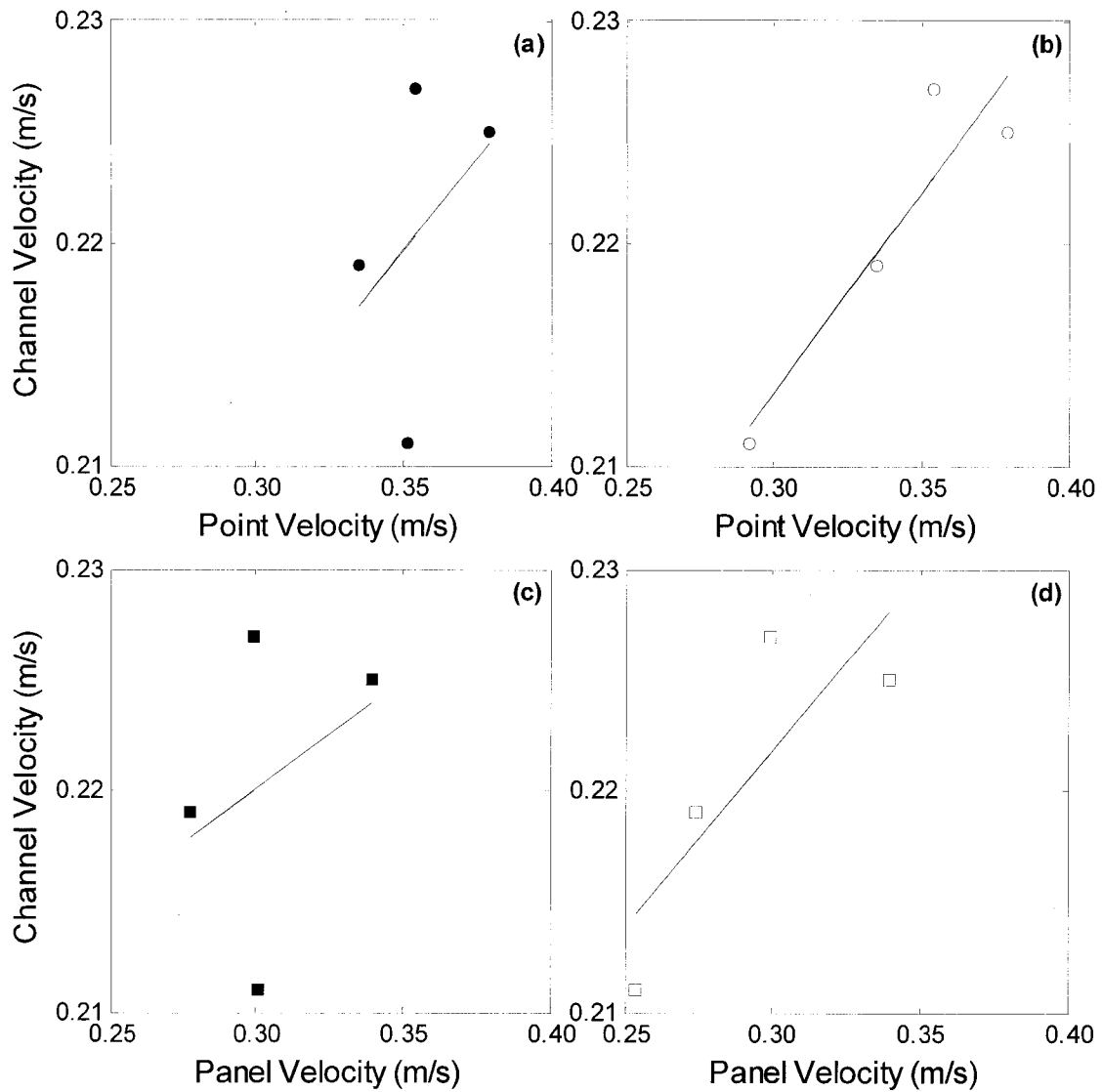
Figure 2.16. Summary data for Little Smoky River near Guy (07GH002): circles denote point velocities; squares denote panel velocities; closed symbols denote maximum values over the entire cross section; open symbols denote values obtained at the panel of maximum depth: (a) u_{max} ($R^2 = 0.80$, p = 0.58), (b) $u_{maxdepth}$ ($R^2 = 0.92$, p = 0.08), (c) V_{max} ($R^2 = 0.90$, p = 0.65), (d) $V_{maxdepth}$ ($R^2 = 0.88$, p = 0.18).

69
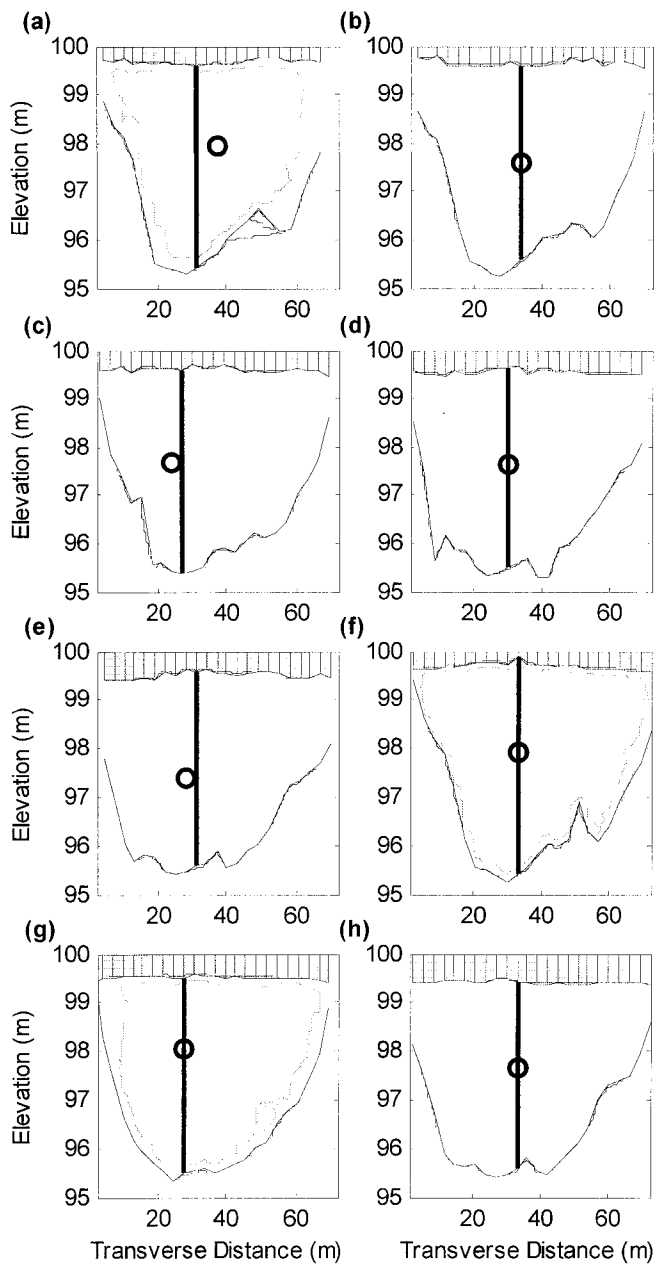
Figure 2.17. Velocity contour data for Yellowknife River at Outlet of Prosperous Lake (07SB002): circle indicates location of u_{max} and heavy vertical line indicates location of V_{max} (contour interval = 0.1 m/s): (a) 20-Dec-89, (b) 09-Jan-90, (c) 15-Feb-90, (d) 14-Mar-90, (e) 04-Apr-90, (f) 10-Dec-90, (g) 28-Jan-91, (h) 12-Mar-91.

70
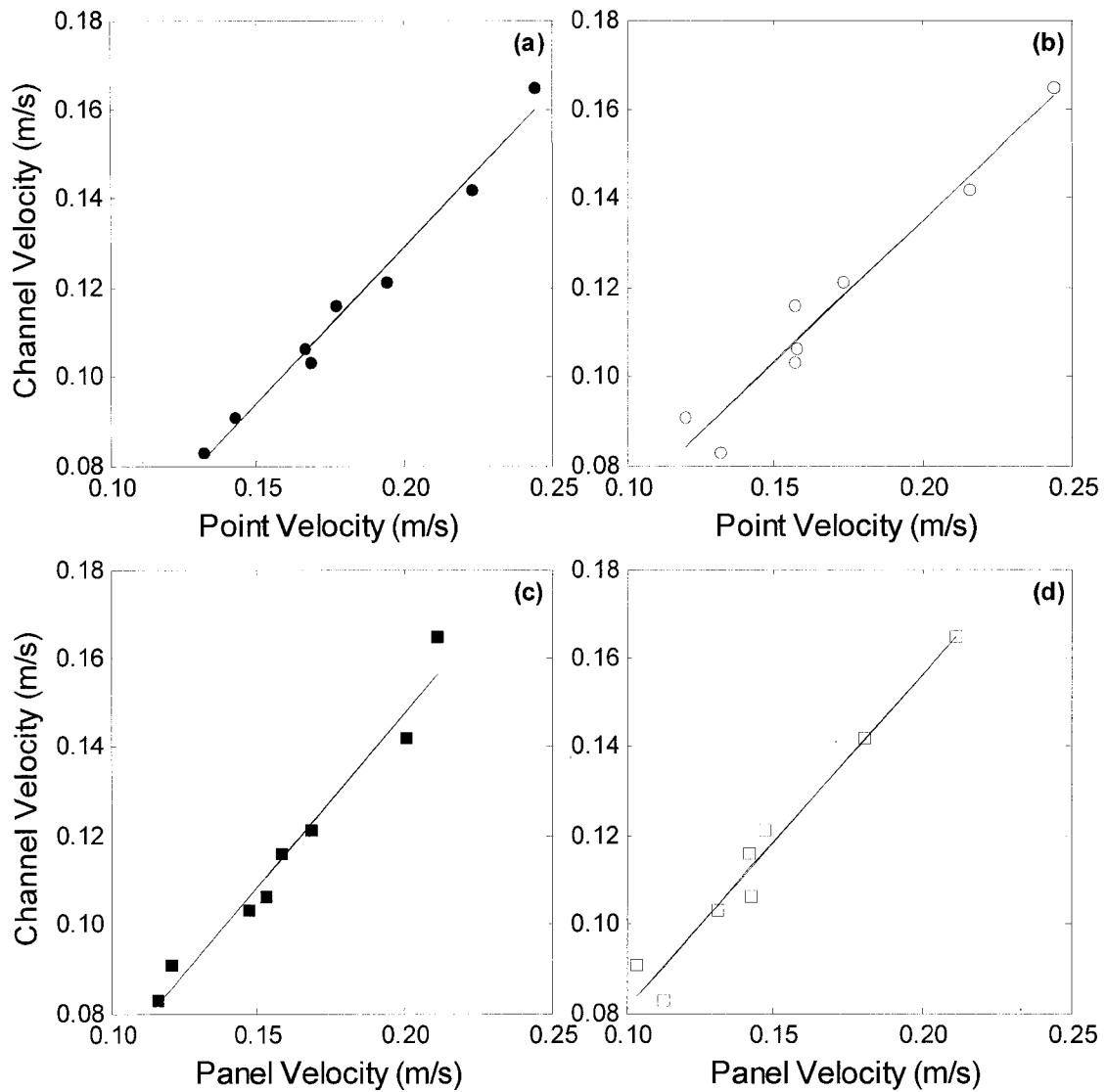
Figure 2.18. Summary Data Yellowknife River at Outlet of Prosperous Lake (07SB002): circles denote point velocities; squares denote panel velocities; closed symbols denote maximum values over the entire cross section; open symbols denote values obtained at the panel of maximum depth: (a) u_{max} ($R^2 = 0.98$, p = 0.00), (b) $u_{maxdepth}$ ($R^2 = 0.95$, p = 0.00), (c) V_{max} ($R^2 = 0.96$, p = 0.00), (d) $V_{maxdepth}$ ($R^2 = 0.96$, p = 0.00).

71
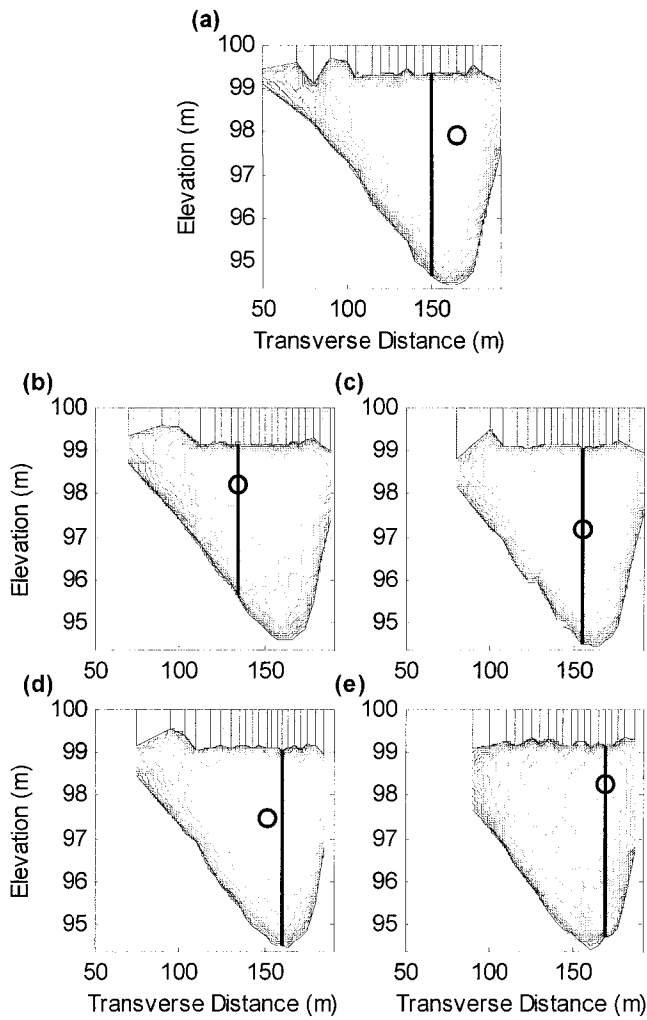
Figure 2.19. Velocity contour data for Yukon River at Carmacks (09AH001): circle indicates location of u_{max} and heavy vertical line indicates location of V_{max} (contour interval = 0.1 m/s): (a) 17-Jan-90, (b) 14-Feb-90, (c) 13-Mar-90, (d) 27-Mar-90, (e) 24-Jan-91, (f) 27-Mar-91, (g) 17-Apr-91, (h) 25-Apr-91, (i) 22-Feb-93, (j) 17-Mar-93, (k) 05-Apr-93.
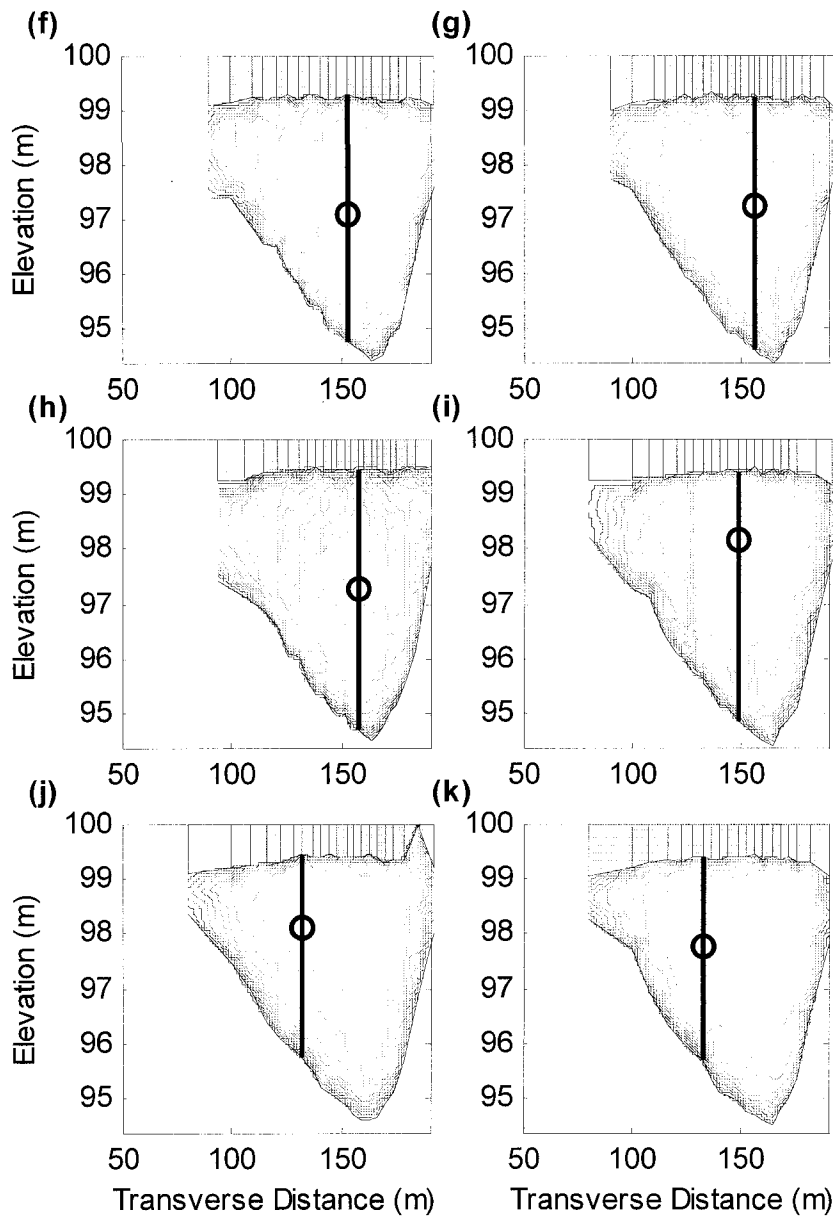
Figure 2.19 (continued). Velocity contour data for Yukon River at Carmacks (09AH001): circle indicates location of u_{max} and heavy vertical line indicates location of V_{max} (contour interval = 0.1 m/s): (a) 17-Jan-90, (b) 14-Feb-90, (c) 13-Mar-90, (d) 27-Mar-90, (e) 24-Jan-91, (f) 27-Mar-91, (g) 17-Apr-91, (h) 25-Apr-91, (i) 22-Feb-93, (j) 17-Mar-93, (k) 05-Apr-93.
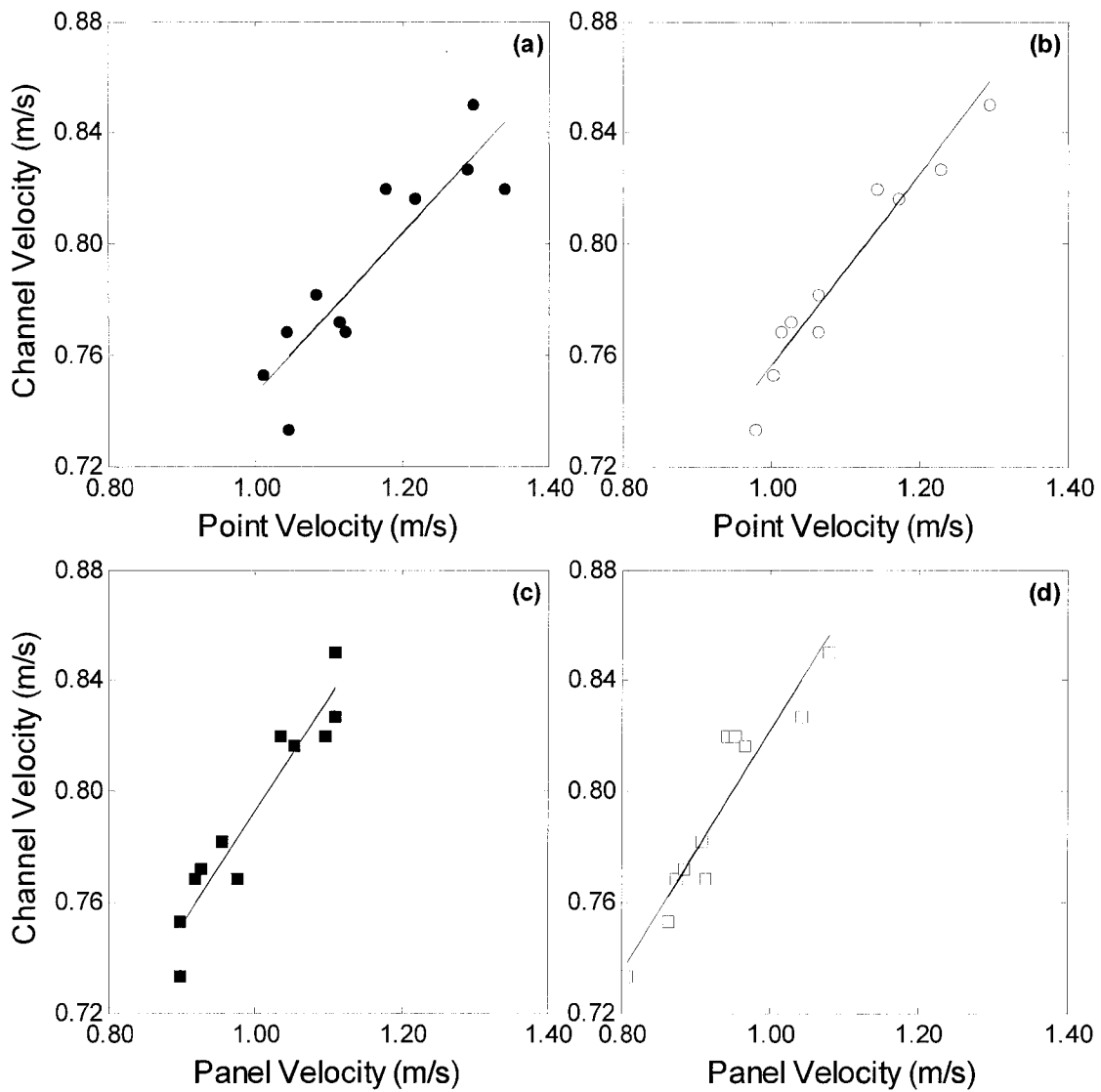
Figure 2.20. Summary data for Yukon River at Carmacks (09AH001): circles denote point velocities; squares denote panel velocities; closed symbols denote maximum values over the entire cross section; open symbols denote values obtained at the panel of maximum depth: (a) u_{max} ($R^2 = 0.80$, p = 0.00), (b) $u_{maxdepth}$ ($R^2 = 0.92$, p = 0.00), (c) V_{max} ($R^2 = 0.90$, p = 0.00), (d) $V_{maxdepth}$ ($R^2 = 0.88$, p = 0.00).

74
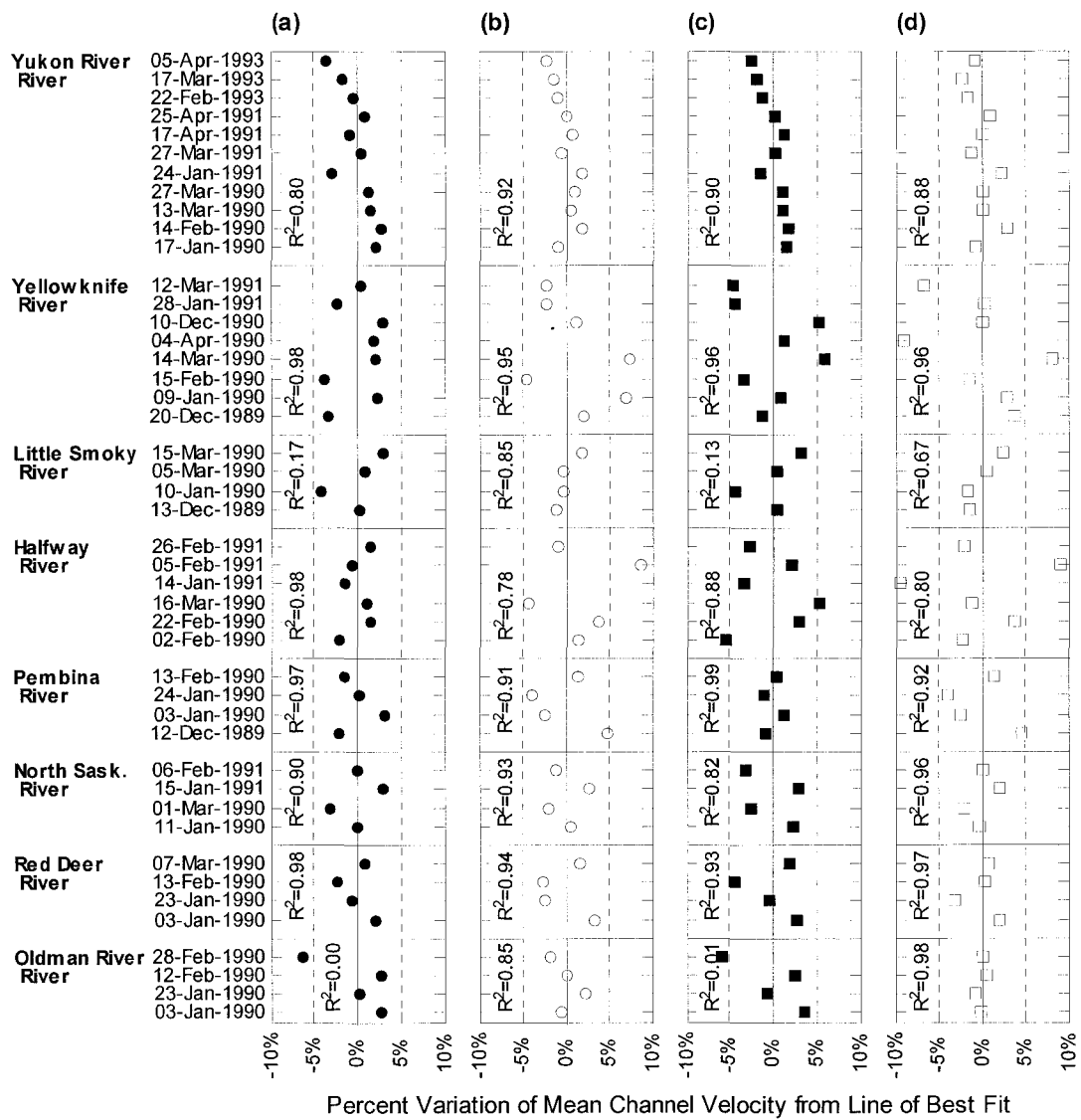
Figure 2.21. Percent variation of line of best fit for index velocities (a) u_{max}, (b) $u_{maxdept}$, (c) V_{max}, and (d) $V_{maxdepth}$.

75

2.7 References

Carter, R.W. and Anderson, I.E. 1963. Accuracy of current meter measurements. ASCE Journal of the Hydraulics Division, Vol. 89, HY4, pp. 105-115.

Chiu, C.L. 1988. Entropy and 2-D velocity distribution in open channels. ASCE Journal of Hydraulic Engineering, Vol. 114, No. 7, pp. 738-756.

Chiu, C.L. 1989. Velocity distribution in open channel flow. ASCE Journal of Hydraulic Engineering, Vol. 115, No. 5, pp. 576-594.

Chiu, C.L., Lin, G.F., and Lu, J.M. 1993. Application of probability and entropy concepts in pipe-flow study. ASCE Journal of Hydraulic Engineering, Vol. 119, No. 6, pp. 742-756.

Fulton, J.W. 1999. Comparison of conventional and probability-based modeling of open channel flow in the Allegheny River, Pennsylvania, USA. Unpublished M.S. Thesis, School of Engineering, University of Pittsburgh.

Hamilton, A.S., Hutchinson, D.G., and Moore, R.D. 2001. Estimation of winter streamflow using a conceptual hydrologic model: a case study, Wolf Creek, Yukon Territory. Proceedings of the 11th Workshop on the Hydraulics of Ice Covered Rivers, Ottawa, pp. 111-125.

Healy, D., and Hicks, F. 2001. Experimental observations on ice jam shoving. Proceedings of the 11th Workshop on the Hydraulics of Ice Covered Rivers, Ottawa, pp.

76

126-144.

Healy, D., Hicks, F., and Loewen, M. 2002. Unsteady velocity profiles under a floating cover. Ice in the Environment: Proceedings of the 16th IAHR International Symposium on Ice, Dunedin, New Zealand, Vol. 1, pp. 83-90.

Hicks, F.E., and Healy, D. 2003. Determining winter discharge based on hydraulic modeling. Canadian Journal of Civil Engineering, Vol. 30, No. 1, pp. 101-112.

Melcher, N.B. and Walker, J.F. 1992. Evaluation of selected methods for determining streamflow during periods of ice effect. U.S.G.S. Water Supply Paper 2378, 47 p.

Moore R.D., Hamilton A.S. and Scibek J. 2002. Winter streamflow variability, Yukon Territory, Canada. Hydrological Processes, Vol. 16, pp. 763-778.

Pelletier, P.M. 1988. Uncertainties in single determination of river discharge: a literature review. Canadian Journal of Civil Engineering, Vol. 15, No. 5, pp. 834-850.

Pelletier, P.M. 1989. Uncertainties in streamflow measurement under winter ice conditions a case study: the red river at Emerson, Manitoba, Canada. Water Resources Research, Vol. 25, No. 8, pp. 1857-1867.

Tsai, W.F., and Ettema, R. 1994. Modified eddy viscosity model in fully-developed asymmetric channel flows. ASCE Journal of Engineering Mechanics, Vol. 120, No. 4, pp. 720-732.

Teal, M.J., and Ettema, R. 1994. Estimation of mean flow velocity in ice-covered channels. ASCE Journal of Hydraulic Engineering, Vol. 120, No. 12, pp. 1385-1400.

Walker, J.F., and Wang, D. 1993. Measurement of flow under ice covers in North America. ASCE Journal of Hydraulic Engineering, Vol. 123, No. 11, pp. 1037-1040.

Wang, D. 1993. Cross-sectional velocity distribution of flow under ice. Proceedings of the CSCE Annual Conference, Fredericton, N.B., pp. 119-129.

3.0 Experimental Study of Ice Jam Formation Dynamics[2]

3.1 Introduction

River ice jams often cause very damaging flood events. For improved floodplain management, and to minimize the threat to public safety, it is desirable to be able to predict flood levels associated with river ice jam occurrence. A number of steady state computer models are available to the practitioner for calculating ice jam profiles, such as the U.S. Army Corps of Engineers' HEC-RAS model (Daly and Vuyovich 2003) and the RIVJAM model (Beltaos and Wong 1986). The ice jam routine used in HEC-RAS is essentially the same as that developed by Flato and Gerard (1986). However, since these models assume steady flow and ice jam formation is generally considered to be a highly dynamic process, predictions from such models may not be sufficiently representative of real ice jams. More sophisticated models incorporating dynamic ice jam formation effects have been developed (e.g. Shen et al. 1995; Zufelt and Ettema 2000). However, to date there is still a lack of validation data available to model developers.

---

[2] This chapter was submitted for publication in the ASCE Journal of Cold Regions Engineering. It has completed the first round of review and a revised manuscript was submitted to the editors in late February 2006.

A key factor limiting the availability of such data is the fact that it is logistically difficult, and extremely unsafe, to attempt to measure the variation in discharge and ice accumulation thickness during an actual ice jam consolidation event. Thus, experimental investigations are necessary to complement our understanding of the underlying processes gained from field studies at specific sites. However, experimental studies of ice jams to date have been limited either to steady flow (Saadé and Sarraf 1996) or to primarily qualitative observations of the unsteady processes (Zufelt 1990 and 1992). Lever et al. (1997) conducted physical model tests of an ice control structure (ICS). The published results focused mainly on the performance of the ICS with little attention to the resulting ice jam accumulations. Although these studies were extremely valuable in developing an understanding of ice jam evolution processes, quantitative data are still needed for the validation of modern numerical models. The purpose of this study was to investigate the dynamic processes associated with ice jam formation, and in particular to provide quantitative observations of thickness and discharge variations during ice jam formation events.

Ice jam development is an inherently unsteady process as water goes into storage when the ice cover thickens and roughens. Even if the supply flow upstream of the jam (carrier discharge) in a stream is relatively constant, temporal and spatial variations in discharge can be expected during ice cover consolidation ("shoving"). For this investigation, ice jam formation under steady carrier flow conditions was investigated such that any unsteady variations in carrier discharge, ice thickness and water level could be directly attributed to the ice jam formation dynamics.

80

3.2 Experimental Apparatus

Figure 3.1 presents a schematic of the experimental apparatus used. The experiments were carried out in a 32 m long recirculating flume located in the T. Blench Hydraulics Lab at the University of Alberta. This rectangular flume had 0.91 m high sidewalls, a width of 1.22 m, and was set to a constant slope of 0.00164 for all runs. The bed was sheet metal (slightly rusted and rough textured) and the walls were Plexiglas. Manning's n for the channel, under open water flow conditions, ranged from 0.020 to 0.025. For most experiments, a wire mesh was attached to the sides of the flume to facilitate the development of an "ice-ice" shear interface along the walls; the interface was believed to be more representative of natural conditions. A series of tests without the wire mesh (smooth Plexiglas walls only) were also conducted for comparison.

3.3 Test Configuration

For the tests described herein, discharges of 35 to 65 L/s were supplied to the head tank. The flow entering the flume was conditioned with a combination of flow "straighteners" and steel pipes to ensure flow symmetry in the measurement zone (confirmed by detailed velocity measurements). At the downstream end of the flume, water levels were controlled with a 0.15 m high broad crested weir, along with a series of adjustable vertical vanes spaced across the channel. A 1.9 cm x 1.22 m x 1.22 m sheet of plywood was positioned 24.5 m downstream of the head box to simulate an intact ice cover; this sheet was allowed to float freely. Floating rigid insulation was used downstream of this plywood sheet for the remainder of the flume's length, to simulate an intact ice cover. A

81

heavy wire screen was fastened to the upstream edge of the plywood to facilitate initiation of an ice accumulation.

3.4 Model Ice Material

Ice floes were simulated using a mixture of rectilinear polyethylene pieces of varying size (specific gravity = 0.92). Preliminary tests were run using uniform sizes; however, it was found that ice transport, rather than consolidation, dominated the ice cover thickening process unless a mixture of sizes were used. The distribution of sizes used in the composite mixture is presented in Table 3.1, chosen to approximate typical size distributions and floe-size-to-river-width ratios found in the field. Table 3.1 provides the most precise and meaningful description of the mass of model ice material used in these tests. While appropriate for materials that lend themselves to a grain size analysis, a median particle diameter, or other such descriptive term, for our model ice material is not offered since for our particle "distribution", it would not be very meaningful.

Choice on the size and nature of the mixture of floes were based on previous investigations (Hicks and Bonneville 1998) and were developed mainly by a trial and error approach to ensure reproducibility in ice cover consolidation behavior. For this reason, large anomalous pieces (although also typical of many field situations) were not incorporated in the mixture. The bulk porosity, defined as the porosity of the ice mixture when randomly poured in a bucket, was found to average 0.49, based on repeated measurements (Table 3.2). The synthetic ice floes used had sufficient tensile and compressive strengths to be considered unbreakable and incompressible.

82

Perhaps the most limiting characteristic of using polyethylene and other similar materials as a synthetic ice material is its non-wetting tendency, which raises the potential significance of surface tension effects. Previous investigators have suggested that surface tension effects could be minimized "by allowing natural accumulation of micro-organisms" (Wuebben 1995) and in this study it was found that when the model ice material was left wet for several days, surface tension effects were minimized by what appeared to be the development of a biological film on the surface of the plastic pieces. Zufelt (1992) also found that when "plastic beads" were left wet for several days, surface tension effects were minimized.

A series of tests were also conducted to determine both the dry and buoyant angle of repose of the synthetic ice mixture (Appendix A). The average dry angle of repose was 29°, the average buoyant angle of repose was 42° for model ice that was initially dry, and 46° for model ice that had soaked in water for several days. Figure 3.2 illustrates the techniques used to determine the dry and so-called buoyant angle of repose. The method used to determine the different angle of repose values was not intended to be an exhaustive method for determining the relative strength of the model ice rubble. It was used mainly for interpretive purposes and to get a first approximation of the relative difference in the strength of the model ice material under two different conditions (dry and buoyant). Differences in the surface irregularities for the dry and buoyant cases were indistinguishable. Also, it is plausible that the porosities were different for both cases and that a floating ice jam may pack differently than was observed under the quiescent test conditions.

3.5 Testing Procedures and Measurement Techniques

At the beginning of each experiment, a steady discharge was introduced under open water conditions with the plywood sheet and rigid insulation in place (Figure 3.1). The flow was allowed to stabilize and the resulting open water surface profile upstream of the plywood sheet was measured using a point gauge equipped with a vernier, enabling measurements to the nearest 0.1 mm.

Figure 3.3 presents photos taken during the introduction of the model ice material to the flow and a view from the top of the accumulation as the ice was being delivered. The model ice material was manually fed into the flow from a hopper located at the upstream end of the flume (Figure 3.3b). A piece of rigid plastic, positioned below the hopper, was used as a chute to facilitate the manual introduction of the model ice floes onto the water surface with minimal disturbance. Efforts were made to keep the delivery rate constant, yet the duration of loading did vary from 10 to 24 minutes, with an average of 17 minutes. Once the ice cover stabilized (typically after 1 to 1.5 hours) the jam was assumed to be in static equilibrium and the resulting water surface and ice thickness profiles were measured. The average transverse thickness of the ice accumulation was viewed from the side using a scale and setsquare. Temperature readings were also taken periodically during each test and the variations over a full day of testing were less than one degree Celsius.

Continuous water level, ice thickness, point velocity and discharge data were also collected during each test. The following parameters were measured directly and

84

recorded to a digital file using a personal computer and the LabView$^{©}$ data collection software program: discharge indicated by the magnetic flow meter; point velocities at stations 10 and 20 m downstream from the head tank (indicated by Prandtl tubes equipped with pressure transducers); and discharge over the outlet weir (indicated by an automated water level transmitter). The date and time associated with each sample (sampler rate = 1 Hz) was attached to the digital file. Details of these specific measurements are presented below.

3.5.1 Flume Inflow and Outflow Measurements

Inflow to the flume was measured directly by the magnetic flow meter where the meter output in volts was converted directly to a discharge value by the LabView$^{©}$ software package and recorded directly to a digital file. The accuracy of the magnetic flow meter was evaluated by comparison to direct discharge measurements obtained from detailed integrated velocity profile data taken under open water conditions at measurement station 20 m for a variety of steady carrier discharges. Appendix B presents the results of this analysis, indicating that the actual discharge was consistently overestimated by the magnetic flow meter by 4% (R^2 = 1.0). Consequently, all inflow discharge data obtained by the magnetic flow meter were corrected accordingly.

Outflow (discharge over the outflow weir) was deduced from water level data collected over the weir using an automated capacitance water level recorder. It was determined that there was a linear relationship between discharge and the water level transmitter output, in volts (R^2 = 0.9997). This linear relationship facilitated direct estimates of

85

discharge over the weir with knowledge of the initial and final steady state discharge values provided by the magnetic flow meter.

3.5.2 Water Level and Ice Thickness at Measurement Stations 10 and 20 m

Water level and ice thickness data were recorded at measurement stations 10 and 20 m downstream from the head tank using video cameras. A date and time stamp was added to all video data to facilitate synchronization with the digitally recorded data. To improve the visibility of the water surface, a 6 mm inside diameter tap (introduced near the bottom of the flume sidewall) was fitted with a flexible plastic (piezometer) tube with a 6 mm inside diameter, which was then secured to the wall of the flume next to a measurement scale. Dye was also added to the water in the piezometer tube to assist in visualizing water levels. Localized pressure fluctuations due to flow separation effects created by the hole introduced in the wall were expected to cause minor water level variations in the piezometer tube. These expected fluctuations along with an anticipated delay in response in the piezometer-tube were not visually apparent, as compared to the actual observed water levels.

The elevations of the water surface and bottom of ice above the bed were referenced to the known initial water surface elevation recorded at that location prior to the start of each test. The initial water surface elevation was related to the initial water surface level indicated on the scale visible in the video data and subsequent values were adjusted to match changes in readings based on the video data. The data were then interpolated linearly between readings at one-second intervals to facilitate use in subsequent analyses

86

with continuous point velocity data. The uncertainty of the water and bottom of ice levels obtained in this manner were estimated to be ± 1 mm and ± 1 cm, respectively. Due to the rough texture and variable thickness of the ice accumulations, the latter uncertainty was larger.

3.5.3 Discharge Estimates based on Point Velocity Data at Stations 10 and 20 m

Healy and Hicks (2004) demonstrated that the channel centerline's vertically averaged velocity provided a good estimate on the average channel velocity for this experimental apparatus. The resulting relationships between the mean centerline and average section velocity facilitated estimates of the discharge by simply taking the product of the average channel velocity and area of flow. The area of flow was based on the known width of the flume and the depth of flow obtained from measured water surface or bottom of ice elevations.

Point velocity data, measured with Prandtl tubes (velocity probes), were used to obtain estimates of the average centerline velocity. Details on the setup and arrangement of the velocity probes are presented in Appendix B. Figure 3.4 presents a schematic of the two different arrangements used. Figure 3.4a shows the 3-probe arrangement where the lowermost probe was placed between the known initial and estimated final 80% depths of flow. The second and third probes were situated at the known initial and estimated final 20% depths of flow, respectively. The 3-probe arrangement allowed for probes to be situated at both stations 10 and 20 m. Previous investigators (Teal and Ettema 1994) demonstrated that the vertically averaged velocity at an ice covered section can be

87

accurately determined by the average of two point velocities measured at the 20% and 80% depths below the ice. These locations correspond to the theoretical Gauss point locations (i.e. 21.13% and 78.87% of depth) for which the average of the two corresponding point velocities gives the vertically averaged velocity at that section (Hicks and Steffler 1996). Through comparison to Acoustic Doppler Velocimeter data, collected simultaneously with data collected from the velocity probes used in this investigation, Healy et al. (2002) demonstrated that practical estimates of vertically averaged velocities using this method could be made to within 5% accuracy for unsteady flow conditions (also refer to Chapter 2).

Figure 3.4b presents an image of the 8-probe arrangement where 8 evenly spaced probes were placed at the channel centerline at station 20 m, only. For this arrangement, the centerline velocity was taken as the integrated vertical average of all the probes (with knowledge of the bottom of ice elevation). Efforts were made to ensure that the probe tips were oriented in the direction of the flow. Specifications provided by the manufacturer indicated readings to be accurate within 2% for angles of attack of up to 30°. For these experiments the attack angles were generally less than 5° and never more than 15°; thus errors associated with oblique angles of attack could be considered to be negligible.

3.6 Experimental Observations

A total of 40 experimental simulations were conducted over the range of carrier discharges feasible with the apparatus. Table 3.3 presents a summary of the salient

88

parameters associated with these runs.

3.6.1 Qualitative Overview of Ice Jam Formation

During ice cover formation, ice initially accumulated through a combination of juxtaposition, underturning, and hydraulic transport. As the model ice first arrested (at either the floating toe or progressing head of the accumulation) it tended to juxtapose, with pieces rearranging themselves to provide a complete cover of ice over the open water approximately one layer thick. In conjunction with the process of juxtaposition, some of the ice pieces would underturn and deposit under the leading edge and deposit immediately downstream without becoming entrained in the flow. Other pieces would be become entrained in the flow and would transport below the cover and eventually come to rest downstream of the progressing head. This active portion of the accumulation, where the model ice was transported and deposited downstream of the leading edge, consistently extended approximately one to one and a half channel widths downstream from the leading edge. The processes above can be described as hydraulic thickening in which local hydrodynamic forces at the leading edge dominate the resulting jam thickness.

In addition to these hydraulic thickening processes, which were localized to the vicinity of the leading edge, the accumulation would subsequently further thicken by shoving processes. While this consolidation behavior was not dramatic, it was readily apparent when playing back video in accelerated viewing mode. Inspection of additional video observations, obtained from a submersible camera looking up from the channel bed

89

confirmed this shoving behavior. The degree of shoving varied from test to test and in some cases portions of the accumulation appeared to consolidate more in the middle to upper reaches than in the downstream reaches near the floating toe.

3.6.2 Stable Ice Accumulation Thickness Profile Characteristics

Figure 3.5 illustrates the resulting model ice jam profiles created during three representative tests under constant carrier discharges of 34, 39, and 48 L/s. The profiles described in Figure 3.5 were measured after there was no detectable movement of either the individual ice pieces or the entire ice jam. The shaded regions of the jam profile indicate the mid-portion of the jam used to describe the average formation jam thickness associated with subsequent figures and analyses. The accumulations at higher discharges were completely consolidated (e.g. Figure 3.5c) while for lower discharges the thickness of the covers were not entirely attributable to consolidation. Near the head, the jams were in some cases thicker than at the downstream portion, due to the entrainment and subsequent deposition of ice pieces near the leading edge (e.g. Figure 3.5a). In other instances, near the toe region the forces were taken up partially by the floating plywood cover; that is, not all of the forces were taken up by the flume walls. Thinner accumulations resulted in this area (e.g. Figure 3.5a and 5b). The forces were transferred to the floating plywood sheet directly through juxtaposed surface ice. For the tests with higher discharges the resisting capacity of these juxtaposed pieces was exceeded and they rearranged to allow for thickening by consolidation, creating a more classical jam shape near the toe region (e.g. Figure 3.3c). To facilitate comparison of the various measured ice jam profiles, dimensionless plots were generated based on the following parameters:

90

- non-dimensional position = the streamwise distance from the leading edge of the model ice jam (head), x, divided by the length of the ice jam, L_{jam};

- non-dimensional thickness along the length of the model ice jam = the observed thickness, t_{jam} at location x, divided by the average jam thickness, t_{avg}.

Figure 3.6 presents plots of non-dimensional thickness versus non-dimensional length, grouped in accordance to their carrier discharge. As described above and indicated in Figure 3.5, the accumulations tended to be slightly thicker than average near the head and slightly thinner than average near the toe for lower discharges (Figures 6a and 6b); while the thickness of accumulations resulting from higher carrier discharges were larger and tended to be more constant over the full length of the accumulation. Inspection of the formation jam profiles with thinner ice thickness near the toe region would suggest that perhaps the covers did not have adequate time to fully consolidate. However, once these jams had stabilized, usually within fifteen to thirty minutes, there was no perceptible change in the profile thickness or length over additional periods of some hours. The accumulations had reached a state of equilibrium for the given discharge and flume arrangement.

Figure 3.7 presents a plot of the average thickness of the formation jam versus the constant carrier discharge. The groupings corresponding to Figures 6(a) through 6(d) , are also indicated on Figure 3.7. Closed symbols denote those tests where the wire mesh was in place, while open symbols denote those tests where the wire mesh was not used on the sidewalls. In general, Figure 3.7 suggests that the average jam thickness increased

91

with carrier discharge. For comparable discharges, the average thickness values varied by 10 to 25%, and the presence or absence of the wire mesh had no apparent impact on the resulting jam thickness.

Observations indicated that there were three distinct regions that could be identified over the length of the observed formation jams. The first, denoted as the toe region, corresponded to the downstream limit of the jam where hydrodynamic forces near the surface were minimized by the presence of the floating cover and wire screen. As a result, hydraulic thickening was minimized and the thickness tended to be less in this area. The second region extended upstream from the toe region towards the leading edge of the jam. Upon the initial formation of the jam (shortly after the last pieces of ice were added to the flow), this middle region of the jam, extended upstream to a point very close to the leading edge. However, after all of the ice had arrived at the leading edge, further erosion and deposition at the leading edge occurred, creating a thicker region in the vicinity of the leading edge; thus defining a third region denoted as the head.

For each test a middle portion of the jam was defined such that the thickness did not depend on the localized effects experienced in the head and toe regions. These mid-jam portions are indicated as the shaded areas on Figure 3.5. Existing theories describing the thickness of an accumulation are primarily concerned with this region and for special cases this region is believed by conventional wide-jam theory to maintain a constant thickness referred to as its equilibrium thickness. This equilibrium thickness has generally been associated with the maximum water level attainable by an ice jam for a given steady discharge (Beltaos 1995, Ashton 1986). However, recent computational

92

modeling investigations suggest that the so-called equilibrium thickness and accompanying water level may not be represent the maximum for jams formed under a constant discharge (Zufelt and Ettema 1997, 2000).

Figure 3.8 presents the relationship between the average observed jam body thickness, non-dimensionalized by the depth to the phreatic surface, and the corresponding Froude number, $F = V_h^2/(gh)^{0.5}$, where V_h is the average velocity under the main jam body, h is the depth of flow under the main jam body, and g is the acceleration due to gravity. The plot demonstrates a clear relationship between the Froude number and the resulting thickness profile, suggesting that the ratio of inertial to gravity forces is important to the jam formation process. More specifically, the jam thickness is largely a function of gravity, depth of flow, and velocity. These parameters combined, define the applied forces experienced by the ice jam accumulation – the down-slope component of weight and the shear exerted by the flow underneath the accumulation. Also included on the plot is the line describing the theoretical jam thickness corresponding to hydraulic thickening of a narrow type jam. The data suggest that these experimental jams were thickened by processes in addition to those associated with the classical narrow jam formation and perhaps these jams behaved more like the wide type ice jam, thus confirming the observation of consolidation in the formation of these accumulations. Further investigations suggested that there was no apparent relationship between accumulation porosity and either jam thickness or Froude number. It is likely that the ice jams were too thin to produce substantial compaction, thus minimizing the relative dependence on porosity.

93

3.6.3 Continuous Observations during Formation of the Stable Accumulations

Figures 3.9 through 3.13 present the continuous time series data obtained for the tests presented in this paper corresponding to constant carrier discharges of 34, 39 and 48 L/s. In each of these figures, subfigure (a) presents the observed elevation of the water surface, bottom of ice, fixed probe locations, and theoretical Gauss point locations – all with respect to a bed elevation of 0 m. Subfigure (b) presents the estimated centerline and respective channel section velocities. For the cases where the 3-probe arrangement was used (Figures 3.9, 3.10, 3.12, and 3.13), the centerline velocity was taken as the average of the lowermost probe (assumed to represent the theoretical 80% Gauss point depth) and the nearest of the two uppermost probes to the theoretical 20% Gauss point depth. A decision was made as to the point at which the 20% Gauss point velocity switched from one probe to the other; this point is referred to as the demarcation point and is indicated in subfigure (a). Where the 8-probe arrangement was used (Figure 3.11), the centerline velocity was taken as the vertically integrated average represented by the 8 probes. The demarcation point also indicated the point at which the index velocity relationship between the centerline average and channel section average changed. For comparison, the velocity, $V=Q_{IN}/A$, was also included where: Q_{IN} is the carrier discharge recorded by the magnetic flow meter and A is the product of the flume width and depth of flow. Subfigure (c) presents the continuous discharge, $Q_{sta\ 10m}$ or $Q_{sta\ 20m}$ (depending on the location), estimated as the product of the average channel velocity and the depth of flow. The carrier discharge, Q_{IN}, and flow exiting the system over the weir, Q_{out}, are included for comparison. Subfigures (d) and (e) provide a visual representation of the index

velocity relationships used to find the average channel velocity from the centerline velocity. The "selected relationship", indicated by the solid line is superimposed over observed data for index relationships under steady state conditions. Subfigures (d) and (e) describe the relationships used before and after the demarcation point shown in subfigure (a), respectively.

While inflow and outflow for the system in each test were near constant, there were apparent variations in the estimated discharge at measurement stations 10 and 20 m. Inspection of the figures suggested that the flow exiting the system, Q_{OUT}, did not vary significantly over the duration of each test and by conservation of mass, the variations in discharge at station 10 and 20 m should be of a comparable magnitude as those variations experienced at the exit of the system. To explore this matter further a simple analysis on storage estimates was carried out. It was expected that as the jams formed water would go into storage. The amount of water that went into storage could then be estimated by two methods. A comparison of storage estimates by these methods is illustrated in Figure 3.14. The first method was to compare the measured open water surface profiles to the formation jam profile some time after it had reached its final stable condition. Storage estimates made in this manner suggested that while the level of the phreatic surface increased slightly for each test, the water entering the system did not in fact go into storage since the apparent increase in storage represented by higher water levels was exceeded by the volume of ice added in each test to the addition of the model of ice (approximately 0.35 m³). There was a slight net outflow from the system for each test. Storage volume estimates found in this manner were then compared to those estimated by

95

integrating the difference between the inflow and outflow hydrographs. Storage estimates found by this second approach varied by plus or minus 0.8 m^3, while storage estimates found by the first approach were more closely grouped and varied by about 0.5 m^3. The length of the time the inflow and outflow hydrographs were integrated over was 30 minutes. The absolute storage volumes calculated by this approach were nearly 1 m^3. To achieve this volume over the integration interval an average difference in discharge would be roughly half a liter per second (around 1% of a typical carrier discharge). Accuracies of 1% were not achieved by any of the methods used for estimates on discharge. Thus, the volume of water attributed to storage for any of these tests was considered to be negligible when compared to the expected accuracy of the instrumentation.

The data presented in Figure 3.9 suggest discharge variations at station 10 m of up to 25%. Estimates on the average channel velocity for this case are suspect. These differences are most likely due to a lack in "performance" of the selected index velocity relationship and poor capture of point velocity data at the theoretical Gauss point location. For the same test, estimates of the average channel velocity at station 20 m provided discharge estimates that appeared reasonable (Figure 3.10), and suggested that the discharge in the accumulation was near constant throughout the duration of the test. Figure 3.11 presents the results of a test where the 8-probe arrangement was used at measurement station 20 m. Here the estimated discharge appeared to vary by up to roughly 7%. Figure 3.12 presents discharge estimates at station 10 m for a constant carrier discharge of 48 L/s. The head of the formation jam never reached this station.

96

The probes captured the 20% depth well and good estimates on the average channel velocity were achieved. The estimated discharge at this station closely followed the steady carrier discharge throughout the duration of the test. Figure 3.13 shows that reasonable estimates on discharge were achieved before and after passage of the progressing head of the jam during formation, even when the 20% depth was missed by the middle probe. A sharp increase in discharge was estimated upon the initial arrival of the ice front at the measurement station. It is suspected that this jump in flow was not realized and is attributed to poor representation by both the actual centerline average velocity and selected index velocity relationship.

With respect to all of the estimates of the average channel velocities, additional sources of error in discharge estimation were in some instances attributable in part to localized effects in the vicinity of the velocity probes due to the movement of ice. Also, it was not uncommon for model ice pieces to interfere with the probe tips and these effects, combined with the potential for larger coherent eddy structures forming in the vicinity of the probes due to local roughness elements (larger than the average of the cross section), all contributed to measurements indicating an exaggerated unsteadiness in the flow at these locations.

Thus, overall, the observations suggested that the discharge did not vary significantly within the accumulation and that noticeable apparent variations were largely attributable to deficiencies in capturing appropriate point velocity data representative of the channel average.

97

3.7 Discussion

The generally accepted classifications describing ice jams follow the pioneering work of Pariset et al. (1961) and Pariset et al. (1966) who introduced the concepts of narrow and wide channel type ice jams. For the narrow case, the thickness is largely dictated by the hydrodynamic forces encountered at the leading edge, with the following conditions satisfied for narrow jams:

$$[3\text{-}1] \quad V_u = \sqrt{2g(1-p)(1-s_i)t} \, ,$$

where: V_u is the average velocity under the jam; g is the acceleration due to gravity; p is the jam porosity; s_i is the specific gravity of the model ice (0.92); and, t is the thickness of the narrow jam.

Figure 3.15 presents a comparison between the observed average thickness of the middle portion of the jam, $t_{observed}$, and that obtained using equation [3-1] illustrating that, for all of the formation jams observed in this investigation, accumulations were thicker than predicted by the narrow jam theory. The thinnest accumulations were roughly 25% thicker than predicted by equation [3-1] and the thickest were approximately twice that predicted by equation [3-1]. This confirms that, while the hydrodynamic forces associated with narrow jam thickening were present, they did not entirely account for the resulting jam thicknesses observed in these experiments.

The second class of ice jams defined by Pariset et al. (1961, 1966) are the so-called wide channel jams, for which all of the applied forces on the ice accumulation are transferred

98

through the mass of ice and ultimately taken up by the banks. By applying the usual uniform flow assumptions and neglecting cohesive forces within the ice accumulation, the following relationship can be used to describe the equilibrium thickness of a wide jam for a rectangular channel (Ashton 1986),

$$[3\text{-}2] \quad \mu(1 - \frac{\rho_i}{\rho})\rho_i g t_{eq}^2 - (g\rho_i SB)t_{eq} - \tau_i B = 0,$$

where: μ is a coefficient defining the internal strength of the ice accumulation; t_{eq} is the equilibrium ice thickness; S is the stream slope; B is the width of the channel; and τ_i represents the applied forces under the ice cover resulting from the flow. Defining $\tau_i = \rho g R_i S_f$ (R_i is the hydraulic radius of the ice-influenced portion of the flow and S_f is the friction slope), the equilibrium thickness can be written as:

$$[3\text{-}3] \quad t_{eq} = \frac{BS}{2\mu(1-s_i)}\left\{1 + \sqrt{1 + \frac{4R_i\mu(1-s_i)}{s_i BS}}\right\},$$

where, the specific gravity of ice, $s_i = \rho_i/\rho$.

Figure 3.16 presents a comparison between the observed average thickness of the jam body, $t_{observed}$, and the theoretical wide channel jam equilibrium thickness defined by equation [3-3]. In most cases the main body did appear to have a section of near constant thickness. However, it may be reasonable to argue that sufficiently long accumulations were not achieved to get a true equilibrium section. The internal strength of the accumulation is defined by the parameter ϕ, which for usual soil mechanics theory represents the internal angle of friction, which for cohesionless, incompressible

99

materials (e.g. sands) can be approximated as the dry angle of repose. The angle of repose, ϕ, describes the internal strength of the accumulation and appears in the well know jam stability coefficient, μ. shown in equation [3-3] as $\mu = k_o k_1 K_x (1-p)$, where k_o is a coefficient of lateral thrust roughly taken as 1/3, k_o=tan(ϕ), K_x=tan^2(45+ϕ/2), and p is porosity. Here, taking the dry angle of repose as the internal angle of friction suggests that the theoretical equilibrium thickness exceeds those observed in the experiments; whereas applying the buoyant angle of repose, the theoretical equilibrium thickness underestimates the observed thickness. Thus, in general, the wide jam approach seems to potentially describe the observed thickness, depending on the choice of the angle of repose.

Neglecting cohesive forces and assuming $s_i = 0.92$, Beltaos (1983) developed the following non-dimensional depth relationship for wide channel equilibrium ice jams:

$$[3\text{-}4] \quad \eta = \frac{H}{SB} = 0.63 f_o^{1/3} \Omega + \frac{5.75}{\mu} \left[1 + \sqrt{1 + 0.11 \mu f_o^{1/3} (f_i / f_o) \Omega} \right],$$

where: η is the non-dimensional depth; H is the depth of water from the bed to the phreatic surface; f_o is the composite friction factor for the flow under the ice cover; f_i is the friction factor associated with ice-affected portion of flow; and the dimensionless discharge parameter $\Omega = (q^2/gS)^{1/3}/SB$ (where q is the discharge per unit width of channel, g is the acceleration due to gravity, S is the slope of the channel, and B is the width of the channel). The main independent variable found in equation [3-4] is Ω, which combines discharge, channel width, and slope. Figure 3.17 presents the field data collected/collated

100

by Beltaos (1983) using the non-dimensional relationship in equation [3-4], as well as the laboratory results from this investigation. The plot suggests that these experimental results compare well with the field observations.

3.8 Conclusions

Experimental investigations of river ice jam formation under steady carrier flow discharge conditions were conducted in a rectangular flume using synthetic (polyethylene) ice pieces of varying size. In addition to documenting the resulting ice jam profiles, continuous measurements of the variations in flow depth, ice thickness and discharge were obtained at key stations within the developing ice jam.

A total of 40 experimental runs were conducted over a range of steady discharges, and the resulting observations suggest that all accumulations initially developed by hydraulic thickening (narrow jam formation), and then subsequently thickened further by consolidation (wide jam formation). The upstream end of the accumulation (approximately 1 to 1.5 channel widths in length) continued to thicken hydraulically throughout the formation period. The presence or lack of a wire mesh along the inside of the Plexiglas walls did not appear to have an affect on the configuration of the resulting ice jams. Comparison of experimental observations to narrow channel jam theory confirm that hydraulic thickening dominated the ice jams formed at lower discharges, but did not fully explain the ultimate thickness of these accumulations. With increasing discharge, ice jam formation departed consistently further from the narrow channel jam theory predictions.

101

These experiments involve the first measurements of discharge variation during ice jam formation, providing new insights on ice jam formation processes. Because the experiments involved ice jam formation under steady carrier discharges, any observed spatial or temporal discharge variations would be attributable to the ice jam formation itself. The observations for these 40 experimental runs all support the conclusion that discharge variations during ice jam formation under steady ambient flow conditions are small; and generally found to be within the measurement errors of the experimental method. Comparison of the observed experimental ice jam thicknesses with existing steady flow theories indicate that wide channel ice jam theory provides a reasonable approximation of the formation jams studied in this investigation. As expected, the experimental observations suggest that the analyses of jams formed under steady ambient (carrier) flow conditions lend themselves well to steady state hydraulic analysis – partly because discharge variations were small. Also, the presence or lack thereof wire mesh on the flume walls had no apparent impact on the thickness of the ice jams (at least for the experimental arrangement and range of flow conditions used in this investigation).

Table 3.1. Model ice floe size distribution.

Ice dimension (cm)	Proportion of full mixture by volume
1.27 x 1.27 x 0.32	21.4 %
1.27 x 1.27 x 0.64	8.4 %
1.27 x 1.27 x 5.08	26.7 %
5.08 x 5.08 x 0.64	23.5 %
5.08 x 5.08 x 1.27	20.0 %
Total	100.0 %

Table 3.2. Determination of model ice accumulation bulk porosity.

Test	Bucket Volume (mL)	Voids Volume (mL)	Porosity
1	22900	11540	0.50
2	22500	10840	0.48
3	22500	10785	0.48
4	22900	11500	0.50
Average	22700	11166	0.49

103

Table 3.3. Summary of formation jam tests.

Test date	Discharge (L/s)	Mesh in (yes/no)	# of probes at 10 m	# of probes at 20 m	L_{jam} (m)	$t_{main\ body}$ (cm)	p	F
18-Jun-01	38.5	no	3	3	17.0	3.2	0.45	0.10
19-Jun-01	38.4	no	3	3	15.0	4.0	0.53	0.10
20-Jun-01	38.5	no	3	3	15.0	3.8	0.51	0.10
21-Jun-01	38.3	no	3	3	14.0	5.1	0.61	0.10
22-Jun-01	38.0	no	3	3	12.0	6.1	0.57	0.10
25-Jun-01	43.0	no	3	3	8.5	7.5	0.57	0.10
26-Jun-01	43.3	no	3	3	9.5	7.2	0.57	0.10
27-Jun-01	43.3	no	3	3	8.0	8.3	0.57	0.11
28-Jun-01	47.7	no	3	3	7.5	8.0	0.52	0.11
29-Jun-01	48.0	no	3	3	7.0	9.3	0.55	0.11
3-Jul-01	52.7	no	3	3	6.0	9.9	0.50	0.11
4-Jul-01	52.1	no	3	3	6.5	10.0	0.55	0.11
5-Jul-01	33.5	no	3	3	15.0	2.9	0.47	0.09
9-Jul-01	33.6	no	3	3	16.0	3.0	0.47	0.09
10-Jul-01	33.6	no	3	3	16.5	3.3	0.53	0.09
11-Jul-01	33.8	no	3	3	14.5	3.8	0.50	0.09
12-Jul-01	33.8	no	3	3	15.5	3.3	0.48	0.09
13-Jul-01	33.8	no	3	3	16.0	3.3	0.51	0.09
16-Jul-01	38.5	no	3	3	12.0	6.1	0.57	0.10
17-Jul-01	43.1	no	3	3	8.5	8.0	0.51	0.10
18-Jul-01	42.9	no	3	3	8.0	7.5	0.50	0.10

104

Table 3.3. Summary of formation jam tests (continued).

Test date	Discharge (L/s)	Mesh in (yes/no)	# of probes at 10 m	# of probes at 20 m	L_{jam} (m)	$t_{main\,body}$ (cm)	p	F
19-Jul-01	42.9	no	3	3	7.5	7.9	0.50	0.10
20-Jul-01	38.3	no	3	3	14.5	4.0	0.48	0.10
23-Jul-01	38.6	no	3	3	12.0	5.2	0.50	0.10
25-Jul-01	48.3	no	0	8	6.5	8.5	0.50	0.11
26-Jul-01	38.5	no	0	8	13.5	4.9	0.54	0.10
30-Jul-01	33.4	no	0	8	16.5	3.4	0.47	0.09
31-Jul-01	33.7	no	0	8	17.0	3.4	0.52	0.09
1-Aug-01	33.5	no	0	8	17.0	3.8	0.56	0.09
2-Aug-01	47.7	no	0	8	8.0	7.6	0.58	0.11
3-Aug-01	38.7	no	0	8	13.0	5.0	0.55	0.10
7-Aug-01	38.2	no	0	8	15.5	4.5	0.54	0.10
8-Aug-01	43.1	no	0	8	10.5	6.9	0.55	0.10
9-Aug-01	47.6	no	0	8	7.5	8.9	0.54	0.11
10-Aug-01	33.1	no	0	8	18.5	2.7	0.45	0.09
13-Aug-01	33.6	no	0	8	15.5	3.7	0.52	0.09
14-Aug-01	33.3	no	0	8	15.5	3.8	0.55	0.09
15-Aug-01	33.7	no	0	8	14.0	4.2	0.53	0.09
16-Aug-01	33.5	no	0	8	15.5	3.5	0.51	0.09
17-Aug-01	33.6	no	0	8	15.5	3.8	0.55	0.09

105
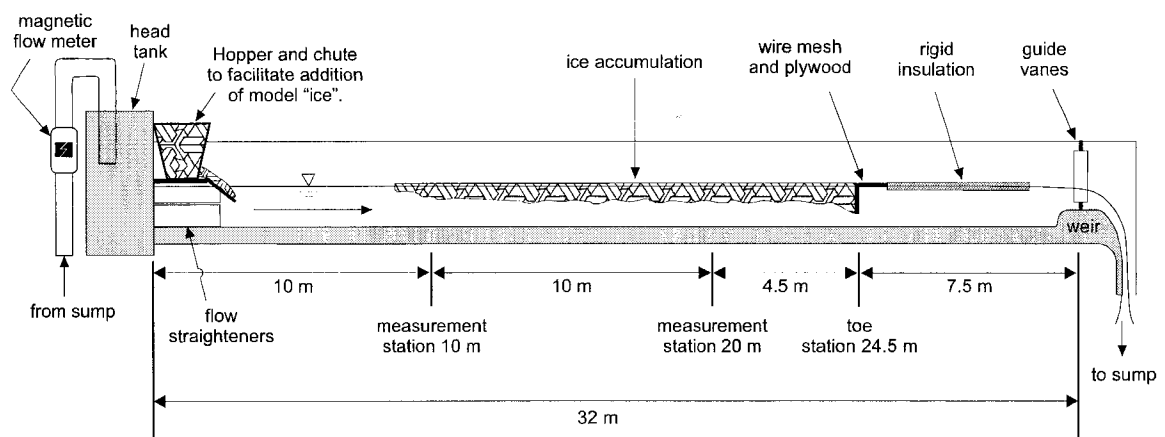
Figure 3.1. Experimental flume apparatus.

106

(a)

rough steel bed

air

ϕ_{dry}

(b)

ice added from top

$\phi_{buoyant}$

still water
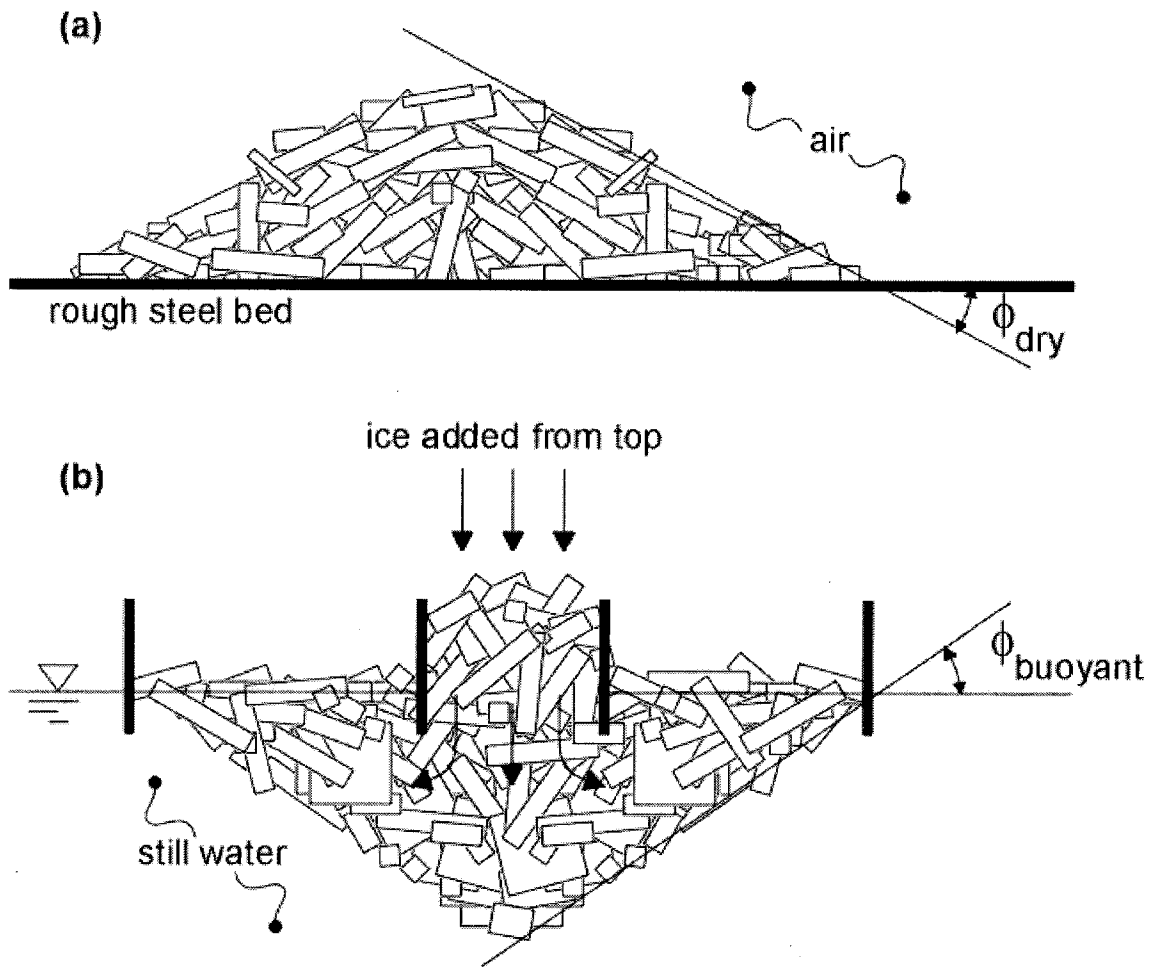
Figure 3.2. Schematic of test arrangement for determining, ϕ_{dry} and $\phi_{buoyant}$, the dry and buoyant angle of repose, respectively.

107
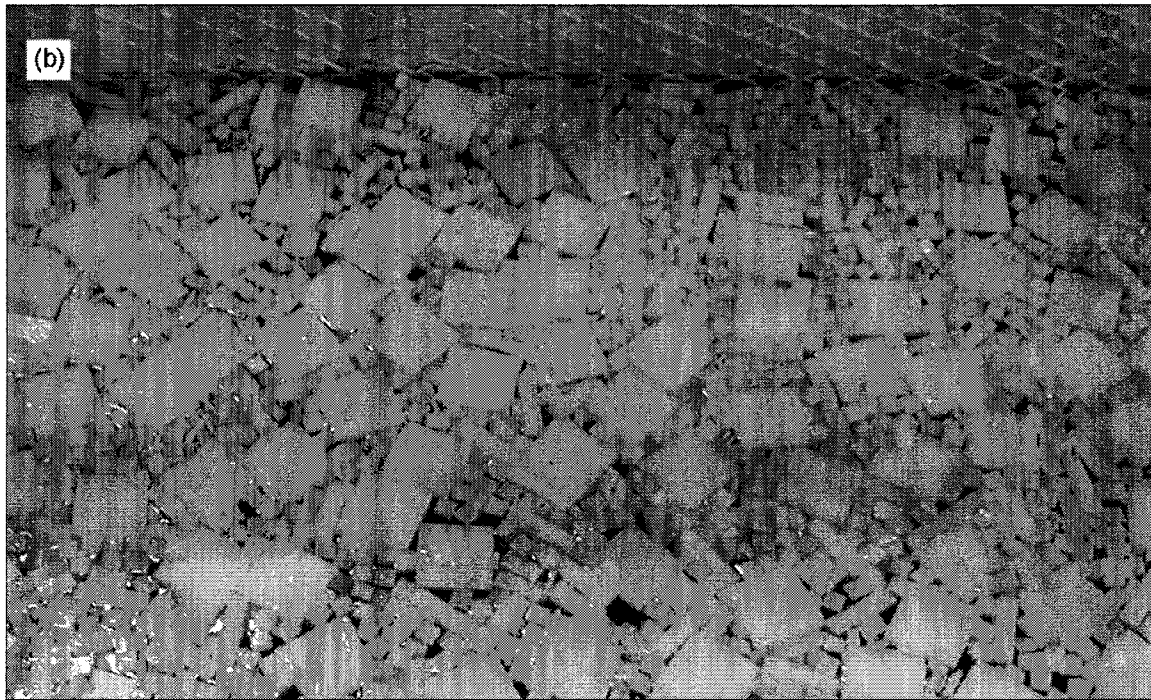
Figure 3.3. Experimental photos of test arrangement showing (a) controlled manual
introduction of model ice and (b) the resulting cover viewed from the top.

108
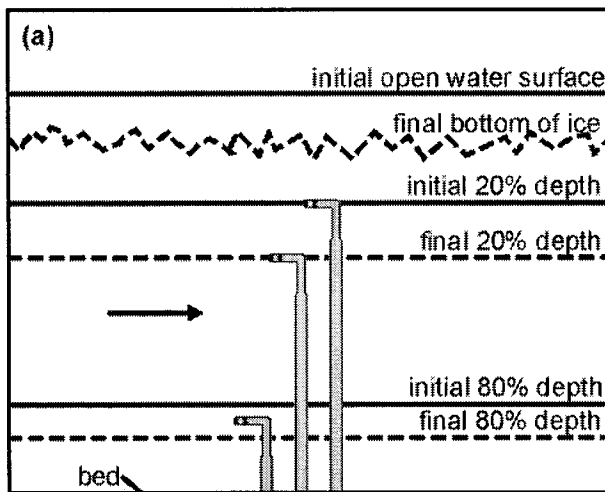
Figure 3.4. Prandtl tube arrangements for (a) idealized 3-probe placement to estimate average Gauss point velocity and (b) 8-probe arrangement to estimate vertically integrated average velocity.

109
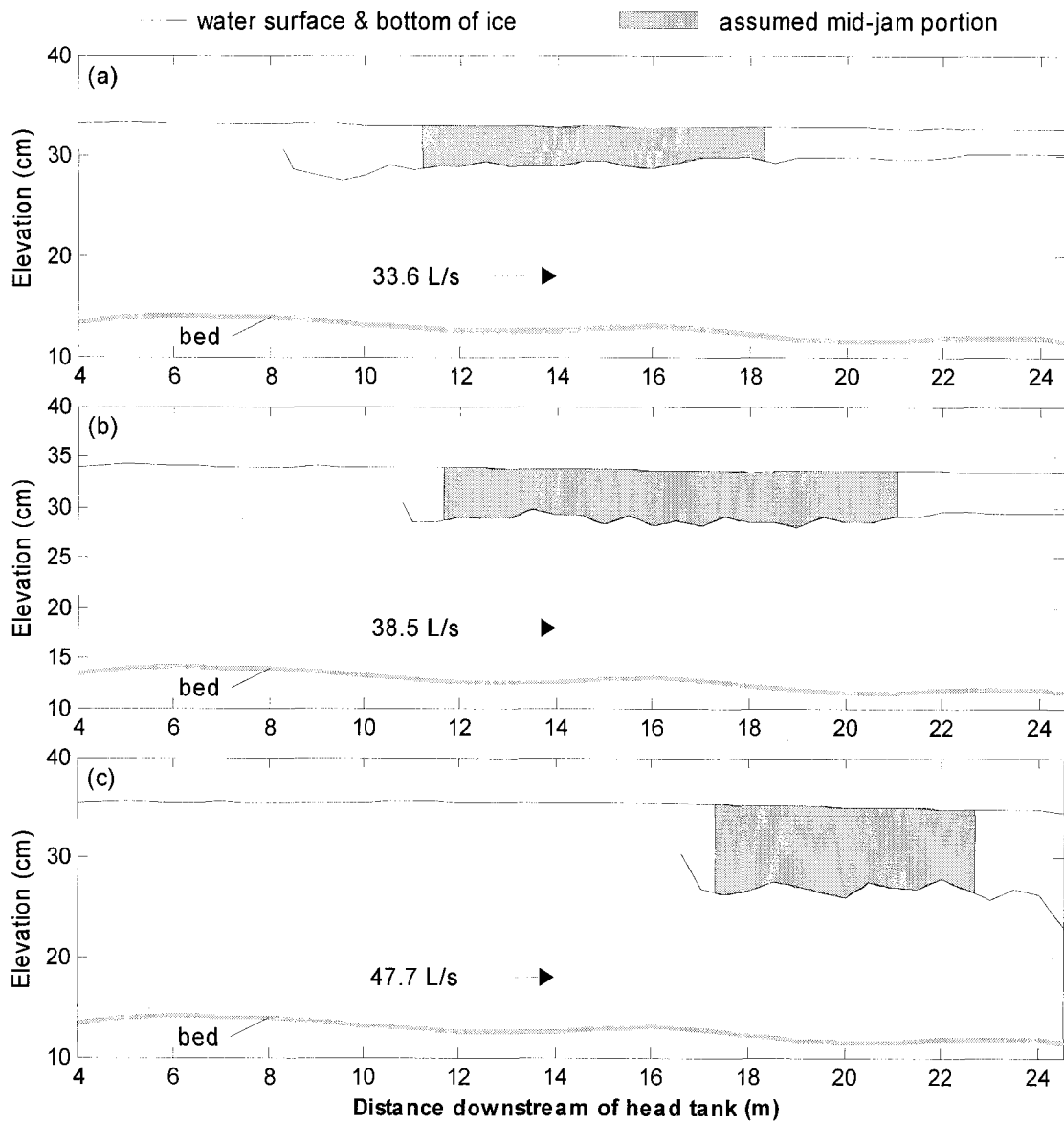
Figure 3.5. Typical formation jam thickness profiles for steady carrier discharge of (a) 34 L/s, (b) 39 L/s, and (c) 48 L/s.

110
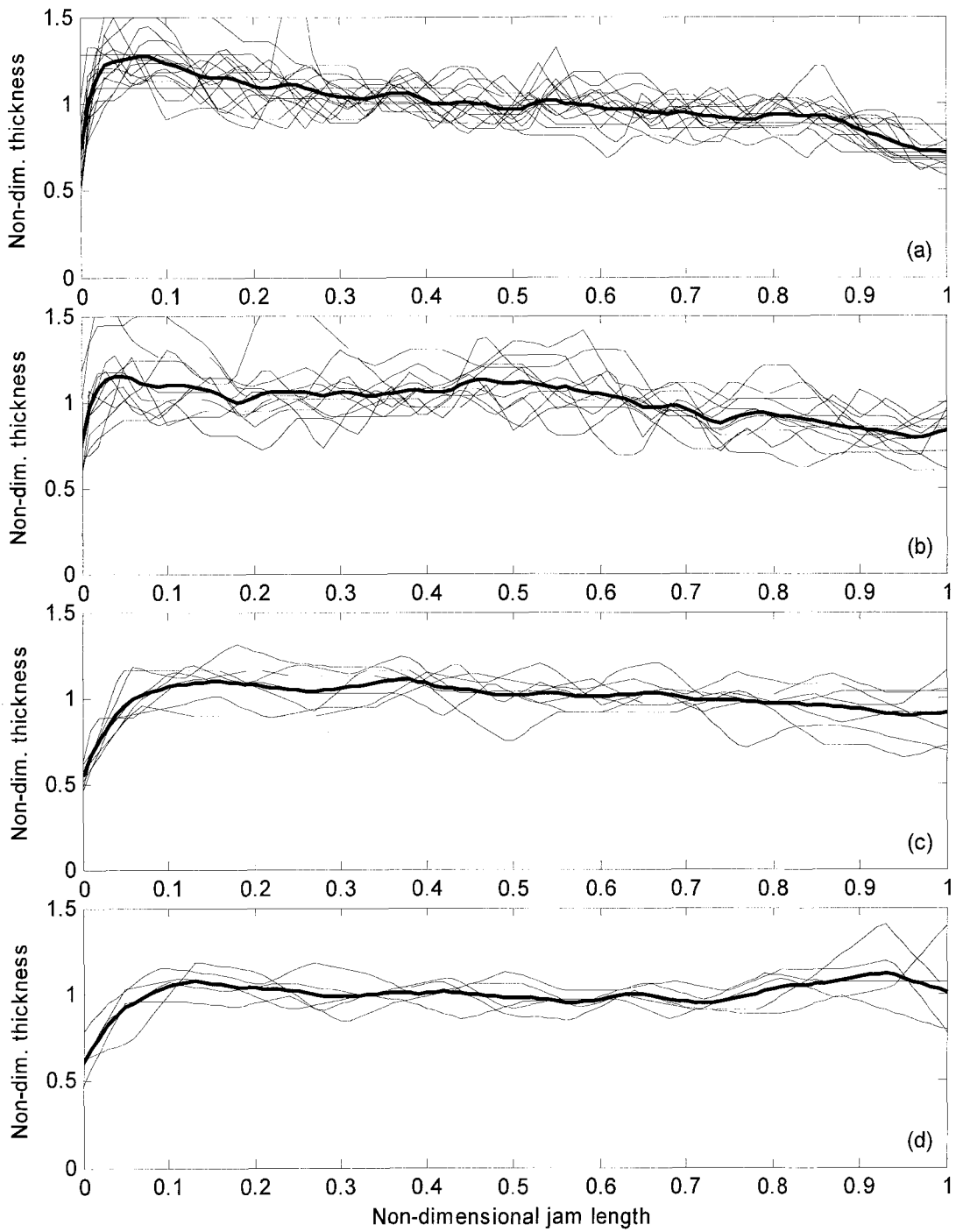
Figure 3.6. Dimensionless plot of formation jams grouped according to discharge:

(a) 34 L/s, (b) 38 L/s, (c) 43L/s, and (d) 48 L/s,

111
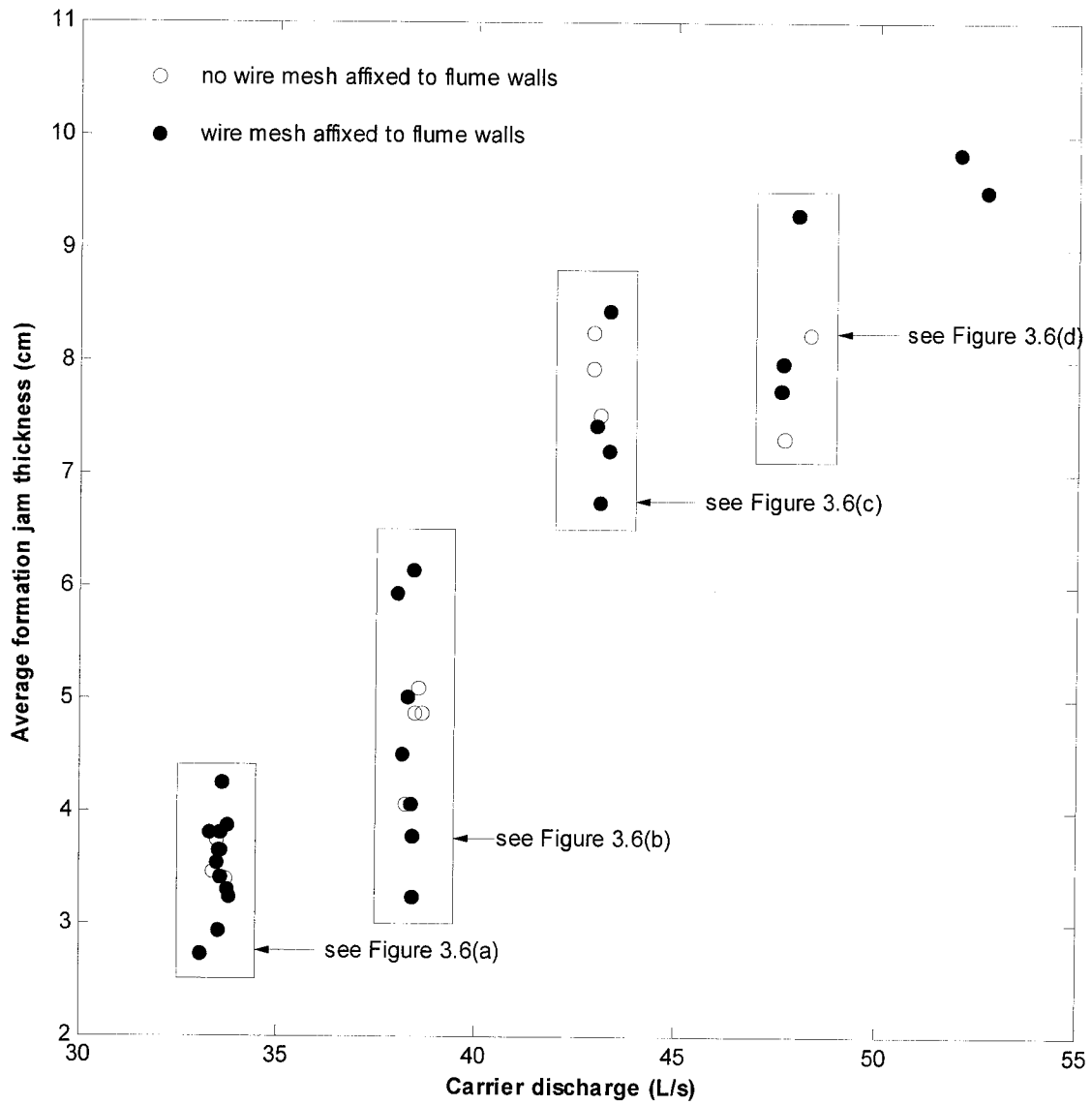
Figure 3.7. Average formation jam thickness versus carrier discharge.

112
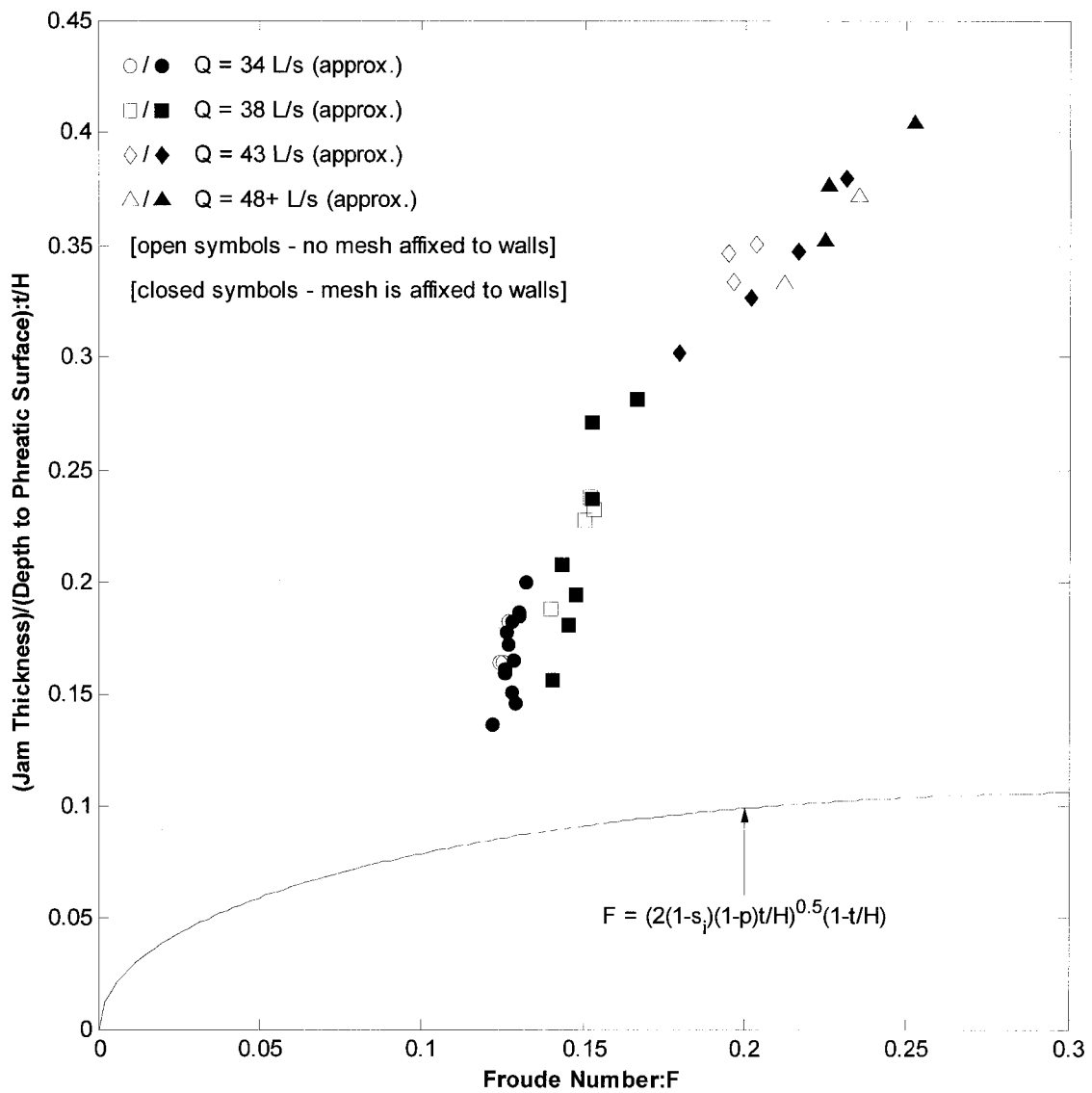
Figure 3.8. Average jam thickness versus Froude number.

The chart shows "(Jam Thickness)/(Depth to Phreatic Surface):t/H" on the y-axis (ranging from 0 to 0.45) versus "Froude Number:F" on the x-axis (ranging from 0 to 0.3).

Legend:
○ / ●   Q = 34 L/s (approx.)
□ / ■   Q = 38 L/s (approx.)
◇ / ◆   Q = 43 L/s (approx.)
△ / ▲   Q = 48+ L/s (approx.)

[open symbols - no mesh affixed to walls]
[closed symbols - mesh is affixed to walls]

$$F = (2(1-s_i)(1-p)t/H)^{0.5}(1-t/H)$$
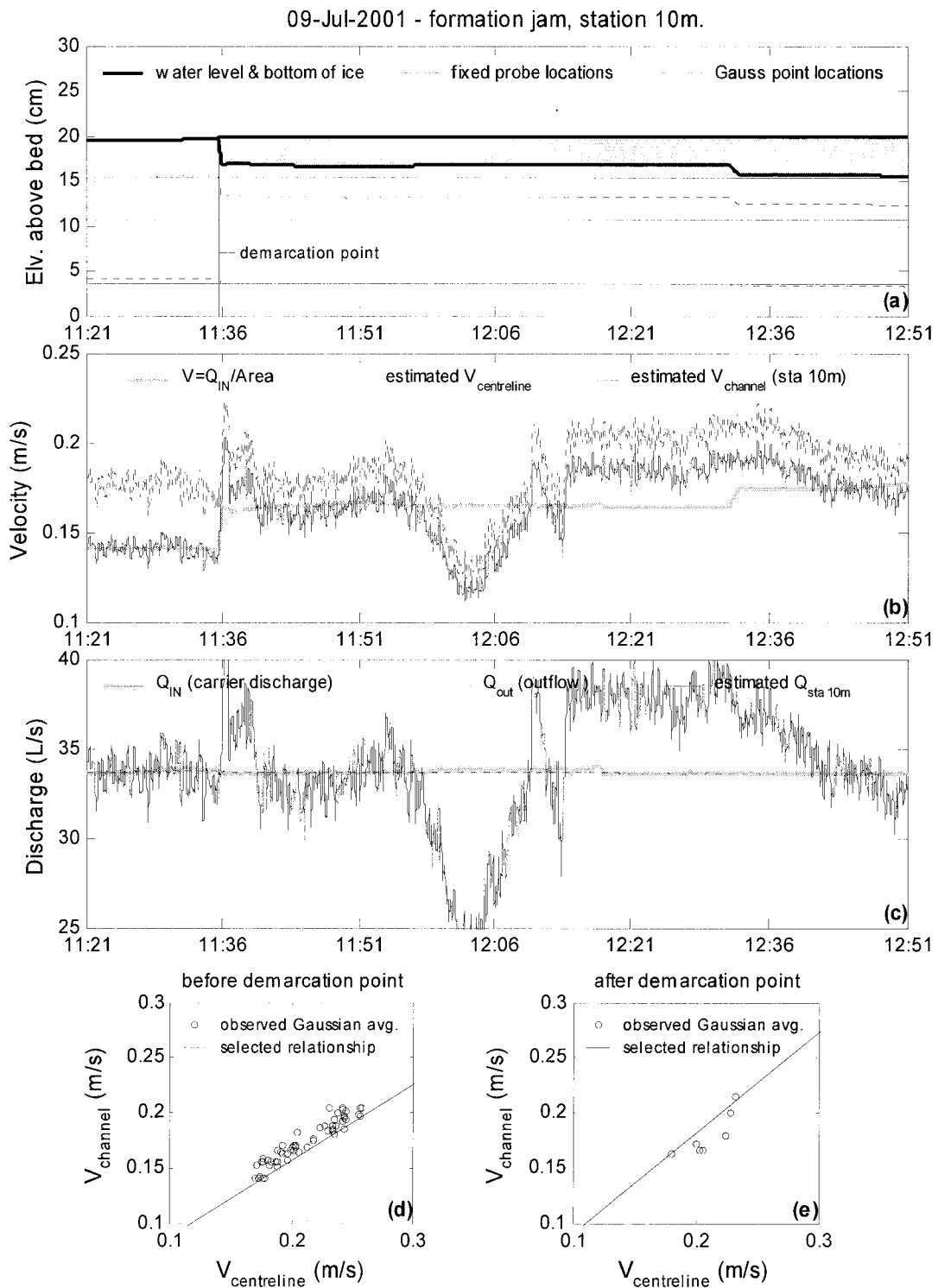
Figure 3.9. Continuous observations taken at station 10 m for formation jam created under constant carrier discharge of 34 L/s.

114
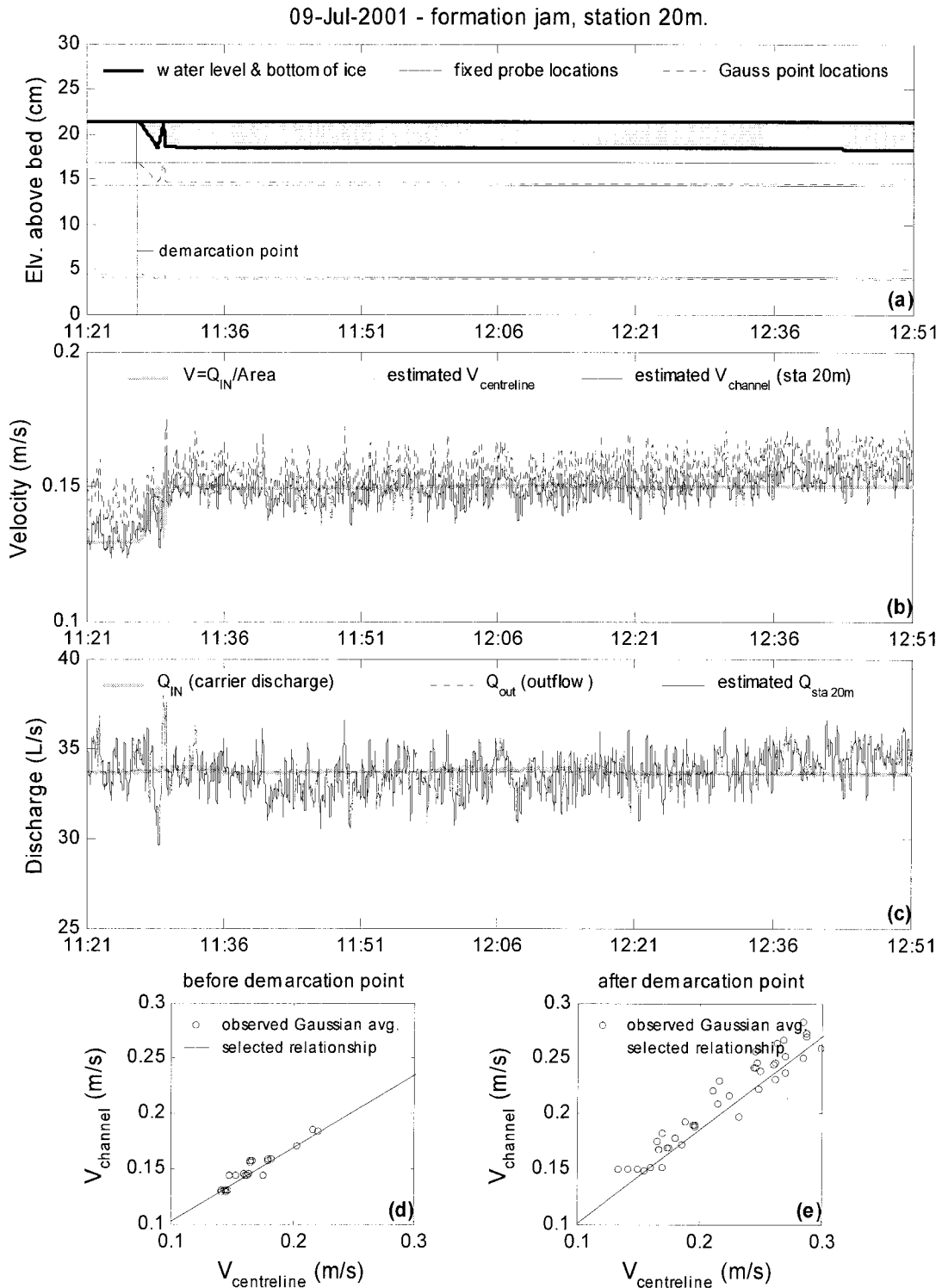
Figure 3.10. Continuous observations taken at station 20 m for formation jam created under constant carrier discharge of 34 L/s.
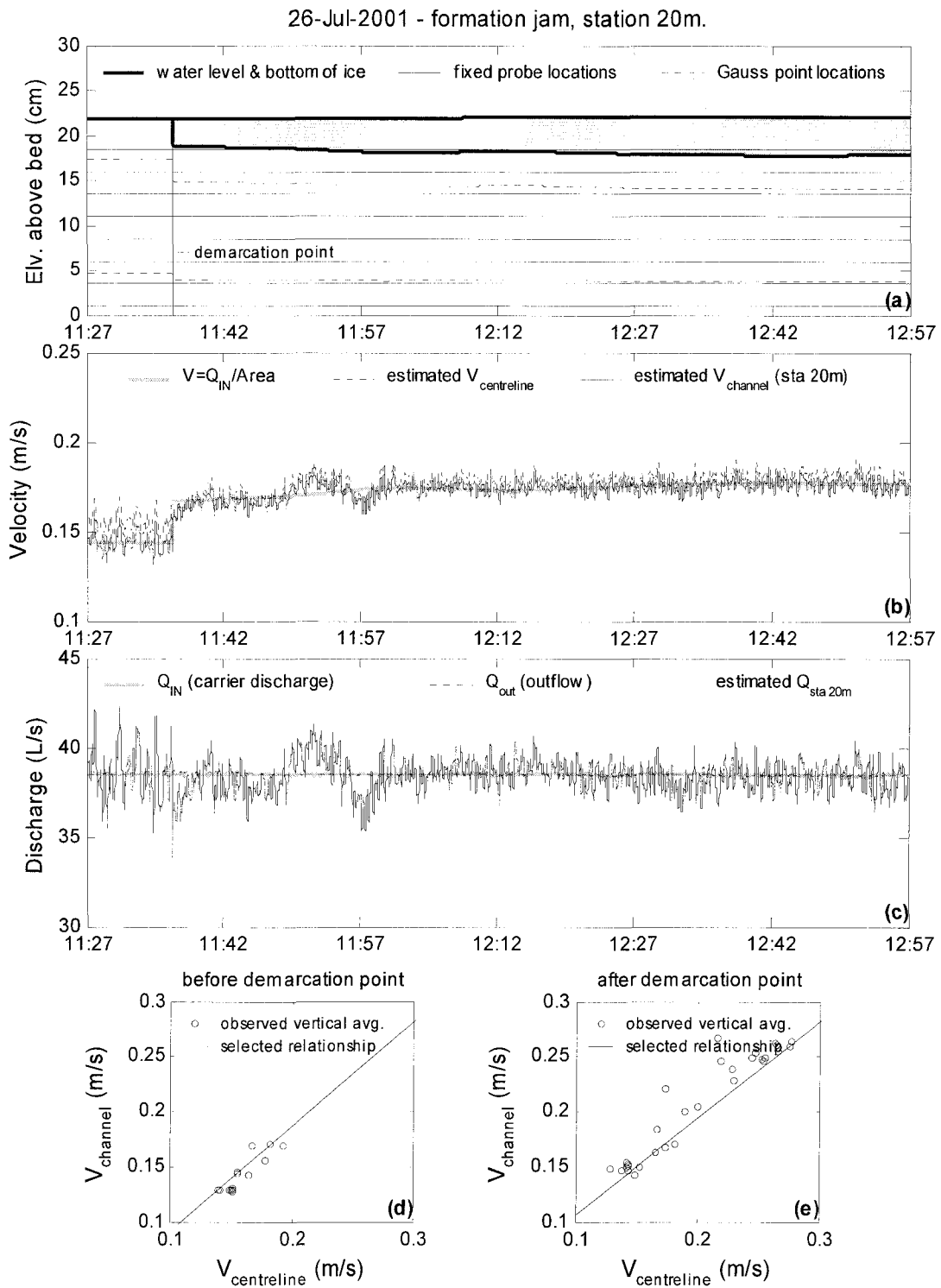
Figure 3.11. Continuous observations taken at station 20 m for formation jam created under constant carrier discharge of 39 L/s.
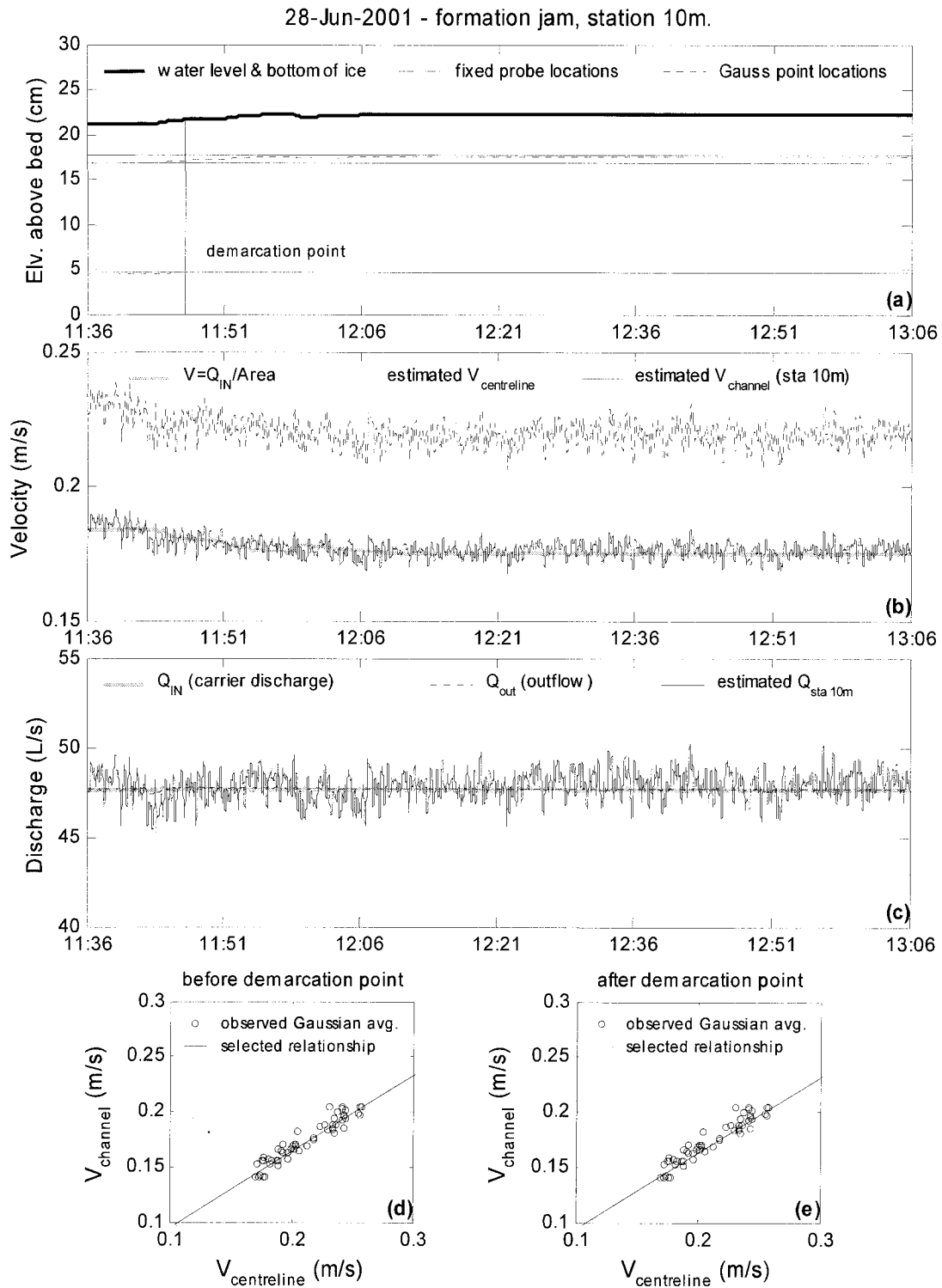
Figure 3.12. Continuous observations taken at station 10 m for formation jam created under constant carrier discharge of 48 L/s.
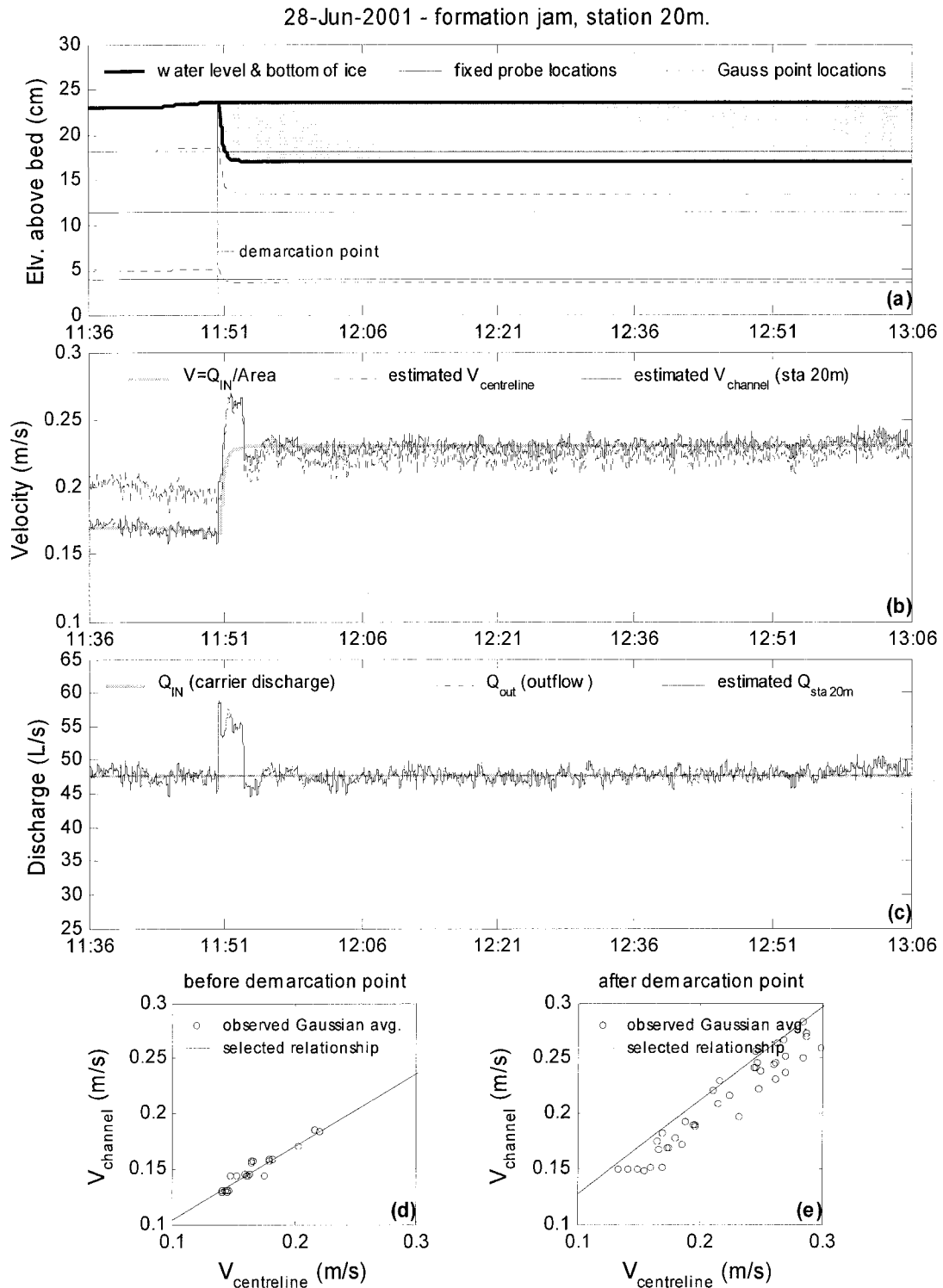
Figure 3.13. Continuous observations taken at station 20 m for formation jam created under constant carrier discharge of 48 L/s.
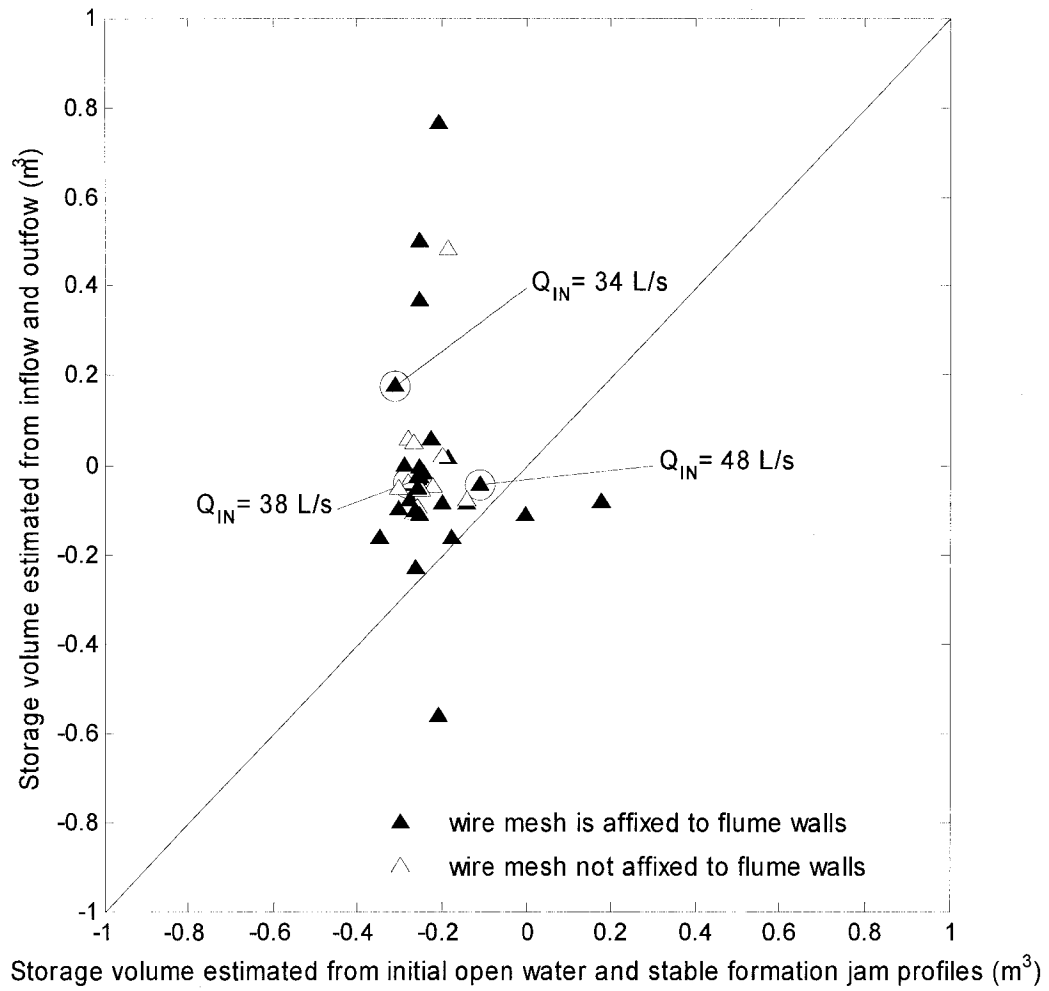
Figure 3.14. Comparison of storage estimates based on jam profiles and continuous discharge measurements.

119
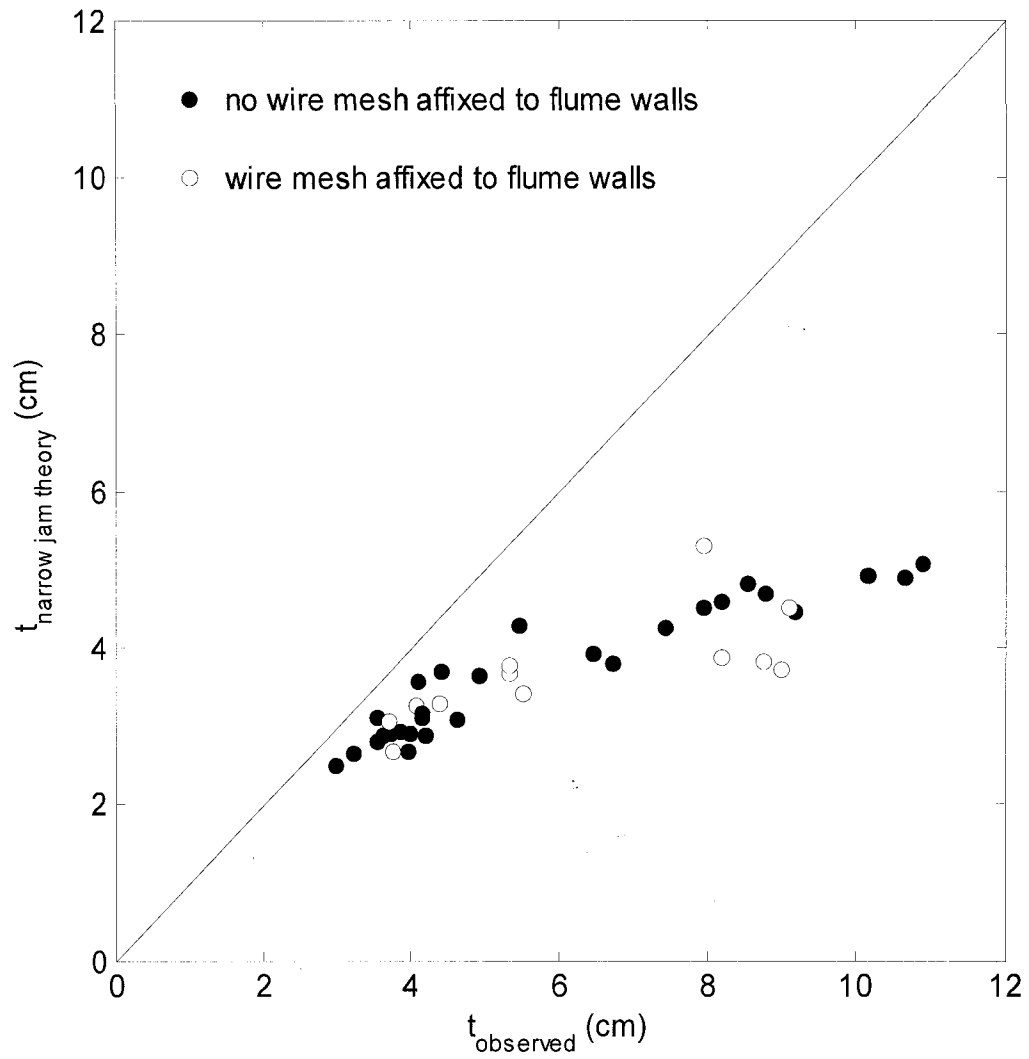
Figure 3.15. Observed thickness versus "narrow-jam" thickness.
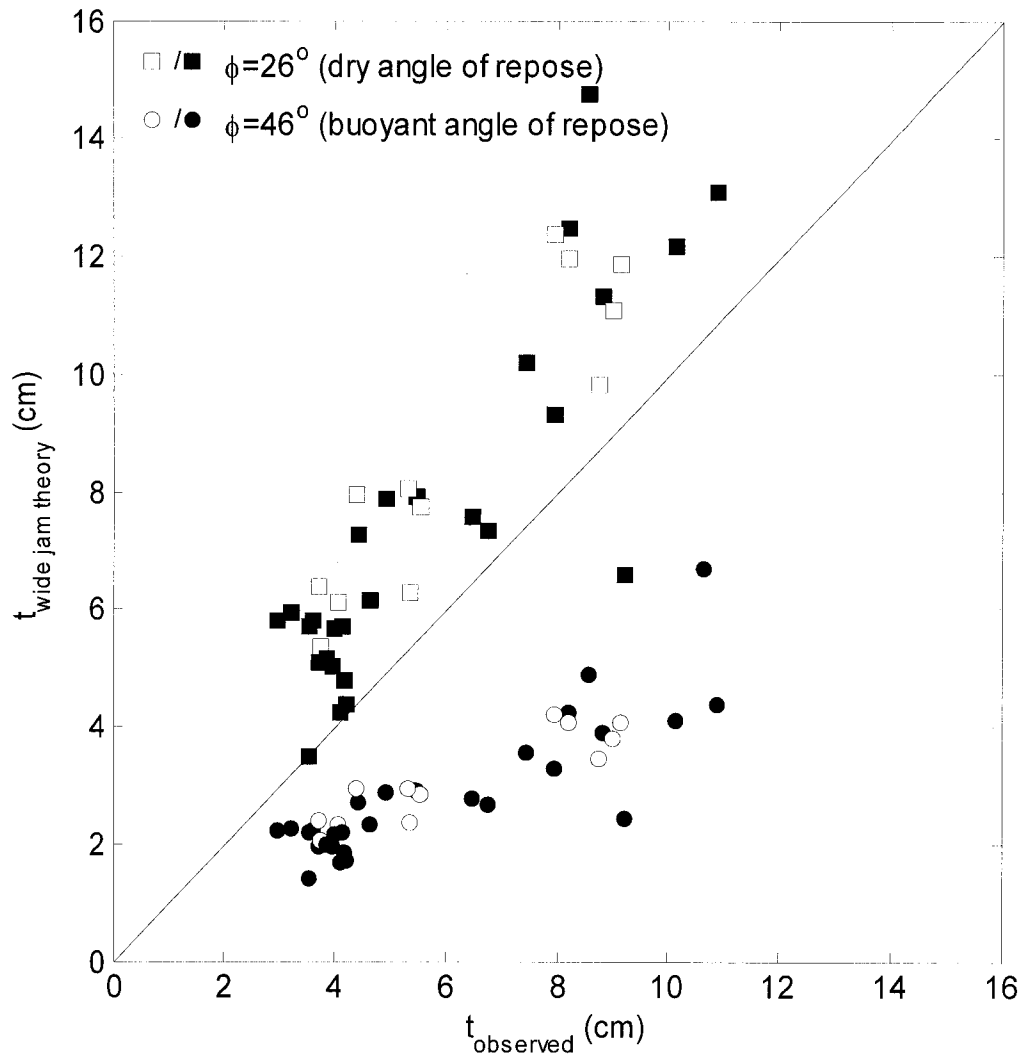
Figure 3.16. Observed thickness versus "wide-jam" thickness. Open symbols denote no wire mesh on side walls and closed symbols denote wire mesh on side walls.

121
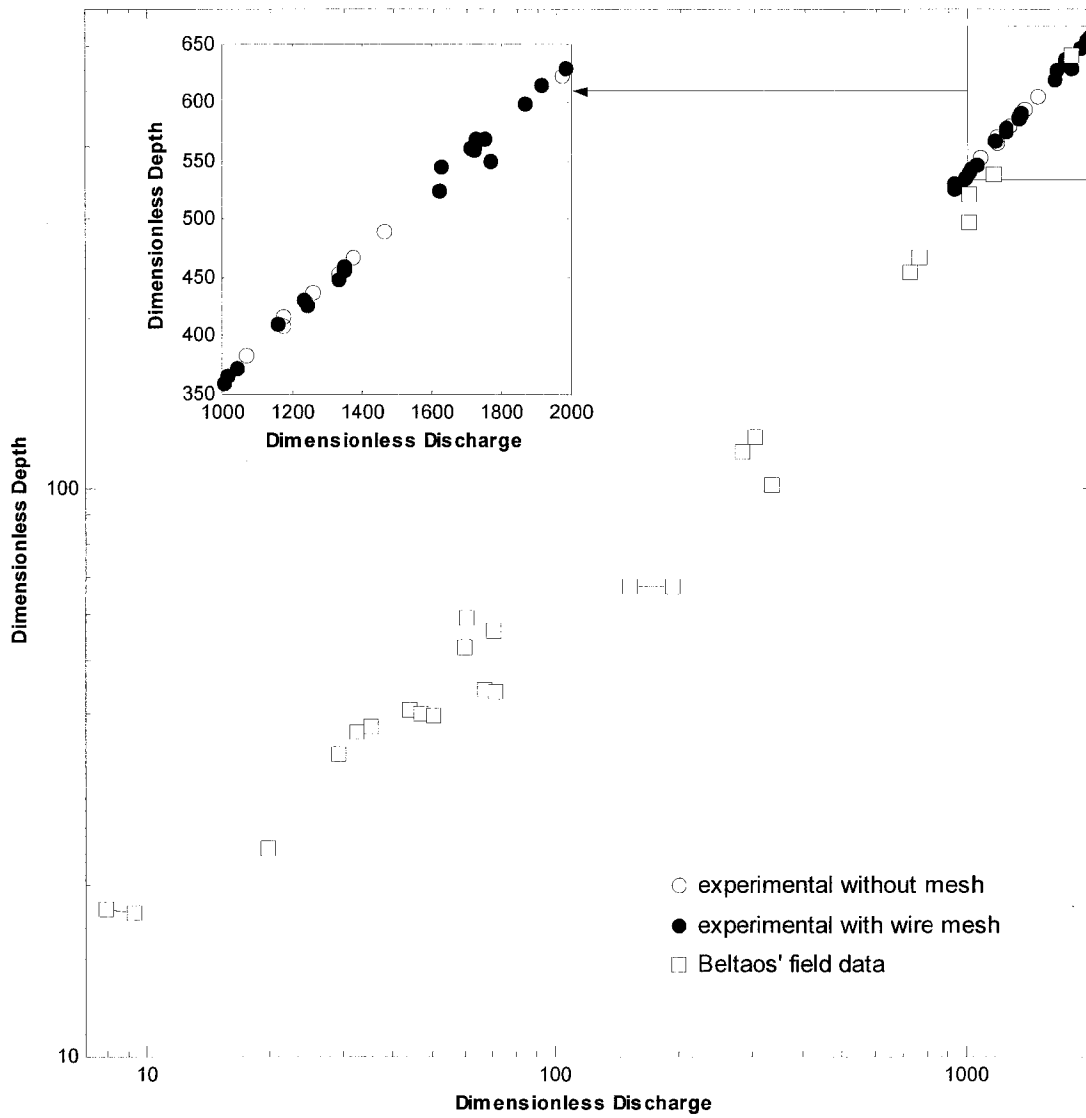
Figure 3.17. Dimensionless depth versus discharge.

122

3.9 References

Ashton, G. D. 1986. River and lake ice engineering. Water Resources Publications, Littleton, Colorado, 485 p.

Beltaos, S. 1983. River ice jams: theory, case studies, and applications. ASCE Journal of Hydraulic Engineering, Vol. 109, No. 10, pp. 1338-1359.

Beltaos, S., ed. 1995. River ice jams. Water Resources Publications, Littleton, Colorado.

Beltaos, S., and Wong, J. 1986. Downstream transition of river ice jams. ASCE Journal of Hydraulic Engineering, Vol. 112, No. 2, pp. 91-110.

Daly, S. F., and Vuyovich, C. M. 2003. Modeling river ice with HEC-RAS. Proceedings of the 12th Workshop on River Ice, Canadian Geophysical Union - Hydrology Section, Comm. on River Ice Processes and the Environment, Edmonton, Alberta, pp. 280-290.

Flato, G. and Gerard, R. 1986 Calculation of ice jam thickness profiles. Proceedings of the Fourth Workshop on Hydraulics of River Ice, Montreal, pp. C3.1-C3.25.

Healy, D., and Hicks, F. E. 2004. Index velocity methods for winter discharge measurement. Canadian Journal of Civil Engineering, Vol. 30, No. 1, pp. 407-419.

Healy, D., Hicks, F. and Loewen, M. 2002. Unsteady velocity profiles under a fixed floating cover. Proceedings of the 16th IAHR International Symposium on Ice, Dunedin, New Zealand, Vol. 1, pp. 83-90.

Hicks, F. E. and Bonneville, C. 1998. Modelling ice jam evolution processes. Proceedings of the 14th International Association for Hydraulic Research Ice Symposium, Postdam, New York.

Hicks, F. E. and Steffler, P.M. 1996. a discussion of: Estimation of mean flow velocity in ice-covered channels, by M. Teal and R. Ettema (Vol. 120, No. 12, 1385-1400), ASCE Journal of Hydraulic Engineering, Vol. 122, No. 8, pp. 475-476.

Lever, J.H., Gooch, G., Tuthill, A., and clardk, C. 1997. Low-cost ice-control structure. ASCE Journal of Cold Regions Engineering, Vol. 11, No. (3), pp. 198-220.

Pariset, E., and Hausser, R. 1961. Formation and evolution of ice covers in rivers. Transactions of the EIC, Vol. 5, No. 1, pp. 41-49.

Pariset, E., Hausser, R., and Gagnon, A. 1966. Formation of ice covers and ice jams in rivers. Journal of the Hydraulics Division, Vol. 92, No. HY6, pp. 1-24.

Saadé, R. G., and Sarraf, S. 1996. Phreatic water surface profiles along ice jam – an experimental study. Journal of Nordic Hydrology, Vol. 27, No. 3, pp. 185-202.

Shen, H.T., Wang, D.S., and Wasantha Lal, A.M. 1995. Numerical simulation of river ice processes. ASCE Journal of Cold Regions Engineering, No. 9, Vol. 3, pp. 107-118.

Teal, M.J., and Ettema, R. 1994. Estimation of mean flow velocity in ice-covered channels. ASCE Journal of Hydraulic Engineering, Vol. 120, No. 12, pp. 1385-1400.

Wuebben, J. L. 1995. River ice jams, editor: Spyros Beltaos, Water Resources Publications, Littleton, Colorado, Chapter 6 – Physical Modeling, pp. 173-199.

Zufelt, J. E. 1990. Experimental observations of shoving and thickening – comparison to equilibrium thickness theory. Proceedings of the 10th IAHR Symposium on Ice, Helsinki, Finland, pp. 504-510.

Zufelt, J. E. 1992. Modes of ice cover failure during shoving and thickening. Proceedings of the 11th IAHR Symposium on Ice, Banff, Canada, pp. 504-510.

Zufelt, J. E. 1996. Ice jam dynamics. Ph.D. thesis submitted to the Department of Civil and Environmental Engineering, University of Iowa, 203 p.

Zufelt, J. E., and Ettema, R. 1997. Unsteady ice jam processes. CRREL Rep. 97-7, U.S. Army Cold Regions Research and Engineering Laboratory, Hanover, N.H.

Zufelt, J. E., and Ettema, R. 2000. Fully coupled model of ice-jam dynamics. ASCE Journal of Cold Regions Engineering, Vol. 14, No. 1, pp. 24-41.

4.0 Experimental Study of Ice Jam Thickening under Dynamic Flow Conditions.[3]

4.1 Introduction

Due to a lack of specific knowledge about the potential impacts of sudden flow changes on a developing river ice cover, many hydro-power facilities are forced to curtail their hydro-peaking operations in winter, in order to avoid the potential risk of initiating an ice jam and associated flooding. For example, in Alberta (Canada) flow controls, limiting the range of discharge fluctuations, are implemented on a number of regulated rivers. These flow controls often persist over much of the winter period, representing a significant financial impact to the affected hydro companies in terms of lost revenue. Perhaps even more significant, this results in a significant energy deficit during a high demand period, which is made up with fossil fuel energy generation, an undesirable alternative in the context of current concerns associated with the potential for anthropogenic climate warming.

---

[3] This chapter was submitted for publication in the ASCE Journal of Cold Regions Engineering. It was submitted in July 2005 and is still under review.

Significant efforts have been directed toward the development of sophisticated numerical models that would enable hydro-power regulators to design and implement optimal hydro-peaking schemes safely (e.g. Shen et al. 1995; Zufelt and Ettema 2000). Complementary quantitative data are needed to increase our understanding of the complex processes involved and to provide essential validation data for numerical models of this type. One of the key factors limiting the availability of such data is that it is logistically difficult, and often unsafe, to try to measure discharge and ice thickness variations during ice cover consolidation events. Furthermore, because of imposed flow controls, opportunities to document the impacts of significant flow changes on a developing ice cover seldom arise. Thus, experimental investigations are necessary to complement, and enhance, the understanding of the underlying processes gained from field studies at specific sites.

Earlier experimental studies of ice jams have provided quantitative data describing ice jam formation under steady carrier flow conditions (e.g. Saadé and Sarraf 1996, and see Chapter 3), as well as primarily qualitative observations of the unsteady processes (Zulfelt 1990, 1992). In this experimental investigation, stable ice accumulations formed under a steady carrier discharge were subjected to sudden and significant flow increases, while associated variables (e.g. ice thickness, flow velocity, water levels, and ice cover consolidation rates) were monitored to provide a quantitative time varying record of the dynamic response.

127

4.2 Experimental Apparatus

Figure 4.1 presents a schematic diagram of the experimental apparatus used in this investigation. The work presented herein is a direct extension of the previous investigations on stable ice accumulations formed under constant discharge conditions presented in Chapter 3, and employed the same apparatus and many of the same measurement techniques.

The experiments were conducted in a 32 m long rectangular flume located in the T. Blench Hydraulics Laboratory at the University of Alberta. This flume had 0.91 m high sidewalls, a width of 1.22 m, and was set to a constant slope of 0.00164 for all runs. The bed was slightly rusted sheet metal and the walls were Plexiglas. Manning's n for the channel, under open water flow conditions ranged from 0.020 to 0.025. For most experiments, a coarse wire mesh was attached to the sides of the flume to facilitate the development of an "ice-ice" shear interface along the walls; the interface was believed to be more representative of natural conditions. A series of tests without the wire mesh (smooth Plexiglas walls only) were also conducted for comparison purposes. Ice floes were simulated using a mixture of rectilinear polyethylene pieces of varying size (specific gravity = 0.92). The distribution and quantity of "ice" pieces was the identical to that used in the previous tests outlined in Chapter 3. Again, as in that study, to minimize surface tension effects the ice mixture was kept wet between experiments.

Discharges ranging from 35 to 65 L/s were supplied to the head tank, and downstream water levels were controlled by a weir and guide vanes. The toe of the accumulation was

128

initiated by a floating plywood cover, fixed with a screen positioned 24.5 m downstream of the head box. The test configuration and instrumentation were essentially the same as that used in the previous study described in Chapter 3; the major exception being the inclusion of a system of video cameras positioned above the flume and placement of transverse markers along the length of the ice cover, to track the consolidation progression during the tests. Manual tracking of the cover consolidation was also conducted by direct observation to verify the results interpreted from the overhead video cameras.

4.3 Test Procedures and Measurement Techniques

Stable ice jam accumulations were established at the beginning of each experiment under a constant carrier discharge. The resulting water surface profile was measured using a point gauge and the average ice thickness profiles were measured from the side of the flume using a ruler and set square as illustrated in Appendix B. Next, "tracking particles" were placed on the surface of the stable accumulation at regular intervals along the length of the ice cover, to facilitate consolidation monitoring by the overhead cameras. These tracking particles were exactly the same as the sample ice, except that they were colored various patterns of black, for easy identification. Care was taken when placing these tracking particles, so as to minimize disturbance to the stable accumulation. Details on the methodology for "tracking" the progression of the cover are outlined in Appendix B.

Inflow to the system was increased rapidly by manually opening a valve to a predetermined discharge. The flow was then kept constant for the remainder of the test.

129

Efforts were made to open the valve at a consistent rate for all tests. Direct estimates on the celerity of the resulting wave were made by measuring the time difference between the first observable increases in water level at the observation stations located 10 and 20 m downstream of the head tank. Figure 4.2 presents a comparison of these observed wave speeds with theoretical wave speeds for both progressive dynamic waves, $V_{dynamic} = V_{initial} + (gh_{initial})^{0.5}$, and kinematic waves, $V_{kinematic} = 1.5V_{initial}$ (coefficient determined based on Manning equation), where $V_{initial}$ and $h_{initial}$ were the average velocity and average depth of flow under the initial accumulation, respectively and g is the acceleration due to gravity. Inspection of Figure 4.2 reveals that the waves that passed through the system were dynamic in nature for all of the tests.

The response of the initially stable accumulation to this rapid increase in discharge was monitored continuously until steady flow conditions resumed and the resulting ice accumulation had stabilized to the point where there was no perceptible change in the cover movement or thickness. The resulting water surface and ice thickness profiles were then measured. Figure 4.3 illustrates a representative model ice accumulation formed by the shoving of an initial stable ice accumulation by a rapid increase in discharge. Figure 4.3a shows the downstream portion of the stable ice accumulation where the wire screen attached to the freely floating cover is visible in the far right end of the photo. Subfigures 4.3b and 4.3c illustrate the texture of the ice jam viewed from the bottom and surface, respectively.

130

4.3.1 Continuous Data Measurements

The following continuous data sets were obtained for each test:

- inflow and outflow of the flume;

- water level and ice thickness data at measurement stations located 10 and 20 m downstream from the head tank;

- discharge estimates at stations 10 and 20 m downstream from the head tank; and

- streamwise progression of the cover during secondary consolidation.

The methodology and instrumentations used for these measurements was the same as that described in Chapter 3 with the exception of the streamwise progression of the cover which is outlined in a separate section of Appendix B. Inflow to the flume was measured directly by a magnetic flow meter; outflow was based on the known stage-discharge relationship for the weir and a continuous record of water level at the outlet, obtained using an automated capacitance model water level recorder; and water level and ice thickness data were recorded at measurement stations 10 and 20 meters downstream from the head tank using video cameras.

3.3.2 Applicability of Prandtl Tubes for Measuring Unsteady Velocities

As for the experiments described in Chapter 3, discharge was obtained indirectly using Prandtl tubes on the channel centerline at station 20 m, positioned at various depths to facilitate determination of the average centerline velocity throughout the experiment.

131

This centerline velocity was then related to mean channel velocity through a pre-established relationship, providing mean channel velocity at station 20 m, which together with the continuous record of water level facilitated a discharge determination. A more complete description of the method is outlined within a section of Appendix B.

The distinction between this study and the previous one outlined in Chapter 3 is that, in this case, the ice cover consolidation was precipitated by the introduction of a sudden flow increase to the channel, rather that having the ice jam form under steady carrier flow conditions. This has implications for the accuracy of the discharge measurement method, because of the dynamic nature of the waves introduced (as demonstrated in Figure 4.2). Prandtl tubes are generally used to measure mean flow velocities; they are not suited for measuring turbulent fluctuations, and to the authors' knowledge, there has been few, if any, reported attempts to use pressure differential probes to capture variations in mean velocity or unsteady flow conditions. Therefore additional tests were conducted to evaluate the validity of this approach. To achieve this, velocity measurements taken using a Prandtl tube were compared directly to measurements taken using an Acoustic Doppler Velocimeter (ADV) for highly unsteady conditions.

Figure 4.4 presents an example time series of the raw data collected simultaneously using both a Prandtl tube and an ADV. Inspection of Figure 4.4 indicates that the velocity time series data collected by the Prandtl tube tended to lag behind the ADV data by a couple of seconds. It was also apparent that the inherent fluctuations in velocity were damped, with the higher frequency variations being missed altogether. The Prandtl tube's response to the actual velocity fluctuations was analogous to a filter having a cut-off

132

frequency of roughly 0.1 Hz and a time lag in the order of one second. Since the sampling rate for the Prandtl tube data collected in this investigation was set at 1 Hz, the Prandtl tubes were considered to adequately capture the degree of "unsteadiness" desirable for this investigation. That is, the time interval between measured data points neared or exceeded the time required for the Prandtl tube to "respond" to the actual changes in velocity. Healy et al. (2002) provided a detailed description of the full investigation comparing the ADV and Prandtl tube measurements (this paper is presented in Appendix C). In essence, the data presented herein were expected to accurately capture changes in velocity represented by averages over one second intervals.

4.4 Experimental Observations

A total of 40 experimental simulations were conducted for this investigation. Table 4.1 presents a summary of the salient parameters associated with these runs. The Reynolds numbers for all of the tests ranged from 27,000 to 43,000 (see Table 4.1). The jam length was the full streamwise dimension of a stabilized accumulation from the head to the toe. The jam thickness was the average thickness of a representative section along the middle portion of the jam (and is indicated by the shaded areas in Figures 4.5 through 4.7). The jam porosity was determined based on the known volume of ice added for each test and the measured bulk volume determined from the measured jam profile. Subscripts initial and final denote the initial stable ice accumulation formed under steady carrier flow conditions, and the final stable ice accumulation resulting from the rapid increase in discharge, respectively.

Of the 40 tests, three were selected for detailed presentation in this paper. Appendix D provides full details of the results for all 40 tests. Figures 4.5 through 4.10 present results specific to each of these tests which began with similar initial conditions: for the first test (Figure 4.5 and 4.8) the discharge was increased by 30%; for the second test (Figure 4.6 and 4.9) the discharge was increased by 55%; and for the third test (Figure 4.7 and 4.10) the discharge was increased by 85%.

4.4.1 Cover Mobilization

Inspection of the video data at stations 10 and 20 m downstream of the head tank indicated steady, monotonic increases in water levels followed by a downstream movement of the cover immediately following the rapid increase in discharge. There was no apparent delay in cover movement following the rise in water levels and the cover appeared to move as a single mass, although the tracking particles indicated that different portions of the ice cover consolidated at different rates.

Figures 4.5, 4.6, and 4.7 present the measured initial and final ice jam profiles along with the results of the particle tracking analysis, illustrating the progression of the cover. In general, the secondary consolidations were thicker and shorter than their initial accumulations. As was expected, for the same initial discharge conditions, thicker and shorter accumulations resulted from the higher relative increases in discharge. The middle portion of the jam used for estimating the average jam thickness is also indicated on the figures by shaded areas.

134

4.4.2 Cover Progression

Figures 4.5c, 4.6c, and 4.7c present the results of the particle tracking analysis and illustrate the progression of the cover throughout the duration of the test. Each line essentially tracks the downstream movement of a transverse slice of the cover. The vertical axis describes the elapsed time since a rapid increase in discharge was reported by the magnetic flow meter. Strictly speaking, these lines follow only the surface movements of the accumulation. However, during each test visual observations consistently indicated that the surface movements were representative of the movement of the entire thickness at that location. Those lines that do not extend the full length of the particle tracking analysis period indicate instances where the tracking particles were no longer distinguishable in the video data.

The ice in the upstream portions of the accumulation moved downstream a greater distance than the ice in the downstream portions of the cover and, for the early portions of the test, there was little to no observable under-turning or under ice transport; this implies that the ice cover thickened mostly in a telescopic manner (i.e. by shoving). After the bulk of the ice cover consolidation was complete, local thickening at the head (due to entrainment of particles at the leading edge) was common. Therefore, in many cases the final stable ice jam accumulation profiles (measured well after the bulk of the cover movement and erosion of the head ceased) show shorter lengths than indicated by the particle tracking data that was limited to roughly the first half hour of the test. The local thickening at the head also accounts for the apparent "hook-like" features associated with the head of the final (secondary) consolidations, visible in Figures 4.6b and 4.7b.

135

The relative rate of cover progression diminished asymptotically throughout the duration of the test, as it approached its final position. For those tests with higher relative increases in discharge the progression rates were higher and the model ice accumulation came to its final stable position sooner, than in those tests with lower relative increases in discharge. In some cases the ice cover progression slowed and then experienced a minor increase for several minutes before diminishing again and ultimately reaching its final stable condition (e.g. as seen in Figure 4.5c).

4.4.3 Continuous Observations during Cover Progression

Figures 4.8, 4.9, and 4.10 present the continuous time series data obtained at station 20 m downstream of the head tank for the three tests presented in Figures 4.5, 4.6, and 4.7 (corresponding to rapid increases in carrier discharges of 30%, 55%, and 85%, respectively). Three subfigures are presented in each figure and are described as follows. In these figures, subfigure (a) presents the continuous time series elevation data with respect to the bed for the observed water surface and bottom of ice. Subfigure (b) presents the average channel velocity. Subfigure (c) presents the continuous discharge 20 m downstream of the head tank which was based on the observed depth of flow and the measured velocities. The observed discharges entering and exiting the system are also indicated for comparison.

In a general sense, the following observations can be drawn from these figures. As the discharge increased, the water surface elevation and thickness of the cover increased while the depth of flow under the ice jam tended to remain relatively constant

136

(Figures 4.8a, 4.9a, and 4.10a). Consequently the average channel velocity under the jam increased to facilitate the increased flow rate (Figures 4.8b, 4.9b, and 4.10b).

Subfigures 4.8c, 4.9c, and 4.10c, illustrate continuous discharge measurements for the system inflow, system outflow, and estimated discharge within the accumulation at station 20 m downstream of the head tank. As expected, there was some attenuation of the relatively steep faced dynamic wave front as it passed through the system and water went into storage during the test (as can be seen by visual comparison of the inflow and outflow hydrographs).

Figure 4.11 presents a comparison of the volume of water that went into storage estimated by two different approaches. The first, and most direct, method was to compare the volume of stored water represented by the difference between the initial and final stable ice jam water surface profiles. The second approach was to integrate the difference in the inflow and outflow hydrographs. As indicated in the figure, the cumulative storages found by these two methods were similar. The difference in storage estimates obtained by the two approaches fell roughly within a plus or minus 15% error band (as illustrated in Figure 4.11).

4.4.4 Comparison between Initial and Final Ice Jam Profiles

Figure 4.12 presents a comparison between the relative increase in average jam thickness versus the relative increase in the initial and final steady discharge, both expressed as percent increases from the initial. The figure suggests that there is no strong relationship between the relative increases in thickness to the relative increase in discharge for the

137

tests carried out in this investigation. It appears that the final jam thickness is not strongly correlated to the conditions of formation for the initial ice accumulation (at least for the experimental arrangement used in this study).

4.5 Discussion

Pariset and Hausser (1961, 1966) defined the so-called wide channel jam where all of the applied forces on the ice accumulation are transferred through the mass of ice and ultimately taken up by the banks. By applying the usual uniform flow assumptions and neglecting cohesive forces within the ice accumulation, the following relationship can be used to describe the equilibrium thickness of a wide jam for a rectangular channel (Ashton 1986),

[4-1] $\mu(1 - \frac{\rho_i}{\rho})\rho_i g t_{eq}^2 - (g\rho_i SB)t_{eq} - \tau_i B = 0$,

where: μ is a coefficient defining the internal strength of the ice accumulation; t_{eq} is the equilibrium ice thickness; S is the stream slope; B is the width of the channel; and τ_t represents the applied forces under the ice cover resulting from the flow. Neglecting cohesive forces and assuming $s_i = 0.92$, Beltaos (1983) developed the following non-dimensional relationship for the depth of flow under the ice jam combined with the equilibrium ice thickness (H) for a wide channel jam:

[4-2] $\eta = \frac{H}{SB} = 0.63 f_o^{1/3} \Omega + \frac{5.75}{\mu} \left[1 + \sqrt{1 + 0.11 \mu f_o^{1/3} (f_i / f_o) \Omega} \right]$,

138

where: η is the non-dimensional depth; H is the depth of water from the bed to the phreatic surface; f_o is the composite friction factor for the flow under the ice cover; f_i is the friction factor associated with ice-affected portion of flow; and the dimensionless discharge parameter after Beltaos (1983), $\Omega = (q^2/gS)^{1/3}/SB$ (where q is the discharge per unit width of channel, g is the acceleration due to gravity, S is the slope of the channel, and B is the width of the channel).

Figure 4.13 presents the field data collected/collated by Beltaos (1983) using the non-dimensional relationship in equation [4-2] along with the results of the shoved jams observed in this investigation. Data for ice jams, formed under steady carrier flow conditions, presented previously in Chapter 3, are also presented for comparison. The plot suggests that all experimental results compare well with the field observations.

The theoretical equilibrium thickness presented in Chapter 3 (equation [3-3]) was also compared to the observed thickness associated with the middle portion of each shoved ice jam accumulation. A comparison of this middle portion of the accumulation (indicated by the shaded areas in Figures 4.5, 4.6, and 4.7) to the theoretical equilibrium thickness is provided in Figure 4.14. This figure suggests that the theoretical ice jam thickness defined by steady state ice jam theory fell within the observed ice jam thicknesses for the experiments conducted in this investigation. The theoretical equilibrium thickness based on the buoyant angle of repose overestimated the observed thickness and underestimated the observed thickness when based on the dry angle of repose. It is likely that the accumulations were not sufficiently long enough to achieve the true so-called equilibrium section. The work of Zufelt and Ettema (1996) suggested that equilibrium theory may

not sufficiently describe the resulting ice jam thickness of a collapsed accumulation and that momentum forces supplied by the moving ice would result in ice jams thicker than those predicted by equilibrium theory. They suggested that for relative increases of discharge greater than roughly 50% momentum forces would become important and equilibrium theory would likely underestimate the resulting ice jam thickness. Those events where discharges were increased by more than 50% are indicated in Figure 4.14 by cross hairs superimposed over each respective data point. Inspection of Figure 4.14 does not suggest any clear significant trend defining the relative importance of the relative rate of discharge increase (as was also suggested in Figure 4.12).

Zufelt (1992) introduced two qualitative modes of ice jam failure (as defined in Chapter 1); complete cover failure where the cover failed more or less completely along the length of the accumulation; and, progressive failure where the cover failed progressively from the head to toe of the accumulation. From inspection of the particle tracking data (see Figures E.65 through E.105) a qualitative assessment on the mode of failure was made for each of the 40 tests conducted during this study. For each test, the mode of failure was defined as either progressive or complete based on the qualitative descriptions of Zufelt (1992). The observed failure modes for each test are presented in Table 4.1 along side of the relative increase in discharge expressed as a percentage. Zufelt (1992) suggested that progressive failures would be expected for relative discharge increases less than 50% and the qualitative assessments on the failure modes for this study generally agree with this value.

For the given experimental arrangement it was difficult to assess the relative importance

140

of having roughened side walls that promote an ice-ice interface. For these tests it appears that the presence or lack of presence of the wire mesh had little effect on the resulting ice jam profiles.

4.6 Conclusions

Experimental investigations were conducted investigating the effects of dynamic flow fluctuations in the destabilization (shoving) of ice accumulations created under steady carrier flow conditions. In addition to documenting the resulting ice jam profiles, continuous measurements of the variations in flow depth, ice thickness and discharge were obtained at key stations within the ice jam during consolidation.

For the range of parameters in the experiments, the final ice jam thickness did not carry any significant dependence on the relative increase in discharge the ice jam experienced through its initial to final stable geometries. It is plausible that the relative increase in discharge would carry have an effect on the final ice jam configuration for cases outside of those described by the range of flows and conditions for the experimental arrangement used in this study. While this study, the final ice jam configuration seemed to not dependent on the relative increase in discharge, the so-called failure mode defined as either progressive or complete did. A relative increase in discharge of roughly 50% used to define a demarcation point for these two failure modes agreed with the qualitative assessments on failure modes observed during this investigation.

The observations obtained from a total of 40 tests (conducted over a range of rapid discharge increases) suggest that the final stable accumulations closely follow the jam

141

stability equation defining wide-jams formed under steady state conditions.

Table 4.1. Summary of shoved jam tests.

Test Date	Q (L/s) initial	final	ΔQ (%)	Failure Mode	Length (m) initial	final	t_{middle} (cm) initial	final	Porosity initial	final	Reynolds No. initial	final
18-Jun-01	38.5	48.5	26%	progressive	17	10.5	3.2	6.1	0.45	0.46	31000	27000
19-Jun-01	38.4	49.5	29%	progressive	15	9	4	6.5	0.53	0.52	29000	27000
20-Jun-01	38.5	58	51%	complete	15	6.5	3.8	8.8	0.51	0.52	33000	27000
21-Jun-01	38.3	62.1	62%	complete	14	7.5	5.0	7.0	0.61	0.58	30000	33000
22-Jun-01	38	62.1	63%	complete	12	7	5.9	7.0	0.57	0.48	28000	33000
25-Jun-01	43	53.8	25%	progressive	8.5	6.5	7.4	8.5	0.57	0.52	24000	26000
26-Jun-01	43.3	62.3	44%	complete	9.5	6.5	7.2	8.9	0.57	0.52	27000	29000
27-Jun-01	43.3	61.9	43%	complete	8	5.5	8.4	9.8	0.57	0.46	25000	27000
28-Jun-01	47.7	58.3	22%	progressive	7.5	6	8.0	9.8	0.52	0.5	25000	25000
29-Jun-01	48	57.3	19%	progressive	7	5.5	9.3	9.8	0.55	0.48	21000	25000
03-Jul-01	52.7	62.4	18%	progressive	6	5	9.5	10.6	0.5	0.47	23000	27000
04-Jul-01	52.1	62.6	20%	progressive	6.5	5.5	9.8	10.4	0.55	0.5	25000	26000
05-Jul-01	33.5	40.6	21%	progressive	15	11	2.9	5.9	0.47	0.46	26000	22000
09-Jul-01	33.6	43.4	29%	progressive	16	11	3.6	5.7	0.47	0.45	28000	24000
10-Jul-01	33.6	54.7	62%	no data	16.5	6	3.4	8.7	0.53	0.52	32000	23000
11-Jul-01	33.8	52.9	57%	complete	14.5	7.5	3.9	6.1	0.5	0.51	30000	29000
12-Jul-01	33.8	61.9	83%	complete	15.5	5.5	3.2	9.6	0.48	0.54	33000	28000
13-Jul-01	33.8	43.7	29%	progressive	16	12	3.3	4.9	0.51	0.48	28000	26000
16-Jul-01	38.5	44.6	16%	progressive	12	9.5	6.1	7.0	0.57	0.57	24000	23000
17-Jul-01	43.1	53.5	24%	progressive	8.5	6	7.5	8.7	0.51	0.46	22000	24000
18-Jul-01	42.9	53.1	24%	progressive	8	7	7.9	8.7	0.5	0.48	23000	25000
19-Jul-01	42.9	53	23%	progressive	7.5	6.5	8.2	9.0	0.5	0.5	22000	24000
20-Jul-01	38.3	57.7	51%	complete	14.5	8	4.1	6.1	0.48	0.53	31000	32000

143

Table 4.1. Summary of shoved jam tests (continued).

Test Date	Q (L/s) initial	Q (L/s) final	ΔQ (%)	Failure Mode	Length (m) initial	Length (m) final	t_{middle} (cm) initial	t_{middle} (cm) final	Porosity initial	Porosity final	Reynolds No. initial	Reynolds No. final
23-Jul-01	38.6	57.5	49%	complete	12	8	5.1	5.9	0.5	0.49	29000	32000
25-Jul-01	48.3	57.7	19%	progressive	6.5	6	8.2	8.8	0.5	0.5	24000	26000
26-Jul-01	38.5	58.2	51%	complete	13.5	6.5	4.9	7.5	0.54	0.51	29000	29000
30-Jul-01	33.4	43.5	30%	progressive	16.5	10.5	3.5	5.8	0.47	0.47	27000	24000
31-Jul-01	33.7	52.4	55%	progressive	17	7.5	3.4	5.9	0.52	0.51	31000	28000
01-Aug-01	33.5	61.9	85%	complete	17	6.5	3.7	6.9	0.56	0.53	32000	33000
02-Aug-01	47.7	62.2	30%	progressive	8	5	7.3	9.9	0.58	0.55	26000	27000
03-Aug-01	38.7	49.3	28%	progressive	13	9	4.9	6.9	0.55	0.53	27000	26000
07-Aug-01	38.2	52.8	38%	progressive	15.5	10.5	4.5	6.2	0.54	0.54	30000	29000
08-Aug-01	43.1	57	32%	complete	10.5	7	6.7	8.0	0.55	0.49	27000	27000
09-Aug-01	47.6	60.6	27%	progressive	7.5	6.5	7.7	8.7	0.54	0.52	25000	26000
10-Aug-01	33.1	38.9	18%	progressive	18.5	16.5	2.7	2.9	0.45	0.42	27000	27000
13-Aug-01	33.6	49.9	49%	progressive	15.5	8	3.6	7.1	0.52	0.53	29000	25000
14-Aug-01	33.3	57.4	72%	complete	15.5	5.5	3.8	9.1	0.55	0.5	32000	25000
15-Aug-01	33.7	61.8	84%	complete	14	6.5	4.3	7.6	0.53	0.5	31000	33000
16-Aug-01	33.5	48.5	45%	complete	15.5	9	3.5	6.4	0.51	0.52	29000	28000
17-Aug-01	33.6	57.5	71%	complete	15.5	6.5	3.8	7.8	0.55	0.52	32000	28000

144
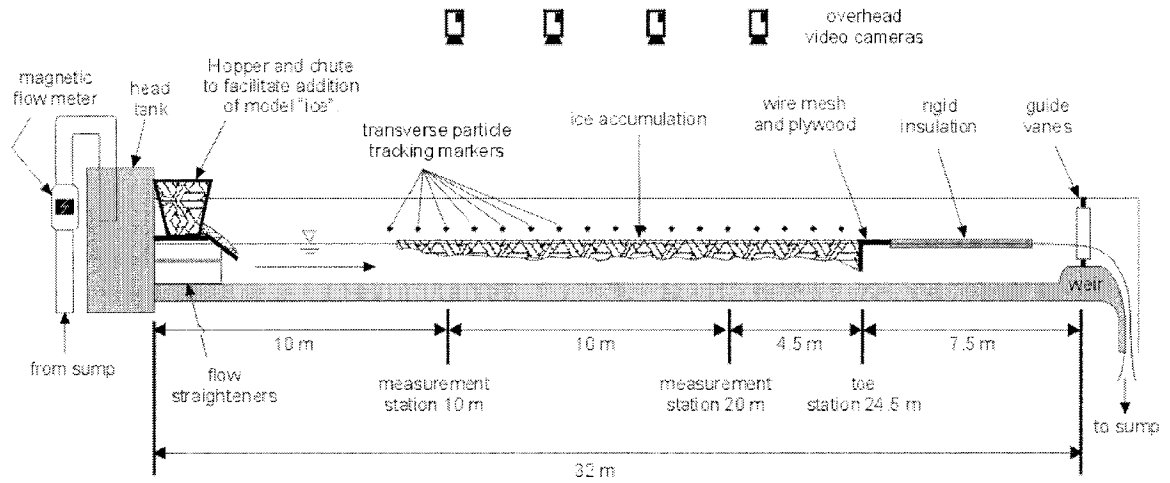
Figure 4.1. Experimental flume apparatus.

145
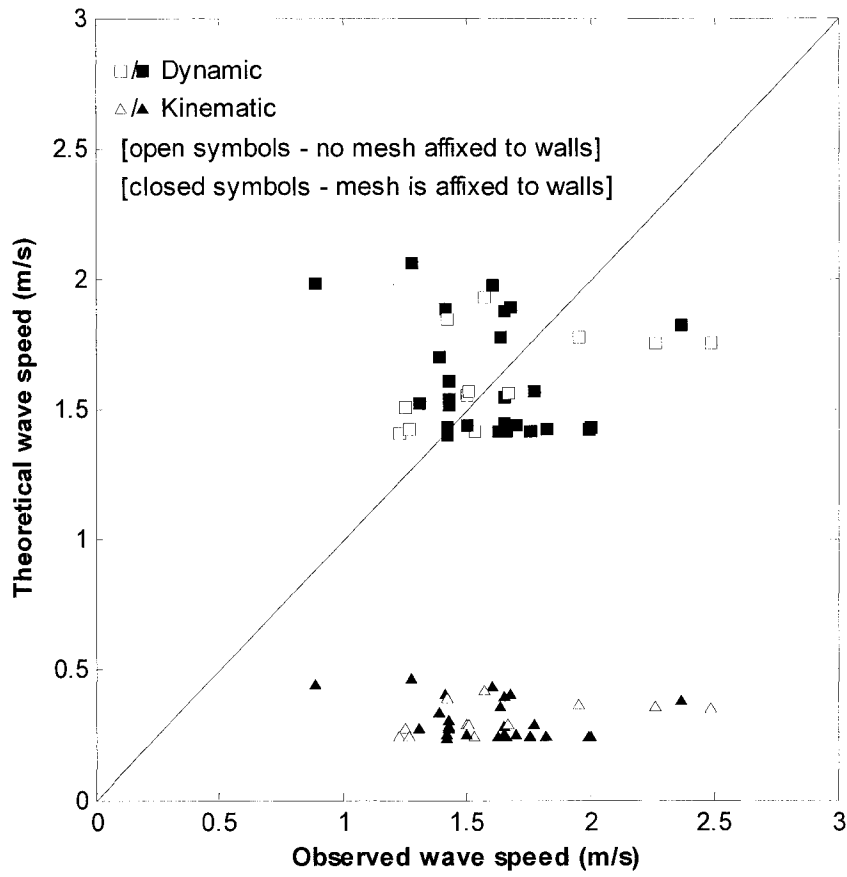
Figure 4.2. Observed versus theoretical wave speeds.

146
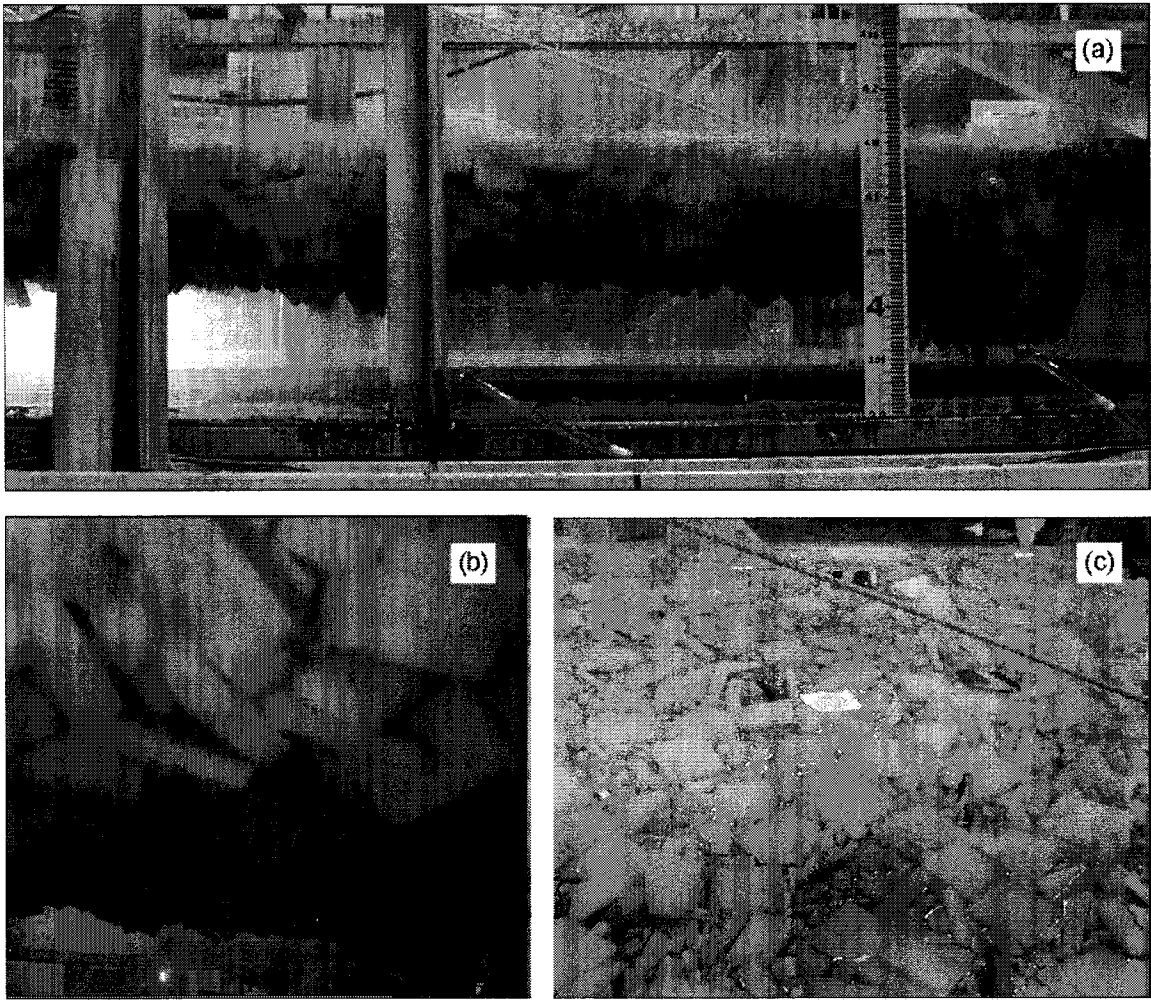
Figure 4.3. Experimental photos of a shoved jam viewed from (a) the side, (b) the bottom, and (c) the top.

147
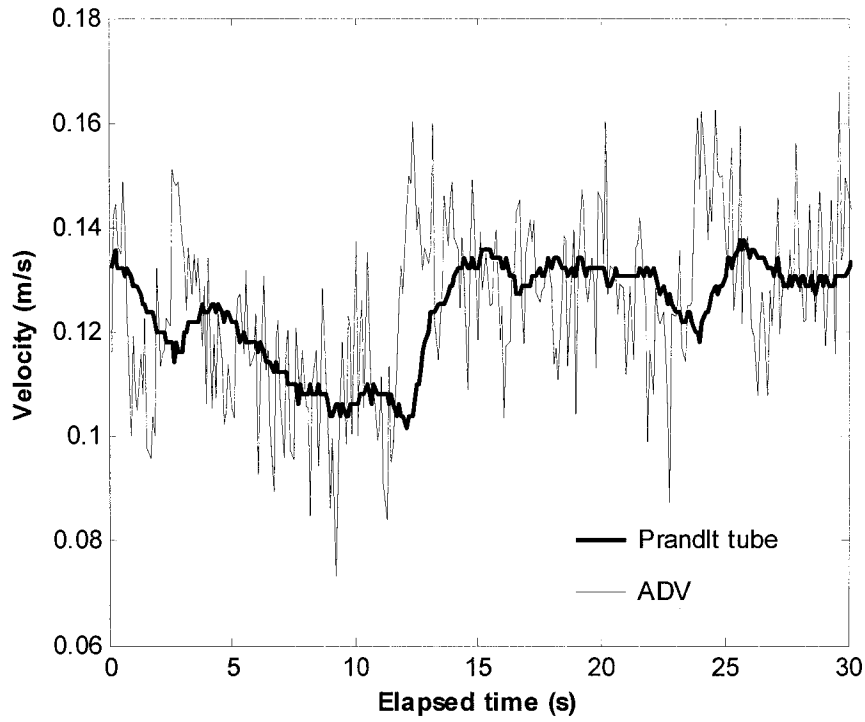
Figure 4.4. Velocity data comparison between Prandtl tube and ADV.

30-Jul-2001 - jam profile and cover progression summary

------- water surface & bottom of ice   ▨▨▨ assumed mid-jam portion
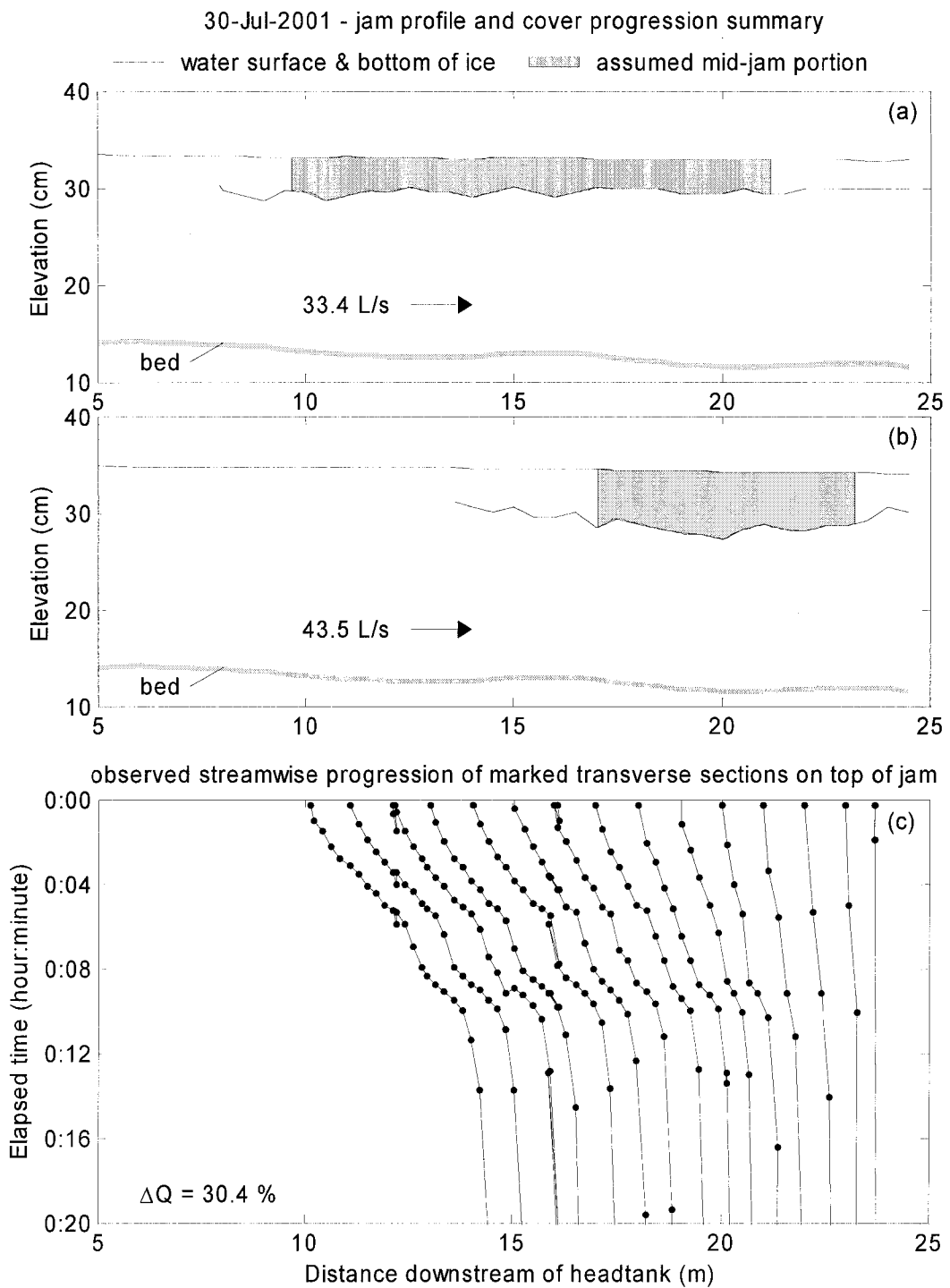
Figure 4.5. Initial ice jam profile (a), final ice jam profile (b), and cover progression (c) for 30% rapid increase in discharge.
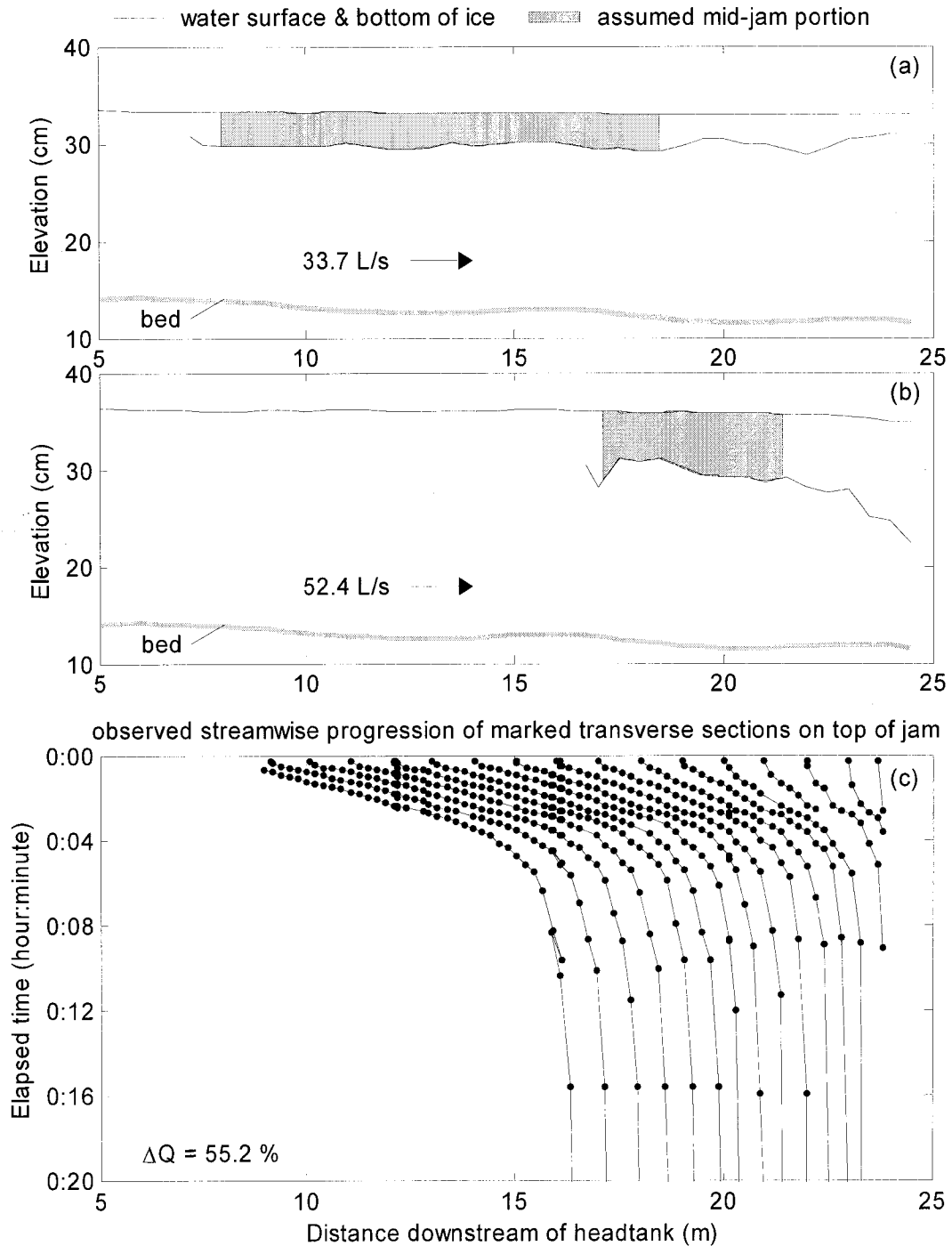
Figure 4.6. Initial ice jam profile (a), final ice jam profile (b), and cover progression (c) for 55% rapid increase in discharge.

150

01-Aug-2001 - jam profile and cover progression summary
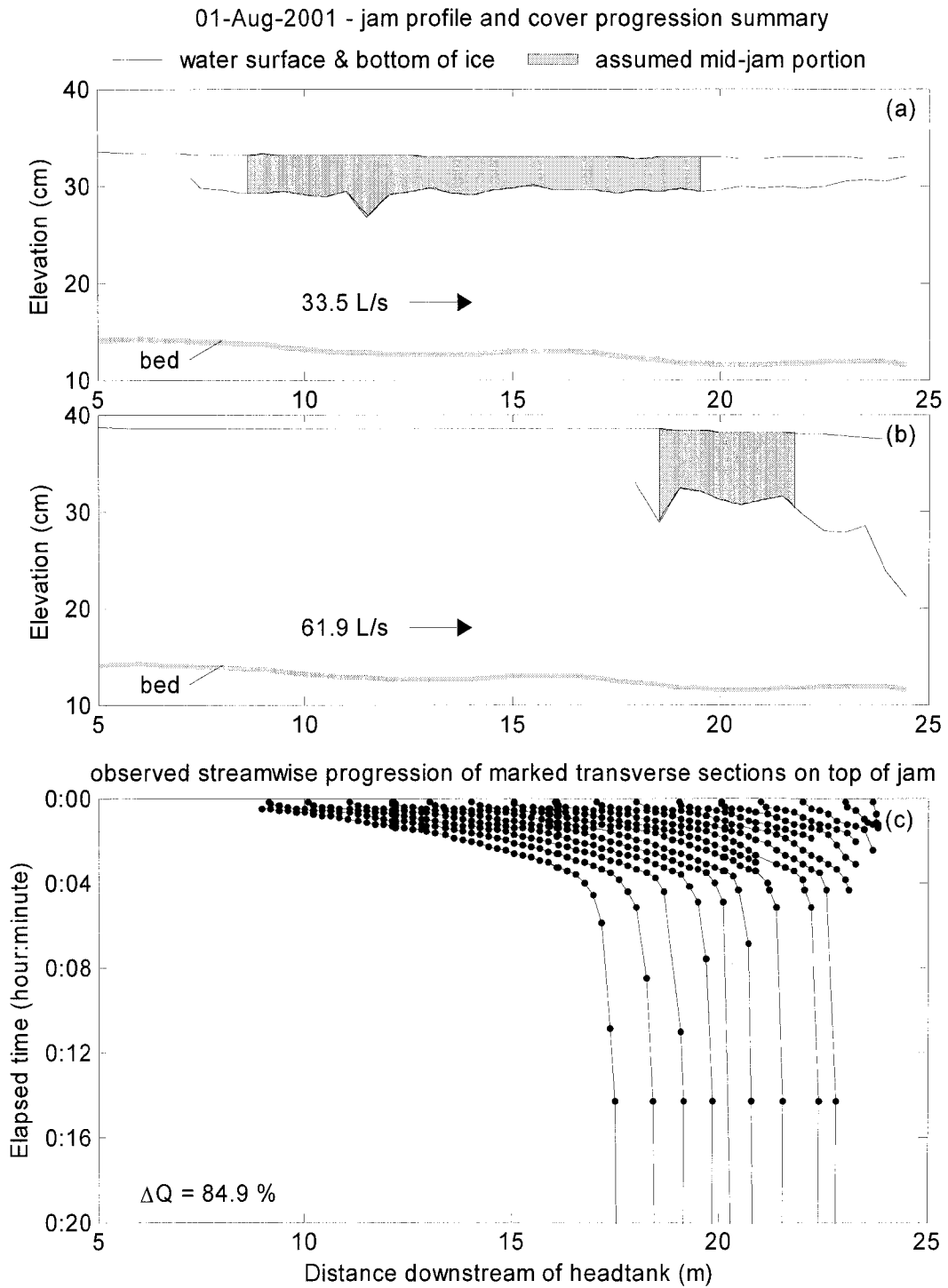
Figure 4.7. Initial ice jam profile (a), final ice jam profile (b), and cover progression (c) for 85% rapid increase in discharge.
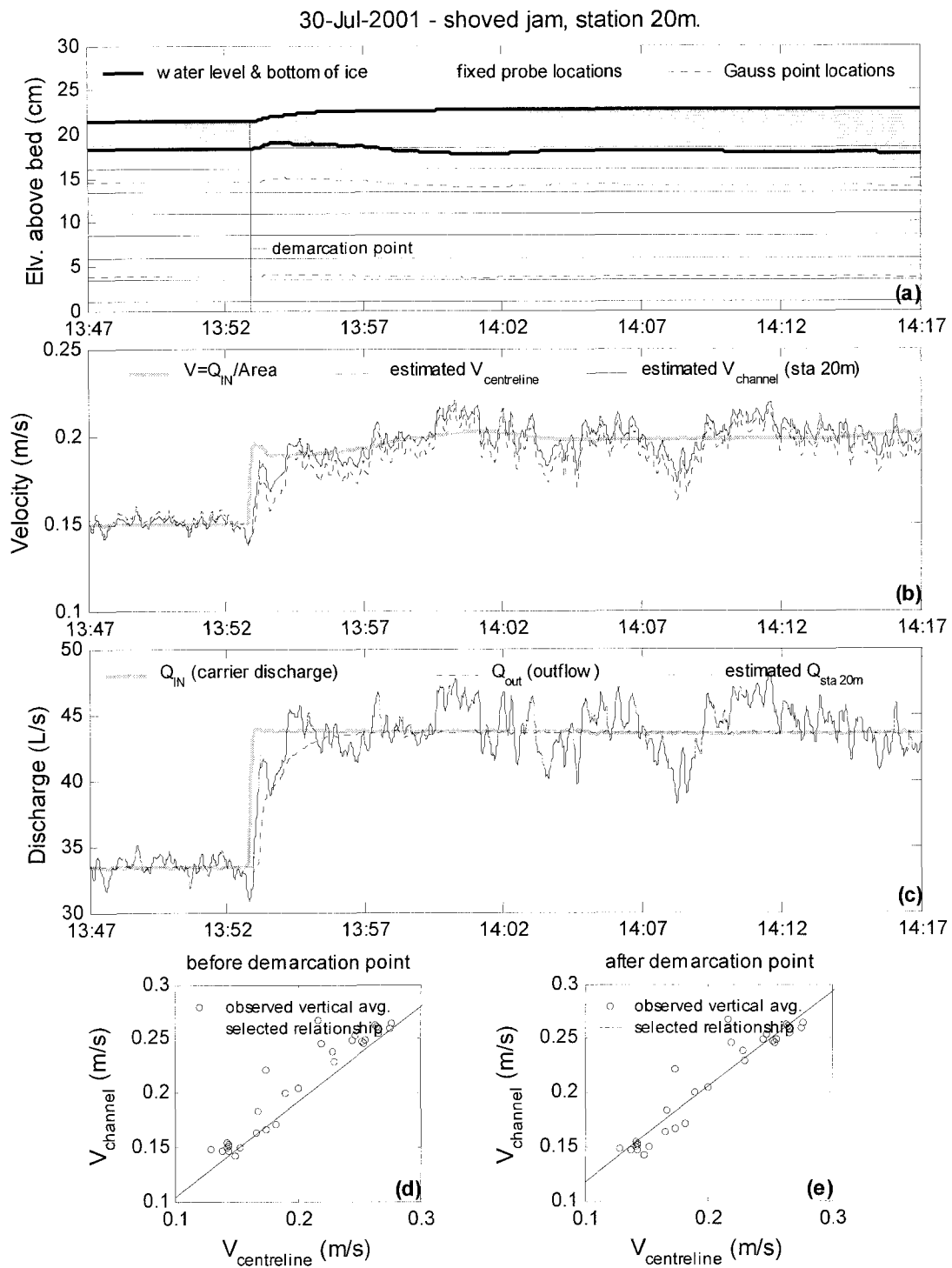
Figure 4.8. Continuous observations at station 20 m downstream of headtank for 30% rapid increase in discharge.
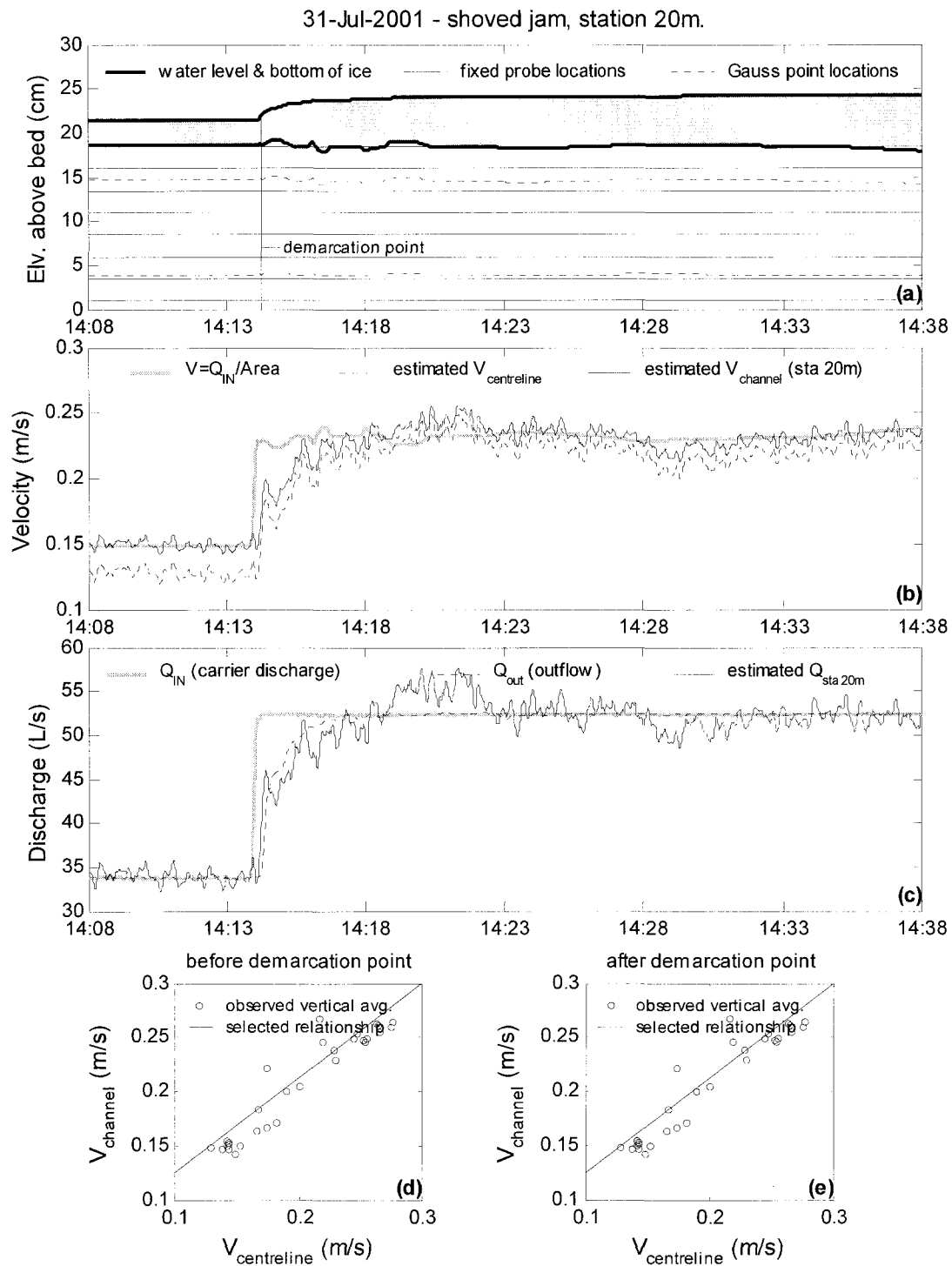
Figure 4.9. Continuous observations at station 20 m downstream of headtank for 55% rapid increase in discharge.

153
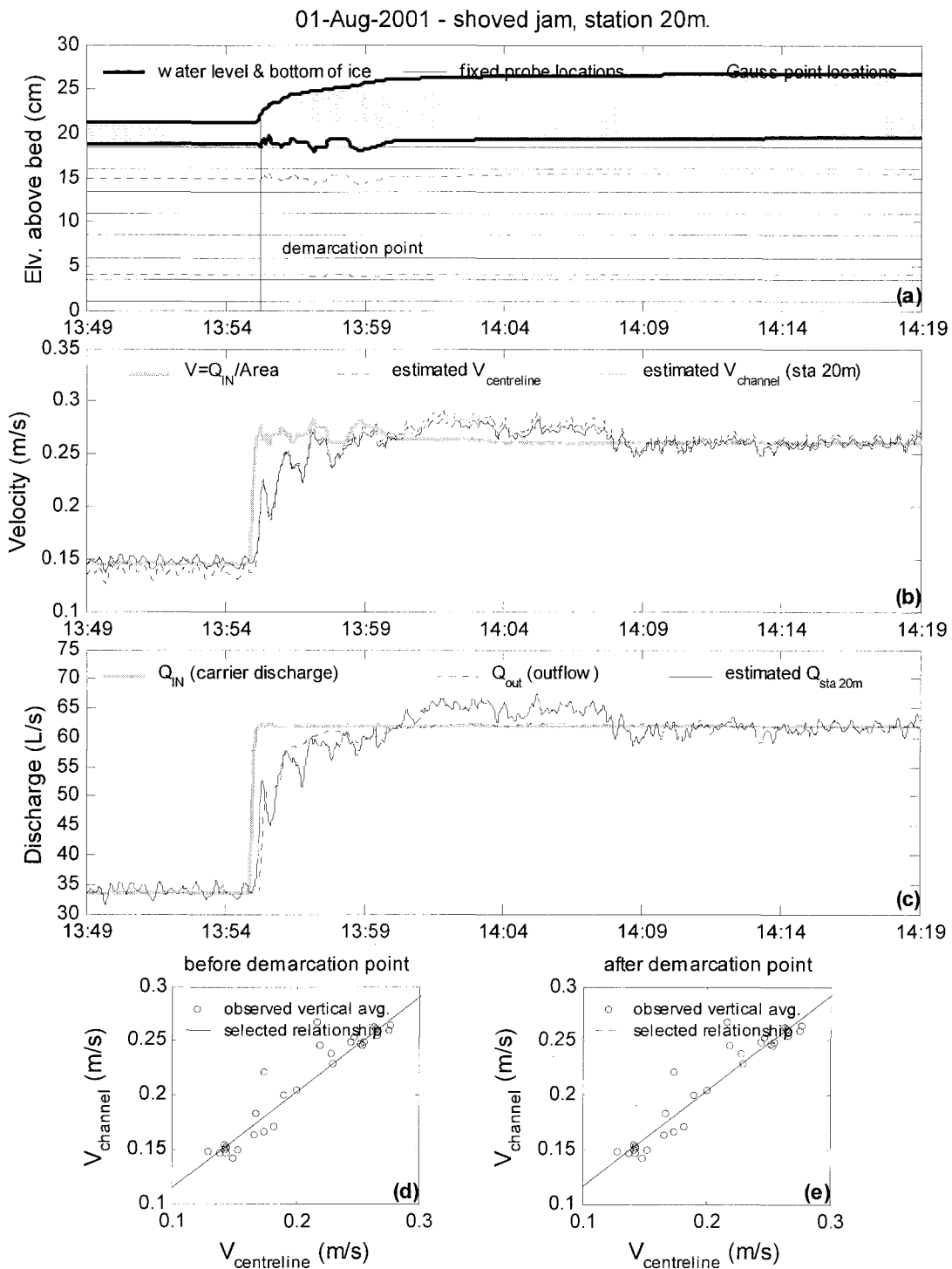
Figure 4.10. Continuous observations at station 20 m downstream of headtank for 85% rapid increase in discharge.
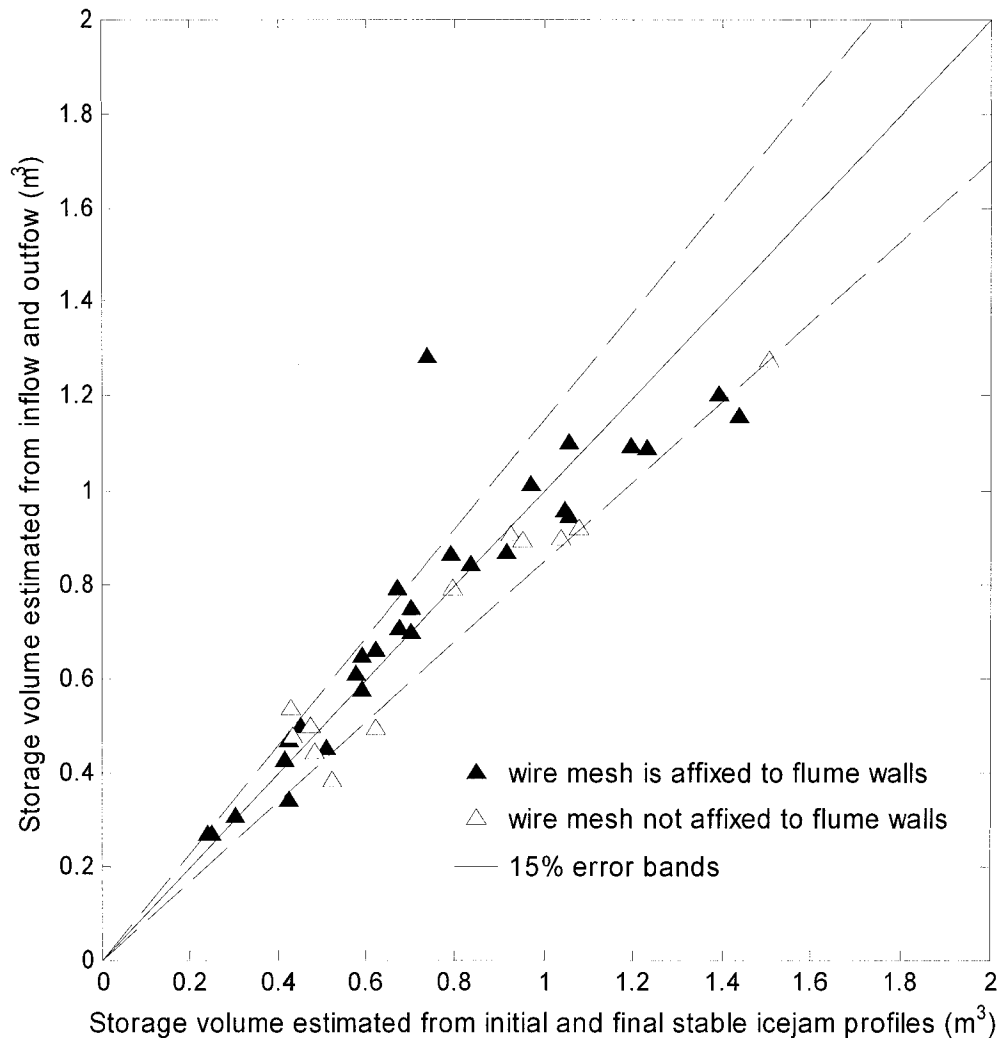
Figure 4.11. Comparison between storage volume based on difference in initial and final jam profiles and storage based on cumulative difference between measured system inflow and outflow.

155
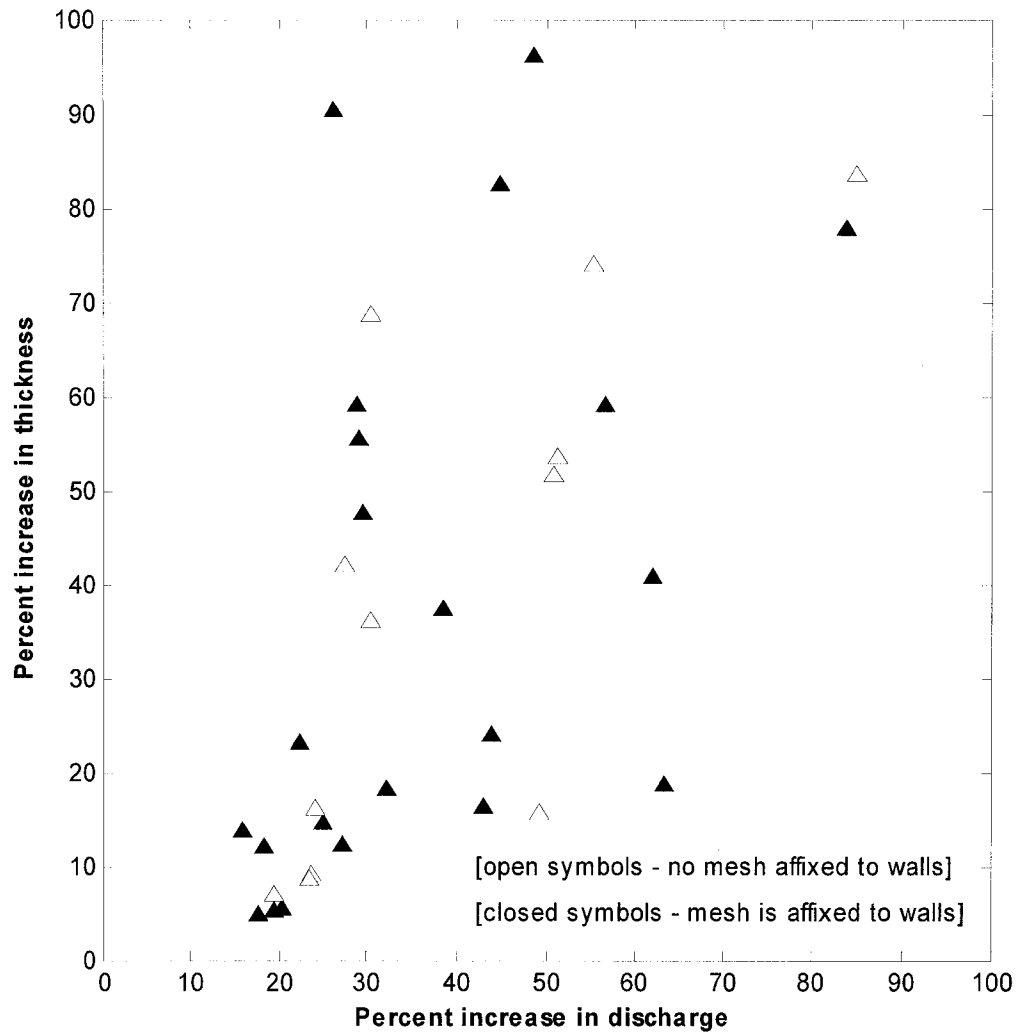
Figure 4.12. Percent increase in jam thickness as a function of the percent of rapid increase in discharge.

156
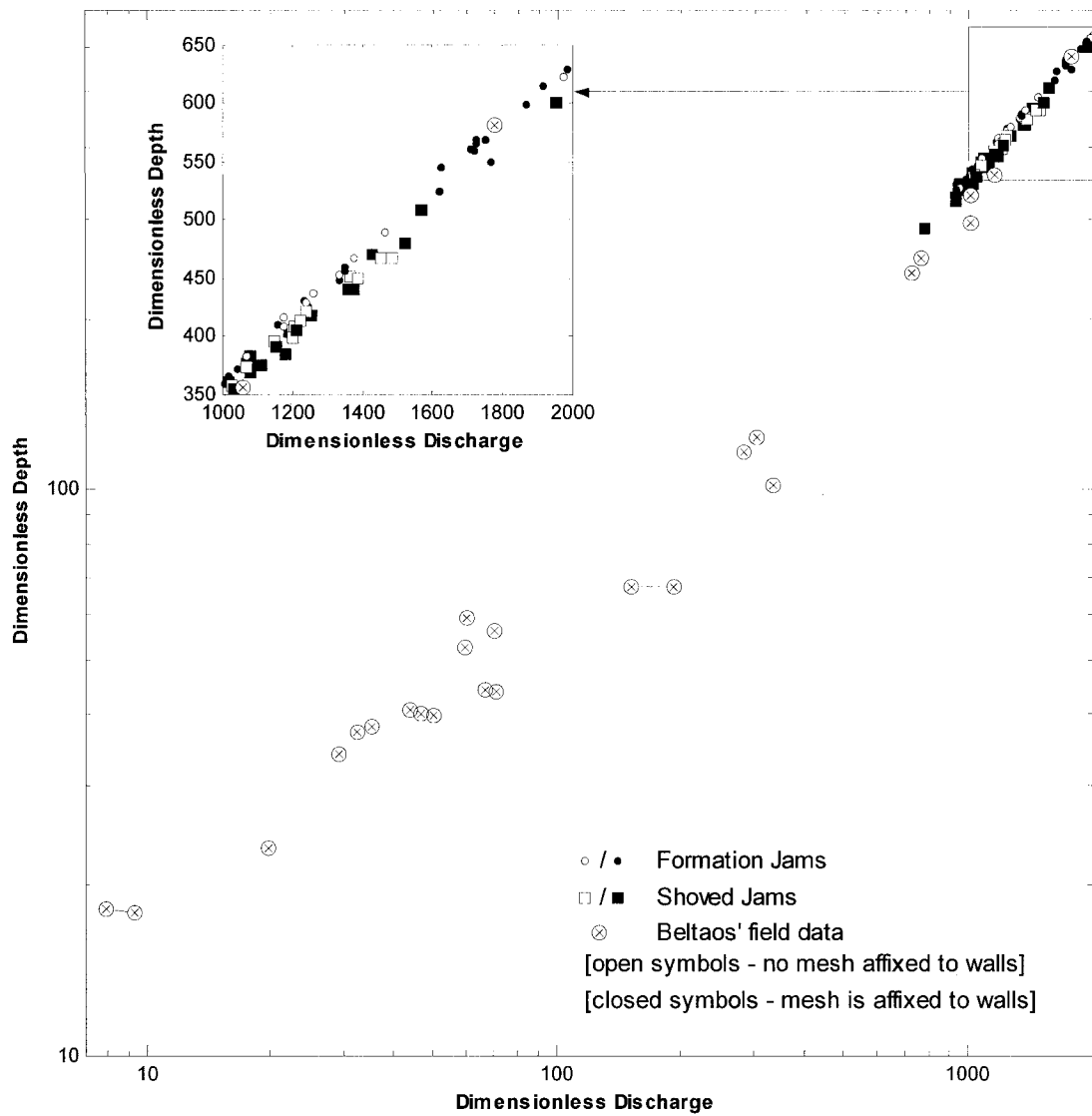
Figure 4.13. Dimensionless depth versus discharge.

157
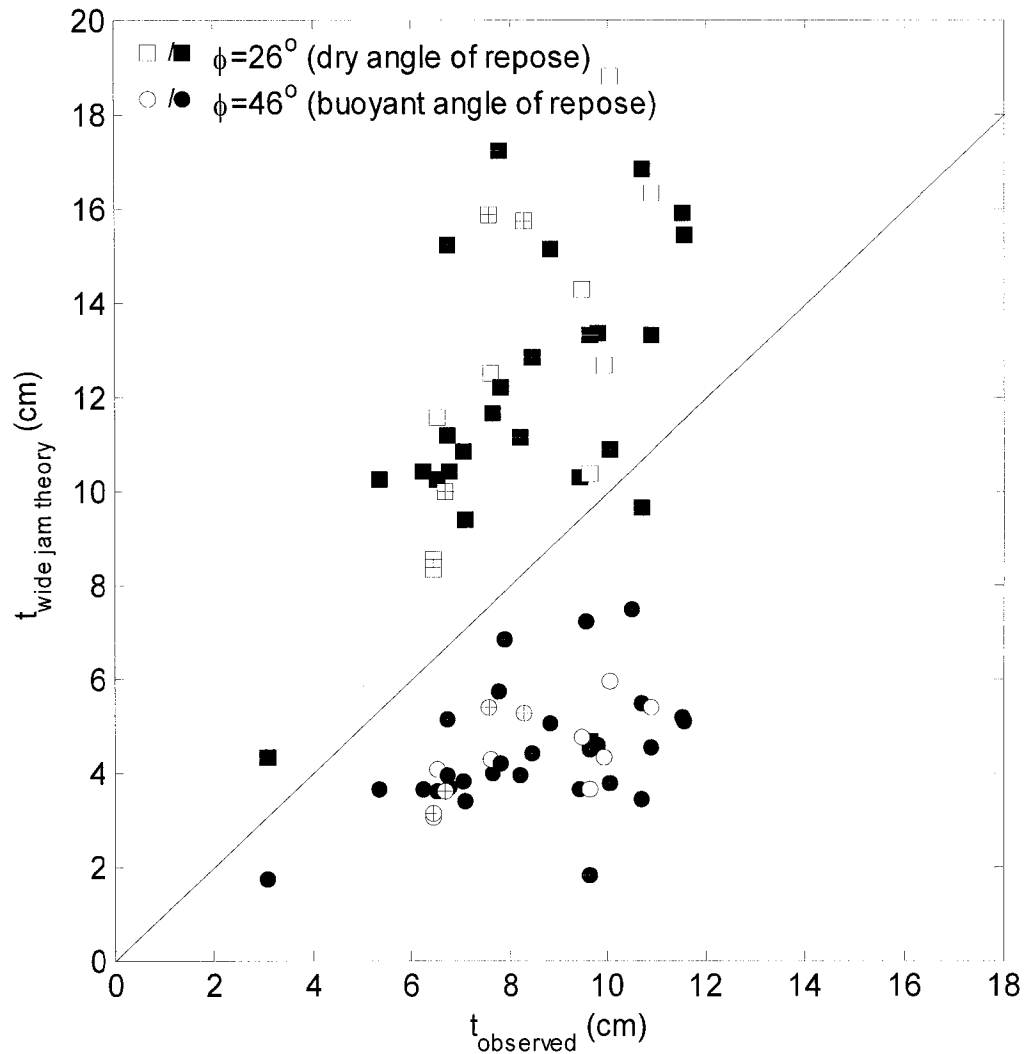
Figure 4.14. Comparison between the observed ice jam thickness within the middle portion of the shoved ice jam to the corresponding theoretical equilibrium thickness. Closed symbols denote wire mesh attached to flume walls and open symbols denote no wire mesh attached to flume walls. Symbols with a crosshair indicate denote those cases where the relative increase in discharge from the initial to final ice jam accumulation was greater than 50%.

158

4.7 References

Ashton, G. D. 1986. River and lake ice engineering. Water Resources Publications, LLC, 485 p.

Beltaos, S. 1983. River ice jams: theory, case studies, and applications. ASCE Journal of Hydraulic Engineering, Vol. 109, No. 10, pp. 1338-1359.

Healy, D., Hicks, F. and Loewen, M. 2002. Unsteady velocity profiles under a fixed floating cover. Proceedings of the 16th IAHR International Symposium on Ice, Dunedin, New Zealand, Vol. 1, 83-90.

Pariset, E., and Hausser, R. 1961. Formation and evolution of ice covers in rivers. Transactions of the EIC, Vol. 5, No. 1, pp. 41-49.

Pariset, E., Hausser, R., and Gagnon, A. 1966. Formation of ice covers and ice jams in rivers. Journal of the Hydraulics Division, Vol. 92, No. HY6, pp. 1-24.

Saadé, R. G., and Sarraf, S. 1996. Phreatic water surface profiles along ice jam – an experimental study. Journal of Nordic Hydrology, Vol. 27, No. 3, pp. 185-202.

Shen, H.T., Wang, D.S., and Wasantha Lal, A.M. 1995. Numerical simulation of river ice processes. ASCE Journal of Cold Regions Engineering, Vol. 9, No. 3, pp. 107-118.

Zufelt, J. E. 1990. Experimental observations of shoving and thickening – comparison to equilibrium thickness theory. Proceedings of the 10th IAHR Symposium on Ice, Helsinki, Finland, pp. 504-510.

Zufelt, J. E. 1992. Modes of ice cover failure during shoving and thickening. Proceedings of the 11th IAHR Symposium on Ice, Banff, Canada, pp. 504-510.

Zufelt, J. E. 1996. Ice jam dynamics. Ph.D. thesis submitted to the Department of Civil and Environmental Engineering, University of Iowa, 203 p.

Zufelt, J. E., and Ettema, R. 1997. Unsteady ice jam processes. CRREL Rep. 97-7, U.S. Army Cold Regions Research and Engineering Laboratory, Hanover, N.H.

Zufelt, J. E., and Ettema, R. 2000. Fully coupled model of ice-jam dynamics. ASCE Journal of Cold Regions Engineering, Vol. 14, No. 1, pp. 24-41.

160

5.0 Summary and Conclusions

5.1 Summary

The objective of this work was to improve our understanding of the dynamic aspects of ice jam formation through observations of model ice jams under controlled laboratory conditions. The dynamic aspects refer to how the key parameters describing the ice jam vary with respect to time. Never before has such a comprehensive set of observations on these key parameters (flow rate, depth, ice jam thickness, and cover progression) been documented.

Methods were successfully devised to obtain continuous direct observations of inflow, outflow, depth, and ice jam thickness. However, there was no means for obtaining direct observations of flow at measurement stations within the ice jam; estimates of flow at these locations were deduced from measured point velocities and flow depths. The first paper in this thesis explored the viability of using such an approach through a detailed examination of velocity profile measurements taken under stable ice covers in natural streams. The data, made available from Water Survey Canada, suggested the existence of index velocities that related well to the section average velocity. A practical method for estimating discharge under ice covers in the field was also suggested and the approach is currently being pursued by Water Survey Canada. More imporatantly, the existence of index velocity relationships were established for the experimental arrangement used for the ice jam experiments presented in Chapters 3 and 4.

161

5.2 Main Conclusions and Recommendations

The experimental work carried out in this thesis study investigated two different ice jam formation scenarios which corresponded to extreme carrier discharge conditions that may be expected in natural channels. The first scenario explored the relative importance of the dynamic aspects of ice jam formation on the ultimate ice jam profile for ice jams formed under a constant carrier discharge. The second scenario looked at the case where an otherwise stable ice jam accumulation was caused to fail and collapse by shoving to form a thicker new stable ice jam through a very rapid increase in discharge to a higher constant flow rate. A total of 40 model runs were conducted over the full range of discharges permitted by the experimental arrangement. In addition to documenting the resulting ice jam profiles, continuous measurements of the variations in flow depth, ice thickness and discharge were obtained within the developing ice jam.

For all of the ice jams formed under a constant carrier discharge described in Chapter 3, the ice accumulations initially developed by hydraulic thickening processes, and then subsequently by varying degrees of consolidation. Comparison of the resulting ice jam thicknesses within the middle portion of the jam with existing steady flow theories, indicated that the analysis of jams formed under a constant carrier discharge lend themselves well to the usual steady state ice jam formulations. While the process of ice jam formation is dynamic the results of this investigation suggested that steady ice jam analysis based on the dominant carrier discharge is likely sufficient for most practical applications.

The second series of tests outlined in Chapter 4 investigated the effects of very dynamic flow fluctuations on the destabilization of stable ice jams initially formed under steady carrier flow conditions. In addition to documenting the difference in the resulting ice jam profiles, continuous measurements of the variations in flow depth, ice thickness and discharge were obtained at key stations within the ice jam during consolidation (shoving). The resulting observations suggested that the final stable accumulations followed the theoretical relationships used to describe ice jams formed under steady state conditions. Even for highly dynamic events, characterized by a rapid increase in discharge, an appropriate steady discharge can be used in cooperation with the usual steady state ice jam formulations to achieve estimates on ice jam thicknesses and resulting water surface elevations for most practical design scenarios.

The experimental arrangement used in this study was not sophisticated enough to explore the passing of various hydrograph shapes in a controlled manner. The author recommends that future investigations explore this further. Also, existing dynamic ice jam models should be tested against the results of this thesis investigation to further verify their application and by doing so, perhaps narrow the focus of our understanding of ice jam formation dynamics.

Additional future work recommended by the author would be the development of a semi-analytical model describing index velocity relationships under an ice cover, complemented by a more rigorous field investigation. This would serve to increase the level of confidence in using such methods in full scale discharge measurement programs.

The combined work of the two series of tests presented in Chapter 3 and 4 provides the most comprehensive and exhaustive set of data relating to dynamic ice jam formation available. It also represents the first published efforts of obtaining discharge estimates within a developing ice jam.

164

Appendix A – Salient Properties of the Model Ice Material

Ice floes were simulated using polyethylene pieces with a specific gravity of 0.92. Table A.1 presents the proportions of floe sizes used for the experiments where the resulting mixture had a bulk porosity of 0.49. The bulk porosity was defined as the porosity of the ice mixture when randomly placed in a bucket. This was determined by first filling a bucket of known volume with the model material and then adding water to fill the voids until it had reached the top of the container. The ratio of the volume of water required to fill the voids to the volume of the empty bucket represented the bulk porosity. Table A.2 lists the results of the series of tests conducted to determine the bulk porosity. The bulk porosity was very consistent from test to test. Knowing the bulk porosity of the material in the buckets was necessary since the total volume of model ice added to the flow for each experiment was based on the total number of buckets of model ice added.

A.1 Model Ice Strength

The ice processes investigated in this study were limited to those processes that could be described by a cohesionless mass of detached floes, where each floe is considered to remain intact and incompressible. The ice floes used in this study had sufficient tensile and compressive strengths to be considered both unbreakable and incompressible. Unbreakable floes of this type are commonly used when hydrodynamic processes dominate (Wuebben 1995) – as was the case for this investigation.

Where cohesive forces between particles can be neglected, an ice jam can be thought to respond to the applied hydrodynamic forces as a floating granular mass of detached particles where basic soil mechanic principles apply. This implies that the internal shearing strength of the accumulation is a function of the angle of shearing resistance, ϕ, which can be considered equivalent to the angle of repose resulting from the deposit of a granular soil by pouring it from a single point above the ground (Holtz and Kovacs 1981). The fundamental theories describing the force distribution in large ice accumulations formed through shoving in a telescopic manner (i.e. wide channel jams) are based on simple Mohr-Coulomb concepts that rely on an internal strength parameter that is often characterized by the dry angle of repose (e.g. Pareset et. al 1966; and Uzuner and Kennedy 1976). Therefore, it was appropriate to make an attempt to determine the shearing angle of the model ice material used in this investigation.

A series of tests were conducted to determine both the dry, and "buoyant" angle of repose (ϕ_{dry} and $\phi_{buoyant}$), both of which are defined schematically in Figure A.1. The dry angle of repose was determined by measuring the side slope of a pile of model ice created by three different methods. The first method involved lifting an inverted a garbage can full of the model ice material (the bottom of which was cut off to facilitate addition of model ice), the second method involved dumping ice slowly into a pile from a bucket, while in the third method, model ice was delivered loosely into a pile using a shovel. Figure A.1a presents a schematic of the resulting pile and the measured angle of repose. Table A.3 presents the results of this test where, for each test, the angle of repose was taken as the average of that viewed from three different sides of the resulting pile. The dry angle of

166

repose is a general indication of a granular material's resistive strength to an applied vertical force (i.e. gravity). However, in a floating accumulation of ice, gravity is not the only acting vertical force; buoyancy also contributes. Therefore, it was deemed appropriate to attempt to define a modified angle of repose that considered buoyancy effects.

A simple test was devised to quantify this so-called buoyant angle of repose, $\phi_{buoyant}$. The basic procedure is illustrated in Figure A.1b. In a tank of still water, two concentric rings, with their axes oriented vertically, were fixed in position so as to span the air-water-interface. Model ice was introduced through the top of the inner ring (through the air-water interface) as illustrated in Figure A.1b. The model ice spanned outwards to the outer ring and then began to form an upside down cone as additional model ice was added to the base of the inverted cone through the inner ring. The model ice eventually began to escape past the bottom edge of the outer ring and more model ice was added in this manner until a constant angle of repose was maintained (regardless of any additional model ice added to the inner ring). The resulting angle of the inverted side slope was then measured (see Figure A.1b). Variations in the ratio of the inner and outer ring diameters were found to have no impact on the resulting angle of repose. Table A.4 presents the results of this test for two separate cases where, for each test, the angle of repose was taken as the average of that viewed from four sides of the tank. In the first case the model ice material was dry initially and in the second case the model ice had been soaking in water for 5 days (these two cases were investigated to explore any possible difference in the model ice's non-wetting tendency – discussed below).

167

The values for ϕ_{dry} and $\phi_{buoyant}$ should differ since the applied forces are quite different for each case. In on case the mass of the model ice material experiences buoyant forces while the other case does not. There was no convenient means for determining the uncertainty in values determined for ϕ_{dry} and $\phi_{buoyant}$. There were an insufficient number of tests to enable a suitable uncertainty analysis. The point of the tests was to conduct a first level analysis to quantify the relative difference between the two cases and establish that there was indeed a difference in the angle of repose for ice rubble under only the influence of gravity and ice rubble under the influence of gravity and buoyant forces.

A.2 Non-Wetting Tendency of Model Ice

Perhaps the most limiting characteristic of using polyethylene and other similar materials as a model ice material is its non-wetting tendency, which raises the issue of surface tension effects. It was found during previous experiments that when the model ice material was left wet for several days, surface tension effects were minimized. Zufelt (1992) conducted experiments using "plastic beads" and found that "when first added to water, the beads exhibit some surface tension but after a few days in water, they become fully wetted". Similar behaviour was exhibited by the model ice used in the experiments conducted in this study and it was the authors' opinion that the wettability of the model ice increased through the development of a biological film on the surface of the ice pieces. Other investigators have suggested that surface tension effects can be minimized "by allowing natural accumulation of micro-organisms" (Wuebben 1995).

The contact angle, α, between a liquid and a solid surface, can be used as a measure of

168

the "wetting" between a liquid and solid interface. Sugita (1987) defined this contact angle as "the angle between the tangent of the liquid surface and the solid surface through the liquid at the point where the surface of a liquid droplet on a solid surface intersects with the solid surface"; contact angles near zero indicate "complete wetting", contact angles less than $90°$ indicate "partial wetting", and contact angles between $90°$ and $180°$ indicate "hardly any wetting". Sugita (1987) lists the contact angle between water and polyethylene as $94°$ (hardly any wetting) and various organic liquids (e.g. Glycerine and Formamide) having contact angles less than $90°$ (partial wetting). It may be reasonable to suppose that the liquid in direct contact with the model ice material becomes more "organic" due to the development of a biological film consequently decreasing the contact angle and making the material more "wettable". A simple qualitative test was devised to investigate this theory.

Figure A.2 presents a schematic describing this simple test. Since no appropriate microscope was available to make direct measurements on the contact angle, an alternative approach was used to get at least a semi-quantitative indication of the contact angle. To do this, the height and diameter of water droplets laid on both dry model ice, and on model ice that was allowed to soak for several days, were compared. The drops placed on the wet model ice were wider and shorter than those placed on the dry model ice suggesting a decrease in contact angle. Visual inspection of the water drops also indicated a decrease in contact angle from dry to wet ice. The impact of the relative "wetability" of the model ice on the buoyant angle of repose was also explored (see Table A.4) and it was found that drier model ice gave a smaller angle of repose than

169

model ice that had been soaked in water for several days. These results support the author's observed behaviour of the model ice: the materials wettability increased after soaking for several days and surface tension effects were reduced. Therefore, to minimize the impact of surface tension effects, the model ice material was kept wet throughout the entire series of tests conducted for this study.

170

Table A.1 Proportions of individual floe sizes used in model ice mixture.

Ice sizes (cm)	Proportion of entire mixture by volume (%)
1.27 x 1.27 x 0.32	21.4
1.27 x 1.27 x 0.64	8.4
1.27 x 1.27 x 5.08	26.7
5.08 x 5.08 x 0.64	23.5
5.08 x 5.08 x 1.27	20.0

Table A.2 Determination of the model ice bulk porosity.

Test number	Volume of bucket (mL)	Volume of water added to fill voids (mL)	Porosity
One	22,900	11,540	0.50
Two	22,500	10,840	0.48
Three	22,500	10,785	0.48
Four	22,900	11,500	0.50
Average	22,700	11,166	0.49

172

Table A.3 Determination of the dry angle of repose.

Method	Dry angle of repose (degrees)			
	Test 1	Test 2	Test 3	Average
1. Lift inverted garbage can.	30.3	29.3	30.0	29.9
2. Slowly dump ice into a pile from a bucket.	27.7	28.7	29.3	28.6
3. Loose shoveling of ice into a pile.	30.3	30	29	29.8

Table A.4 Determination of the buoyant angle of repose.

Ice Condition	Buoyant angle of repose (degrees)		
	Test 1	Test 2	Average
1. Initially dry.	43	41	42
2. Soaking in water for 5 days.	46	46	46

(a)

air

rough steel bed

ϕ_{dry}

ice added from top

(b)

$\phi_{buoyant}$

still water
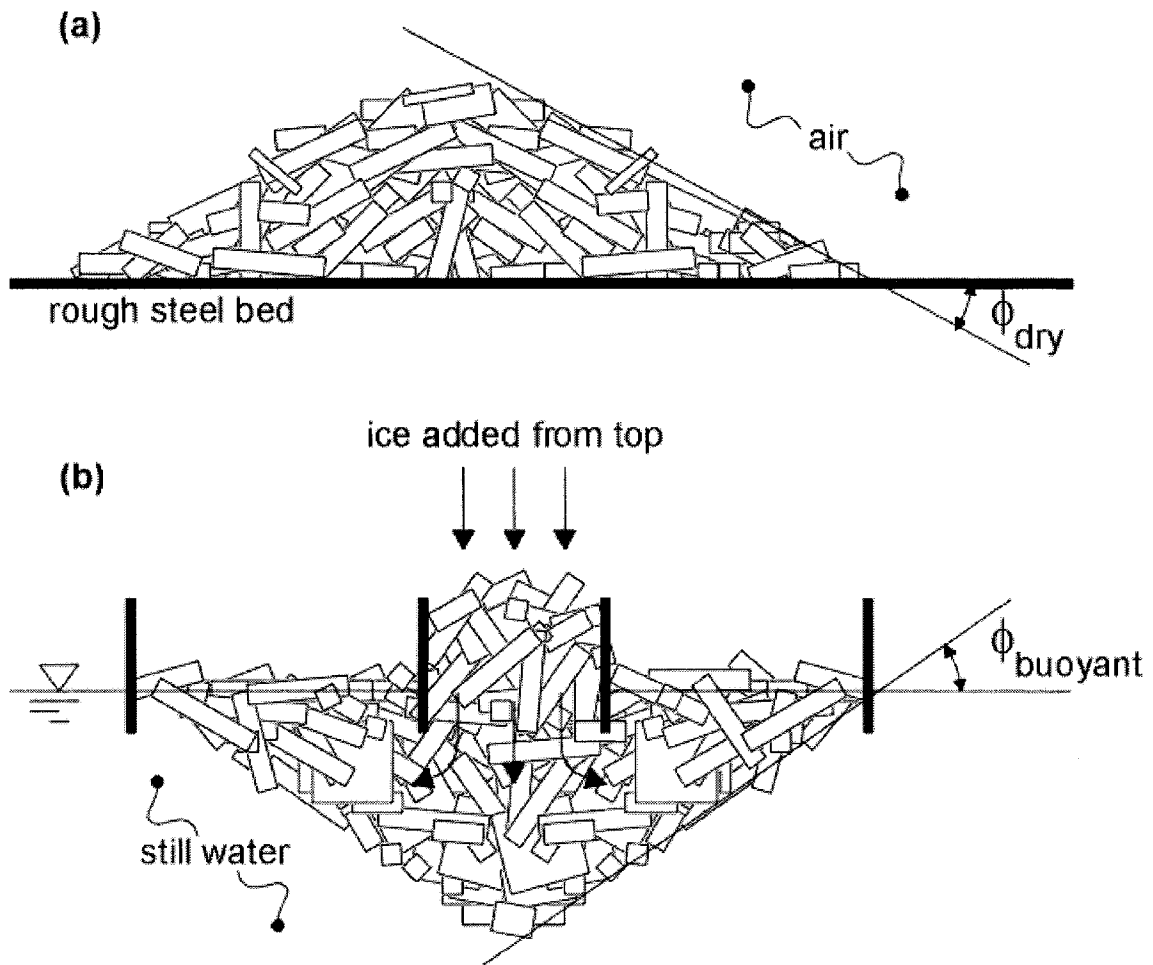
Figure A.1. Schematic of test arrangement for determining, ϕ_{dry} and $\phi_{buoyant}$, the dry and

buoyant angle of repose, respectively.

174
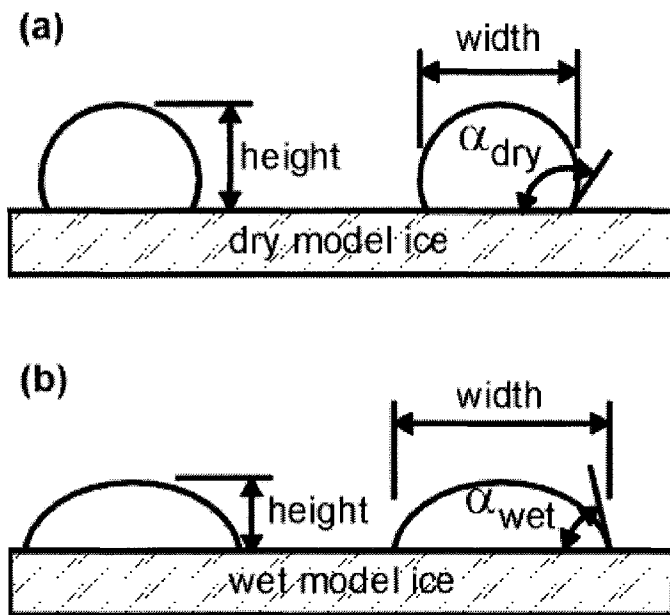
Figure A.2. Schematic of water-drop-test to assess model ice "wetability".

A.3 References

Holtz, R.D., and Kovacs, W.D. 1981. An introduction to geotechnical engineering. Prentice Hall, Inc., Englewodd Cliffs, New Jersey, 733 p.

Pariset, E., Hausser, R., and Gagnon, A. 1966. Formation of ice covers and ice jams in rivers. Journal of the Hydraulics Division, Vol. 92, No. HY6, pp. 1-24.

Sugita, K. 1987. Wettability and adhesion of polymer surfaces. International Polymer Science and Technology, Vol. 14, No. 10, pp. 38-46.

Uzner, M.S., Kennedy, J.F. 1976. Theoretical model of river ice jams. Journal of the Hydraulics Division, Vol. 102, No. HY9, pp. 1365-1383.

Wuebben, J. 1995. Physical modeling. *in* River ice jams. S. Beltaos, ed., Water Resources Publications, LLC, 372 p.

Zufelt, J.E. 1992. Modes of ice cover failure during shoving and thickening. IAHR Proceedings of the International Symposium on Ice, 11th, Banff, Alberata, Canada, Vol. 3, pp. 1507-1514.

Appendix B – Details on Discharge Estimates

B.1 Inflow and Outflow

Inflow was recorded by an inline magnetic flow meter positioned directly downstream of the flow control valve in the feed pipe to the head tank. The accuracy of the magnetic flow meter was evaluated by comparison to direct discharge measurements obtained from detailed integrated velocity profile data taken across a flume section at station 20 m for different steady carrier discharges. The results of this check indicated that the actual discharge was overestimated by the magnetic flow meter by 4%. Consequently, all discharge data obtained by the magnetic flow meter was corrected accordingly.

A unique relationship between discharge and depth that was found over the weir located at the downstream end of the flume. This relationship was confirmed by collecting water surface elevation data over the weir using a point gauge for a range of steady discharges. Figure B.2 illustrates the results of this test. The placement of a water level recorder at this location facilitated reliable estimates of discharge exiting the system for the duration of each test. Continuous water level data was collected at this location using a capacitance model water level recorder made by Delavan Industrial Controls (No. CS54-12). Over the range of depths for the experiments the water level recorder provided a direct relationship between voltage and water level. With knowledge of the initial and final steady discharge values obtained from the magnetic flow meter (inflow) estimates on the discharge over the weir (outflow) were obtained directly from the voltage output readings obtained from the water level recorder. Figure B.3 illustrates the direct

177

relationship between voltage output from the water level recorder and discharge obtained from the magnetic flow meter. Two primary concerns associated with the use of a capacitance type water level recorders are drift in instrument calibration and sensitivity to changes in water temperature. Flume temperatures did not vary by more than 0.5 °C over the duration of a single test and any effects on discharge estimates due to these small temperature changes were negligible. However, changes in the flume water temperature from day to day were in the order of several degrees and these changes combined with expected calibration drift in the instrument were expected to have a significant impact on instrument calibration. Rather than re-calibrating the instrument each day (to account for the effects of temperature changes and calibration drift) and determining the coefficients defining the unique voltage-discharge relationship prior to each test, the unique linear relationship was determined after each test with knowledge of the initial and final steady discharges obtained from the magnetic flow meter. This circumvented the need to calibrate the water level transmitter prior to each test, which would have been logistically prohibitive.

B.2 Station 10 and 20 m Downstream of Head Tank

Continuous estimates on discharge at stations 10 and 20 m downstream of the head tank were based on knowledge of the section average velocity and corresponding flow area.

B.2.1 Water Level and Ice Thickness @ Stations 10 and 20 m

Initial and final steady state water levels were measured directly using a point gauge oriented along the channel centerline. Initial and final and ice thicknesses were measured

178

directly with the aid of a ruler and set square as illustrated in Figure B.4.

Variations in water level and ice thickness data during a test were obtained by visual inspection of the playback of continuous video data recorded at measurement stations 10 and 20 m. For each reading, the time, water level, and bottom of ice level, were manually recorded into a table. Water levels were estimated to the nearest 1 mm and the bottom of ice to the nearest 0.5 cm.

The variations in water elevation and ice thickness were related to the initial measured steady state water surface elevation to obtain continuous water surface elevation and ice thickness values. The data was then interpolated linearly between recorded values at one second intervals to facilitate use in subsequent analyses with the continuous velocity data (collected at 1 second intervals).

B.2.2 Point Velocity Data @ Measurement Stations 10 and 20 m

Point velocity data was obtained using Prandtl tubes equipped with pressure transducers. Each setup was calibrated so that 1" (2.54 cm) of water corresponded to a one-volt output from carrier demodulator that were connected to the pressure transducers. Figure B.5 presents a schematic of a Prandtl tube arrangement used in this investigation along with the variables used to develop a relationship for the velocity immediately upstream of the tip of the probe, u_{probe}, which can be expressed as a function of the difference in stagnation and static pressures – written as follows (White, 1986):

$$[4\text{-}1] \quad u_{probe} = \sqrt{\frac{2(p_o - p_s)}{\rho}} \, ,$$

179

where: ρ is the density of the fluid, p_o and p_s are the stagnation and static pressure, respectively.

Efforts were made to ensure the probe tips were oriented in the direction of the flow. Specifications provided by the manufacturer indicate readings to be accurate within 2% with angles of attack of up to 30 degrees. For the experiments described herein the attack angles were generally less than 5 degrees and never more than 15 degrees; so errors associated with oblique angles of attack were considered to be negligible.

The pressure plates available for this study were designed to have a linear response within a working pressure range of ± 2.54 cm; on the positive scale, this translates to a working velocity range of 0 to 70 cm/s. The range of velocities encountered during these experiments was approximately 15 to 35 cm/s.

B.2.3 Vertically Averaged Centerline Velocities

In an attempt to measure the vertically averaged velocity at a measurement section, Prandtl tubes were positioned so as to try and capture point velocities at the Gauss point locations (as described in Chapters 2 and 3). Healy and Hicks (2003) demonstrated that the centerline vertically averaged velocity provided for a reasonable and direct estimate of the average channel velocity. Figure B.6 illustrates a comparison between the between the average Gauss point velocities and the vertically averaged centerline velocities obtained from measurements taken under steady flow conditions. The measurements include velocities taken under variable ice conditions (e.g. open water or under an ice jam). A strong direct relationship between the centerline average velocity and the

180

average Gauss point velocity was observed. This made it more expedient when obtaining estimates on the average channel velocity. That is, estimates on the average channel velocity was based on the average Gauss point velocity.

Figure B.7 presents a comparison between the average Gauss point velocities and the average channel velocities. The average channel velocity was determined based on the discharge from the magnetic flow meter divided by the area of flow. The area of flow was the depth of flow observed at the channel centerline multiplied by the channel width.

In a general sense, Figure B.7 suggests that there is a strong direct relationship between the average Gauss point velocity and the channel average velocity. However, there is some scatter in the data and the following comments warrant consideration. First the data includes observations made at two different sections in the flume, station 10 m and station 20 – each data point associated with station 10 m is outlined by large diamond shape. It is possible that the relationships at station 10 are different than those for station 20 m. Secondly, the average channel velocity was based on the depth of flow observed at the channel centerline (where the velocity data was obtained). For those instances where there was an ice jam present it is plausible that the depth of flow at the channel centerline differed from the average depth of flow across the channel. The data presented in Figure B.1 is also included for comparison.

B.2.4 Estimating the Discharge at a Measurement Station using Average Centreline Velocities

The method for estimating discharge at stations 10 and 20 m was based on index velocity

181

relationships between the channel centerline velocity and the channel average velocity. It was found that no one unique relationship gave satisfactory estimates for the section average discharge. Figure B.8 presents a comparison of the index velocity relationships for a variety of flow conditions. It was found that the index relationships varied depending on the location (i.e. station 10 or 20 m) and the presence of ice in the flume. These varying conditions are represented by each subfigure in Figure B.8. Also, included on each subfigure is a linear line of fit with the corresponding equation as indicated directly on the figure. It was expected that this relationship would vary slightly from test to test and little success was achieved trying to establish a unique set of values for the coefficients m and b. Alternatively, a unique set of coefficients was determined for each test based on the initial and final steady state values for the average channel velocity and the average centreline velocities. This was done by varying only the intercept, b, as defined in equation B-1, for each test. The average channel velocity, $V_{channel}$, was determined directly from the measured centerline velocity, V_{centre}, taken as either the average Gauss point velocities where the 3 probe arrangement was used or by the vertically integrated average where the 8 probe arrangement was used:

[B-1] $\quad V_{channel} = mV_{Centre} + b$,

where: m and b are coefficients.

182
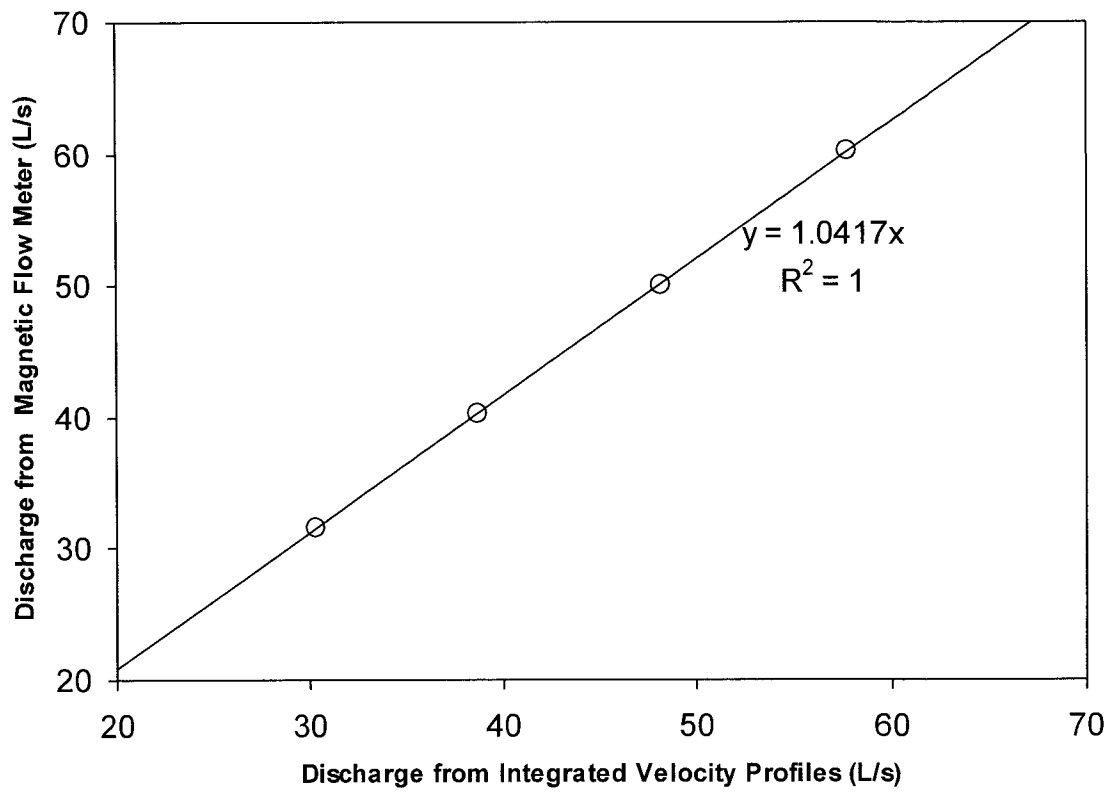
Figure B.1. Magnetic flow meter discharge versus discharge obtained from integrated velocity profiles.

183
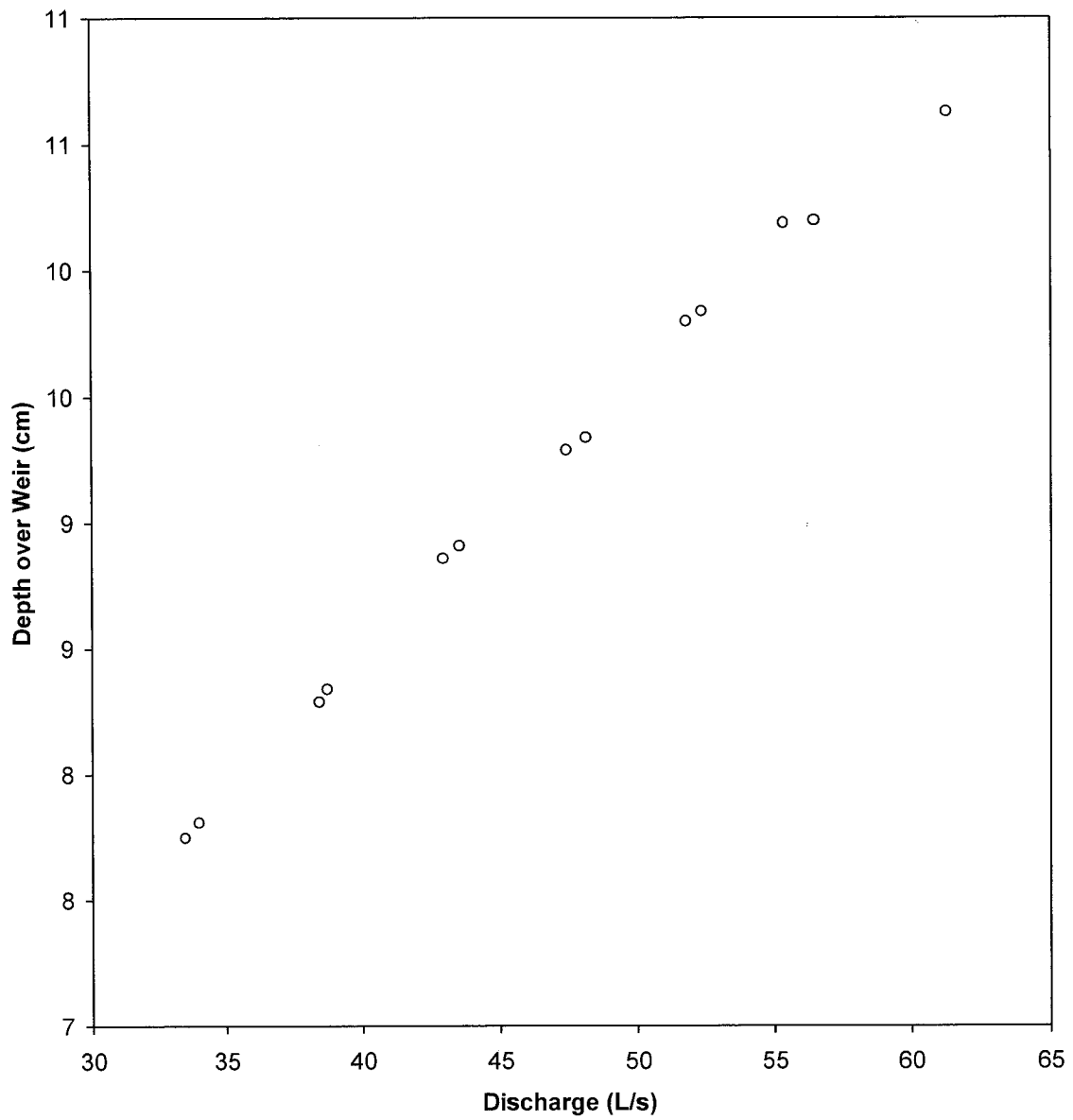
Figure B.2. Linear relationship between depth over the weir and magnetic flow meter discharge.

184
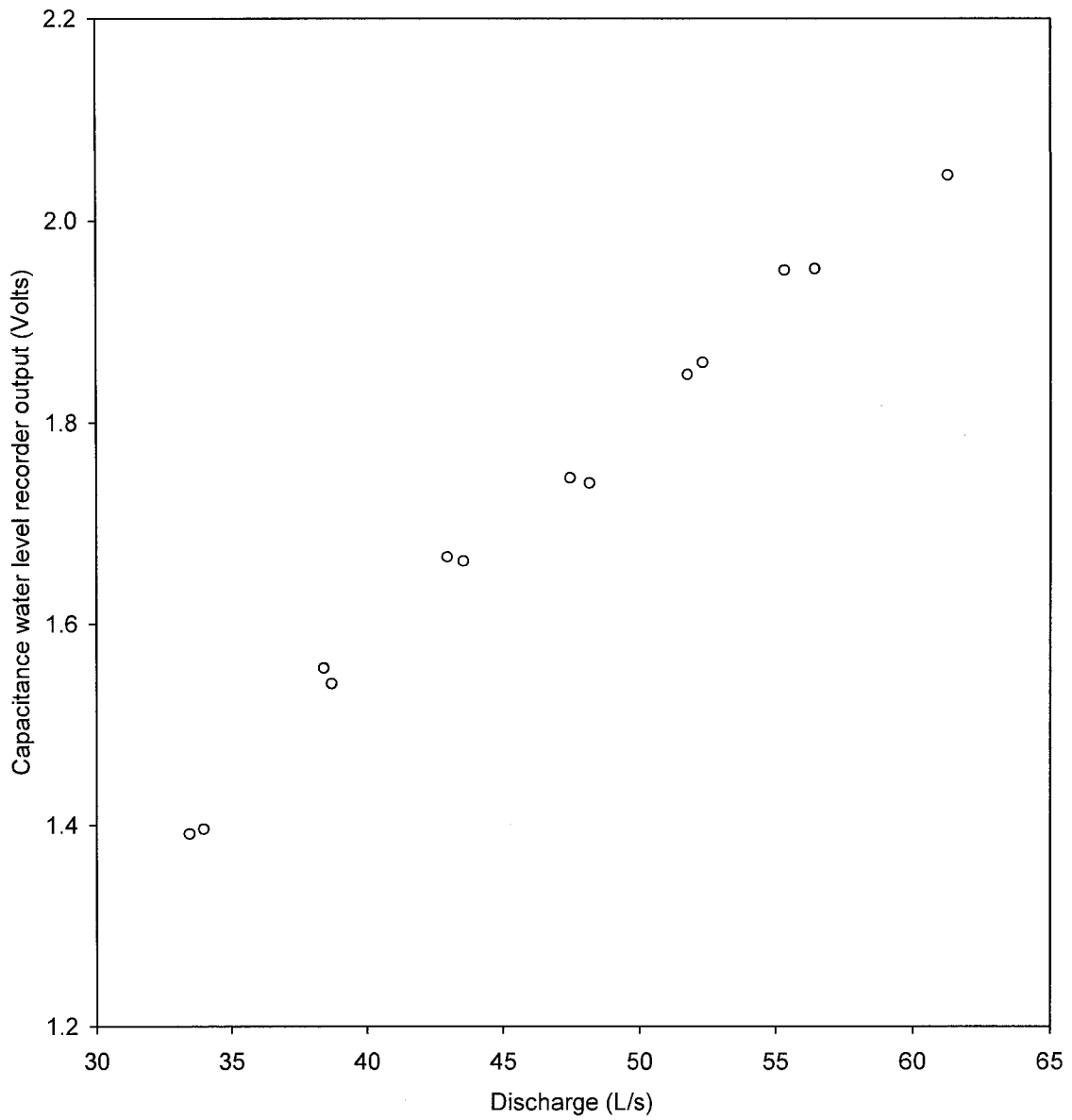
Figure B.3. Linear relationship between capacitance type water level recorder and magnetic flow meter discharge.

185
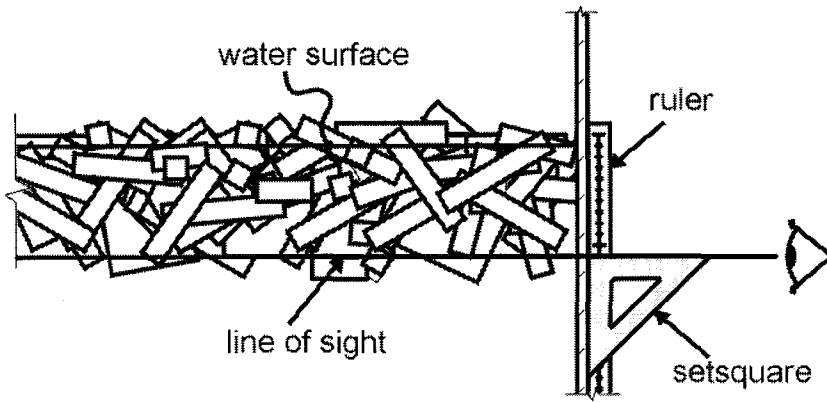
Figure B.4. Measurement technique used for determining static ice jam thickness.

186

static
pressure

u

attack
angle

stagnation
pressure

Prandtl
Tube

Pressure
Transducer

Battery operated digital transducer indicator

0.008

S   Z

span   zero
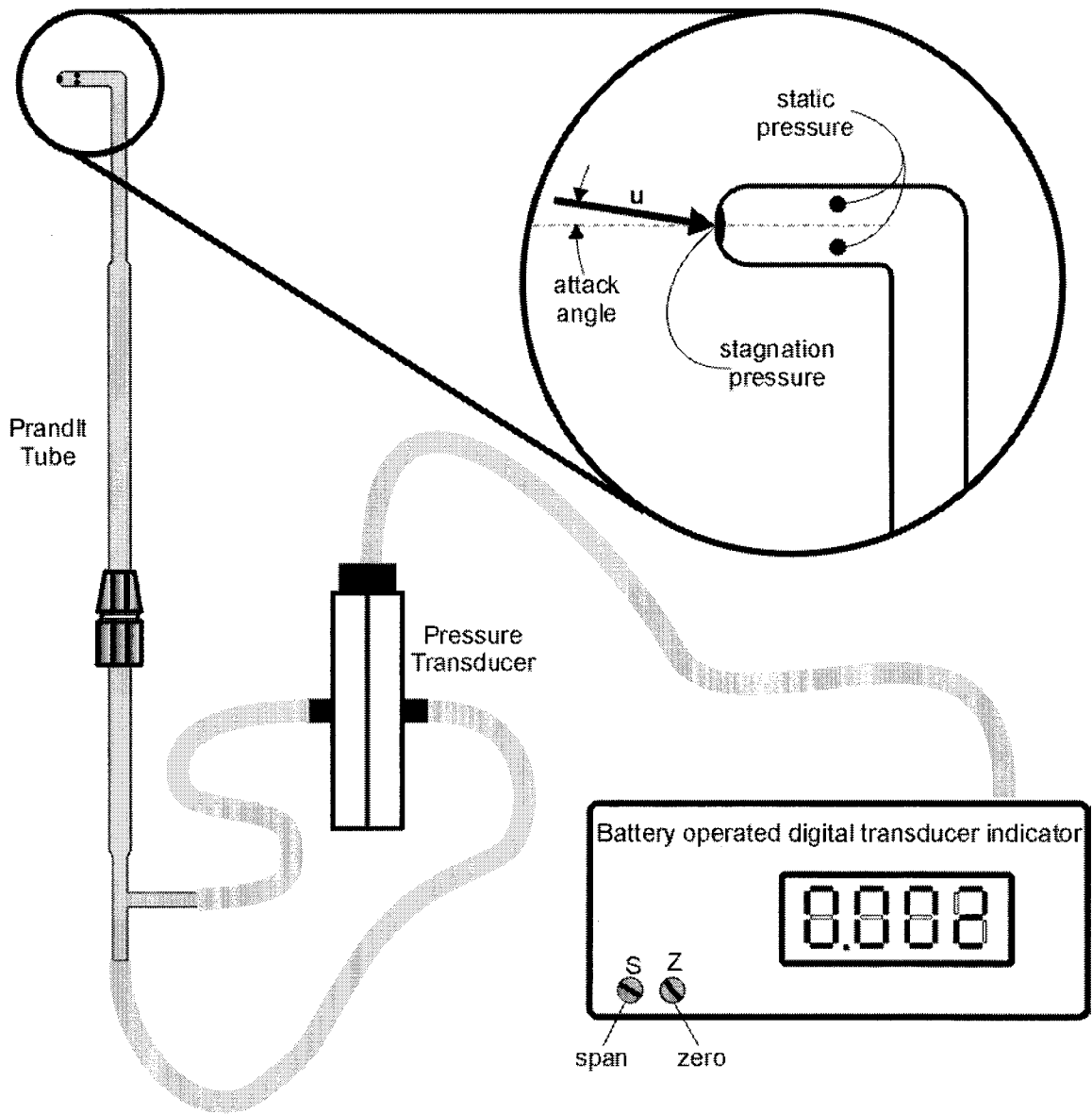
Figure B.5. Schematic of Prandtl tube arrangement.
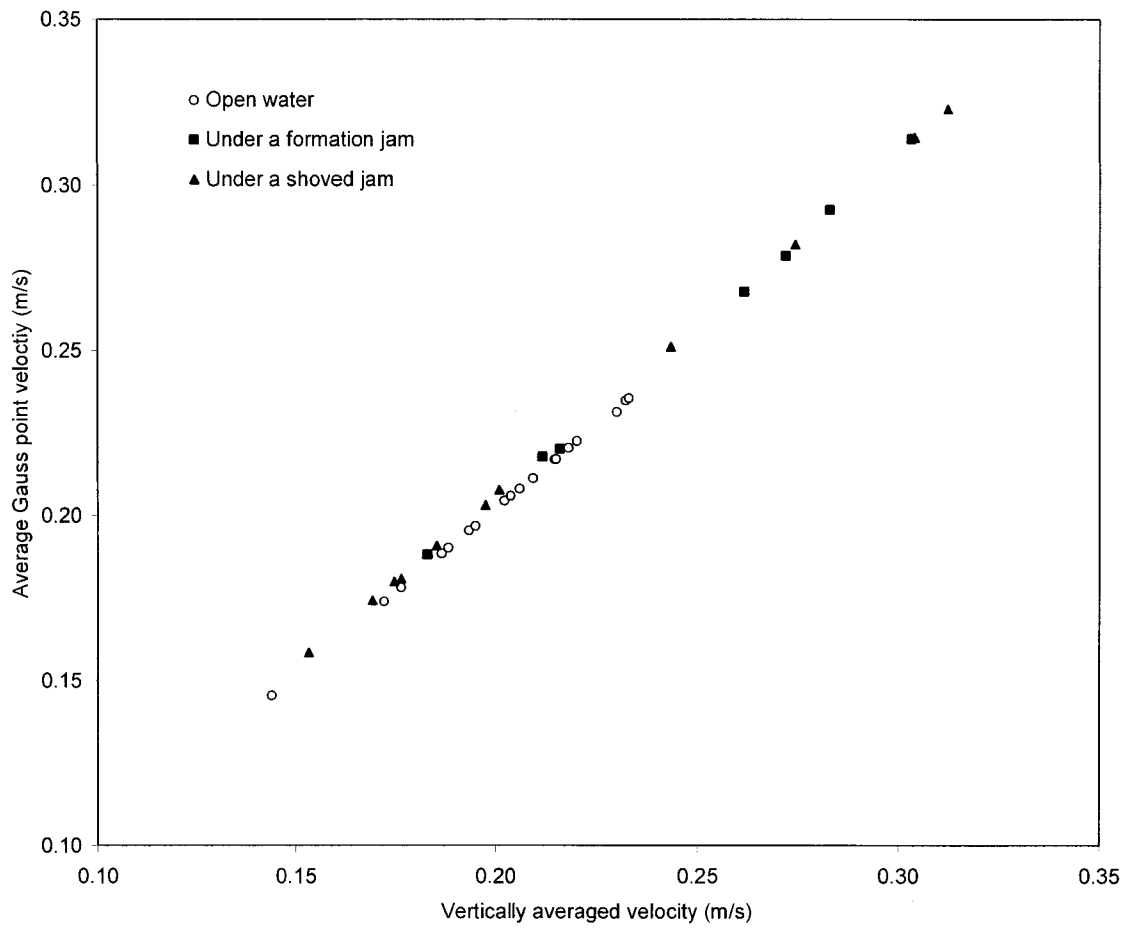
Figure B.6. Average Gauss point velocities versus the vertically averaged velocity for velocity profiles measured at the channel centerline under open water and ice covered conditions.

188
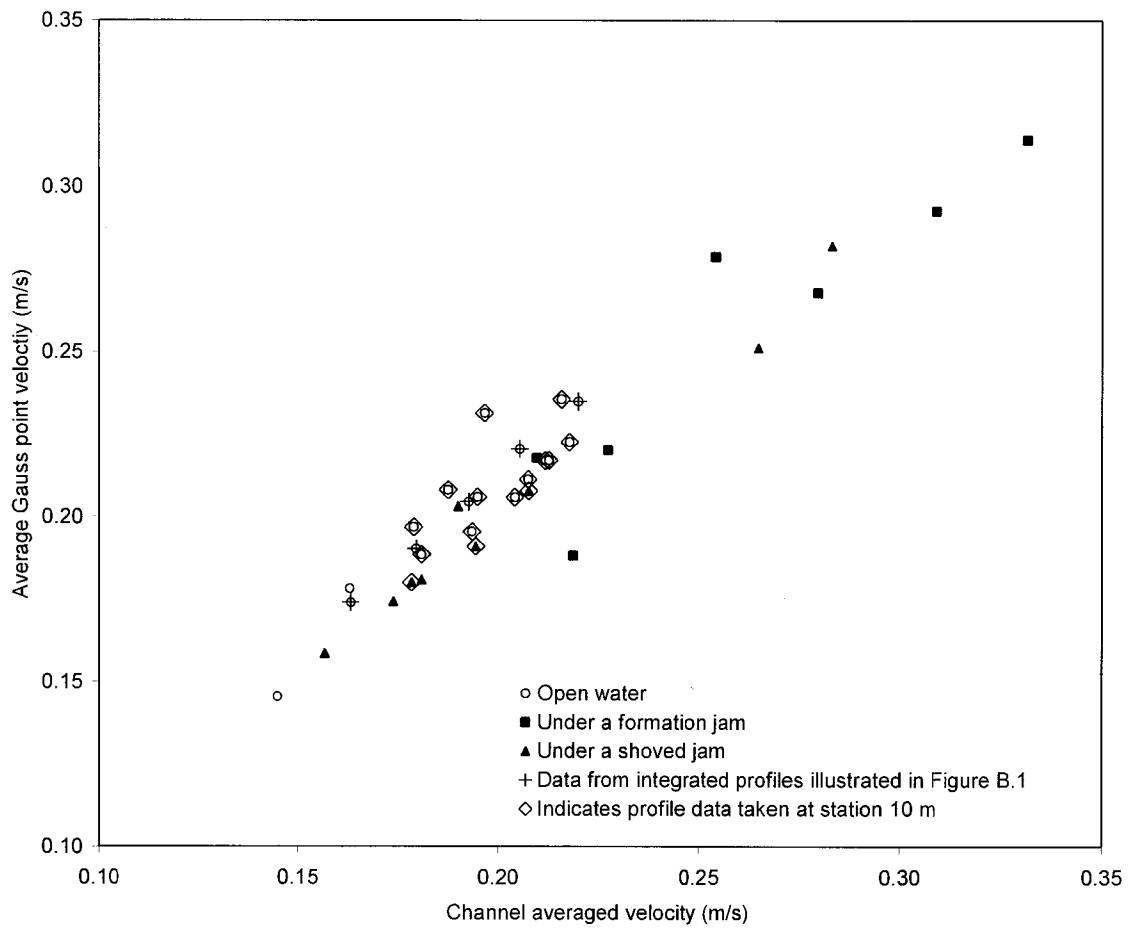
Figure B.7. Average Gauss point velocities from detailed centerline velocity profiles versus the averaged channel velocities under open water and ice covered conditions.

189

190
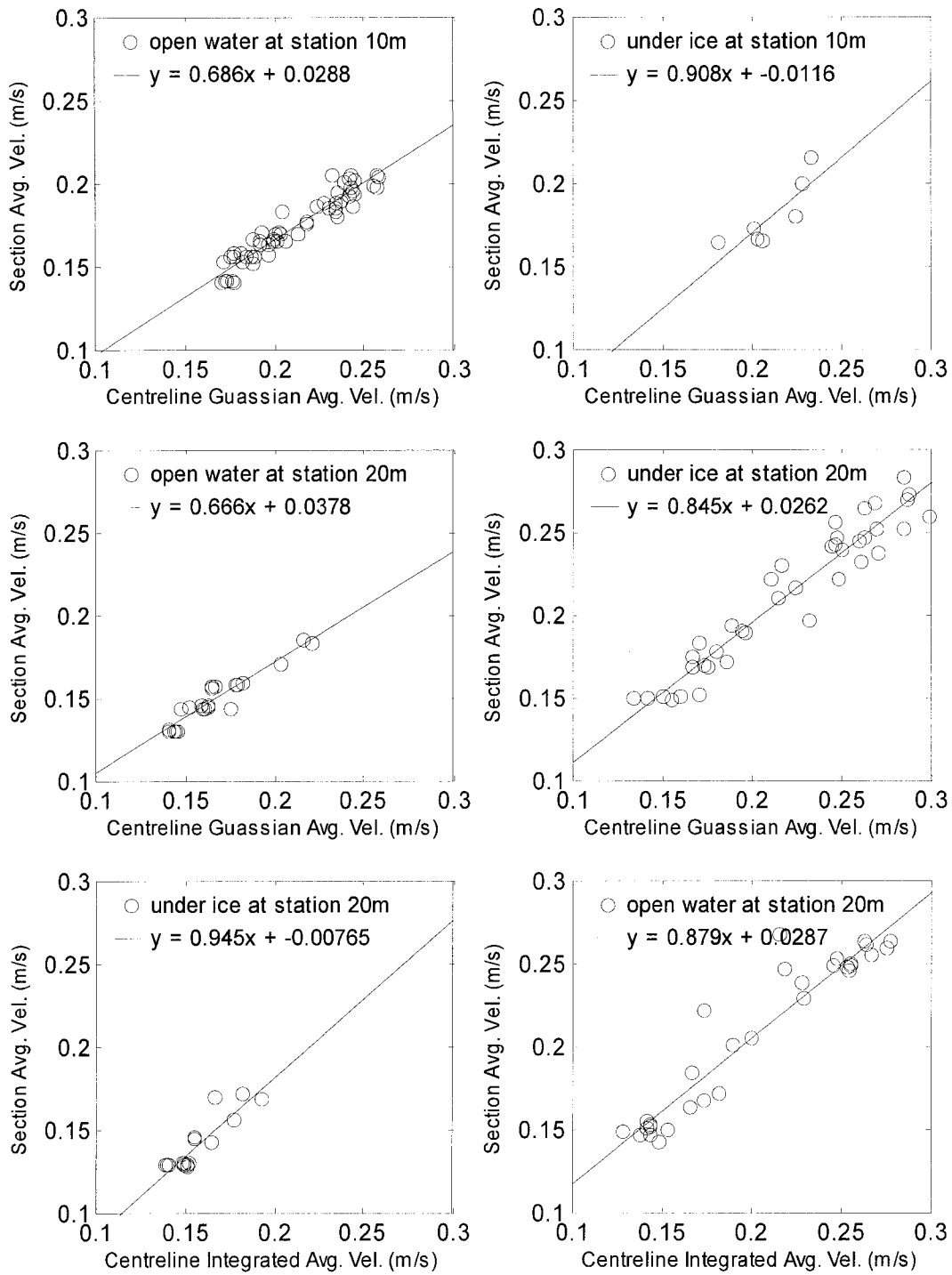
Figure B.8. Index velocity relationships used in computing average channel velocities at stations 10 and 20 m downstream of the head tank.

191

Appendix C – Unsteady Velocity Profiles under a Floating Cover[4]

C.1 Introduction

For both open channel and ice covered flows it is generally assumed that the relationships describing velocity distributions for steady flows are also applicable for unsteady flows. Natural channels are commonly subjected to unsteady flows and many of the dominant river ice processes, such as ice jam formation and surges resulting from their subsequent release, are inherently unsteady. Therefore, it is reasonable to question the applicability of using steady state assumptions for dynamic river ice processes.

Although unsteady velocity distributions have been studied for open channel and closed conduit flows, to the authors' knowledge, no investigations into ice covered (i.e. under a floating cover) flows have been conducted. The current investigation examines the behaviour of velocity profiles for unsteady flow under a floating cover.

C.2 Experimental Apparatus

---

[4] This Appendix was published in the Proceedings of the 16th IAHR International Symposium on Ice, Dunedin, New Zealand, Vol. 1, 83-90. The paper was also presented by the first author at this conference in December 2002.

Figure C.1 presents a schematic of the experimental setup used in this investigation. Experiments were conducted in a 30.5 m long recirculating flume located in the T. Blench Hydraulics Lab at the University of Alberta. This rectangular flume has 0.91 m high side walls and a width of 1.22 m. The bed is sheet metal (though rusted and rough in texture) and the walls are made of plexiglass. Mannings n for the channel, under open water flow conditions, ranges from 0.020 to 0.025.

For the tests described herein, discharges ranging from 40 to 65 L/s were supplied to the head tank. The flow entering the flume was conditioned with a combination of flow straighteners in the floor of the head tank and a bank of 1.2 m long 200 mm diameter steel pipes positioned on the floor immediately downstream of the head tank. At the downstream end of the flume, water levels were controlled with a 150 mm high broad crested weir along with a series of adjustable vertical vanes spaced across the channel. The slope of the flume was set to 0.00164. A 12 m long flexible rubber mat with a rough underside was allowed to float freely and the location of the upstream (leading edge) was fixed at 9 m downstream of the head tank.

Flow rates in the supply line (carrier discharge) were measured with a magnetic flow meter, and flow velocities were measured using eight sets of Prandtl tubes and pressure transducers. The Prandtl tubes were positioned vertically from the bed on the flume centreline at a station 20 m downstream of the head tank. Two water level transmitters were located at station 20 m and over the weir to measure water levels at station 20 m and to estimate the discharge exiting the flume, respectively. All discharge, velocity, and water level measurements were recorded digitally using a Pentium computer running the

193

LabView© data collection software program.

C.3 Using Prandtl Tubes for Unsteady Flow

Prandtl tubes are generally used to measure mean flow velocities, they are not suited for measuring turbulent fluctuations, and to the authors' knowledge, there has been little to no reported attempts to use pressure differential probes to capture variations in mean velocity or unsteady flow conditions. In this investigation the potential use of Prandtl tubes for monitoring mean velocity variations was explored.

Velocity measurements taken using a Prandtl tube (PT) were compared directly to measurements taken using an Acoustic Doppler Velocimeter (ADV). Simultaneous measurements of velocity were taken using both devices where the sample space for the ADV was set immediately upstream of the tip of the Prandtl tube. Under a constant carrier discharge, "continuous" velocity measurements were taken at a sampling rate of 10 Hz. Figure C.2 presents a time series of the raw data collected using both the PT and the ADV. Inspection of Figure C.2 indicates that the velocity time series data collected by the PT tended to lag behind the ADV data by a couple of seconds. It was also apparent that the inherent fluctuations in velocity were damped with the higher frequency variations being missed altogether.

Assuming that the ADV provided a good representation of the real velocity variations it was reasonable to conceive a linear time-invariant "ADV-PT" system where the excitation, $x(t)$, and the response, $y(t)$, were represented by the ADV time series and PT time series, respectively. The system can also be represented in the frequency domain as

194

$Y(f) = H(f)X(f)$, where $Y(f)$ and $X(f)$ are the autospectral densities for the ADV and PT time series data, respectively. The transfer function, $H(f)$, describes the frequency response of the assumed system containing both magnitude and phase components. Figure C.3 illustrates the results of the analysis on the ADV-PT system in the frequency domain. Figure C.3 (a) presents the autospectral density for both the ADV and PT discrete time series measurements. The PT system has a slower response than the ADV and can not adequately identify frequencies much past 0.5 Hz. Figure 3b and c quantitatively describe the magnitude and phase response of the assumed ADV-PT system (which behaves much like a filter). It is generally accepted that the cutoff frequency for a filter corresponds to the point where the magnitude of the transfer function, $H(f)$, drops to 0.7 (the -3dB point), which is roughly 0.1 Hz in this case. The input signal, $x(t)$, also experiences a phase shift as it passes through our assumed ADV-PT system. Figure C.3c illustrates the phase component of the transfer function which indicates that the PT signal lags behind the ADV signal. For example, at a frequency of 0.1 Hz the lag is approximately 1.6 seconds (which can be observed in the time series data provided in Figure C.2). Consequently, all of the raw discrete time series data used for subsequent analyses were passed through a digital filter with a cut-off frequency of 0.1 Hz. The auto spectral densities for the raw data filtered in this manner are also shown in Figure C.3a for comparison.

C.4 Velocity Profile Measurements under a Floating Cover

C.4.1 Steady State Measurements

195

Detailed steady state velocity profiles were measured for discharges ranging from 40 to 65 L/s. Figure C.4 presents the non-dimensional velocity profile for the range of discharges tested where velocity was non-dimensionalized by the centre-line average velocity and distance from the bed was non-dimensionalized by the depth of flow, D.

It is common to make estimates on the average velocity based on point velocities taken at Gauss point locations. Using a two-point approximation, the average of two point velocities taken at $0.2113D$ and $0.8778D$ will give the average of the entire profile (Teal and Ettema 1994). For the non-dimensional velocity profile presented in Figure C.4, the two-point approximation average overestimates the profile average by 2%.

C.4.2 Unsteady Flow Measurements

Point measurements were taken at a frequency of 10 Hz and recorded digitally to a file on a personal computer. The following parameters were measured for each unsteady flow test: magmeter discharge (inflow); discharge over the weir (ouflow); water level at the measurement station; and 8 velocity measurements at the measurement station. For each test the carrier discharge was increased rapidly from a constant "initial" value to constant "final" value. A total of 15 tests were conducted for variable initial and final conditions where discharge increases spanned the range of 9 to 46%.

To facilitate comparison between individual tests a non-dimensional time parameter, T, was defined as the time interval for the change in water surface elevation to reach 90% of its full value between the initial and final steady state values. The time parameter, T, is analogous to a time parameter used by Nezu et al. (1997) for the presentation of mean

196

variations in velocity profile data. Figure C.5 presents the filtered non-dimensional time series of discharge data for the test with the largest increase in carrier discharge (46%). The outflow hydrograph (over the weir) suggests that a portion of the wave was reflected as a result of the outlet conditions. The discharge at the measurement station was deduced from the depth of flow and the vertically averaged centreline velocity (determined through integration of the 8 point velocity measurements). At 0T the time water surface elevation started to rise and at approximately $2T$ the flow returned to a near steady state condition.

The most "dynamic" portion of all tests occurred shortly after $0T$ and unsteady effects were clearly evident up to approximately $1.5T$. For all tests, the vertically averaged velocity tended towards a maximum before the maximum water surface elevation. Similar observations were made for open water conditions by previous investigators (e.g. Song and Graf 1996).

C.5 Initial Observations on Unsteady Velocity Profiles under a Floating Cover

Figure C.6 presents a series of non-dimensional velocity profiles for the same test presented in Figure C.5 at selected intervals spanning the range of 0T to 1T. The '+' and 'x' symbols represent the initial and final average steady state profiles, respectively, while the open circles represent the "instantaneous" profiles spanning the interval $0T$ to $1T$. The most apparent departure from the steady state velocity profile occurs at time $0.1T$ as would be expected as it corresponds to a time when the water surface and vertically averaged velocity are increasing rapidly. However, based on the initial

197

observations of this investigation, the shape of the velocity profile did not vary dramatically under unsteady conditions resulting from a rapid increase in discharge.

Previous and more rigorous investigations under open water conditions suggested that the mean velocity profiles were "little affected" by the unsteadiness of the hydrograph and that some of the usual assumptions on the shape of the velocity profile (e.g. the wall law) for steady flow are applicable to unsteady flow (e.g. Nezu et al. 1997; Song and Graf 1996). An initial interpretation of the data for this investigation qualitatively suggests that similar deductions can be made for unsteady velocity profiles under a floating cover. However, it is interesting to note that qualitative observations taken during this investigation suggested that as the profile affected by the floating cover became steeper the bed-affected profile tended to flatten (and vice versa). This would suggest that as the effective roughness on one wall increases the effective roughness on the other wall decreases – perhaps tending towards a less dramatic change in composite roughness over the unsteady portion of the test.

C.6 Applicability of the two-point approximation for unsteady flow

For the tests conducted in this investigation the two-point approximation appeared to be suitable for both steady and unsteady flow. In all cases the two-point average overestimated the vertically averaged velocity by roughly 5%. Figure C.7 presents a comparison of the vertically averaged velocity with the two-point average for one of the tests with the largest increase in velocity (most "dynamic"). Inspection of Figure C.7 suggests that the two-point approximation is equally suited for both the steady and

198

unsteady portions of the flow.

C.7 Conclusions

Initial observations on velocity profiles under a floating cover suggest that the usual assumptions on the shape of velocity profiles associated with steady flow are also applicable for unsteady flow. Qualitative observations indicate that the shape of the non-dimensional velocity profile does not vary dramatically over the unsteady portion of the tests presented herein. However, during the period associated with the most rapid increase in mean velocity (highly unsteady) the shape of the non-dimensional velocity profile does vary slightly from the steady state non-dimensional velocity profile. And during the period associated with these slight variations, the data suggests that as the profile on one boundary steepens, the profile on the opposite boundary tends to flatten. Finally, for the tests presented herein, the two-point method for estimating mean velocity performs equally well for both steady and unsteady flow – certainly well enough for practical discharge estimates.

199
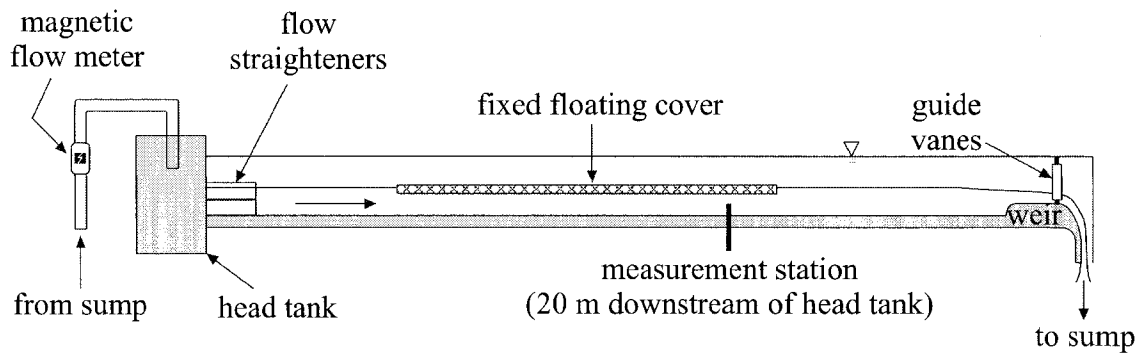
Figure C.1. Experimental flume schematic.
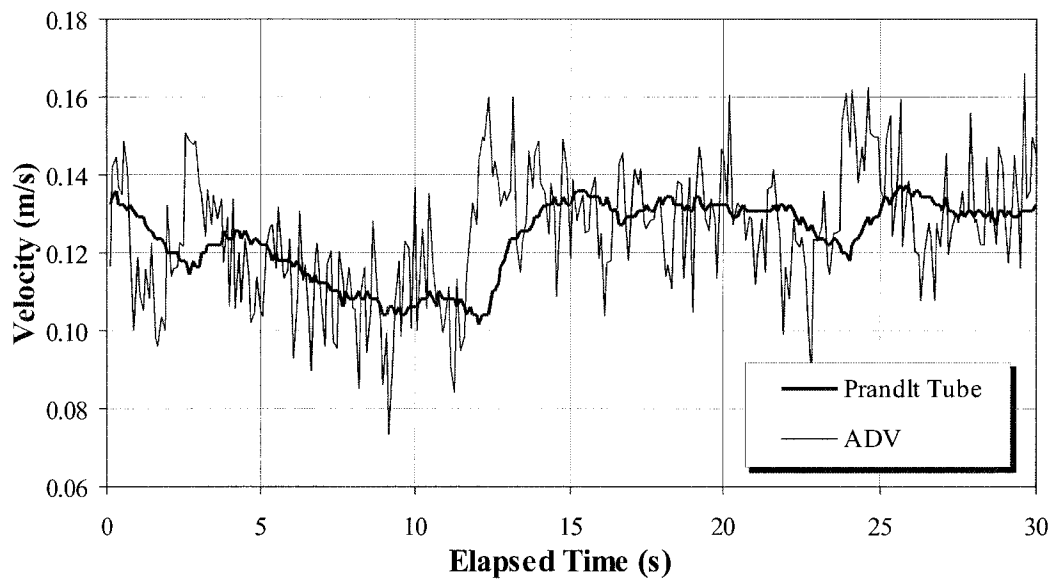
Figure C.2. Velocity data comparison between Prandtl tube and ADV.
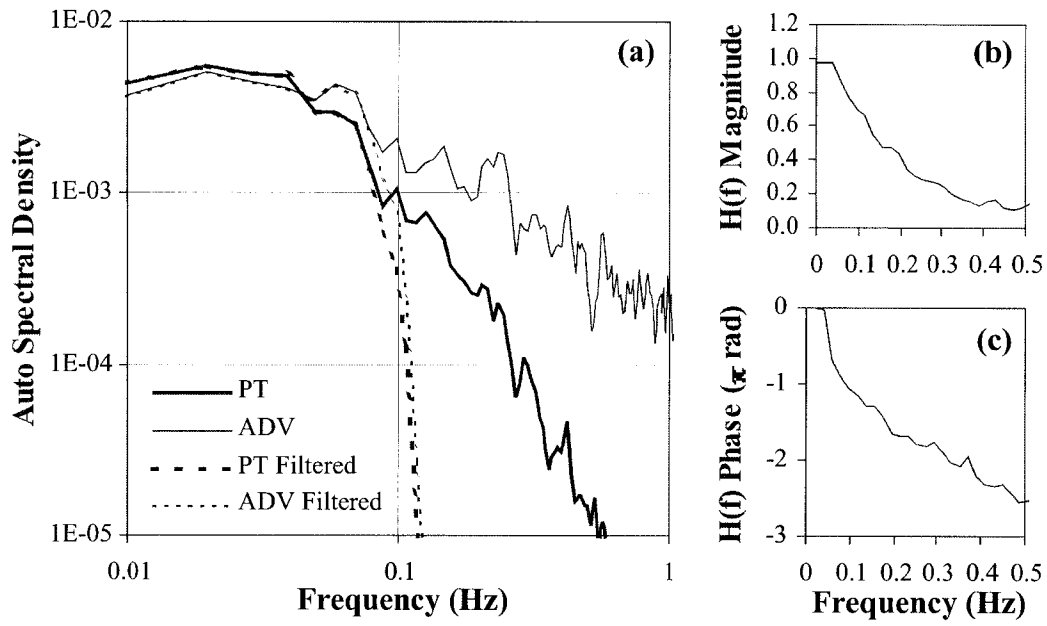
Figure C.3. Autospectral densities for raw and filtered PT and ADV data (a) and ADV-PT system transfer function magnitude (b) and phase (c).

201
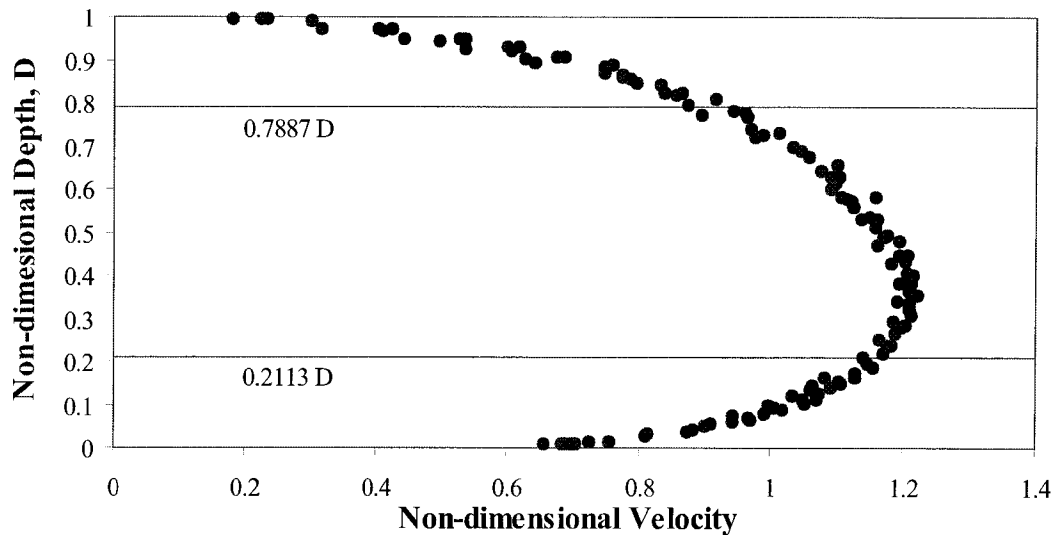
Figure C.4. Non-dimensional velocity profiles under a floating cover.
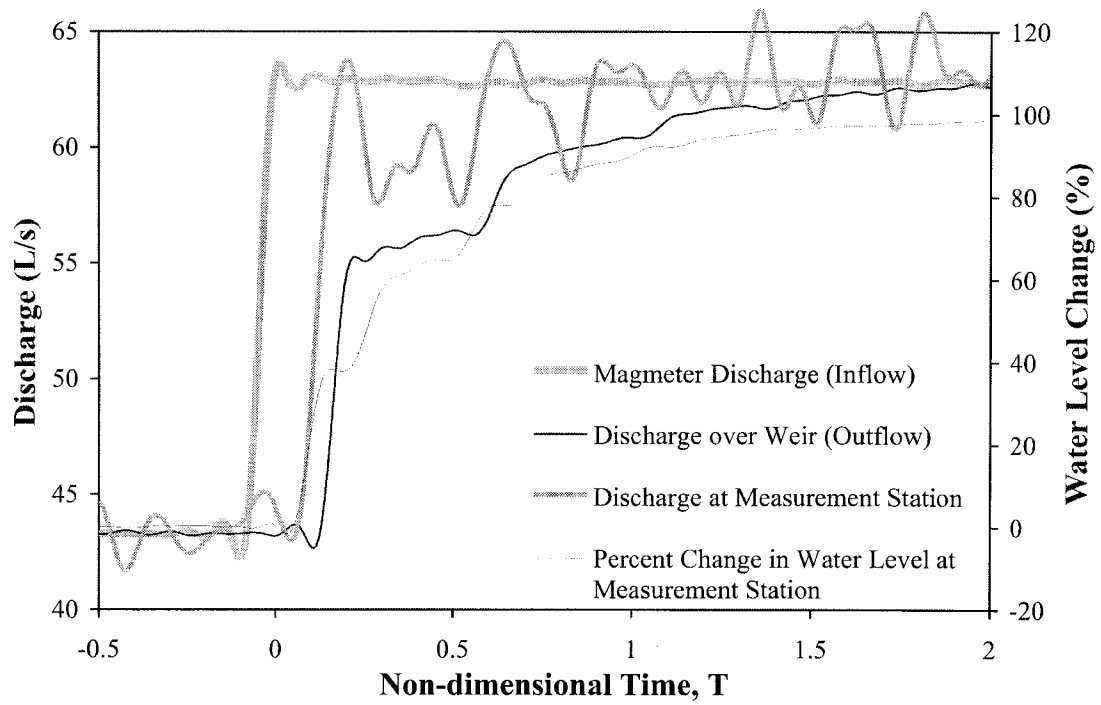
Figure C.5. Non-dimensional time series data describing inflow, discharge at the measurement station, outflow, and percent change in water level.
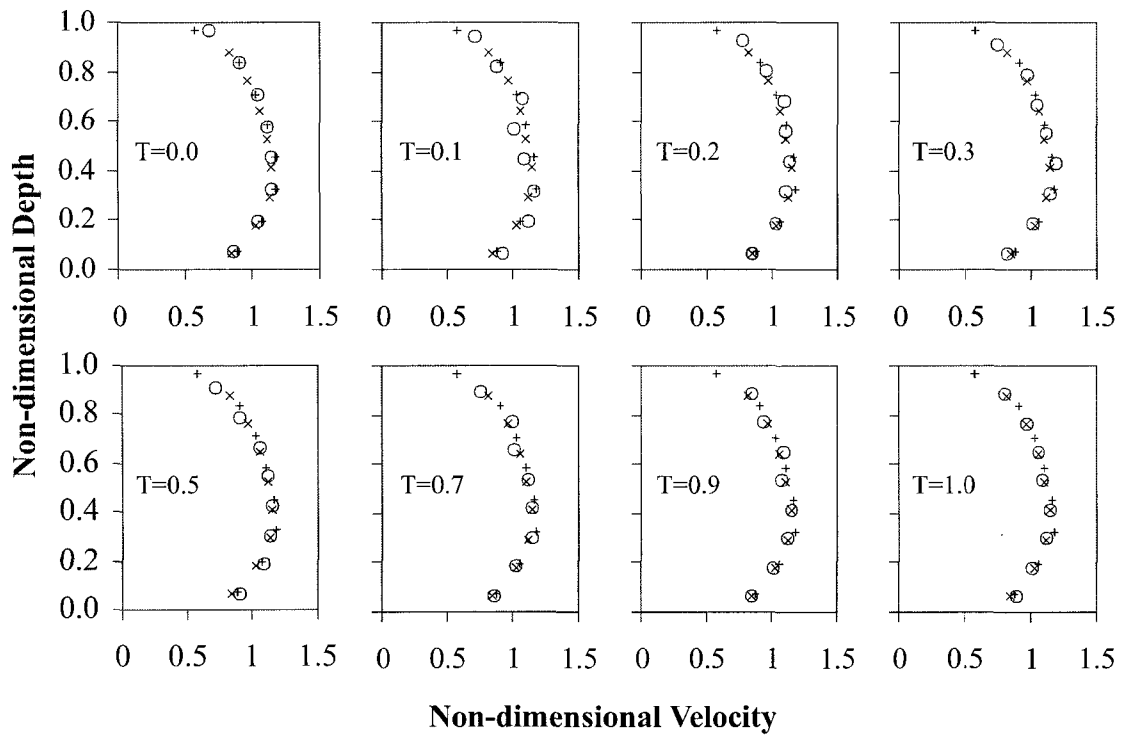
Figure C.6. Non-dimensional velocity profiles under a floating cover during unsteady flow.
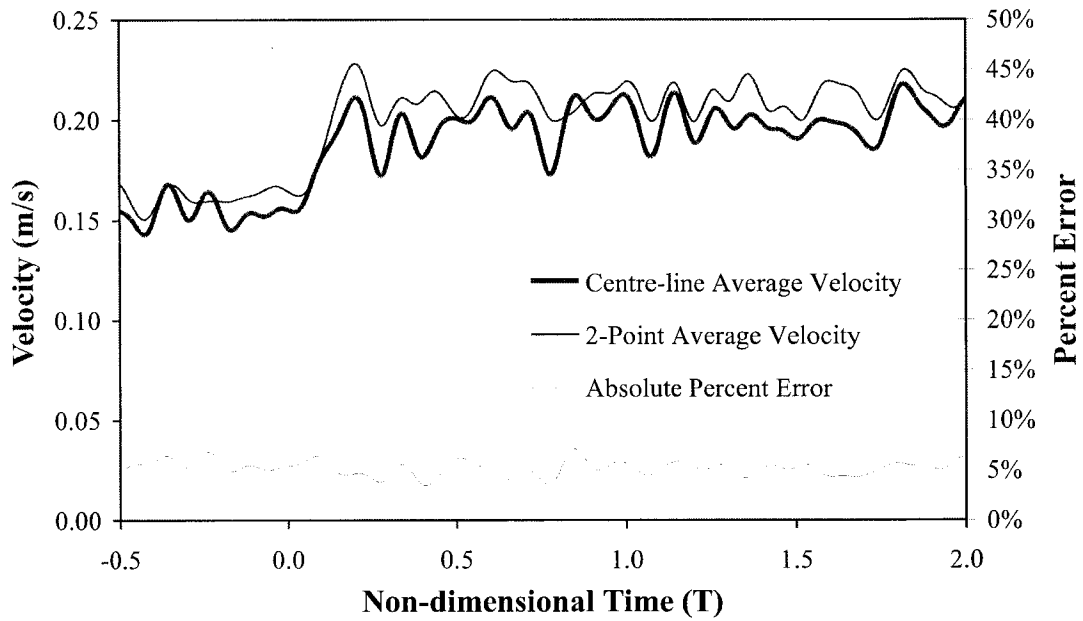
Figure C.7. Comparison between centreline average velocity to two-point average velocity.

C.8 Acknowledgments

204

C.9 References

Nezu, I, Kadota, A, and Nakagawa, H. 1997. Turbulent structure in unsteady depth-varying open channel flows. ASCE Journal of Hydraulic Engineering, Vol. 123, No. 9, pp. 752-763.

Song, T. and Graf, W.H. 1997. Velocity and turbulence distribution in unsteady open-channel flows. ASCE Journal of Hydraulic Engineering, Vol. 122, No. 3, pp. 141-154.

Teal, M. and Ettema, R. 1994. Estimation of mean flow velocity in ice-covered channels. ASCE Journal of Hydraulic Engineering, Vol. 120, No. 12, pp. 1385-1400.

205

Appendix D – Details on Particle Tracking Analysis

D.1 Manual Particle Tracking

For each test, typically two persons (when available) manually tracked particles (Figure D.1). Each person would record the average streamwise location of the tracking particles and corresponding time using watches synchronized (to the nearest second) with the digital time stamp associated with the overhead video cameras viewing the surface of the ice cover from above. This data were then be used as a check on the particle tracking data obtained by the overhead video cameras.

D.2 Automated Particle Tracking

Four downward looking cameras were placed above stations 10, 14, 18, and 22 m downstream from the head tank. Transverse markers (sections of 125 mm diameter metal pipe) were positioned at a fixed elevation above the bed at 1-meter intervals along the length of the flume (see Figure D.1). Video data was collected throughout the duration of the tests where the discharge was increased rapidly (see Chapter 4). After the tests the video data was viewed and the location of the tracking particles along the flume relative to the transverse markers was recorded. The cameras introduced some distortion as to the actual location of the tracking particles in the longitudinal direction and therefore data obtained from the video cameras required further analyses. Figure D.2 presents a schematic describing the effects of the oblique angles introduced by the overhead cameras viewing the top of the cover. Knowledge of the relative location of the cameras

to the flume, locations of each transverse marker, and continuous water level data facilitated estimation of the actual streamwise distance from the head tank of each set of tracking particles. Figure D.3 presents a comparison between particles tracked manually by persons during a test along with corrected data obtained from the overhead video cameras.

207

Figure D.1 Manual particle tracking – note transverse markers and tracking particles.

208

View of tracking particles from overhead video camera.

(a)

tracking particles

station 13   station 14   station 15   station 16

(b)

overhead
video camera

camera "sight-lines"

transverse
marker

tracking
particles

water surface

actual streamwise distance from head tank
perceived streamwise distance from head tank

bed

209
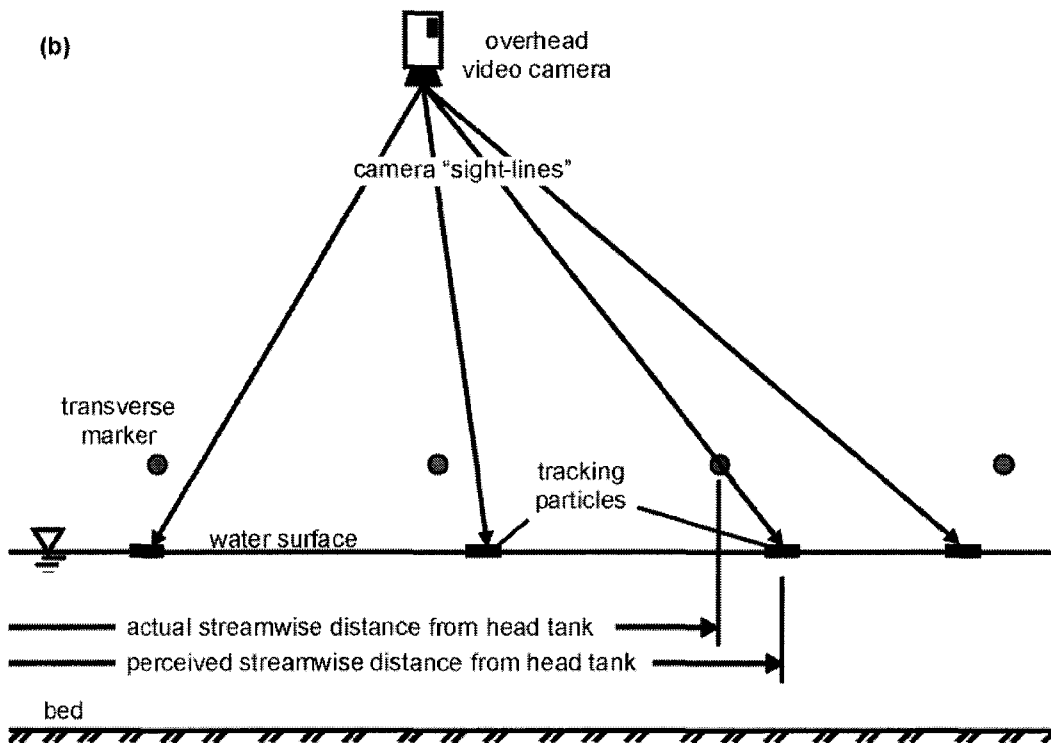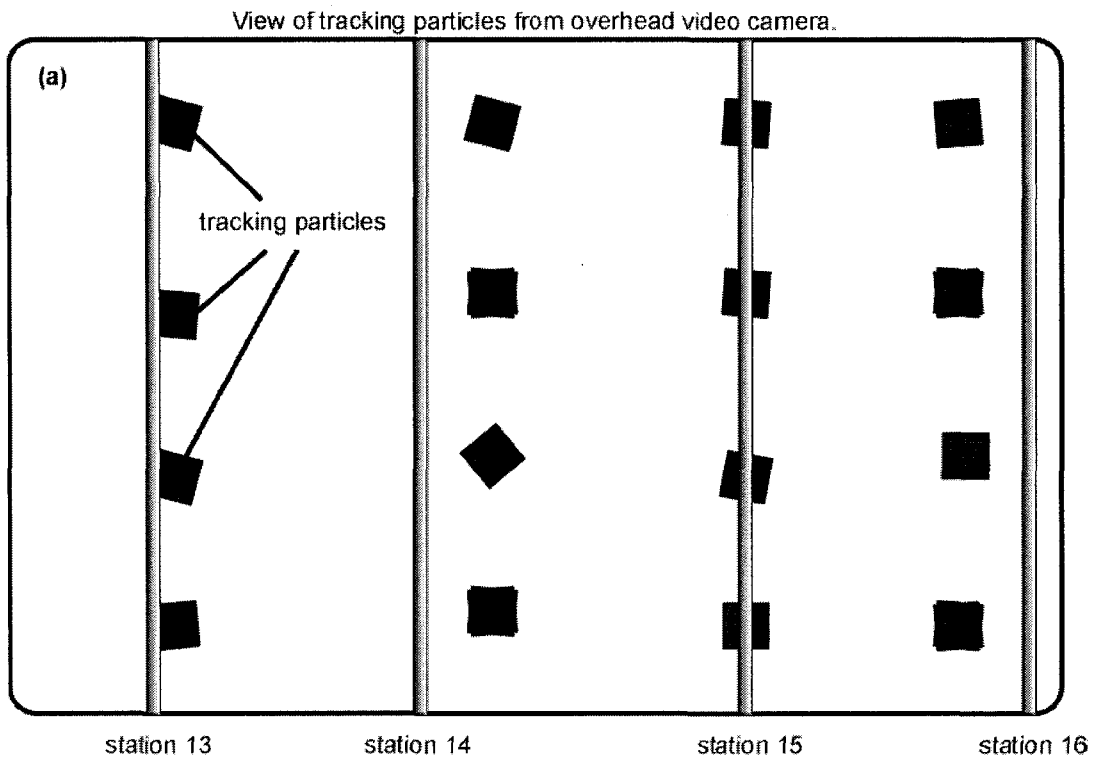
Figure D.2 Schematic of automated particle tracking arrangement depicting effects of oblique camera views on data analysis.
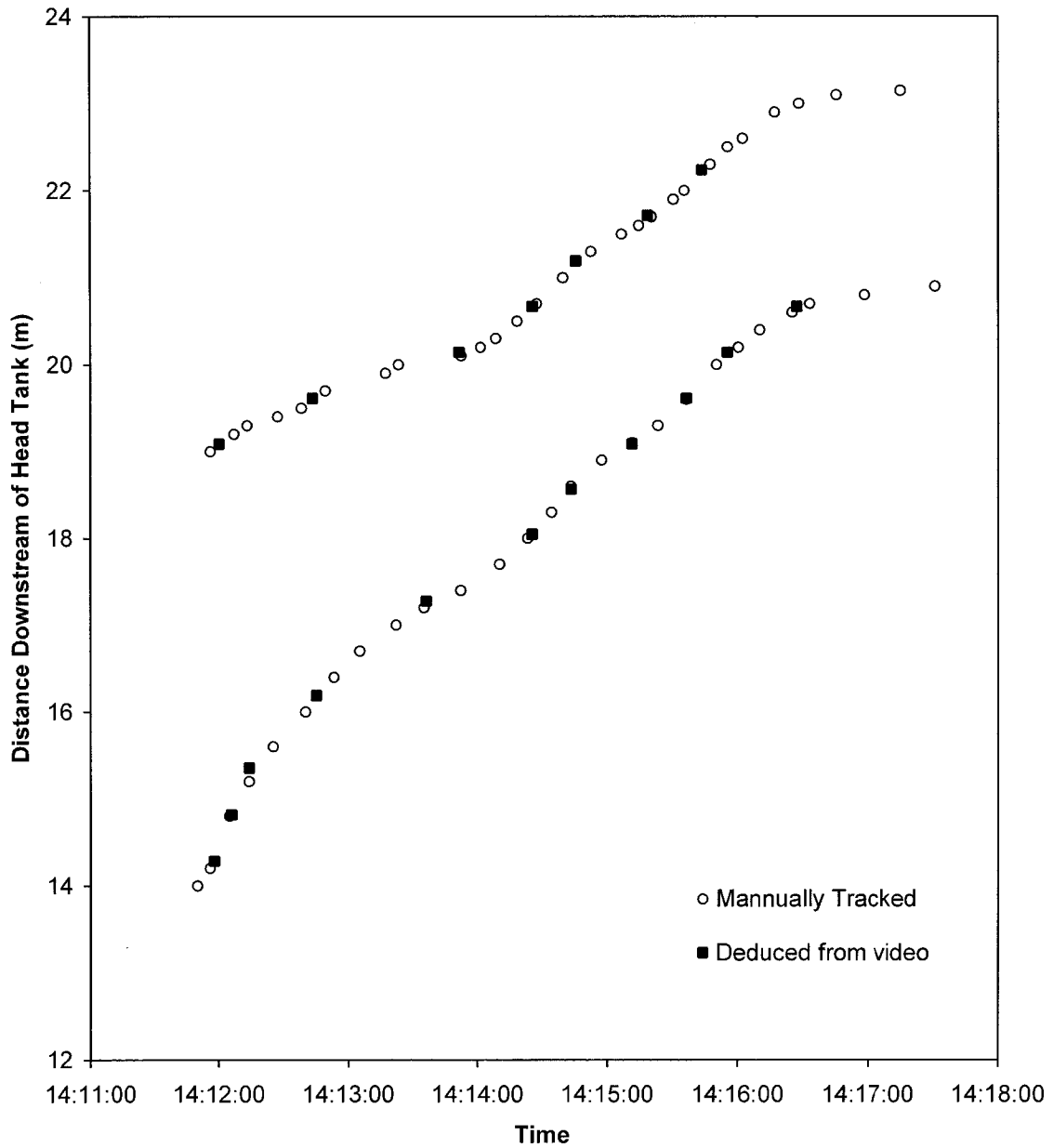
Figure D.3 Comparison between manual and automated particle tracking.

210

Appendix E – Summary of all Test Results for Chapter 4

The results of 40 tests are summarized in this appendix and they compliment the data presented in Chapters 3 and 4. There are three major groups of figures: the first major group presents the continuous time series data collected at stations 10 and 20 m during ice jam formation (Figures E.1 to E.64); the initial "formation" and final "shoved" steady state ice jam profiles and the progression of the cover during ice jam shoving (Figures E.65 to E.104); and the continuous time series data collected at stations 10 and 20 m during ice jam shoving (Figures E.105 to E.168).

The first and last major sets of data warrant further explanation. There are 5 sub-figures contained in each figure summarizing the continuous time series data found in the first and last major groupings of the following figures. In each figure, subfigure (a) presents the elevation of the water surface, bottom of ice, velocity probes, and Gauss point locations. Subfigure (b) presents: the average channel velocity based on the flow area of the corresponding section and the supplied flow rate measured by the magnetic flow meter (carrier discharge); the estimated centerline index velocity; and the estimated channel velocity based on the centerline index velocity. Subfigure (c) presents the estimated discharge at the corresponding section based on the estimated channel velocity and the depth of flow for the section. Subfigures (d) and (e) provide visual representation of the index velocity relationships used to obtain section average velocities from the centerline velocities. A demarcation point is indicated in subfigure (a) and represents the time at which the index velocity relationship changed from the "pre-demarcation"

211

relationship illustrated in subfigure (d) to the "post-demarcation" relationship illustrated in subfigure (e). The circular symbols in subfigures (d) and (e) represent the relationship between the average channel and centerline velocity determined under steady flow conditions and stable ice jams.

212
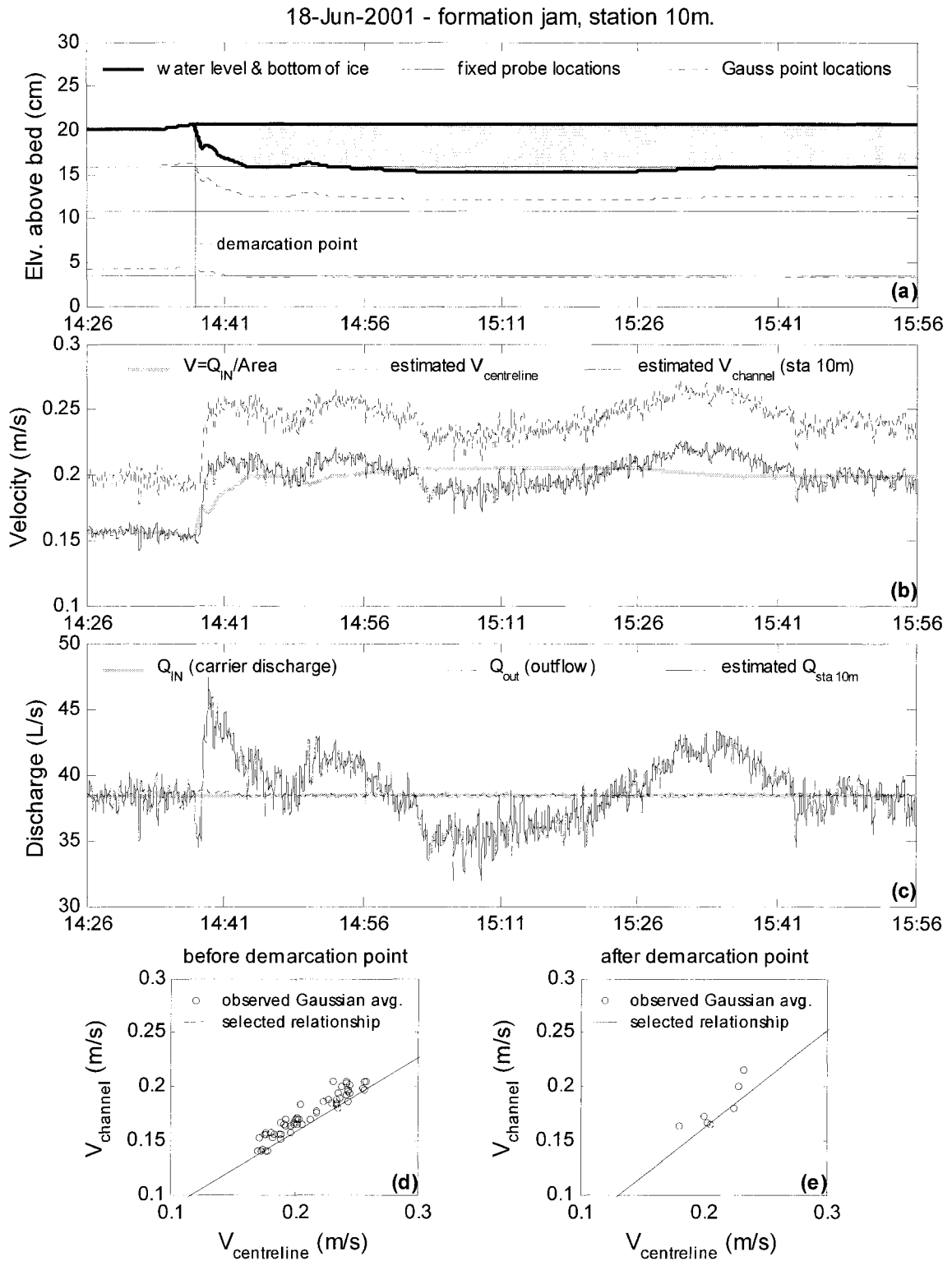
Figure E.1. Summary of continuous observations for a formation jam taken at Station 10m – test date: 18 June 2001.

213

18-Jun-2001 - formation jam, station 20m.

(a) Elv. above bed (cm)

water level & bottom of ice — fixed probe locations — Gauss point locations

demarcation point

(b) Velocity (m/s)

$V=Q_{IN}$/Area — estimated $V_{centreline}$ — estimated $V_{channel}$ (sta 20m)

(c) Discharge (L/s)

Q_{IN} (carrier discharge) — Q_{out} (outflow) — estimated $Q_{sta\,20m}$

before demarcation point

(d) $V_{channel}$ (m/s)

o observed Gaussian avg.
— selected relationship

$V_{centreline}$ (m/s)

after demarcation point

(e) $V_{channel}$ (m/s)

o observed Gaussian avg.
— selected relationship

$V_{centreline}$ (m/s)

Figure E.2. Summary of continuous observations for a formation jam taken at Station 20m – test date: 18 June 2001.

214

19-Jun-2001 - formation jam, station 10m.

(a) Elv. above bed (cm)

water level & bottom of ice — fixed probe locations — Gauss point locations

demarcation point

30 25 20 15 10 5 0
12:15 12:30 12:45 13:00 13:15 13:30 13:45

(b) Velocity (m/s)

$V=Q_{IN}/Area$ estimated $V_{centreline}$ estimated $V_{channel}$ (sta 10m)

0.25 0.2 0.15 0.1
12:15 12:30 12:45 13:00 13:15 13:30 13:45

(c) Discharge (L/s)

Q_{IN} (carrier discharge) Q_{out} (outflow)   estimated $Q_{sta\,10m}$

50 45 40 35 30
12:15 12:30 12:45 13:00 13:15 13:30 13:45

before demarcation point

(d) $V_{channel}$ (m/s) vs $V_{centreline}$ (m/s)

o observed Gaussian avg.
— selected relationship

0.3 0.25 0.2 0.15 0.1
0.1 0.2 0.3

after demarcation point

(e) $V_{channel}$ (m/s) vs $V_{centreline}$ (m/s)

o observed Gaussian avg.
— selected relationship

0.3 0.25 0.2 0.15 0.1
0.1 0.2 0.3

Figure E.3.   Summary of continuous observations for a formation jam taken at Station 10m – test date: 19 June 2001.

215
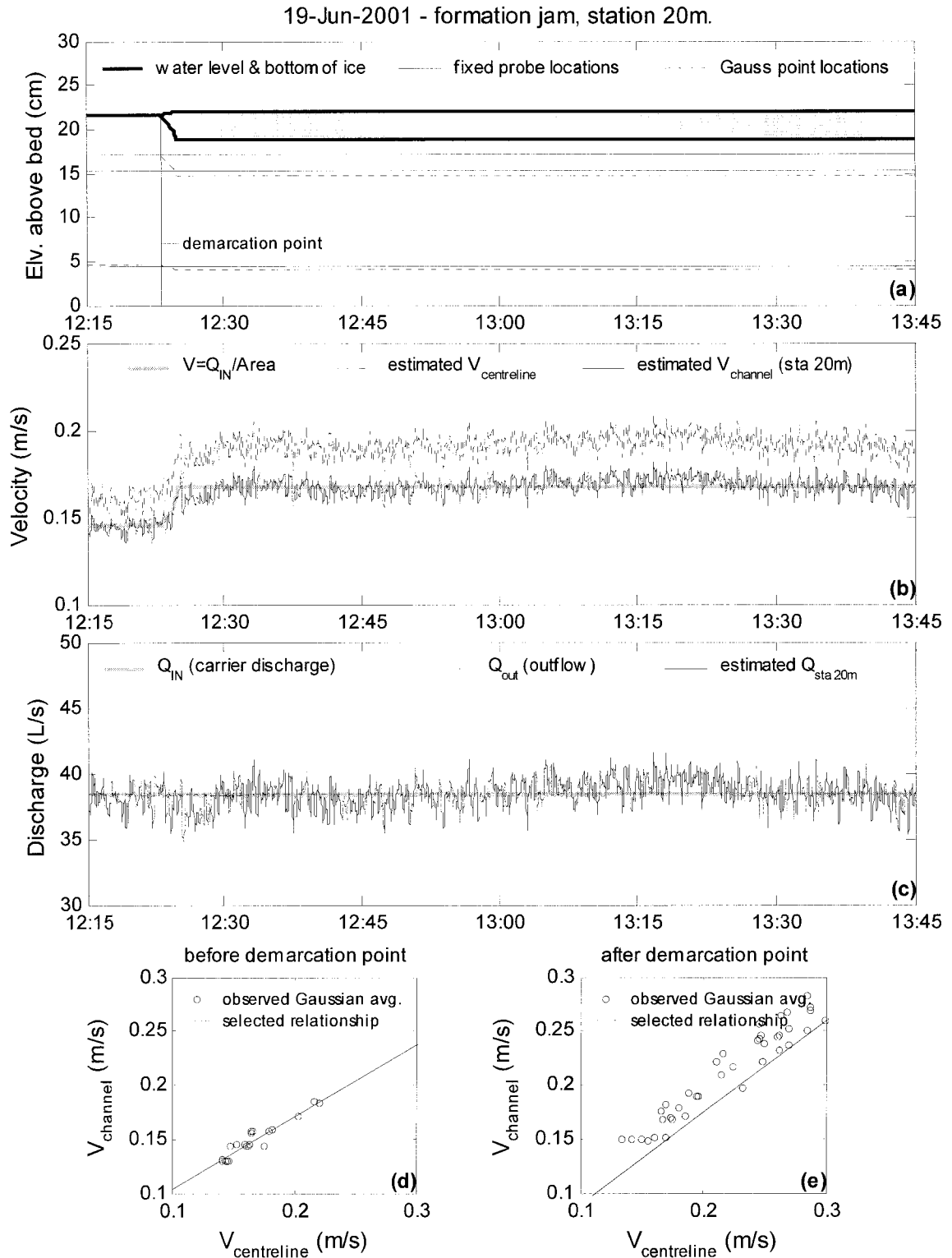
Figure E.4. Summary of continuous observations for a formation jam taken at Station 20m – test date: 19 June 2001.
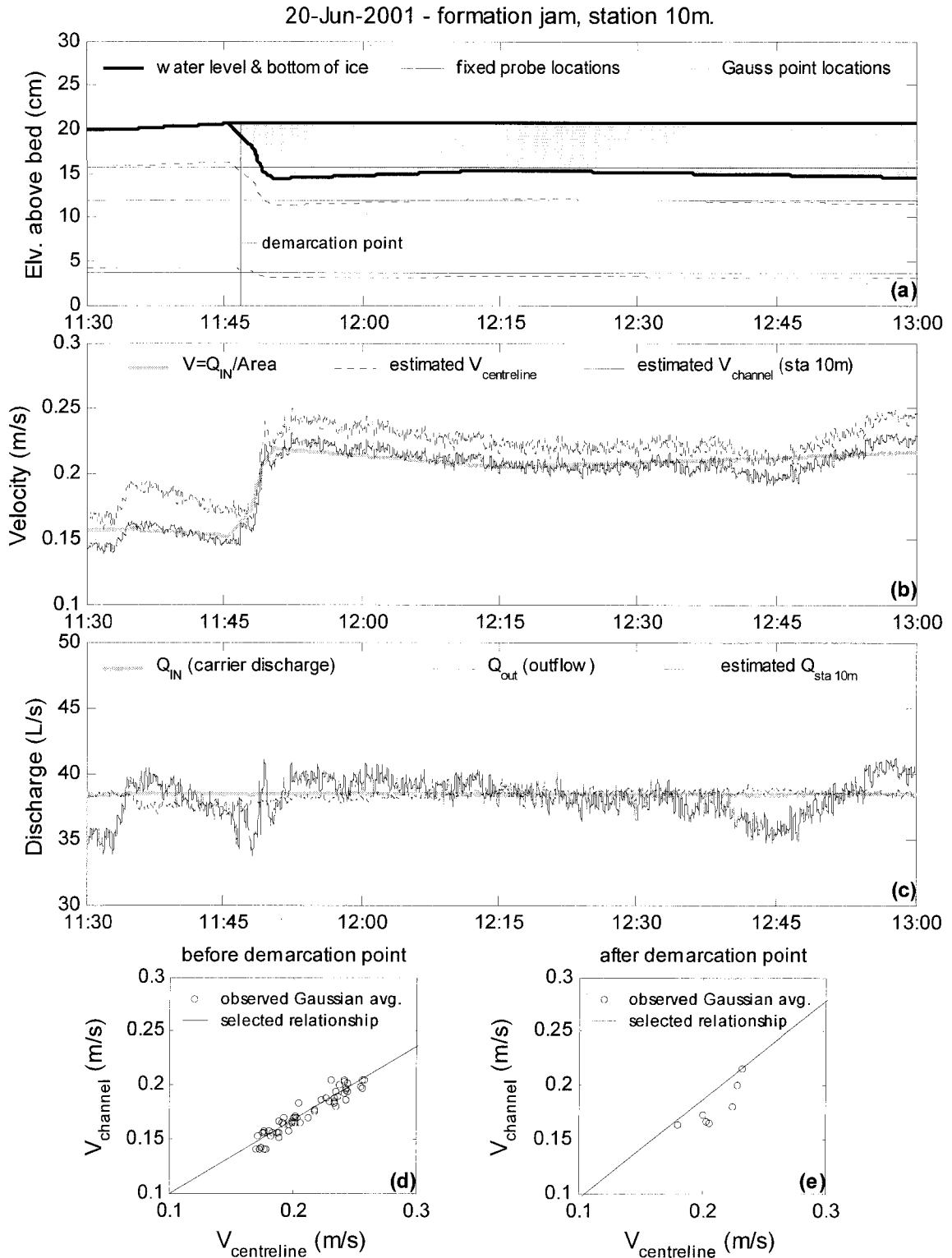
Figure E.5. Summary of continuous observations for a formation jam taken at Station 10m – test date: 20 June 2001.
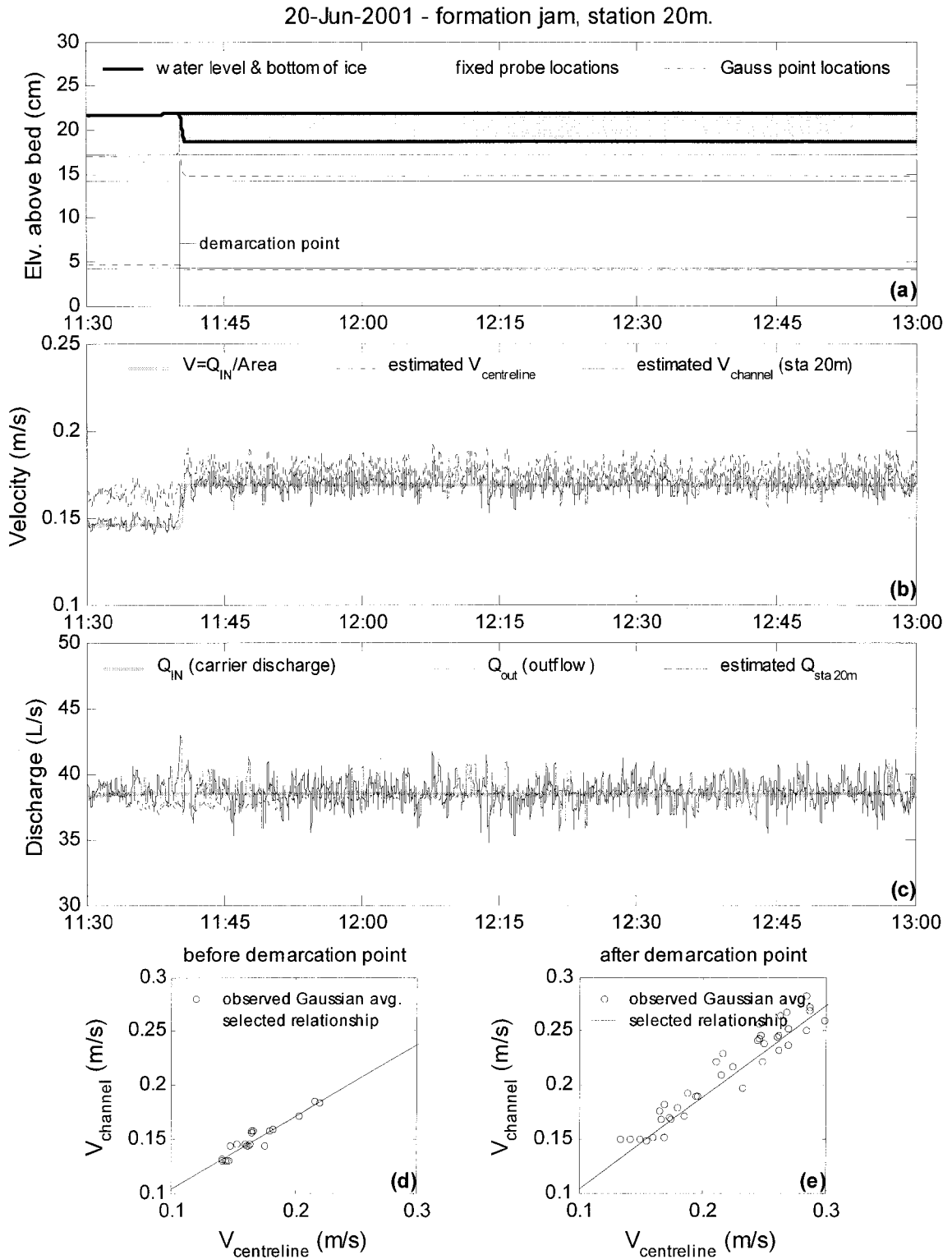
Figure E.6. Summary of continuous observations for a formation jam taken at Station 20m – test date: 20 June 2001.
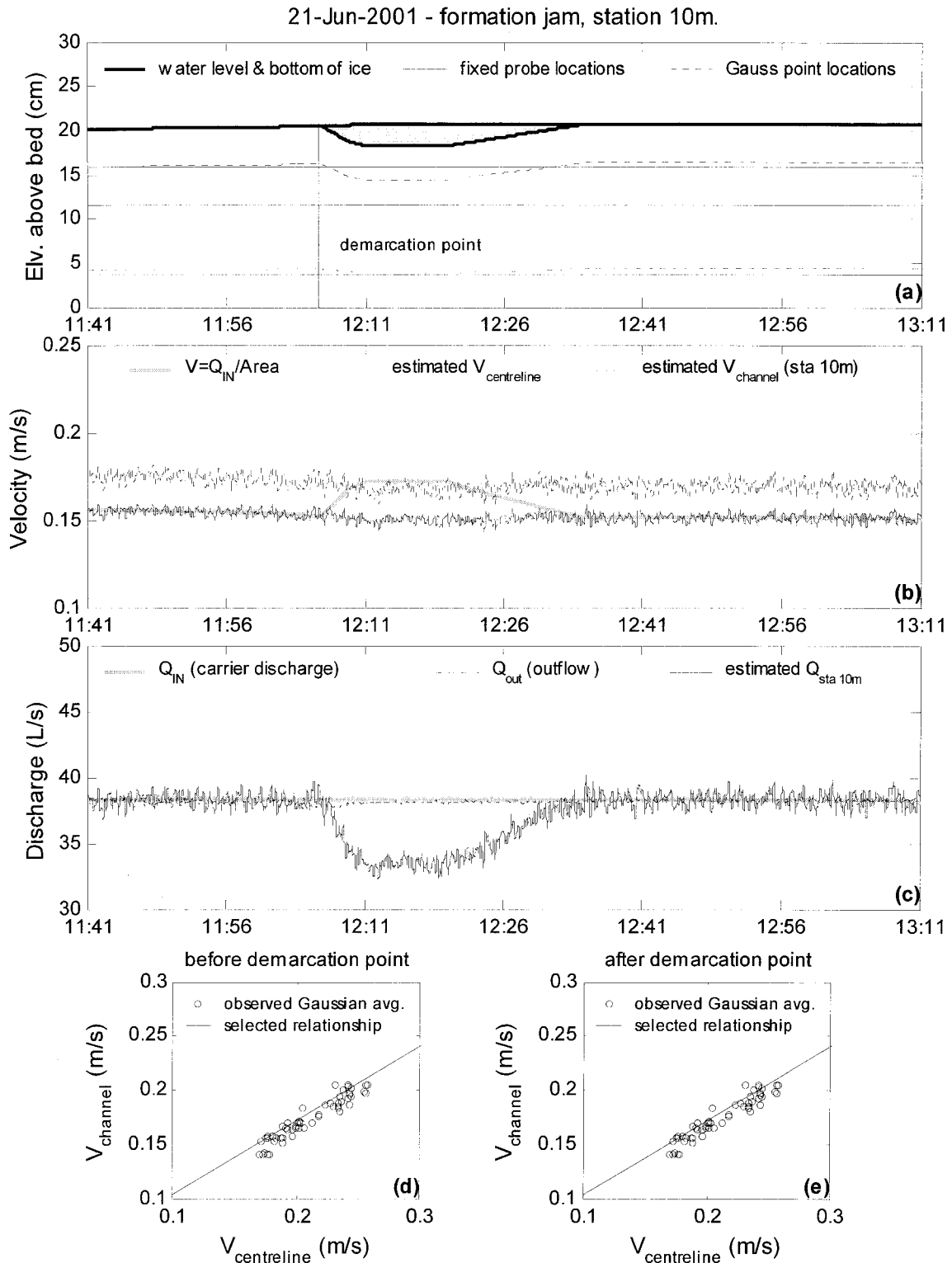
Figure E.7. Summary of continuous observations for a formation jam taken at Station 10m – test date: 21 June 2001.

219
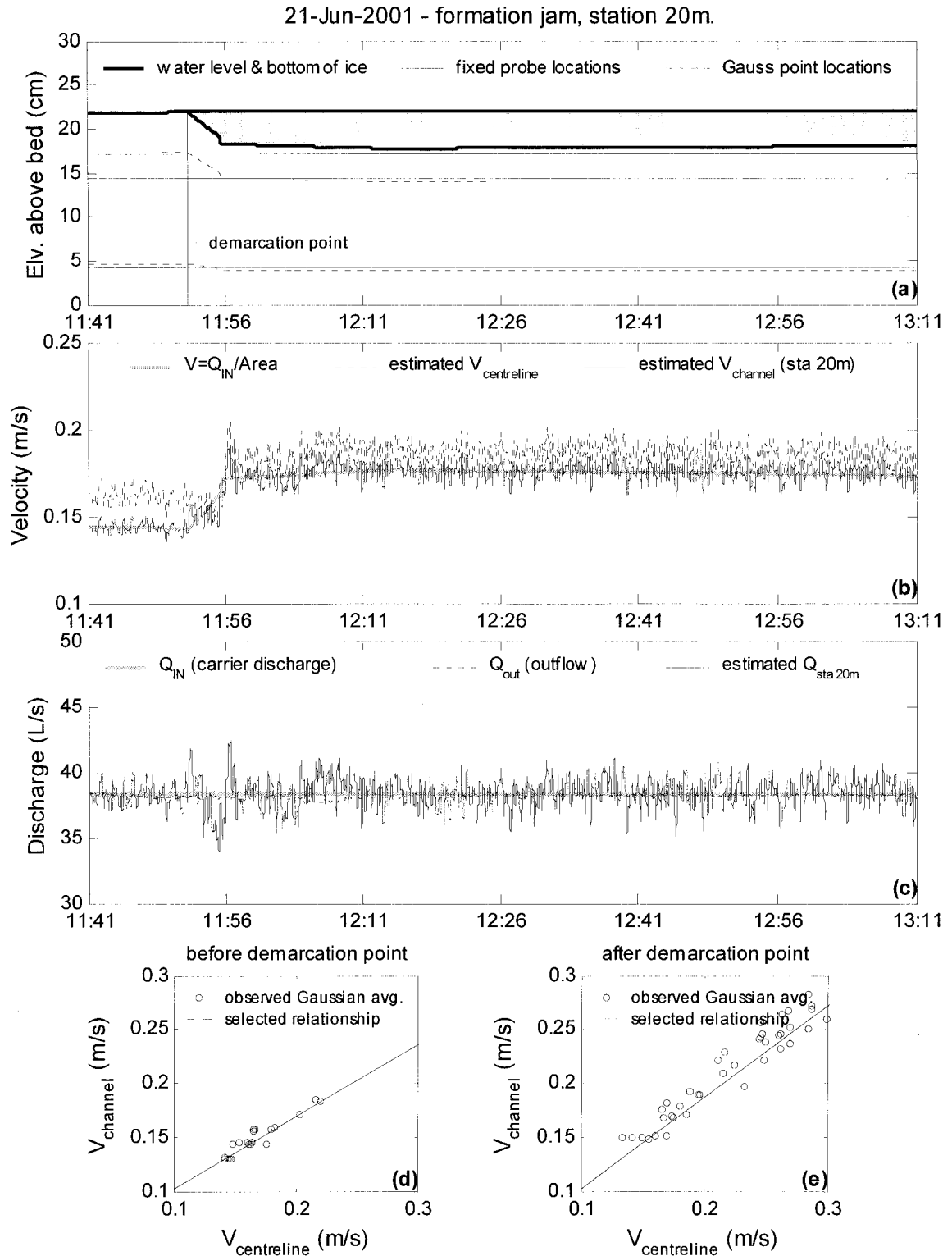
Figure E.8. Summary of continuous observations for a formation jam taken at Station 20m – test date: 21 June 2001.
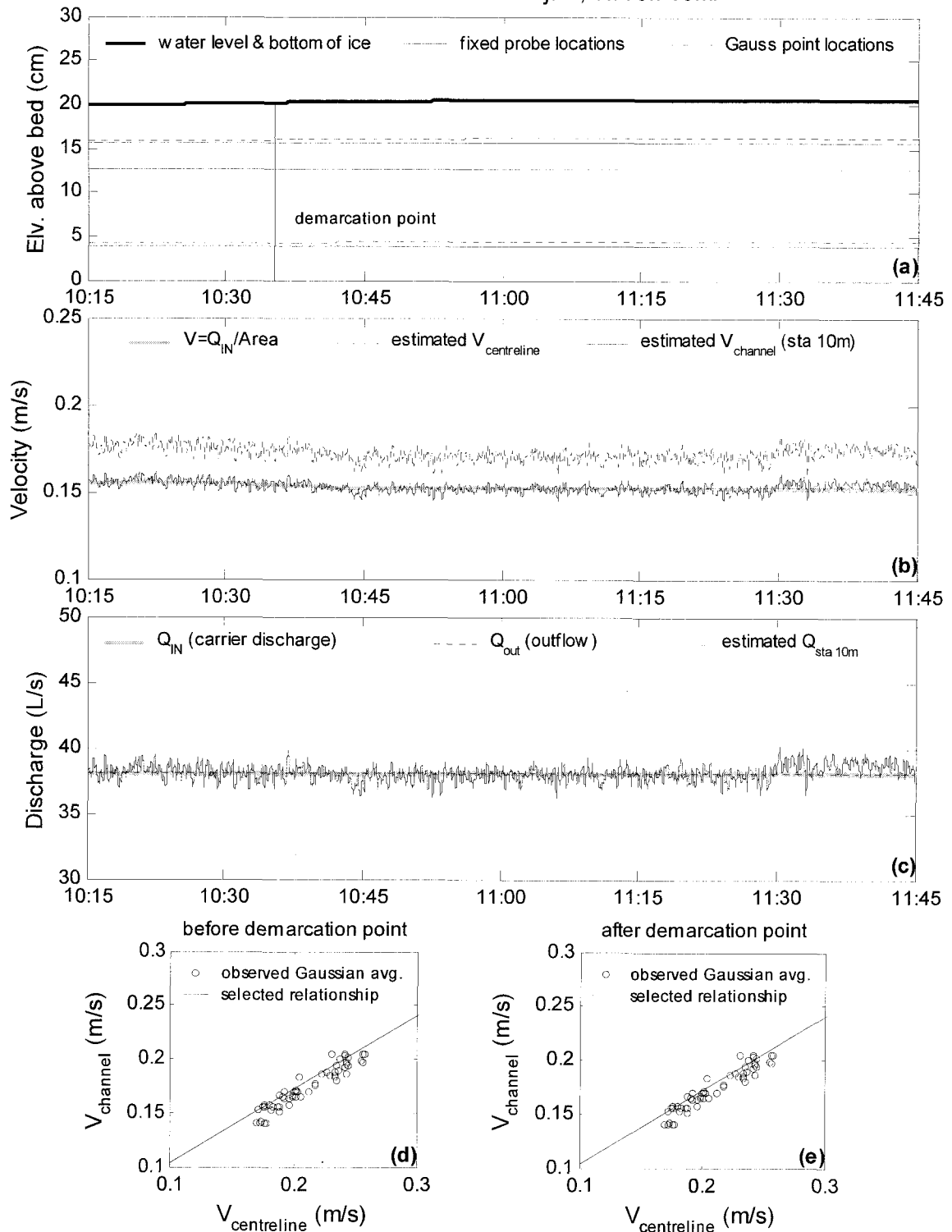
Figure E.9. Summary of continuous observations for a formation jam taken at Station 10m – test date: 22 June 2001.
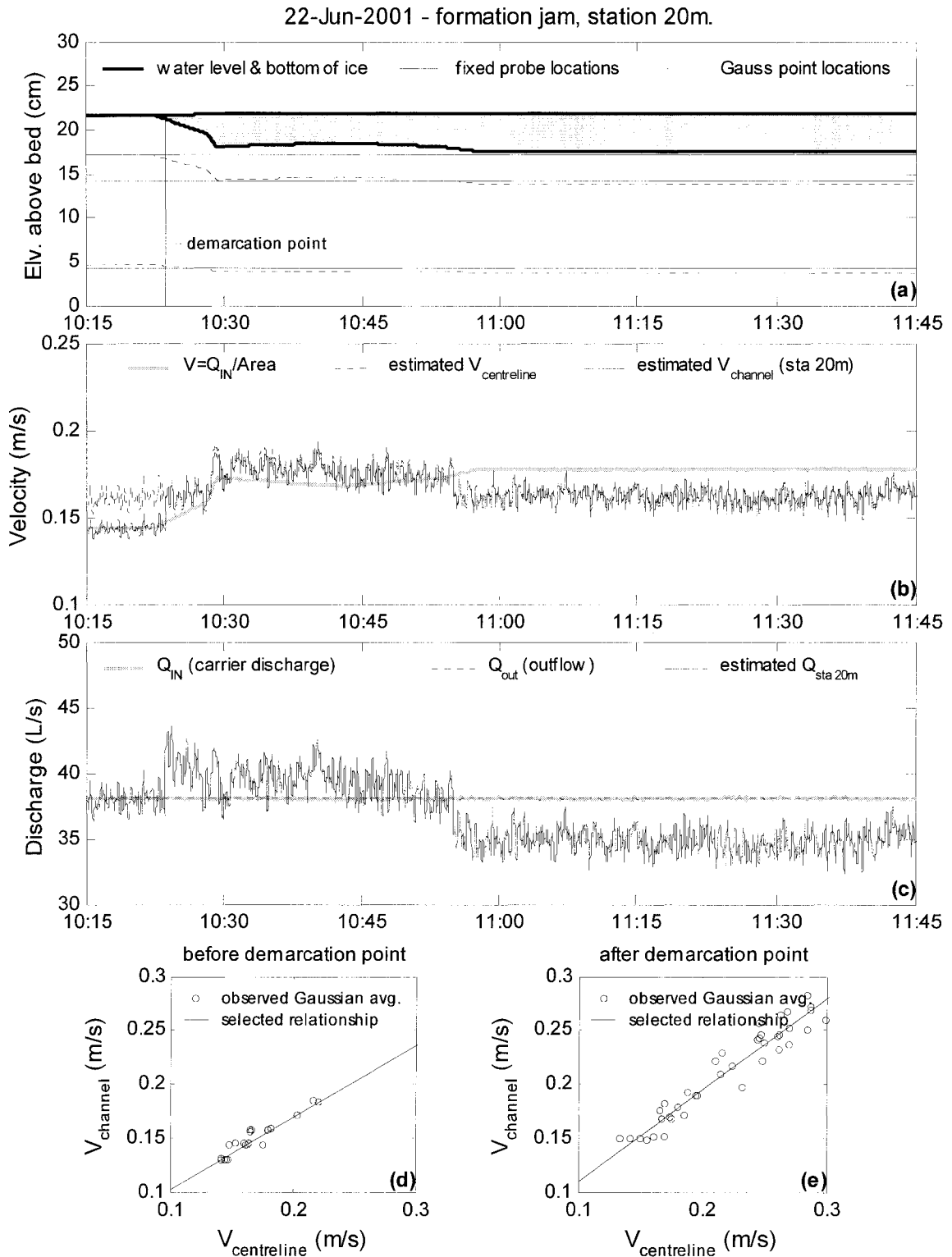
Figure E.10. Summary of continuous observations for a formation jam taken at Station 20m – test date: 22 June 2001.
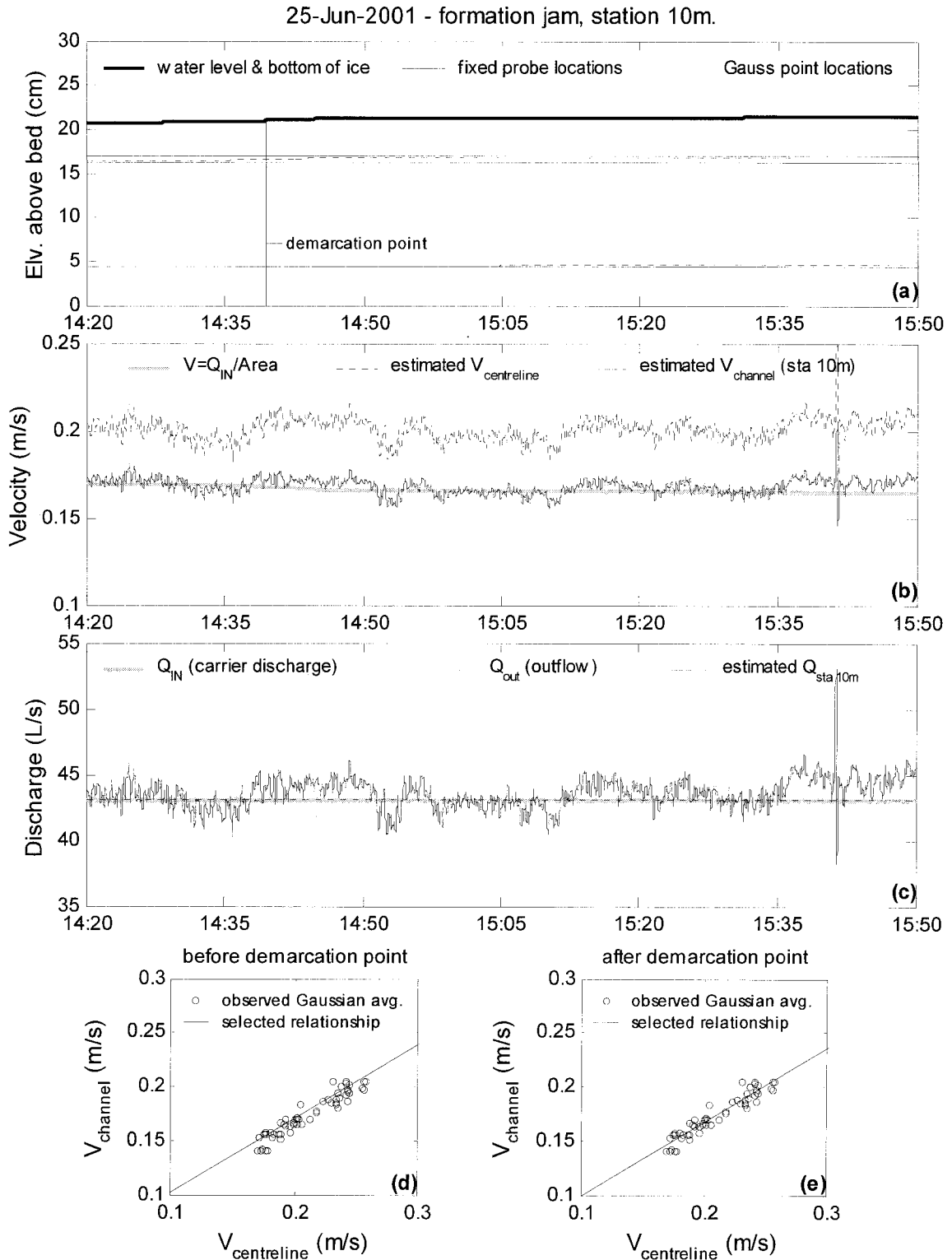
Figure E.11.   Summary of continuous observations for a formation jam taken at Station 10m – test date: 25 June 2001.

223
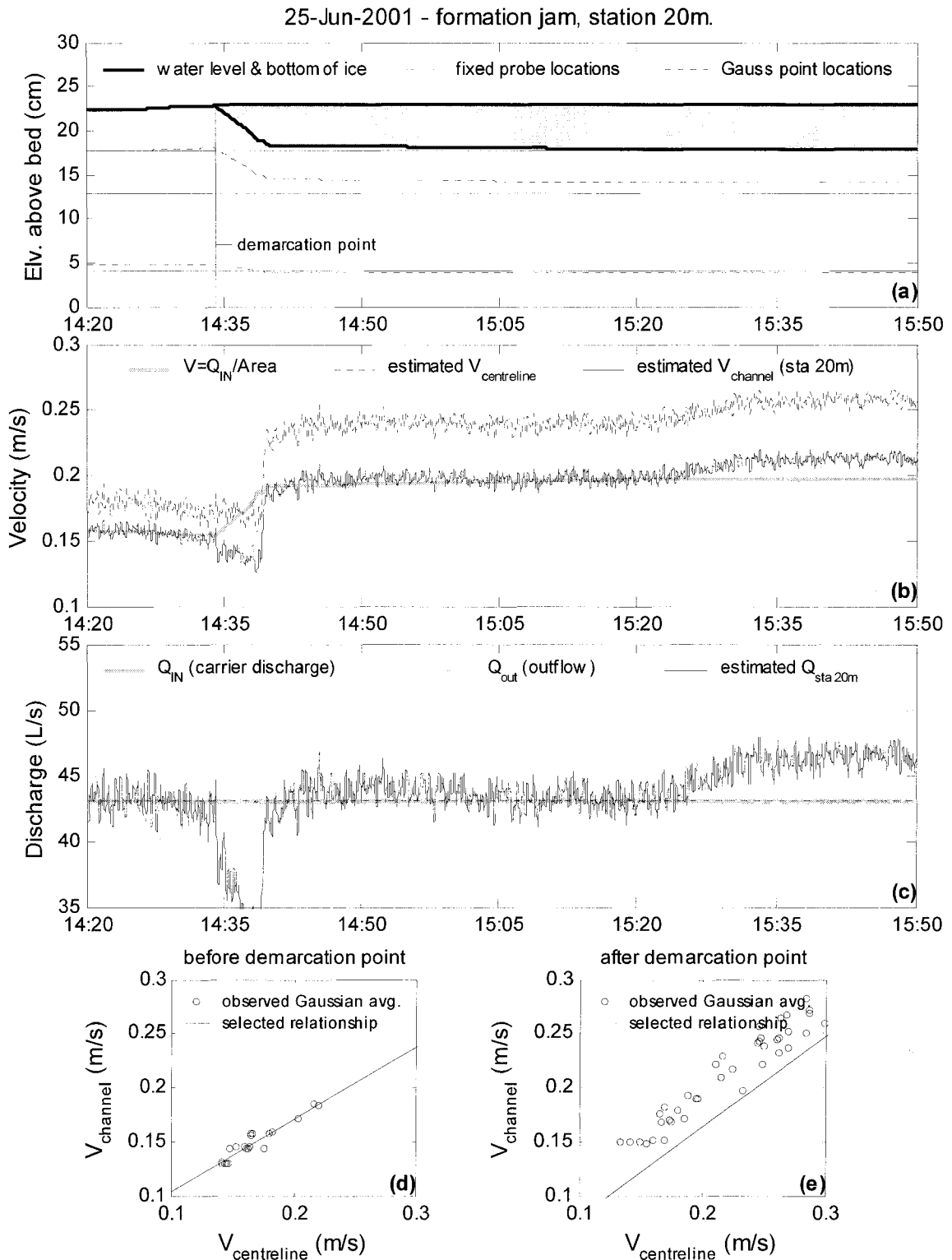
Figure E.12. Summary of continuous observations for a formation jam taken at Station 20m – test date: 25 June 2001.
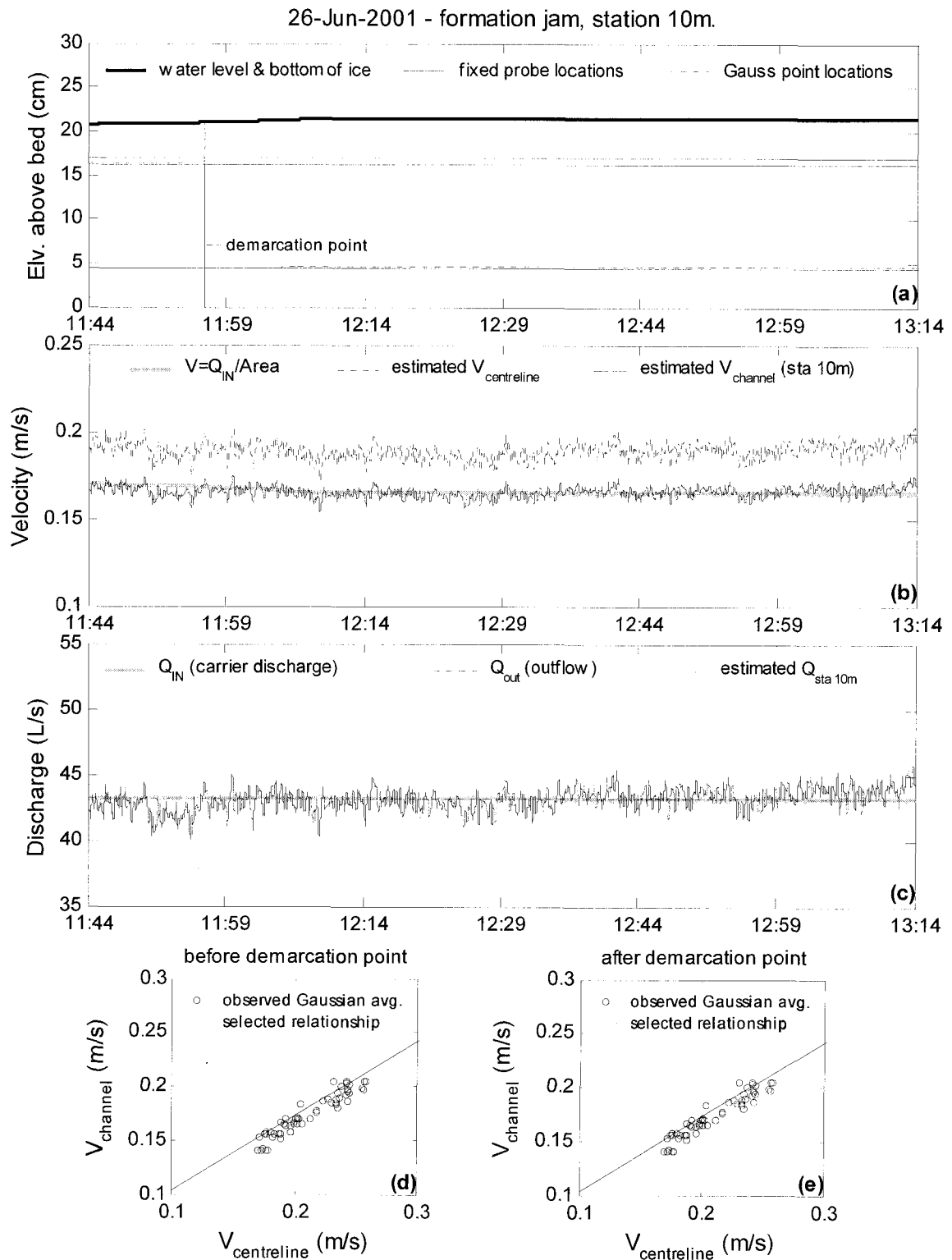
Figure E.13. Summary of continuous observations for a formation jam taken at Station 10m – test date: 26 June 2001.
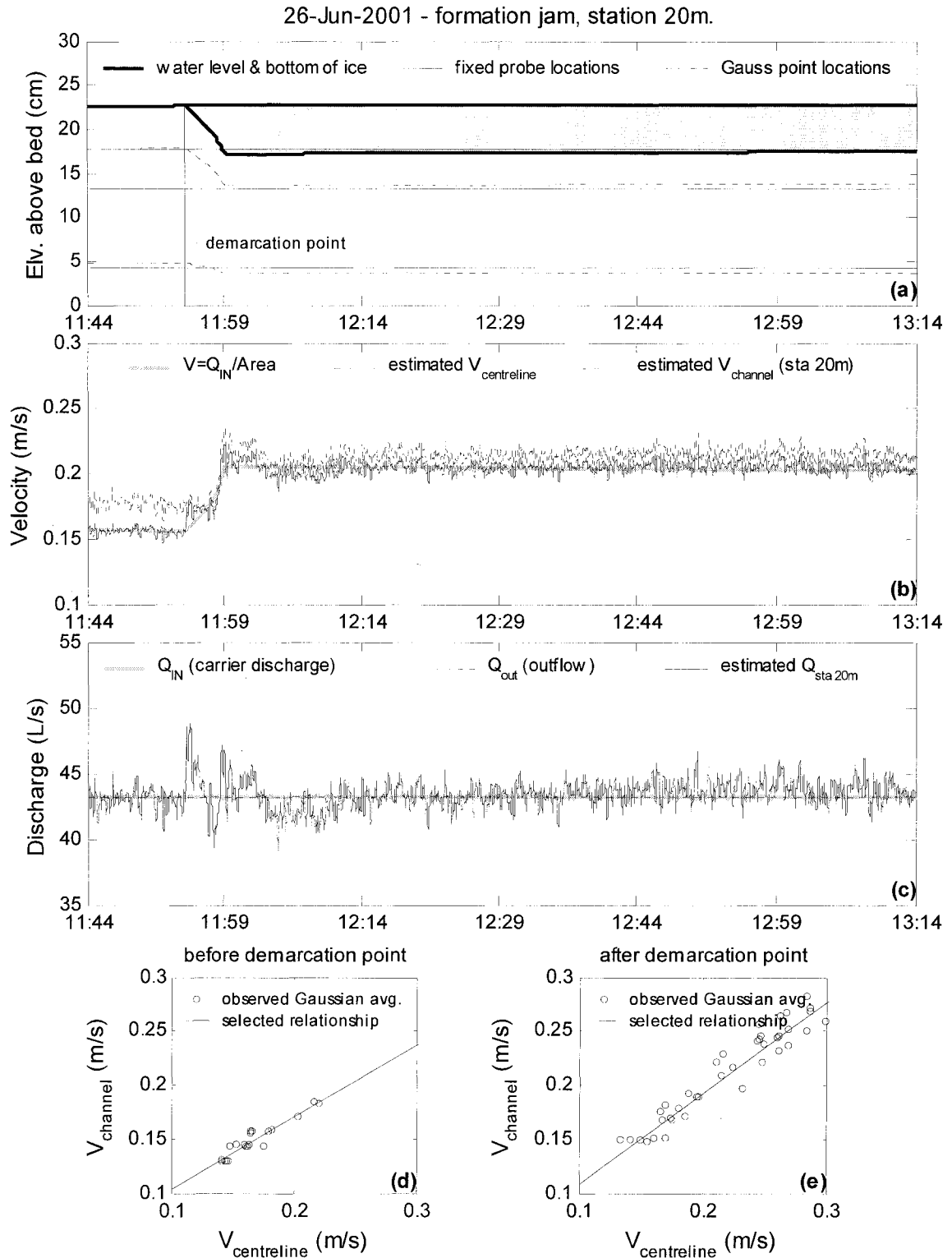
Figure E.14. Summary of continuous observations for a formation jam taken at Station 20m – test date: 26 June 2001.
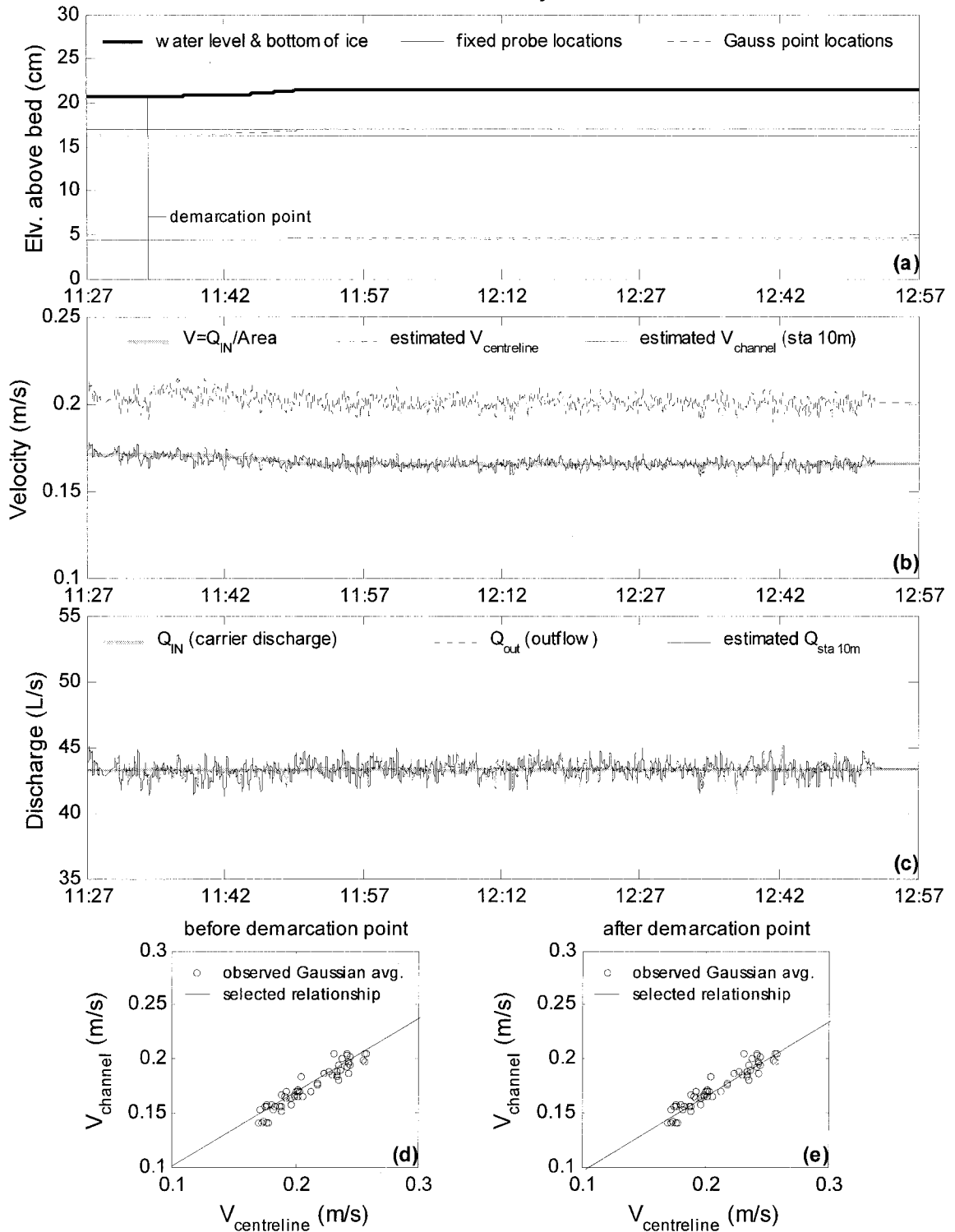
Figure E.15. Summary of continuous observations for a formation jam taken at Station 10m – test date: 27 June 2001.
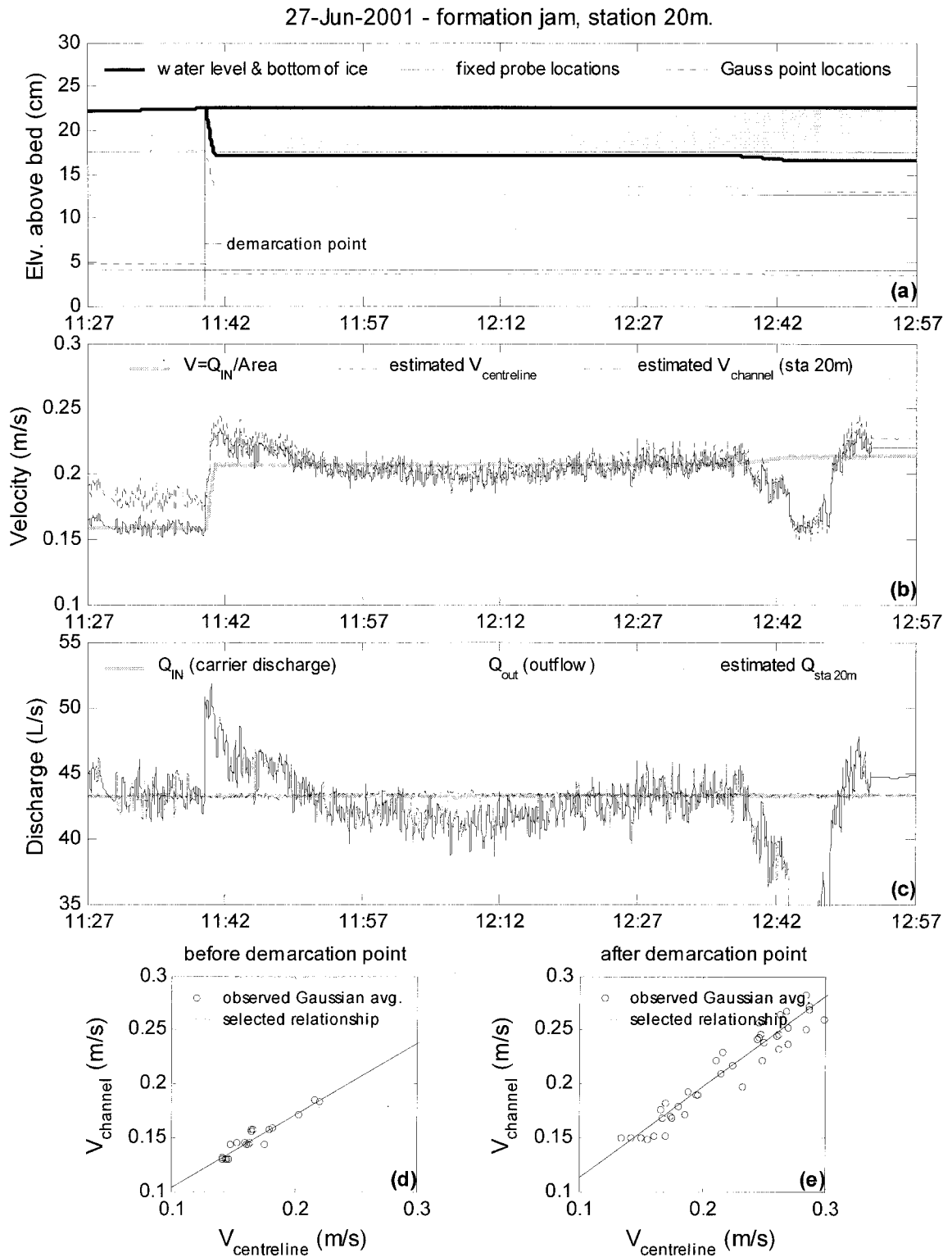
Figure E.16. Summary of continuous observations for a formation jam taken at Station 20m – test date: 27 June 2001.

228
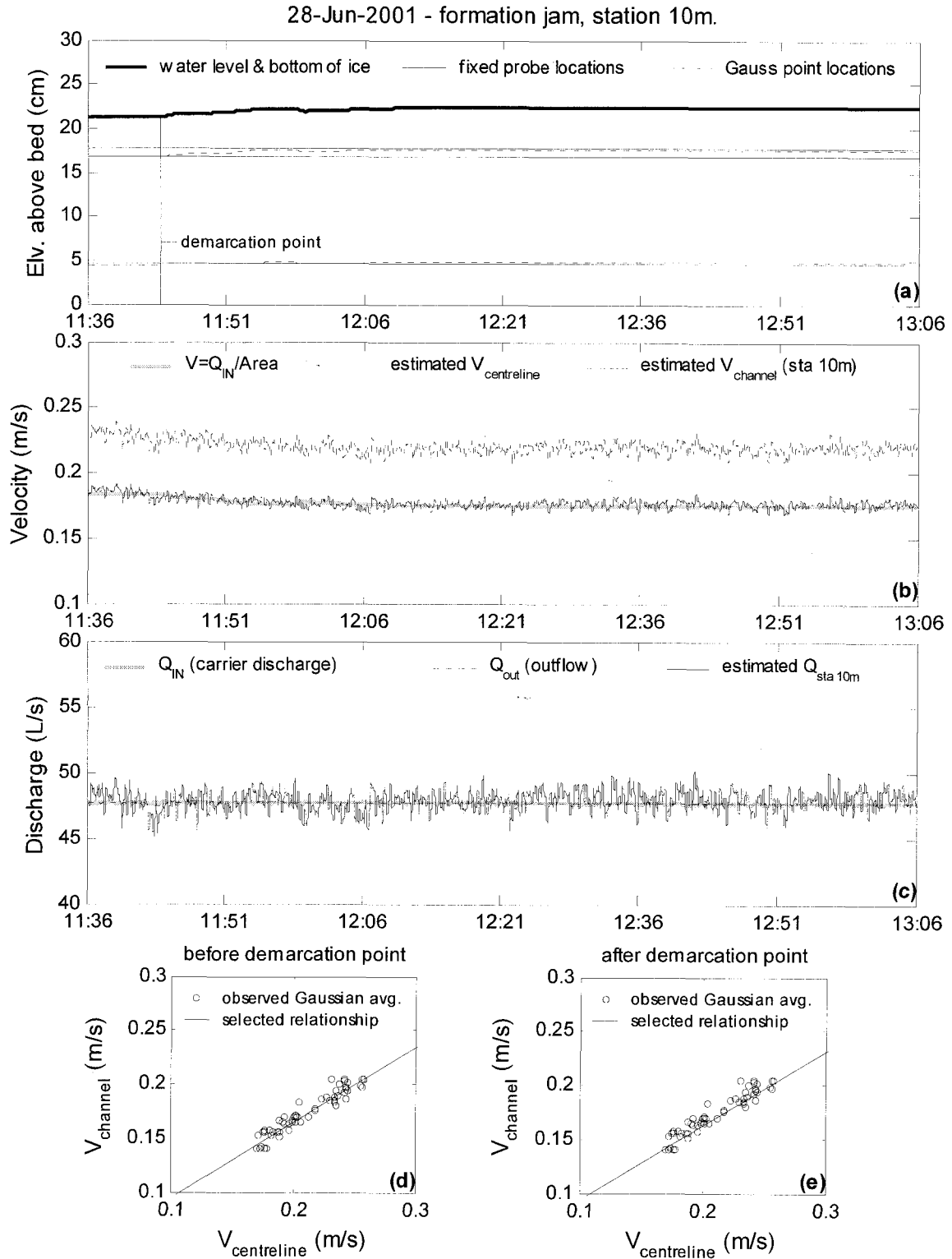
Figure E.17. Summary of continuous observations for a formation jam taken at Station 10m – test date: 28 June 2001.
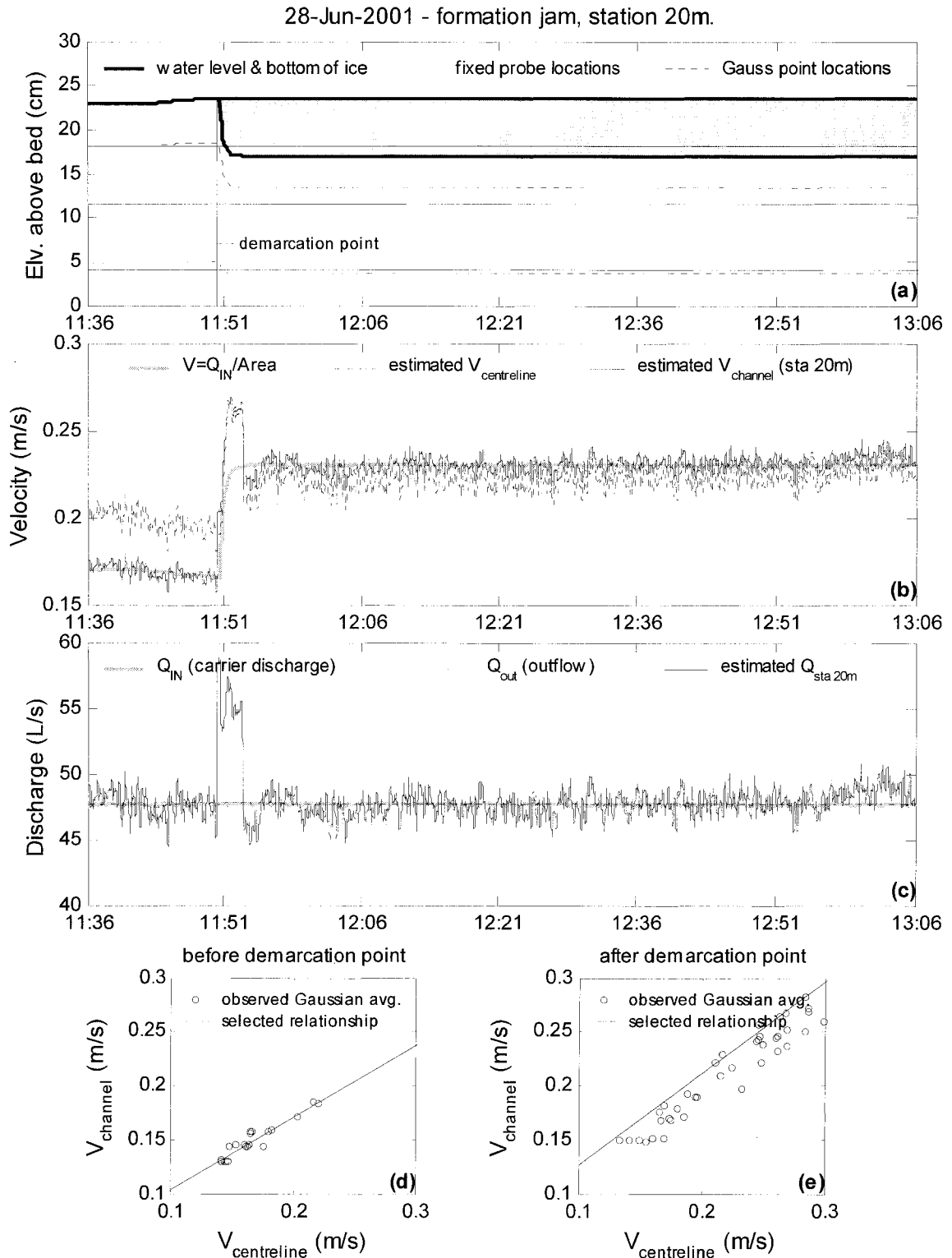
Figure E.18. Summary of continuous observations for a formation jam taken at Station 20m – test date: 28 June 2001.
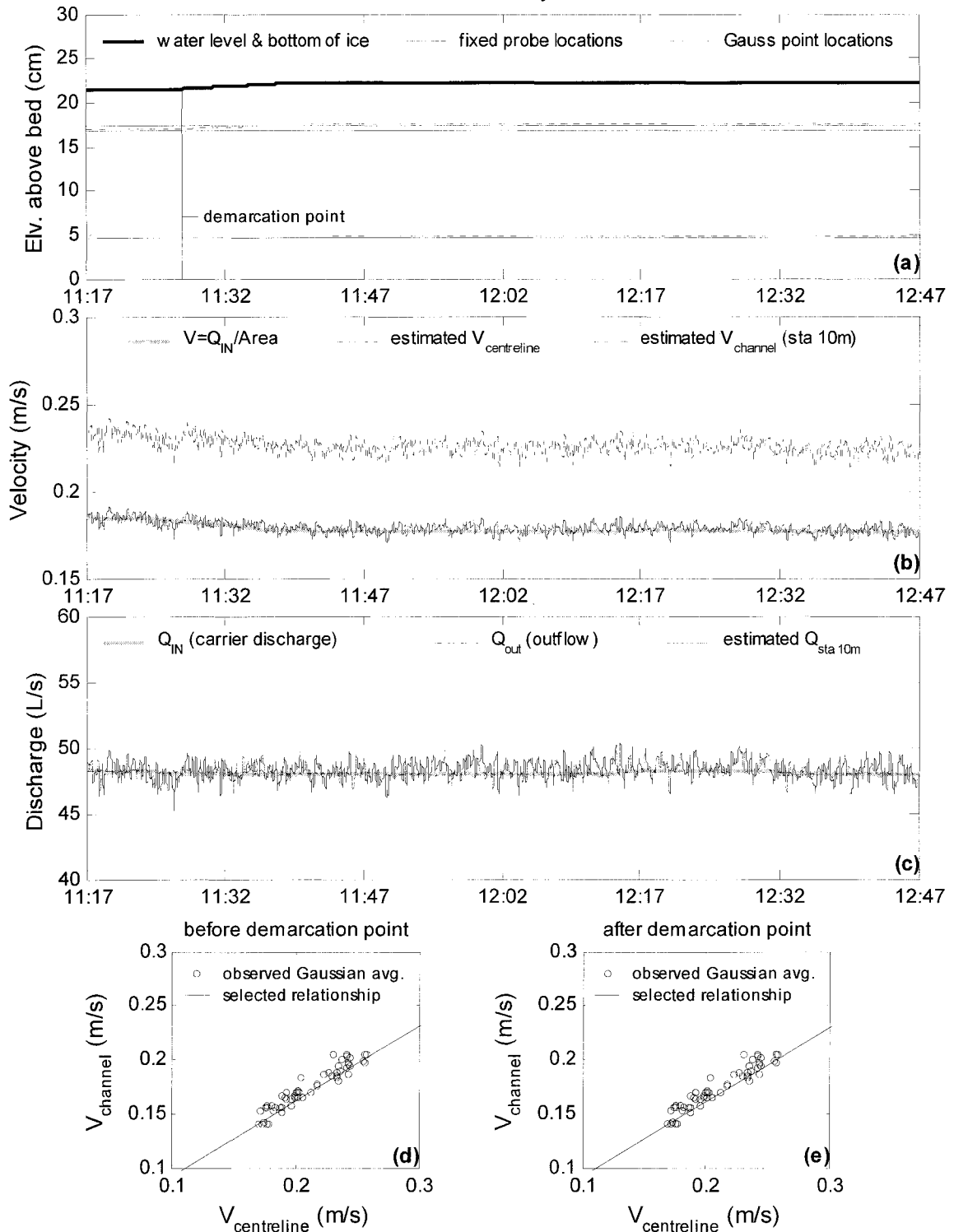
Figure E.19. Summary of continuous observations for a formation jam taken at Station 10m – test date: 29 June 2001.
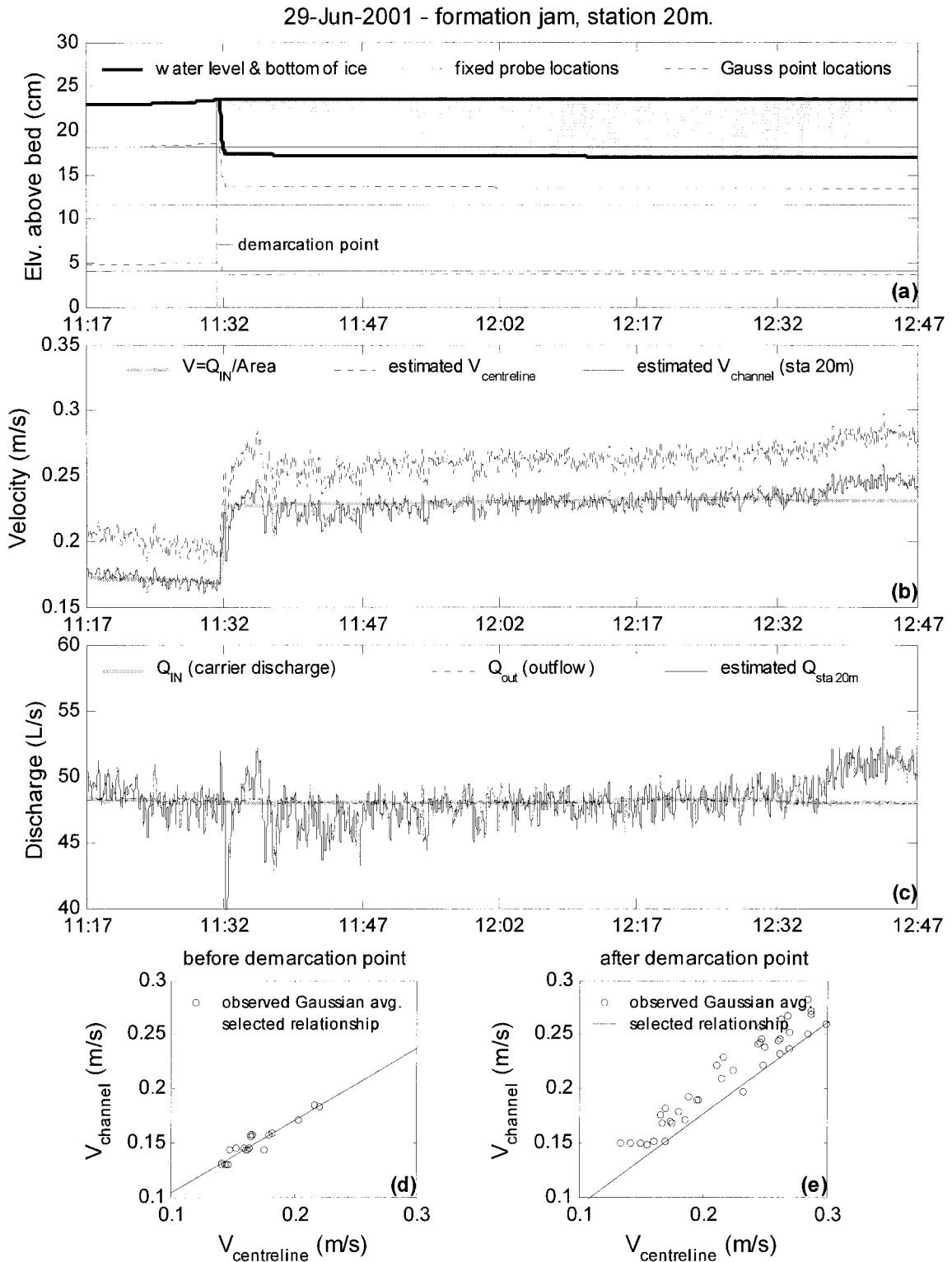
Figure E.20. Summary of continuous observations for a formation jam taken at Station 20m – test date: 29 June 2001.
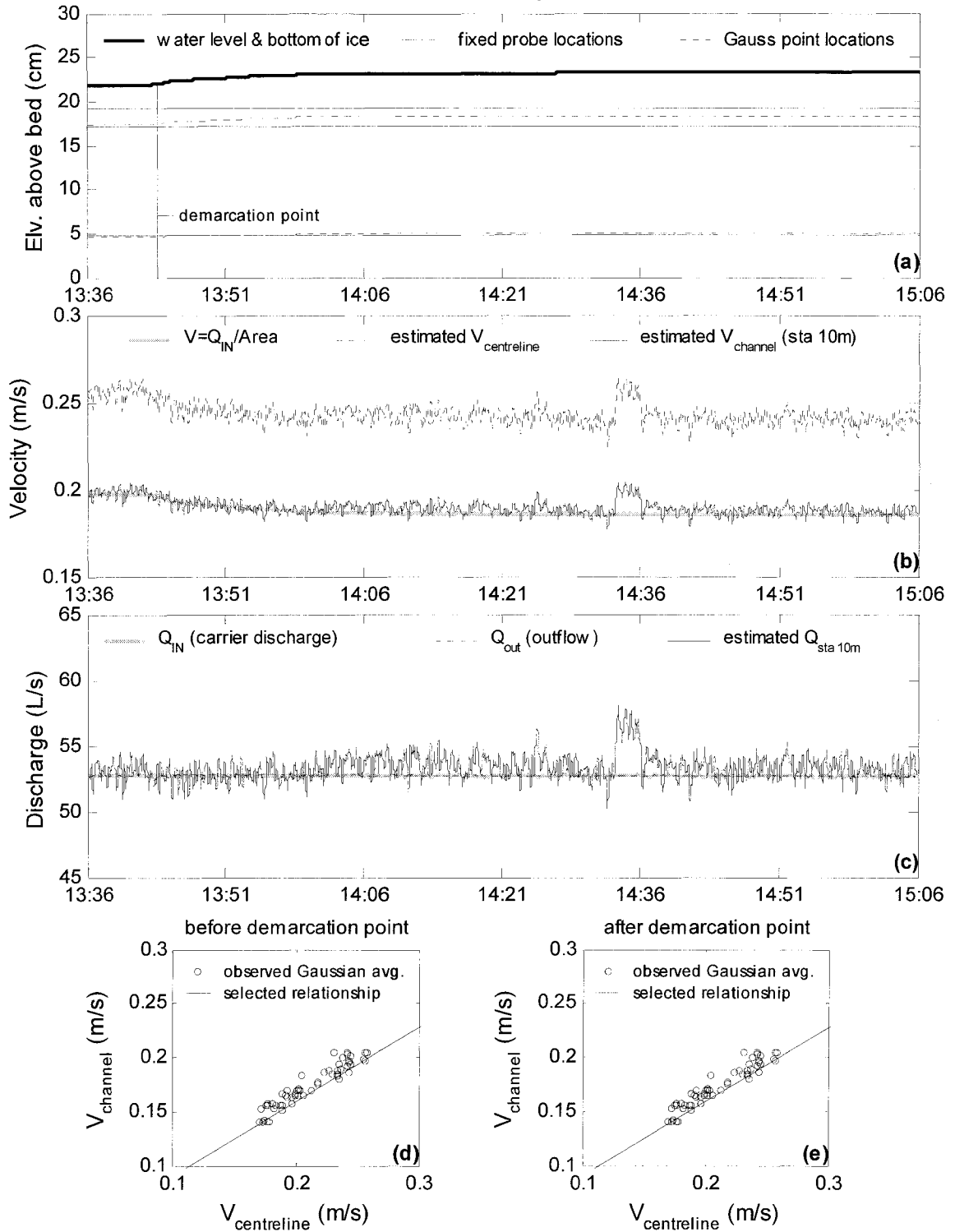
Figure E.21. Summary of continuous observations for a formation jam taken at Station 10m – test date: 03 July 2001.
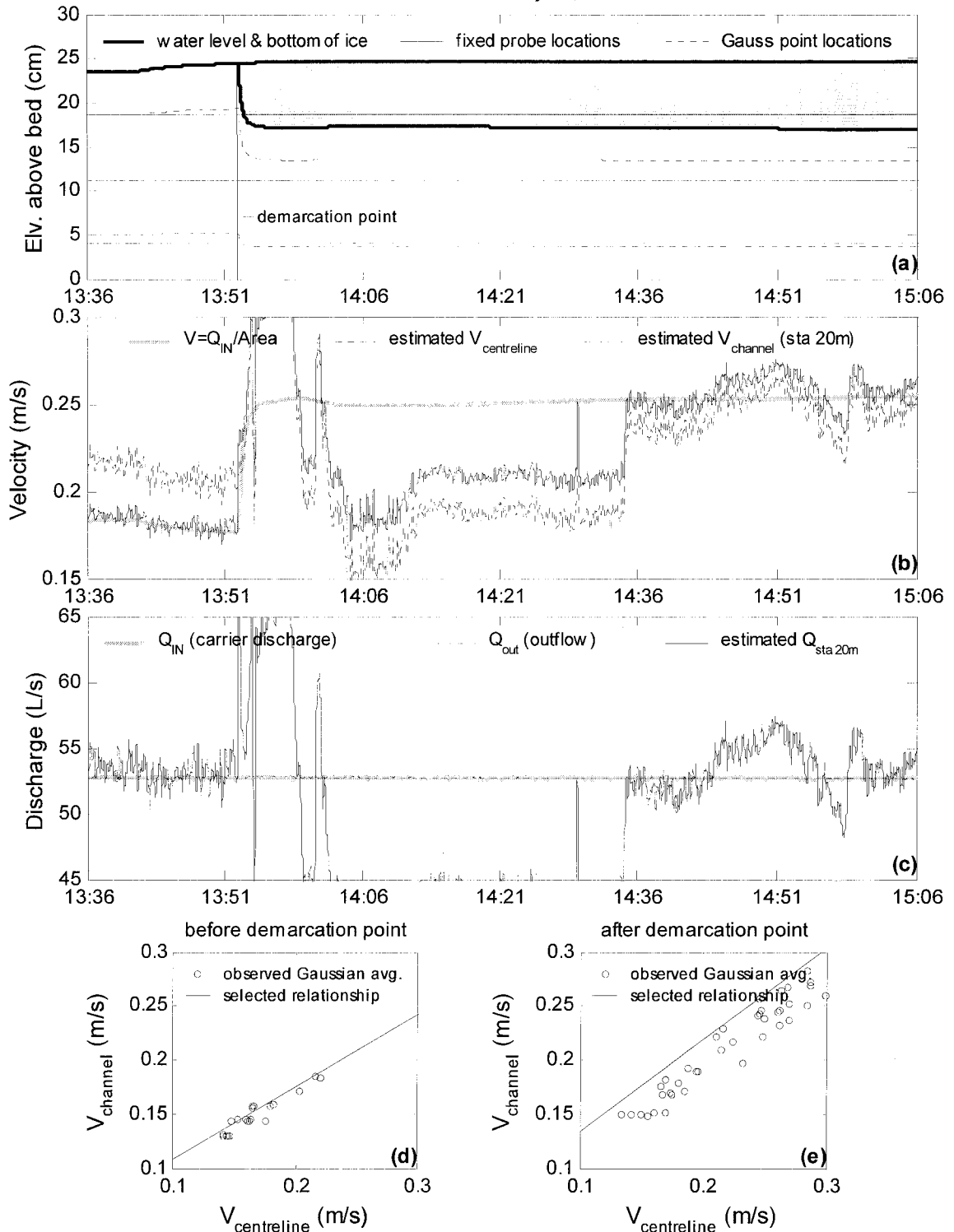
Figure E.22. Summary of continuous observations for a formation jam taken at Station 20m – test date: 03 July 2001.

234
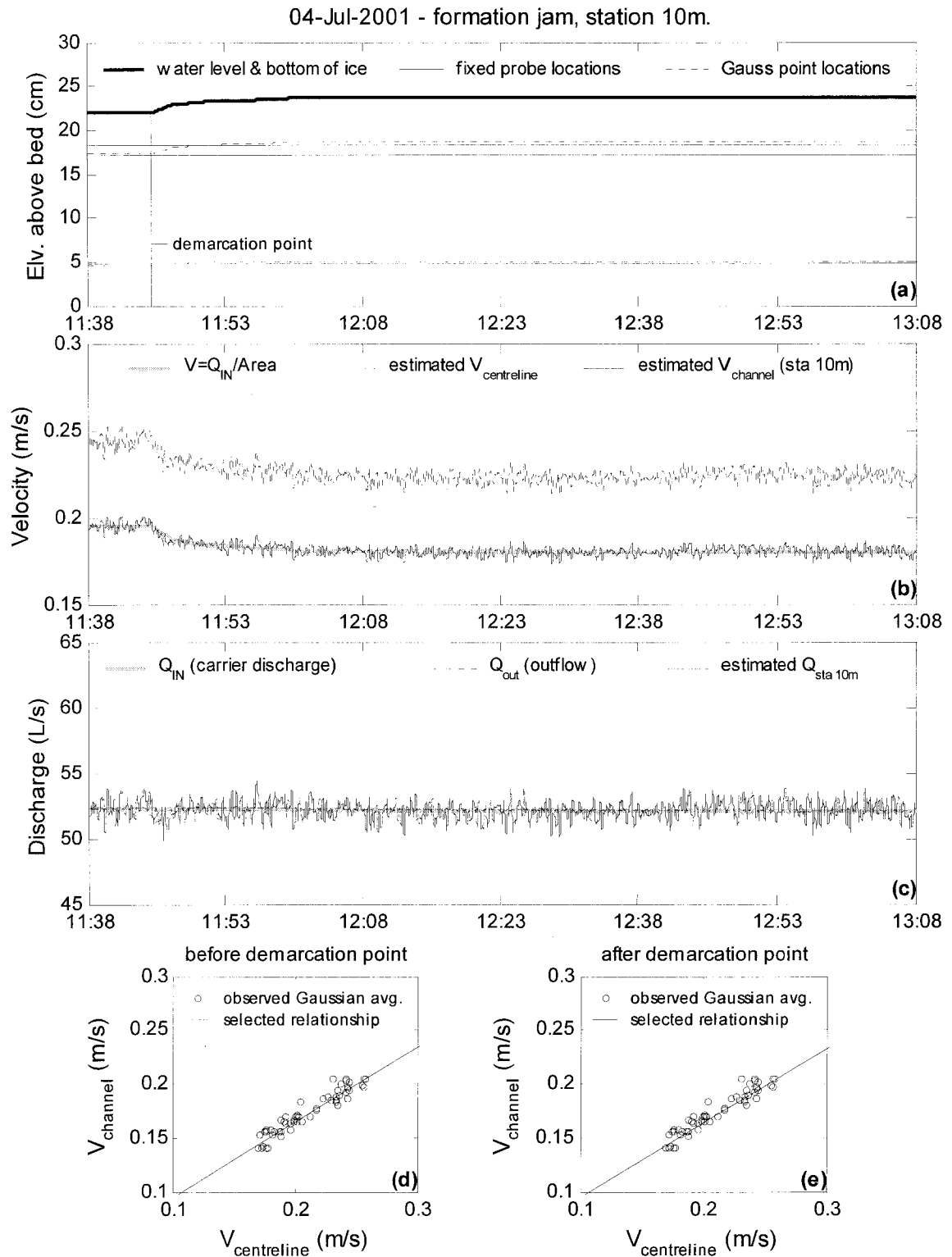
Figure E.23. Summary of continuous observations for a formation jam taken at Station 10m – test date: 04 July 2001.
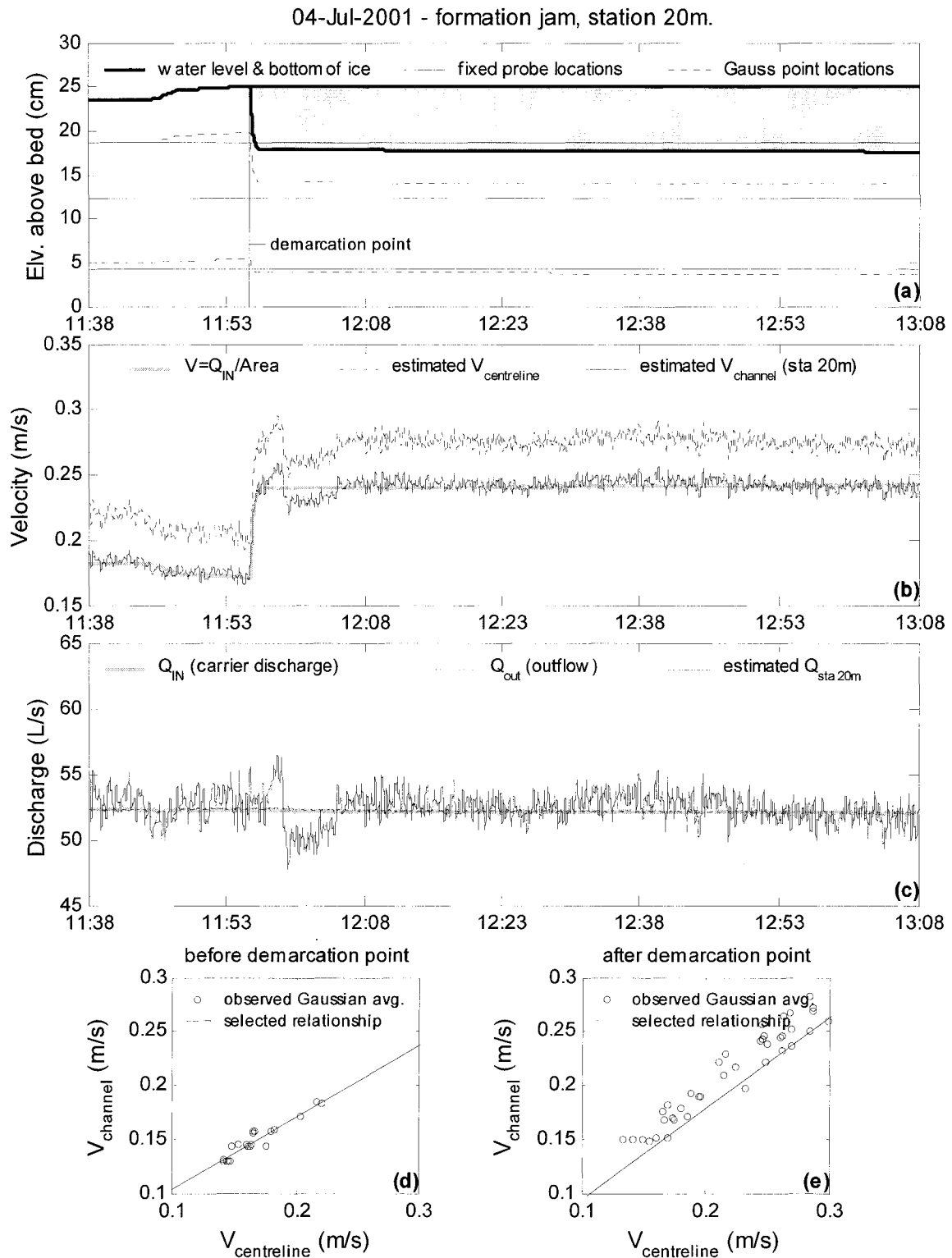
Figure E.24. Summary of continuous observations for a formation jam taken at Station 20m – test date: 04 July 2001.
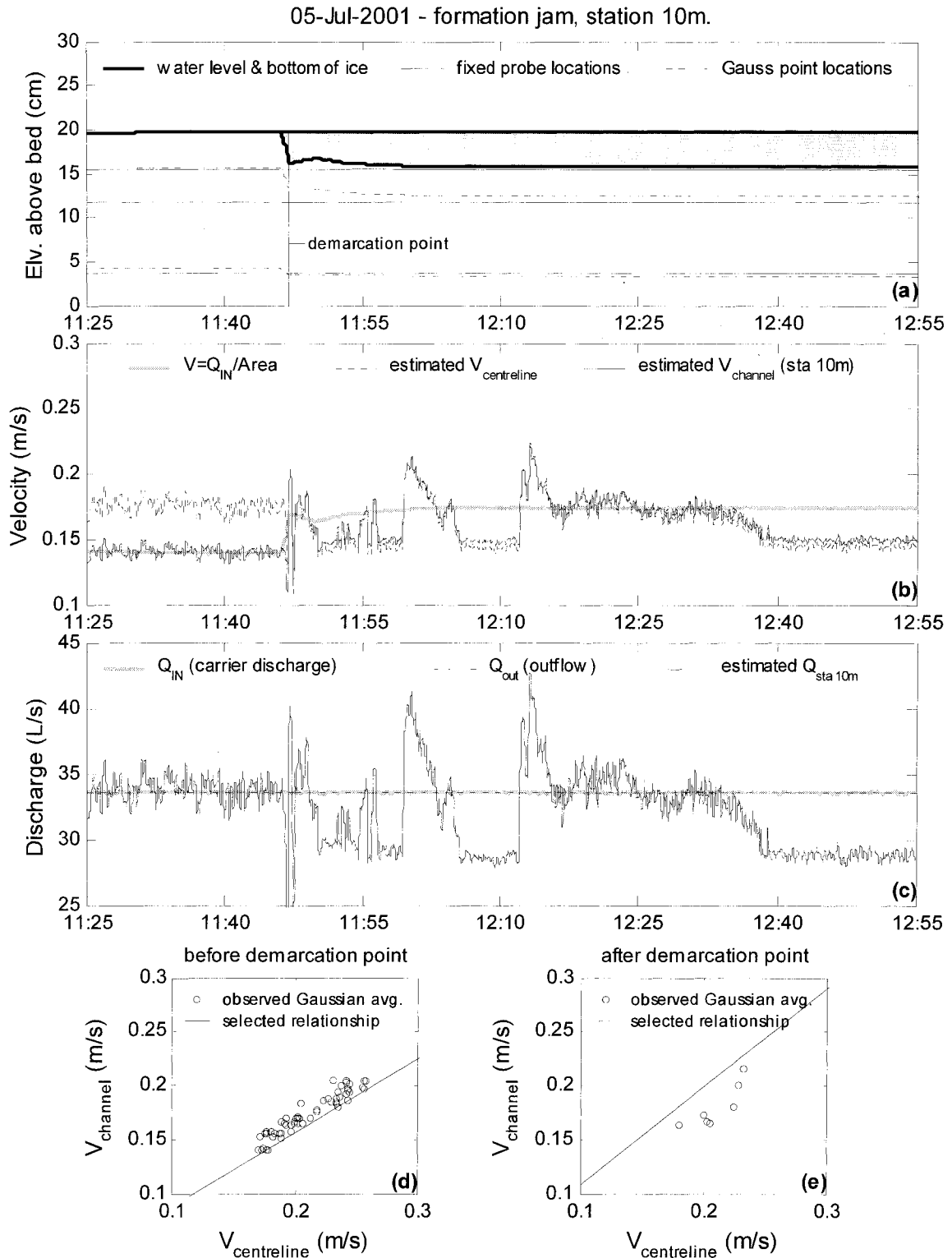
Figure E.25. Summary of continuous observations for a formation jam taken at Station 10m – test date: 05 July 2001.

237
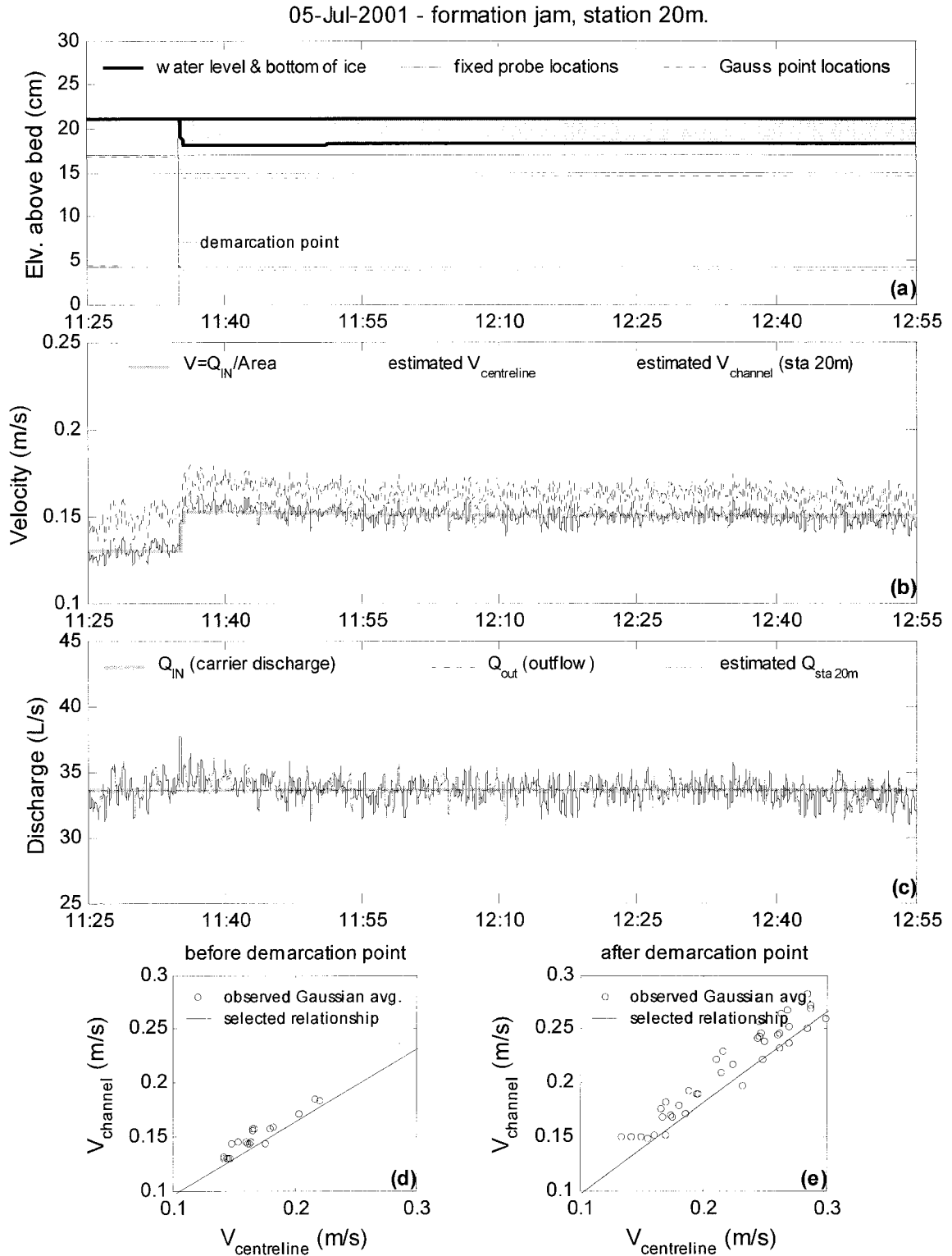
Figure E.26.   Summary of continuous observations for a formation jam taken at Station 20m – test date: 05 July 2001.

238
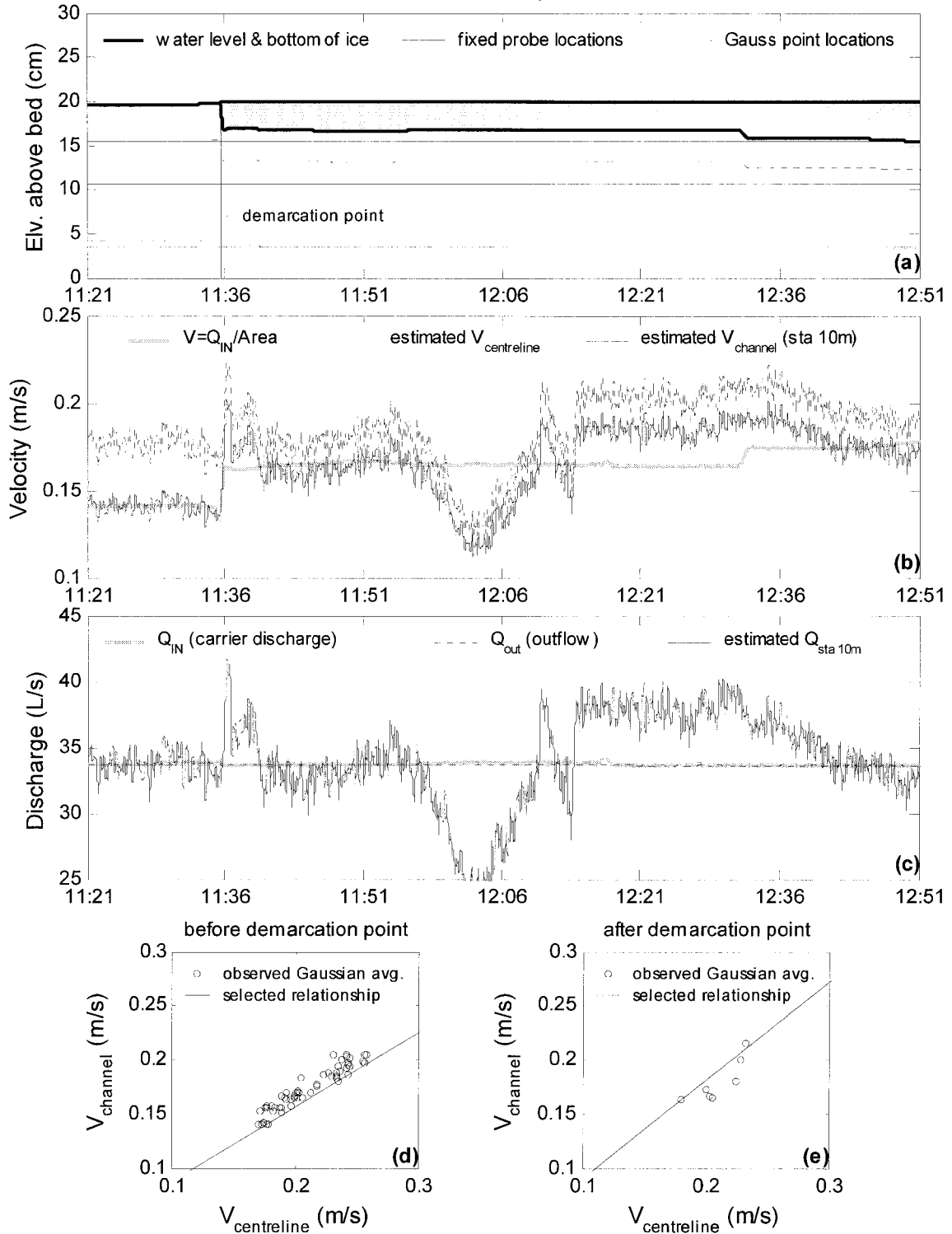
Figure E.27. Summary of continuous observations for a formation jam taken at Station 10m – test date: 09 July 2001.

239
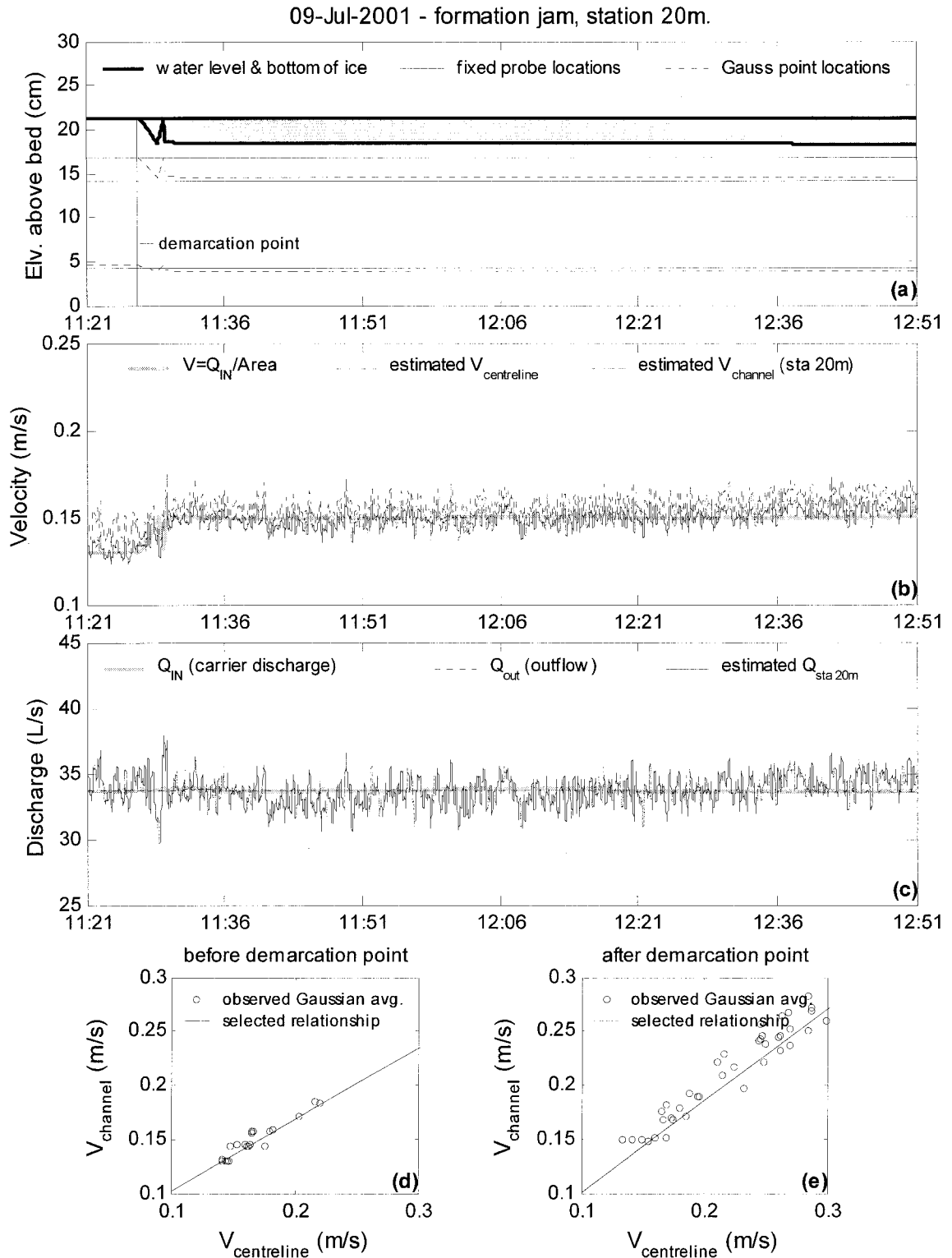
Figure E.28. Summary of continuous observations for a formation jam taken at Station 20m – test date: 09 July 2001.

240
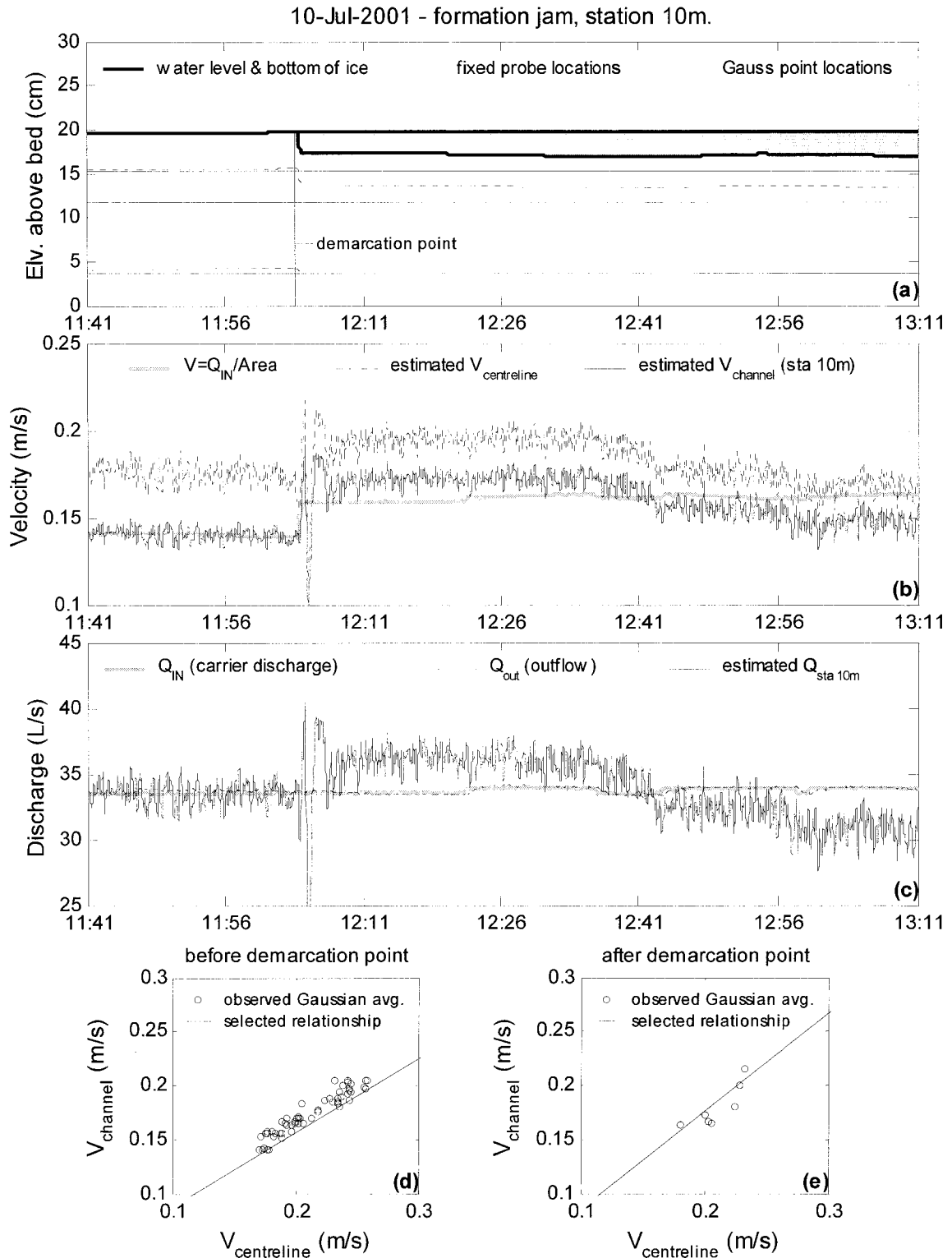
Figure E.29. Summary of continuous observations for a formation jam taken at Station 10m – test date: 10 July 2001.
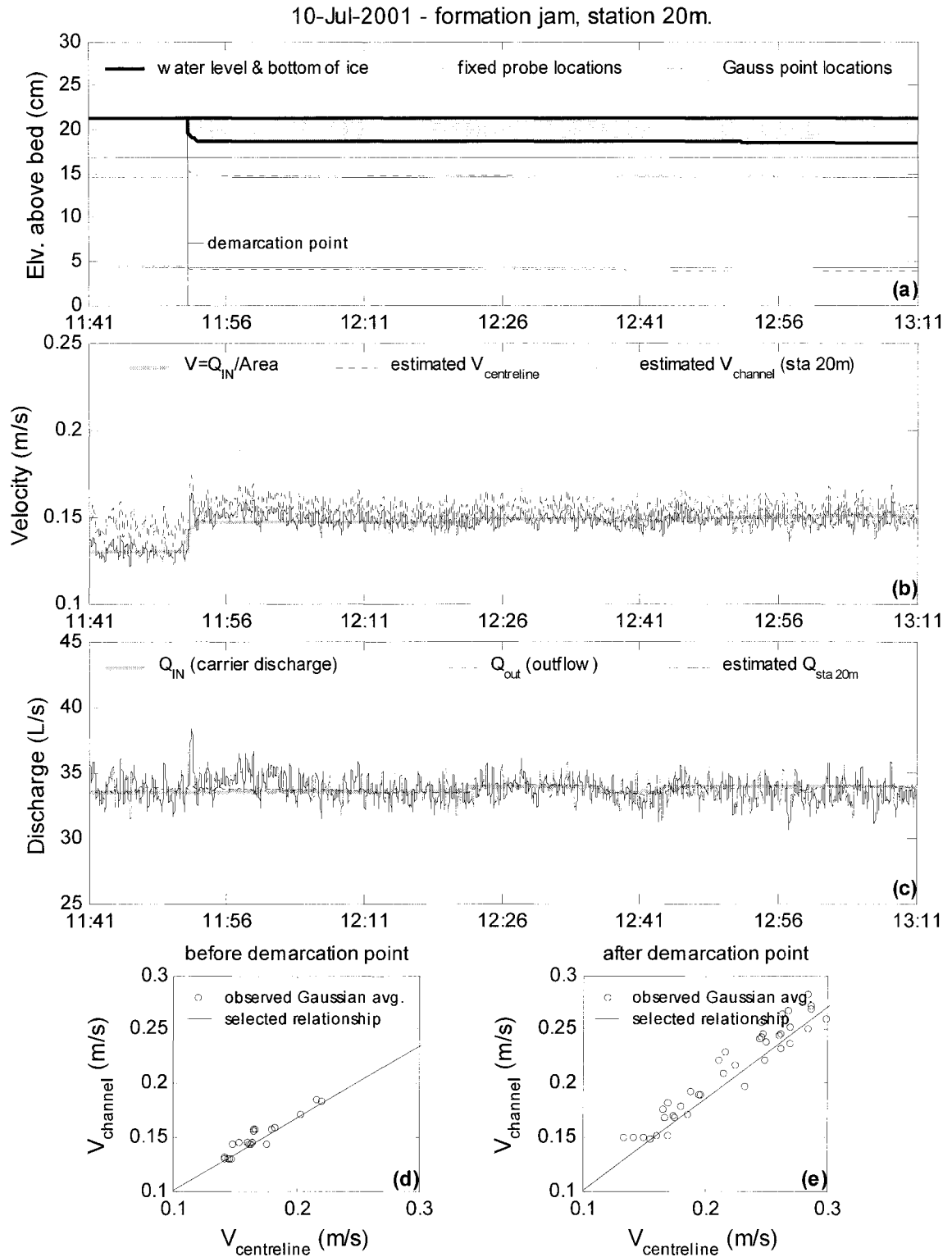
Figure E.30. Summary of continuous observations for a formation jam taken at Station 20m – test date: 10 July 2001.
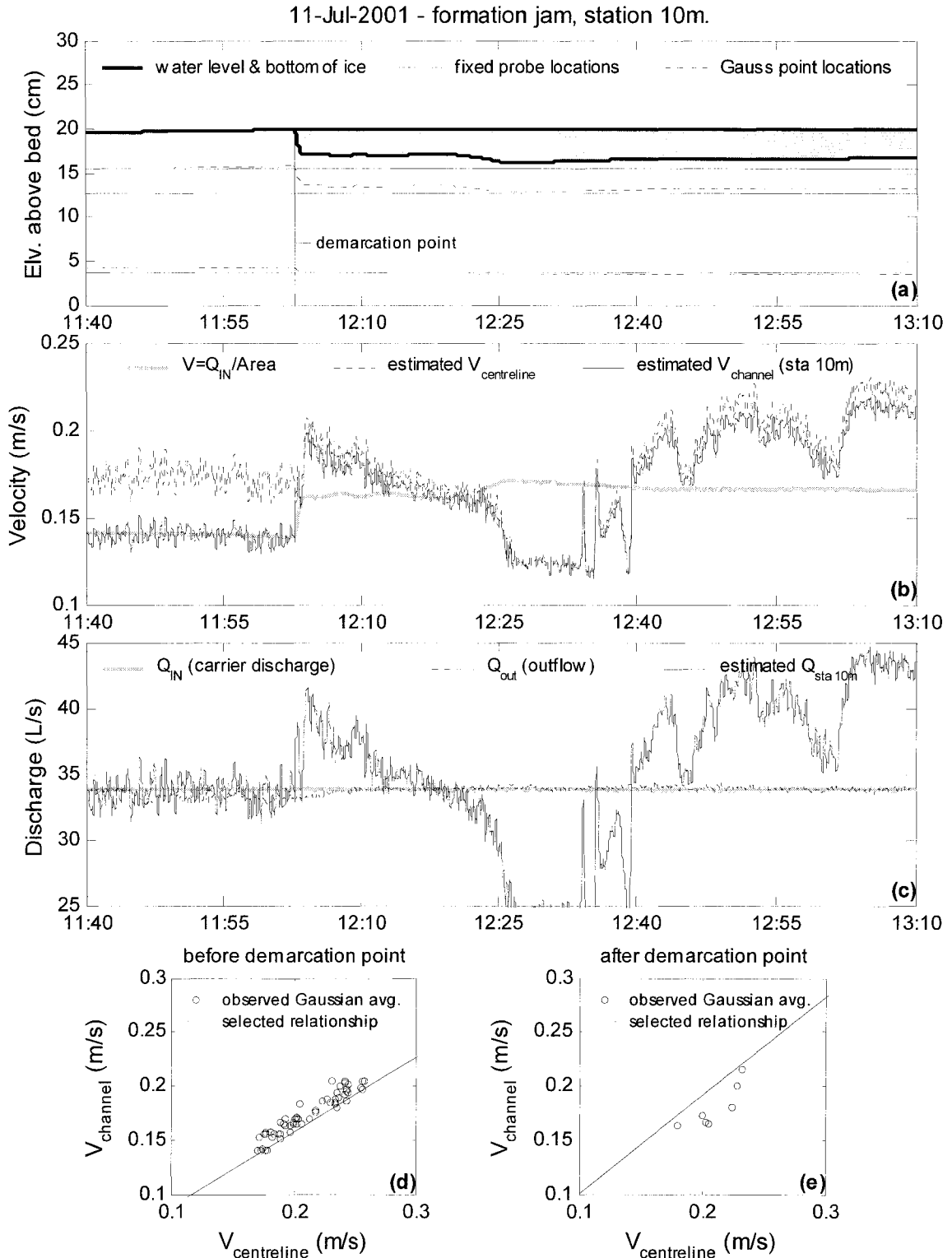
Figure E.31. Summary of continuous observations for a formation jam taken at Station 10m – test date: 11 July 2001.
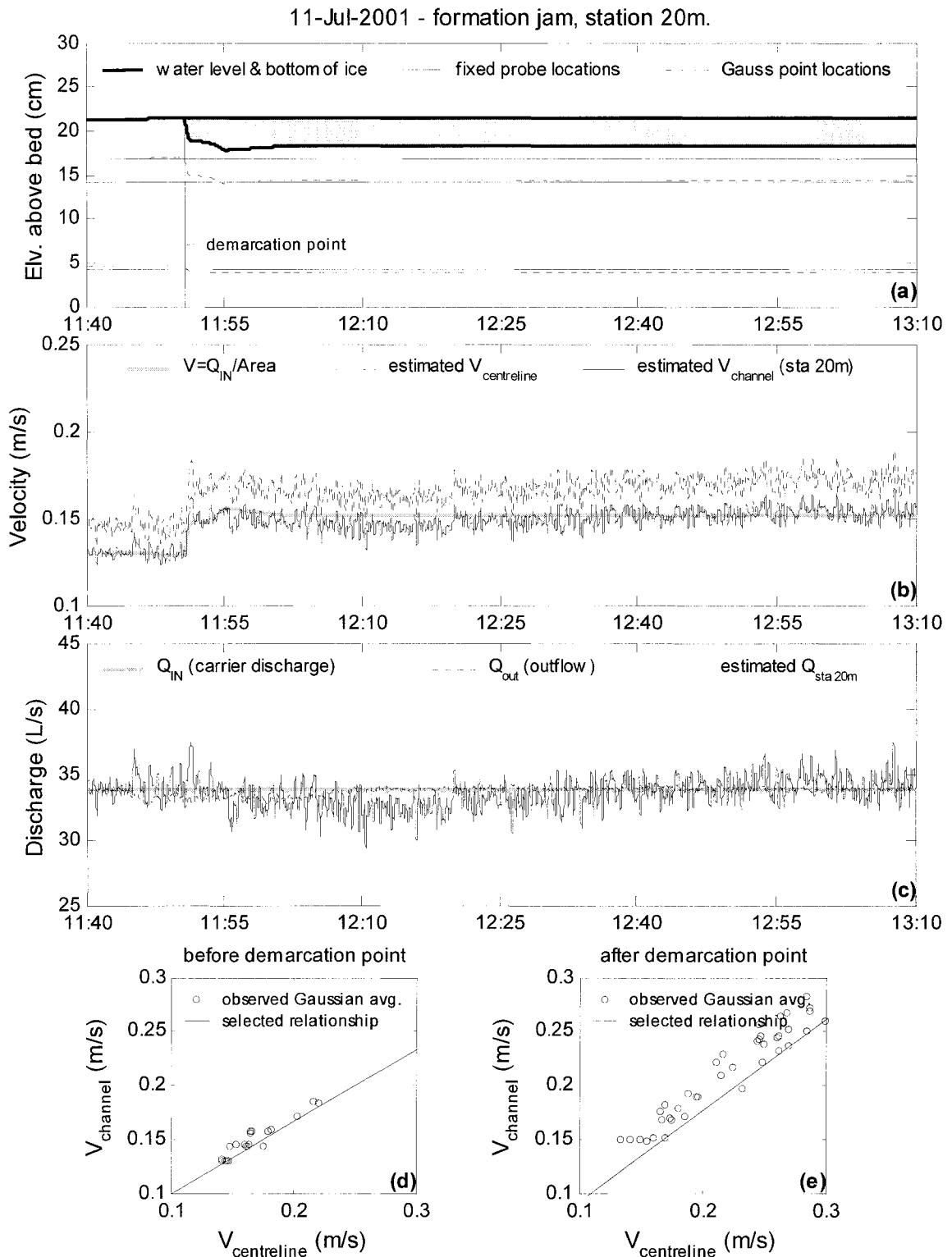
Figure E.32.   Summary of continuous observations for a formation jam taken at Station 20m – test date: 11 July 2001.

244
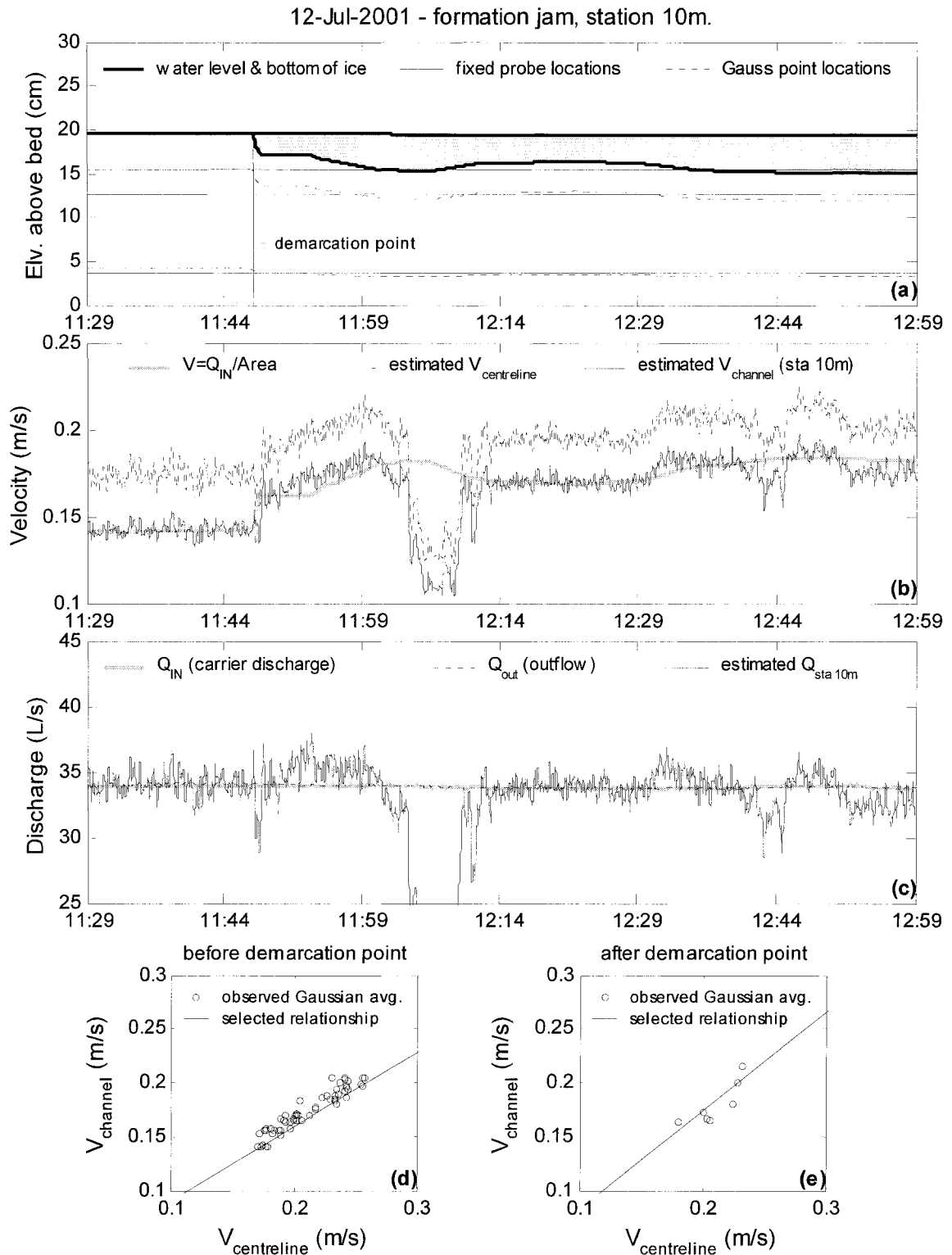
Figure E.33.   Summary of continuous observations for a formation jam taken at Station 10m – test date: 12 July 2001.

245
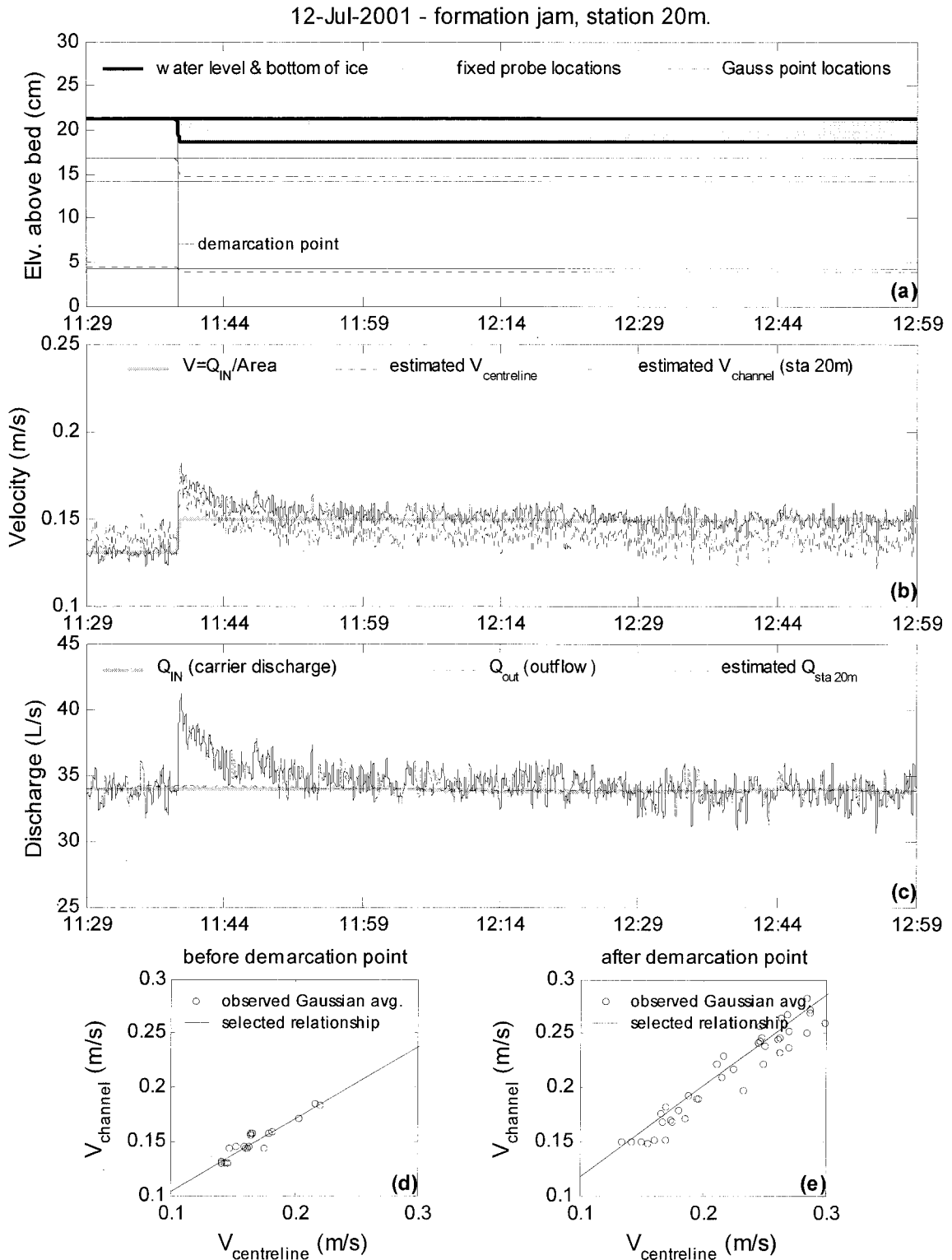
Figure E.34. Summary of continuous observations for a formation jam taken at Station 20m – test date: 12 July 2001.
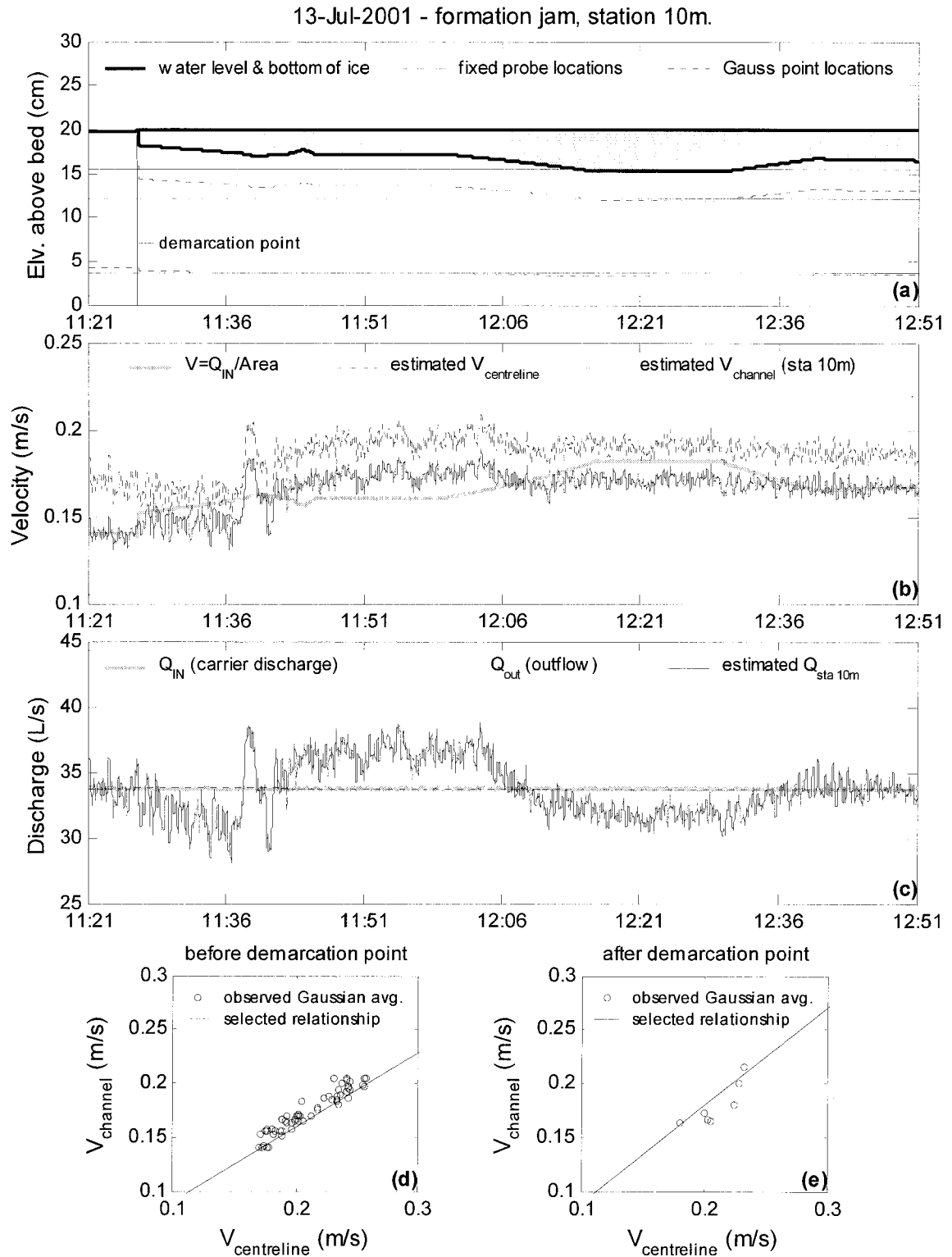
Figure E.35. Summary of continuous observations for a formation jam taken at Station 10m – test date: 13 July 2001.
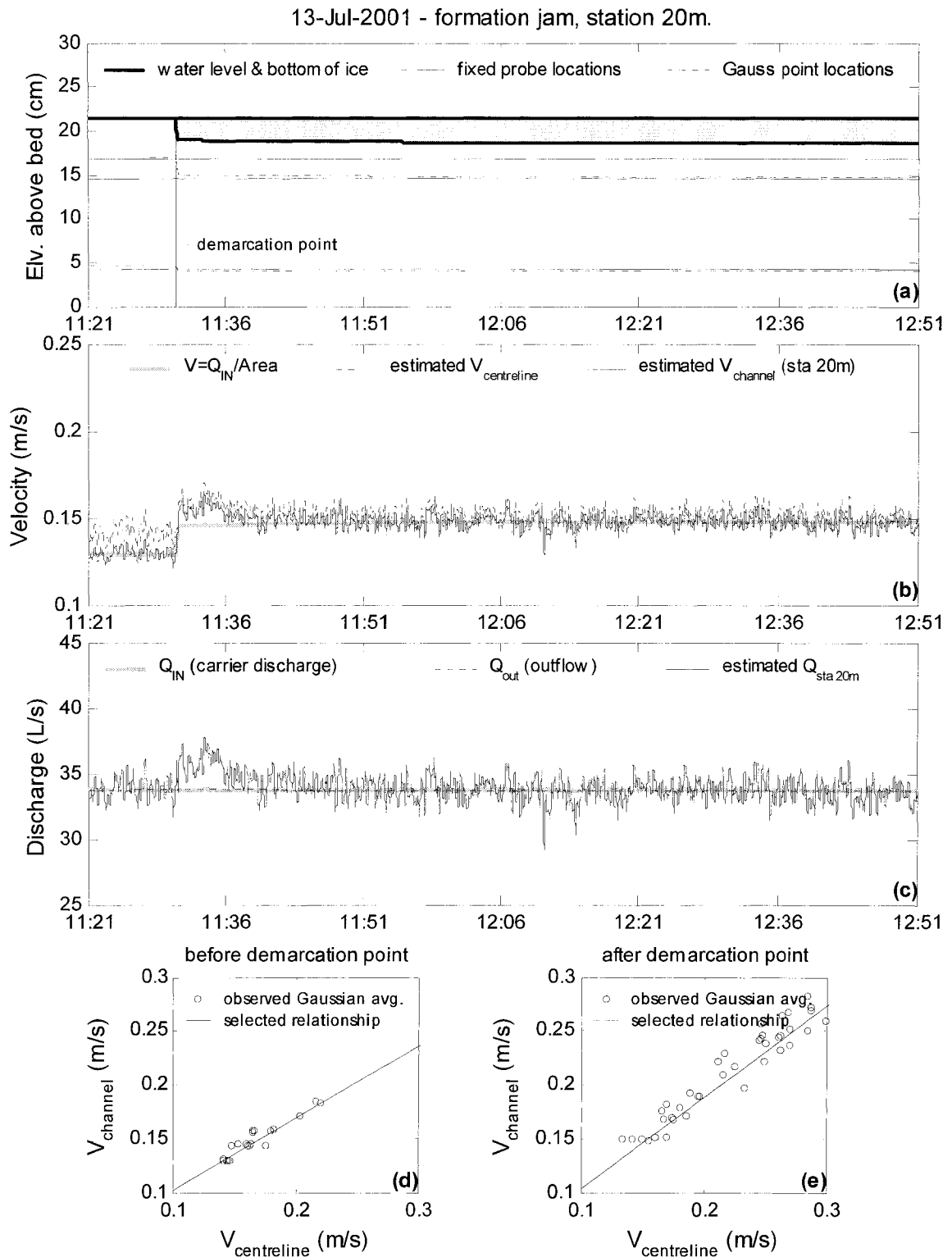
Figure E.36. Summary of continuous observations for a formation jam taken at Station 20m – test date: 13 July 2001.

248
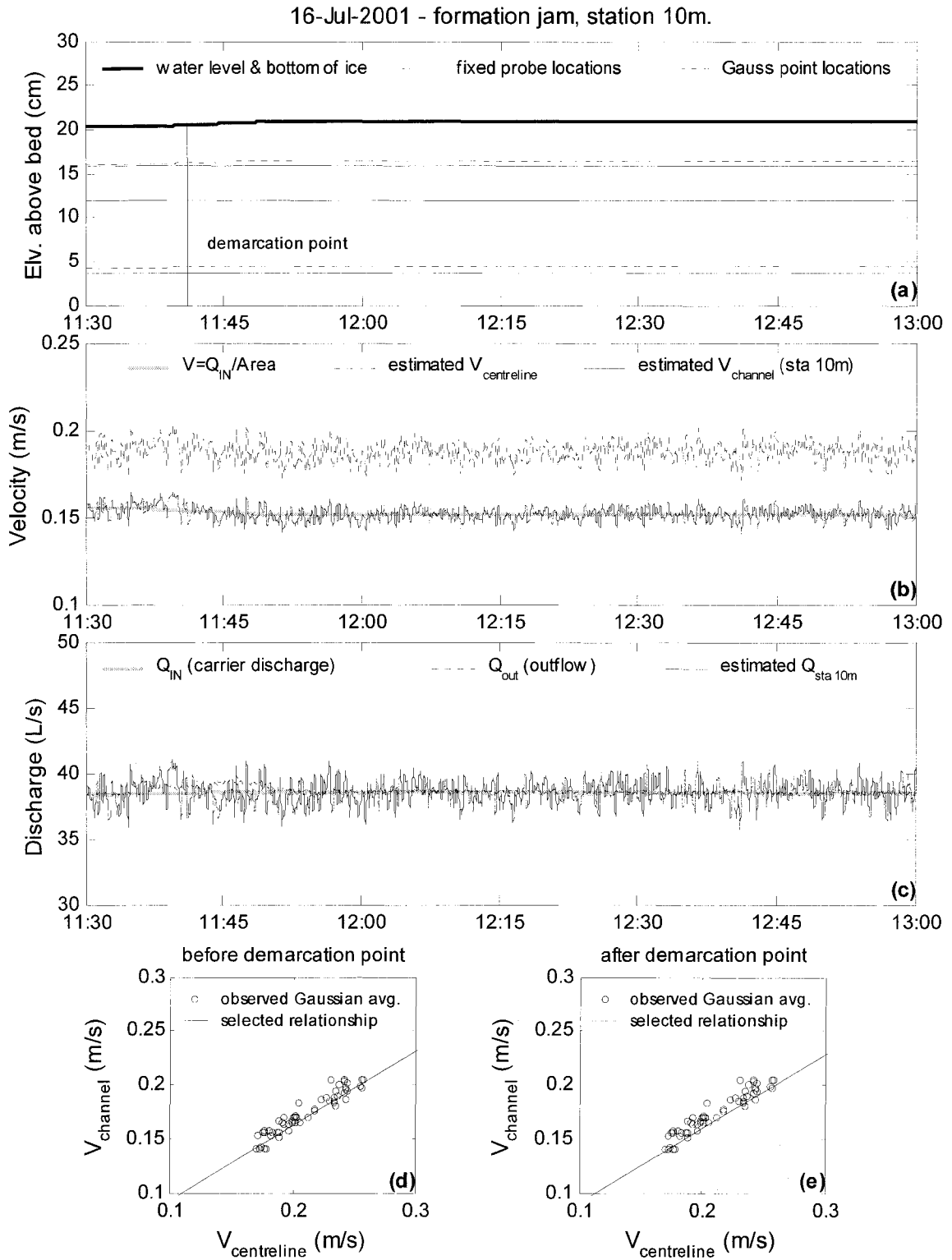
Figure E.37. Summary of continuous observations for a formation jam taken at Station 10m – test date: 16 July 2001.
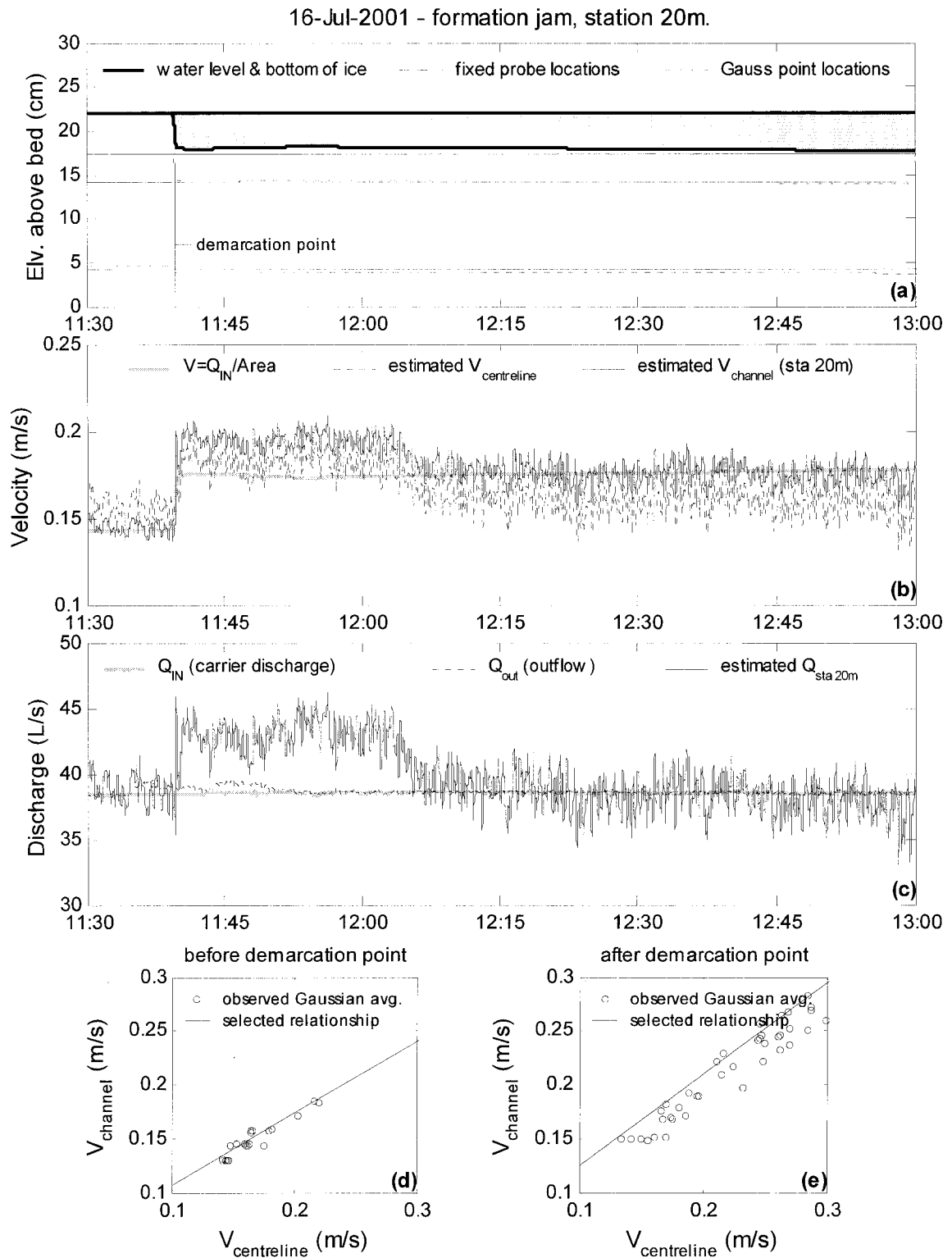
Figure E.38.   Summary of continuous observations for a formation jam taken at Station 20m – test date: 16 July 2001.
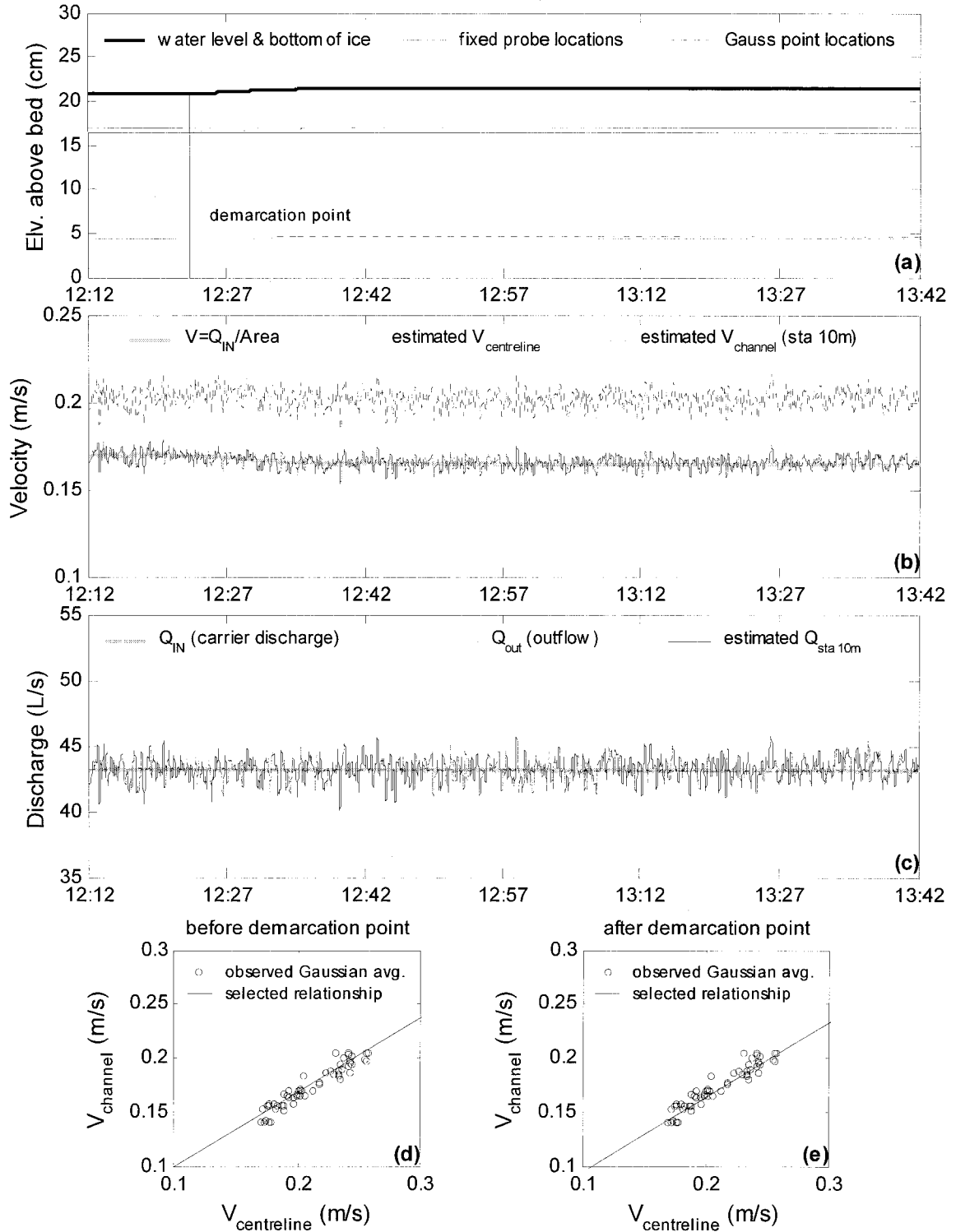
Figure E.39. Summary of continuous observations for a formation jam taken at Station 10m – test date: 17 July 2001.

251
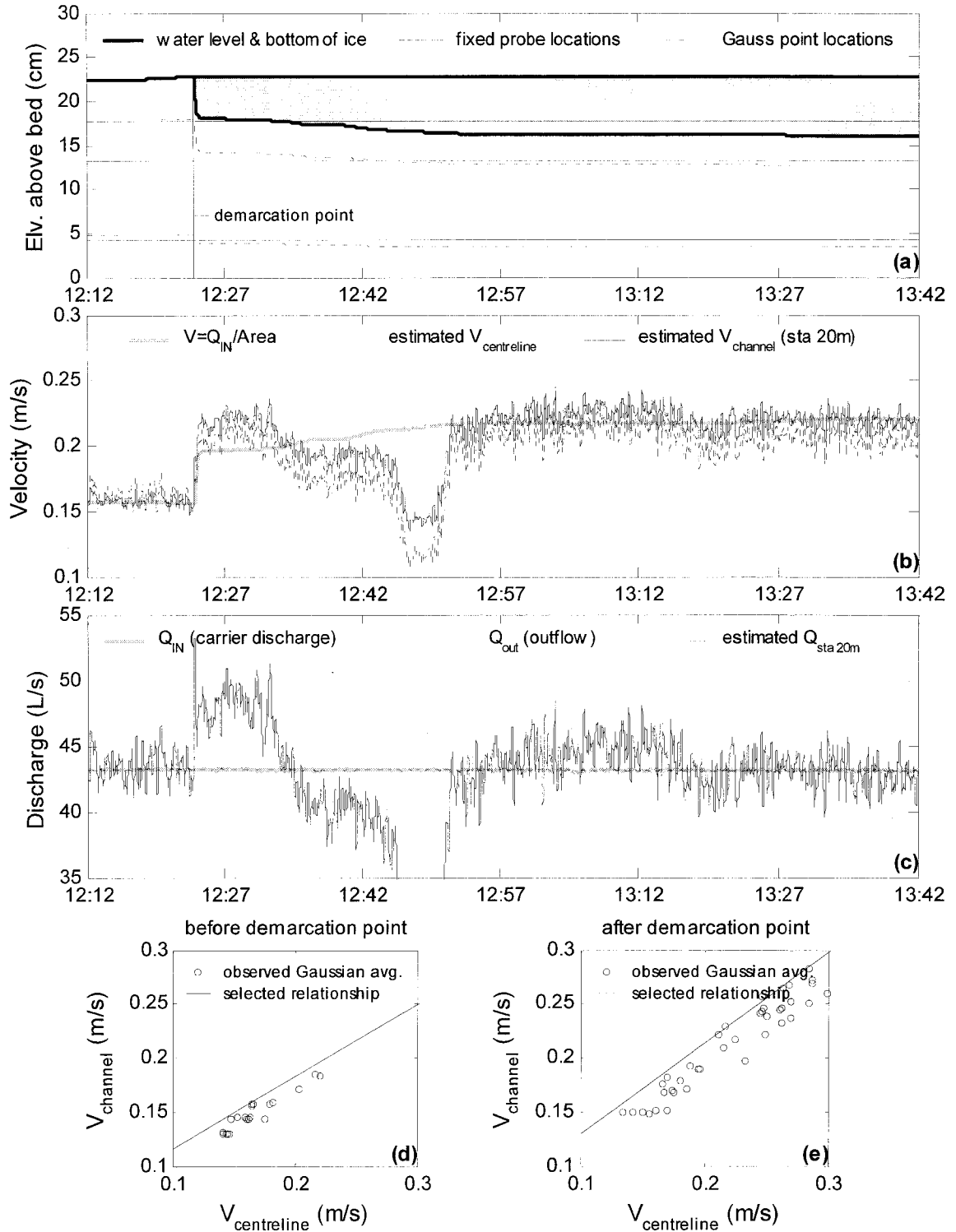
Figure E.40. Summary of continuous observations for a formation jam taken at Station 20m – test date: 17 July 2001.
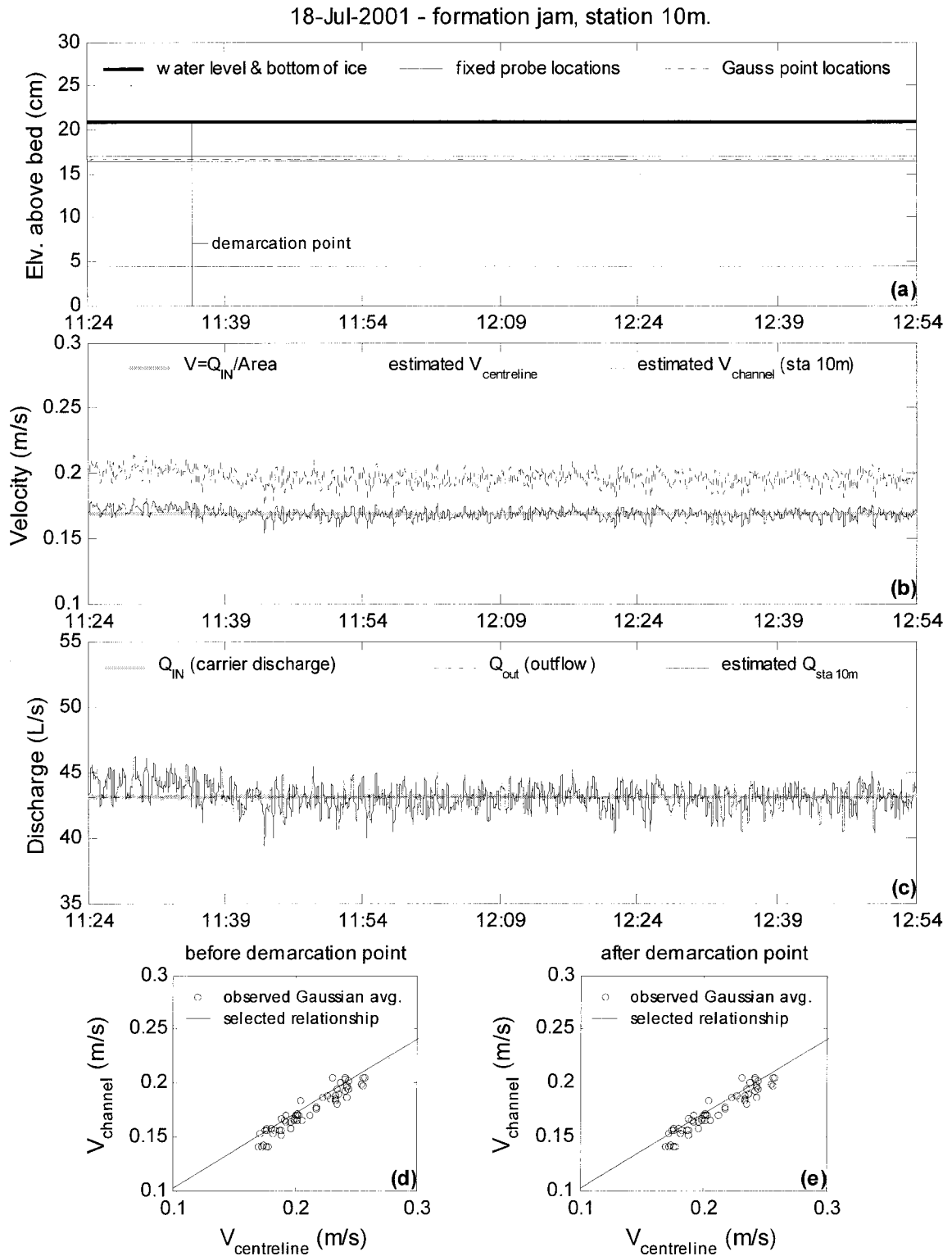
Figure E.41. Summary of continuous observations for a formation jam taken at Station 10m – test date: 18 July 2001.
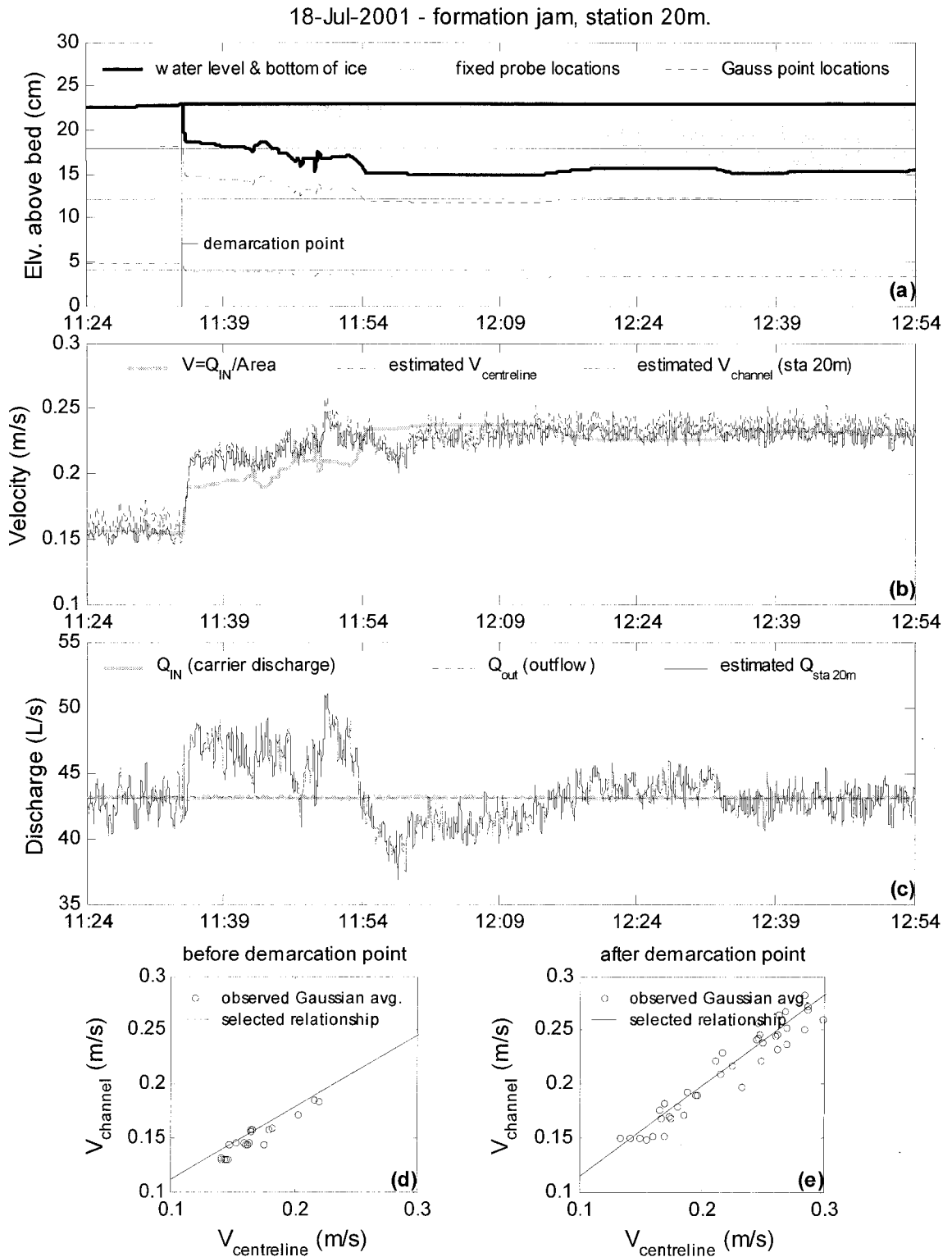
Figure E.42. Summary of continuous observations for a formation jam taken at Station 20m – test date: 18 July 2001.
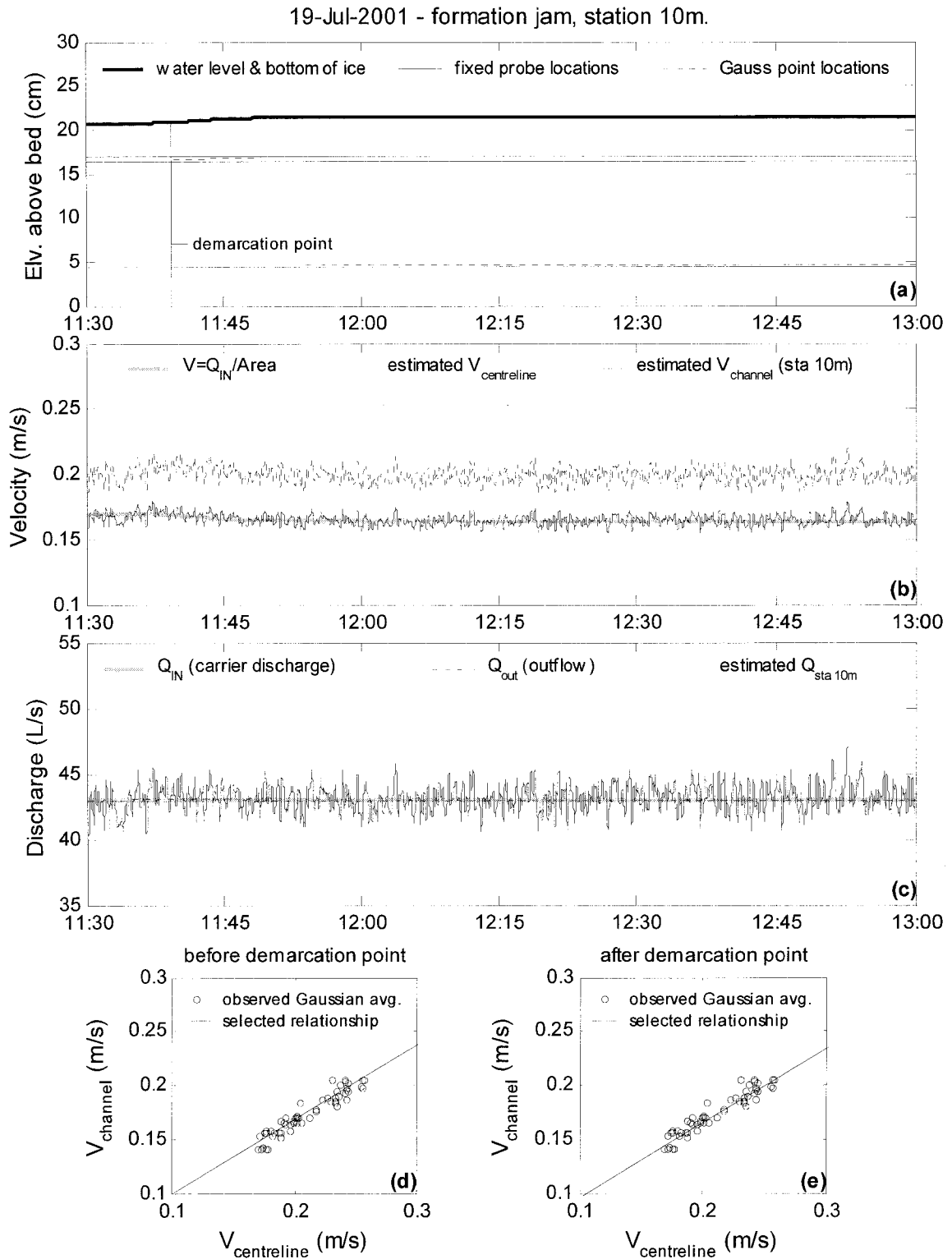
Figure E.43. Summary of continuous observations for a formation jam taken at Station 10m – test date: 19 July 2001.
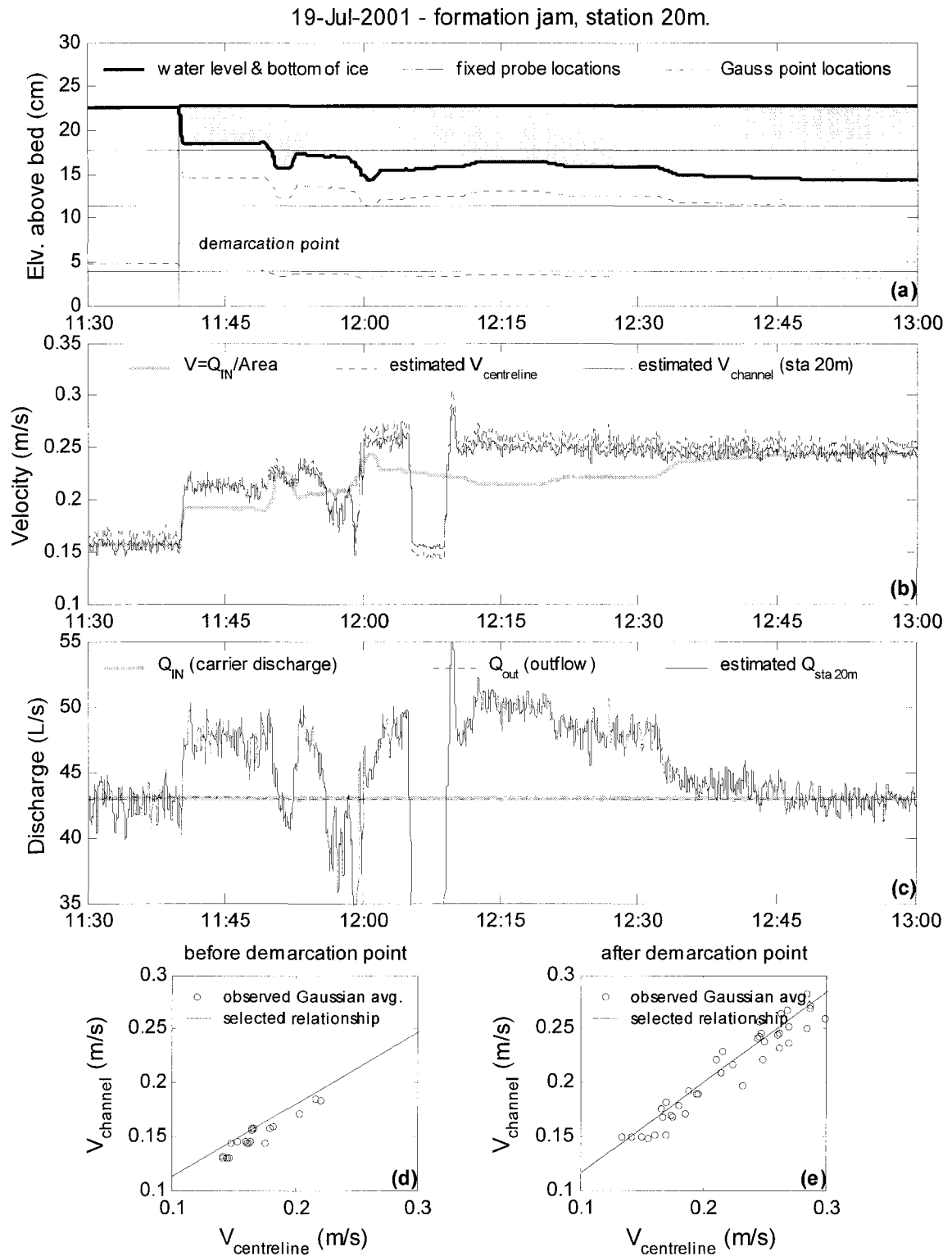
Figure E.44. Summary of continuous observations for a formation jam taken at Station 20m – test date: 19 July 2001.
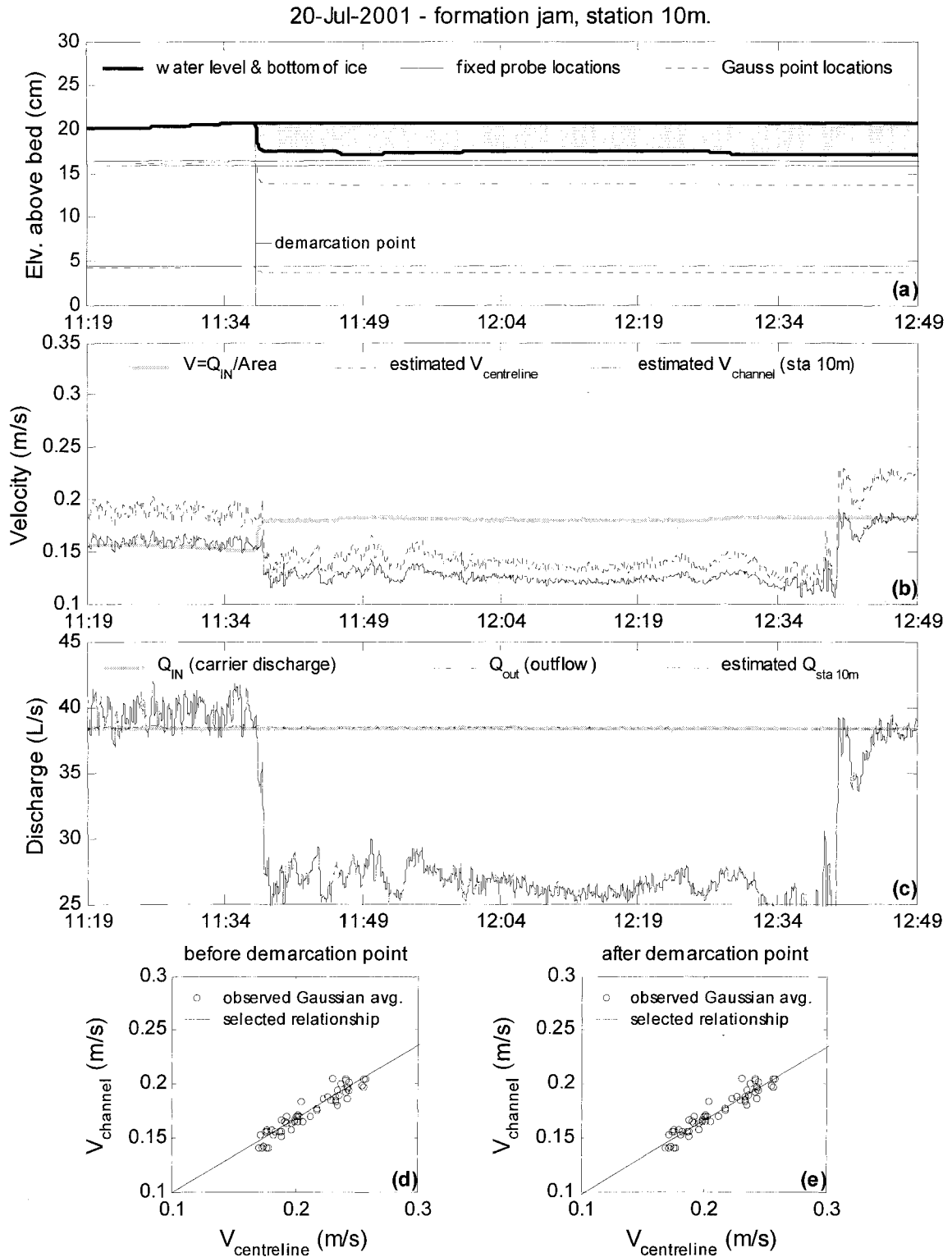
Figure E.45. Summary of continuous observations for a formation jam taken at Station 10m – test date: 20 July 2001.

257
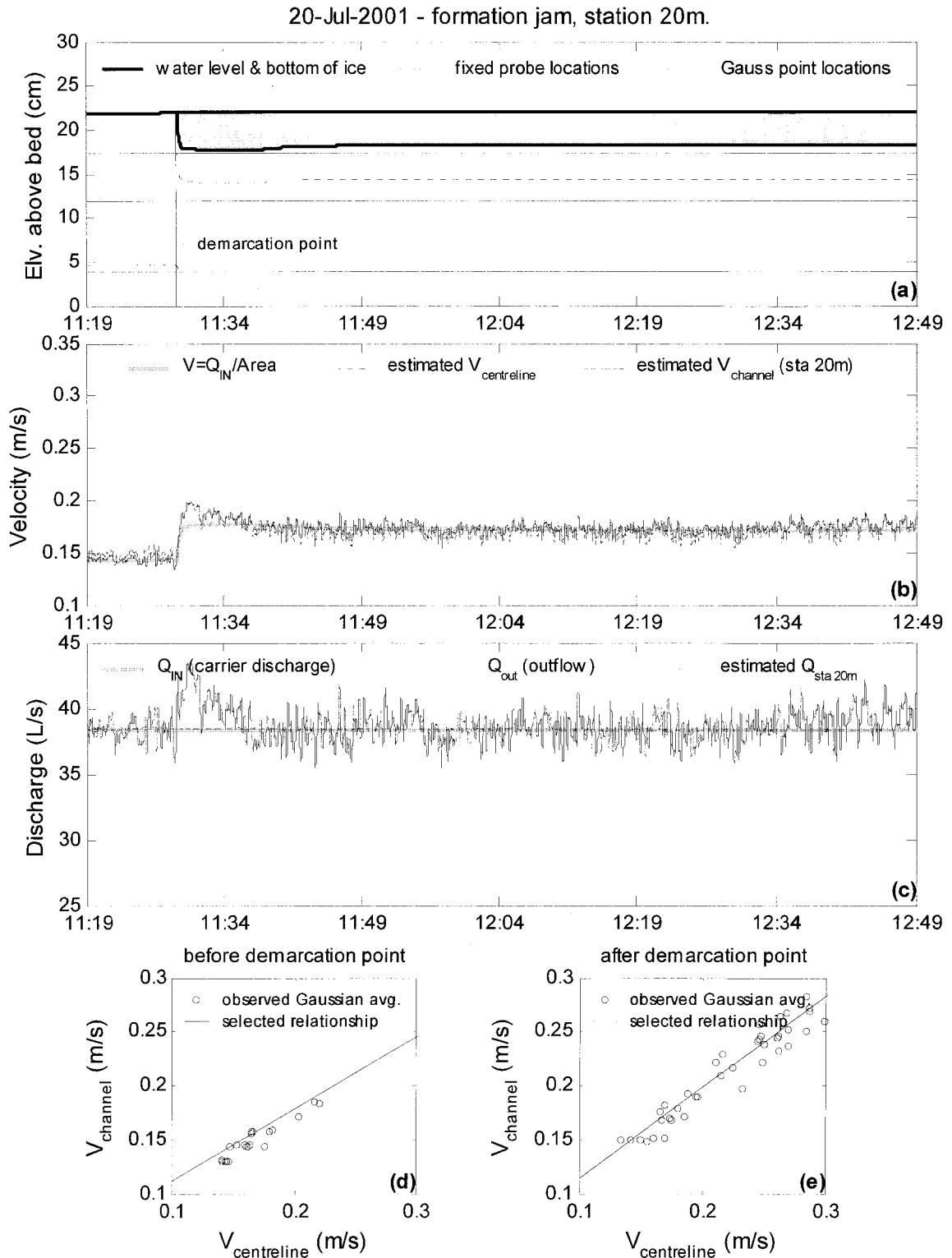
Figure E.46. Summary of continuous observations for a formation jam taken at Station 20m – test date: 20 July 2001.

258
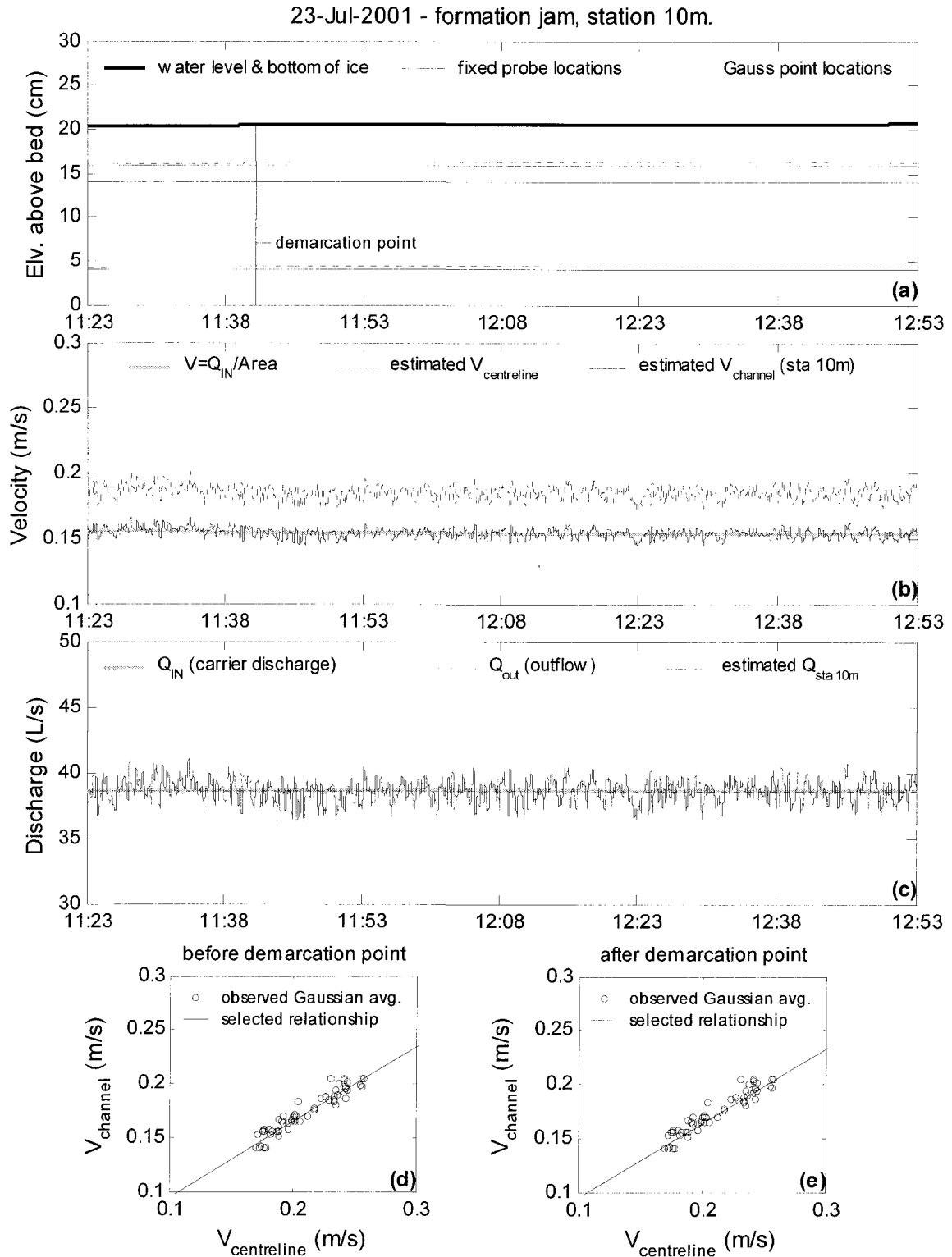
Figure E.47. Summary of continuous observations for a formation jam taken at Station 10m – test date: 23 July 2001.

(a) Elv. above bed (cm) vs time (11:23–12:53)

Legend: water level & bottom of ice — fixed probe locations — Gauss point locations

demarcation point

(b) Velocity (m/s) vs time (11:23–12:53)

Legend: V=Q$_{IN}$/Area — estimated V$_{centreline}$ — estimated V$_{channel}$ (sta 20m)

(c) Discharge (L/s) vs time (11:23–12:53)

Legend: Q$_{IN}$ (carrier discharge) — Q$_{out}$ (outflow) — estimated Q$_{sta 20m}$

(d) before demarcation point — V$_{channel}$ (m/s) vs V$_{centreline}$ (m/s)

Legend: observed Gaussian avg. — selected relationship

(e) after demarcation point — V$_{channel}$ (m/s) vs V$_{centreline}$ (m/s)

Legend: observed Gaussian avg. — selected relationship

Figure E.48. Summary of continuous observations for a formation jam taken at Station 20m – test date: 23 July 2001.

260
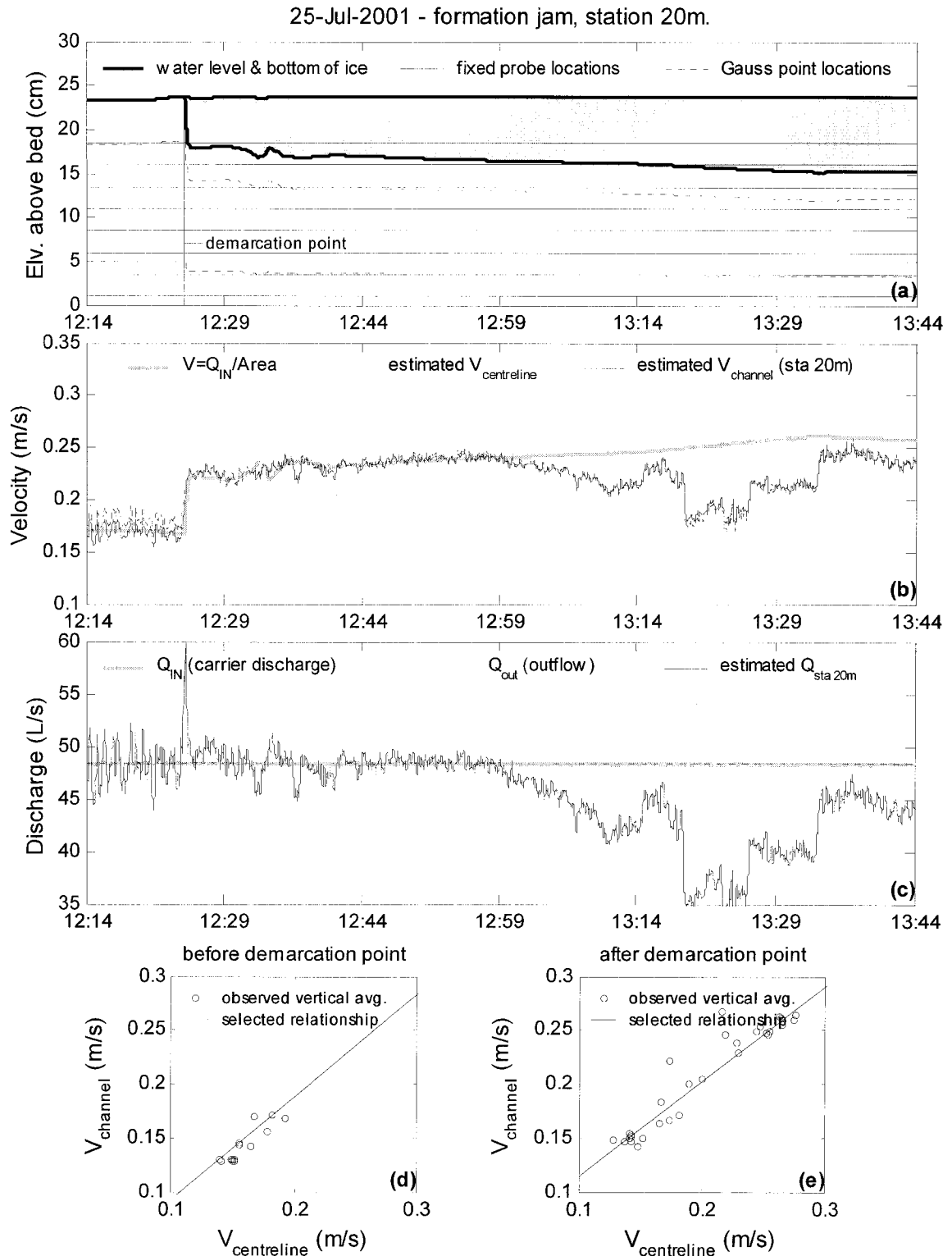
Figure E.49. Summary of continuous observations for a formation jam taken at Station 20m – test date: 25 July 2001.
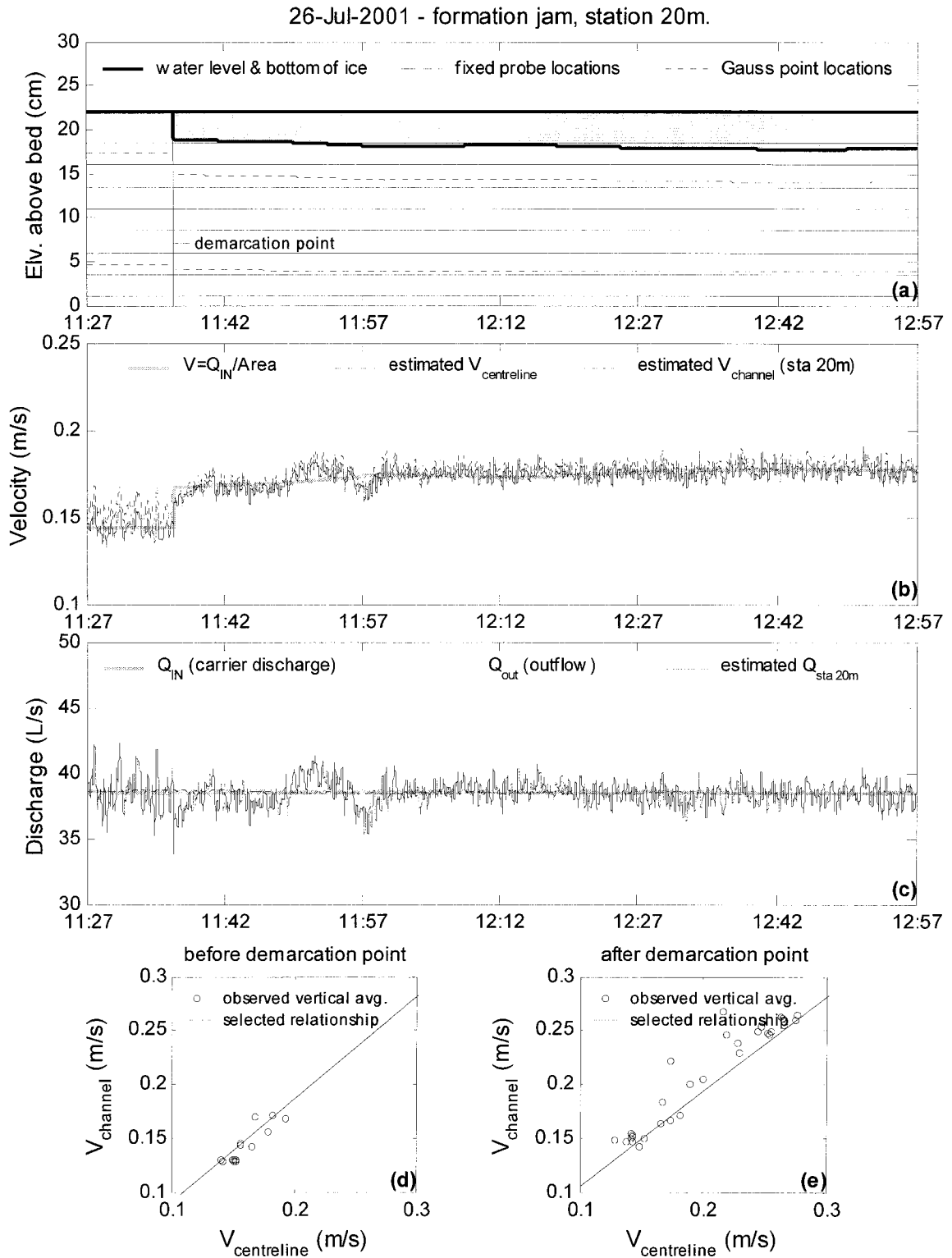
Figure E.50. Summary of continuous observations for a formation jam taken at Station 20m – test date: 26 July 2001.
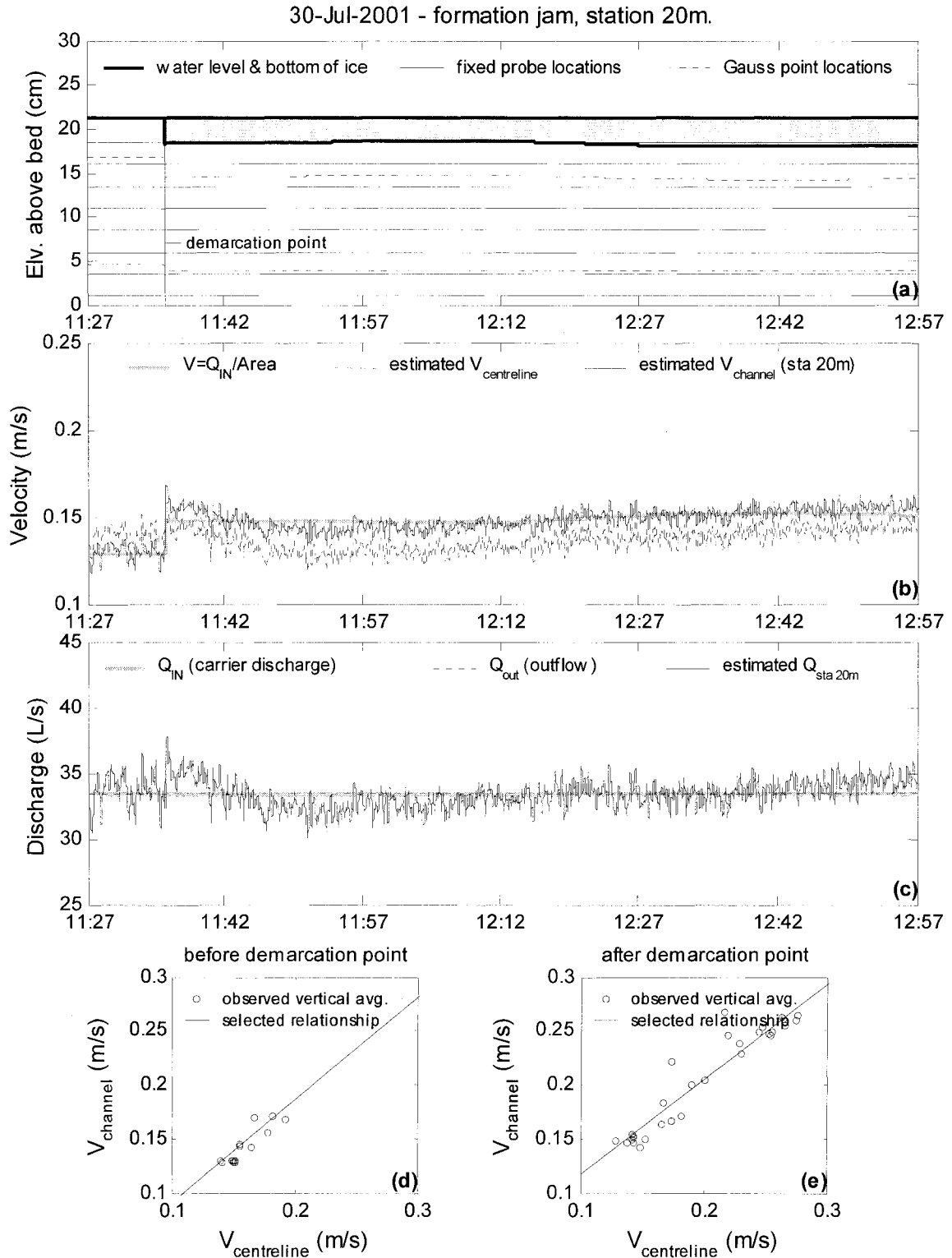
Figure E.51. Summary of continuous observations for a formation jam taken at Station 20m – test date: 30 July 2001.
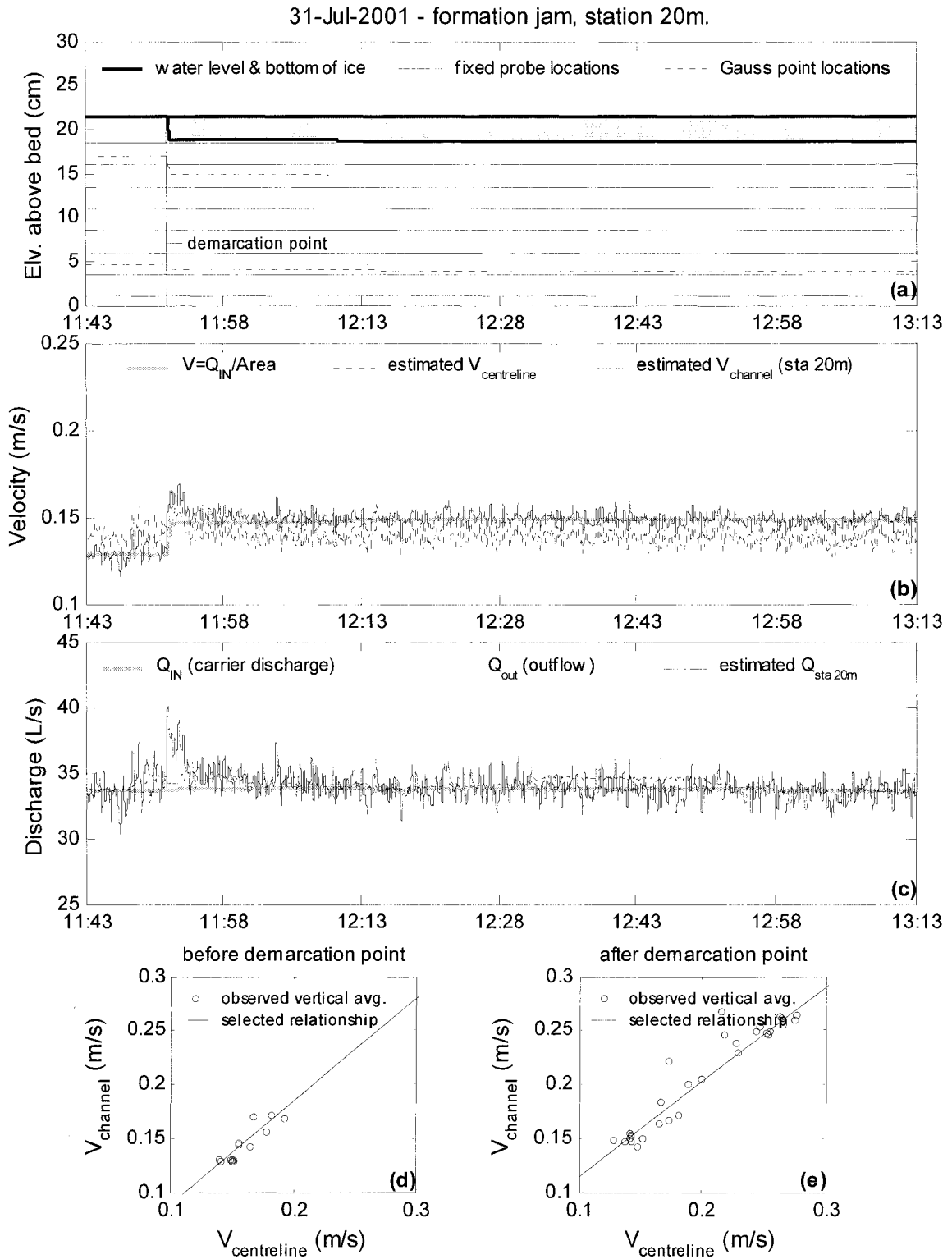
Figure E.52. Summary of continuous observations for a formation jam taken at Station 20m – test date: 31 July 2001.

264
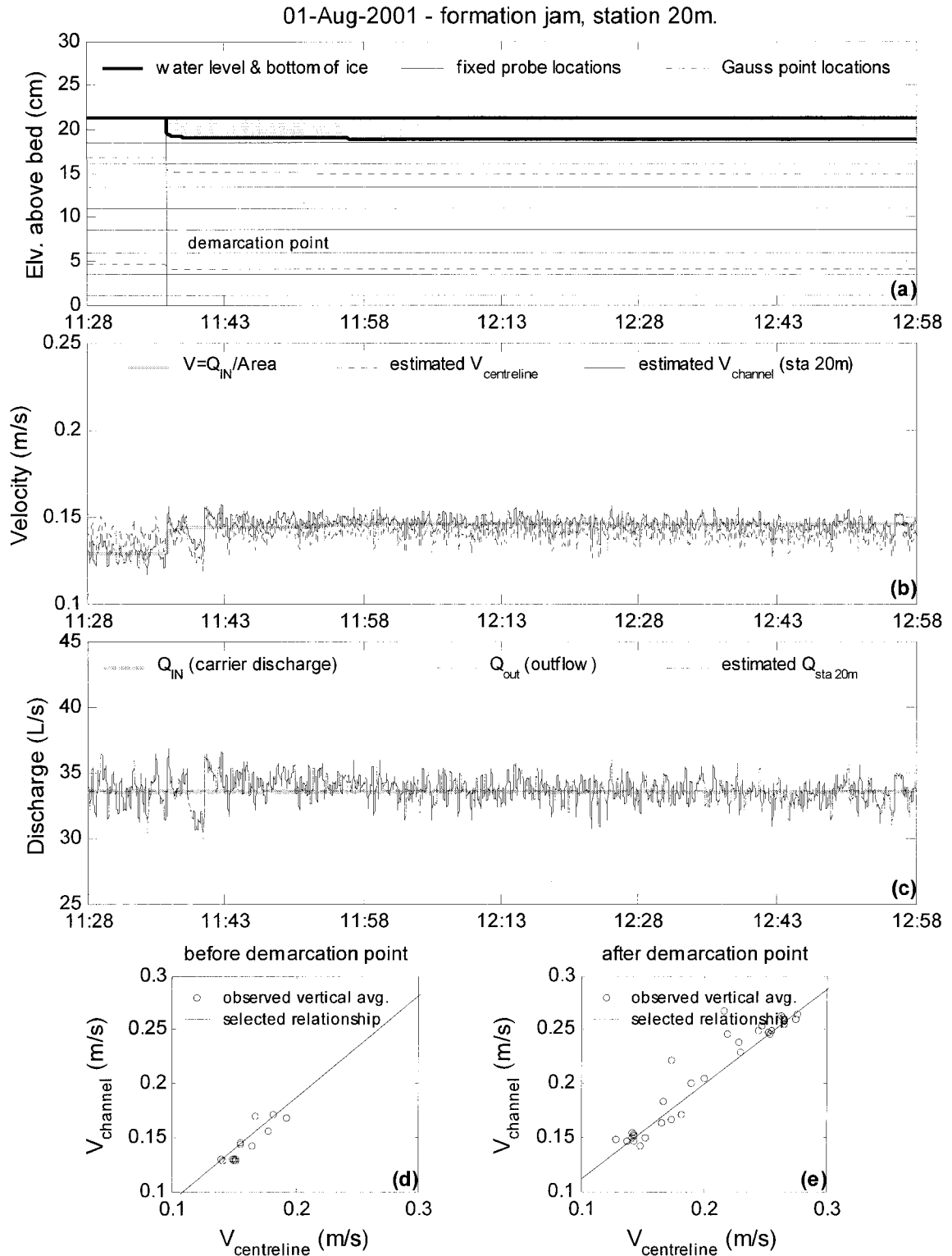
Figure E.53.   Summary of continuous observations for a formation jam taken at
Station 20m – test date: 1 August 2001.

265

02-Aug-2001 - formation jam, station 20m.

(a)
(b)
(c)
(d) before demarcation point
(e) after demarcation point
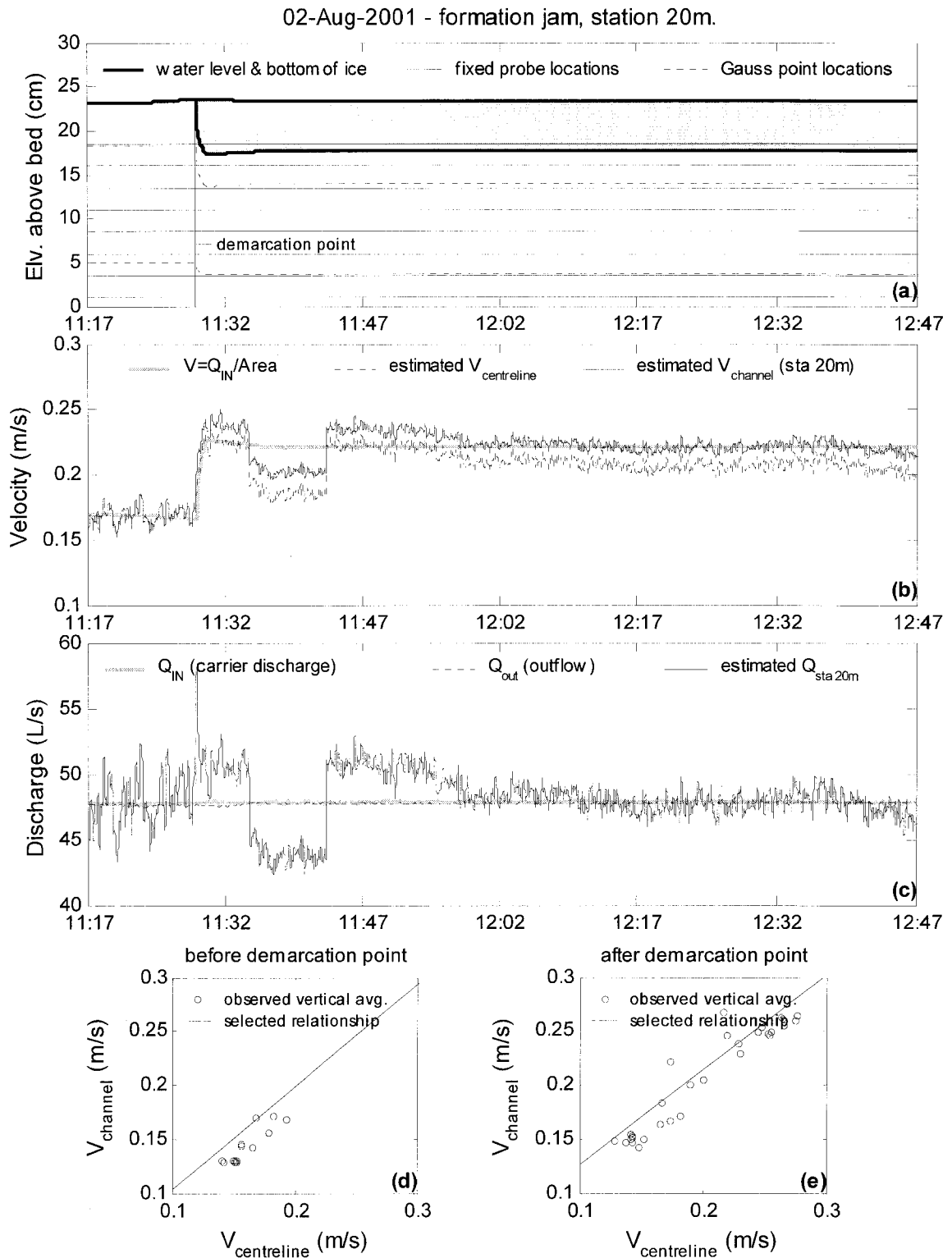
Figure E.54. Summary of continuous observations for a formation jam taken at Station 20m – test date: 2 August 2001.

266
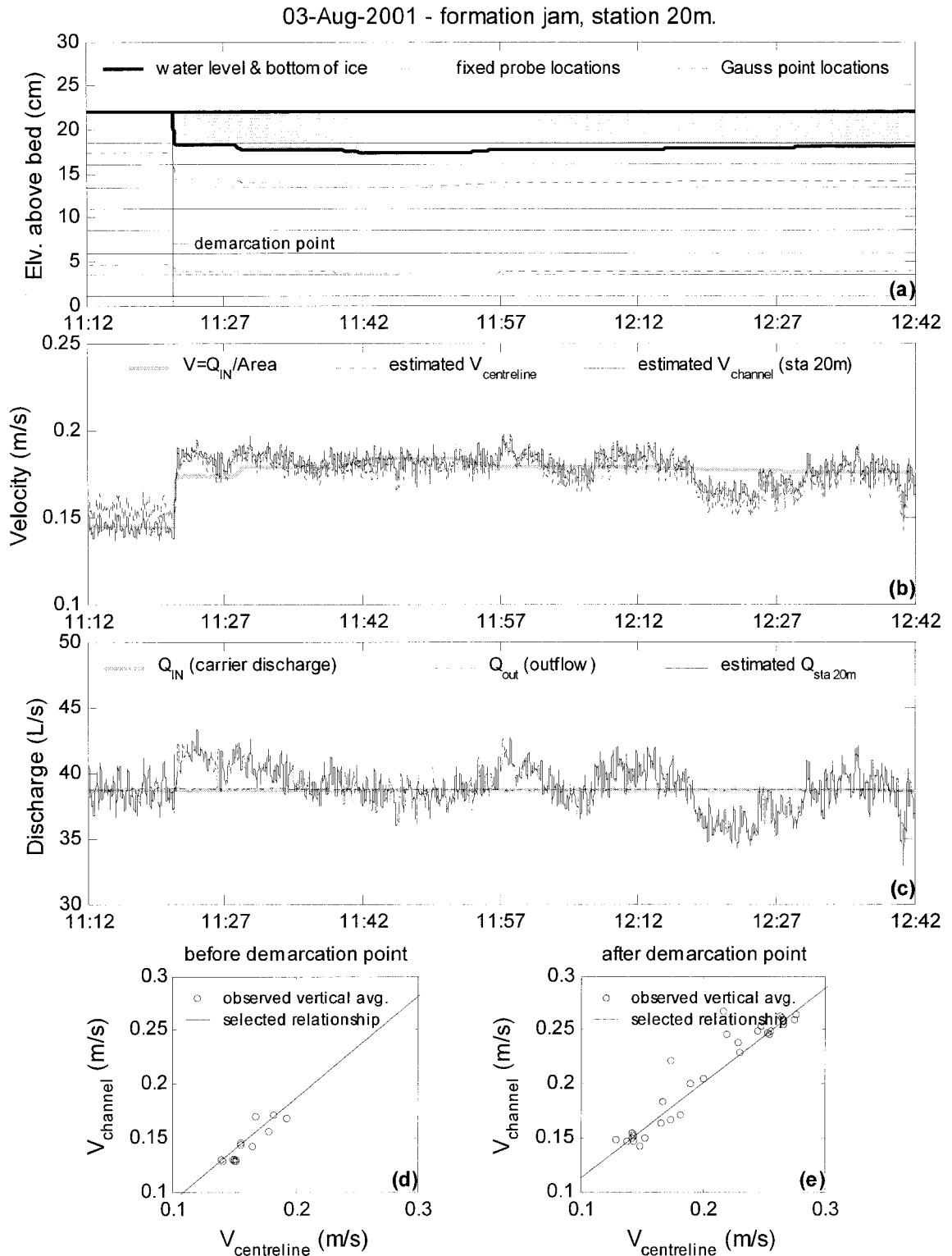
Figure E.55. Summary of continuous observations for a formation jam taken at Station 20m – test date: 3 August 2001.
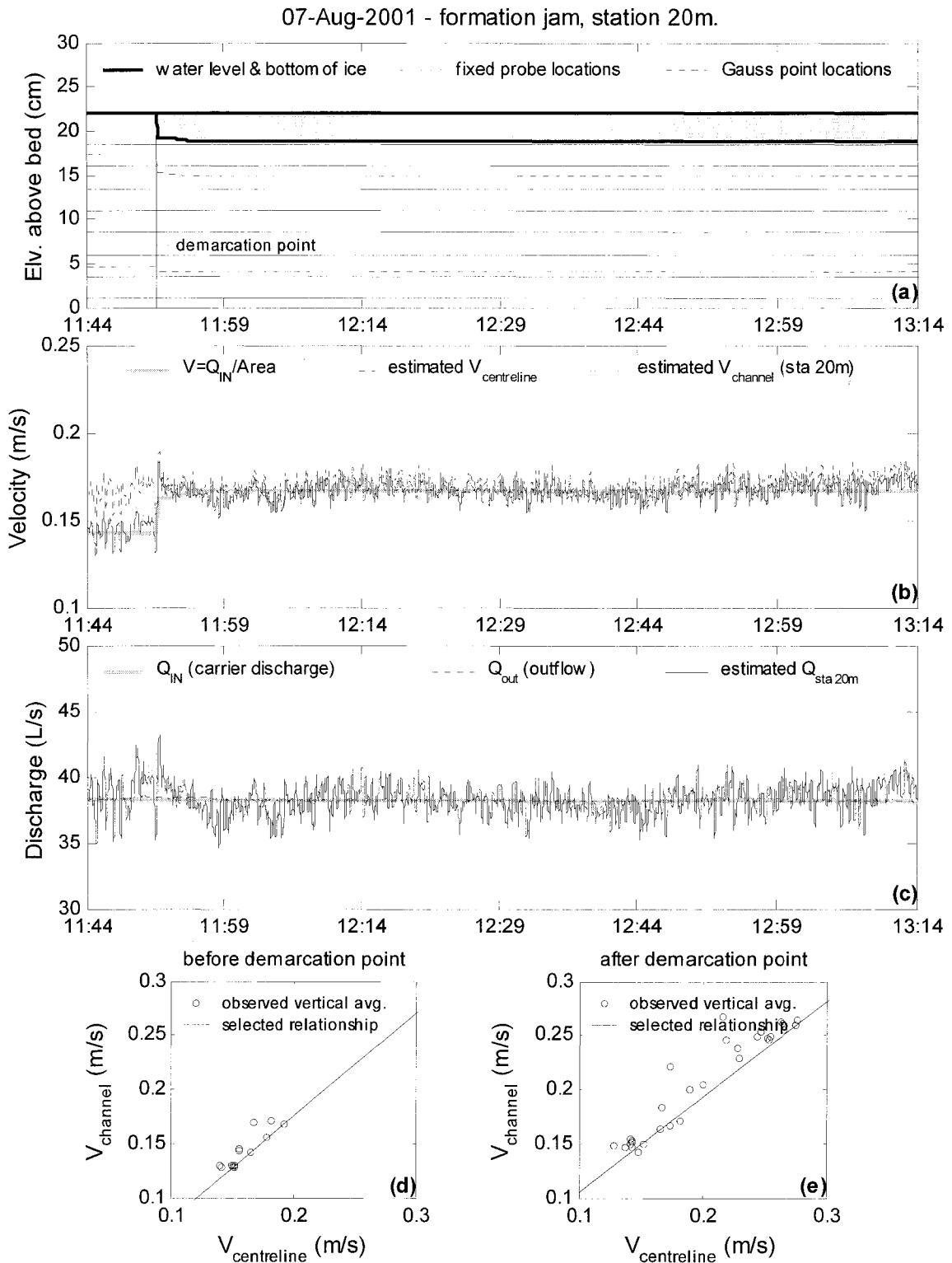
Figure E.56.   Summary of continuous observations for a formation jam taken at Station 20m – test date: 7 August 2001.
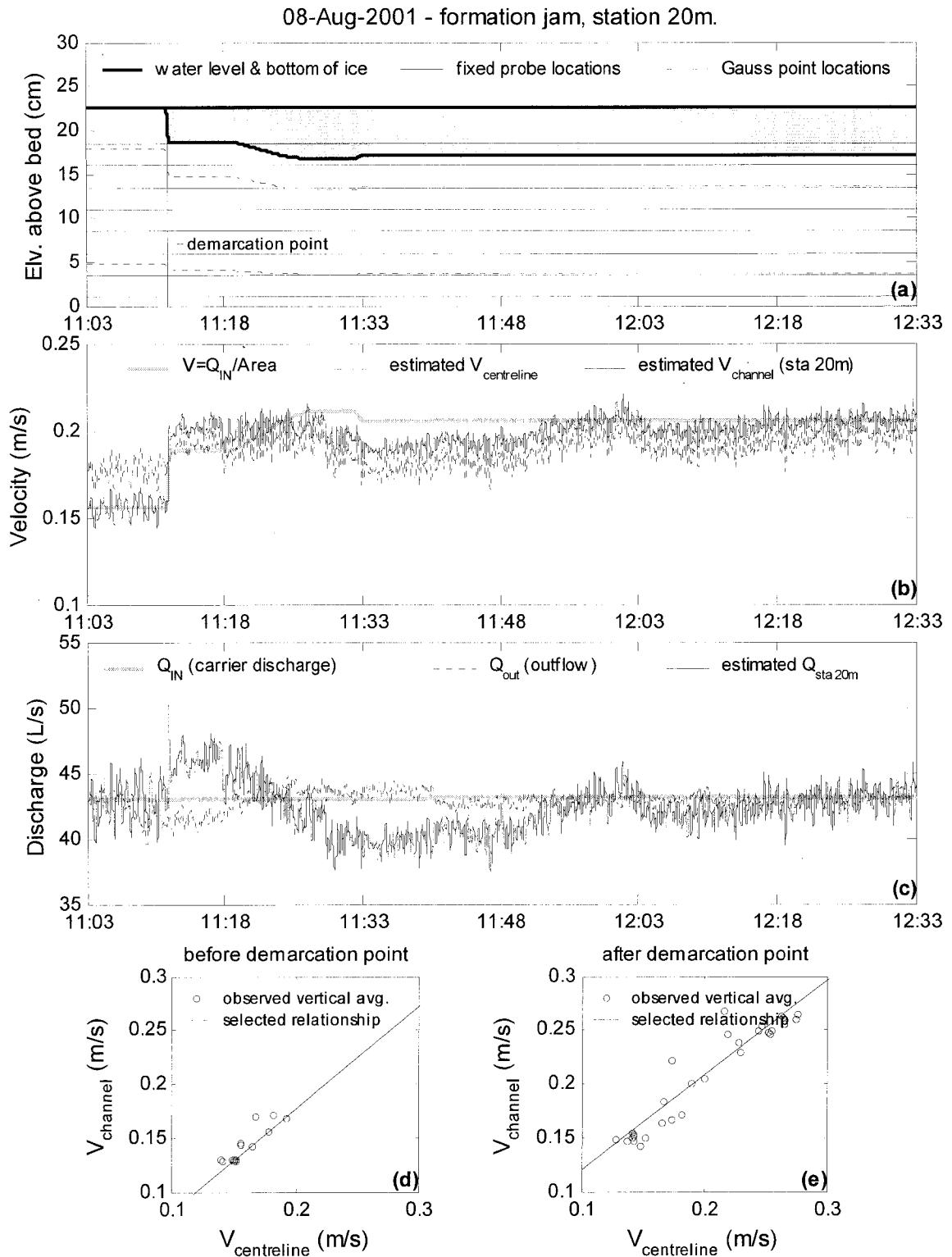
Figure E.57. Summary of continuous observations for a formation jam taken at Station 20m – test date: 8 August 2001.

269
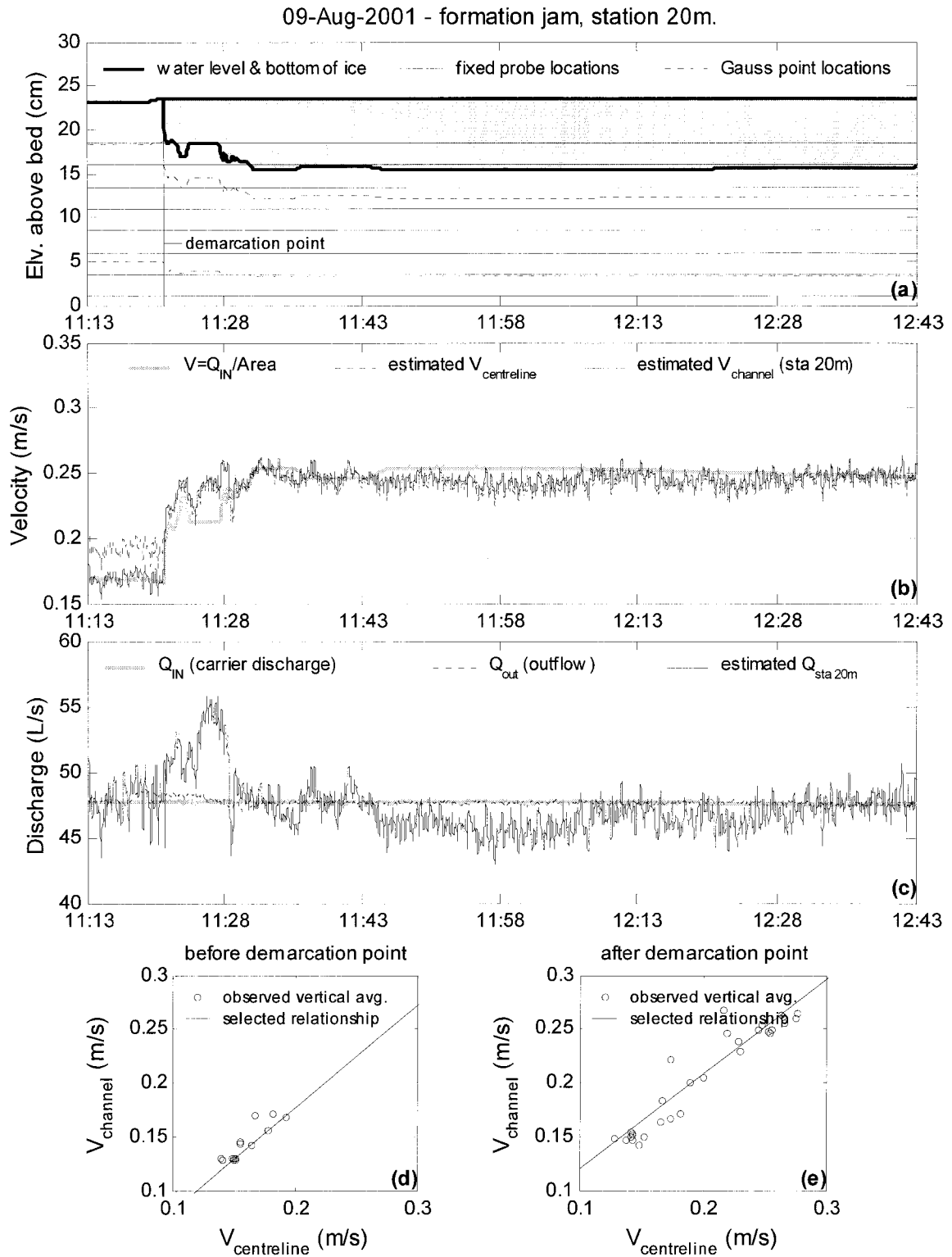
Figure E.58. Summary of continuous observations for a formation jam taken at Station 20m – test date: 9 August 2001.

270
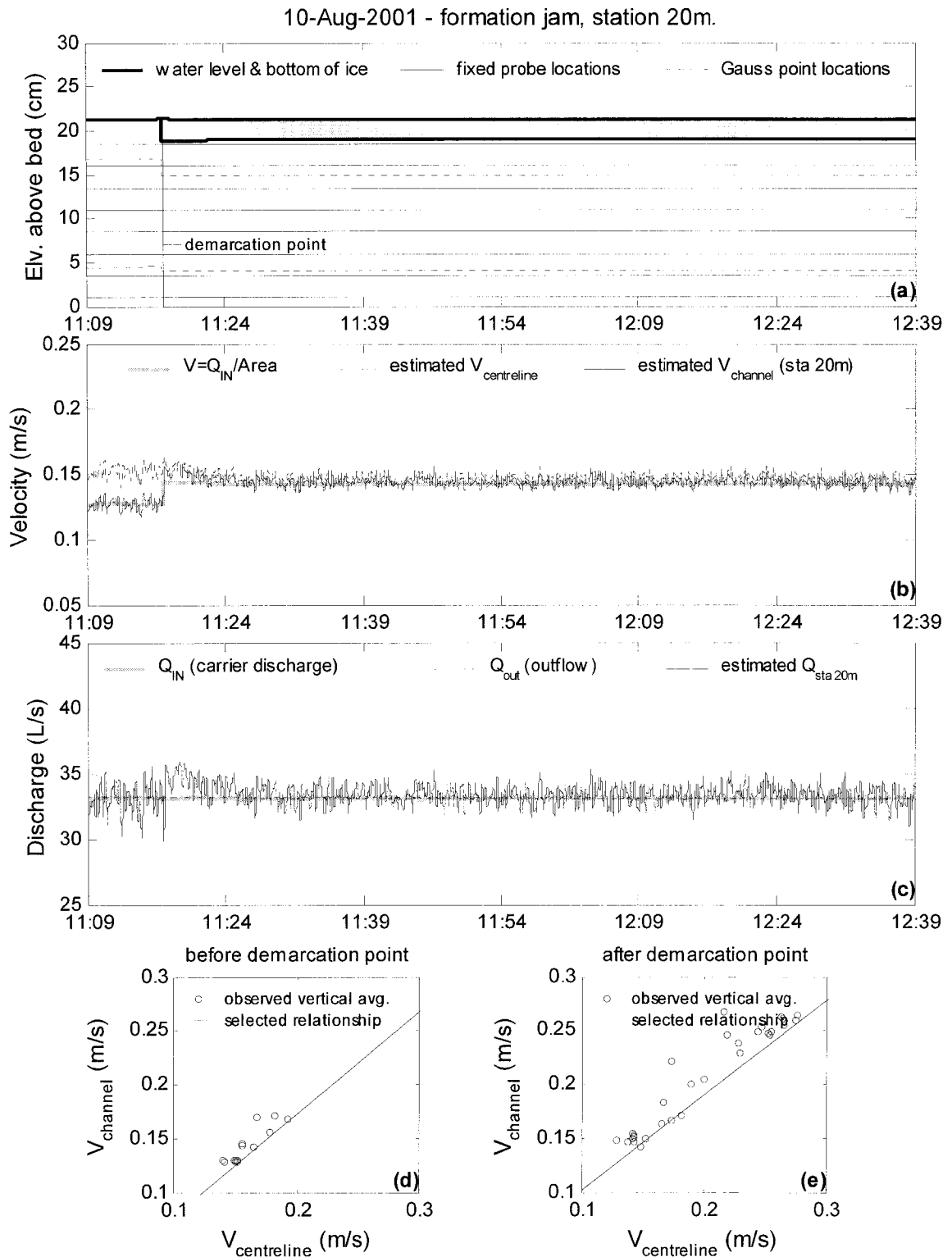
Figure E.59.   Summary of continuous observations for a formation jam taken at Station 20m – test date: 10 August 2001.

271
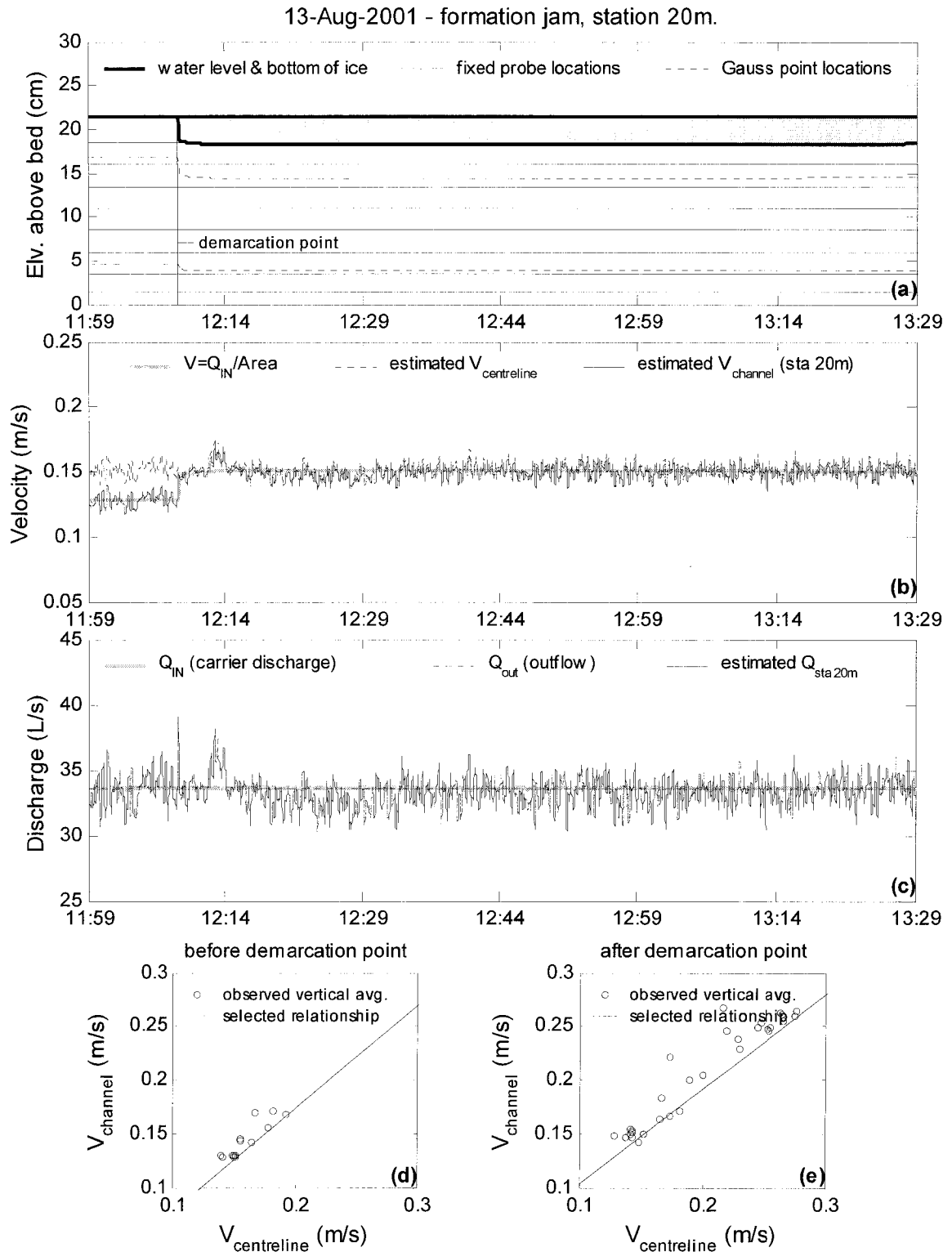
Figure E.60. Summary of continuous observations for a formation jam taken at Station 20m – test date: 13 August 2001.

272
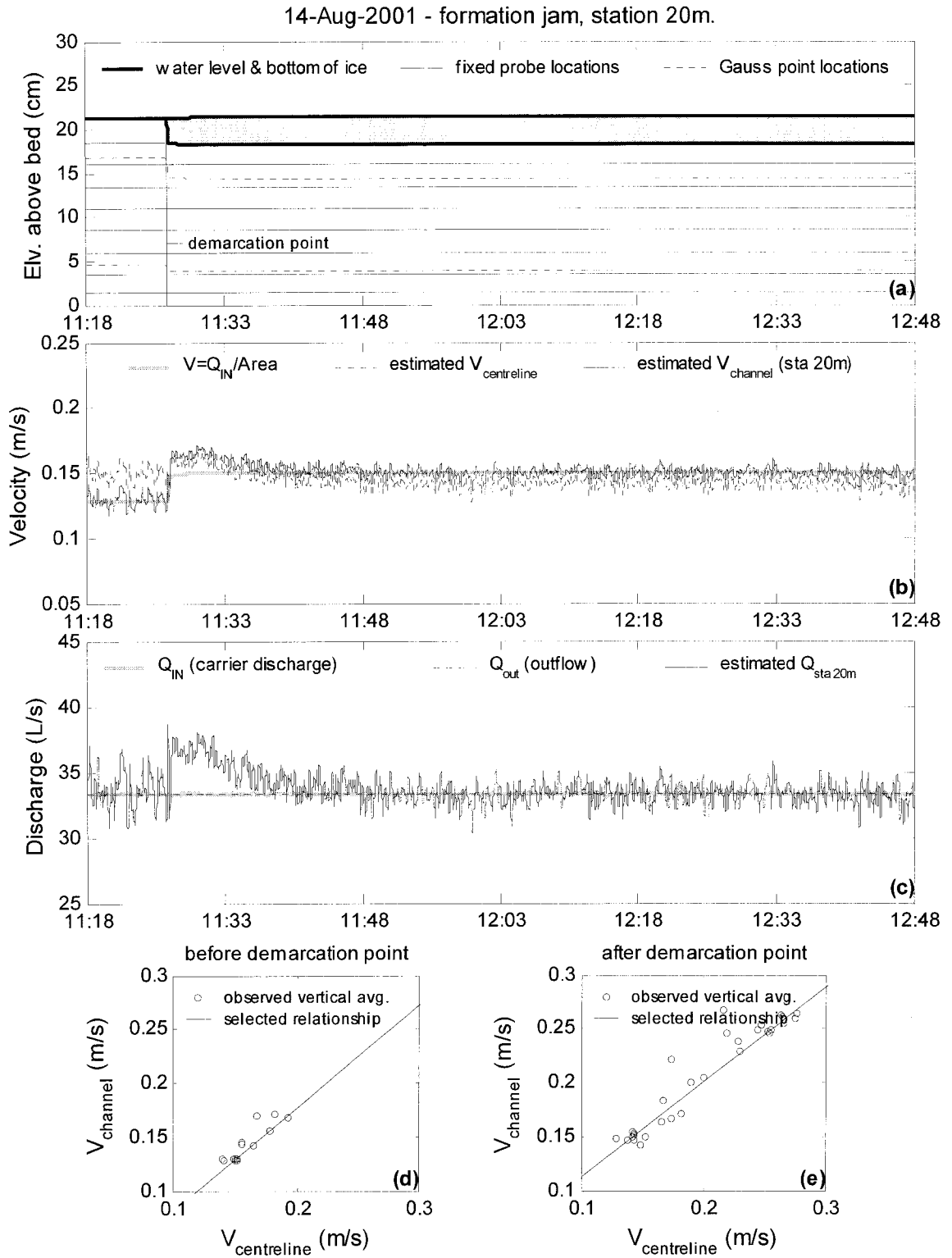
Figure E.61. Summary of continuous observations for a formation jam taken at Station 20m – test date: 14 August 2001.
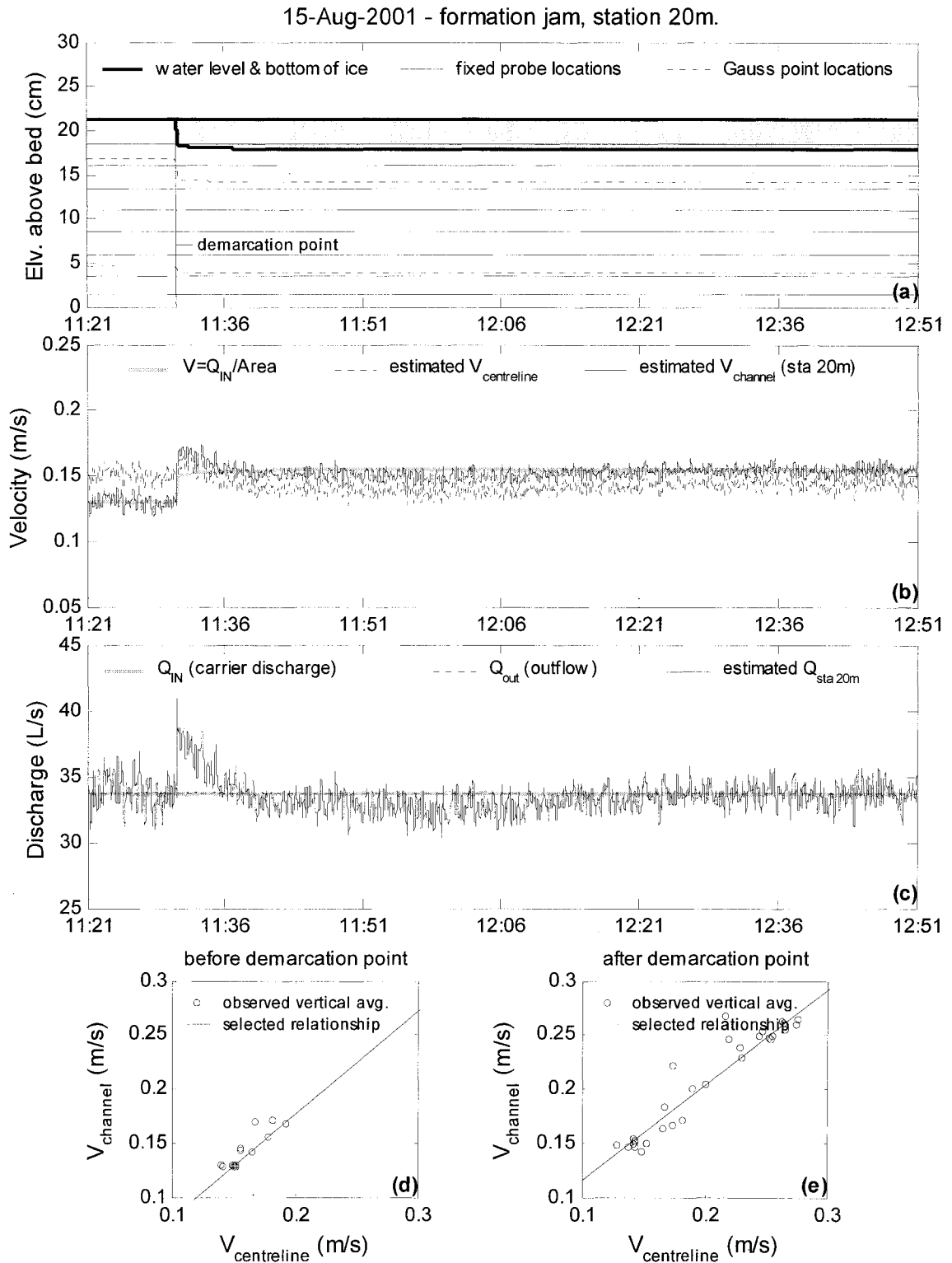
Figure E.62. Summary of continuous observations for a formation jam taken at Station 20m – test date: 15 August 2001.
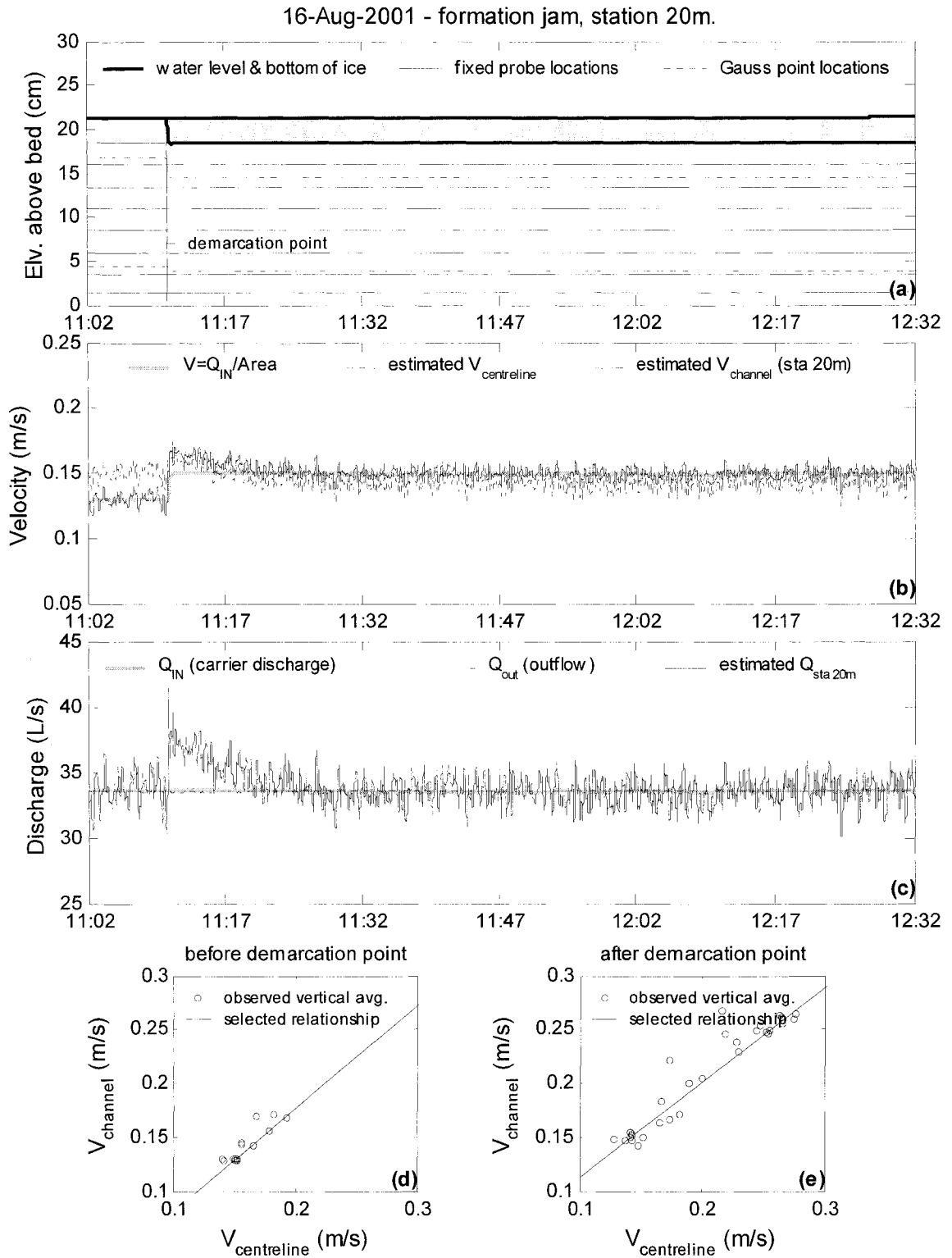
Figure E.63. Summary of continuous observations for a formation jam taken at Station 20m – test date: 16 August 2001.
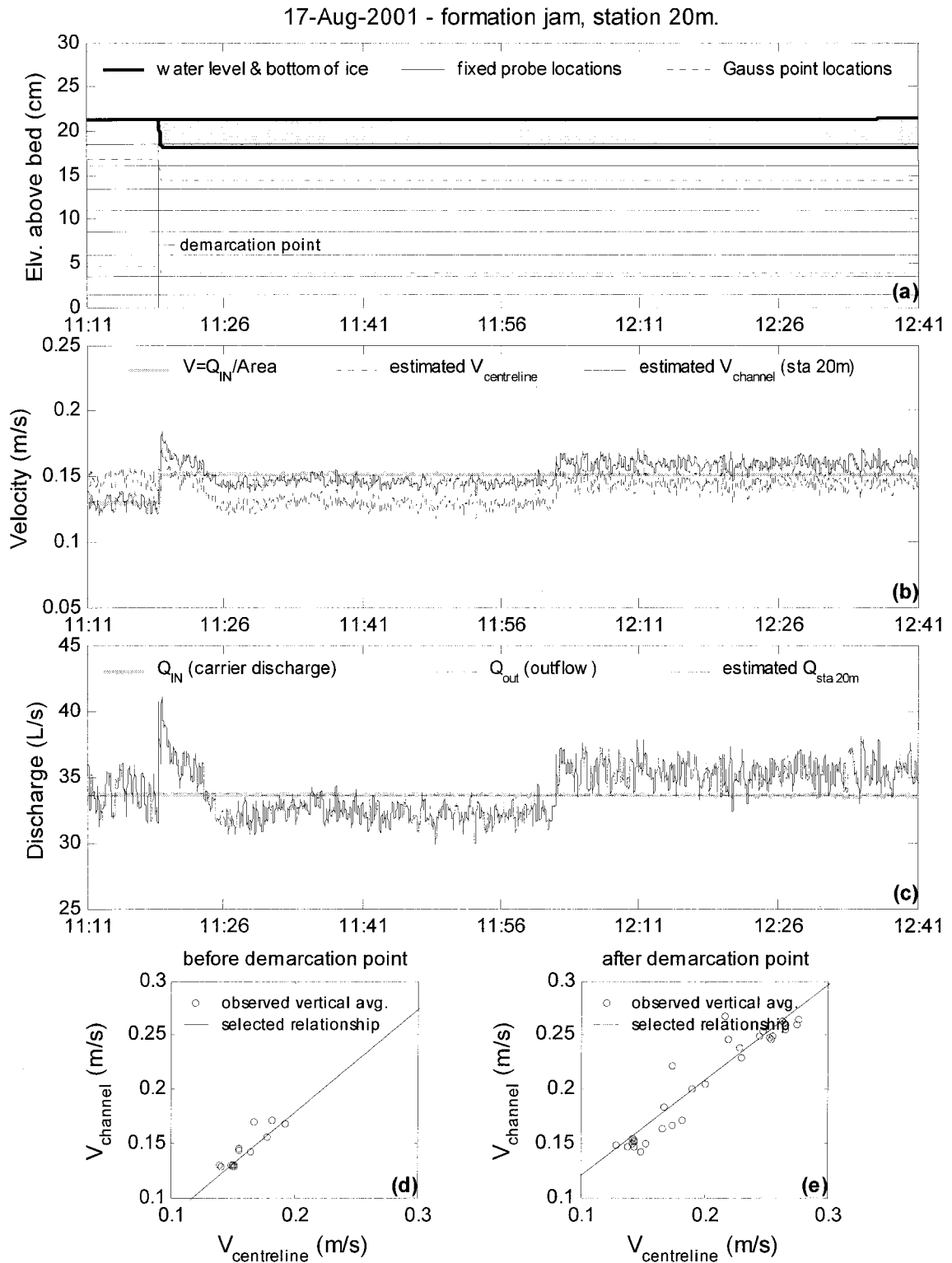
Figure E.64. Summary of continuous observations for a formation jam taken at Station 20m – test date: 17 August 2001.

276
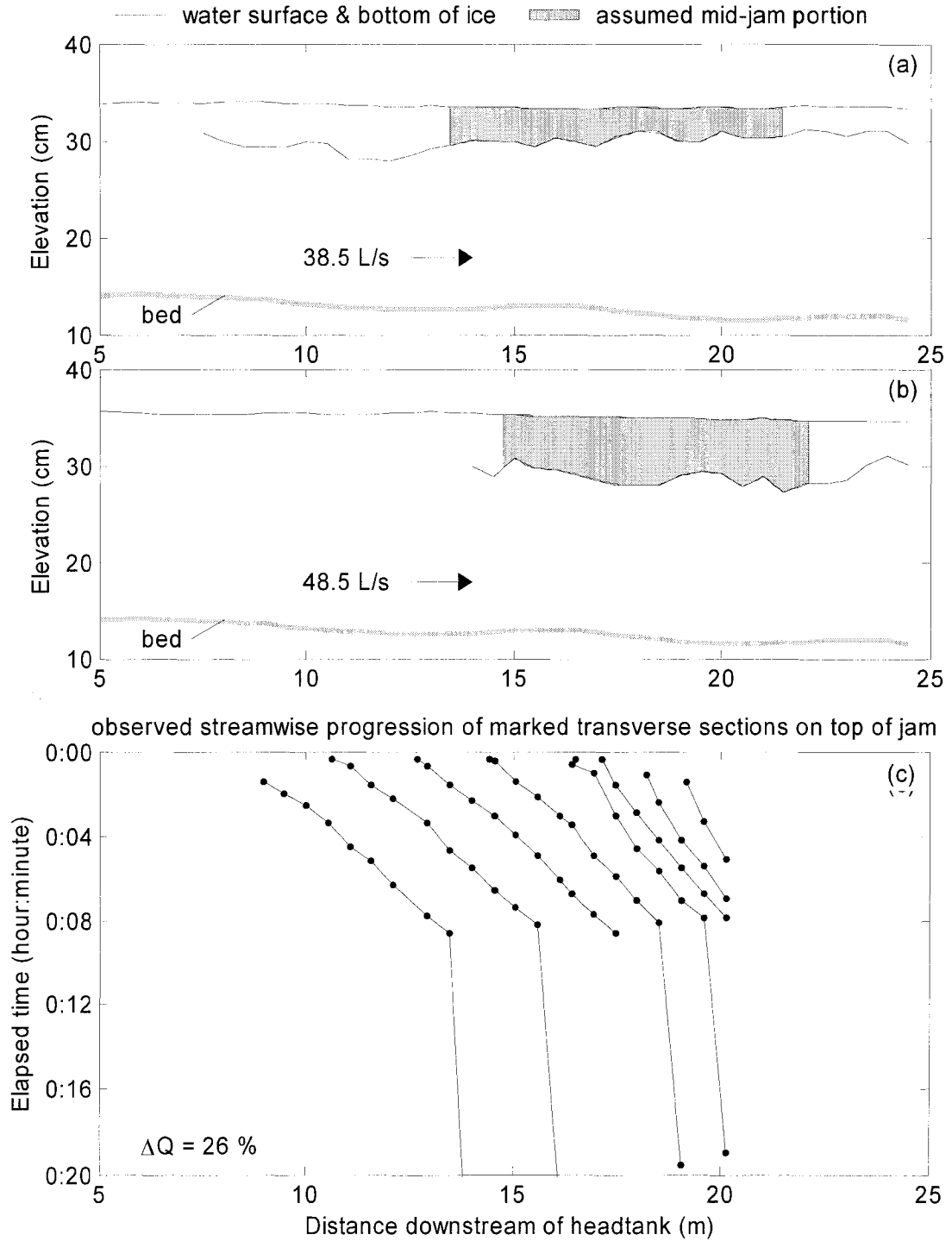
Figure E.65. 18 Jun 2001 initial ice jam profile (a), final ice jam profile (b), and cover progression (c).

277
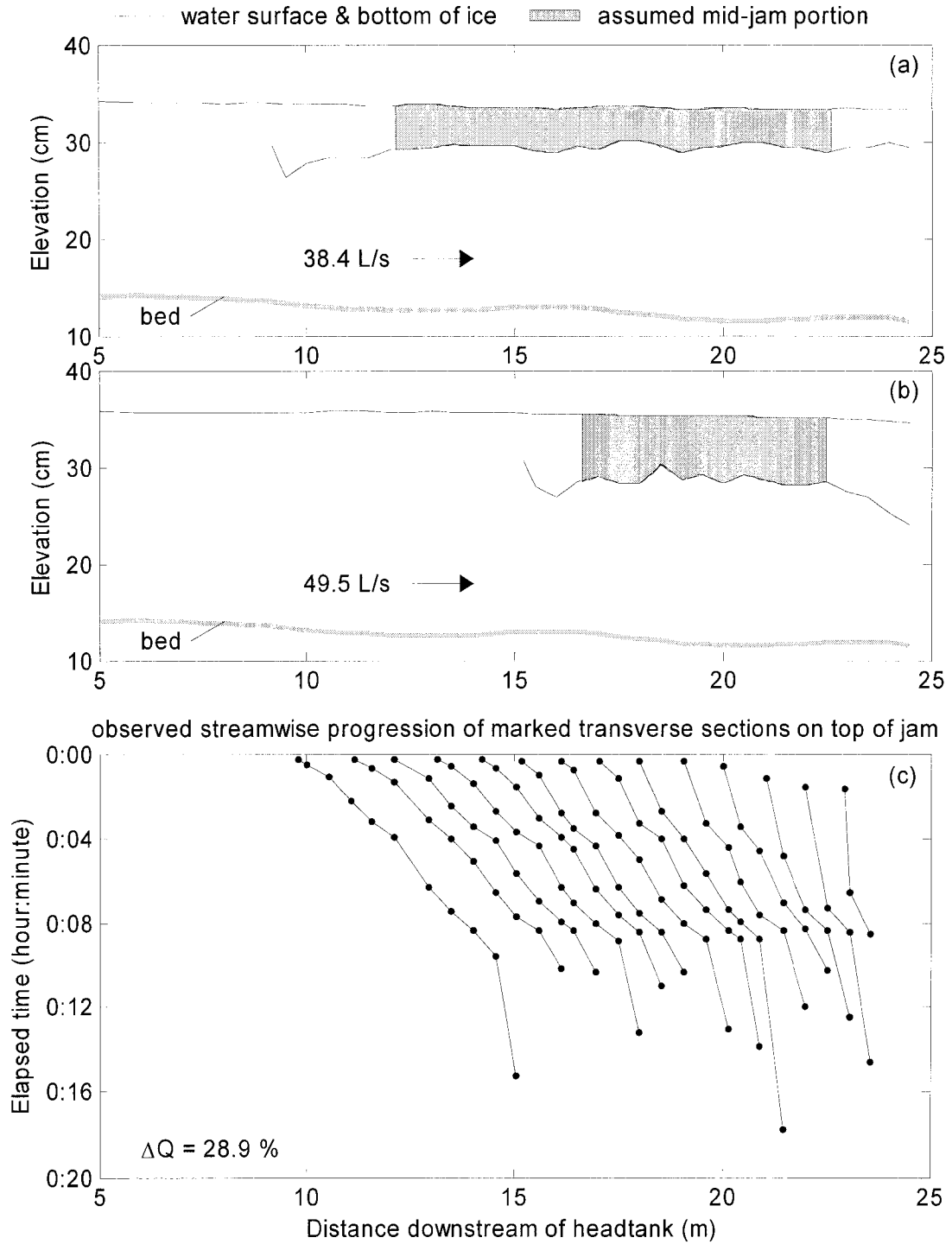
Figure E.66. 19 Jun 2001 initial ice jam profile (a), final ice jam profile (b), and cover progression (c).

278

Figure E.67. 20 Jun 2001 initial ice jam profile (a), final ice jam profile (b), and cover progression (c).

20-Jun-2001 - jam profile and cover progression summary

water surface & bottom of ice ▓▓▓▓ assumed mid-jam portion
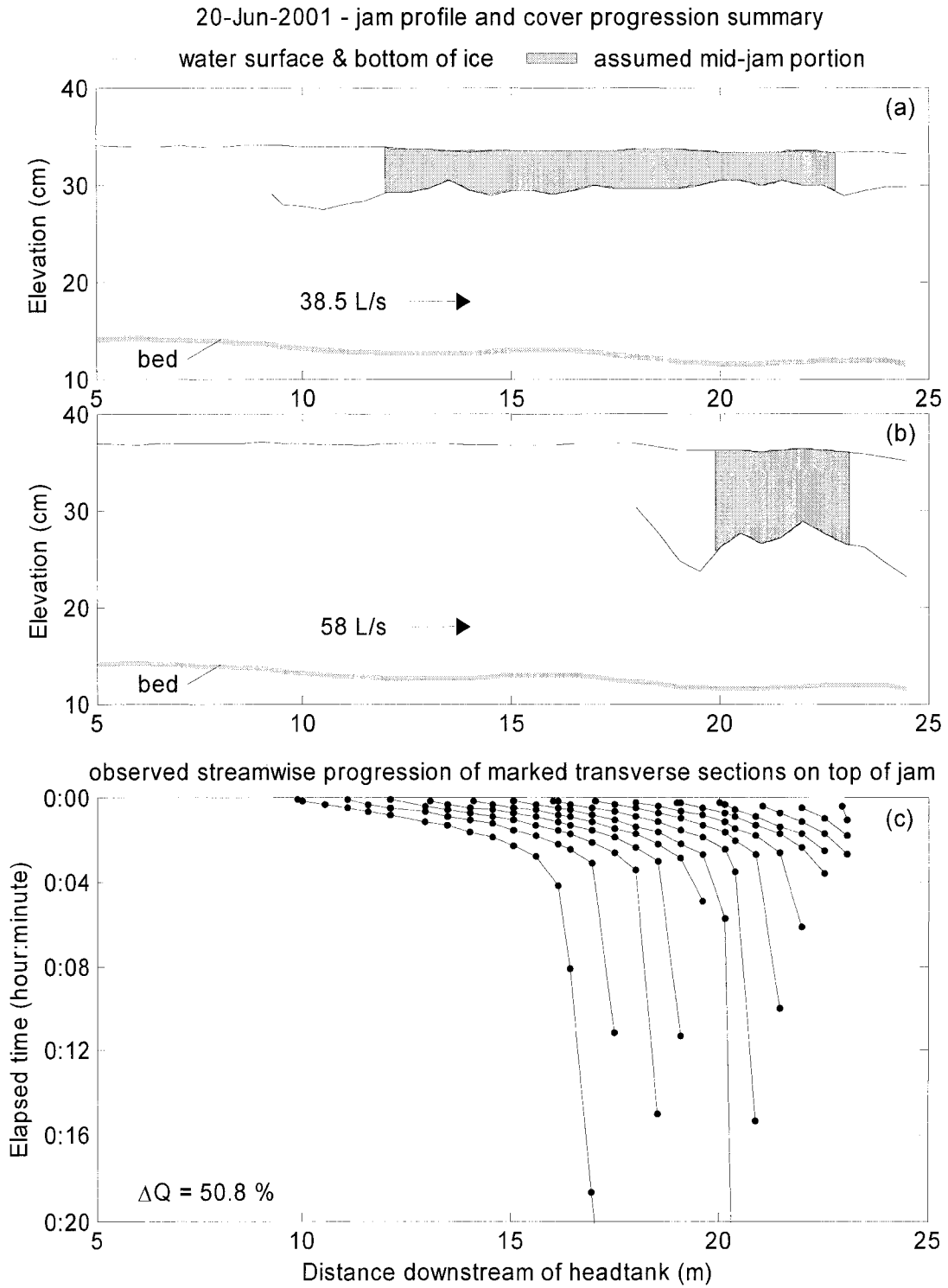
Figure E.68. 21 Jun 2001 initial ice jam profile (a), final ice jam profile (b), and cover progression (c).
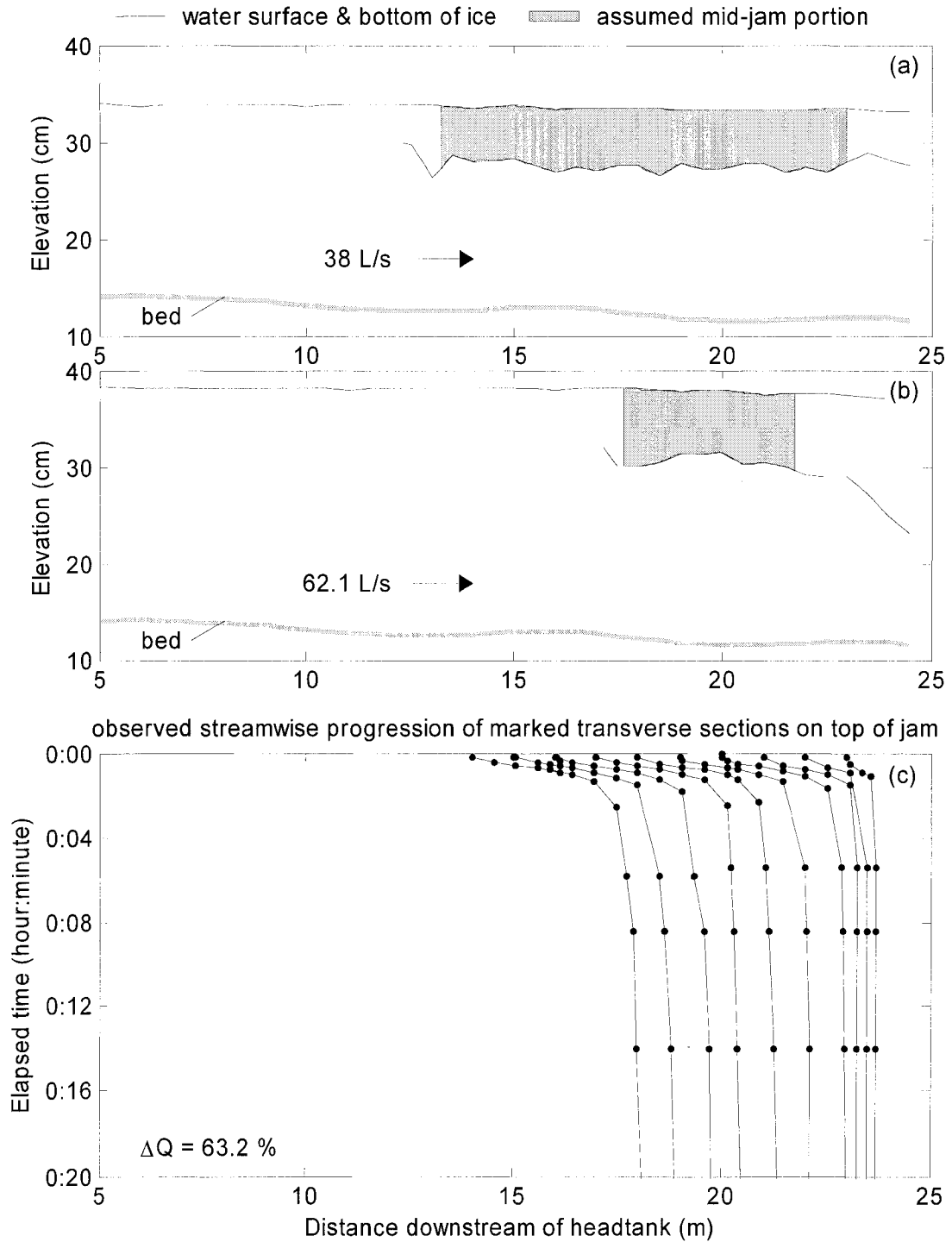
Figure E.69. 22 Jun 2001 initial ice jam profile (a), final ice jam profile (b), and cover progression (c).

25-Jun-2001 - jam profile and cover progression summary
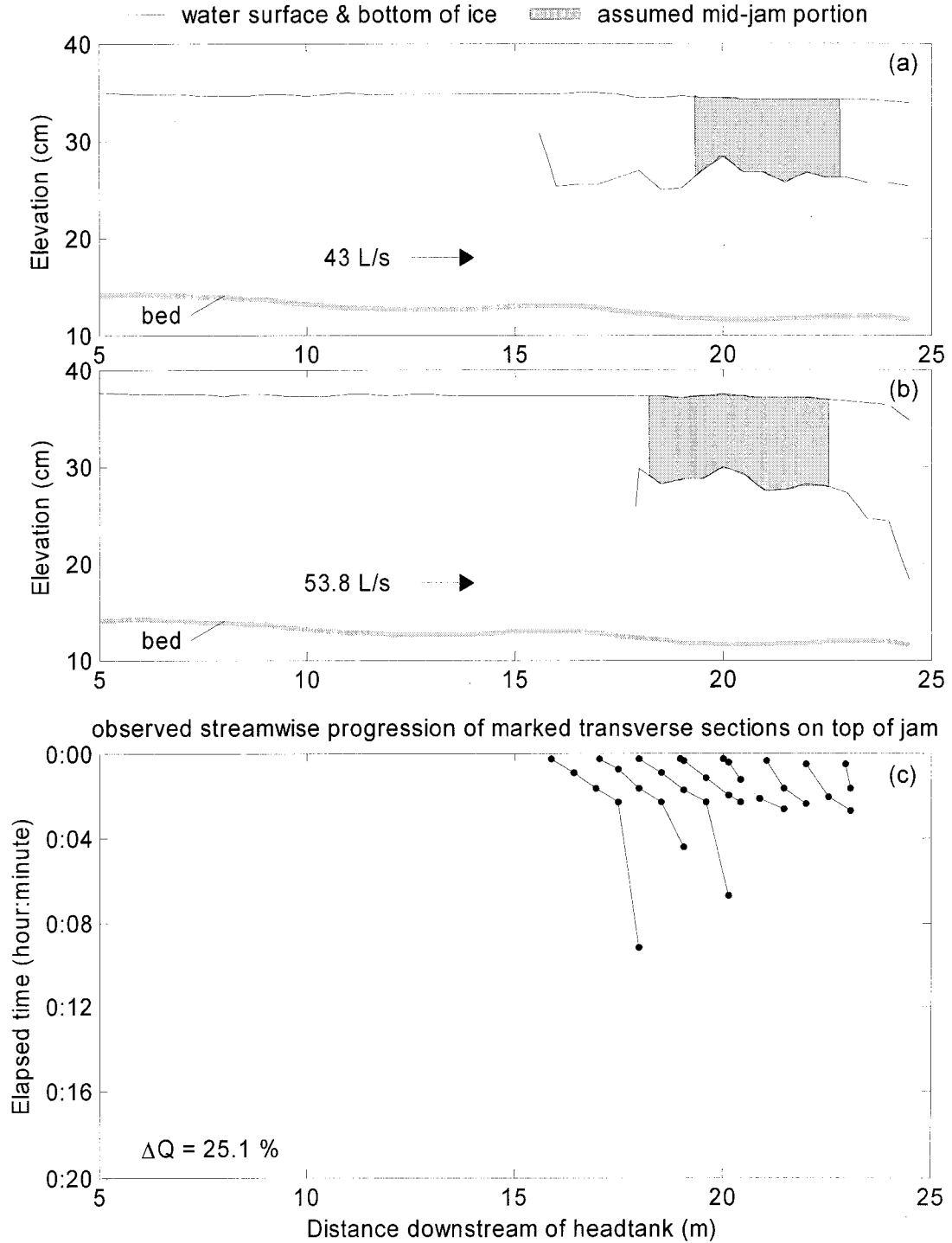
Figure E.70. 25 Jun 2001 initial ice jam profile (a), final ice jam profile (b), and cover progression (c).
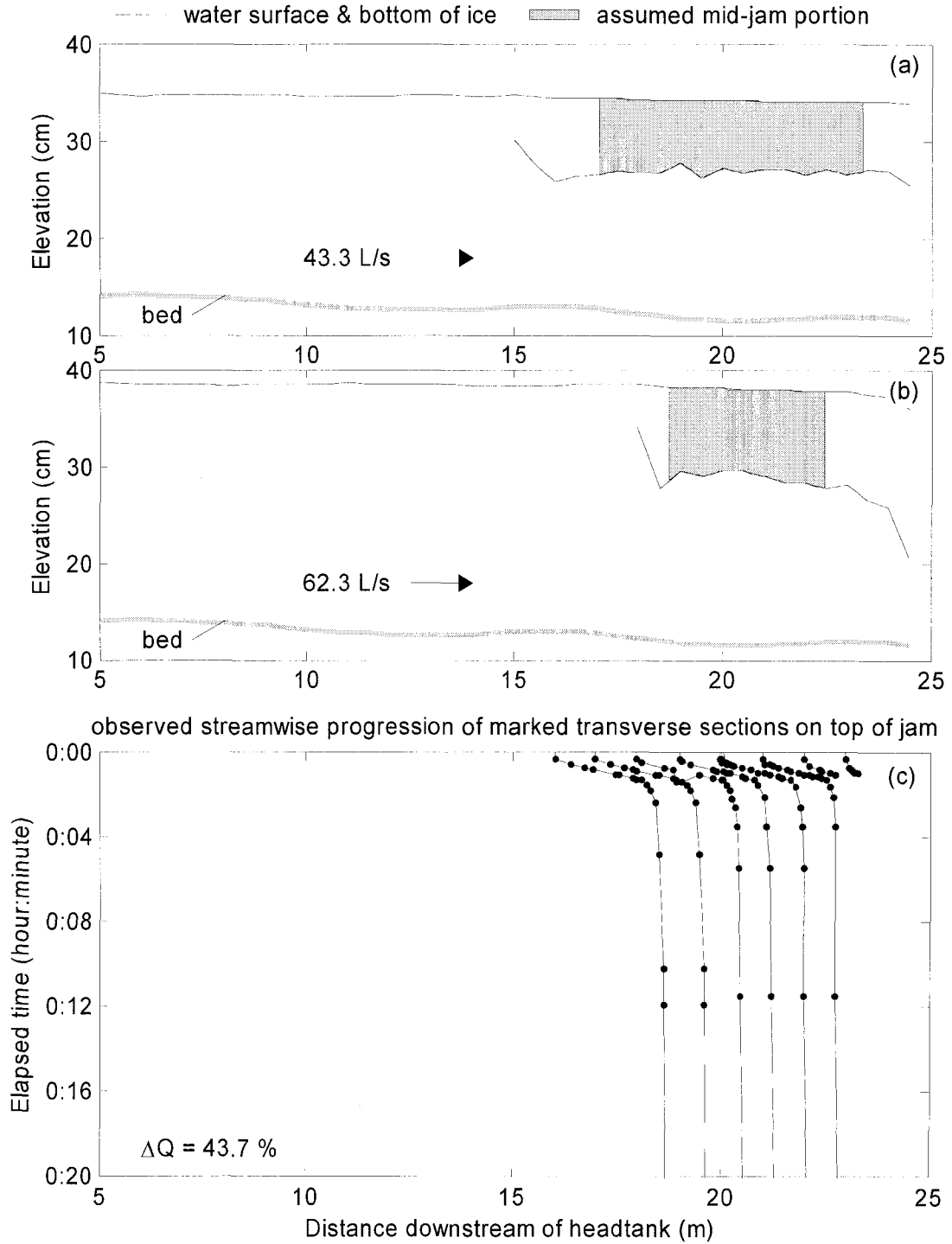
Figure E.71. 26 Jun 2001 initial ice jam profile (a), final ice jam profile (b), and cover progression (c).
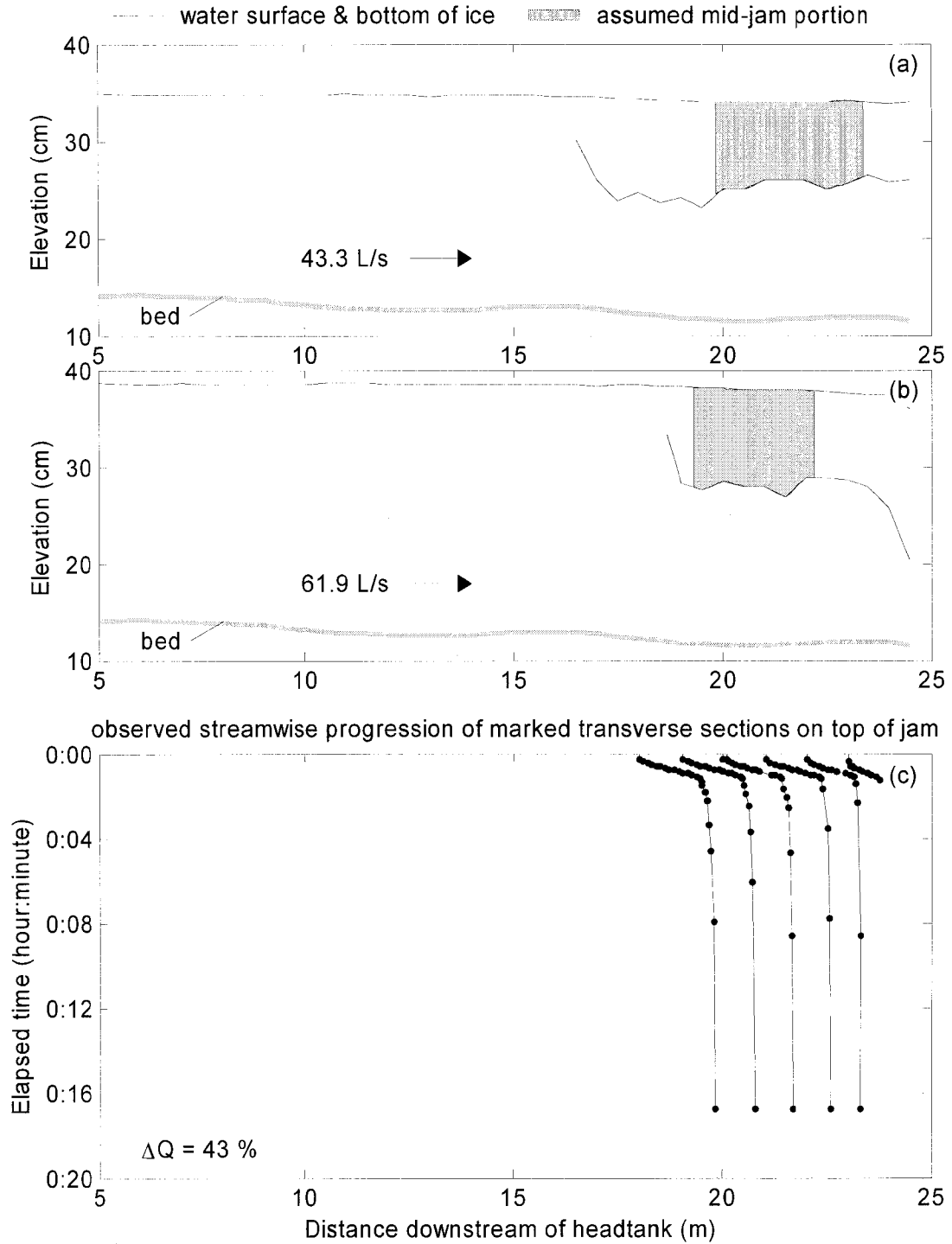
Figure E.72. 27 Jun 2001 initial ice jam profile (a), final ice jam profile (b), and cover progression (c).
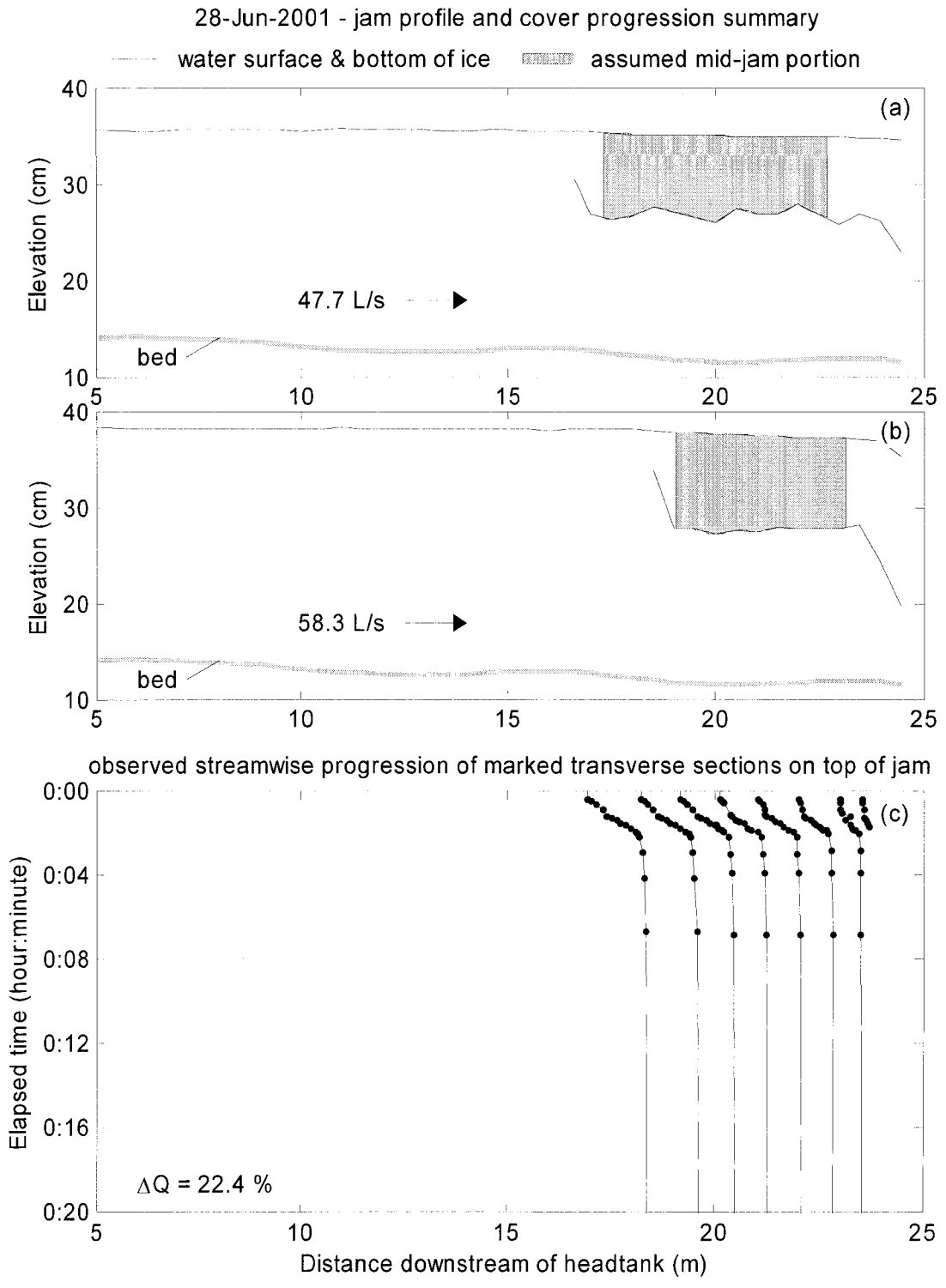
Figure E.73. 28 Jun 2001 initial ice jam profile (a), final ice jam profile (b), and cover progression (c).

285
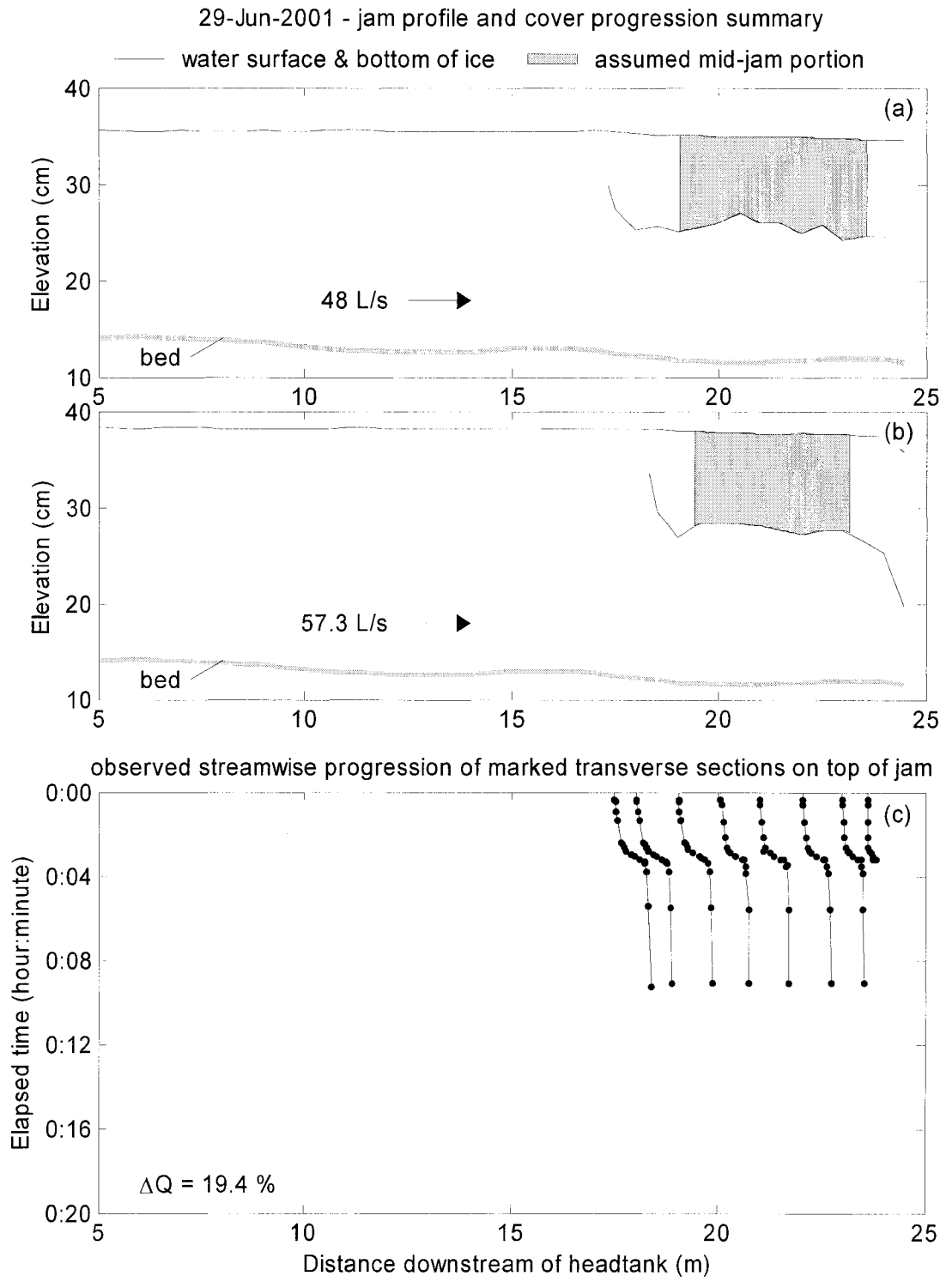
Figure E.74. 29 Jun 2001 initial ice jam profile (a), final ice jam profile (b), and cover progression (c).
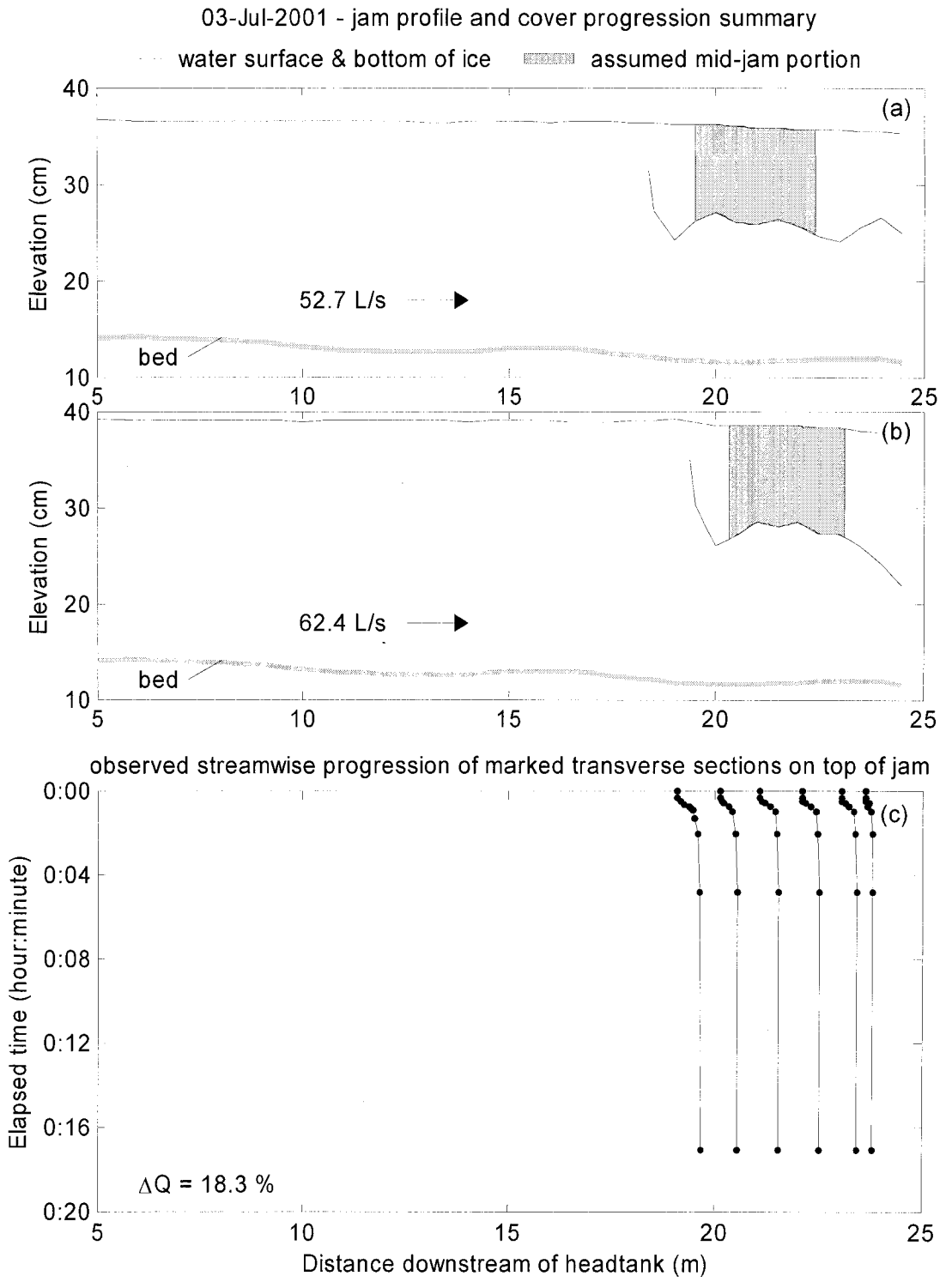
Figure E.75. 03 Jul 2001 initial ice jam profile (a), final ice jam profile (b), and cover progression (c).

287
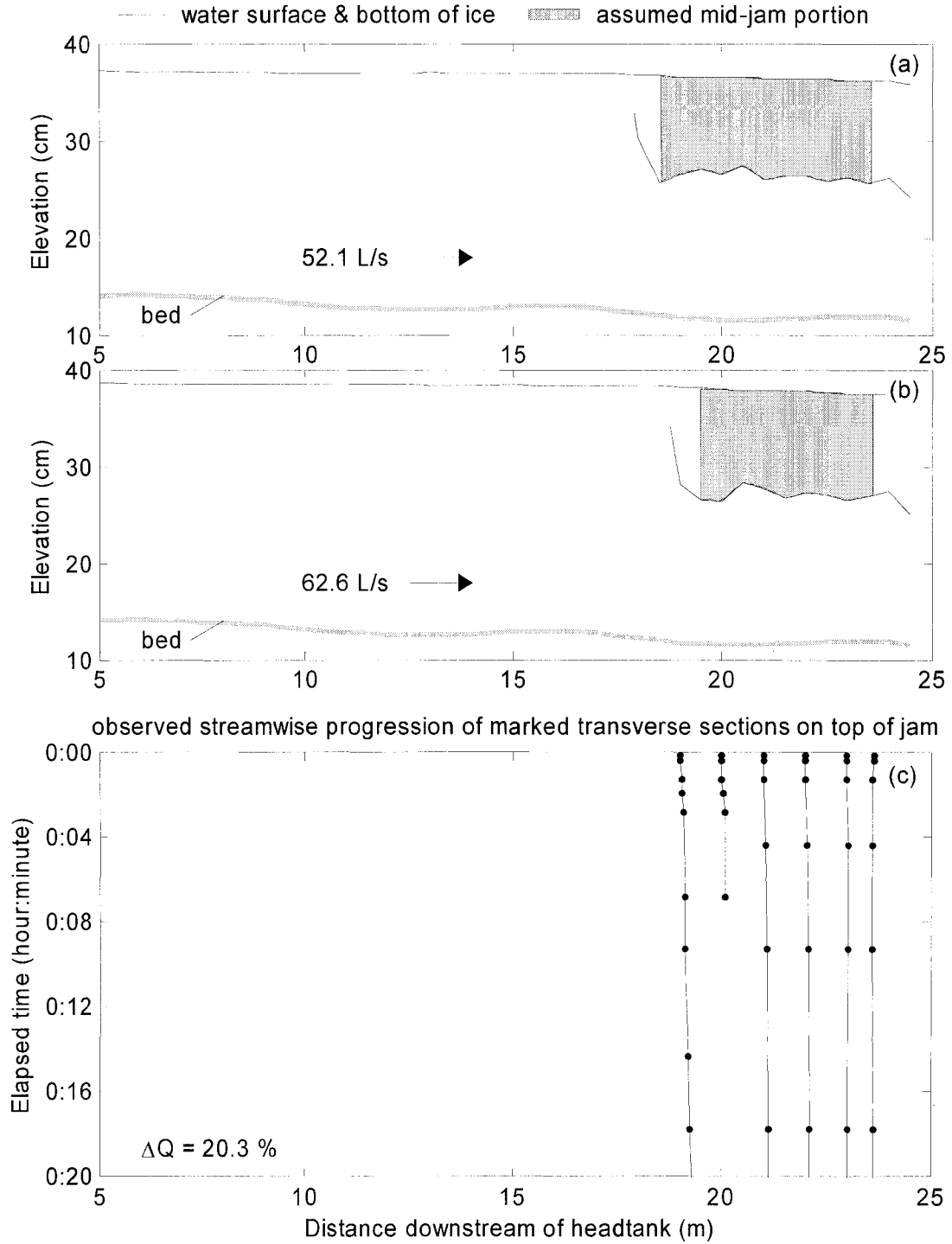
Figure E.76. 04 Jul 2001 initial ice jam profile (a), final ice jam profile (b), and cover progression (c).

05-Jul-2001 - jam profile and cover progression summary

water surface & bottom of ice   assumed mid-jam portion
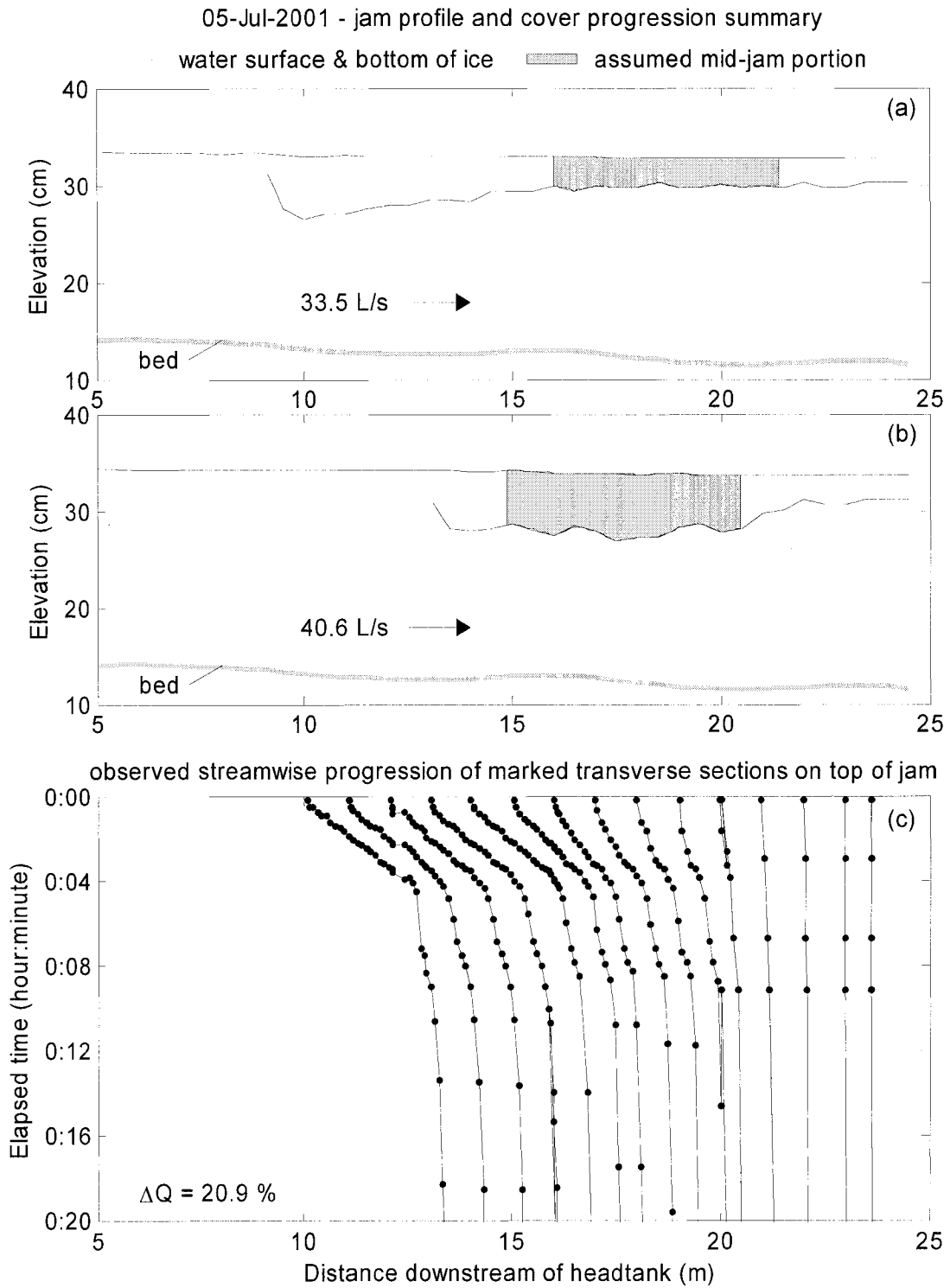
Figure E.77. 05 Jul 2001 initial ice jam profile (a), final ice jam profile (b), and cover progression (c).
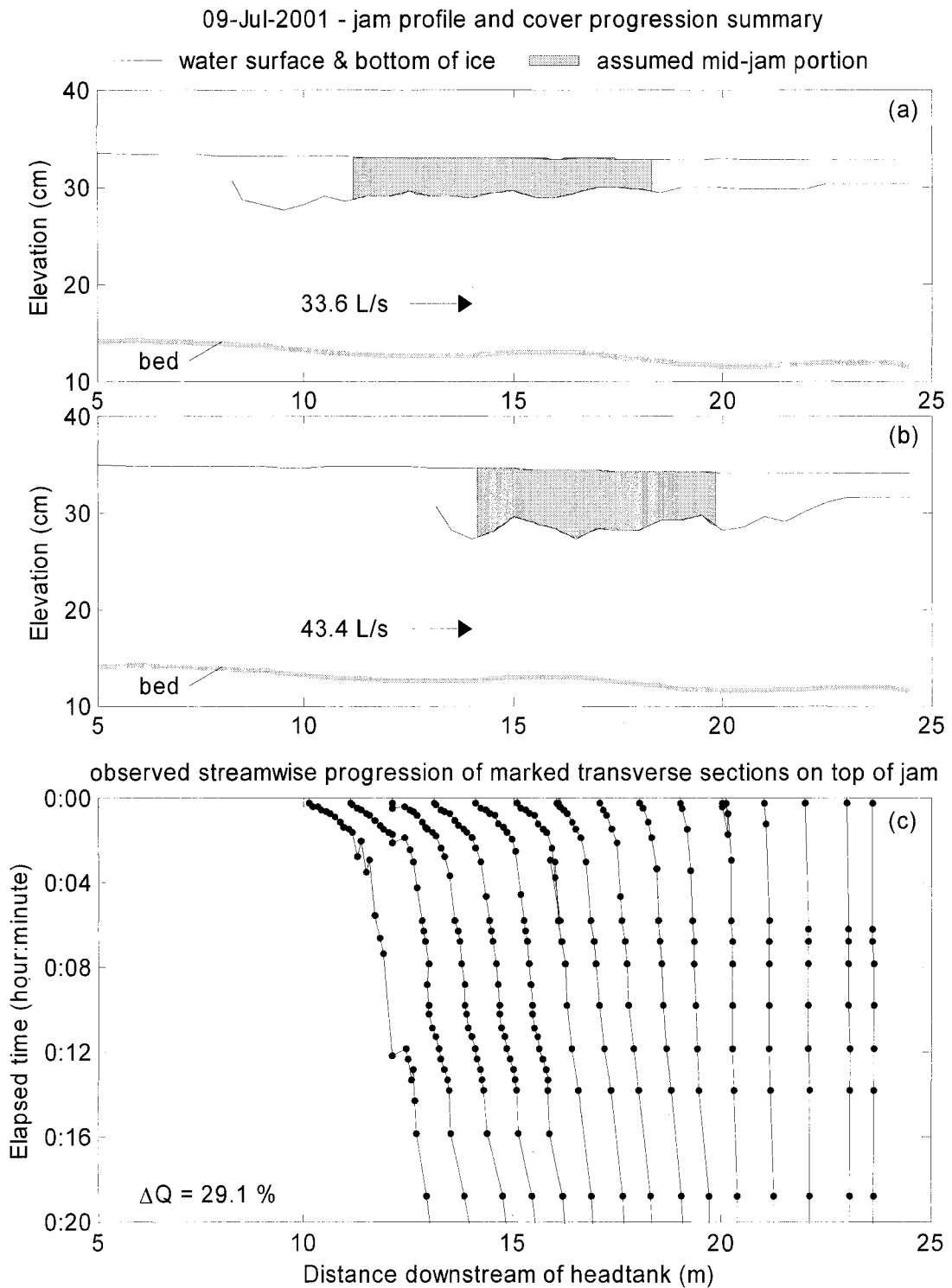
Figure E.78. 09 Jul 2001 initial ice jam profile (a), final ice jam profile (b), and cover progression (c).
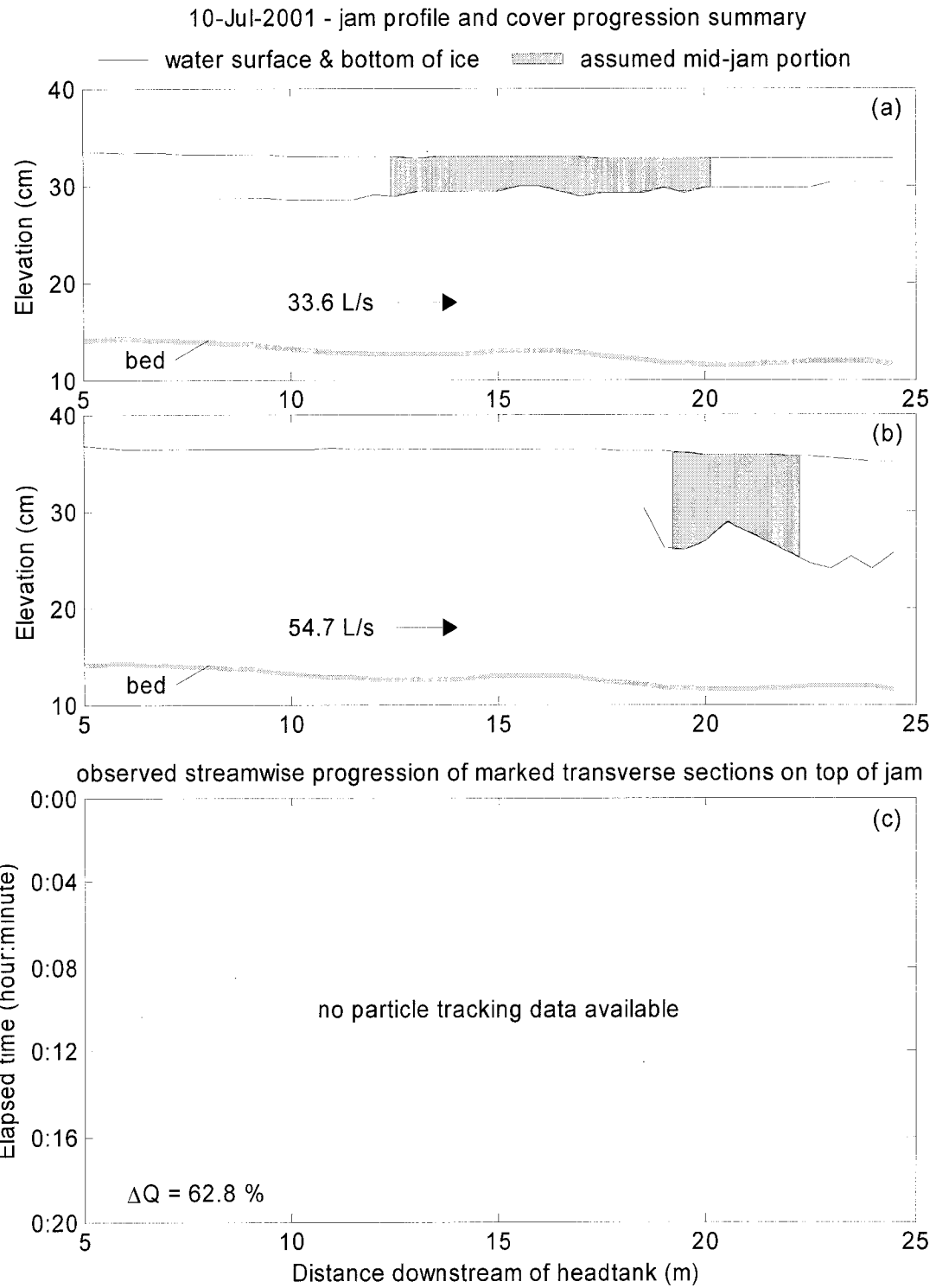
Figure E.79. 10 Jul 2001 initial ice jam profile (a), final ice jam profile (b), and cover progression (c).
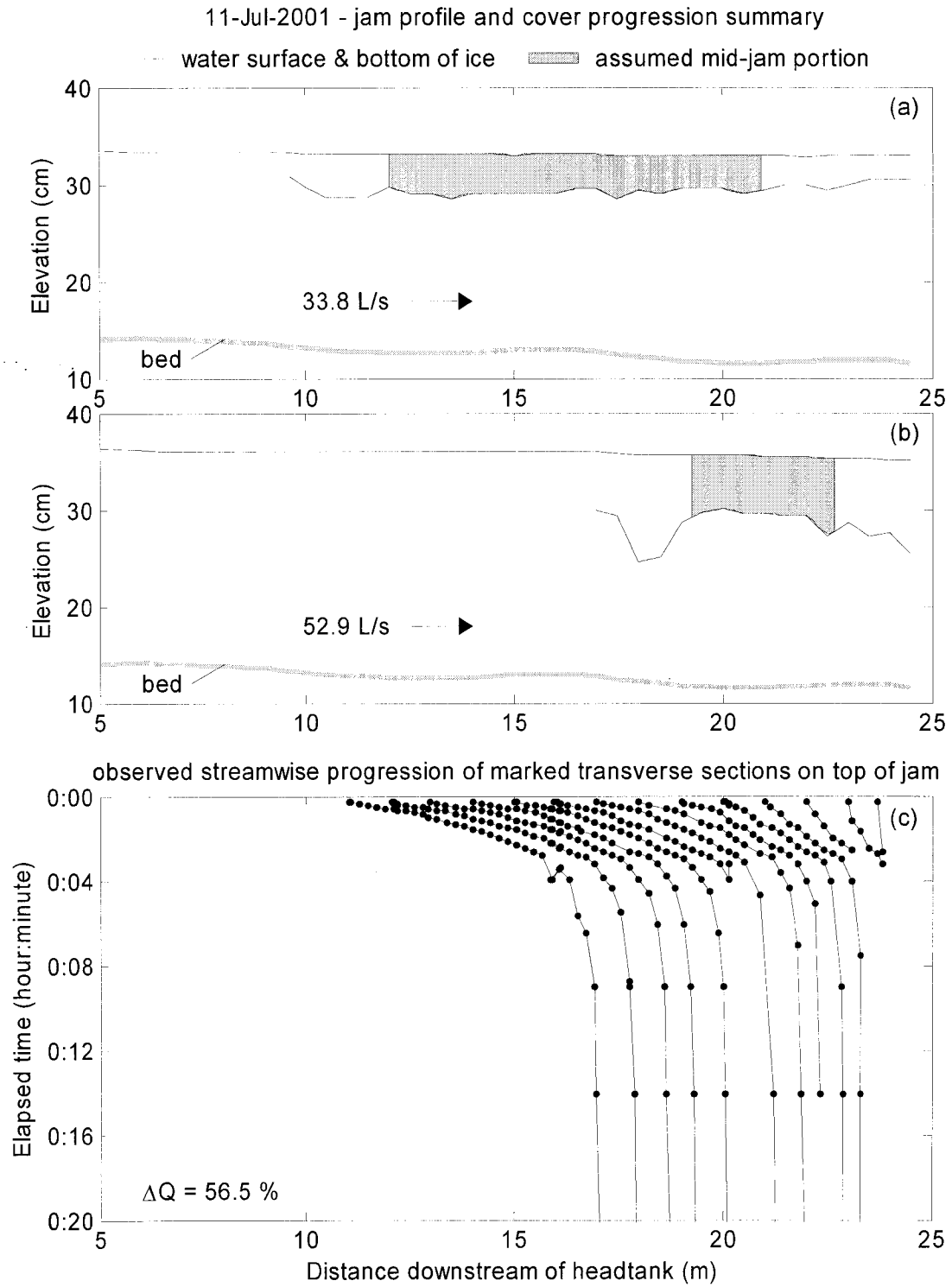
Figure E.80. 11 Jul 2001 initial ice jam profile (a), final ice jam profile (b), and cover progression (c).
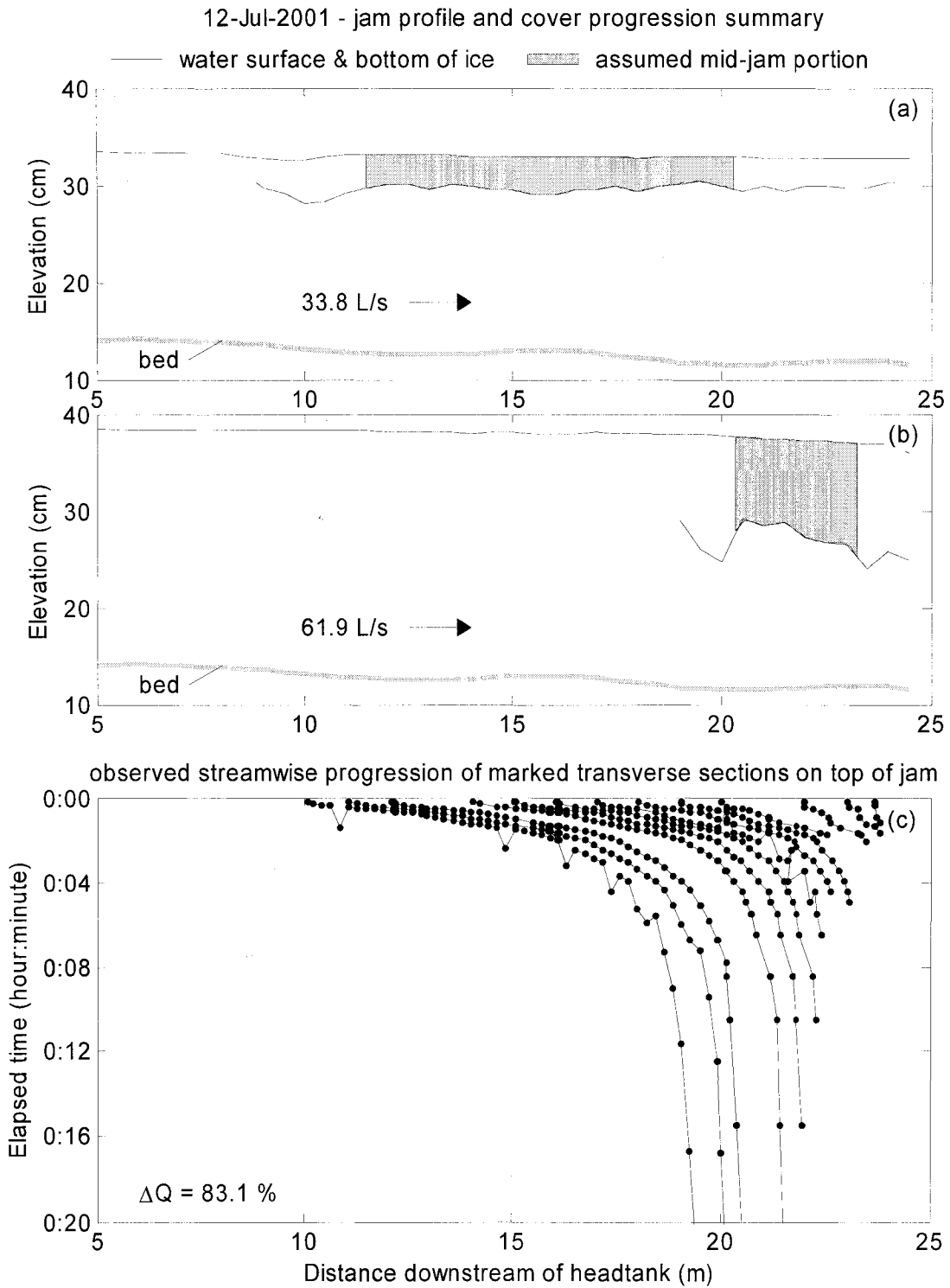
Figure E.81. 12 Jul 2001 initial ice jam profile (a), final ice jam profile (b), and cover progression (c).
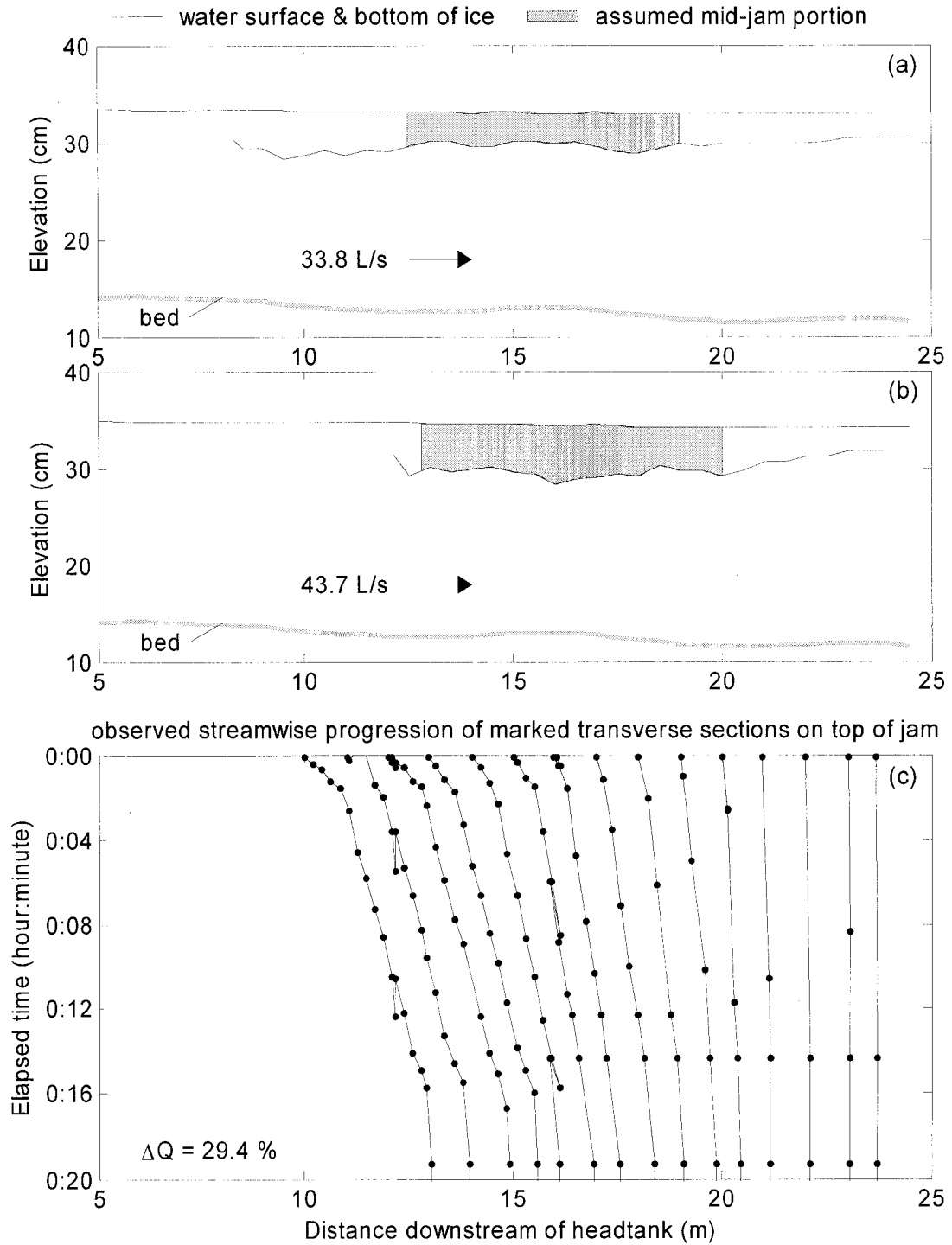
Figure E.82. 13 Jul 2001 initial ice jam profile (a), final ice jam profile (b), and cover progression (c).

294
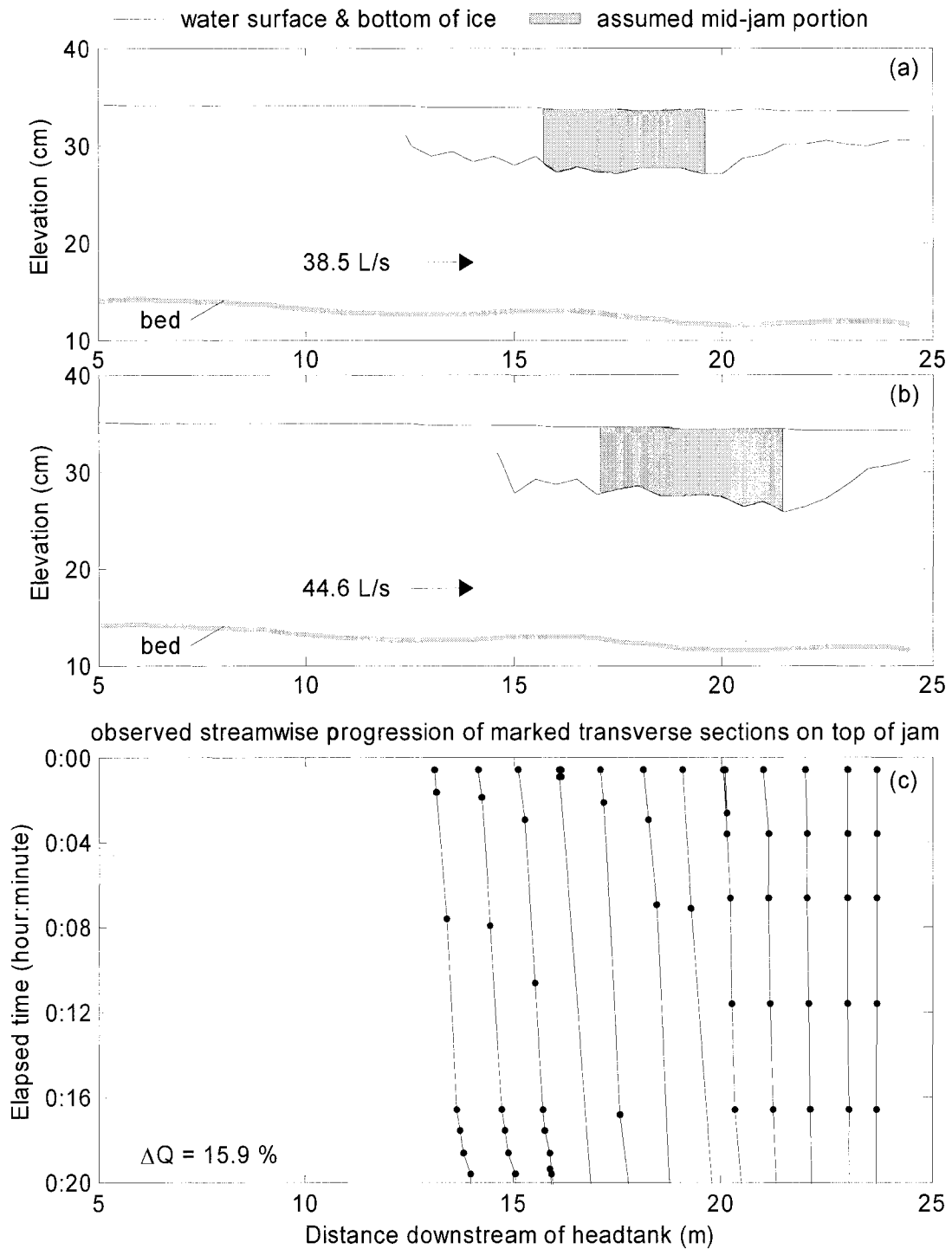
Figure E.83. 16 Jul 2001 initial ice jam profile (a), final ice jam profile (b), and cover progression (c).
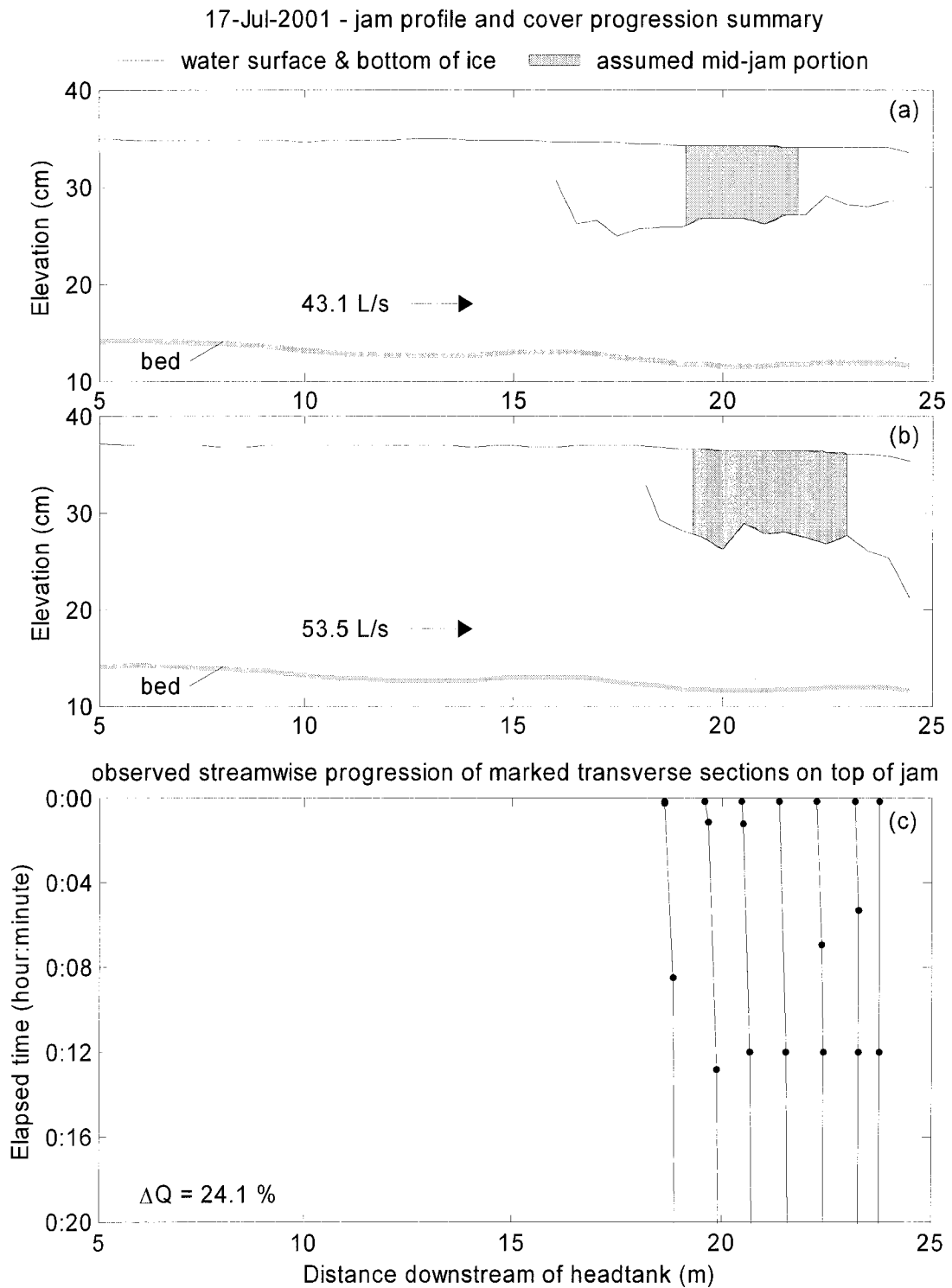
Figure E.84. 17 Jul 2001 initial ice jam profile (a), final ice jam profile (b), and cover progression (c).

18-Jul-2001 - jam profile and cover progression summary

------- water surface & bottom of ice   assumed mid-jam portion

(a)

42.9 L/s   ▶

bed

(b)

53.1 L/s   ⟶▶

bed

observed streamwise progression of marked transverse sections on top of jam

(c)

ΔQ = 23.7 %

Distance downstream of headtank (m)
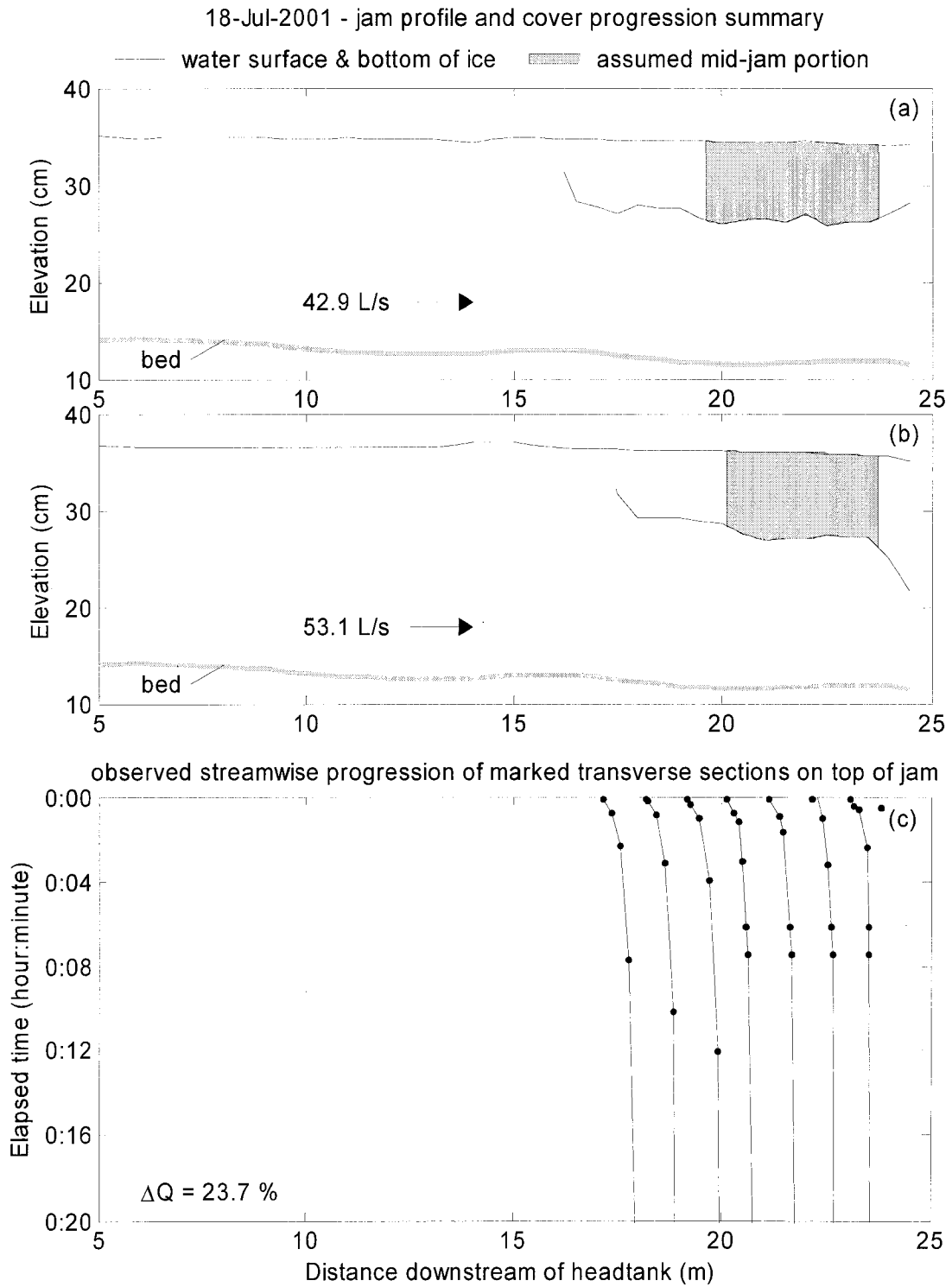
Figure E.85. 18 Jul 2001 initial ice jam profile (a), final ice jam profile (b), and cover progression (c).

297

19-Jul-2001 - jam profile and cover progression summary

—— water surface & bottom of ice ▓▓▓ assumed mid-jam portion
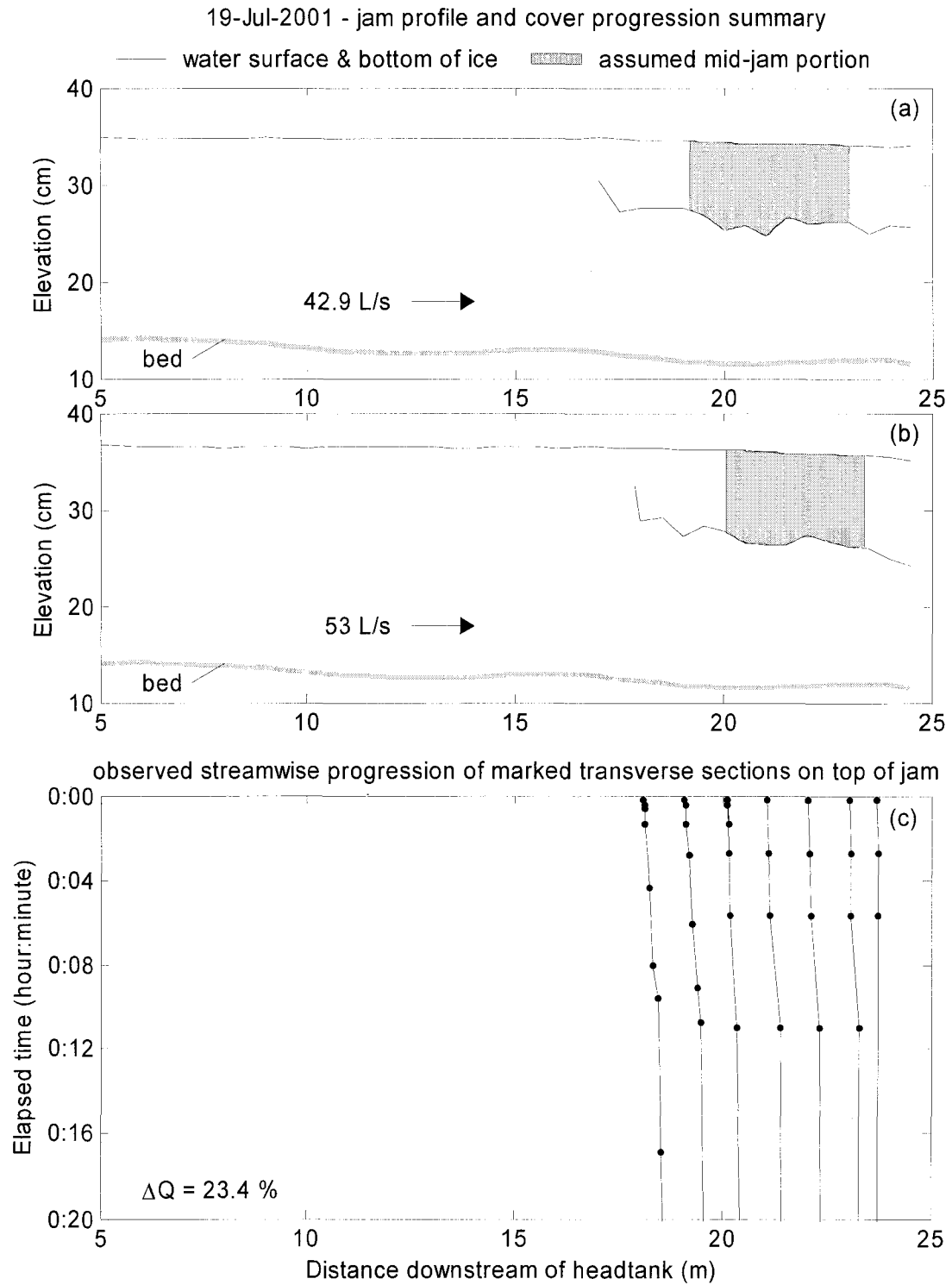
Figure E.86. 19 Jul 2001 initial ice jam profile (a), final ice jam profile (b), and cover progression (c).
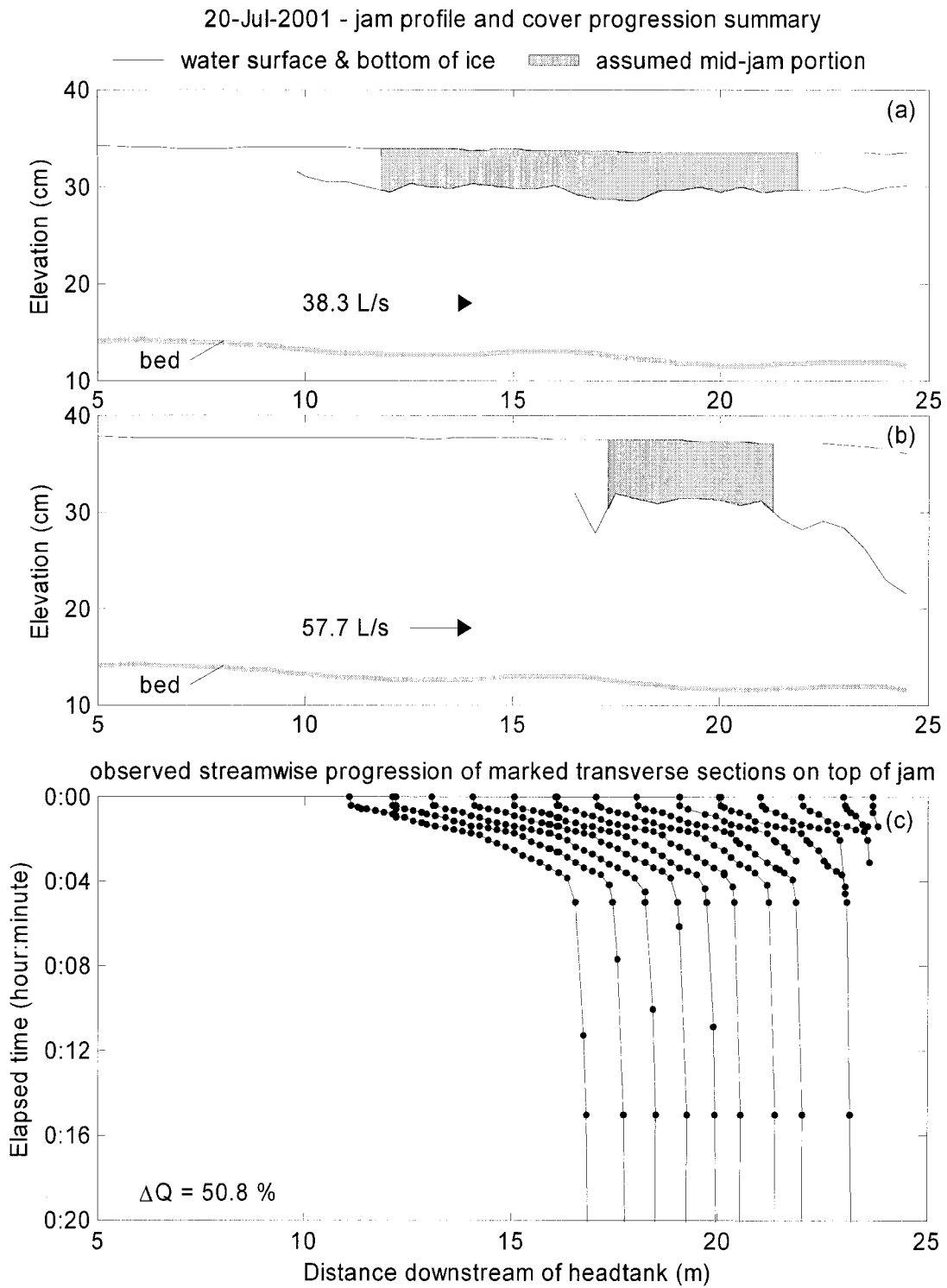
Figure E.87. 20 Jul 2001 initial ice jam profile (a), final ice jam profile (b), and cover progression (c).

299

23-Jul-2001 - jam profile and cover progression summary
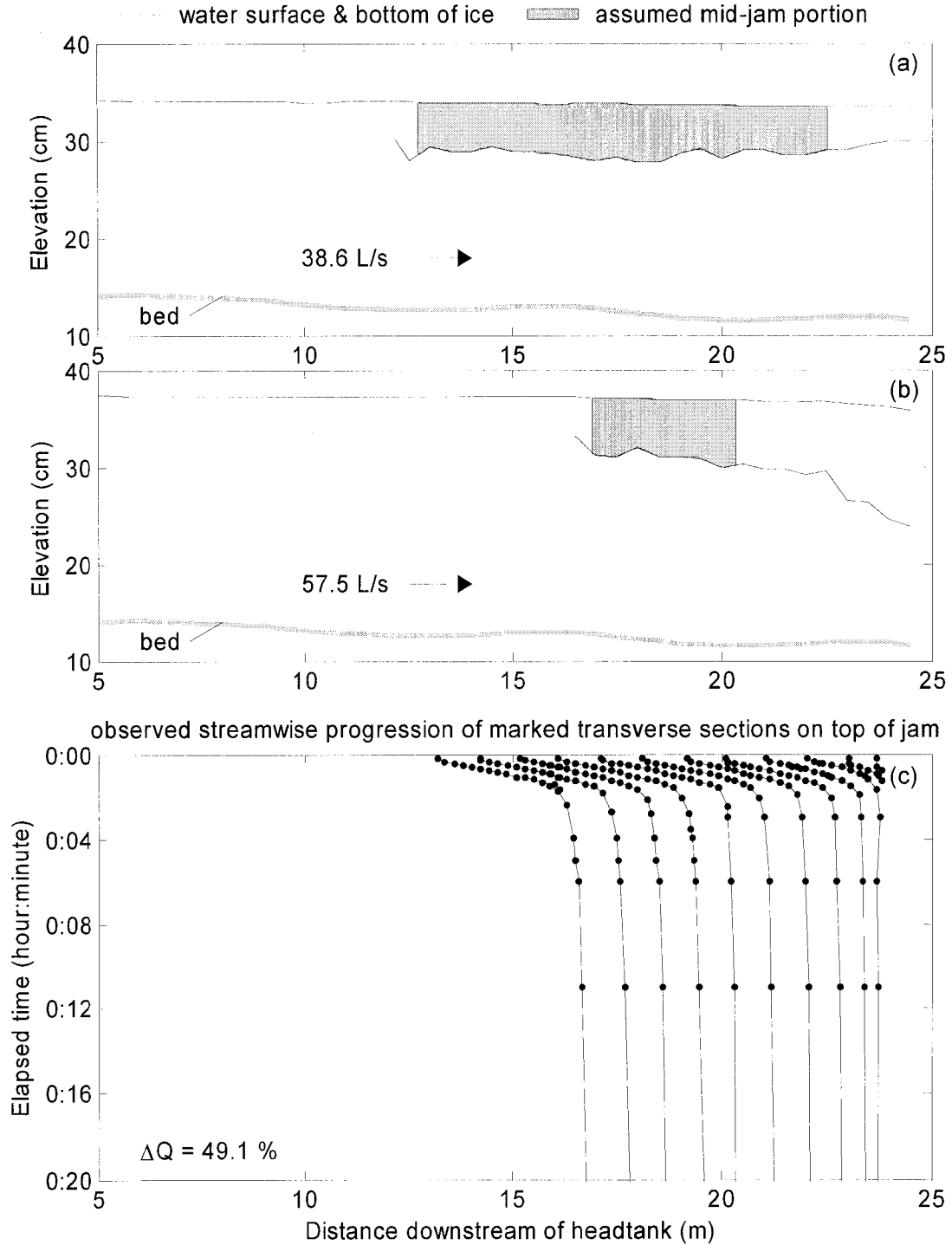
Figure E.88. 23 Jul 2001 initial ice jam profile (a), final ice jam profile (b), and cover progression (c).

25-Jul-2001 - jam profile and cover progression summary

--- water surface & bottom of ice ▦▦▦ assumed mid-jam portion
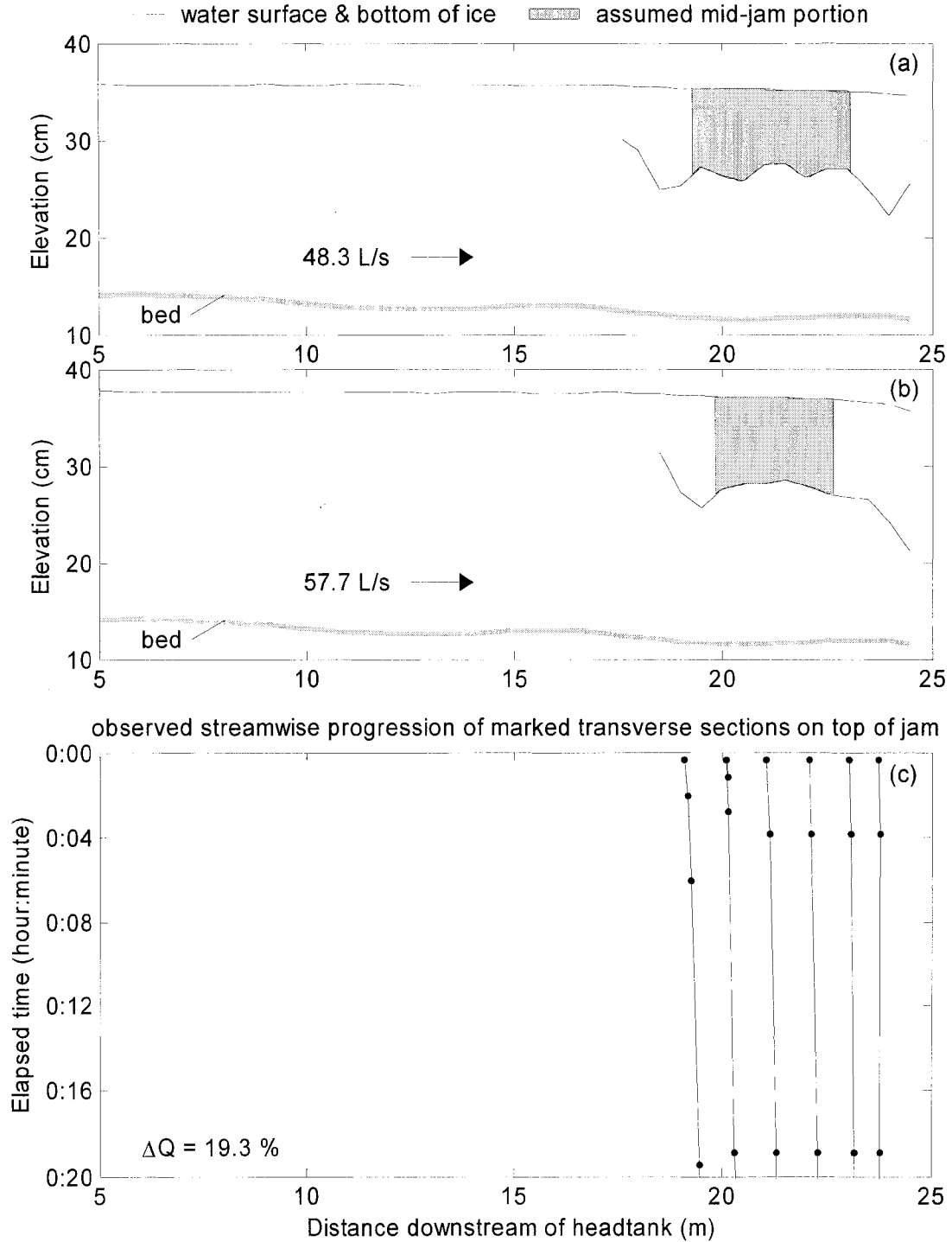
Figure E.89. 25 Jul 2001 initial ice jam profile (a), final ice jam profile (b), and cover progression (c).

301
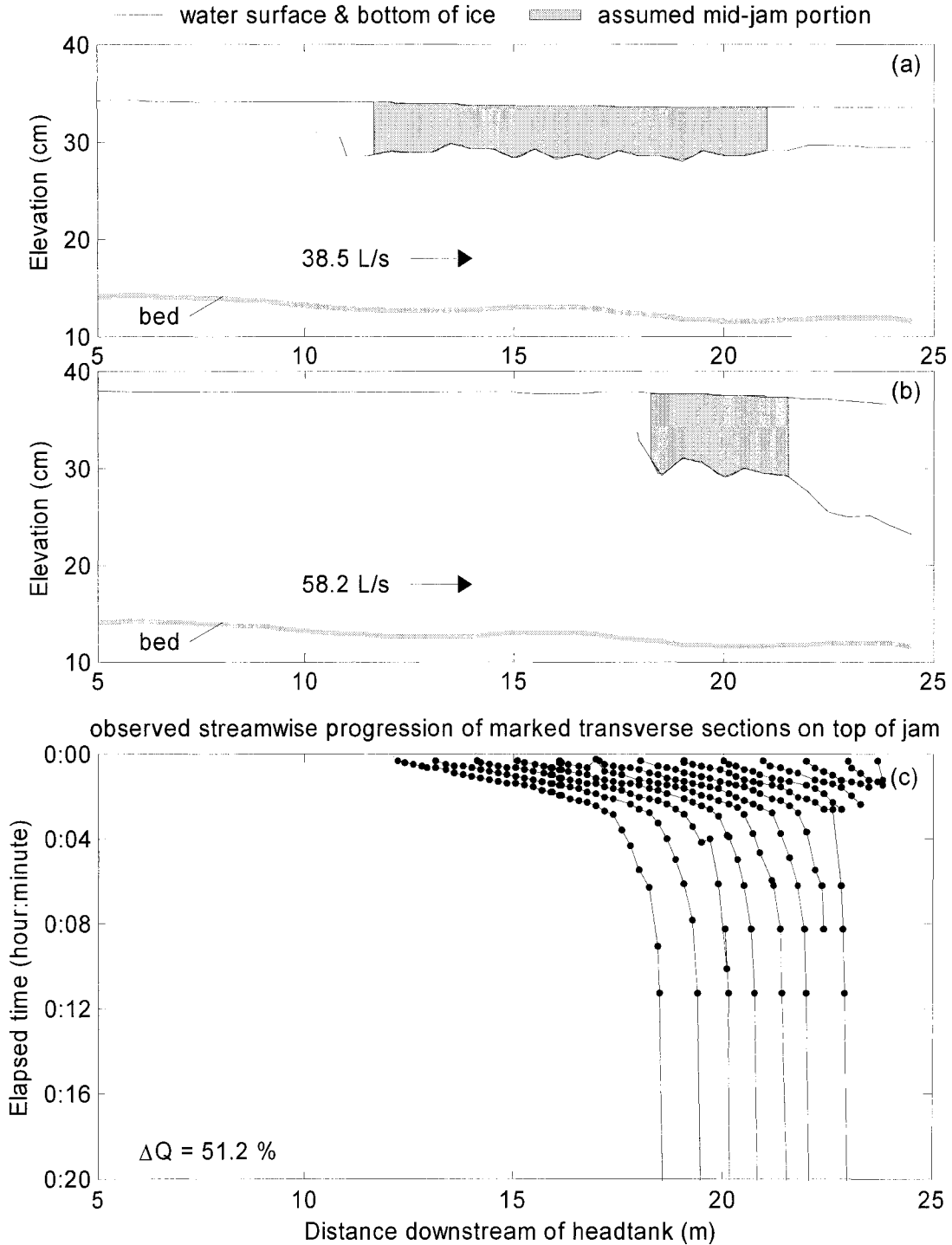
Figure E.90. 26 Jul 2001 initial ice jam profile (a), final ice jam profile (b), and cover progression (c).
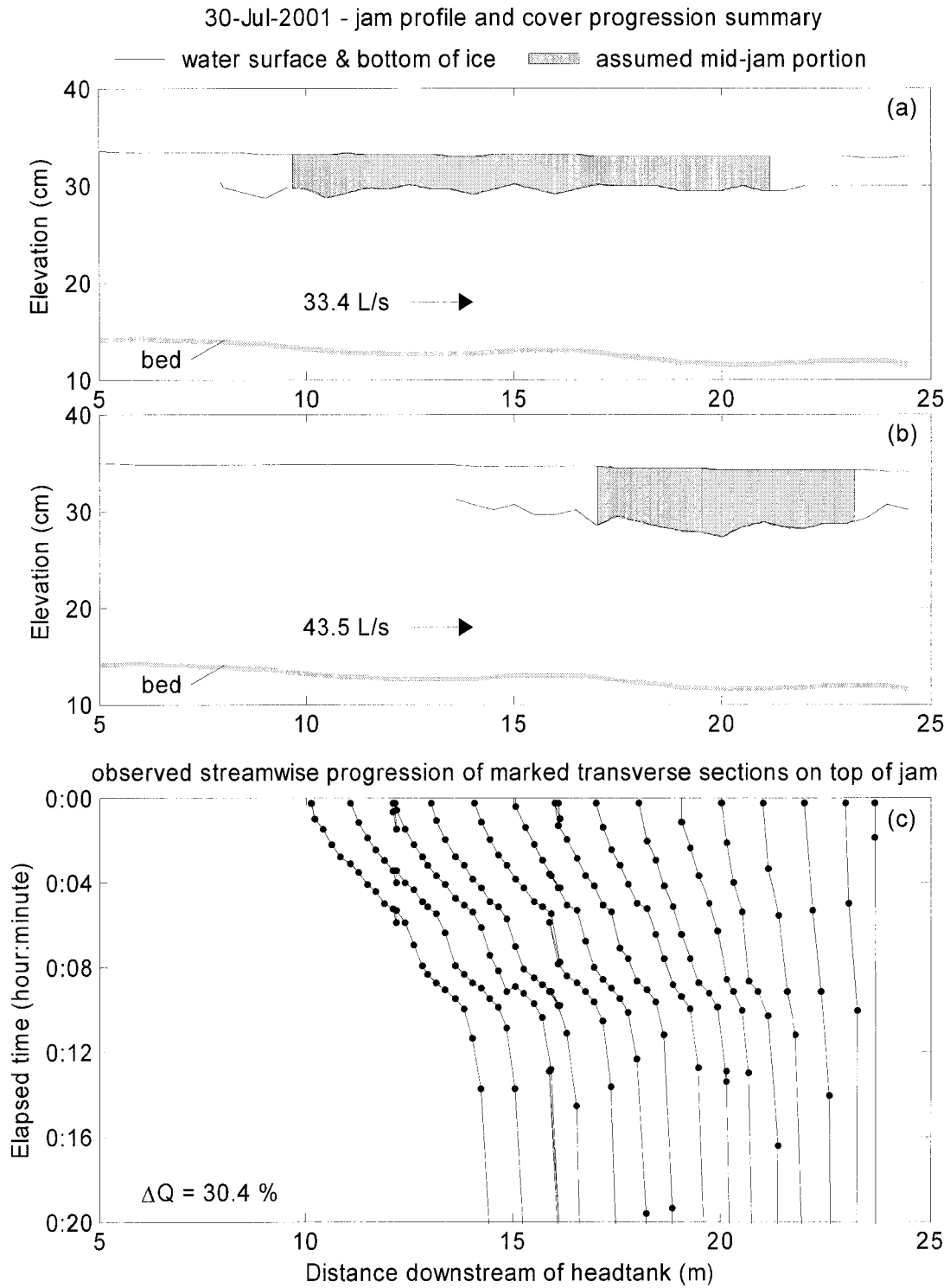
Figure E.91. 30 Jul 2001 initial ice jam profile (a), final ice jam profile (b), and cover progression (c).
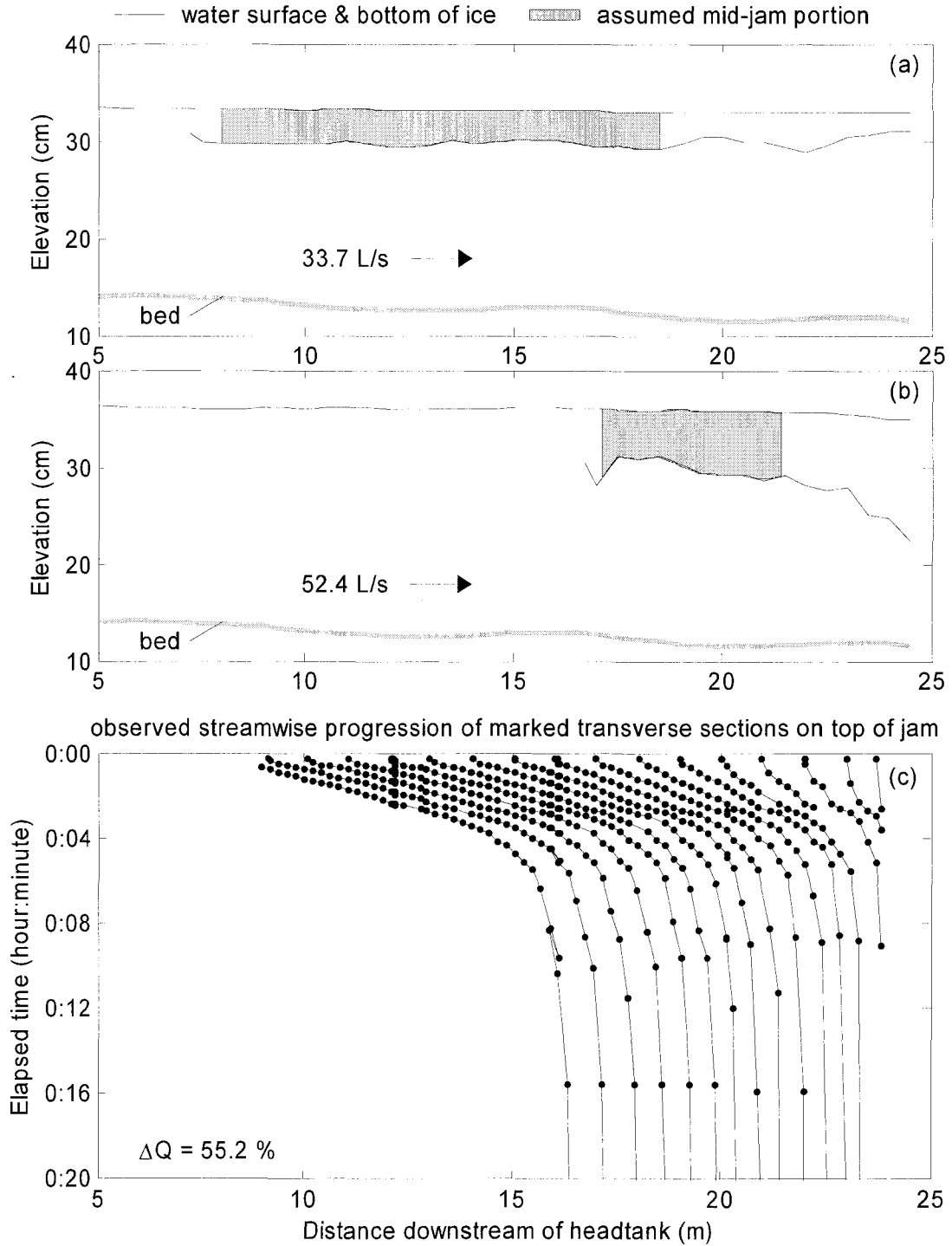
Figure E.92. 31 Jul 2001 initial ice jam profile (a), final ice jam profile (b), and cover progression (c).

304

01-Aug-2001 - jam profile and cover progression summary

—— water surface & bottom of ice ▨▨▨ assumed mid-jam portion
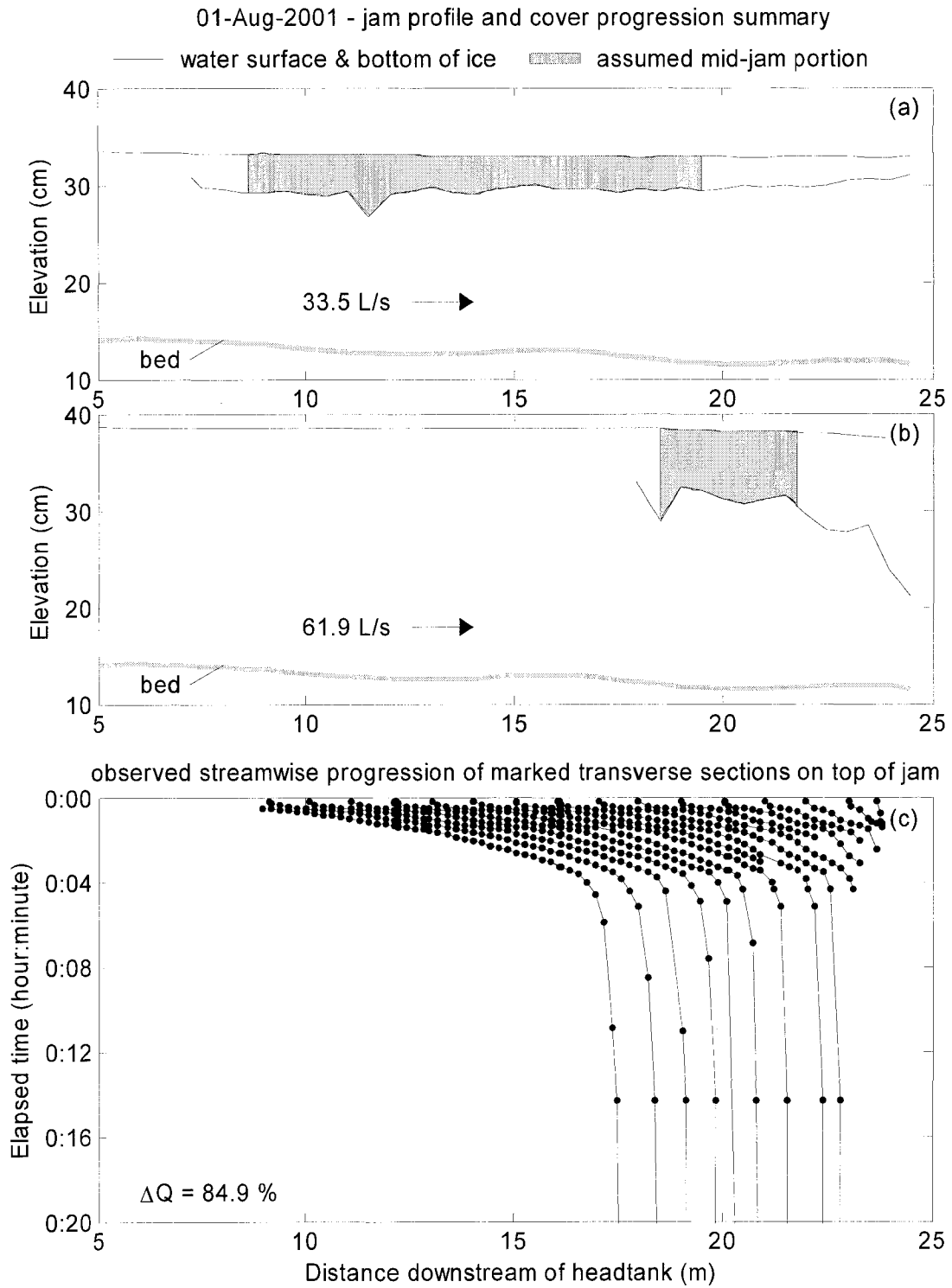
Figure E.93. 01 Aug 2001 initial ice jam profile (a), final ice jam profile (b), and cover progression (c).

305
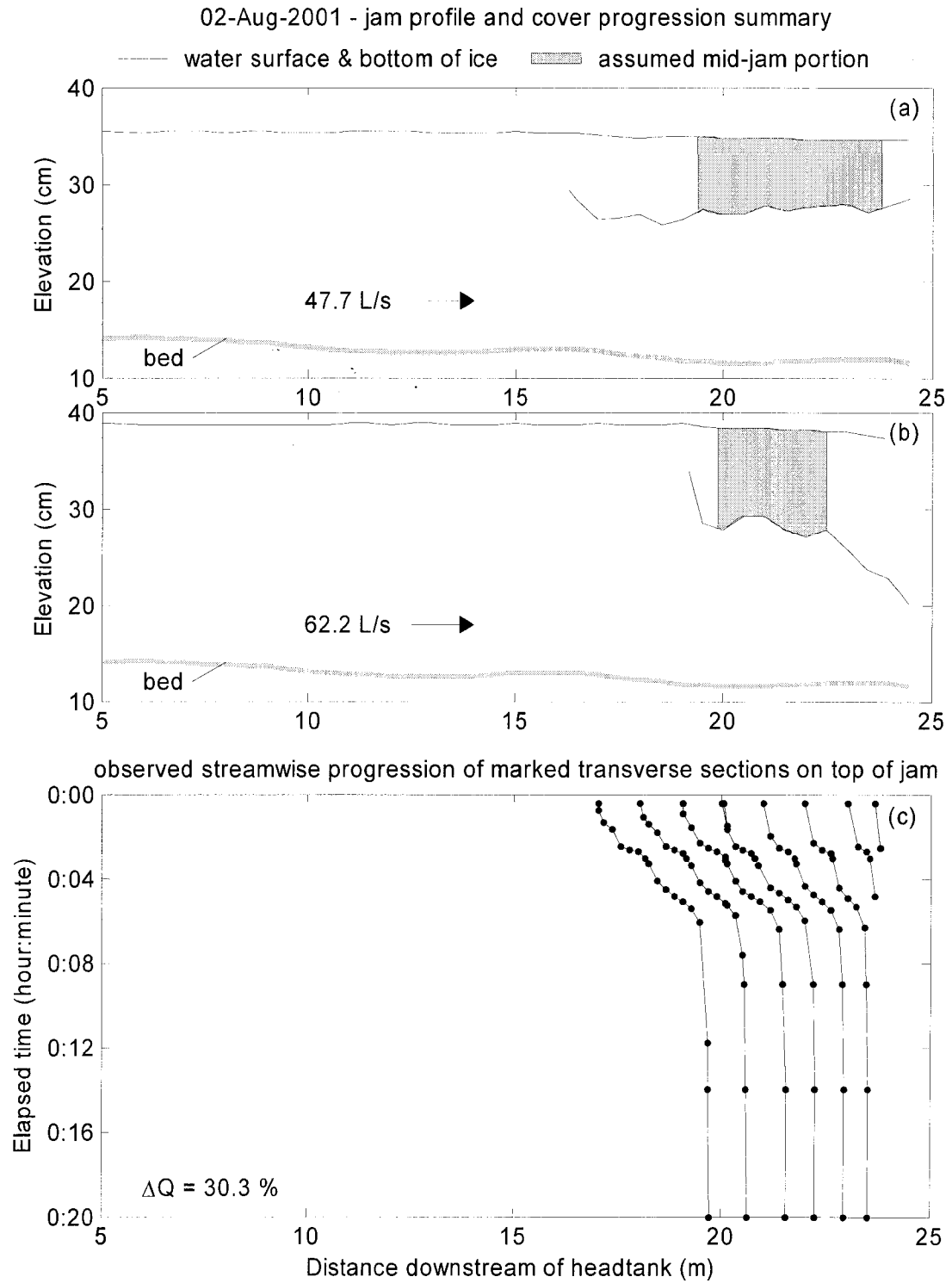
Figure E.94. 02 Aug 2001 initial ice jam profile (a), final ice jam profile (b), and cover progression (c).
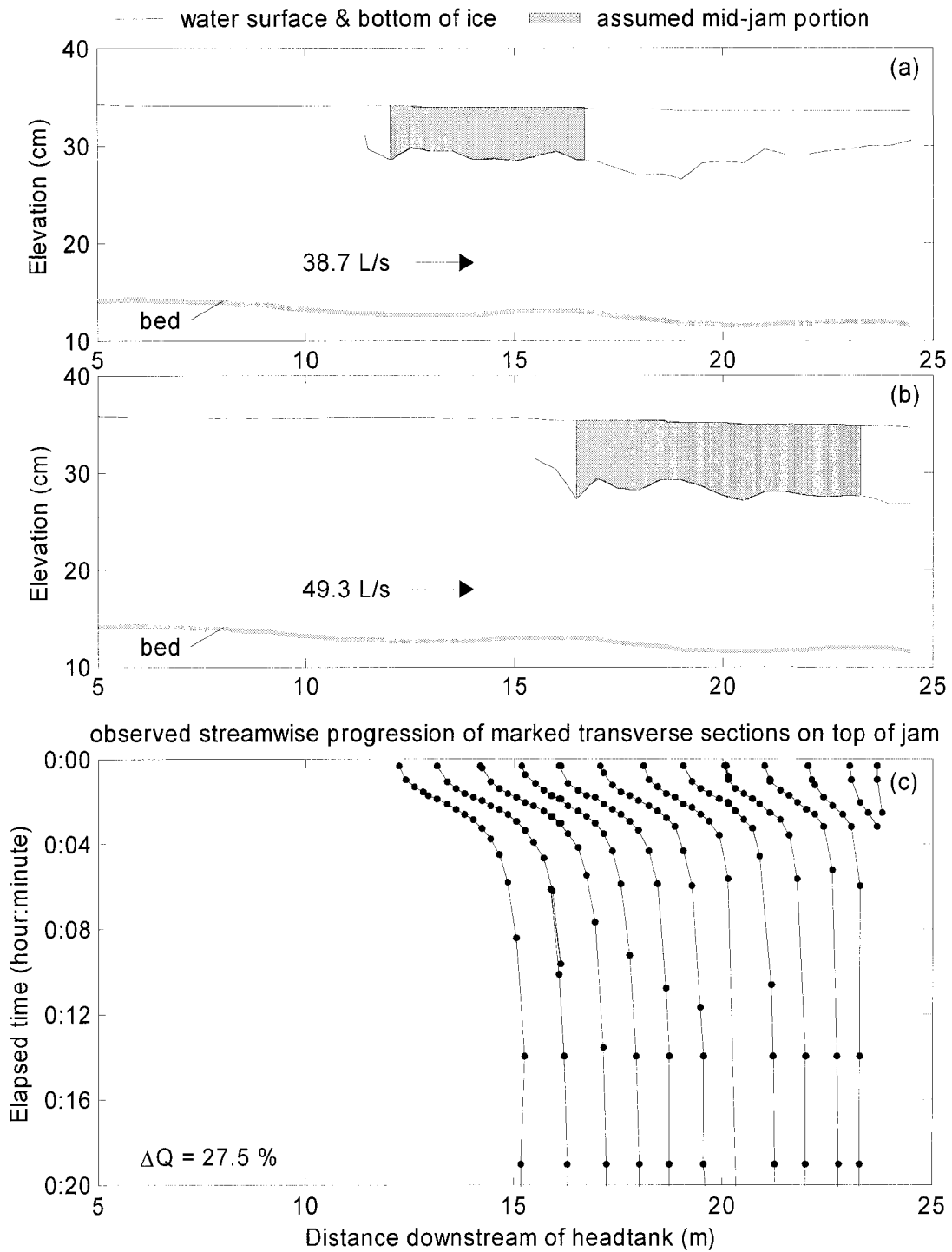
Figure E.95. 03 Aug 2001 initial ice jam profile (a), final ice jam profile (b), and cover progression (c).

307

07-Aug-2001 - jam profile and cover progression summary

—— water surface & bottom of ice ▓▓▓ assumed mid-jam portion
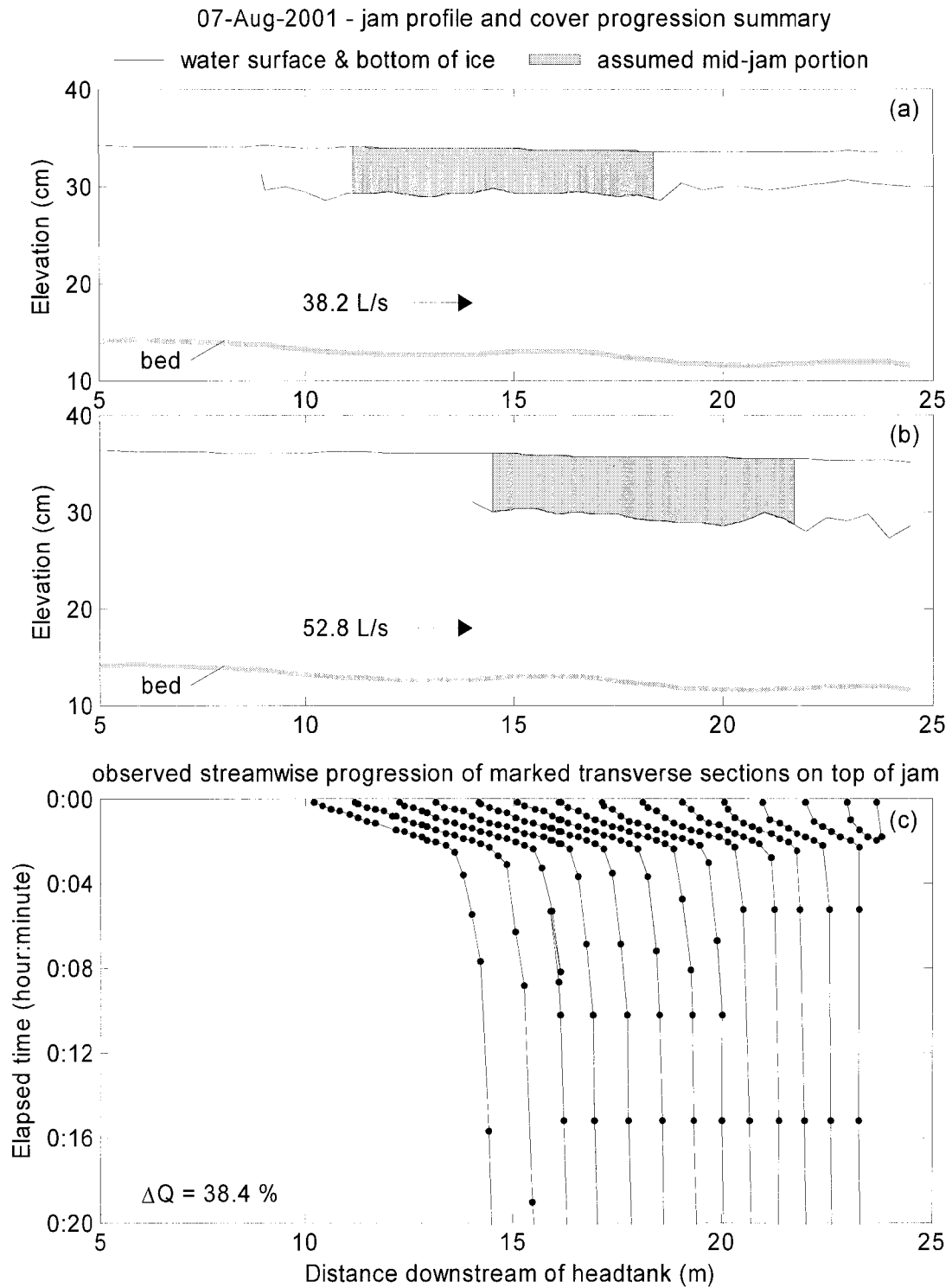
Figure E.96. 07 Aug 2001 initial ice jam profile (a), final ice jam profile (b), and cover progression (c).
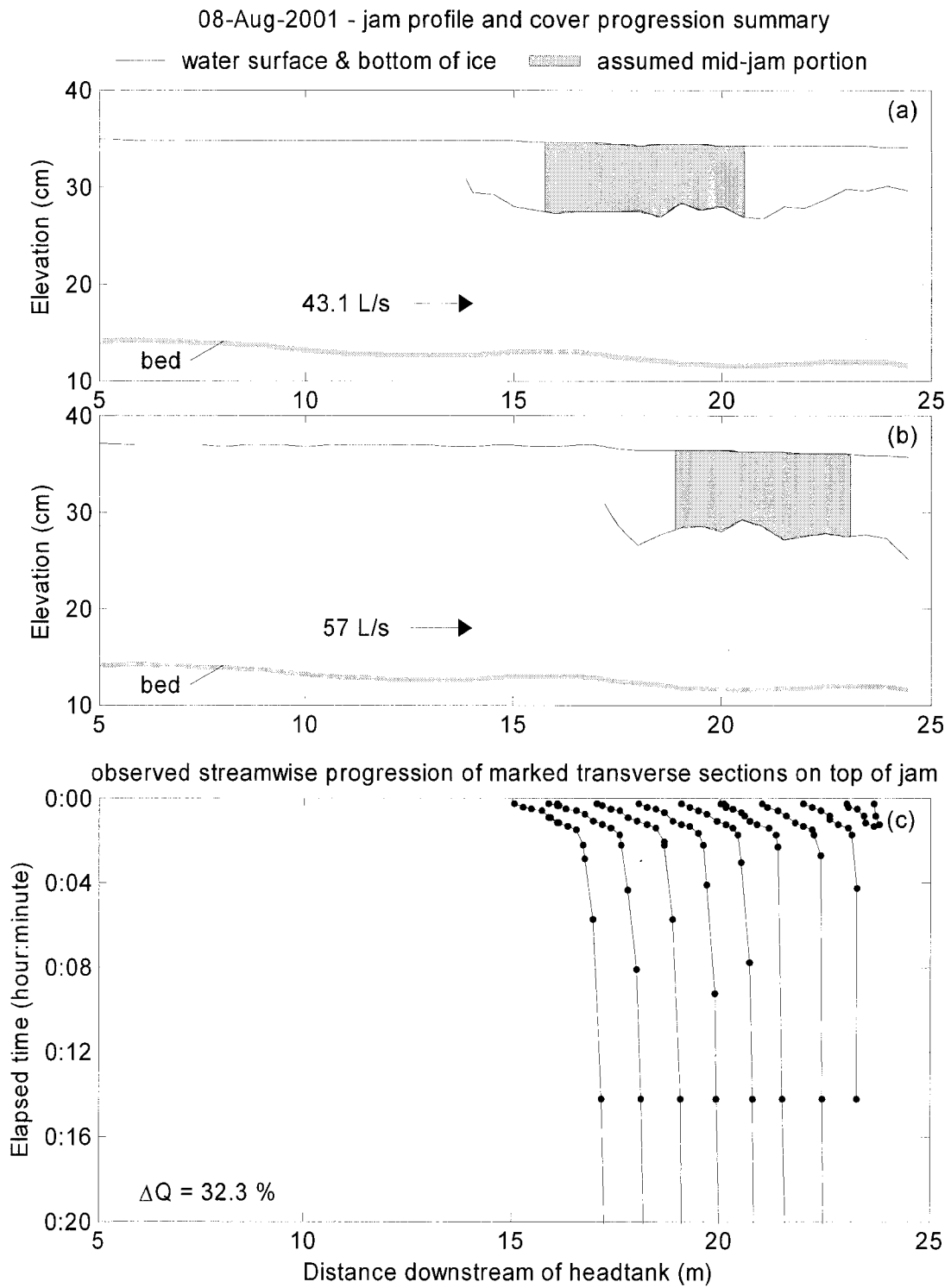
Figure E.97. 08 Aug 2001 initial ice jam profile (a), final ice jam profile (b), and cover progression (c).
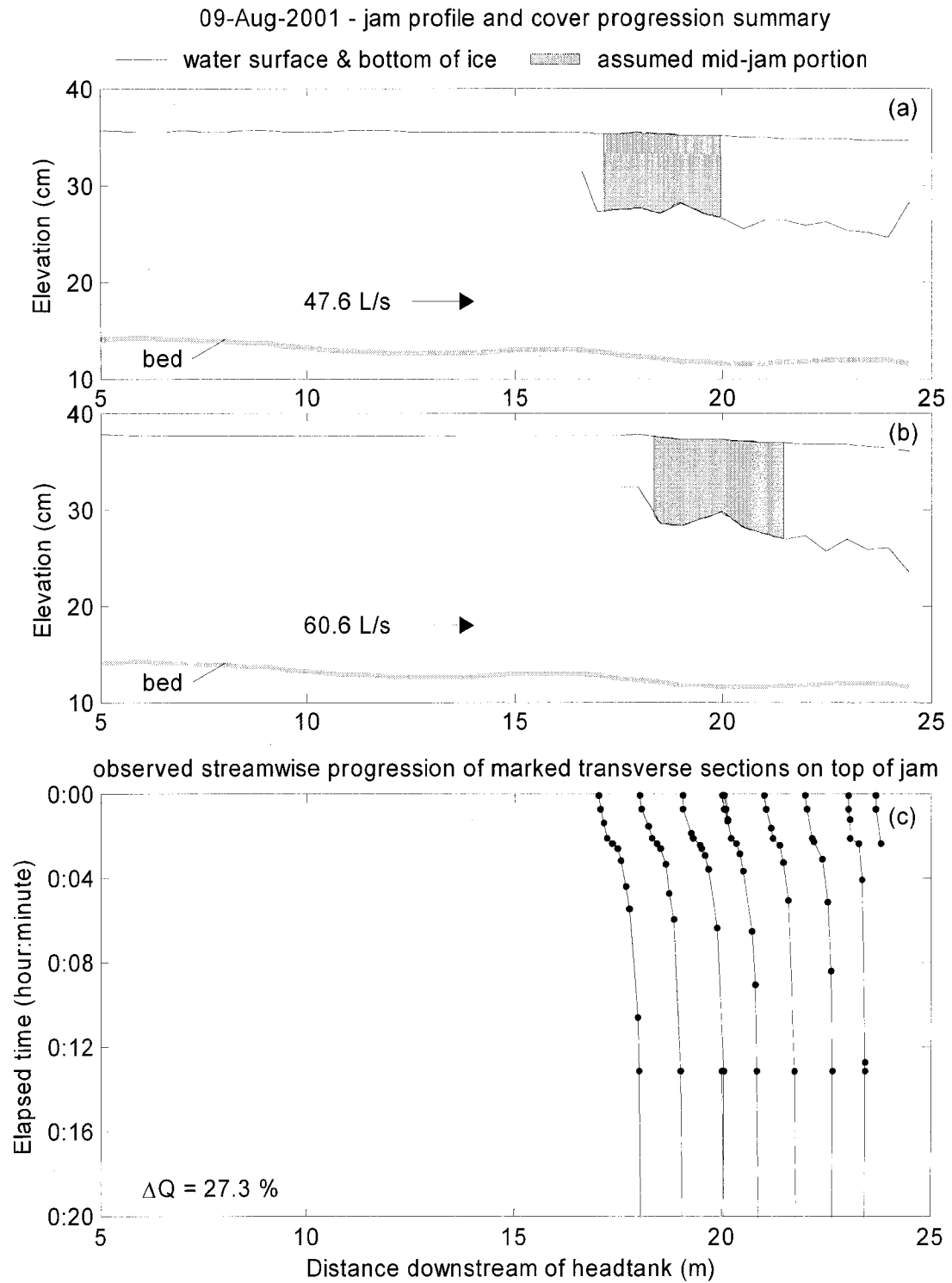
Figure E.98. 09 Aug 2001 initial ice jam profile (a), final ice jam profile (b), and cover progression (c).

310

Figure E.98. 09 Aug 2001 initial ice jam profile (a), final ice jam profile (b), and cover progression (c).

310
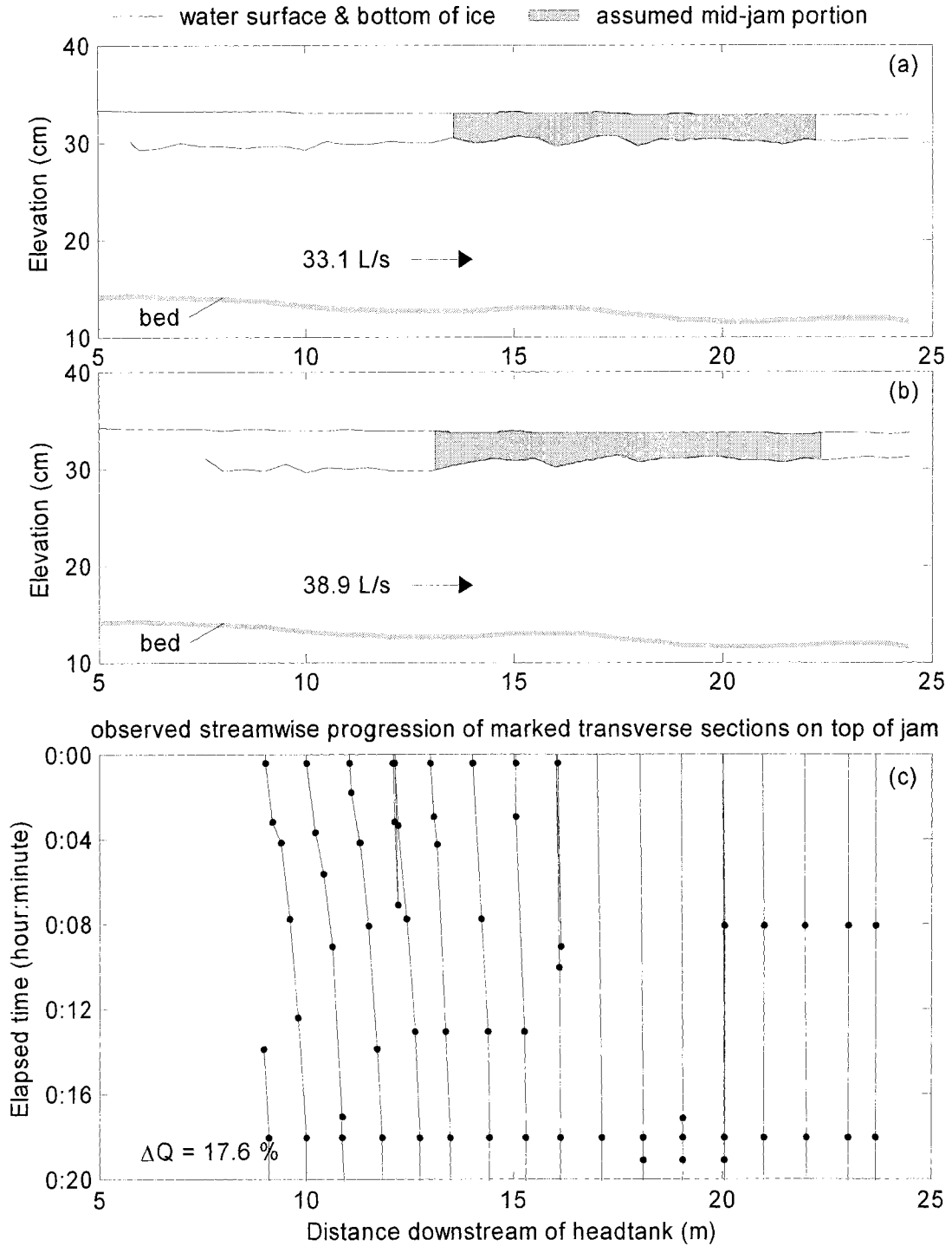
Figure E.99. 10 Aug 2001 initial ice jam profile (a), final ice jam profile (b), and cover progression (c).

311
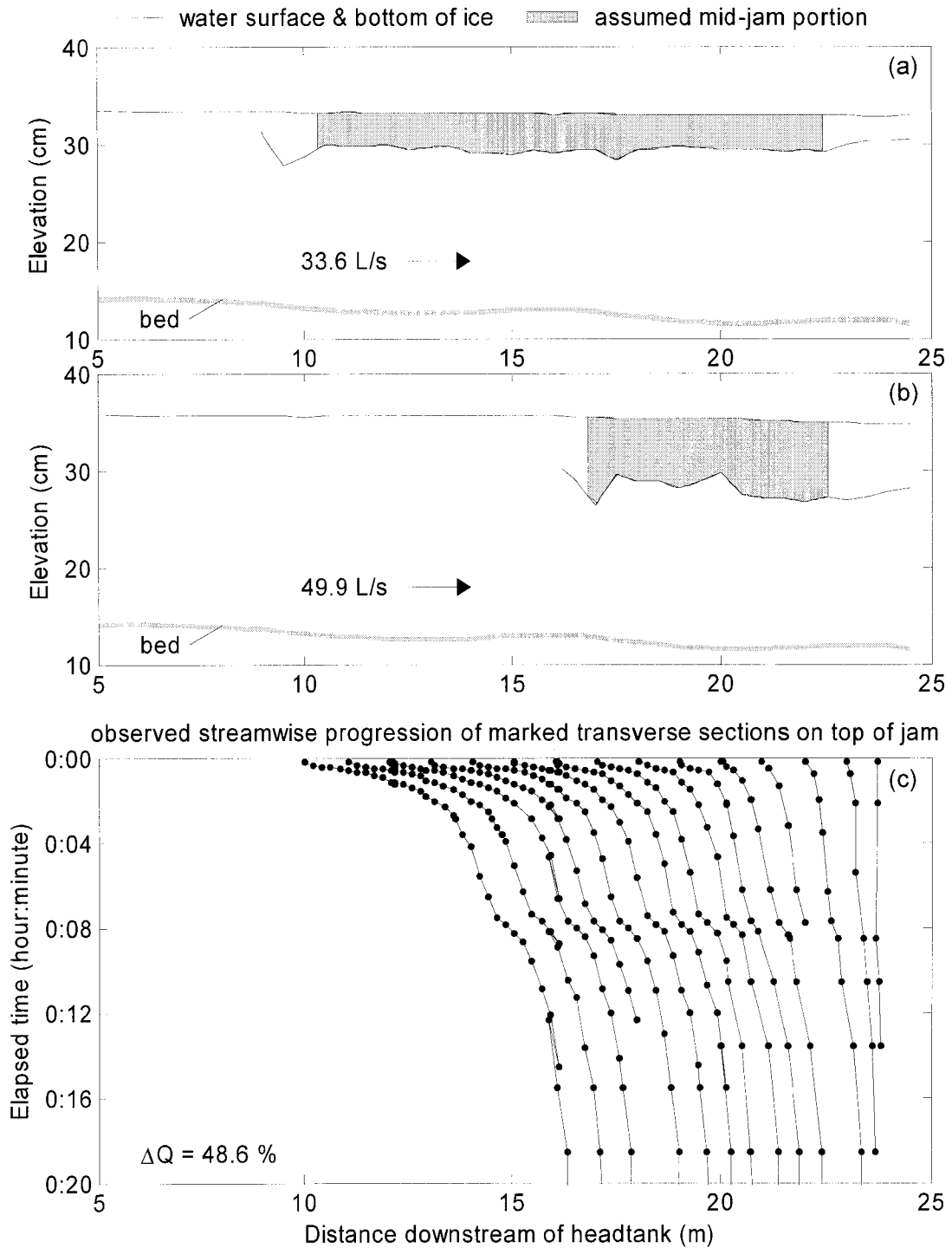
Figure E.100. 13 Aug 2001 initial ice jam profile (a), final ice jam profile (b), and cover progression (c).

312
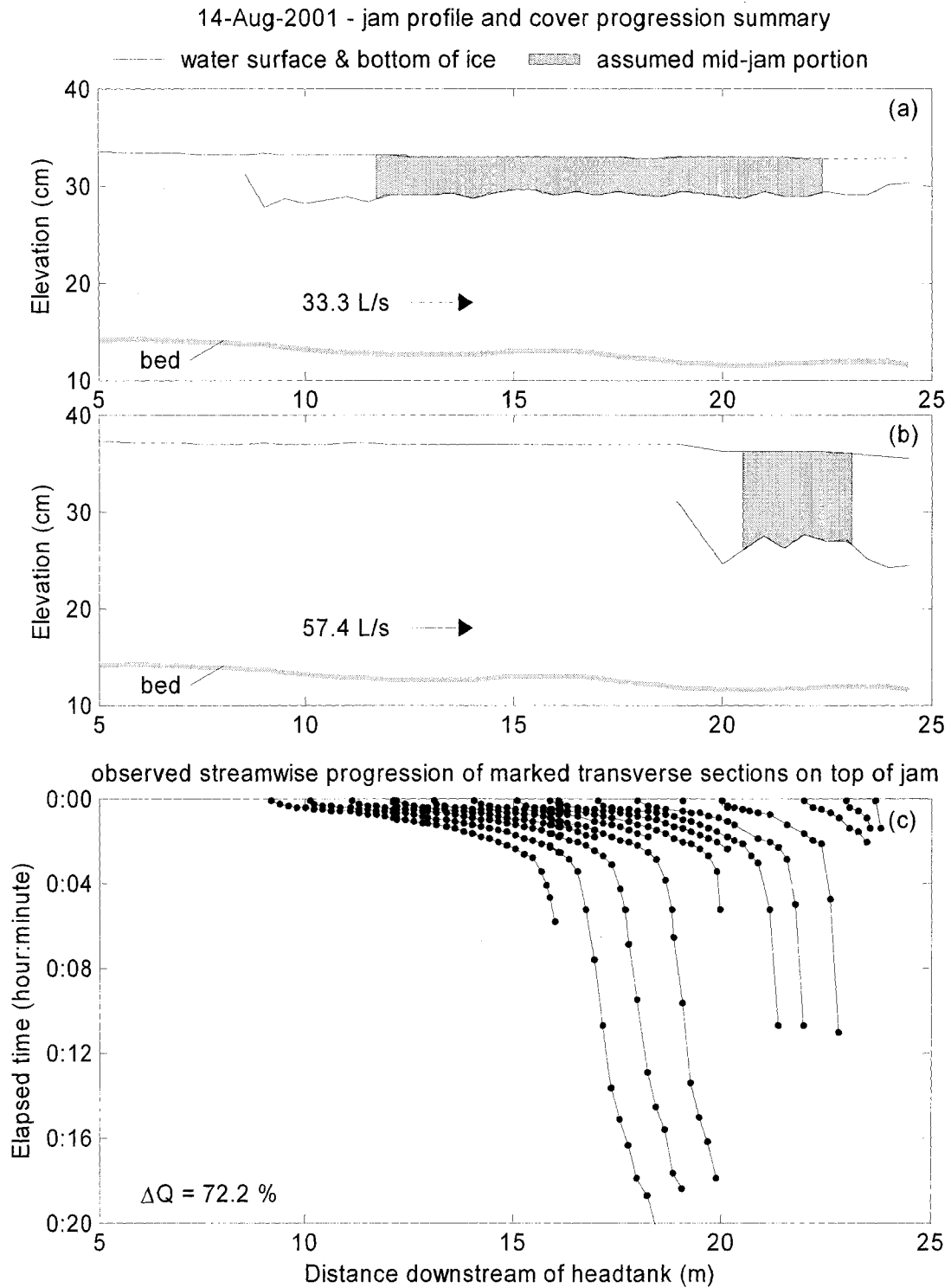
Figure E.101. 14 Aug 2001 initial ice jam profile (a), final ice jam profile (b), and cover progression (c).

313
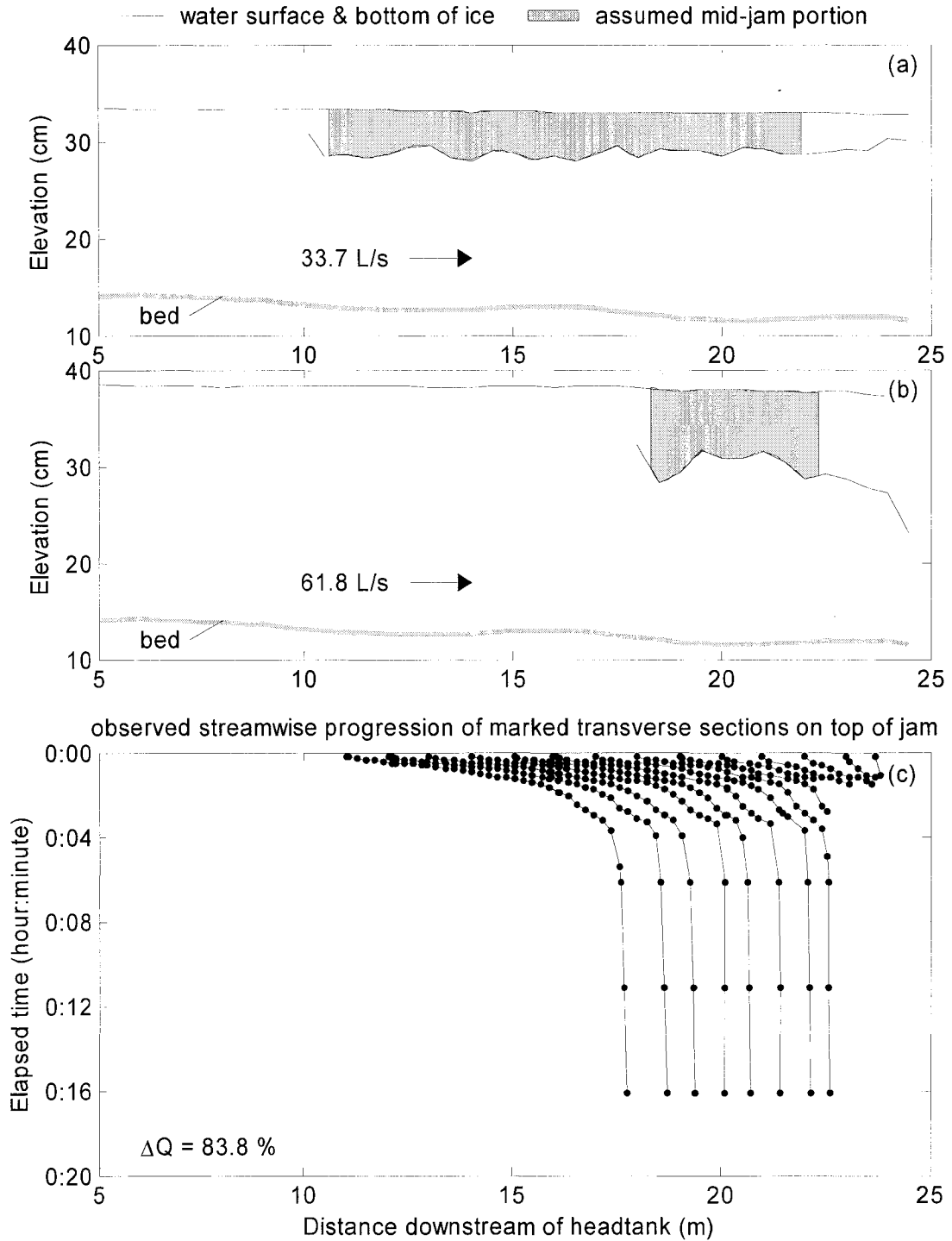
Figure E.102. 15 Aug 2001 initial ice jam profile (a), final ice jam profile (b), and cover progression (c).

314
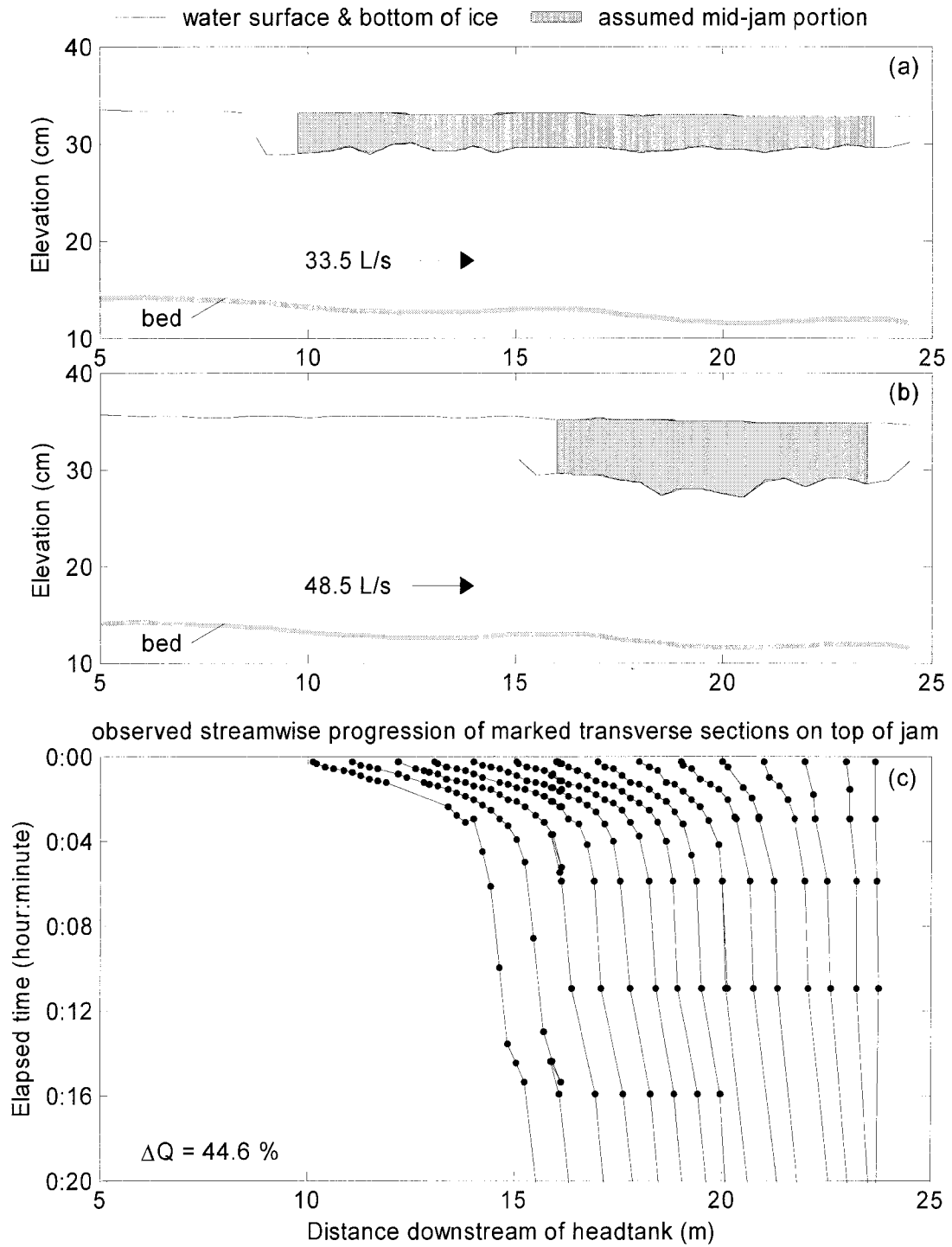
Figure E.103. 16 Aug 2001 initial ice jam profile (a), final ice jam profile (b), and cover progression (c).

315
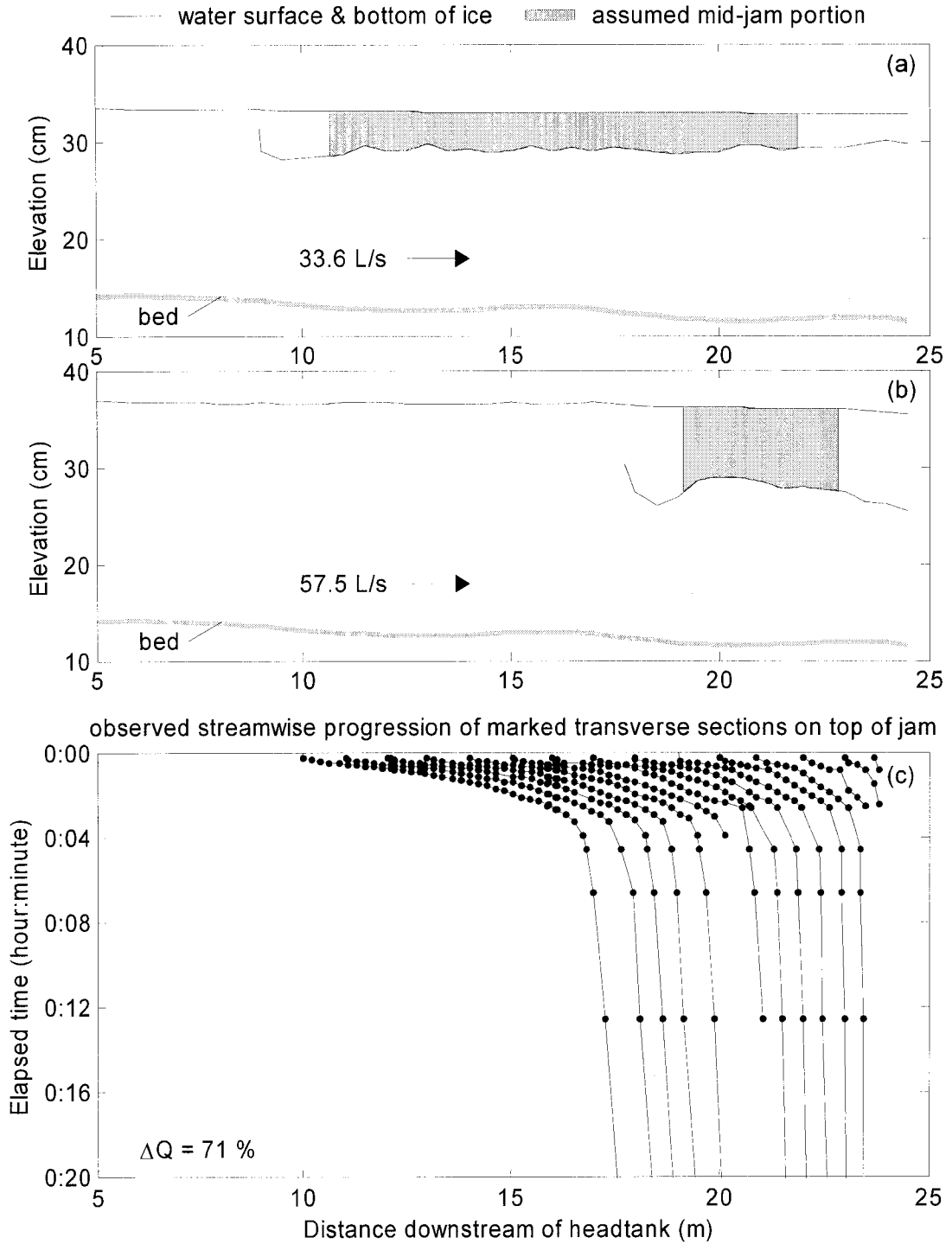
Figure E.104. 17 Aug 2001 initial ice jam profile (a), final ice jam profile (b), and cover progression (c).

316
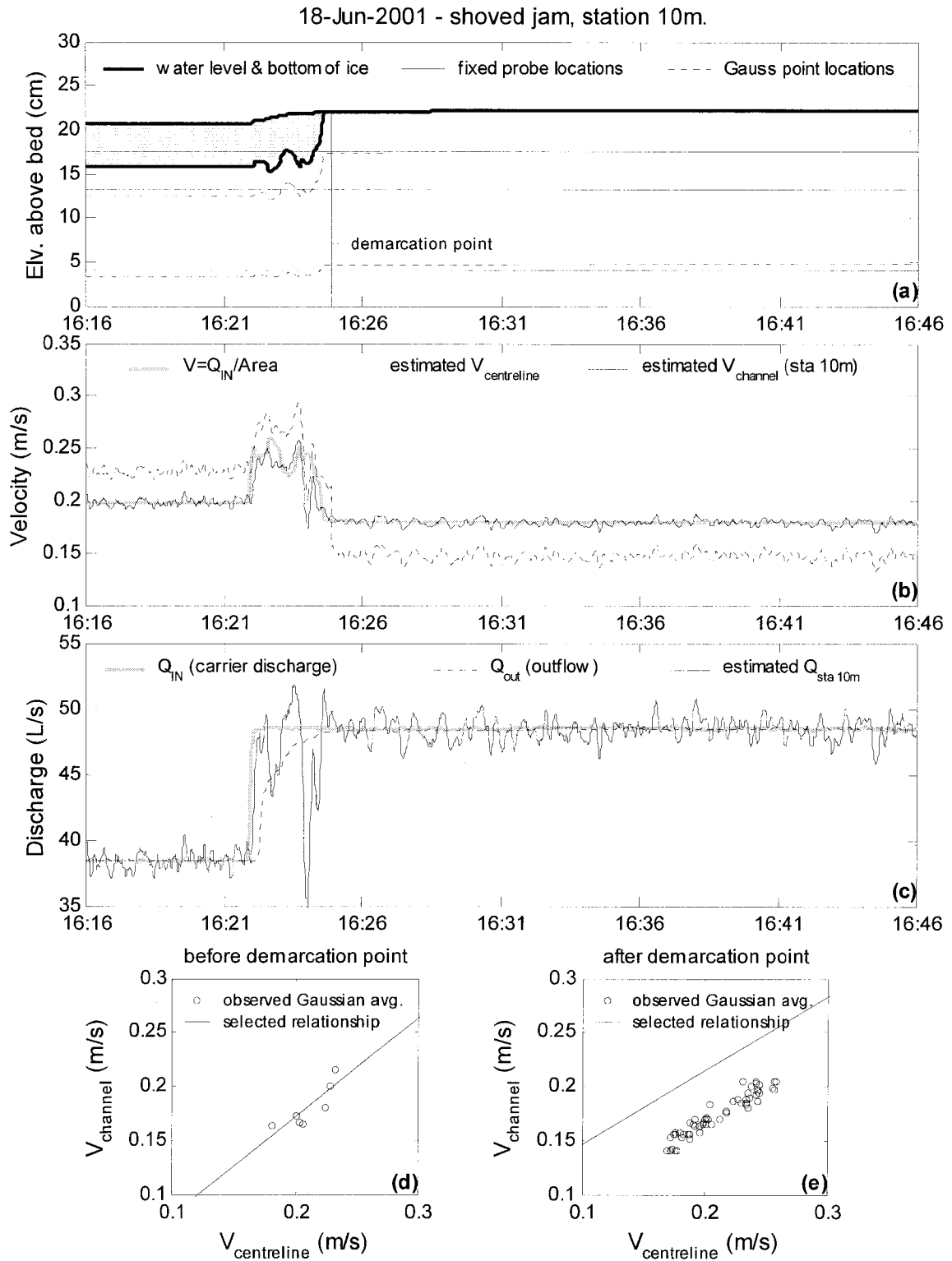
Figure E.105. Summary of continuous observations for a shoved jam taken at Station 10m – test date: 18 June 2001.
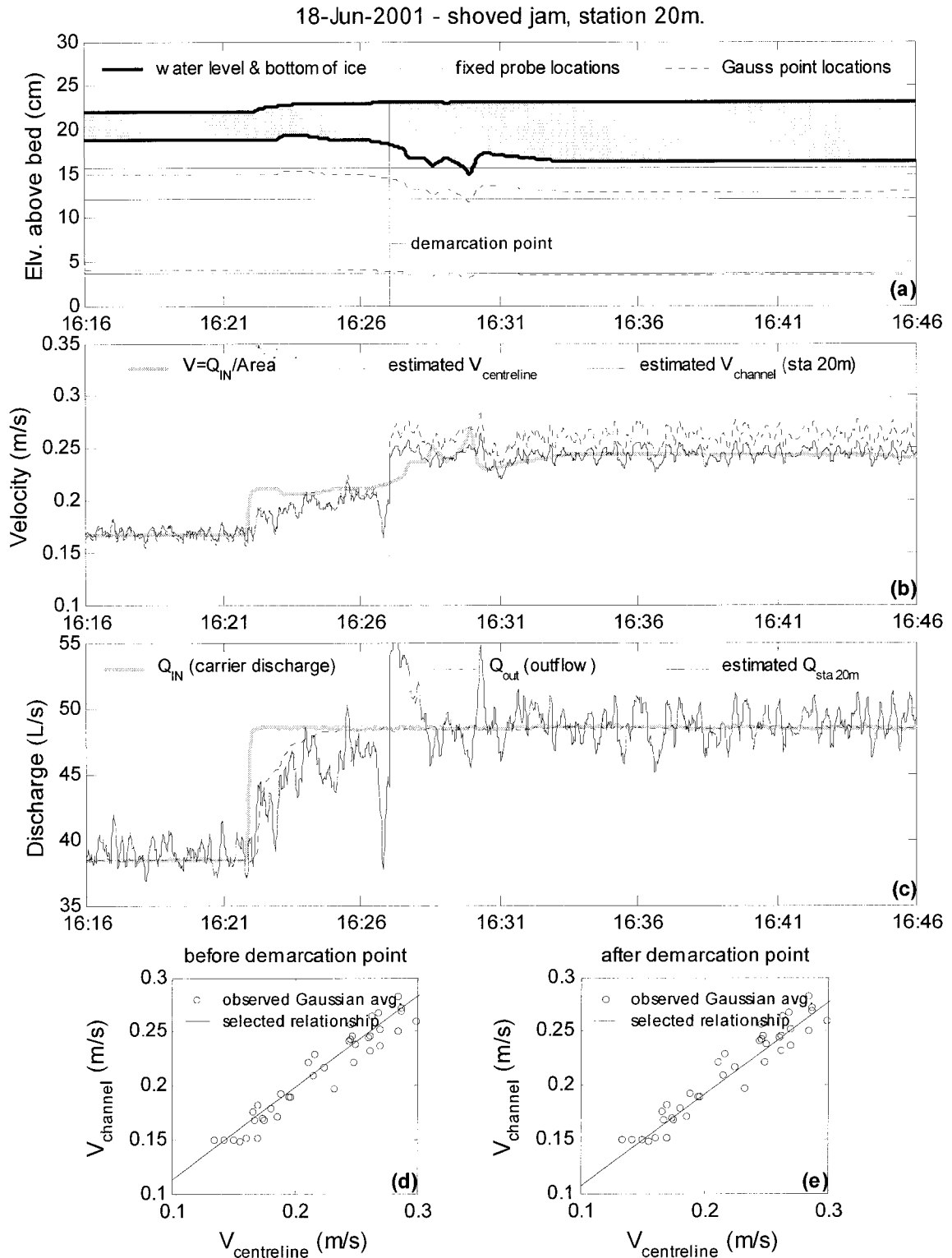
Figure E.106. Summary of continuous observations for a shoved jam taken at Station 20m – test date: 18 June 2001.

318
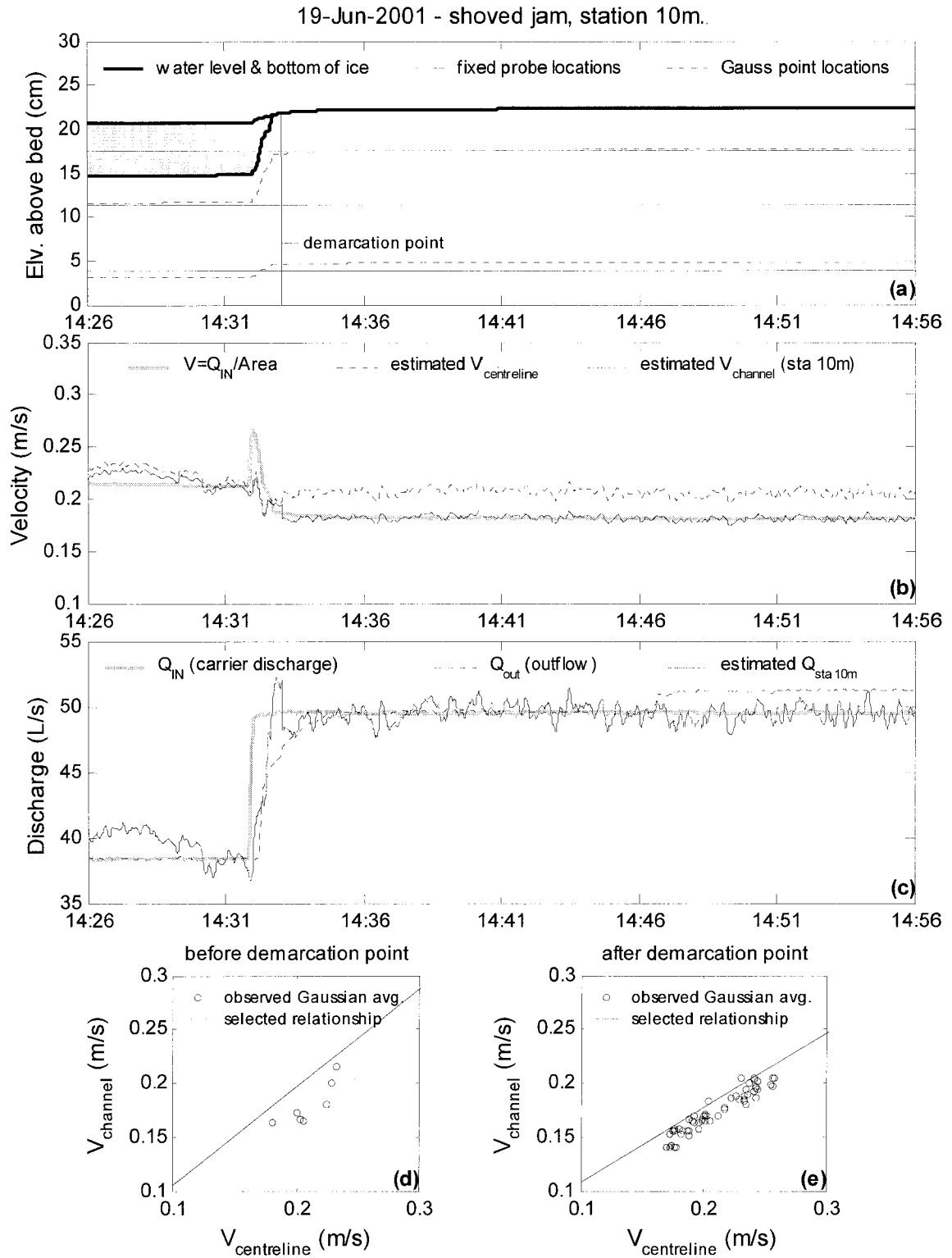
Figure E.107.   Summary of continuous observations for a shoved jam taken at Station 10m – test date: 19 June 2001.

19-Jun-2001 - shoved jam, station 20m.

(a) Elv. above bed (cm)
— water level & bottom of ice   — fixed probe locations   - - - Gauss point locations
demarcation point

(b) Velocity (m/s)
$V=Q_{IN}/Area$ estimated $V_{centreline}$ estimated $V_{channel}$ (sta 20m)

(c) Discharge (L/s)
Q_{IN} (carrier discharge) Q_{out} (outflow)   estimated $Q_{sta 20m}$

(d) before demarcation point
$V_{channel}$ (m/s) vs $V_{centreline}$ (m/s)
o observed Gaussian avg
- - selected relationship

(e) after demarcation point
$V_{channel}$ (m/s) vs $V_{centreline}$ (m/s)
o observed Gaussian avg
- - selected relationship

Figure E.108.   Summary of continuous observations for a shoved jam taken at Station 20m – test date: 19 June 2001.

320
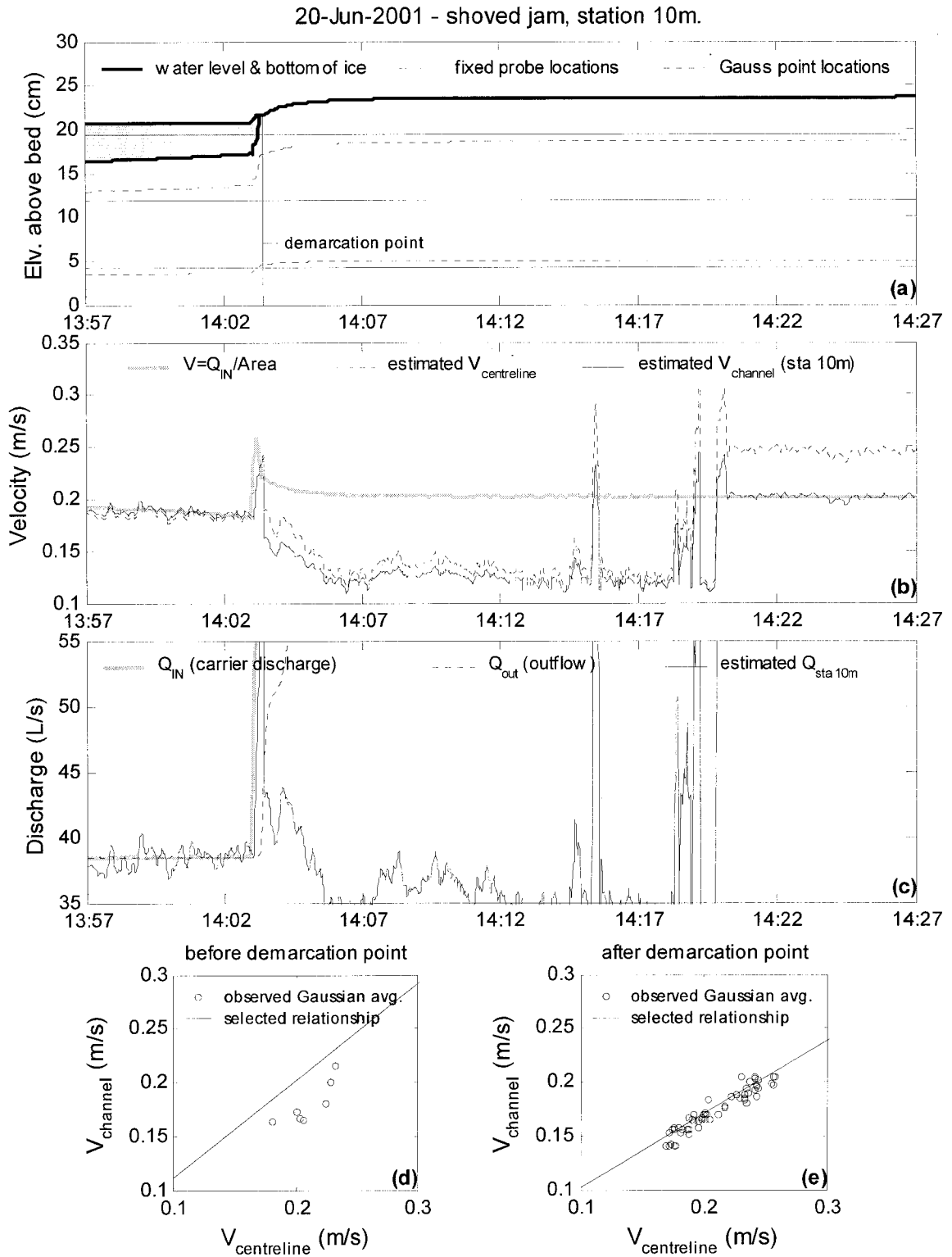
Figure E.109. Summary of continuous observations for a shoved jam taken at Station 10m – test date: 20 June 2001.
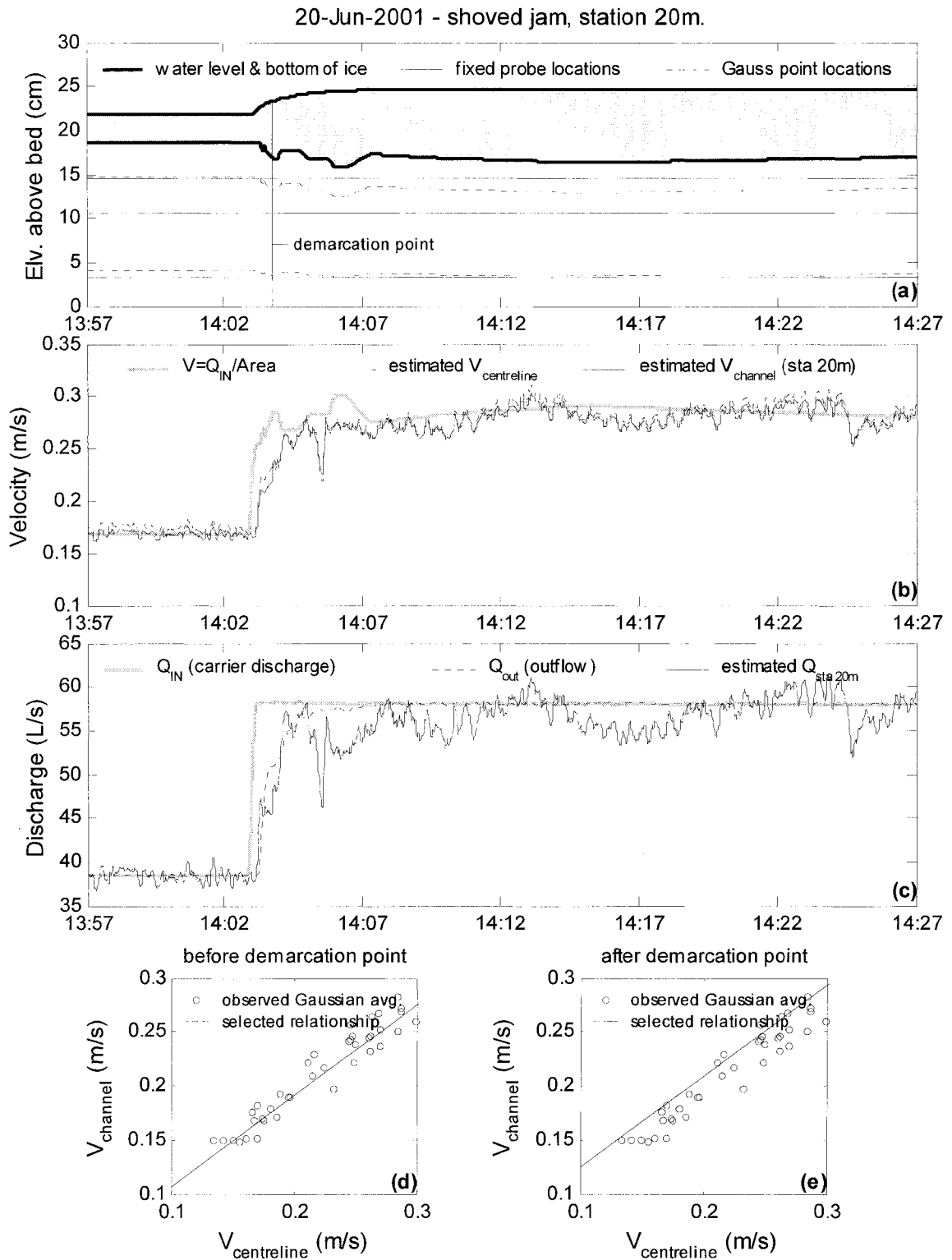
Figure E.110. Summary of continuous observations for a shoved jam taken at Station 20m – test date: 20 June 2001.
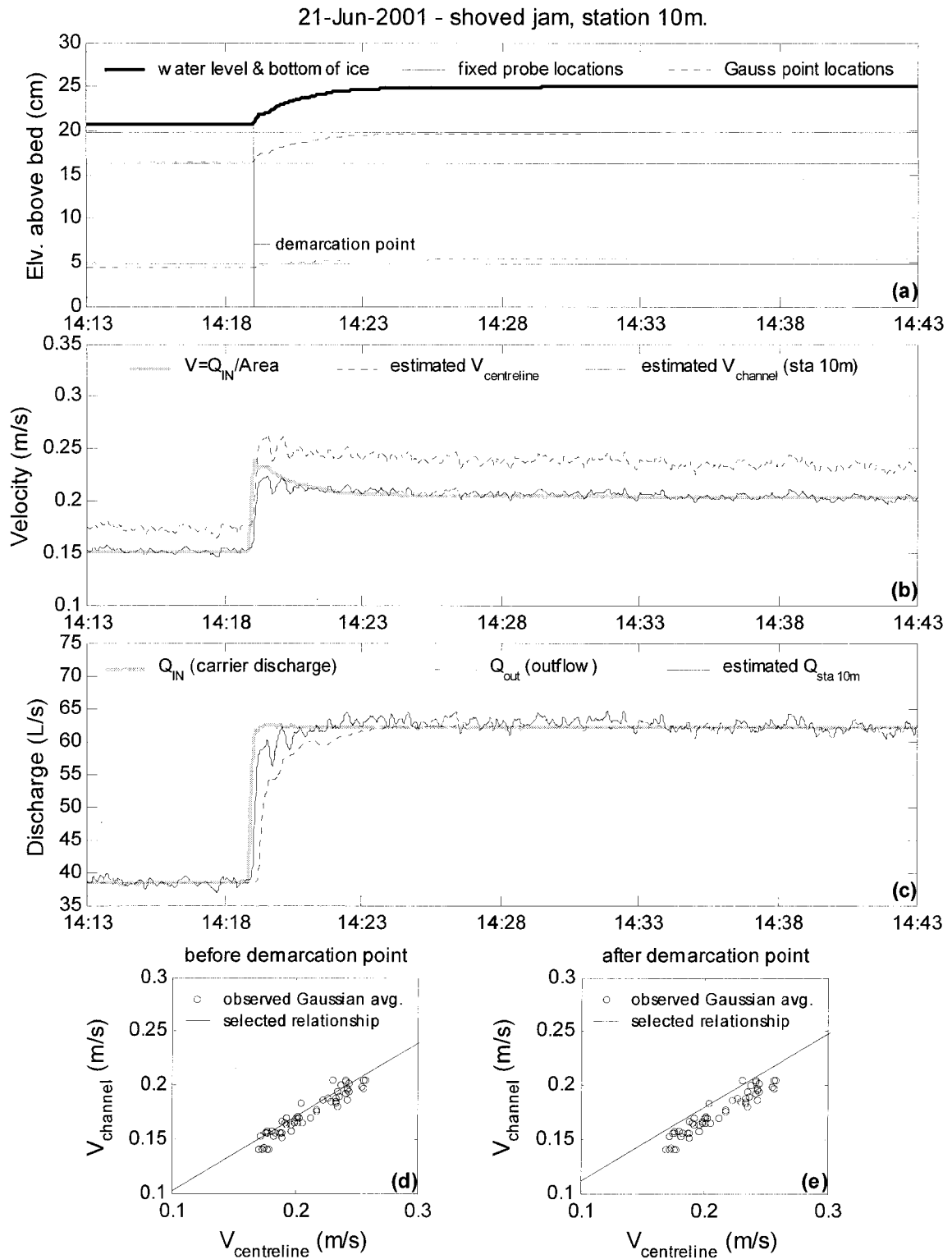
Figure E.111. Summary of continuous observations for a shoved jam taken at Station 10m – test date: 21 June 2001.

323
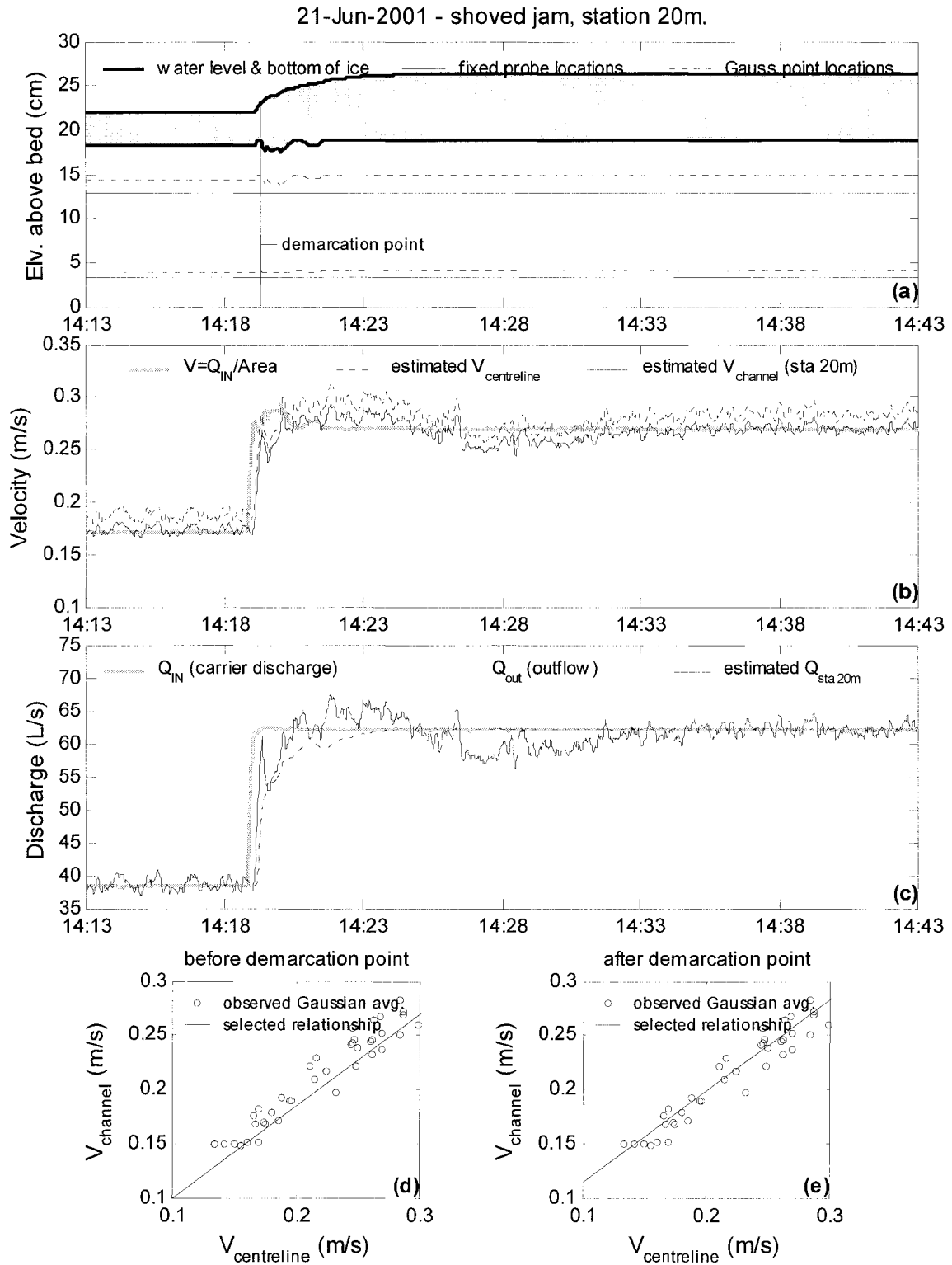
Figure E.112. Summary of continuous observations for a shoved jam taken at Station 20m – test date: 21 June 2001.
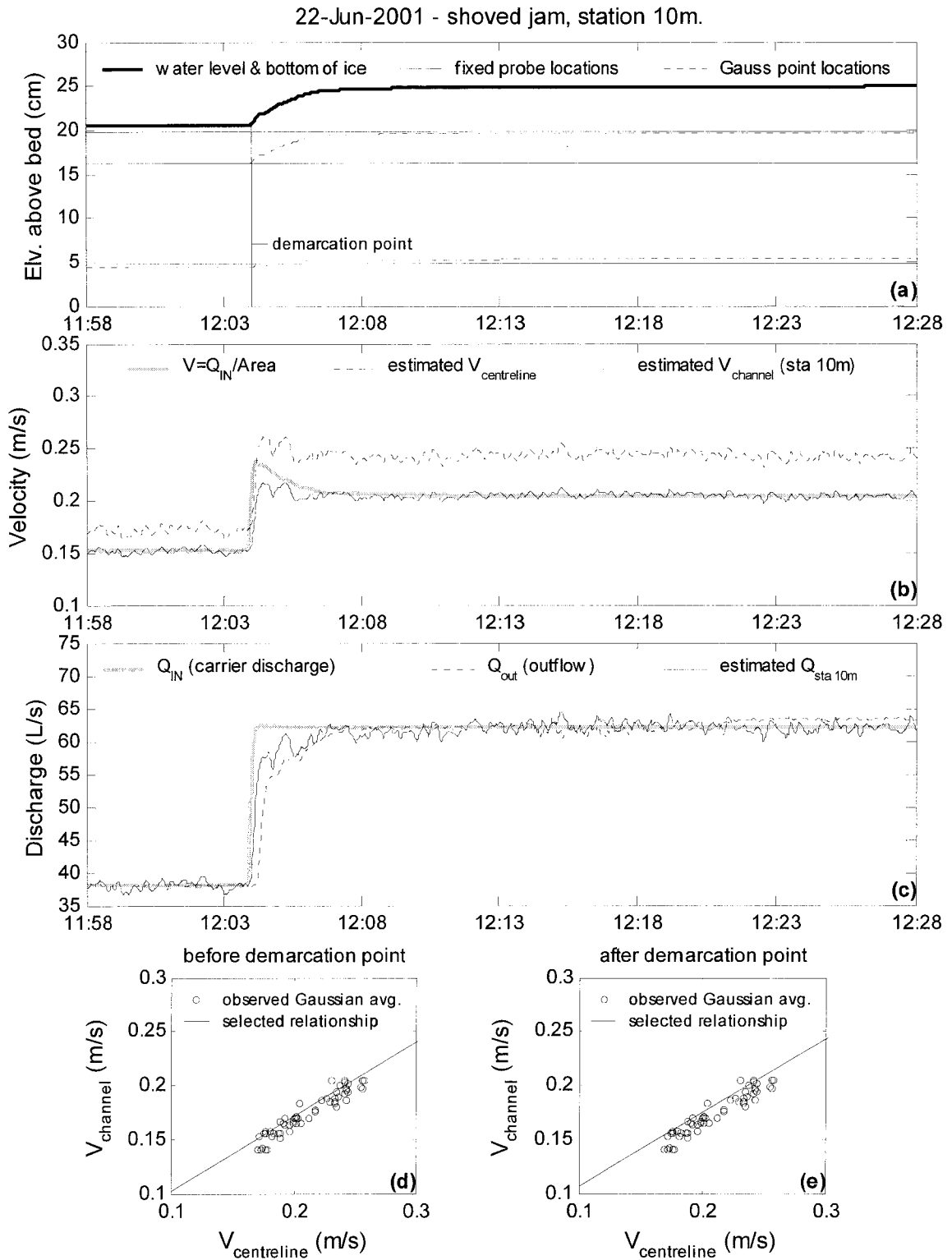
Figure E.113. Summary of continuous observations for a shoved jam taken at Station 10m – test date: 22 June 2001.

22-Jun-2001 - shoved jam, station 20m.
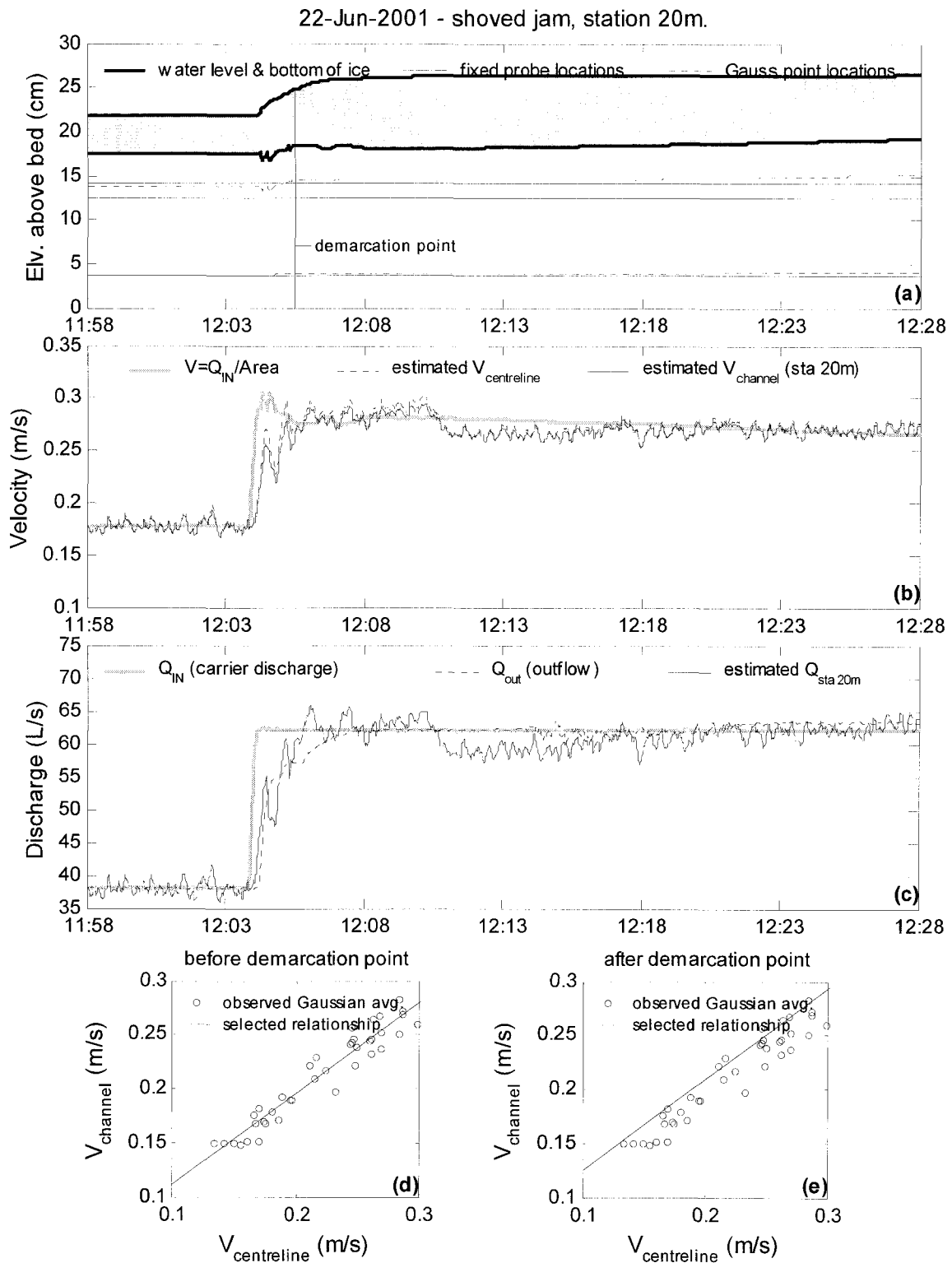
Figure E.114. Summary of continuous observations for a shoved jam taken at Station 20m – test date: 22 June 2001.
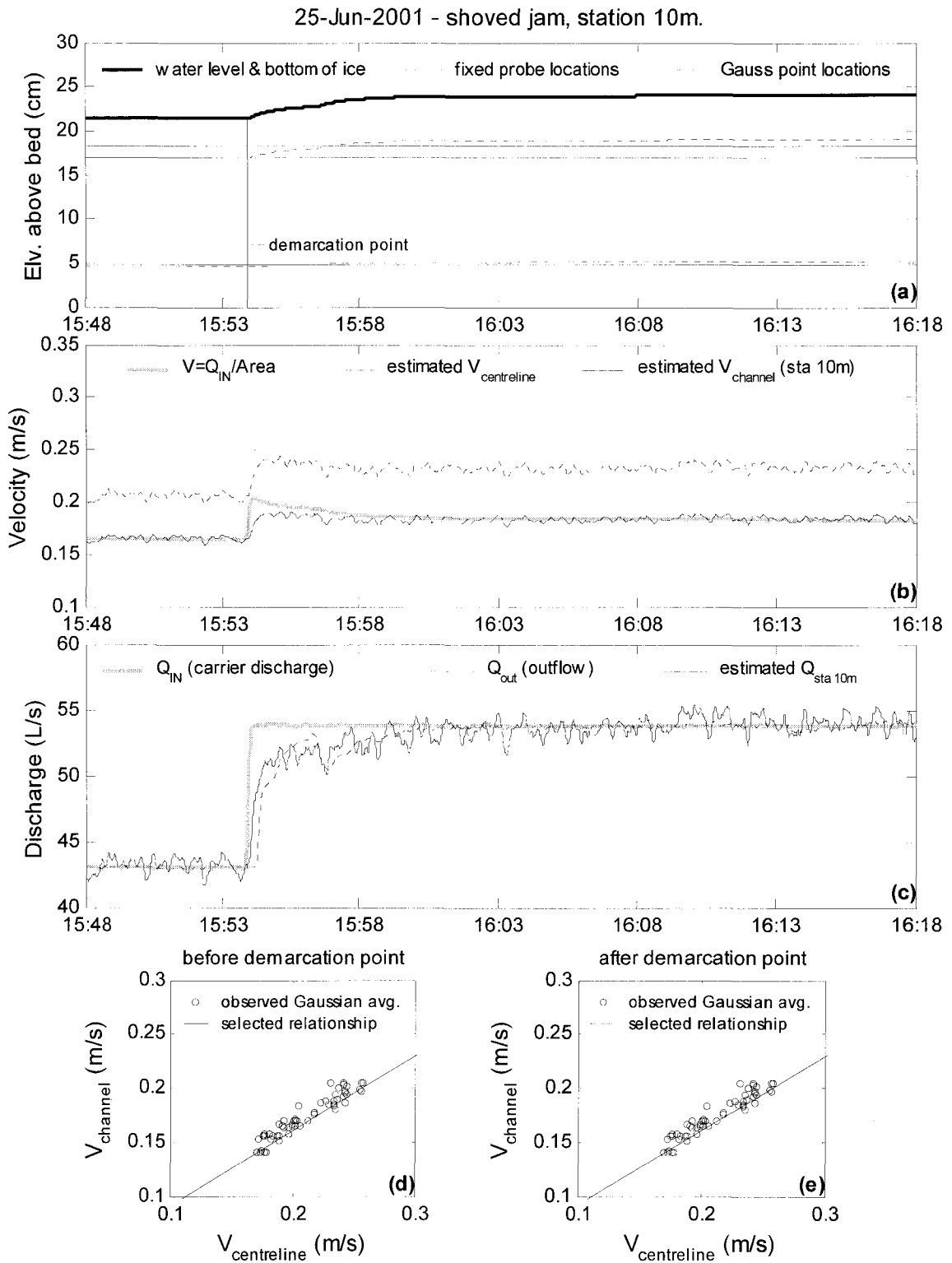
Figure E.115. Summary of continuous observations for a shoved jam taken at Station 10m – test date: 25 June 2001.

327
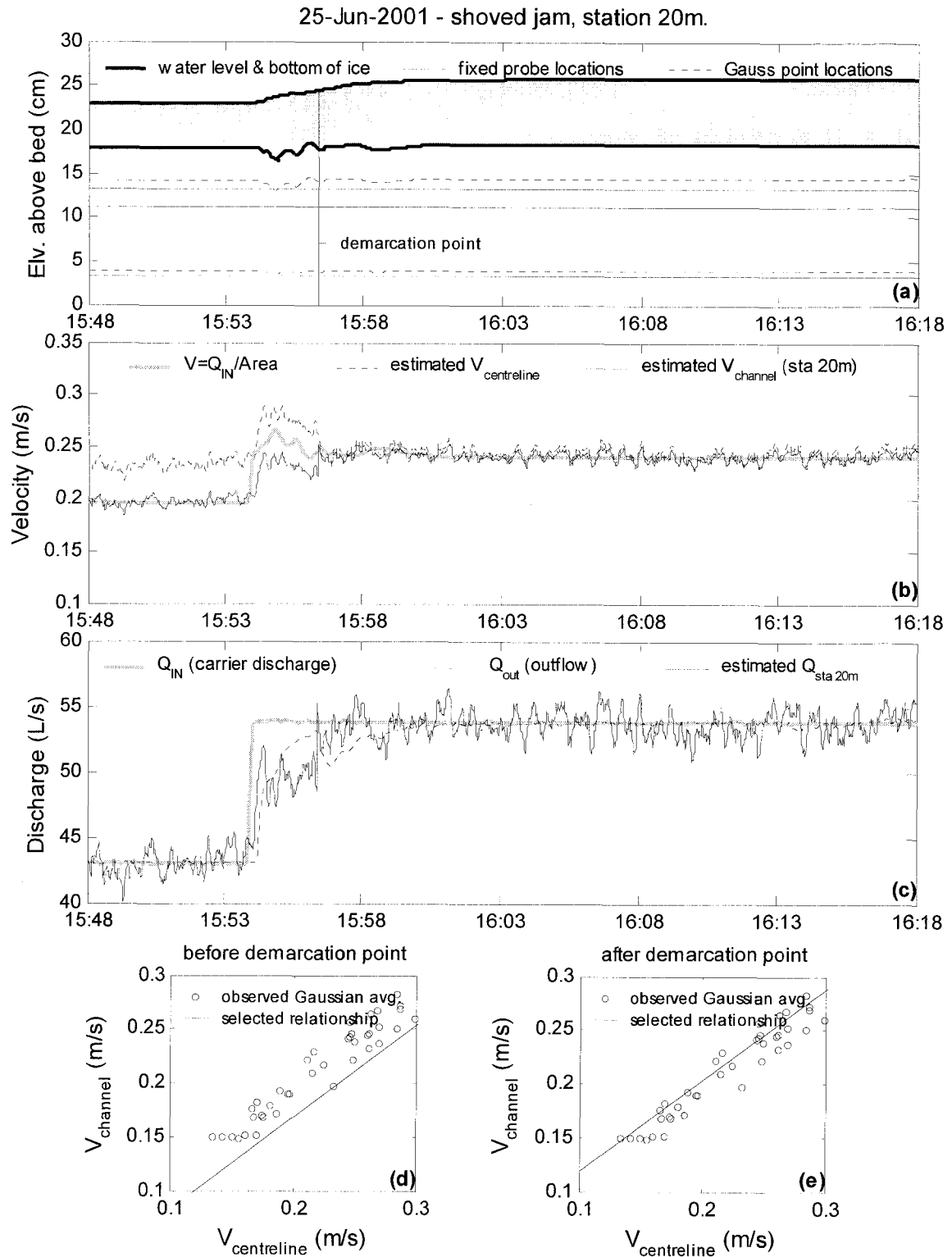
Figure E.116. Summary of continuous observations for a shoved jam taken at Station 20m – test date: 25 June 2001.

328
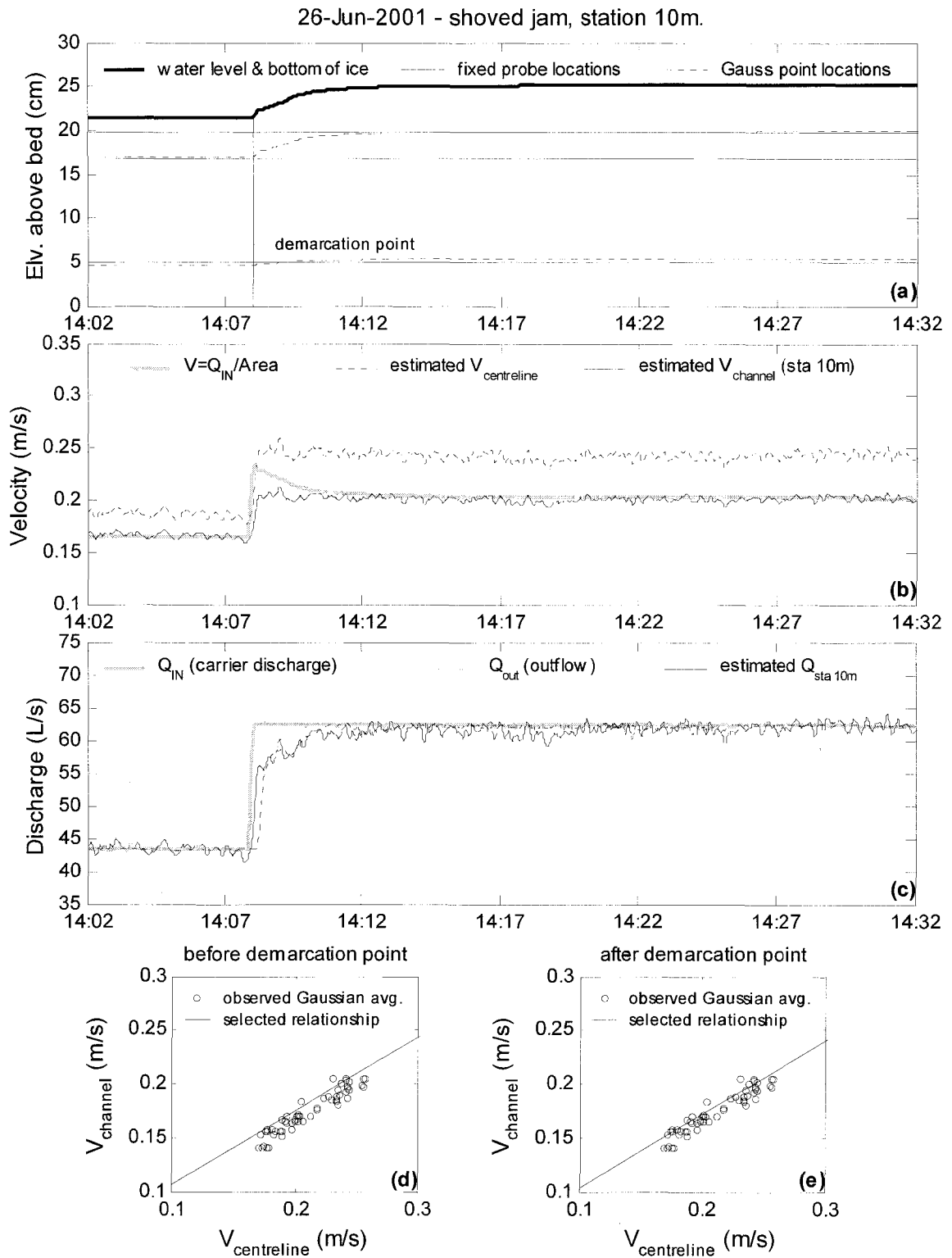
Figure E.117.   Summary of continuous observations for a shoved jam taken at Station 10m – test date: 26 June 2001.

329

26-Jun-2001 - shoved jam, station 20m.

(a) — water level & bottom of ice ········ fixed probe locations — — Gauss point locations

Elv. above bed (cm): 30, 25, 20, 15, 10, 5, 0

demarcation point

14:02 14:07 14:12 14:17 14:22 14:27 14:32

(b) ········ V=Q_{IN}/Area — — — estimated $V_{centreline}$ ········ estimated $V_{channel}$ (sta 20m)

Velocity (m/s): 0.4, 0.35, 0.3, 0.25, 0.2, 0.15

14:02 14:07 14:12 14:17 14:22 14:27 14:32

(c) ········ Q_{IN} (carrier discharge) — — — Q_{out} (outflow) —— estimated $Q_{sta\,20m}$

Discharge (L/s): 75, 70, 65, 60, 55, 50, 45, 40

14:02 14:07 14:12 14:17 14:22 14:27 14:32

before demarcation point

(d) o observed Gaussian avg
     --- selected relationship

$V_{channel}$ (m/s): 0.3, 0.25, 0.2, 0.15, 0.1

$V_{centreline}$ (m/s): 0.1, 0.2, 0.3

after demarcation point

(e) o observed Gaussian avg
     — selected relationship

$V_{channel}$ (m/s): 0.3, 0.25, 0.2, 0.15, 0.1

$V_{centreline}$ (m/s): 0.1, 0.2, 0.3

Figure E.118.   Summary of continuous observations for a shoved jam taken at Station 20m – test date: 26 June 2001.

330
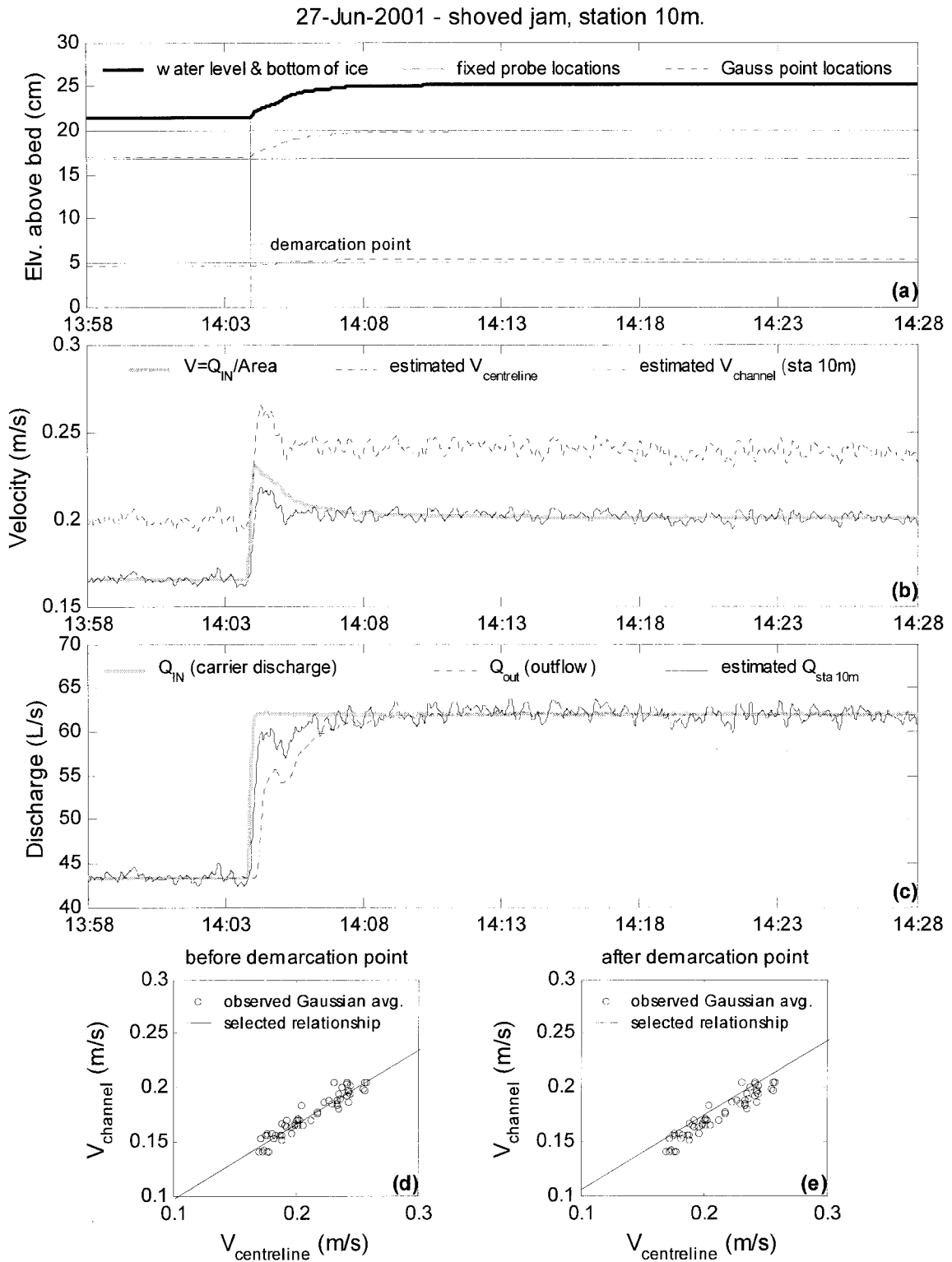
Figure E.119. Summary of continuous observations for a shoved jam taken at Station 10m – test date: 27 June 2001.

331
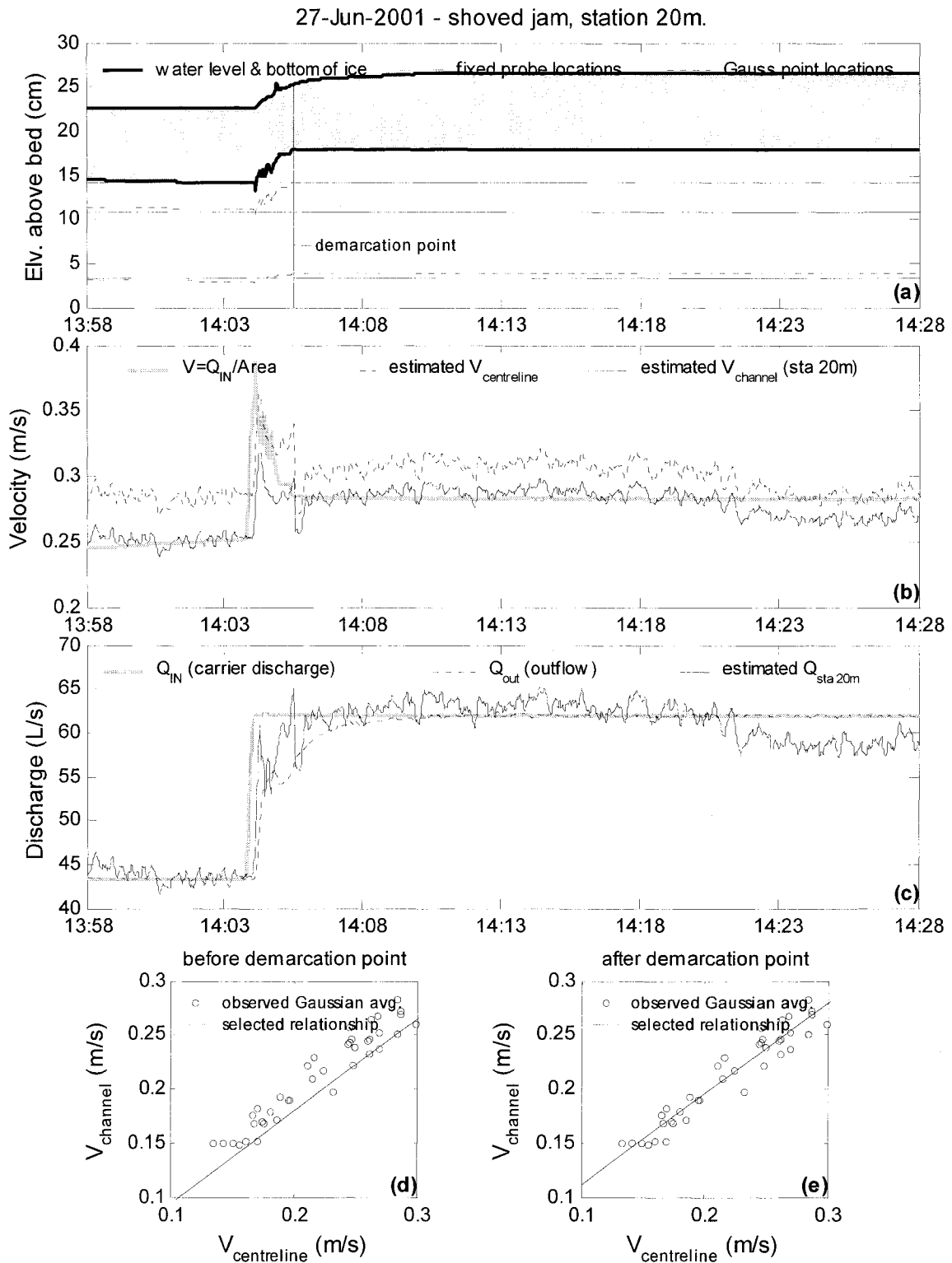
Figure E.120. Summary of continuous observations for a shoved jam taken at Station 20m – test date: 27 June 2001.

332
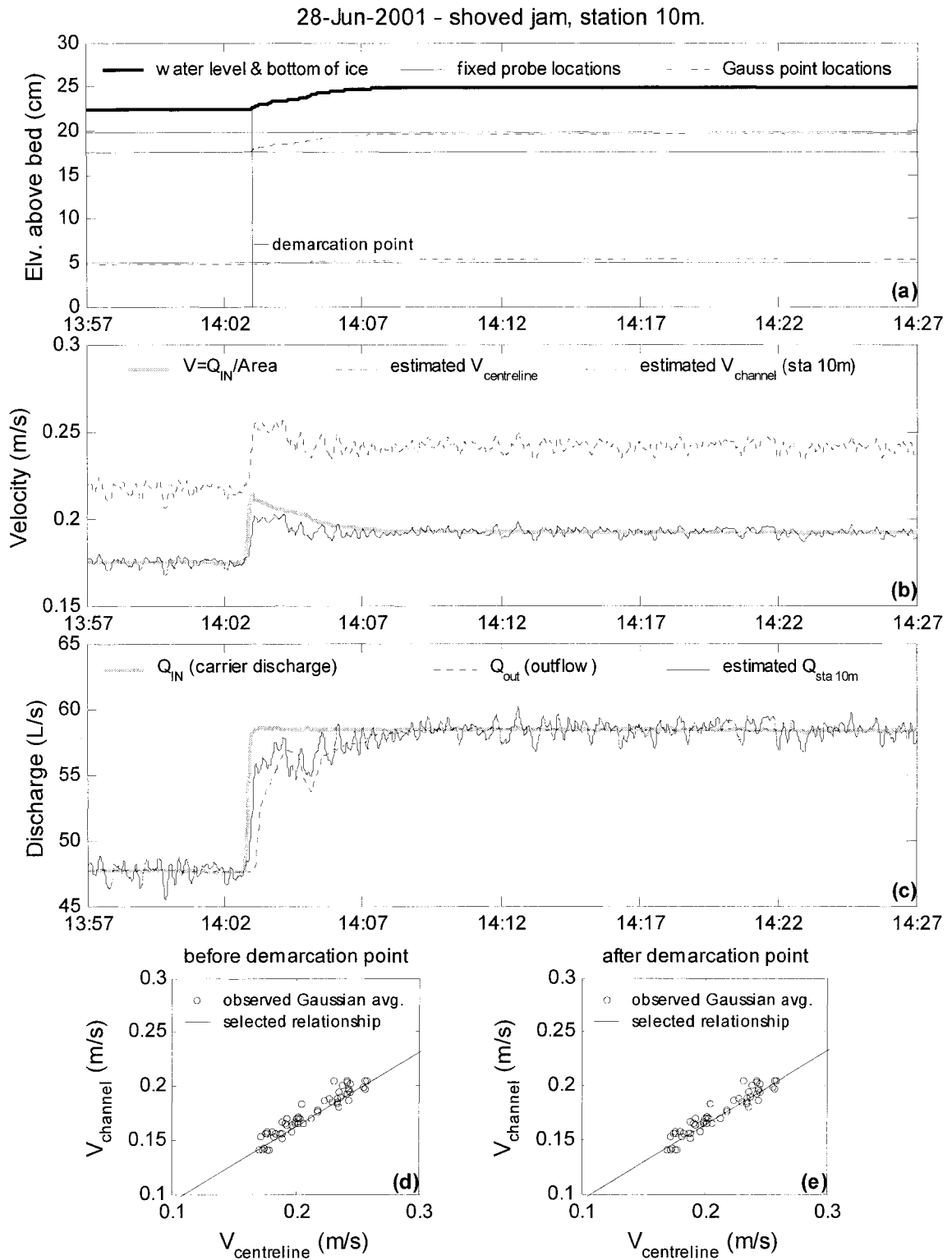
Figure E.121. Summary of continuous observations for a shoved jam taken at Station 10m – test date: 28 June 2001.

333
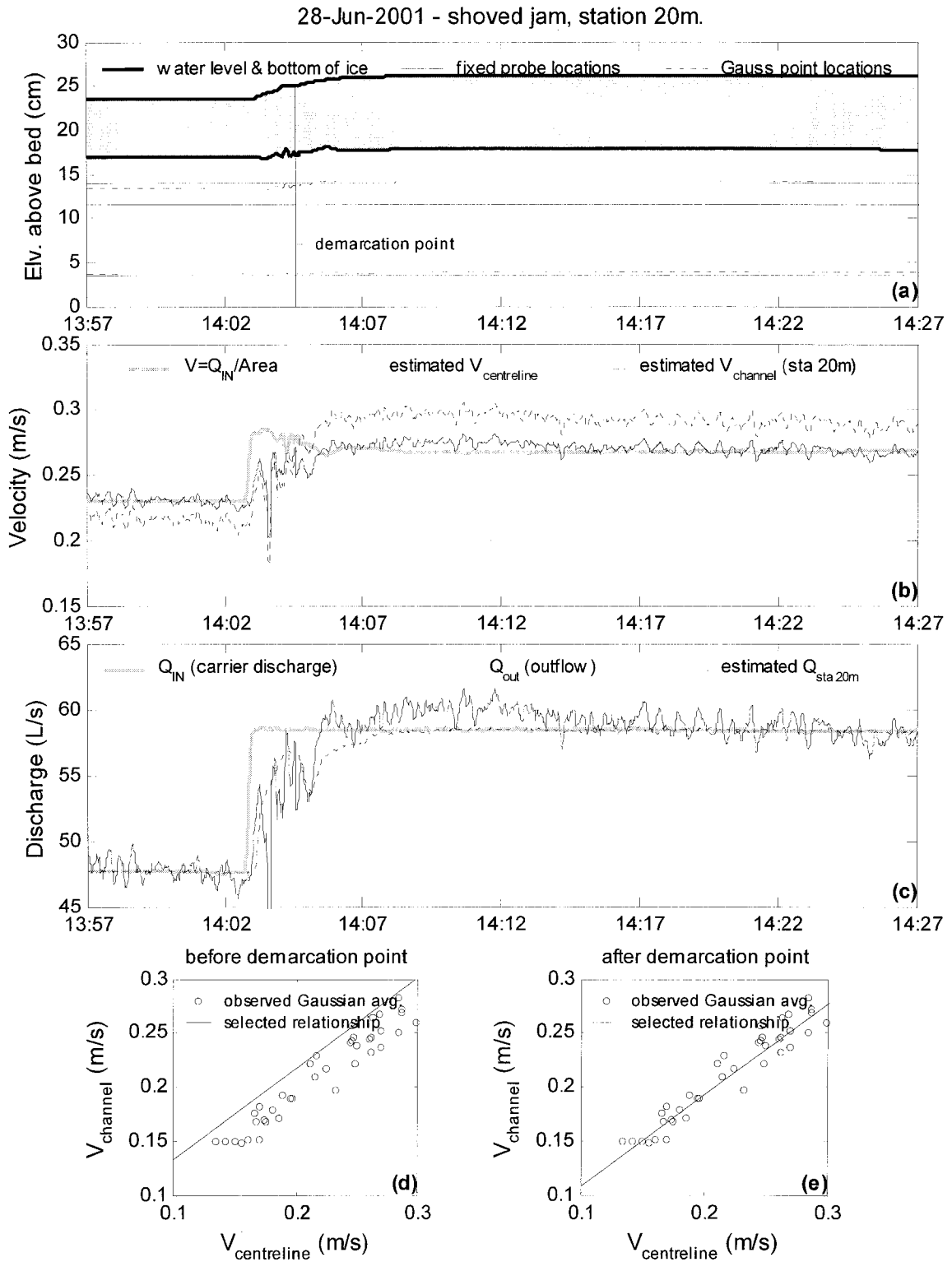
Figure E.122. Summary of continuous observations for a shoved jam taken at Station 20m – test date: 28 June 2001.

334
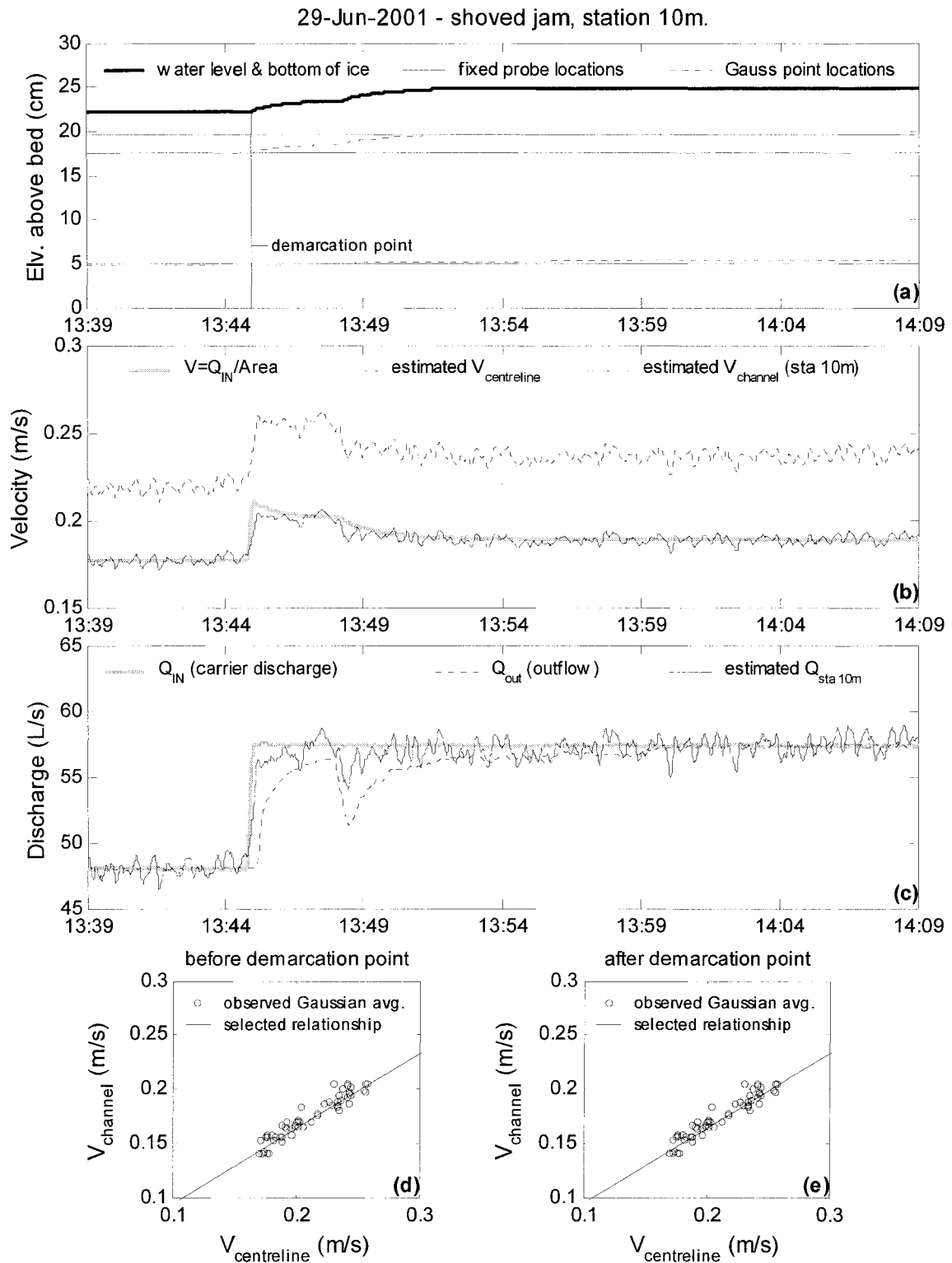
Figure E.123. Summary of continuous observations for a shoved jam taken at Station 10m – test date: 29 June 2001.
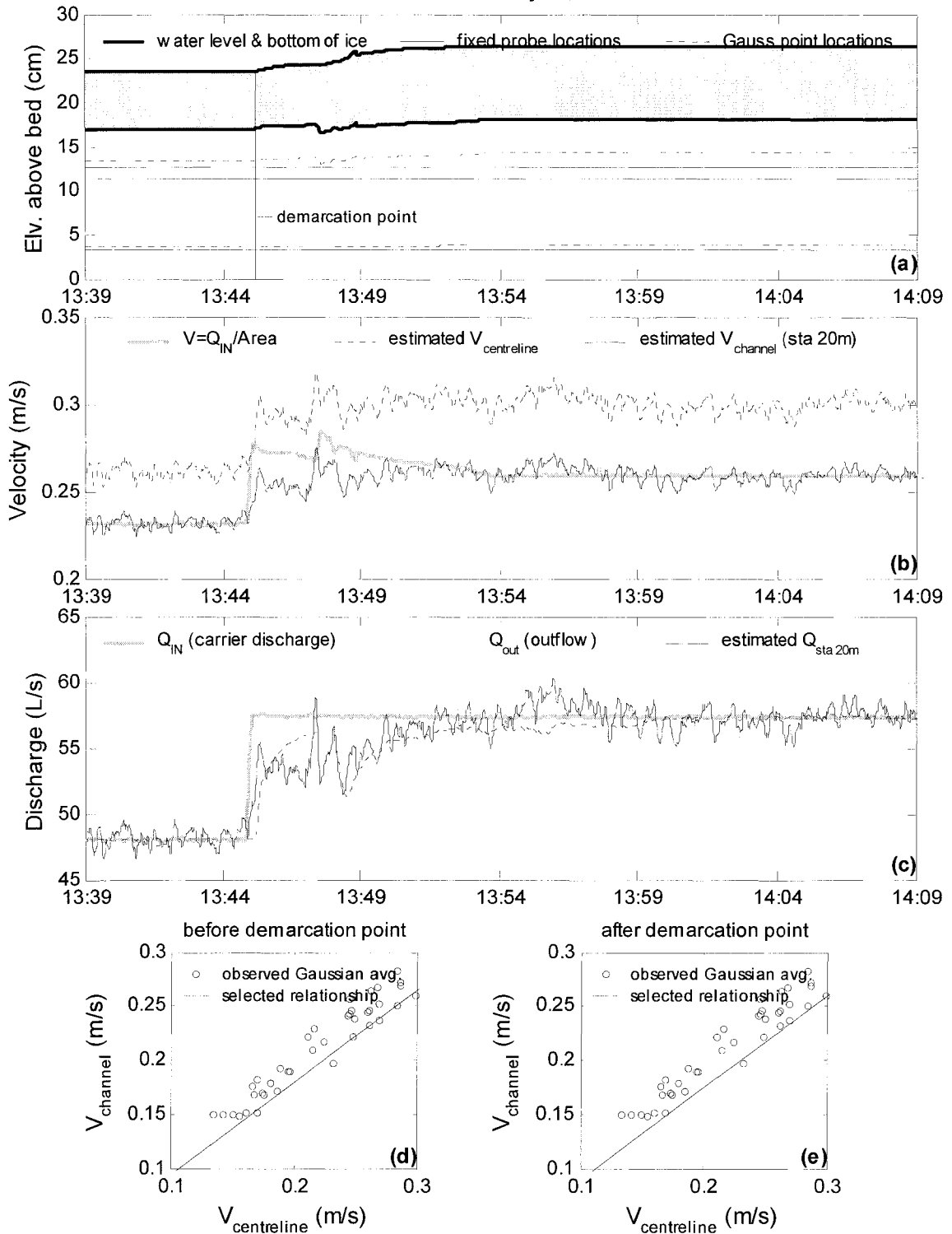
Figure E.124. Summary of continuous observations for a shoved jam taken at Station 20m – test date: 29 June 2001.

03-Jul-2001 - shoved jam, station 10m.

(a)
Elv. above bed (cm)

water level & bottom of ice — fixed probe locations — Gauss point locations

demarcation point

15:16 15:21 15:26 15:31 15:36 15:41 15:46

(b)
Velocity (m/s)

$V=Q_{IN}/Area$ — estimated $V_{centreline}$ — estimated $V_{channel}$ (sta 10m)

15:16 15:21 15:26 15:31 15:36 15:41 15:46

(c)
Discharge (L/s)

Q_{IN} (carrier discharge) — Q_{out} (outflow) — estimated $Q_{sta\,10m}$

15:16 15:21 15:26 15:31 15:36 15:41 15:46

before demarcation point

(d)
$V_{channel}$ (m/s)
o observed Gaussian avg.
selected relationship
$V_{centreline}$ (m/s)

after demarcation point

(e)
$V_{channel}$ (m/s)
o observed Gaussian avg.
selected relationship
$V_{centreline}$ (m/s)

Figure E.125.   Summary of continuous observations for a shoved jam taken at Station 10m – test date: 3 July 2001.

337
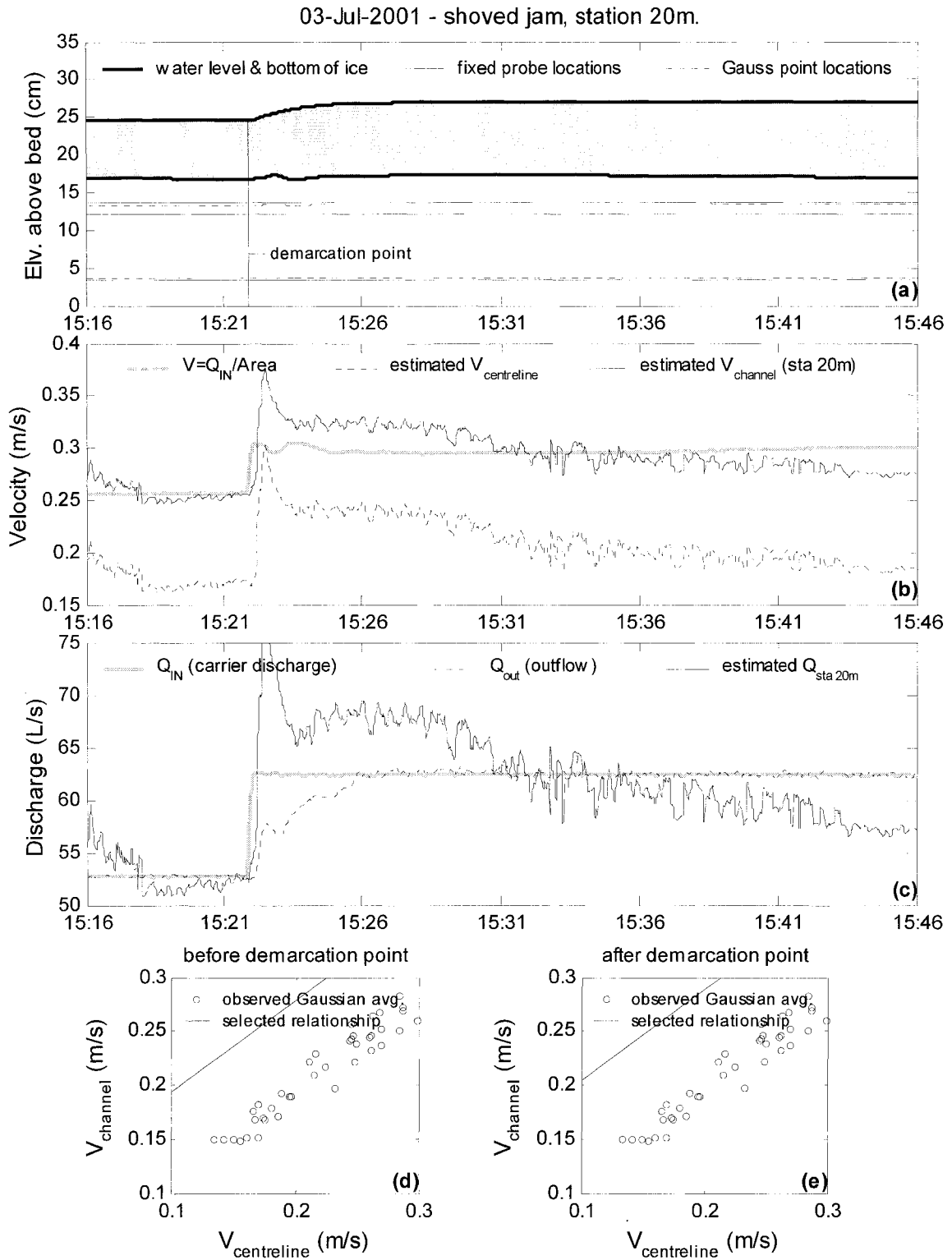
Figure E.126.   Summary of continuous observations for a shoved jam taken at Station 20m – test date: 3 July 2001.

338
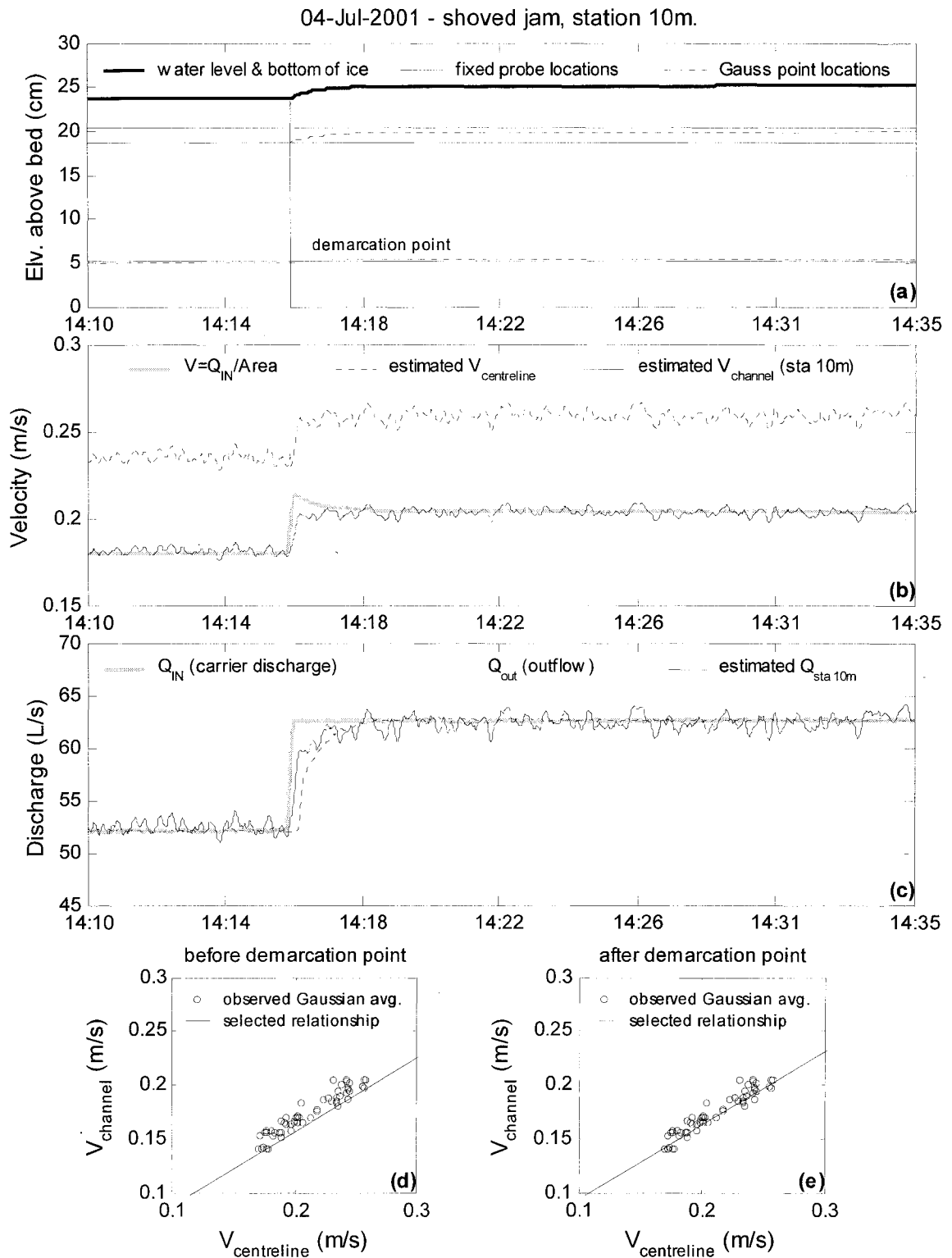
Figure E.127. Summary of continuous observations for a shoved jam taken at Station 10m – test date: 4 July 2001.

339
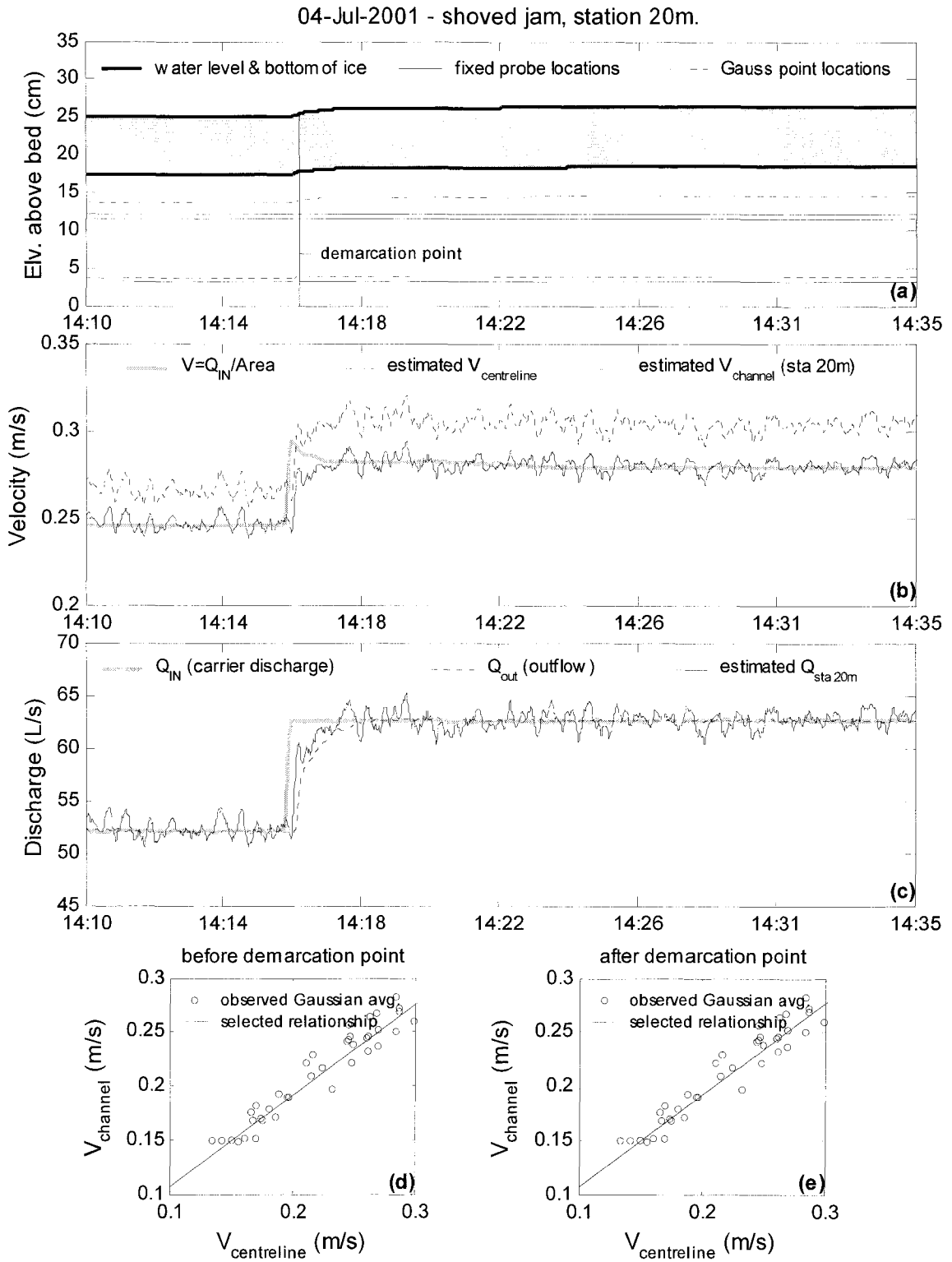
Figure E.128. Summary of continuous observations for a shoved jam taken at Station 20m – test date: 4 July 2001.

340
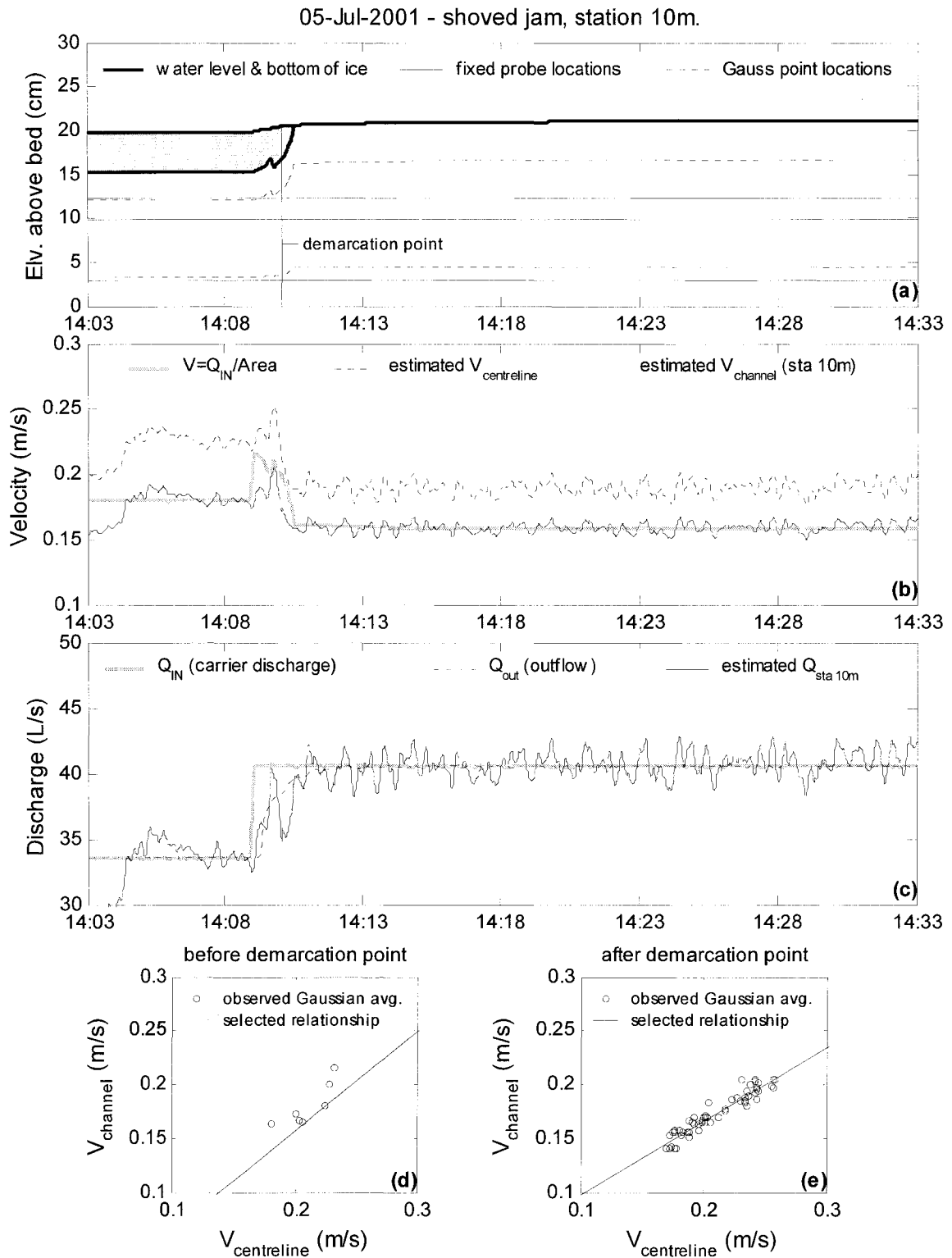
Figure E.129.   Summary of continuous observations for a shoved jam taken at Station 10m – test date: 5 July 2001.

341
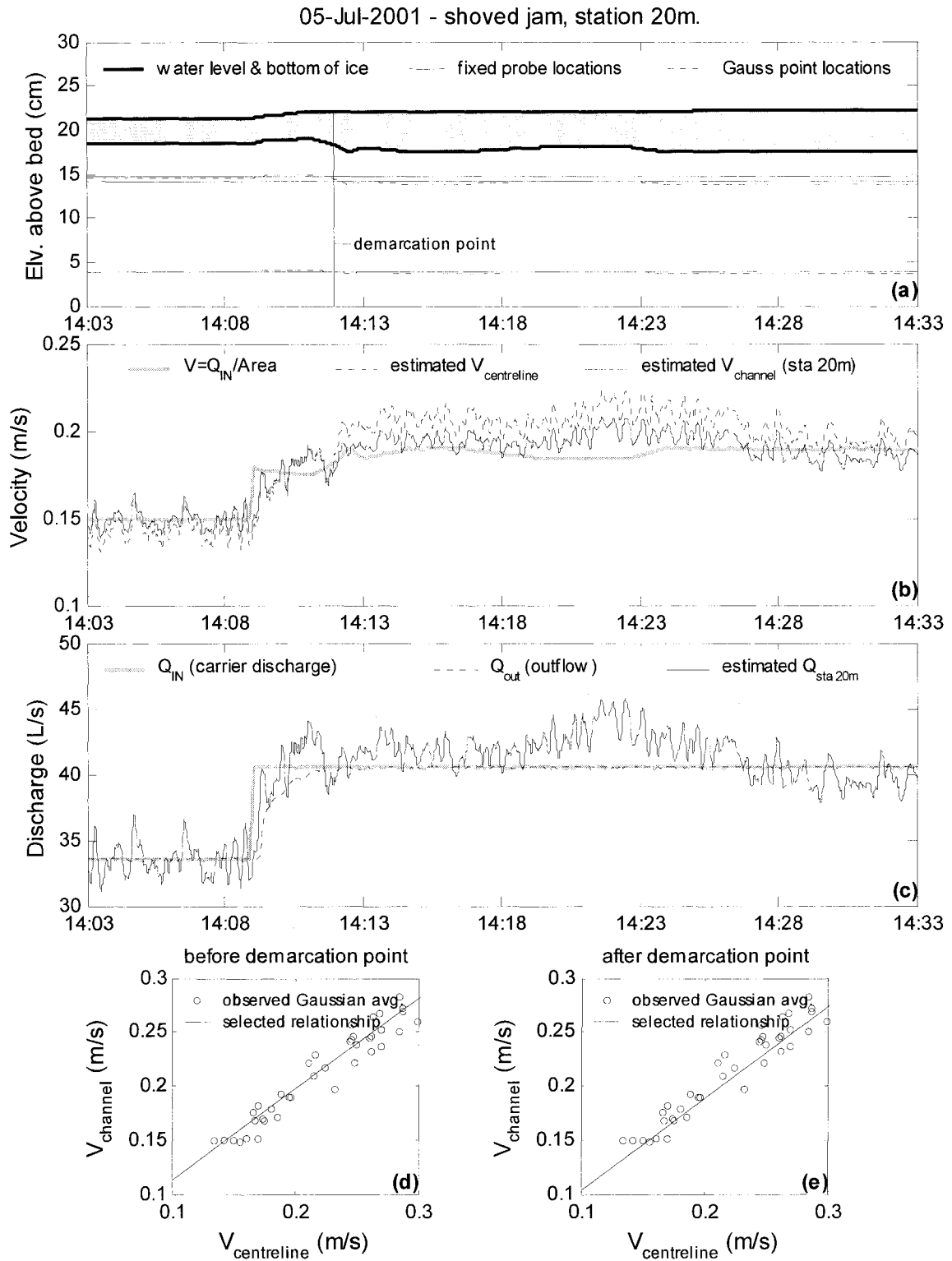
Figure E.130. Summary of continuous observations for a shoved jam taken at Station 20m – test date: 5 July 2001.

342
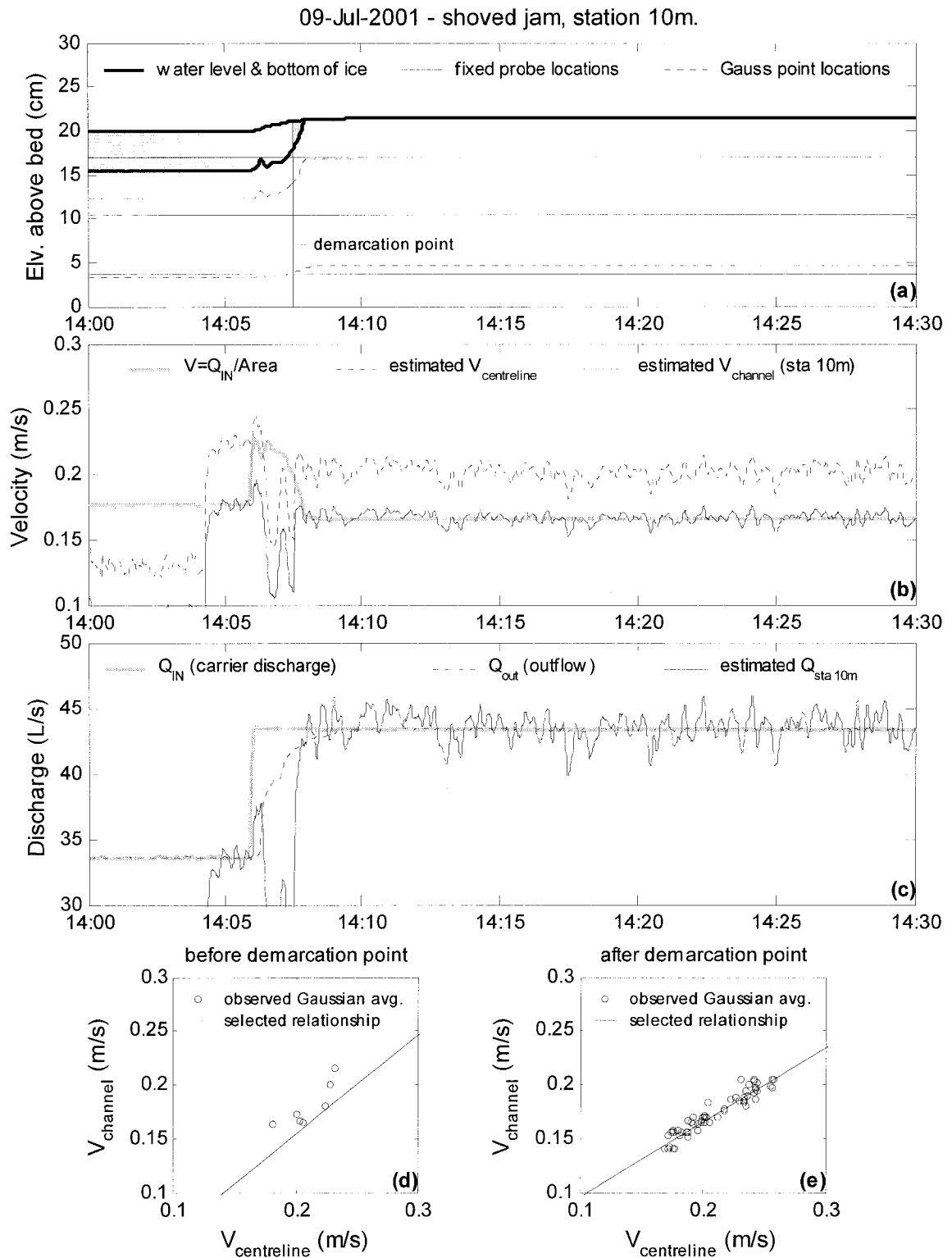
Figure E.131. Summary of continuous observations for a shoved jam taken at Station 10m – test date: 9 July 2001.

343
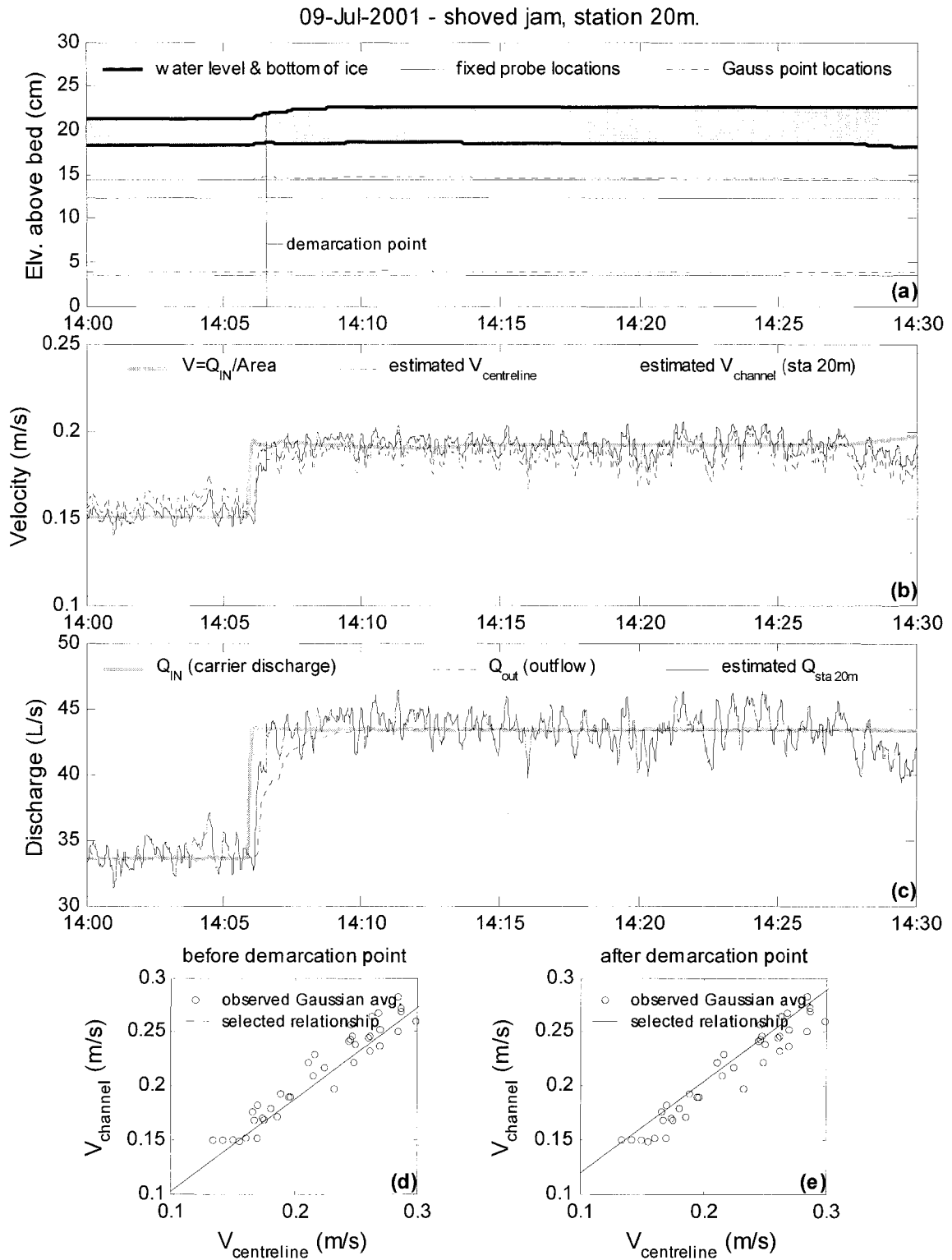
Figure E.132. Summary of continuous observations for a shoved jam taken at Station 20m – test date: 9 July 2001.

344
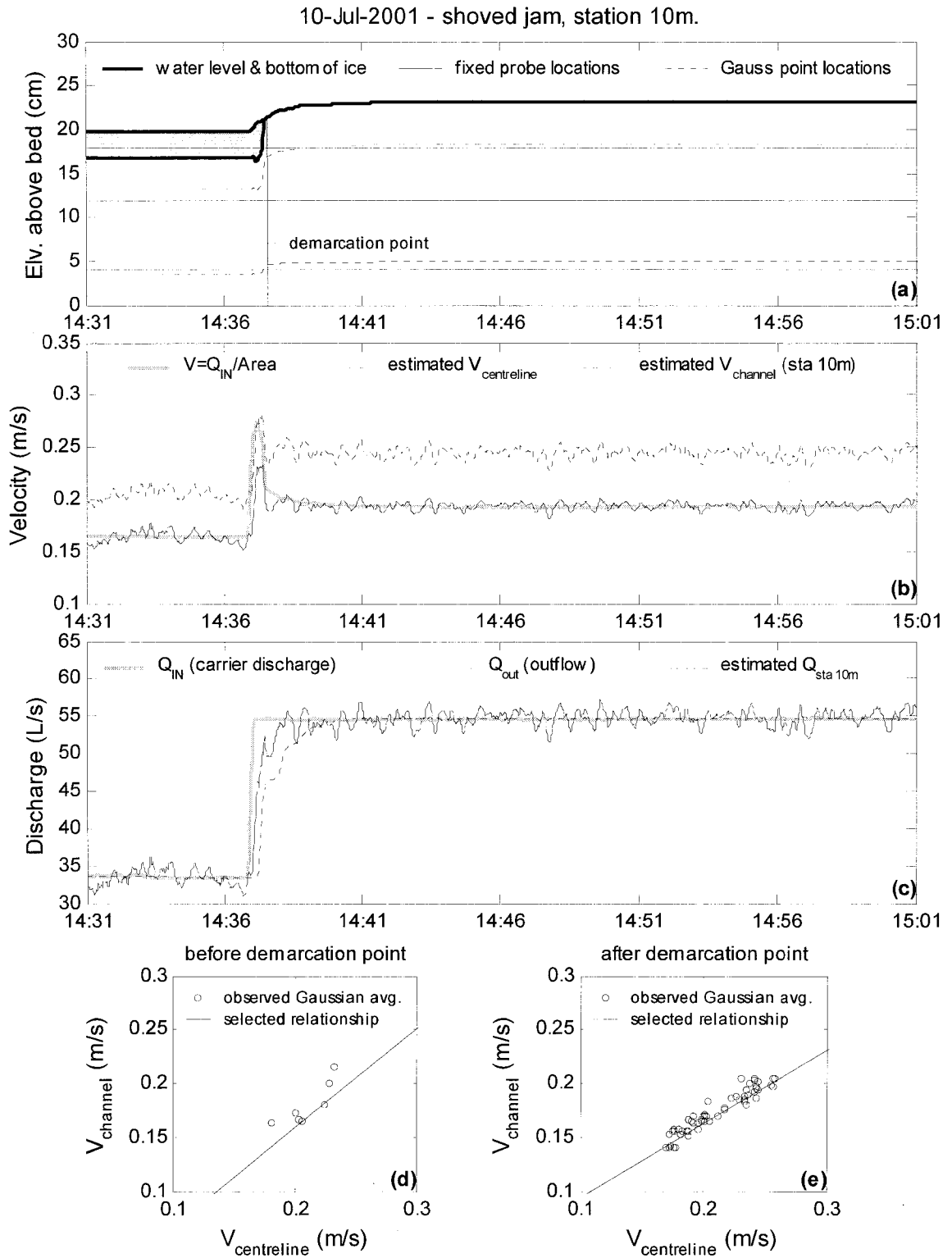
Figure E.133. Summary of continuous observations for a shoved jam taken at Station 10m – test date: 10 July 2001.

345
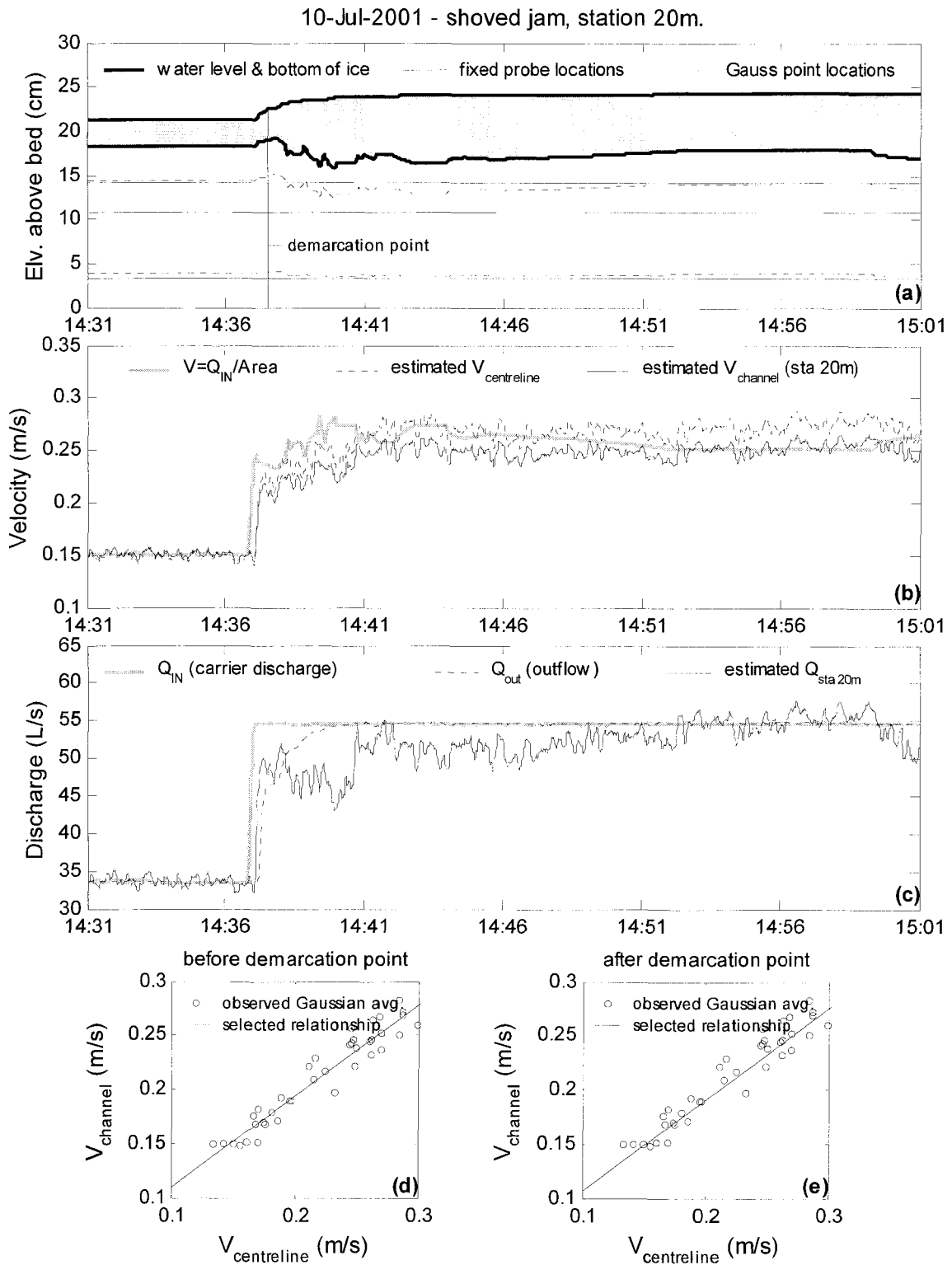
Figure E.134. Summary of continuous observations for a shoved jam taken at Station 20m – test date: 10 July 2001.
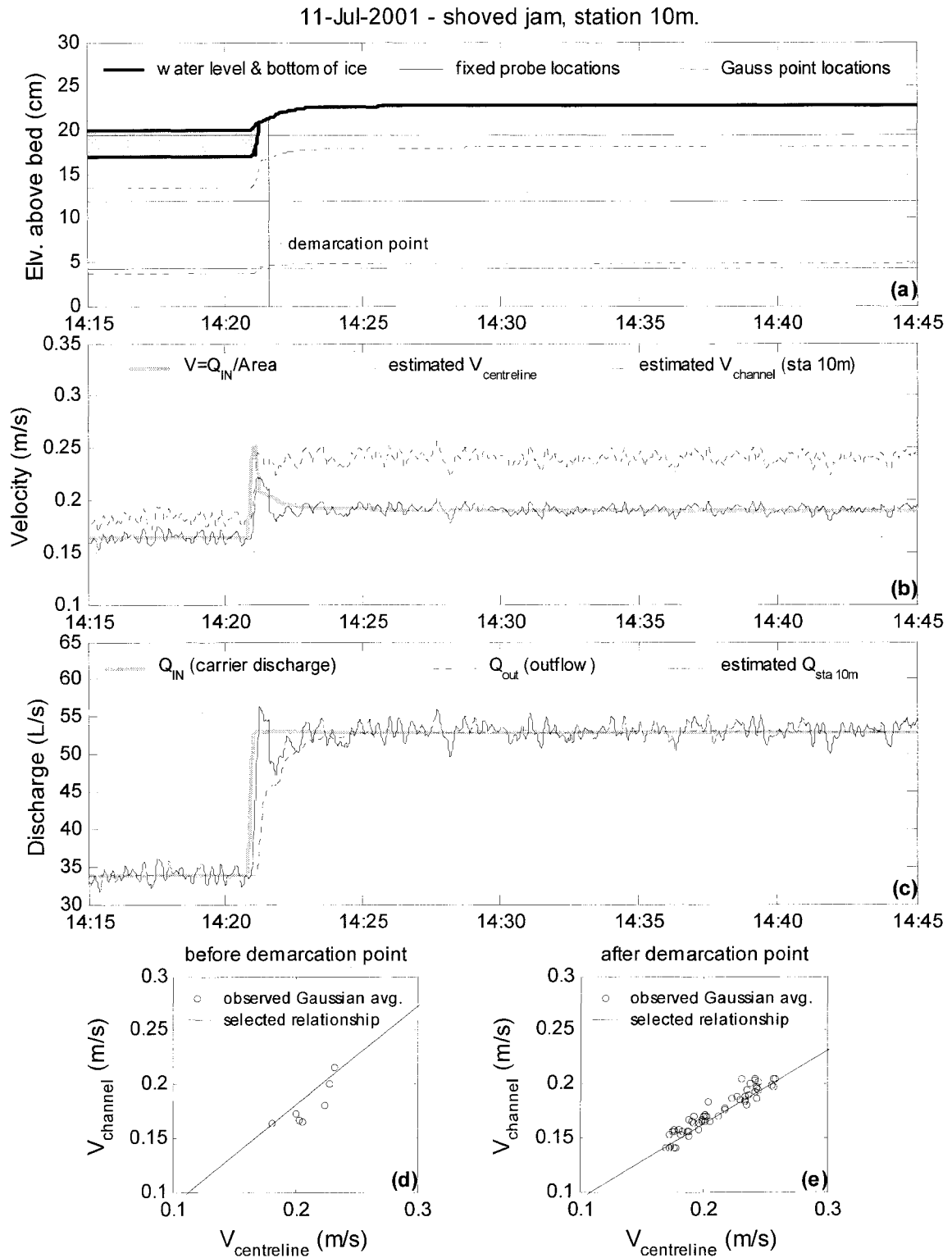
Figure E.135. Summary of continuous observations for a shoved jam taken at Station 10m – test date: 11 July 2001.

347
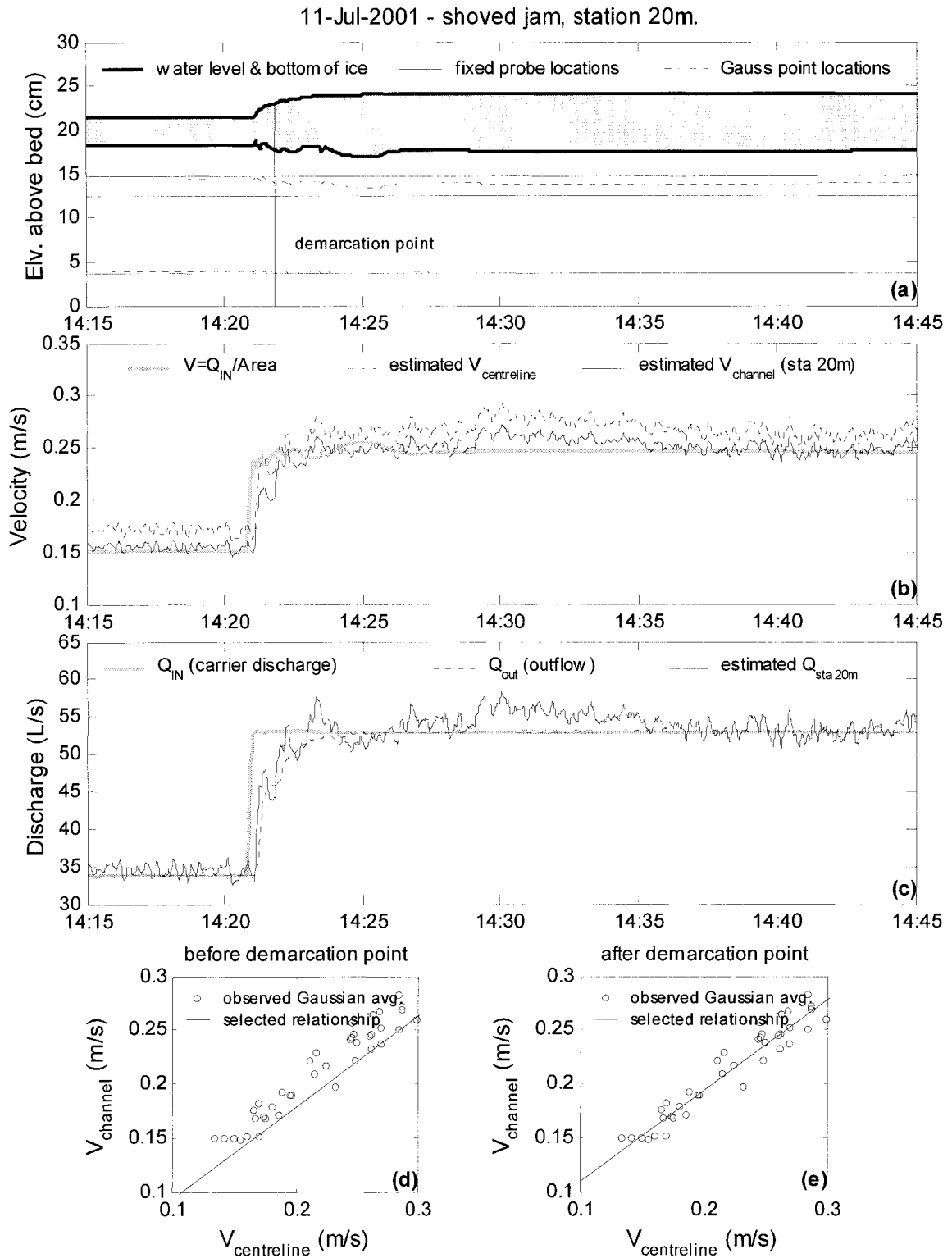
Figure E.136. Summary of continuous observations for a shoved jam taken at Station 20m – test date: 11 July 2001.
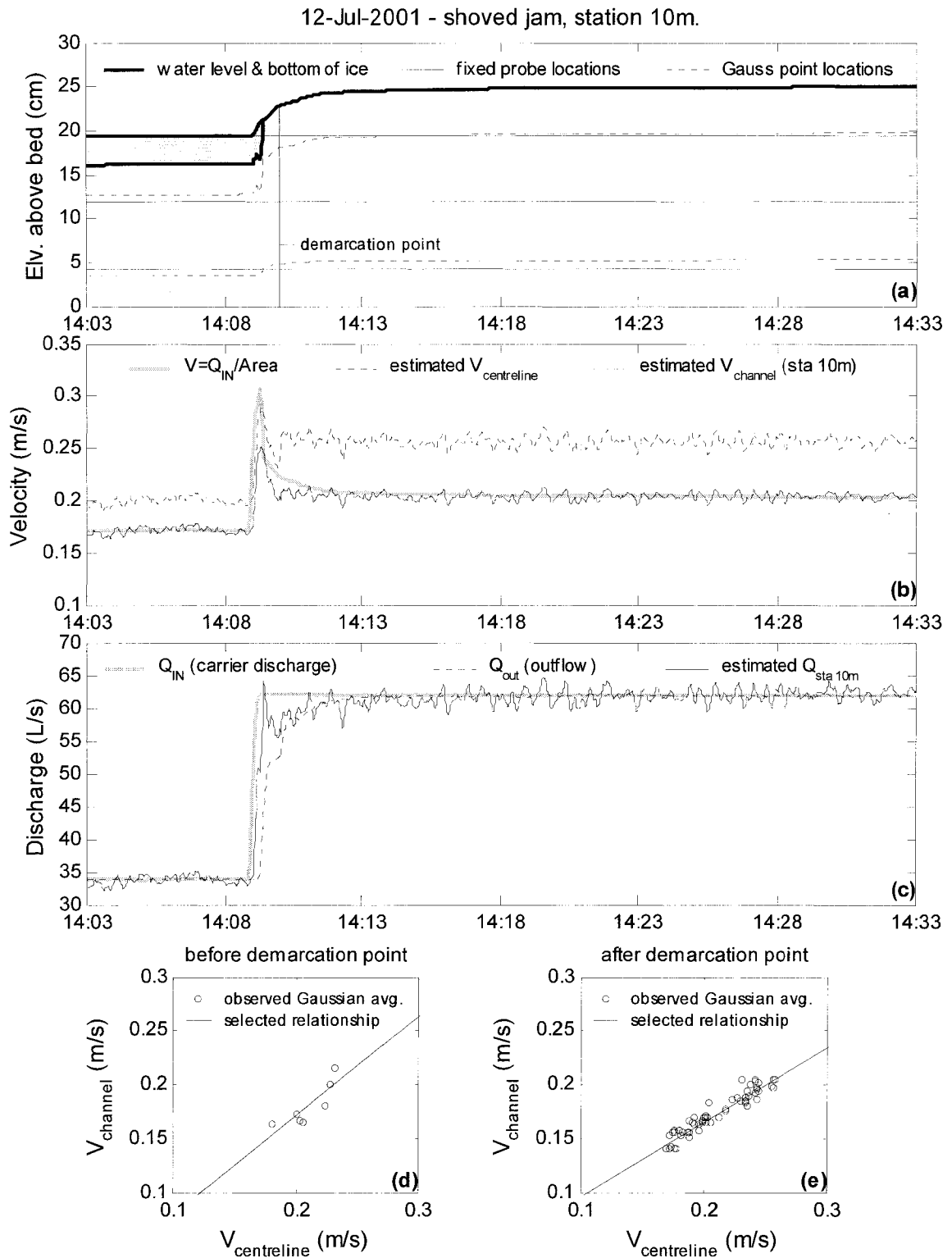
Figure E.137. Summary of continuous observations for a shoved jam taken at Station 10m – test date: 12 July 2001.

349
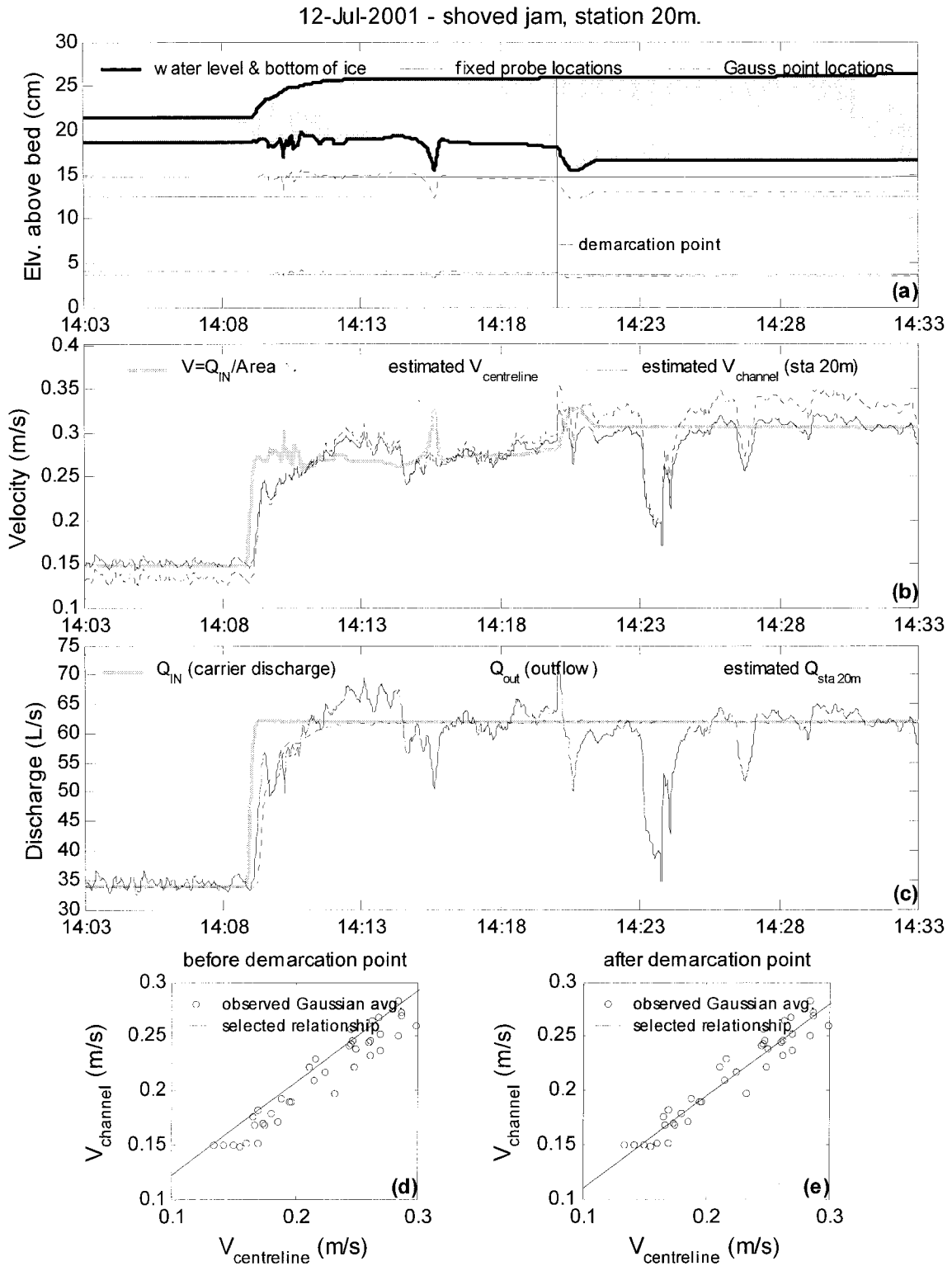
Figure E.138. Summary of continuous observations for a shoved jam taken at Station 20m – test date: 12 July 2001.
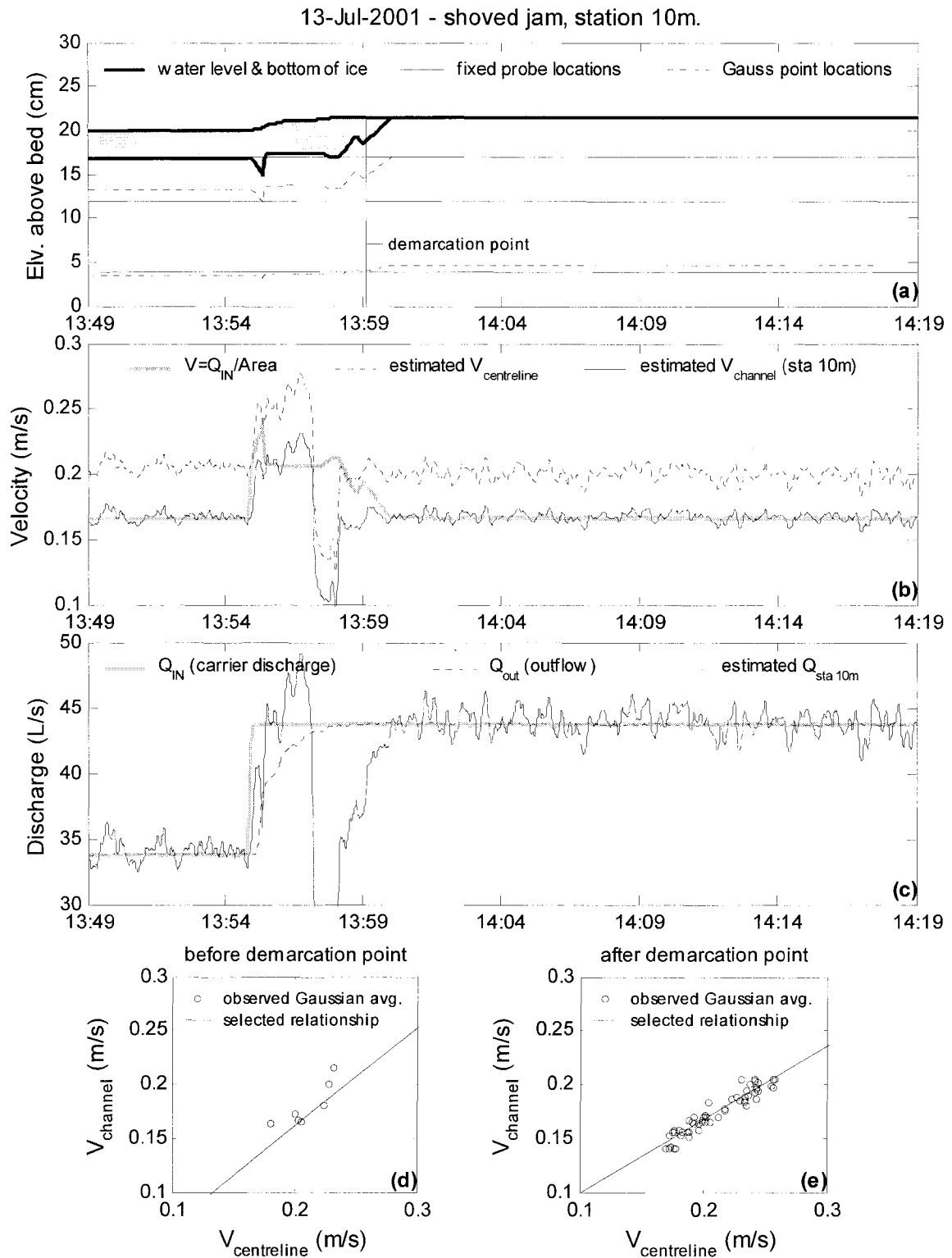
Figure E.139. Summary of continuous observations for a shoved jam taken at Station 10m – test date: 13 July 2001.
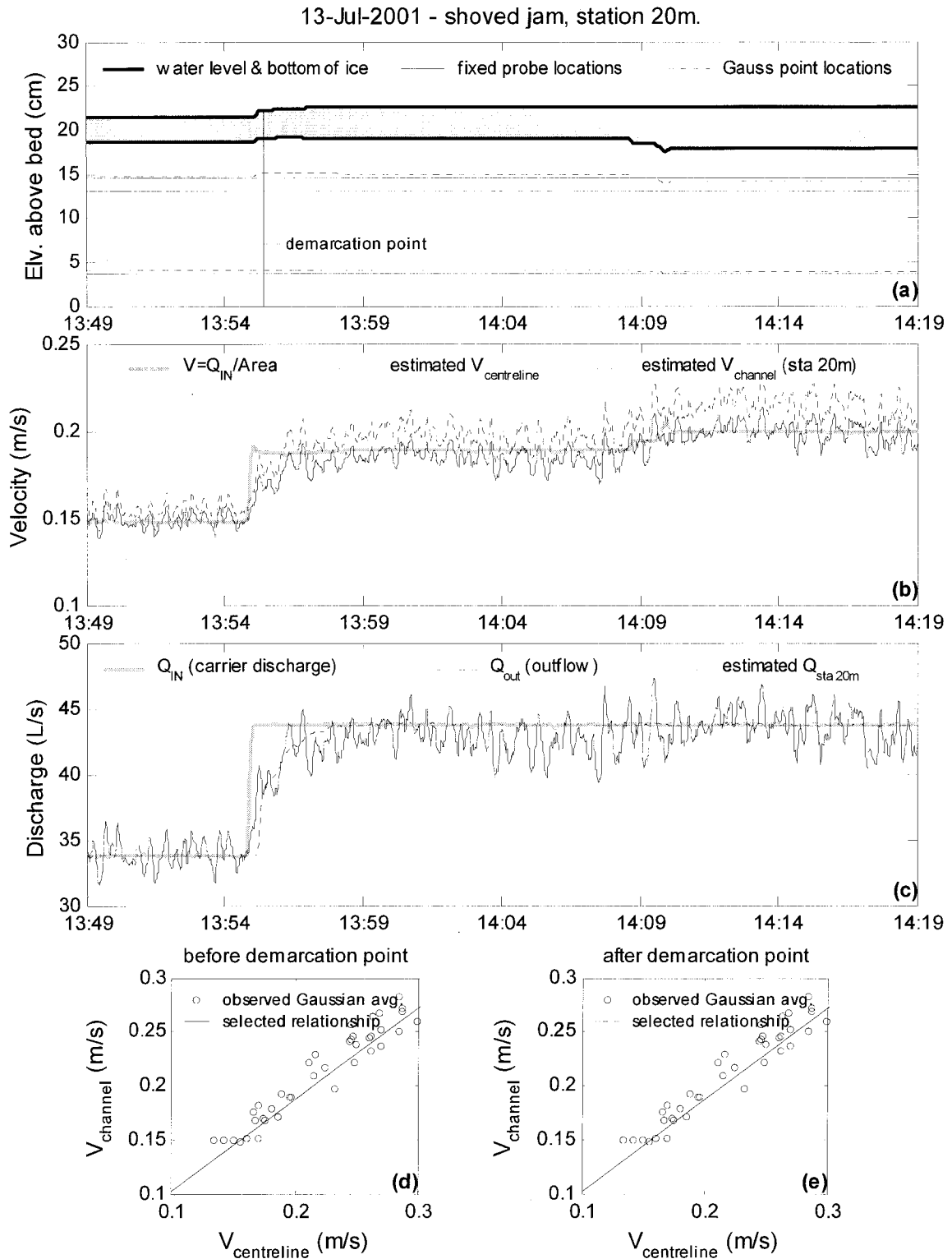
Figure E.140. Summary of continuous observations for a shoved jam taken at Station 20m – test date: 13 July 2001.

16-Jul-2001 - shoved jam, station 10m.

(a)

Elv. above bed (cm)

— water level & bottom of ice   ---- fixed probe locations   -- Gauss point locations

demarcation point

30 25 20 15 10 5 0

14:12 14:17 14:22 14:27 14:32 14:37 14:42

(b)

Velocity (m/s)

$V=Q_{IN}/Area$ estimated $V_{centreline}$ estimated $V_{channel}$ (sta 10m)

0.25 0.2 0.15 0.1

14:12 14:17 14:22 14:27 14:32 14:37 14:42

(c)

Discharge (L/s)

Q_{IN} (carrier discharge) Q_{out} (outflow)   estimated $Q_{sta\,10m}$

50 45 40 35 30

14:12 14:17 14:22 14:27 14:32 14:37 14:42

before demarcation point

(d)

$V_{channel}$ (m/s)

○ observed Gaussian avg.
-- selected relationship

0.3 0.25 0.2 0.15 0.1

0.1 0.2 0.3

$V_{centreline}$ (m/s)

after demarcation point

(e)

$V_{channel}$ (m/s)

○ observed Gaussian avg.
-- selected relationship

0.3 0.25 0.2 0.15 0.1

0.1 0.2 0.3

$V_{centreline}$ (m/s)

Figure E.141.   Summary of continuous observations for a shoved jam taken at Station 10m – test date: 16 July 2001.

353
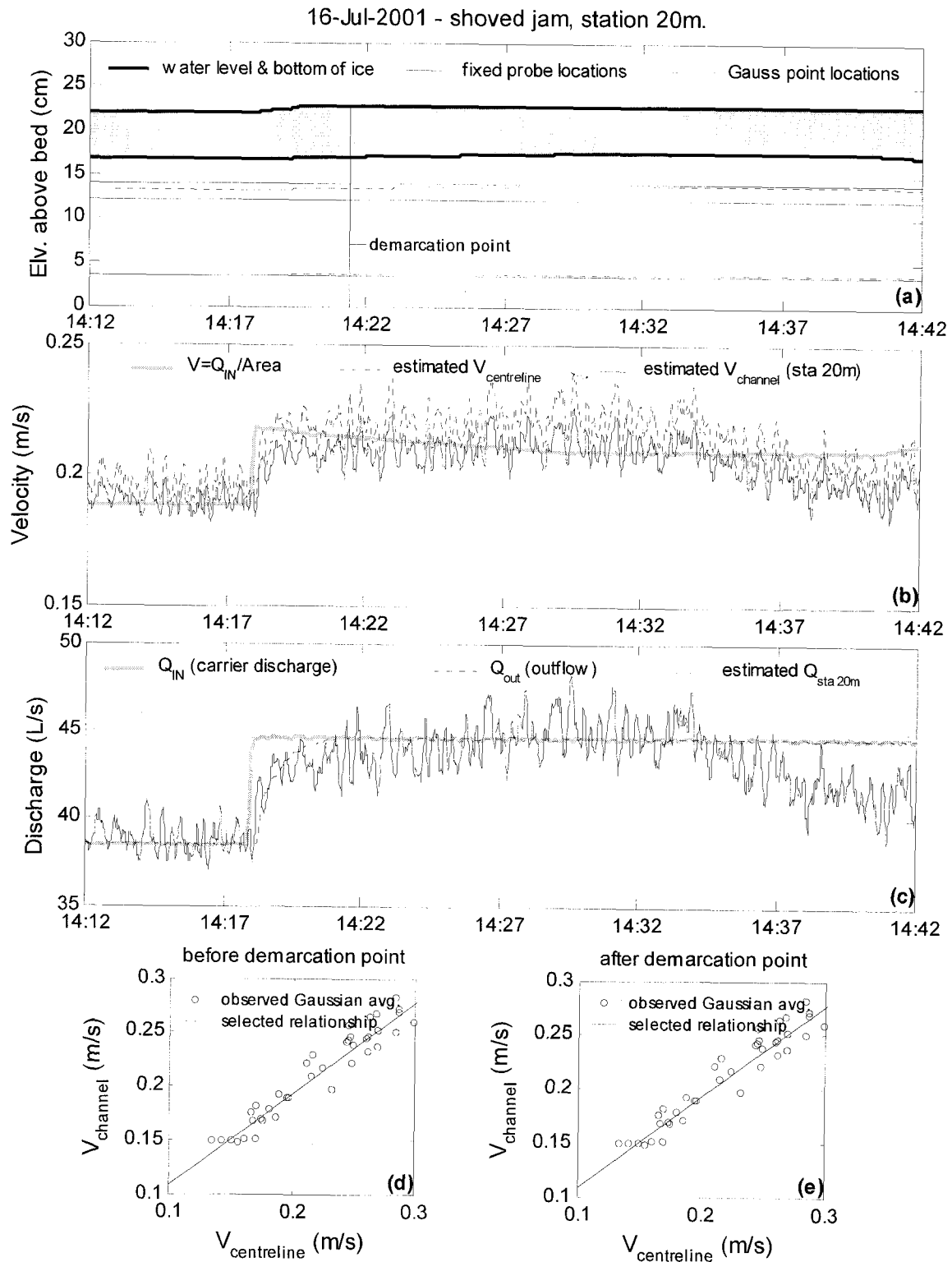
Figure E.142. Summary of continuous observations for a shoved jam taken at Station 20m – test date: 16 July 2001.

354
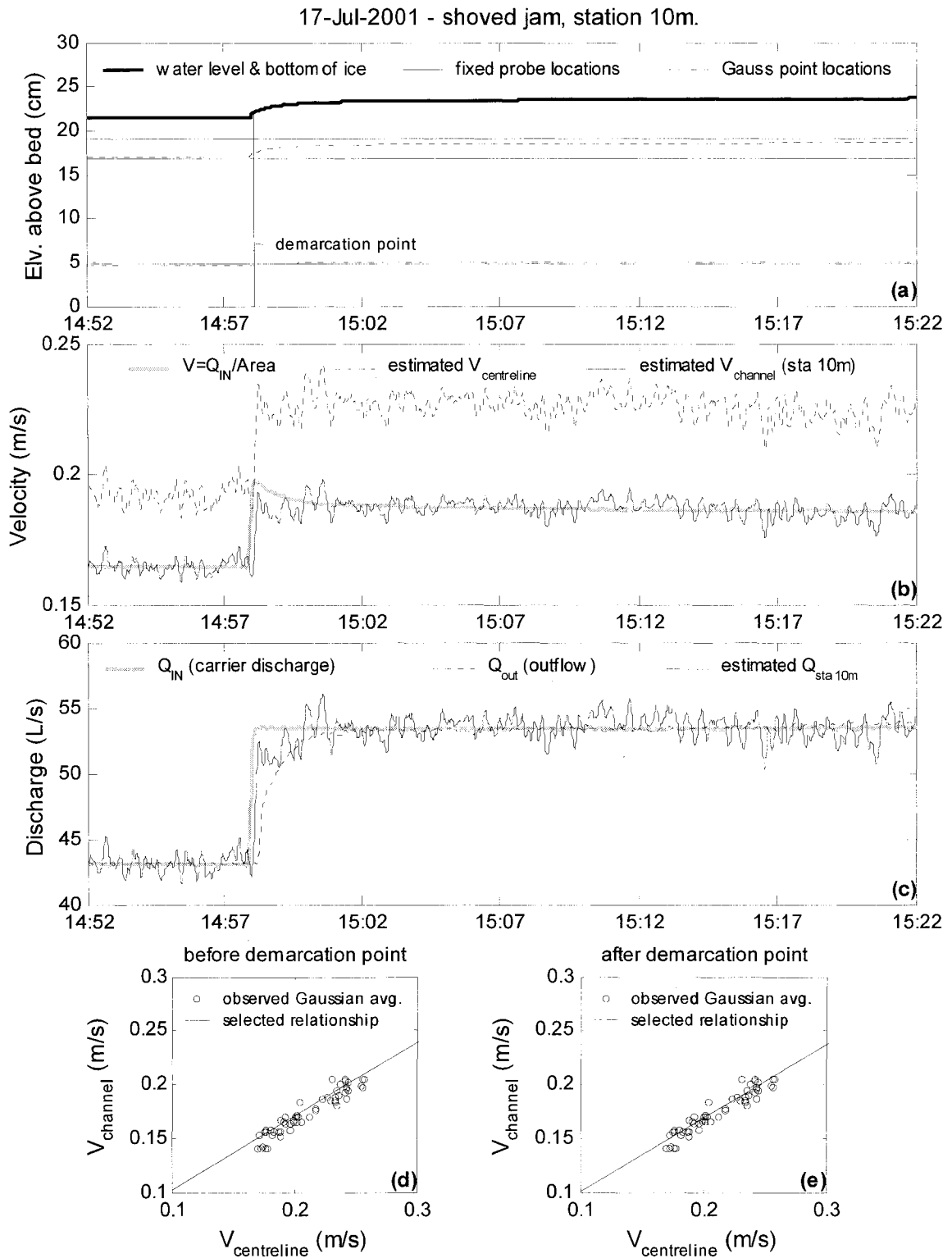
Figure E.143. Summary of continuous observations for a shoved jam taken at Station 10m – test date: 17 July 2001.
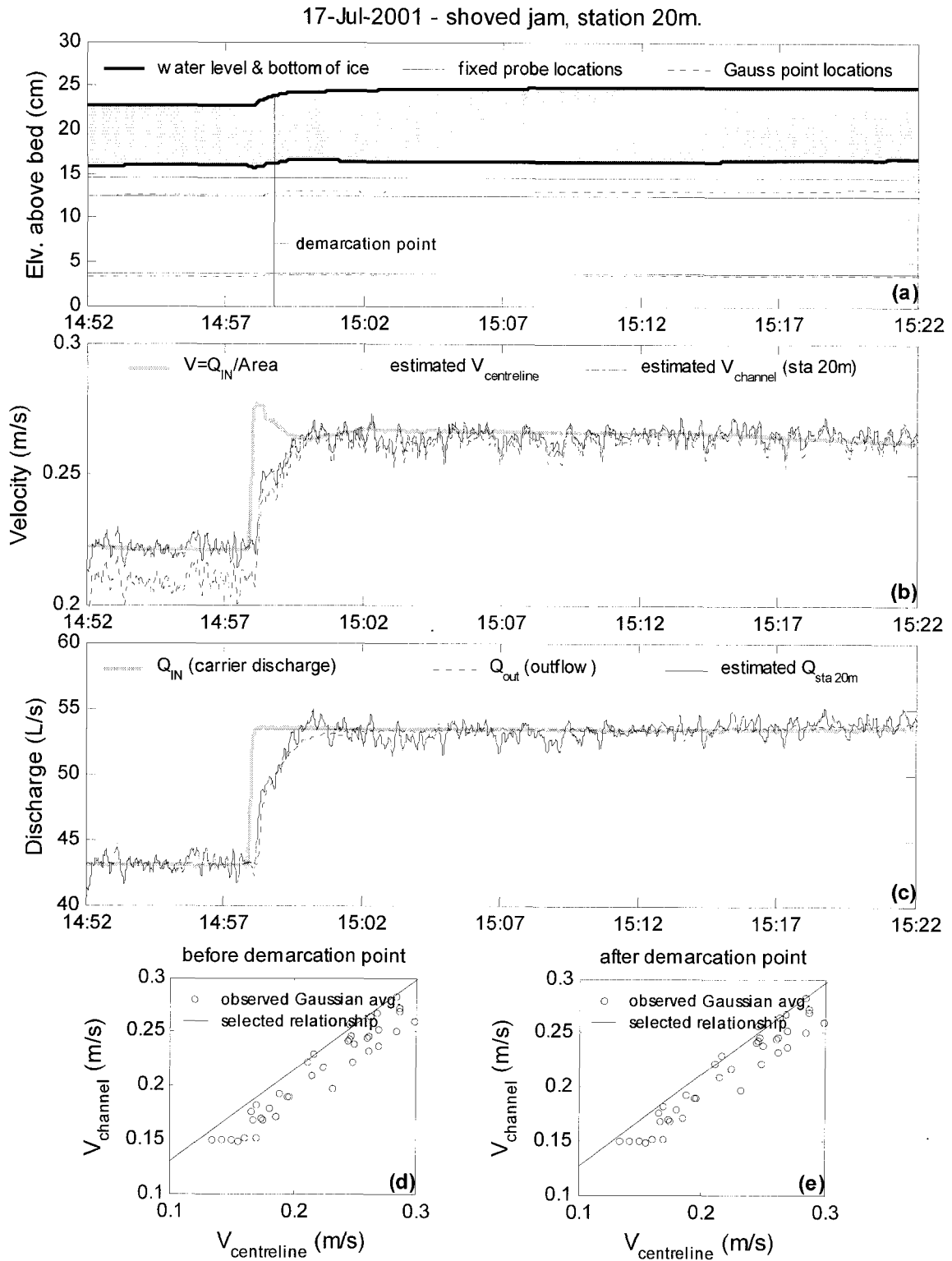
Figure E.144. Summary of continuous observations for a shoved jam taken at Station 20m – test date: 17 July 2001.

356
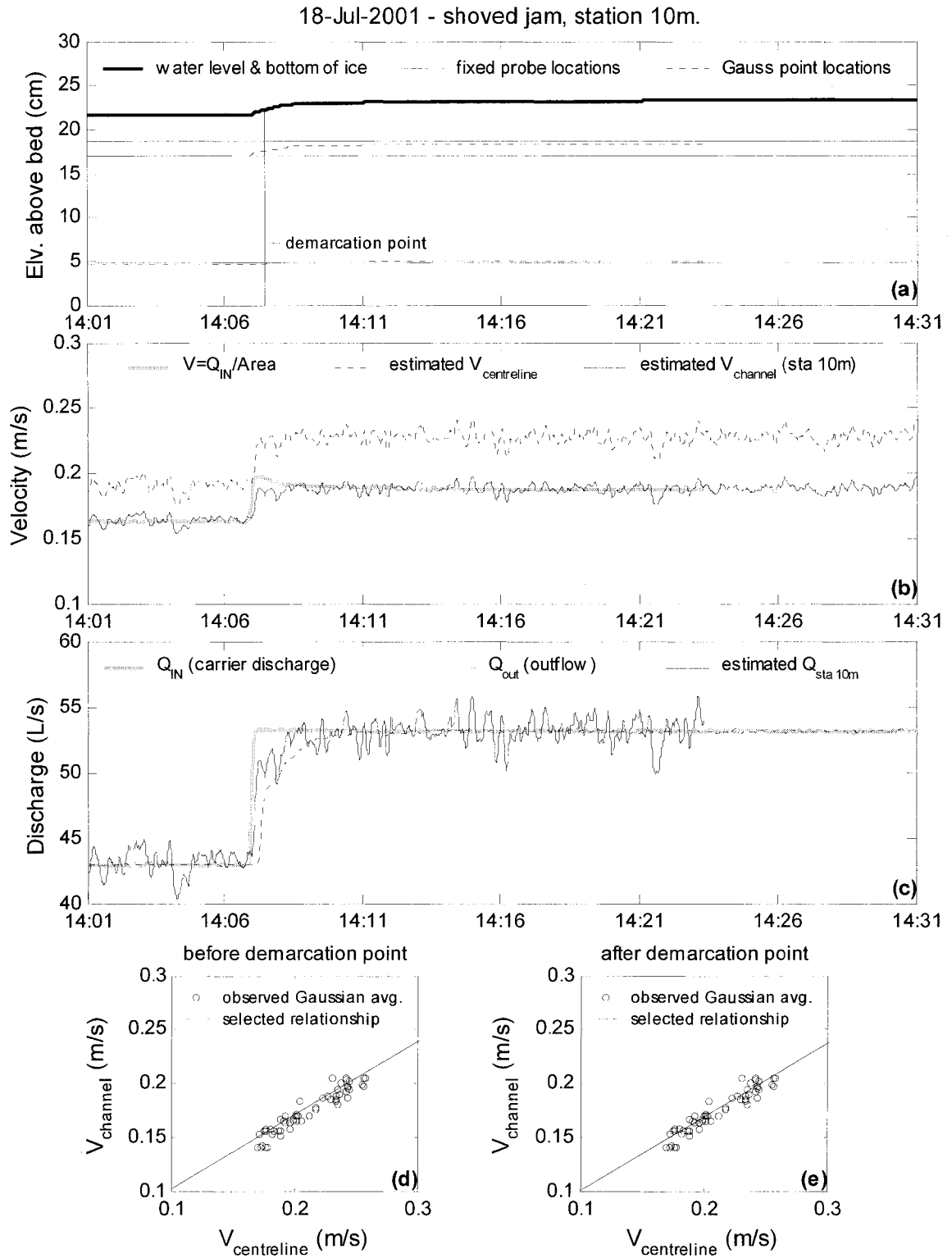
Figure E.145. Summary of continuous observations for a shoved jam taken at Station 10m – test date: 18 July 2001.
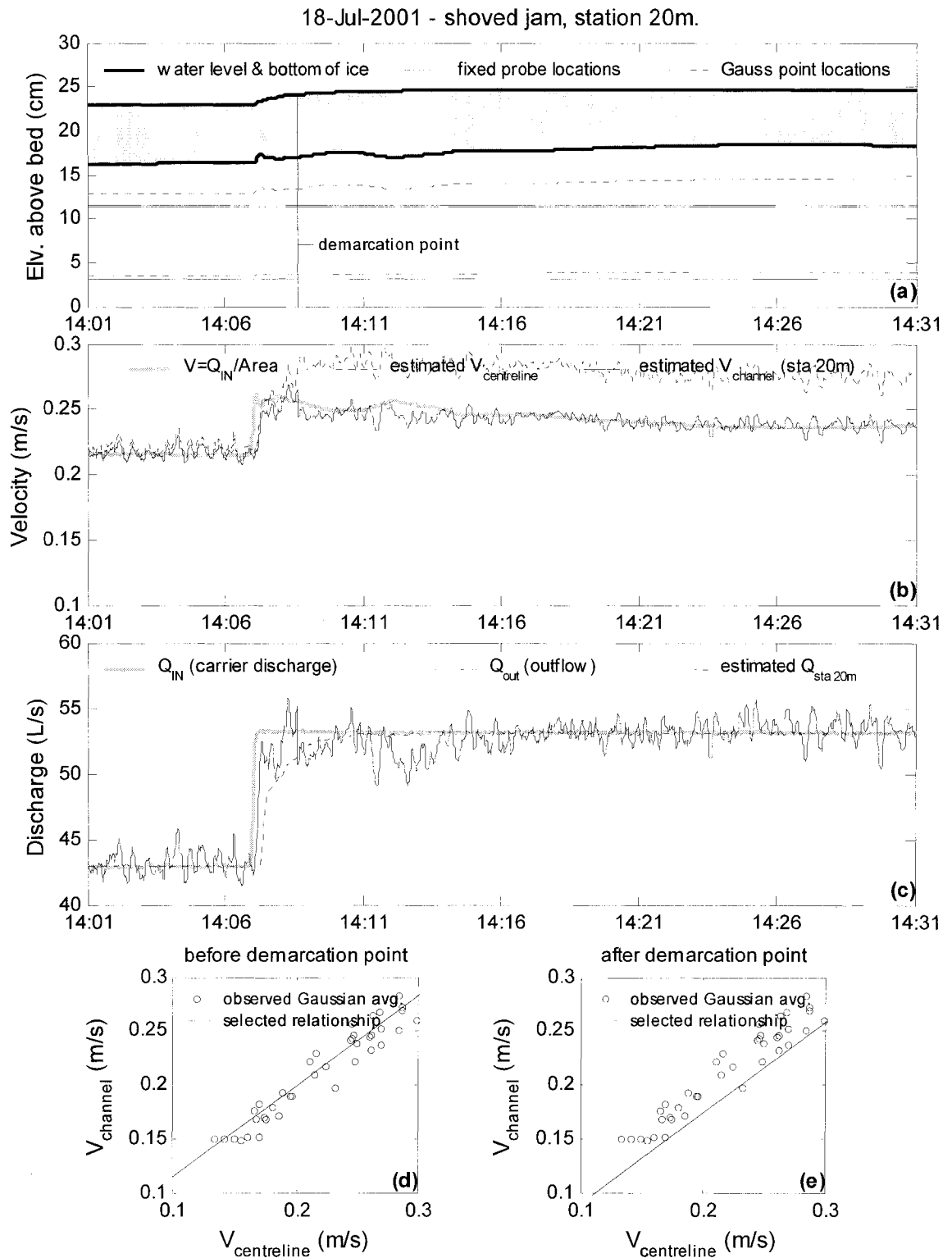
Figure E.146.   Summary of continuous observations for a shoved jam taken at Station 20m – test date: 18 July 2001.
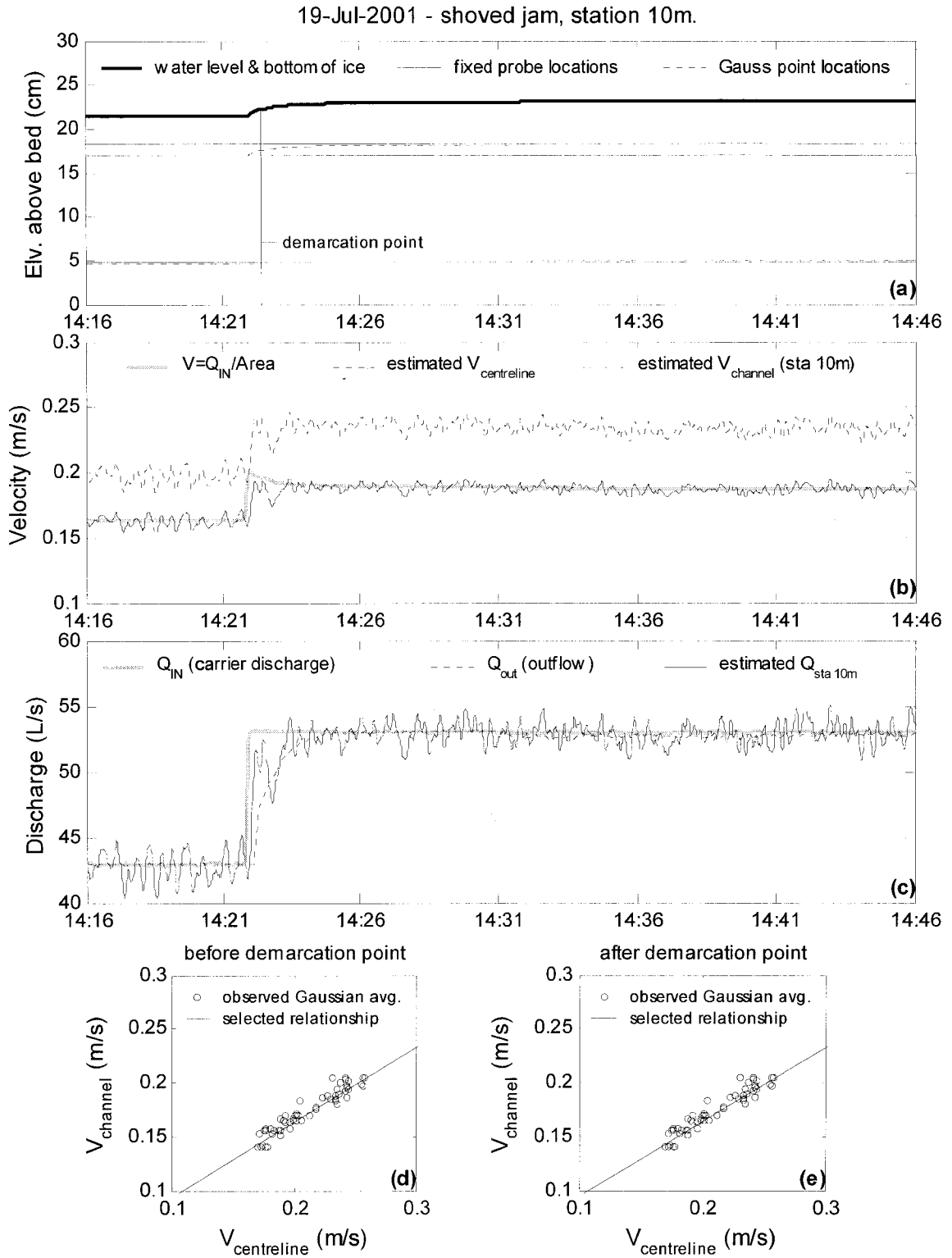
Figure E.147. Summary of continuous observations for a shoved jam taken at Station 10m – test date: 19 July 2001.
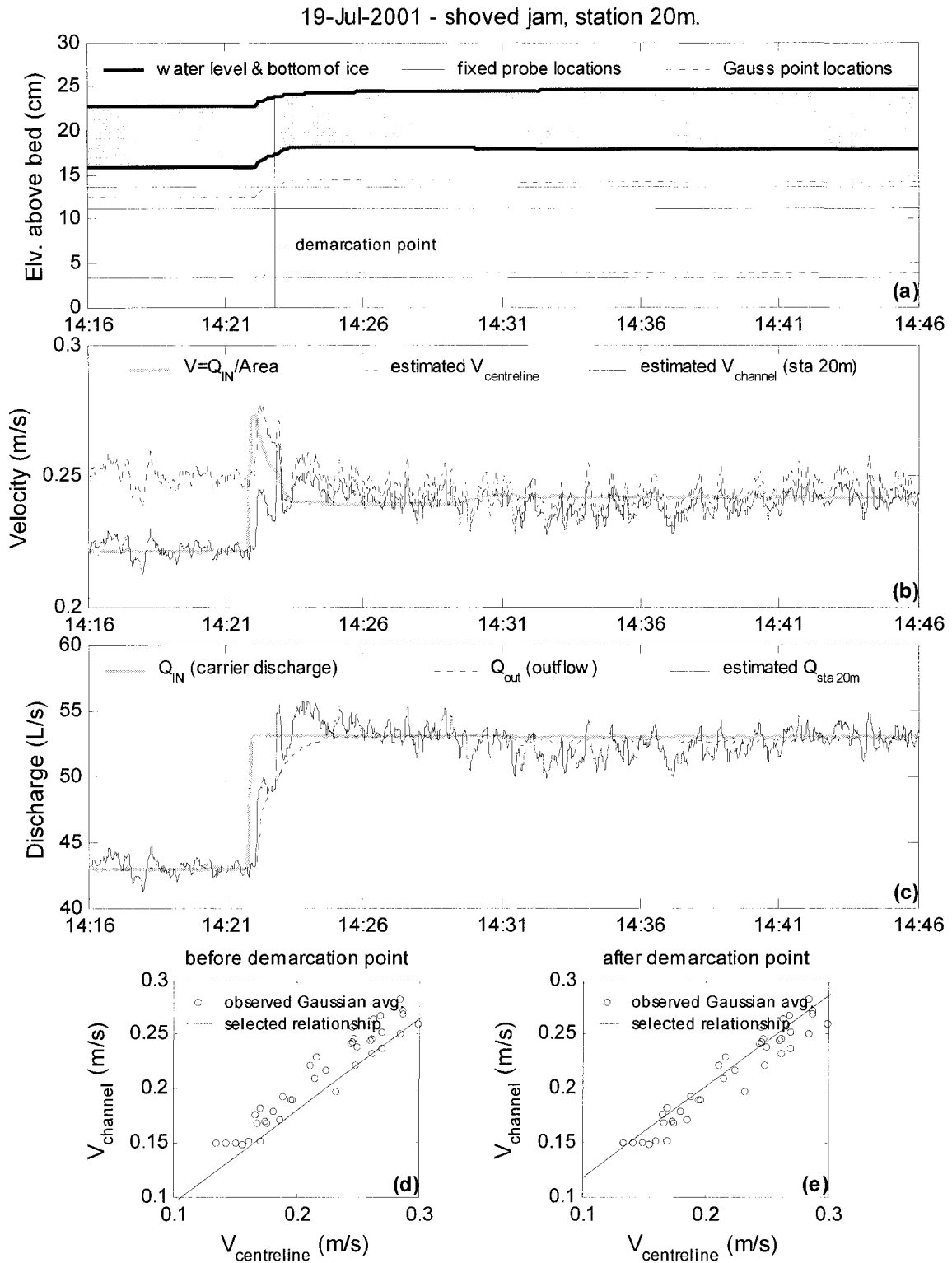
Figure E.148. Summary of continuous observations for a shoved jam taken at Station 20m – test date: 19 July 2001.
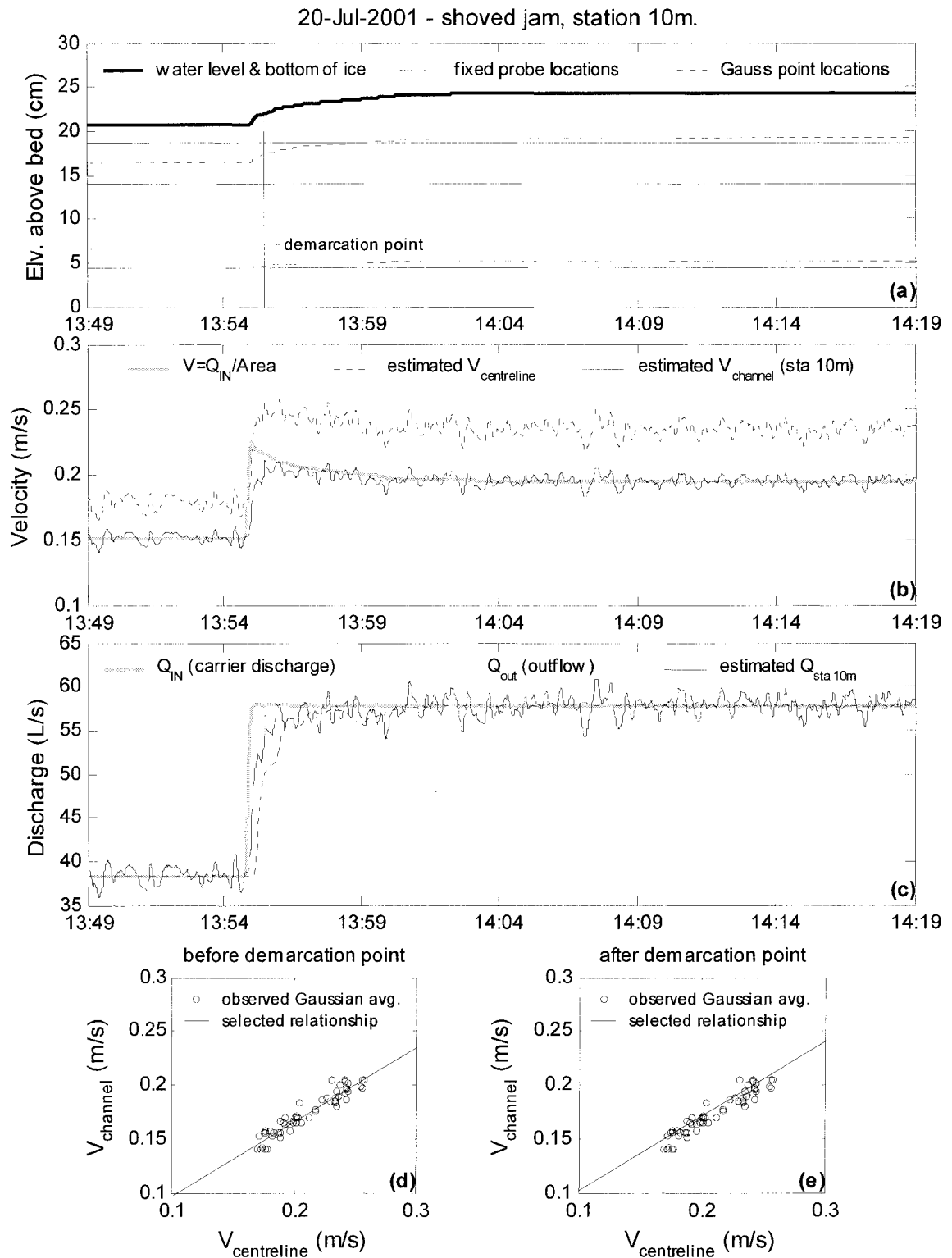
Figure E.149. Summary of continuous observations for a shoved jam taken at Station 10m – test date: 20 July 2001.

361
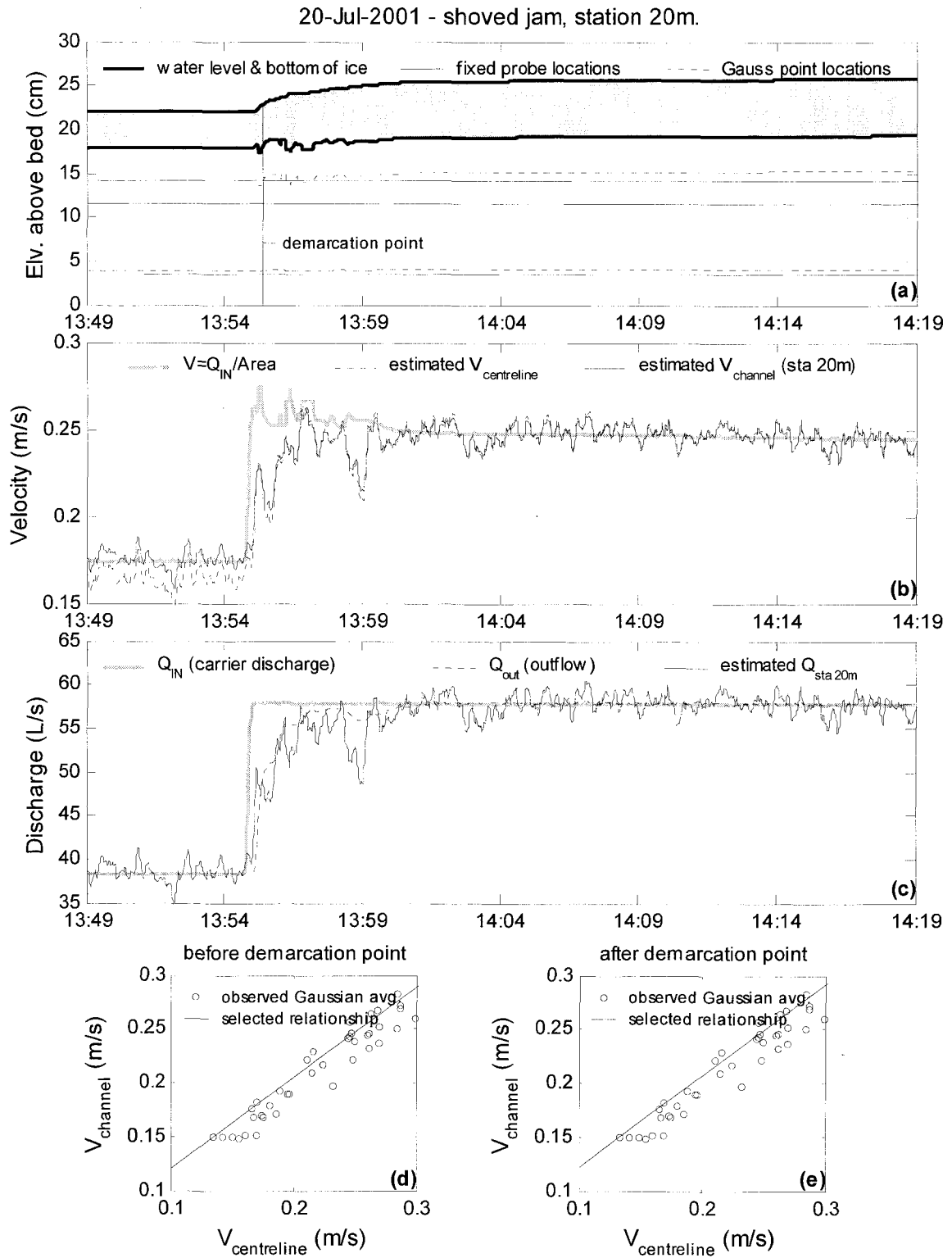
Figure E.150. Summary of continuous observations for a shoved jam taken at Station 20m – test date: 20 July 2001.
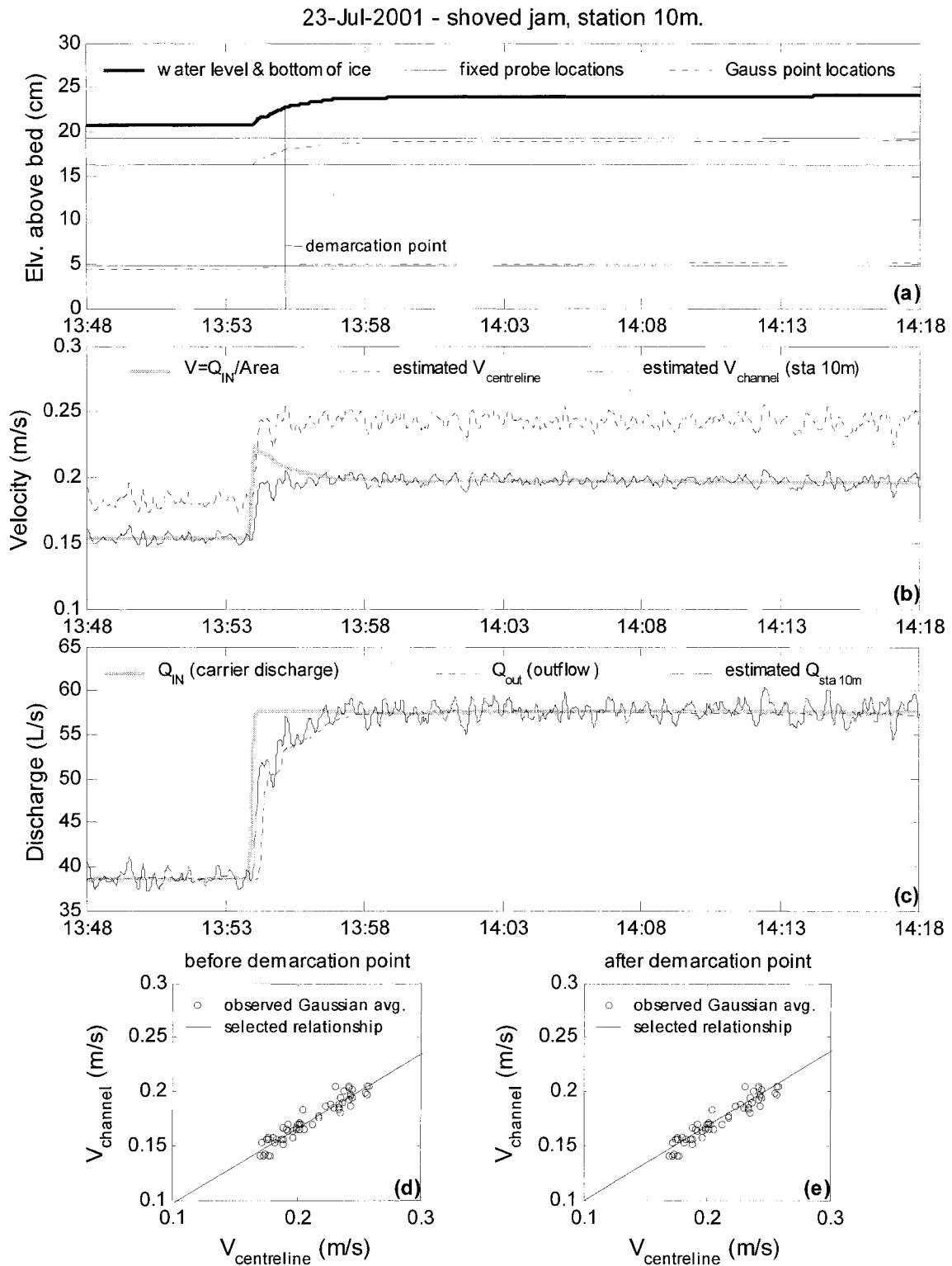
Figure E.151. Summary of continuous observations for a shoved jam taken at Station 10m – test date: 23 July 2001.

363

23-Jul-2001 - shoved jam, station 20m.
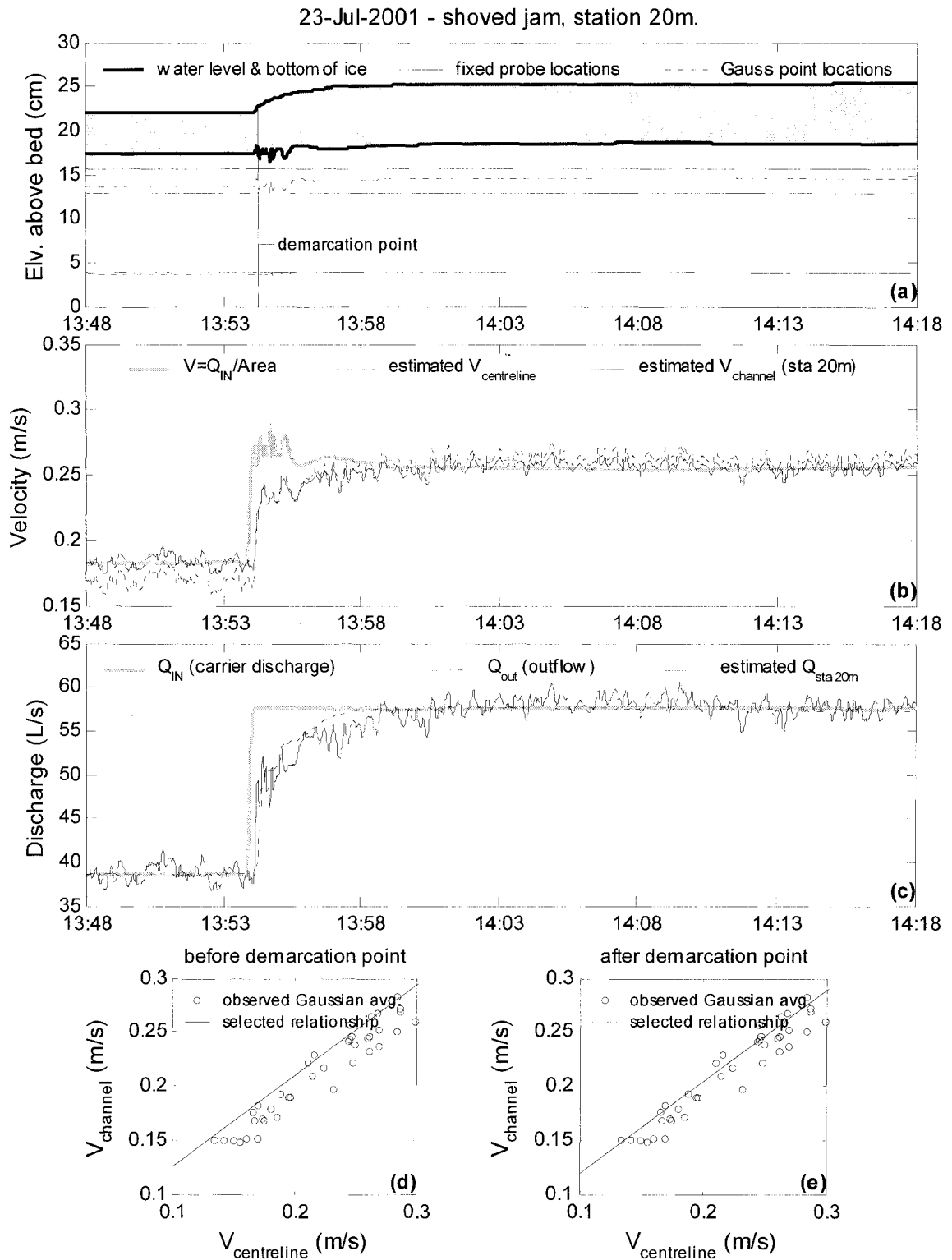
Figure E.152. Summary of continuous observations for a shoved jam taken at Station 20m – test date: 23 July 2001.

364
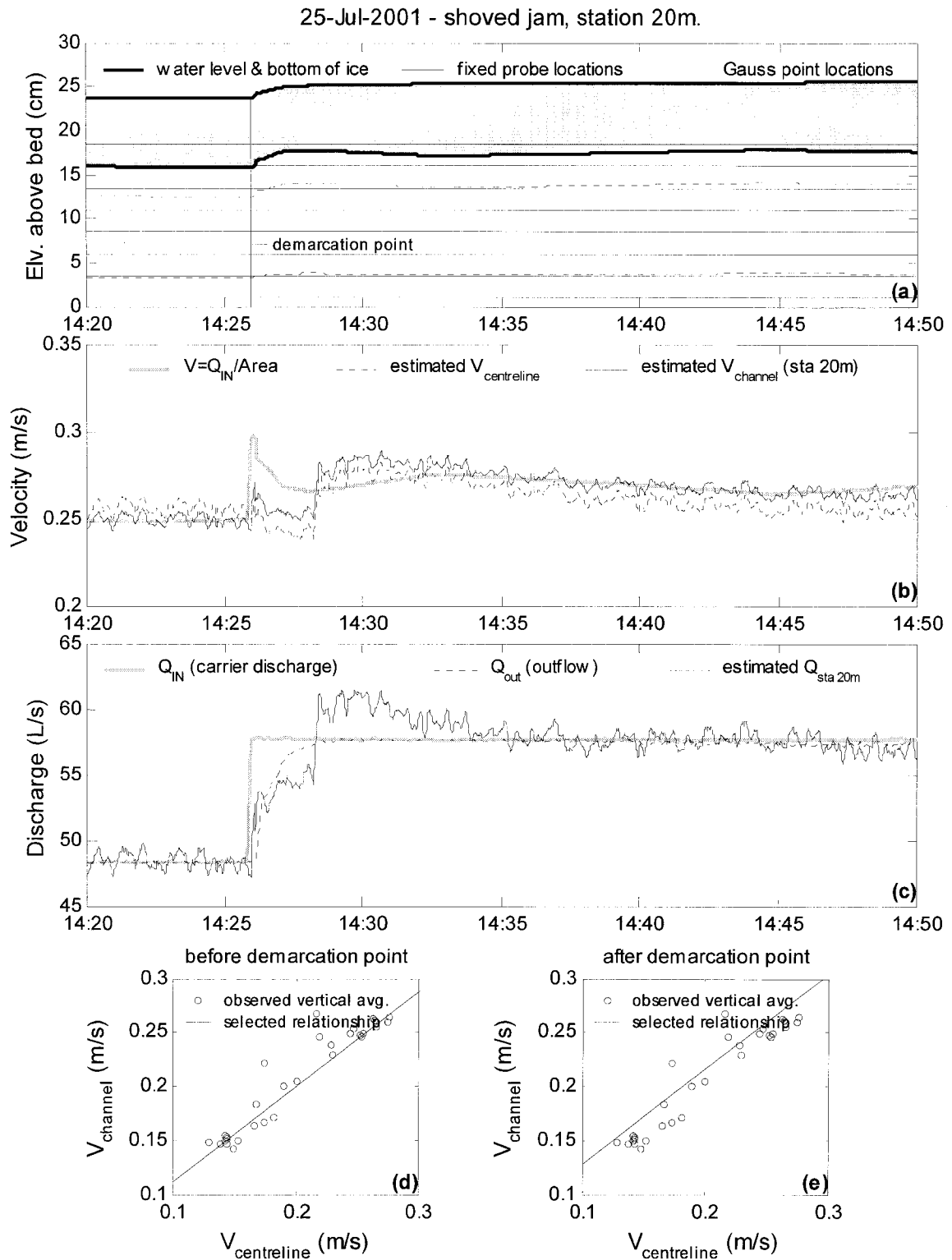
Figure E.153. Summary of continuous observations for a shoved jam taken at Station 20m – test date: 25 July 2001.

365
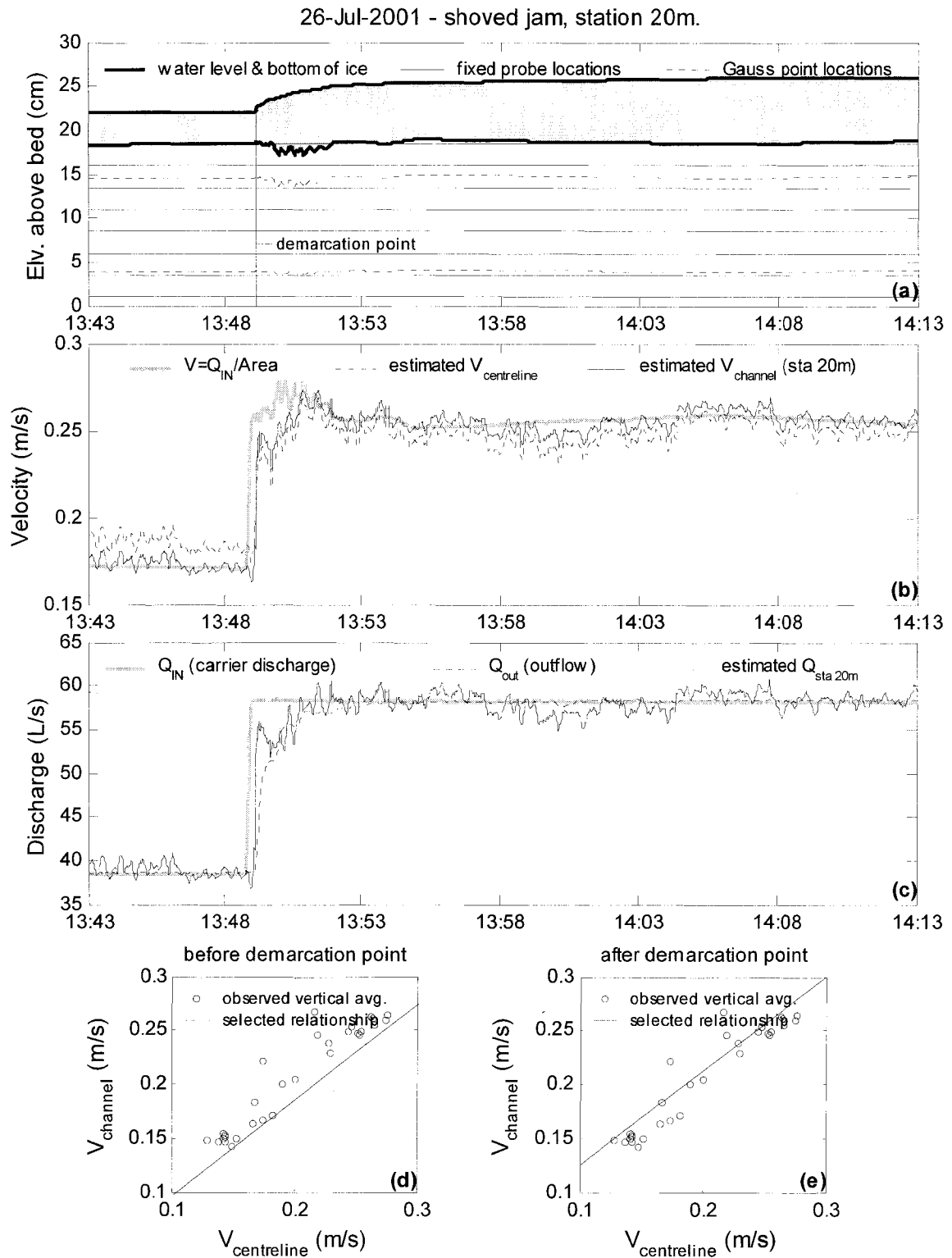
Figure E.154. Summary of continuous observations for a shoved jam taken at Station 20m – test date: 26 July 2001.
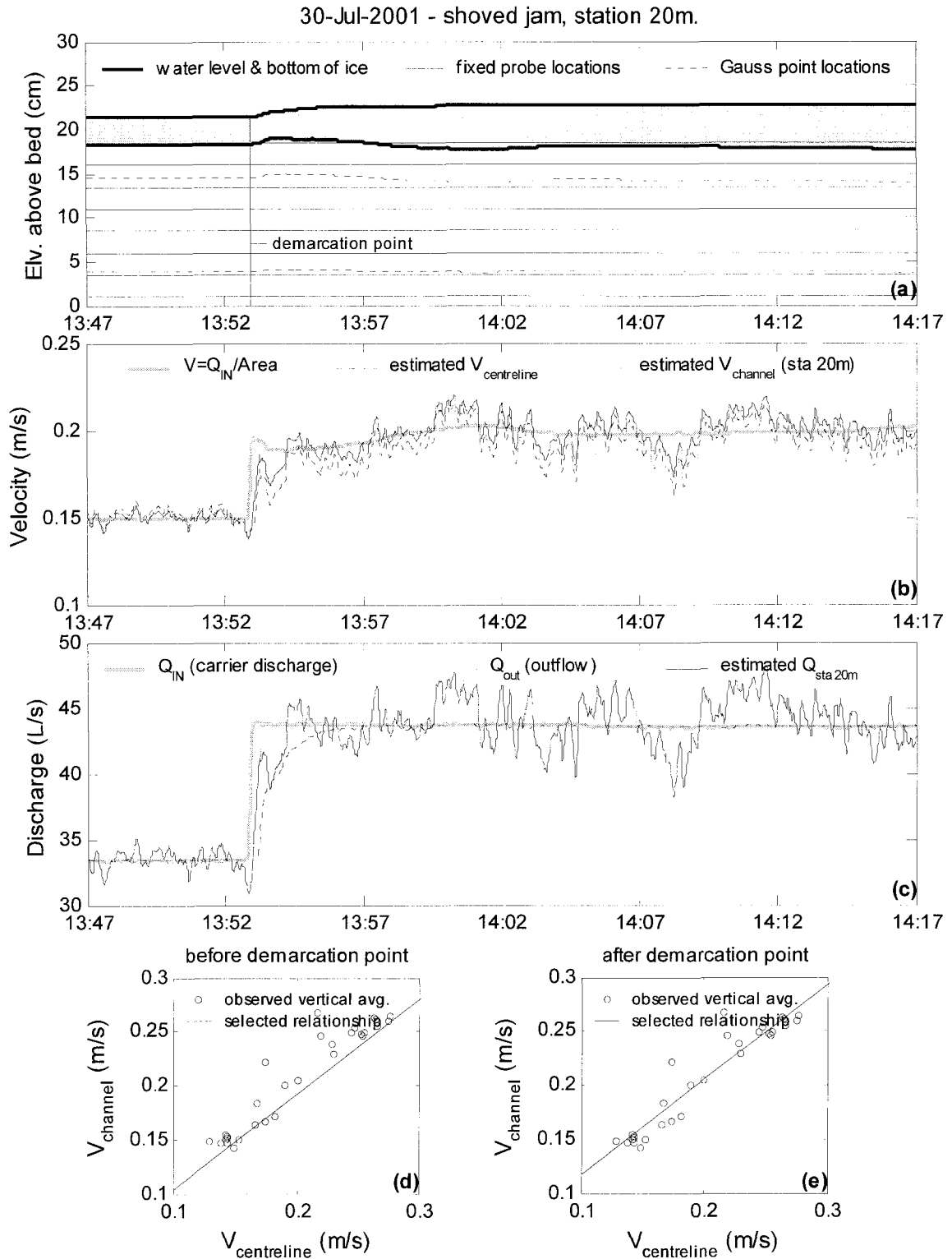
Figure E.155. Summary of continuous observations for a shoved jam taken at Station 20m – test date: 30 July 2001.

367
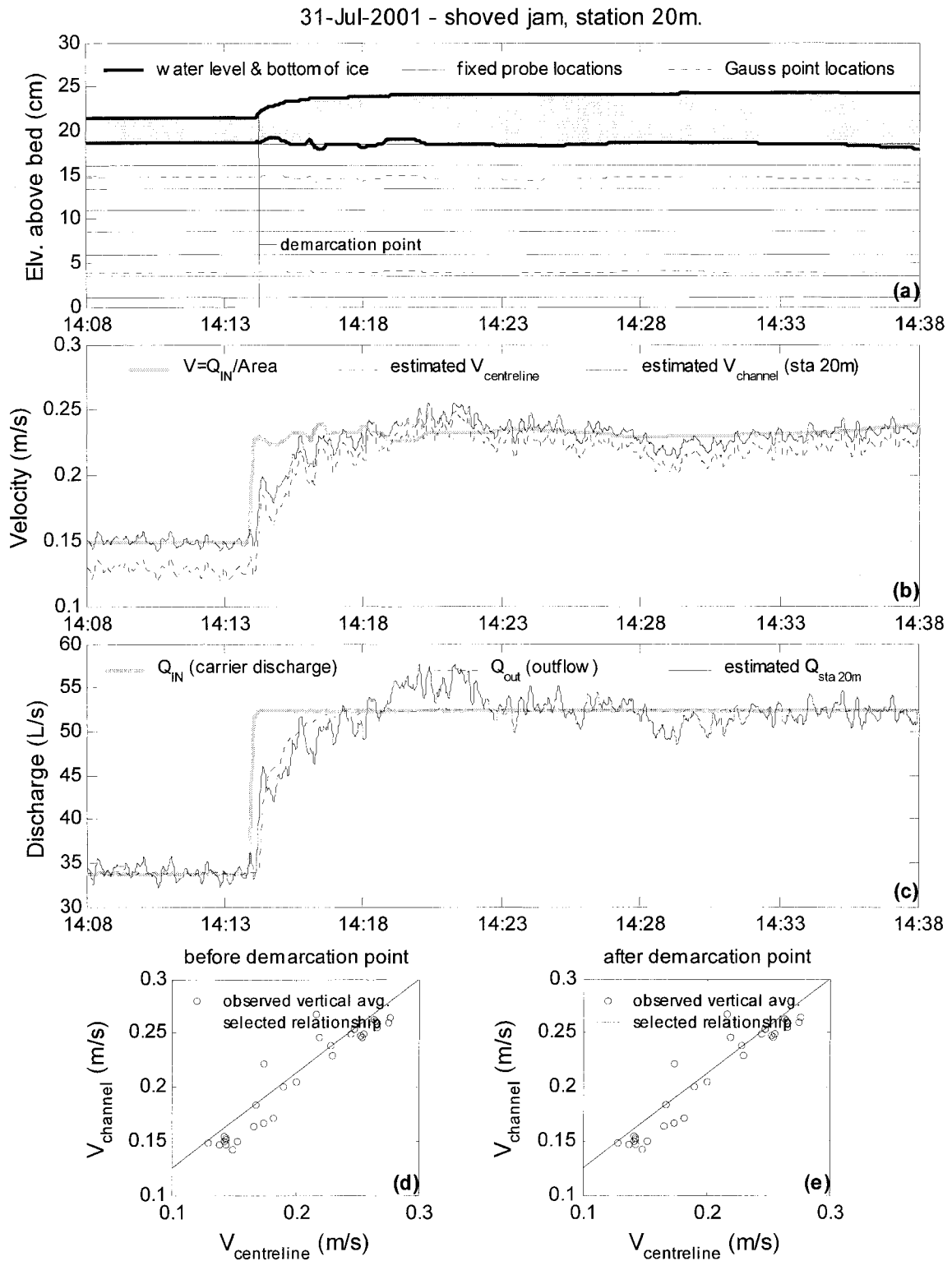
Figure E.156. Summary of continuous observations for a shoved jam taken at Station 20m – test date: 31 July 2001.

01-Aug-2001 - shoved jam, station 20m.

Elv. above bed (cm)

30 25 20 15 10 5 0

water level & bottom of ice   fixed probe locations   Gauss point locations

demarcation point

(a)

13:49   13:54   13:59   14:04   14:09   14:14   14:19

Velocity (m/s)

0.35 0.3 0.25 0.2 0.15 0.1

$V = Q_{IN}/Area$ estimated $V_{centreline}$ estimated $V_{channel}$ (sta 20m)

(b)

13:49   13:54   13:59   14:04   14:09   14:14   14:19

Discharge (L/s)

75 70 65 60 55 50 45 40 35 30

Q_{IN} (carrier discharge) Q_{out} (outflow)   estimated $Q_{sta\,20m}$

(c)

13:49   13:54   13:59   14:04   14:09   14:14   14:19

before demarcation point

$V_{channel}$ (m/s)

0.3 0.25 0.2 0.15 0.1

o observed vertical avg.
selected relationship

(d)

0.1   0.2   0.3
$V_{centreline}$ (m/s)

after demarcation point

$V_{channel}$ (m/s)

0.3 0.25 0.2 0.15 0.1

o observed vertical avg.
selected relationship

(e)

0.1   0.2   0.3
$V_{centreline}$ (m/s)

Figure E.157.   Summary of continuous observations for a shoved jam taken at Station 20m – test date: 1 August 2001.

369
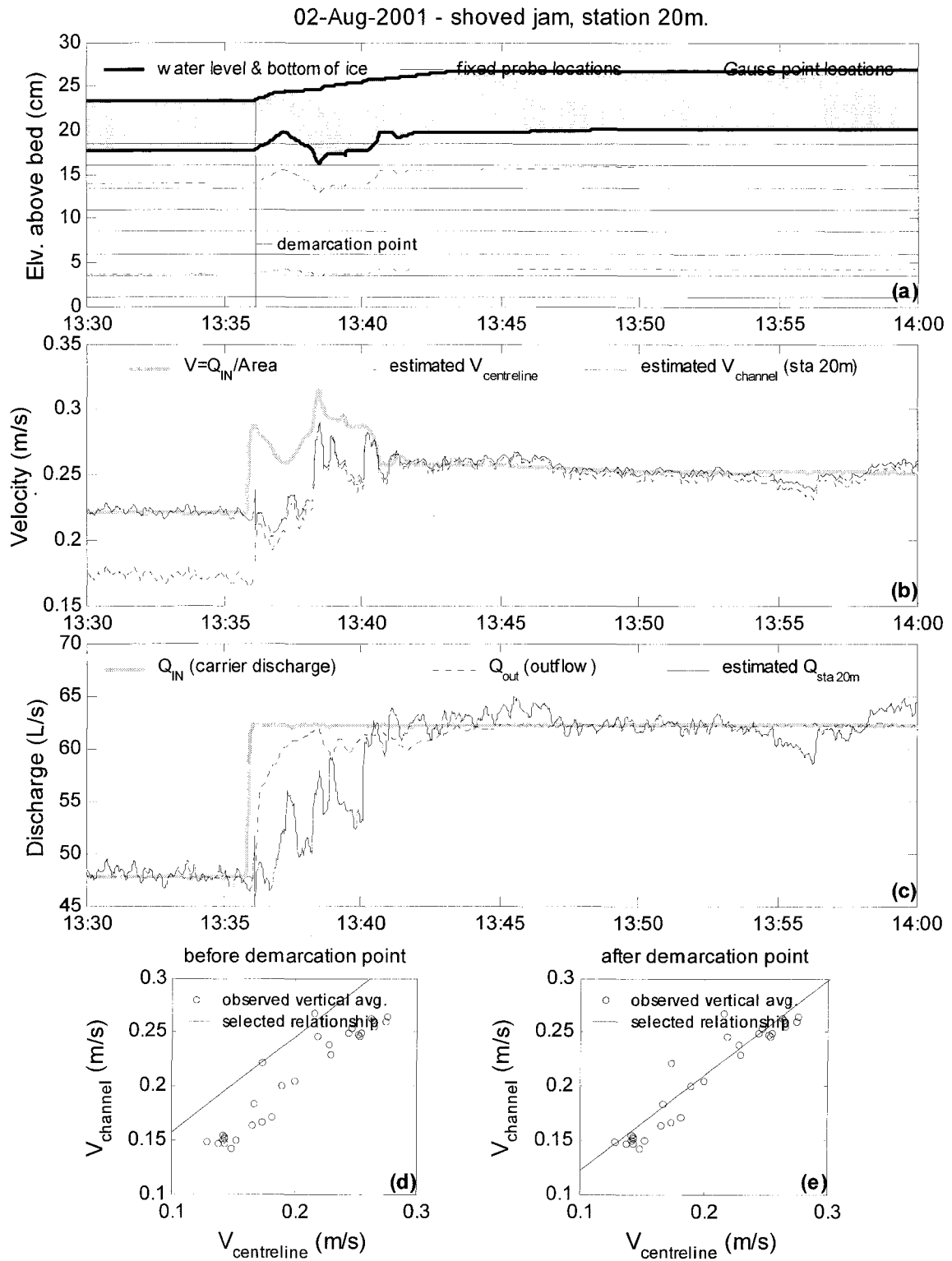
Figure E.158. Summary of continuous observations for a shoved jam taken at Station 20m – test date: 2 August 2001.

370

03-Aug-2001 - shoved jam, station 20m.

(a) Elv. above bed (cm)
— water level & bottom of ice ⋯ fixed probe locations - - - Gauss point locations
demarcation point

x-axis: 13:25 13:30 13:35 13:40 13:45 13:50 13:55

(b) Velocity (m/s)
⋯ V=Q_IN/Area - - - estimated V_centreline — estimated V_channel (sta 20m)

x-axis: 13:25 13:30 13:35 13:40 13:45 13:50 13:55

(c) Discharge (L/s)
⋯ Q_IN (carrier discharge) — Q_out (outflow) — estimated Q_sta 20m

x-axis: 13:25 13:30 13:35 13:40 13:45 13:50 13:55

(d) before demarcation point
○ observed vertical avg.
- - - selected relationship
V_channel (m/s) vs V_centreline (m/s)

(e) after demarcation point
○ observed vertical avg.
- - - selected relationship
V_channel (m/s) vs V_centreline (m/s)

Figure E.159.   Summary of continuous observations for a shoved jam taken at Station 20m – test date: 3 August 2001.

371
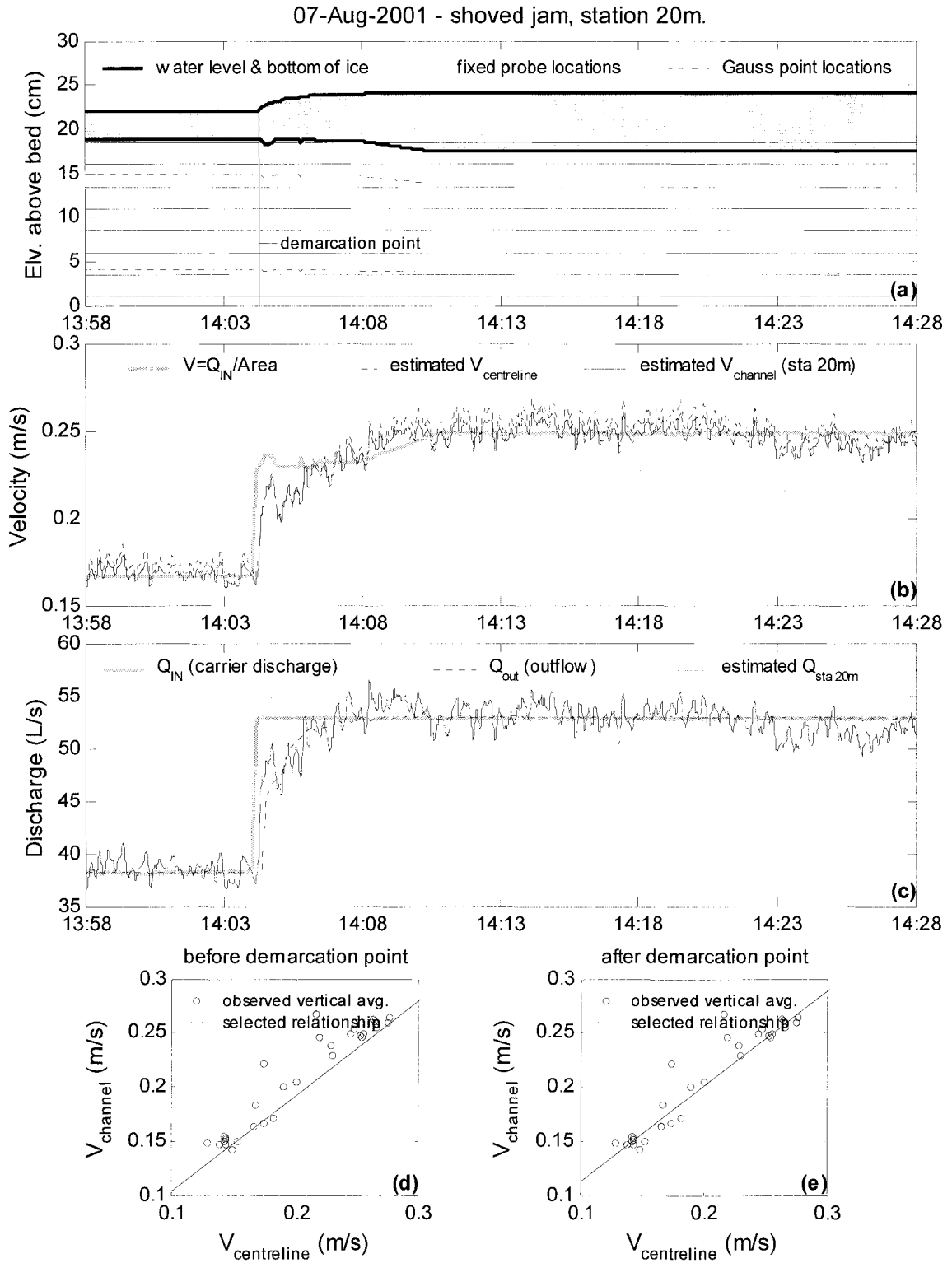
Figure E.160.   Summary of continuous observations for a shoved jam taken at Station 20m – test date: 7 August 2001.

372
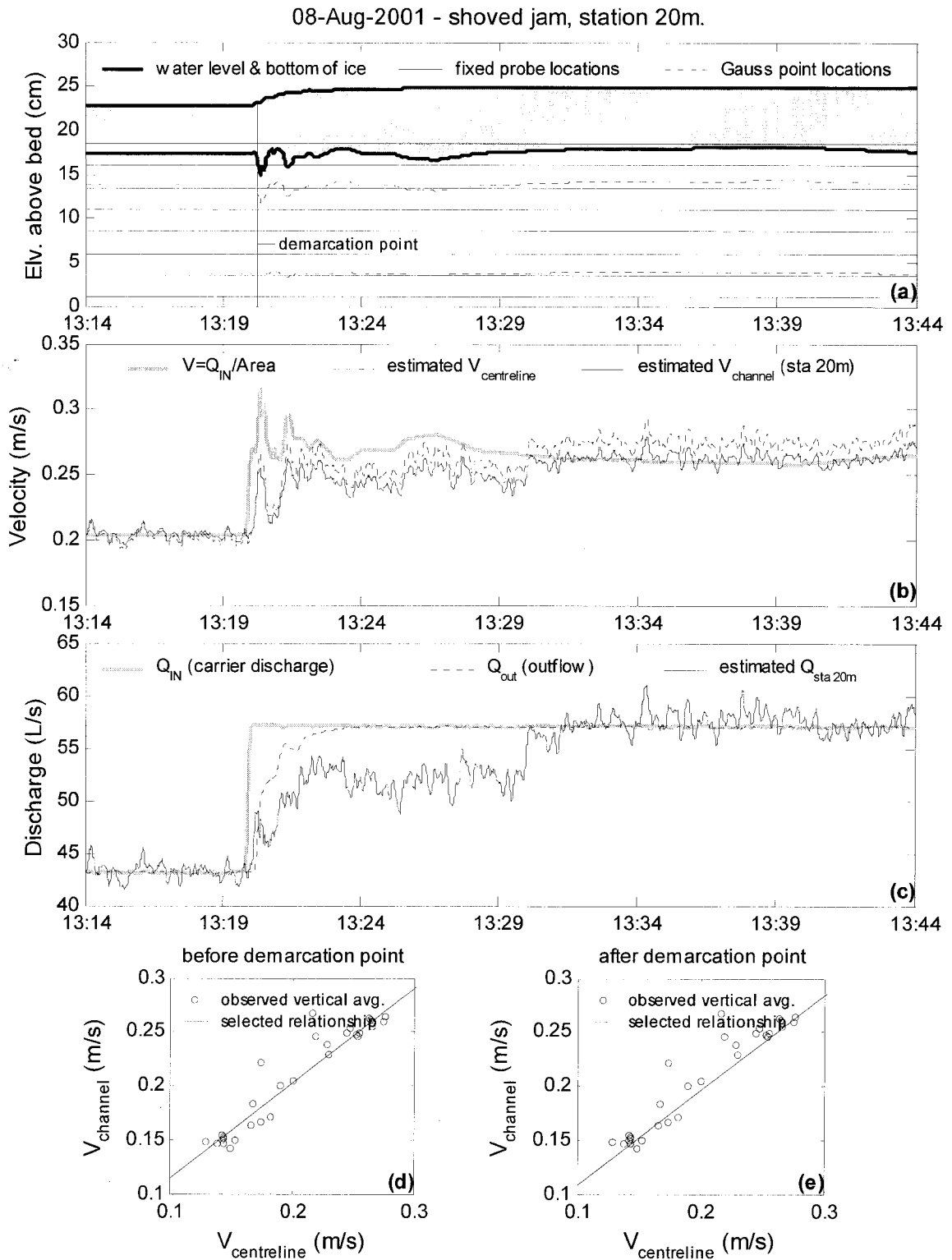
Figure E.161. Summary of continuous observations for a shoved jam taken at Station 20m – test date: 8 August 2001.
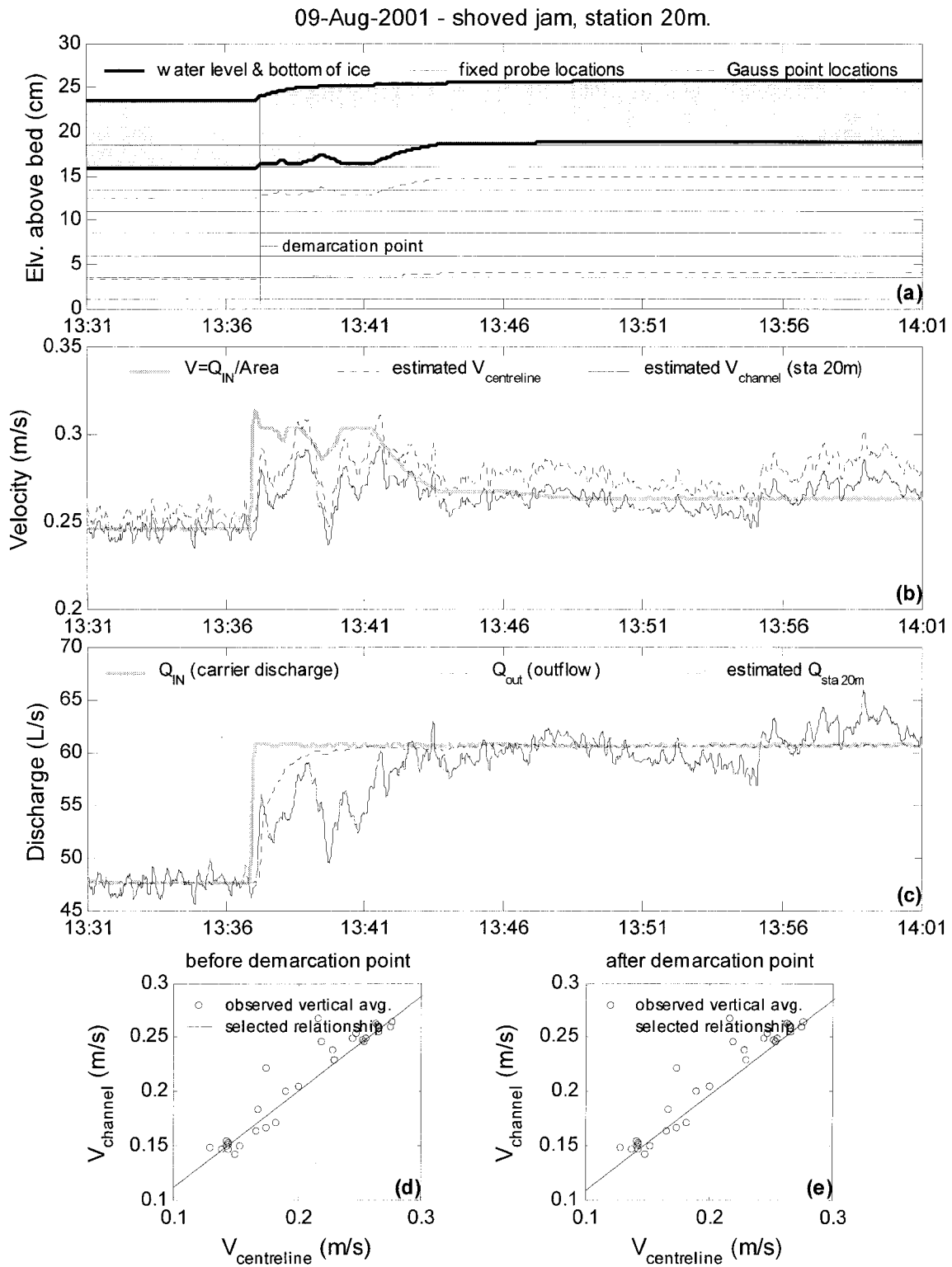
Figure E.162. Summary of continuous observations for a shoved jam taken at Station 20m – test date: 9 August 2001.

374
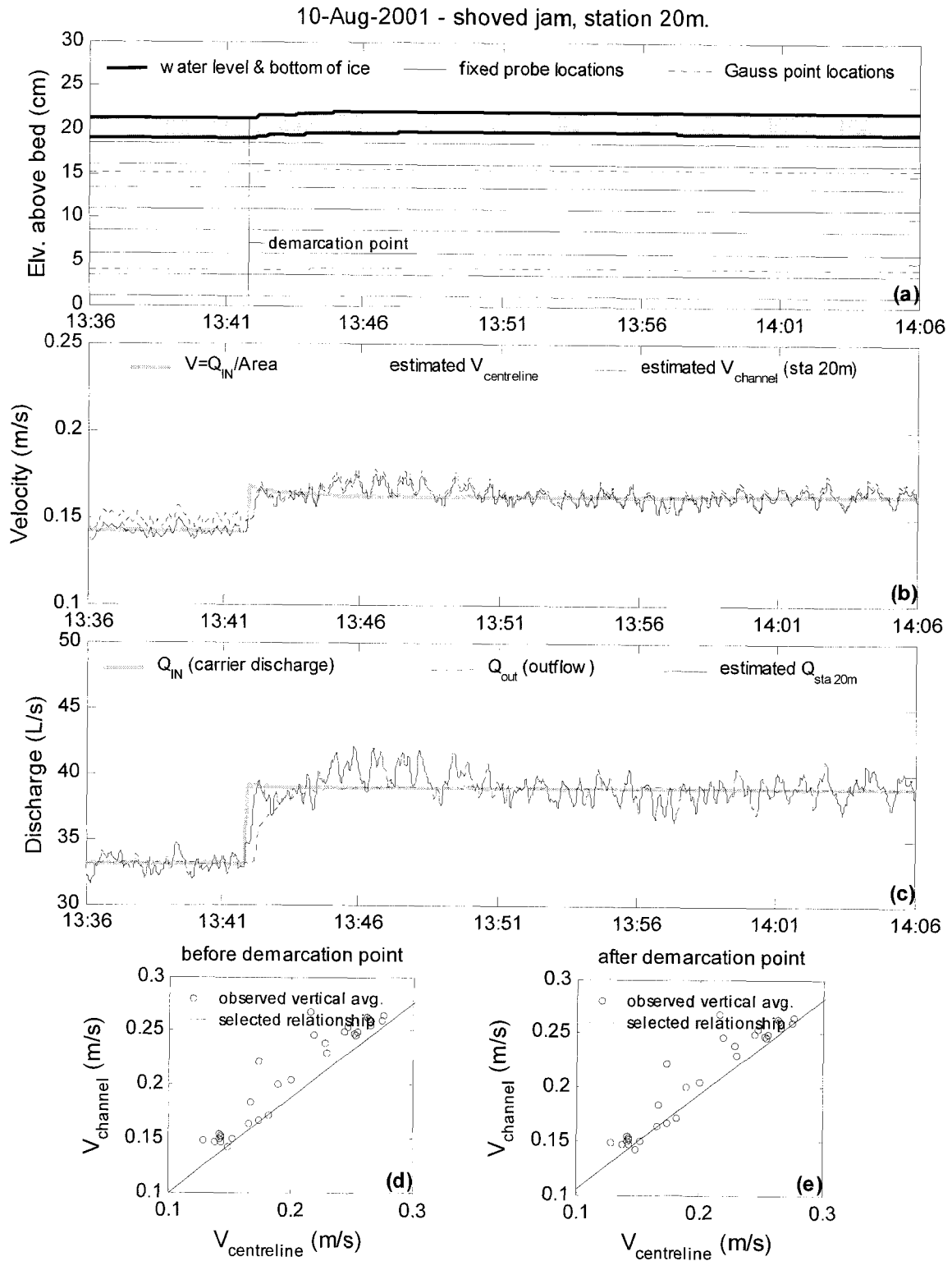
Figure E.163. Summary of continuous observations for a shoved jam taken at Station 20m – test date: 10 August 2001.

375
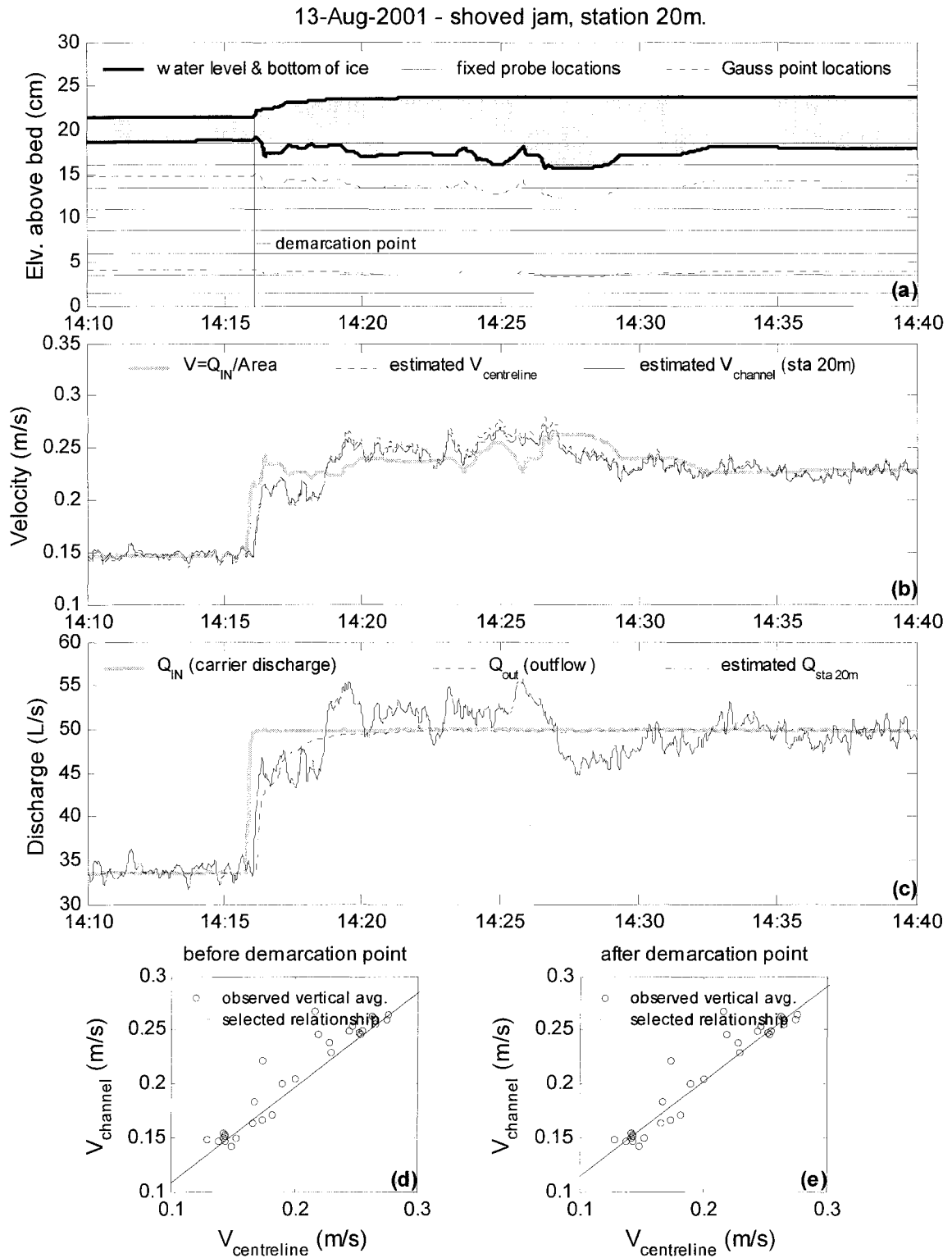
Figure E.164. Summary of continuous observations for a shoved jam taken at Station 20m – test date: 13 August 2001.

14-Aug-2001 - shoved jam, station 20m.

(a) Elv. above bed (cm) — water level & bottom of ice, fixed probe locations, Gauss point locations, demarcation point. Time axis 13:31 to 14:01.

(b) Velocity (m/s) — $V=Q_{IN}/\text{Area}$, estimated $V_{centreline}$, estimated $V_{channel}$ (sta 20m).

(c) Discharge (L/s) — Q_{IN} (carrier discharge), Q_{out} (outflow), estimated $Q_{sta\,20m}$.

(d) before demarcation point — $V_{channel}$ (m/s) vs $V_{centreline}$ (m/s): observed vertical avg., selected relationship.

(e) after demarcation point — $V_{channel}$ (m/s) vs $V_{centreline}$ (m/s): observed vertical avg., selected relationship.

Figure E.165.   Summary of continuous observations for a shoved jam taken at Station 20m – test date: 14 August 2001.

377
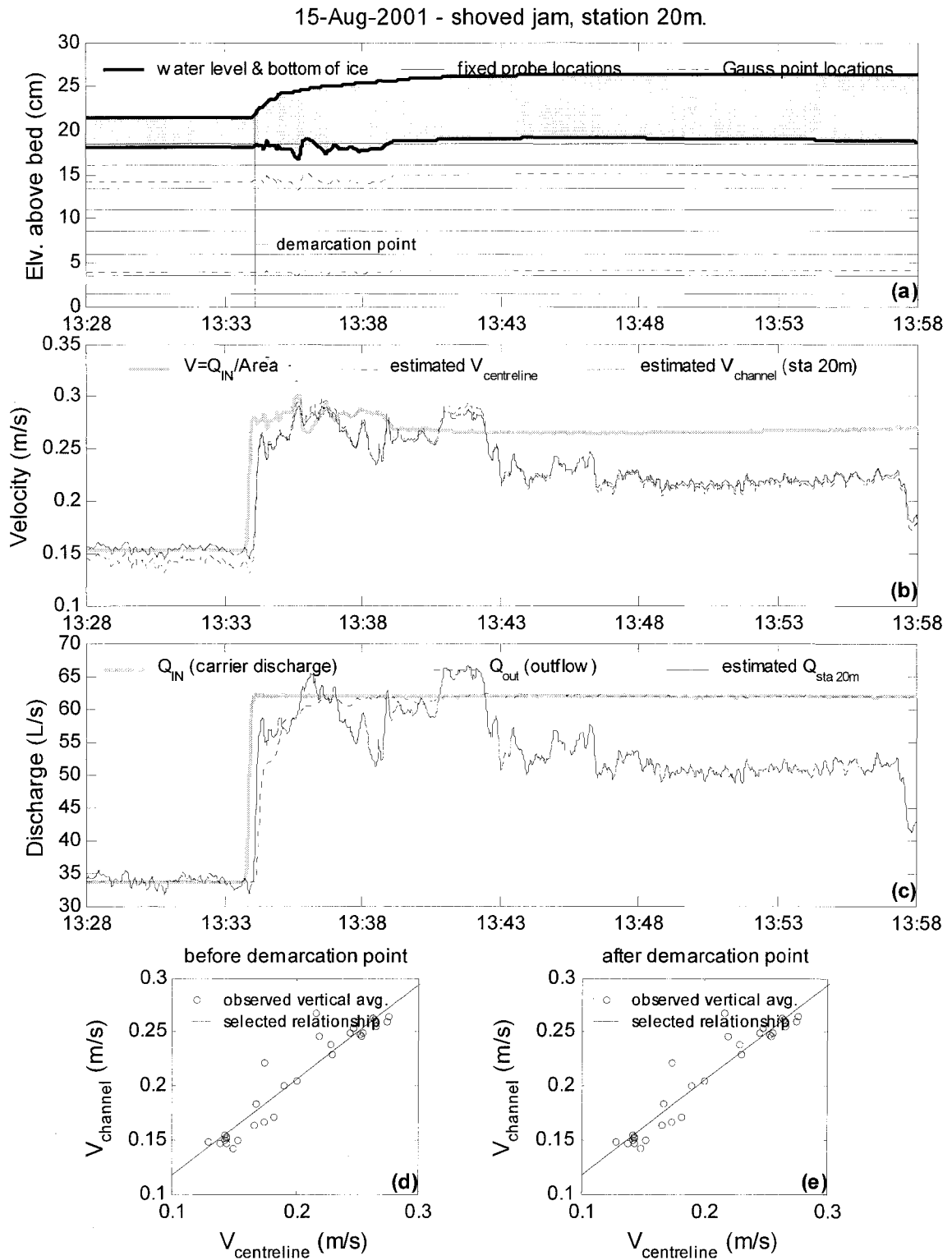
Figure E.166. Summary of continuous observations for a shoved jam taken at Station 20m – test date: 15 August 2001.

378
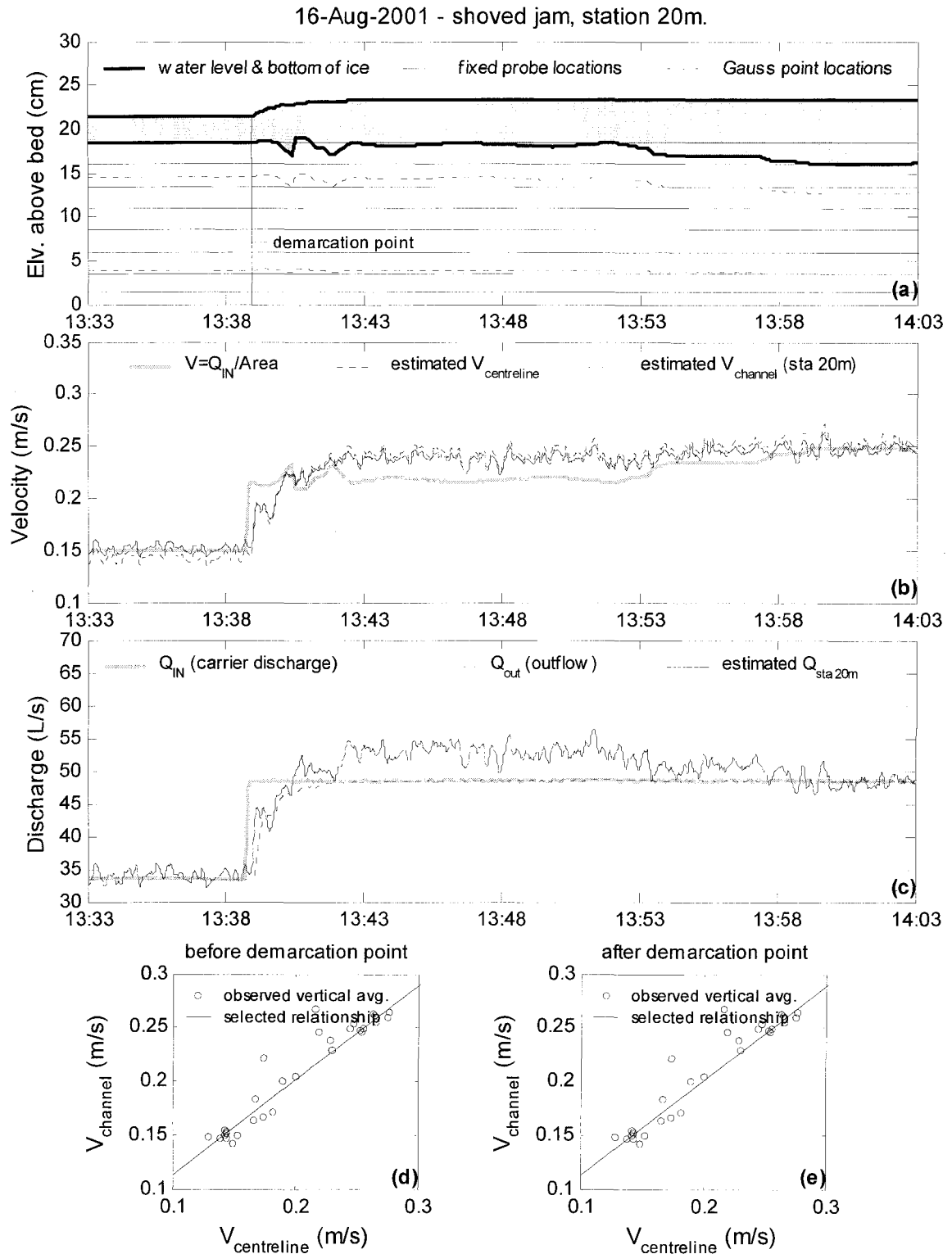
Figure E.167. Summary of continuous observations for a shoved jam taken at Station 20m – test date: 16 August 2001.
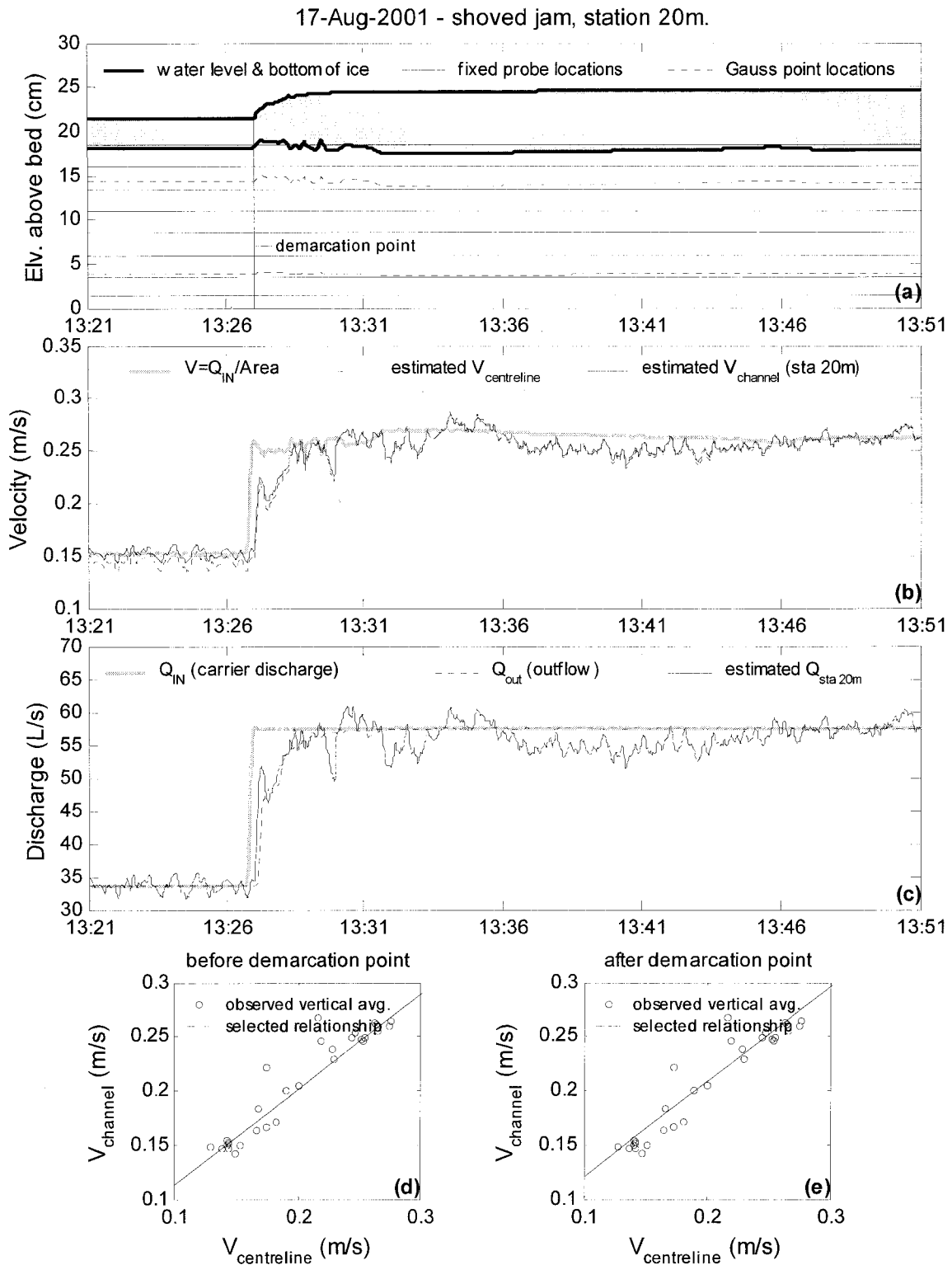
Figure E.168. Summary of continuous observations for a shoved jam taken at Station 20m – test date: 17 August 2001.